Evaluation of Nuclear Spent Fuel Disposal in Clay-Bearing Rock - Process Model Development and Experimental Studies

(M2SF-23SN010301072)

Spent Fuel and Waste Disposition

Prepared for
U.S. Department of Energy
Spent Fuel and Waste Science and Technology

Carlos F. Jové Colón, Carlos M. Lopez,
Tuan A. Ho, Jeffery Greathouse (SNL)

Jonny Rutqvist, Yves Guglielmi,
Mengsu Hu, Tsubasa Sasaki,
Carl I. Steefel, Christophe Tournassat
Utkarsh Mital, Justin Cheng (LBNL)

Florie A. Caporuscio, Amber E. Zandanel,
Marlena J. Rock (LANL)

Mavrik Zavarin, Thomas J. Wolery,
Elliot Chang, Sol-Chan Han (LLNL)

Haruko Wainwright (MIT)

August 31th, 2023
SAND2023-XXXXR

This is a technical report that does not take into account the contractual limitations under the Standard Contract for Disposal of Spent Nuclear Fuel and/or High-Level Radioactive Waste (Standard Contract) (10 CFR Part 961). For example, under the provisions of the Standard Contract, DOE does not consider spent nuclear fuel in multi-assembly canisters to be an acceptable waste form, absent a mutually agreed to contract amendment. To the extent discussions or recommendations in this report conflict with the provisions of the Standard Contract, the Standard Contract provisions prevail.

Sandia National Laboratories is a multimission laboratory managed and operated by National Technology & Engineering Solutions of Sandia LLC, a wholly owned subsidiary of Honeywell International Inc. for the U.S. Department of Energy's National Nuclear Security Administration under contract DE-NA0003525.

SUMMARY

This report represents the milestone deliverable M2SF-23SN010301072 “Evaluation of Nuclear Spent Fuel Disposal in Clay-Bearing Rock - Process Model Development and Experimental Studies” The report provides a status update of FY23 activities for the work package Argillite Disposal work packages for the DOE-NE Spent Fuel Waste Form Science and Technology (SFWST) Program. Clay-rich geological media (often referred as shale or argillite) are among the most abundant type of sedimentary rock near the Earth’s surface. Argillaceous rock formations have the following advantageous attributes for deep geological nuclear waste disposal: widespread geologic occurrence, found in stable geologic settings, low permeability, self-sealing properties, low effective diffusion coefficient, high sorption capacity, and have the appropriate depth and thickness to host nuclear waste repository concepts. The DOE R&D program under the Spent Fuel Waste Science Technology (SFWST) campaign has made key progress (through experiment, modeling, and testing) in the study of chemical and physical phenomena that could impact the long-term safety assessment of heat-generating nuclear waste disposition in clay/shale/argillaceous rock. International collaboration activities comprising field-scale heater tests, field data monitoring, and laboratory-scale experiments provide key information on changes to the engineered barrier system (EBS) material exposed high thermal loads. Moreover, consideration of direct disposal of large capacity dual-purpose canisters (DPCs) as part of the back-end SNF waste disposition strategy has generated interest in improving our understanding of the effects of elevated temperatures on the engineered barrier systemem (EBS) design concepts. Chemical and structural analyses of sampled bentonite material from laboratory tests at elevated temperatures are key to the characterization of thermal effects affecting bentonite clay barrier performance. The knowledge provided by these experiments is crucial to constrain the extent of *sacrificial zones* in the EBS design during the thermal period. Thermal, hydrologic, mechanical, and chemical (THMC) data collected from heater tests and laboratory experiments have been used in the development, validation, and calibration of THMC simulators to model near-field coupled processes. This information leads to the development of simulation approaches to assess issues on coupled processes involving porous media flow, transport, geomechanical phenomena, chemical interactions with barrier/geologic materials, and the development of EBS concepts. These lines of knowledge are central to the design of deep geological backfilled repository concepts where temperature plays a key role in the EBS behavior, potential interactions with host rock, and long-term performance in the safety assessment. This report describes multiple R&D efforts on disposal in argillaceous or clay-bearing geologic media and EBS material behaviors:

- Development and application of coupled THMC process models to represent various phenomena (e.g., reactive transport) based on laboratory- and field-scale testing
- Experimental studies on clay/metal/cement barrier and host-rock (argillite) material
- Molecular dynamic (MD) simulations of H_2 interactions and the evaluation of H_2O adsorption mechanisms in hydrated clay interlayers
- Key advances in thermodynamic and surface complexation database development.

Ultimately, various aspects of this R&D work will inform GDSA integration activities towards the efficient and practical inclusion of coupled THMC processes into the GDSA-PA modeling platform.

As in previous milestone deliverables, this report is a living document that is continuously being updated and structured according to various national laboratory contributions describing their R&D activities on clay/shale/argillite media.

The FY23 R&D activities are summarized as follows:

- **Disposal in Argillite R&D and International Collaborations Activities – SNL (Part I)**
  - **Molecular dynamics (MD) simulations of H_2 interactions and GCMC studies of H_2O adsorption at clay interlayers**
    - Metadynamics molecular simulations were used to investigate the free energy landscape of H_2 intercalation into hydrated clay interlayers. The results indicate that H_2 intercalation is thermodynamically unfavorable.
    - Grand Canonical Monte Carlo (GCMC) metthods were used to evaluate water adsorption isotherms for expandable clay models corresponding to transitions between standard hydration states. This effort has established a method of creating model systems to explore the effect of layer bending on the thermodynamic and mechanical properties of expandable clays.
  - **Reactive-Transport and Reaction Path Modeling of OPC Monolith Leaching**
    - Updates to the 1-D PFLOTRAN model of OPC cement leaching simulation of the EPA 1315 tests generate results that provide good representations of the overall experimental leaching trends for temporal solute concentration profiles.
    - Reaction path model representation of the EPA Method 1313 test for OPC leaching confirms that the cement phase assemblage developed from the PFLOTRAN simulations generate results that are in good agreement with experimental data.
  - **SKB Task 12: 1-D Reactive-Transport Modeling of Cement-Bentonite Interactions**
    - Ongoing PFLOTRAN 1-D reactive-transport model for cement-bentonite interactions has evolved, with more recent modifications to the past year problem description and it is still work in progress.
    - Similar to results reported in FY22, current results of the “blind prediction” show a strong temporal dependence on changes in pore solution chemistry, particularly at early times up to ~100 years.
  - **DECOVALEX2023 Task D: PFLOTRAN Modeling of the S1-3 and S1-4 Bentonite Saturation Experiments, and Full-Scale EBS Experiment at the Honorobe URL Site**

  - **S1-3 isothermal bentonite saturation:** The 1-D PFLOTRAN model can simulate the S1-3 bentonite isothermal saturation experiment whether initially homogeneous or heterogeneous conditions of initial saturation are considered.
  - **S1-4 non-isothermal bentonite saturation:** The refined 1-D PFLOTRAN model to simulate the S1-4 bentonite non-isothermal saturation experiment using a stratified permeability. The approach produced results that are in better agreement with test data.
  - **2-D modeling of the EBS Experiment at the Honorobe URL Site:** Successful simulations have been carried out through the heater test time history through modifications of test conditions to represent temperature profiles.

- **Investigation of Coupled Processes in Argillite Rock: FY23 Progress – LBNL (Part II)**
  - Continued investigations on the effect of shale-creep on the long-term performance of an argillite repository. The creep model was extended to consider anisotropic creep. The analysis showed that the results of long-term repository performance considering anisotropic creep were not significantly different from isotropic creep.
  - LBNL have been participating in three DECOVALEX-2023 tasks that include coupled processes model validation against experiments and necessary model developments:
    - Task A on thermal pressurization and gas fracturing at MHM URL in France,
    - Task B related to gas migration in clay, and
    - Task C related to THM response around the Mont Terri FE Experiment.
  - Continued development of a ML model to predict the HM behavior of a fault in response to high-pressure fluid injection. This work utilized data from the Mont Terri Fault Slip FS-B experiment.
  - LBNL has launched a new task on the use of machine learning (ML) for automatically recognizing multiscale geologic features (such as fractures, faults, rock textures and damage zones) scanned from a borehole, using data from Mont Terri URL.
  - LBNL continued collaboration with international scientists have achieved substantial progress in the study of short- to long-term HM response in argillite host rock through new field studies at Mont Terri and Bure URLs.
  - LBNL has continued work on concrete-clay interfaces involving modeling the Cement–Opalinus Clay Interaction (CI-D) experiment at the Mont Terri URL, with the focus on understanding the reaction-induced porosity, permeability, and diffusivity changes in both the cement and the OPA because of their interaction.

A 3D model has been developed and applied to simulating tracer transport out to 450 days and results compared favorably with the 2D-axisymmetric model.

- **Disposal in Argillite R&D and International Collaborations (FY23) – LANL (Part III)**
  - Continued experimental work on bentonite stability in an argillaceous host rock at temperatures from 150-200 ºC.
  - New results and interpretations from our series of experiments with Opalinus Clay, Wyoming bentonite, steel, and cements (experiments EBS-30 through EBS-34).
  - Findings include montmorillonite was stable over the experimental time period (4 to 8 weeks) at 150 °C in the circumneutral pH values and low bulk system K^+ aqueous concentrations expected in the environment of EBS systems. Recrystallization of montmorillonite to illite was not observed.
  - Argillite International Collaborations – Honorobe URL Research
    - Kunigel bentonite in the presence of the Wakkanai groundwater solution was relatively stable and did not undergo extensive alteration, even at elevated temperatures.
    - QXRD results indicate a preferential loss of non-clay silicates (quartz, feldspars, clinoptilolite) and sulfides (pyrite) compared to the clay phase.
    - Alteration at the boundary of a low-carbon steel included with Kunigel showed significant formation of an Fe-sulfide phase (likely pyrrhotite) and Fe-saponite at the steel surface.
- **Development of the SUPCRTNE and Thermodynamic Database Integration – LLNL (Part IV)**
  - Continued evaluation of the extensive thermodynamic database for minerals by Holland and Powell (2011; HP11) for integration into SUPCRTNE.
  - Significan progress in the calculation of adjustments to the Holland and Powell mineral database (HP11) for consistency with NEA standards. This is part of our effort to build the SUPCRTNE database.
- **Surface Complexation/Ion Exchange Hybrid Model for Radionuclide Sorption to Clay Minerals (LLNL) (Part V)**
  - Continued updates of Surface Complexation/Ion Exchange (L-SCIE) digital sorption database. The L-SCIE database includes 246 references, 2331 datasets, and 27,000 individual data points. A workflow was developed in Microsoft Access with a series of linked tables.
  - Development of database material made available includes: database, how-to videos, and L-SCIE unification code.

- Development of chemistry-informed hybrid machine learning (ML) approach to predict metal adsorption onto mineral surfaces. A manuscript published in June 2023 in Applied Geochemistry (Chang et al., 2023) describes this approach.
- Work on aqueous chemistry and physics constrained autonomous-closed-loop modeling for quantifying adsorption processes as applied to metal-mineral interface geochemistry. This work has been published as a book chapter.

Overall Status and Future Perspectives in Disposal in Argillite R&D:

- **Experimental and thermodynamic modeling studies of barrier material interactions**
  - **Goal**: Conduct experimental and thermodynamic modeling investigations of barrier material interactions from ambient conditions up to elevated pressures and temperatures. Study degradation mechanisms of clay, cement, and metal barriers with implications to in-package chemistry and spent fuel degradation. This may also involve coupling the spent fuel degradation model (source term) with reactive transport modeling of the EBS. Exploit molecular-scale models to simulate fluid transport, water adsorption, and swelling phenomena in bentonite clay. Developments of thermodynamic databases to be used as input feeds to coupled-process models and (geo)chemical reactive transport simulators.
  - **Status & Accomplishments**: Progress on experimental and modeling activities:
    - A comprehensive suite of experiments focused on hydrothermal interactions at elevated temperatures involving bentonite clay, steel materials, cementitious materials, and argillaceous wall rock. This also involves and mechanistic characterization of steel corrosion in the presence of engineered barrier solids (e.g., bentonite, steel, cement) and host rock material.
    - Extensive characterization studies (compositional, structural, geochemical) of experiment run products integrated with thermodynamic modeling to evaluate the occurrence secondary mineralization and clay phase stability at elevated pressures and temperatures.
    - Characterization studies of bentonite samples and argillaceous rock from international repository programs (HotBENT, Mont Terri, JAEA Honorobe) achieved through international collaborations.
    - Thermodynamic database (TDB) development for updated and internally consistent computation of thermodynamic properties of aqueous, solids, and gas species. Bridging existing thermodynamic databases for mineral solids (e.g, Holland and Powell, 2011) with the current TDB development. Representation of SFWST campaign within the NEA-TDB project.

        Sorption database development using data science approaches. Sorption modeling strategies using hydrid machine learning (ML) approaches involving aqueous speciation calculations and sorption data regression.
        - Molecular modeling approaches to evaluate H_2 interactions in clay layers and water adsorption in bent and flat clay layer configurations.
    - **Perpespectives**: Future outlook in experimental and modeling studies:
        - Expand experimental work towards interactions between bentonite clay, cementitious materials, steel material, and argillaceous host rock. Investigate these interactions at various temperatures and pressures to evaluate the alteration mineralogy at the interfaces of these barrier materials.
        - MD studies to evaluate the effect of metal corrosion products such as Fe on clay swelling. Expand modeling of water adsorption in flat and bent clay layers to evaluate structural, thermodynamic, and mechanical properties associated with transitions between these configurations.
        - Continue expansion of thermodynamic database development towards testing and applications to geochemical and reactive transport modeling at elevated pressures and temperatures. Incorporation of machine learning (ML) and data science approaches to sorption data regression and modeling strategies. Expanding the use of novel data-driven strategies to sorption database development.
        - Thermodynamic modeling to describe barrier material interactions focusing on interactions between cementitious and other barrier materials. Expand these evaluations towards the effect on clay phase transformation and the role of zeolite formation, particularly in the presence of cementitious phases and alkaline fluids at elevated temperatures.

- **Coupled-process model development for simulation of near-field thermal, chemical, mechanical, and transport (THMC) interactions.**
    - **Goal**: Development, testing, and validation of coupled-process models for simulation of near-field thermal, chemical, mechanical, and transport (THMC) interactions in the evaluation of barrier material performance. Programmatic engagements and collaborations with international R&D activities (e.g., URL heater tests) in repository sciences.
    - **Status & Accomplishments**: Progress on THMC model development, implementation, and validation

- TOUGH-FLAC THM simulator with applications to disposal in argillite R&D. Bentonite swelling behavior using the BBM (Barcelona Basic Model) and BExM (Barcelona Expansive Model) constitutive model implementations.
- Application of a TOUGH-FLAC shale / clay rock constitutive model: rock anisotropic properties of elasticity, strength, thermal conductivity, permeability, and thermal expansion. Modeling of shale creep behavior and assessment of long-term argillite repository performance.
- Development of TOUGH-FLAC models to simulate permeability and damage behavior in the EDZ.
- TOUGH-RBSN simulator for coupled fracturing processes and gas migration.
- International collaborations:
    - Mont Terri URL
    - SKB EBS Task Force (Task 12)
    - DECOVALEX-2023 (FE Experiment – Mont Terri; COx Clay Stone – Bure, France; Full Scale EBS Experiment, Honorobe URL site, Japan).
- Development of advanced numerical modeling approaches for continuous/discontinuous features such as those in complex fractured rocks.
- Fault activation monitoring experiments using the SIMFIP tool, evaluation of gathered data, and hydromechanical (HM) modeling. These activities are key to complex fault slip dynamics, fault transmissivity and self-sealing, and fault (micro)seismicity and rock failure processes.
- 1D-3D reactive transport modeling under non-isothermal conditions using the PFLOTRAN THC simulator.
    - Focus on multiphase simulations porous bentonite saturation under isothermal and non-isothermal conditions using HPC platforms.
    - Reactive transport simulations of barrier material interactions (e.g., cement leaching) and calibration to experimental data.
    - Reaction path modeling of cement leaching and bentonite hydrothermal interactions. Comparisons to experimental data.
- Modeling of the in-situ Cement-Opalinus Clay Interaction (CI-D) experiment at Mont-Terri using the CrunchClay computer code.

- **Perspectives**: Future outlooks in THMC model development:
    - Continue engagements with international collaborations activities involving heater tests design and process model and validation.
    - Utilize recovered samples from heater tests and sensor data for sample characterization and evaluation of EBS material behavior.
    - Expand development of continuum and discrete modeling approaches to evaluate transport phenomena at different scales.
    - Reactive transport (1D-3D) modeling under isothermal and non-isothermal conditions focusing on barrier material interactions (clay, steel, cement) under variably saturated conditions. Extend this modeling approach to DPC disposal scenarios with high thermal loads. Zero-D reaction path modeling of barrier material interactions.
    - Continue development of new approaches to link coupled process models into GDSA and PA.
    - Applications of the SIMFIP tool for long-term *in situ* monitoring of fault movement, effects of fluid pressure, and leakage.
    - Continue development of coupled hydromechanical numerical model to analyze fault displacement, fluid pressure, and injection flow rate data.
    - Development of coupled chemical-mechanical model at the microscale.
    - Characterization of key microbial-abiotic processes in EBS and host rocks.
    - Development of a predictive computational model of radionuclide retention in bentonites.

Near-Term Thrust Topics (Next 1- to 2-year period)

a) Elucidation of the coupled thermal, hydrologic, mechanical, and chemical (THMC) processes affecting repository performance and

b) Development of multi-fidelity approaches for integration of process models into the GDSA framework

These thrust topics are current focus areas in the disposal in argillite work package, which are planned to continue out over the next five years as well. Continuing work includes expanding the applicability of coupled process models to elevated temperatures and integration of DPC-relevant information related to thermal management and impact on repository design concepts. Longer-term thrusts include the development of reduced order models and/or simplified model outputs for complex argillite process models. Also, integration of mechanistic modeling and experimental studies to describe barrier material behavior.

Longer-Term Thrust Topics (Next 3- to 5-year period)

a) Simplifying the representations of THMC processes occurring within the EBS

b) International collaborations with inputs on field testing and process understanding

Partnerships with current international programs will be nurtured and expanded in the coming years to create a collaboration bridge gaining advanced knowledge of nuclear waste disposal research from URL activities worldwide. Emphasis will be given to THM and HM modeling activities for heater test experiments at international URL's and other relevant activities (e.g., DECOVALEX2023). Specific examples of these are the heater tests at the Honorobe URL site in Japan and HotBENT at the Grimsel test site in Switzerland. The Grimsel site has provided a large suite of barrier material samples (bentonite, cement, rock) for characterization and experimental studies of fluid-bentonite interactions. These activities will continue during the next five years. Additional international collaborations include continued modeling of heater test experiments at Mont Terri and SKB Task Force on EBS (Task 12) on bentonite-cement interactions. Ongoing activities aligned to international thermodynamic database developments (e.g., sorption) and other TDB-related activities are planned to take place within the next two years.

These near- and longer-term thrust topics are excerpts from the deliverable report M2SF-21SN010304054 “SFWST Disposal Research R&D 5-Year Plan – FY2021 Update” by Sassani et al. (2021).

Table listing high priority R&D activities for the safety case relevant to the argillite work package

Importance to the Safety Case (ISC) – High (H) Priority R&D Activities	
A-04	Argillite Coupled THM processes modeling including host rock, EBS, and EDZ)
A-08	Evaluation of ordinary Portland cement (OPC)
C-15*	Design improved backfill and seal materials
E-09	Cement plug/liner degradation
E-11	EBS High Temp experimental data collection- To evaluate high temperature mineralogy /geochemistry changes.
E-14*	In-Package Chemistry
E-17*	Buffer Material by Design
I-04	Experiment of bentonite EBS under high temperature, HotBENT
I-06	Mont Terri FS Fault Slip Experiment
I-08	DECOVALEX-2019 Task A: Advective gas flow in bentonite

Source: DOE SFWST Campaign R&D Roadmap Update (Sevougian et al., 2019)

Activity Designator Legend:

A – Argillite, C – Crystalline, E – Engineered Barrier System, I – International, P – Performance Assessment,

* – indicates Gap Activity

Table listing high priority R&D activities relevant to the argillite work package.

Activity Designator*	Description	Purpose	Crosscut With Other Work Packages	SFWST Argillite R&D Activity	International Collaboration Activity Tie-in
A-04 A-08 E-09 C-15*	Argillite Coupled THM processes modeling including host rock, EBS, and EDZ Evaluation of Ordinary Portland Cement (OPC) Cement plug/liner degradation Design improved backfill and seal materials	Evaluation of mineralogical alteration and evolution in seals and liners	Crystalline, Engineered Barrier System (EBS)	Experimentally verified cement-geomaterial 1D-3D reactive transport model development in PFLOTRAN Experimental and modeling studies of barrier material interactions (cement-bentonite, cement leaching)	DECOVALEX2023 – Task D SKB EBS Task Force (TF) – Cement-Bentonite Interaction Modeling Task
E-11 E-17 I-04	EBS High Temperature Geochemistry/Mineralogy Buffer Material by Design Experiment of Bentonite EBS under High Temperature, HotBENT	Evaluation of mineralogical alteration at the buffer/waste package interface	Crystalline, Engineered Barrier System (EBS)	Hydrothermal experiments evaluating host rock, buffer, buffer additives, and canister materials interactions at elevated temperatures	HotBENT: – Field- and laboratory-scale experiments

*See previous table and report DOE SFWST Campaign R&D Roadmap Update (Sevougian et al., 2019) for details on R&D activity designators.

Activity Designator Legend:

A – Argillite, C – Crystalline, E – Engineered Barrier System, I – International

* – indicates Gap Activity

Sevougian, S.D., Mariner, P.E., Connolly, L.A., MacKinnon, R.J., Rogers, R.D., Dobson, D.C. and Prouty, J.L. (2019) DOE SFWST Campaign R&D Roadmap Update. Milestone Deliverable M2SF-19SN010304042, SAND2019-5179R, Sandia National Laboratories, Albuquerque, NM.

Revision 5
01/15/2018

APPENDIX E

NTRD DOCUMENT COVER SHEET[1]

Name/Title of Deliverable/Milestone/Revision No. Evaluation of Nuclear Spent Fuel Disposal in Clay-Bearing Rock - Process Model Development and Experimental Studies (M2SF-23SN010301072)

Work Package Title and Number Argillite Disposal R&D - SNL / SF-23SN01030107

Work Package WBS Number 1.08.01.03.01

Responsible Work Package Manager Carlos F. Jove Colon
(Name/Signature)

Date Submitted August 31, 2023

Quality Rigor Level for Deliverable/Milestone[2]	☐ QRL-1 ☐ Nuclear Data	☐ QRL-2	☒ QRL-3	☐ QRL-4 Lab QA Program[3]

This deliverable was prepared in accordance with Sandia National Laboratory
(Participant/National Laboratory Name)

QA program which meets the requirements of
☒ DOE Order 414.1 ☐ NQA-1 ☐ Other

This Deliverable was subjected to:

☒ Technical Review

☐ Peer Review

Technical Review (TR)
Review Documentation Provided
☐ Signed TR Report or,
☐ Signed TR Concurrence Sheet or,
☒ Signature of TR Reviewer(s) below

Peer Review (PR)
Review Documentation Provided
☐ Signed PR Report or,
☐ Signed PR Concurrence Sheet or,
☐ Signature of PR Reviewer(s) below

Name and Signature of Reviewers

Yifeng Wang (SNL)

NOTE 1: *Appendix E should be filled out and submitted with the deliverable. Or, if the PICS:NE system permits, completely enter all applicable information in the PICS:NE Deliverable Form. The requirement is to ensure that all applicable information is entered either in the PICS:NE system or by using the NTRD Document Cover Sheet.*

- *In some cases there may be a milestone where an item is being fabricated, maintenance is being performed on a facility, or a document is being issued through a formal document control process where it specifically calls out a formal review of the document. In these cases, documentation (e.g., inspection report, maintenance request, work planning package documentation or the documented review of the issued document through the document control process) of the completion of the activity, along with the Document Cover Sheet, is sufficient to demonstrate achieving the milestone.*

NOTE 2: *If QRL 1, 2, or 3 is not assigned, then the QRL 4 box must be checked, and the work is understood to be performed using laboratory QA requirements. This includes any deliverable developed in conformance with the respective National Laboratory / Participant, DOE or NNSA-approved QA Program.*

NOTE 3: *If the lab has an NQA-1 program and the work to be conducted requires an NQA-1 program, then the QRL-1 box must be checked in the work Package and on the Appendix E cover sheet and the work must be performed in accordance with the Lab's NQA-1 program. The QRL-4 box should not be checked.*

AKNOWLEDGEMENTS

The authors acknowledge our gratitude to Yifeng Wang (SNL), Ed Matteo (SNL), Philippe Weck (SNL), Charles R. Bryan (SNL), Chris Camphouse (SNL), Emily Stein (SNL), Prasad Nair (DOE NE), and Tim Gunter (DOE NE) for their helpful discussions and contributions on various topics covered in this report. We also express our gratitude to Drs. Chen Gruber and Dr. David Kosson of Vanderbilt University for sharing their OPC leaching test data and other technical information along with helpful suggestions. Dr. Liange Zheng and Jens Birkholzer (LBNL) kindly hosted the SKB EBS Task Force meeting #35 at LBNL (April 2023) for which some of the argillite international activites were presented. This work was supported by the Spent Fuel and Waste Disposition (SFWD) office through the Department of Energy's (DOE-NE) Spent Fuel and Waste Science and Technology (SFWST) program.

TABLE OF CONTENTS

Disposal in Argillite R&D and International Collaborations Activities – SNL (Part I)

Investigation of Coupled Processes in Argillite Rock: FY23 Progress – LBNL (Part II)

Argillite Disposal R&D and Argillite International Collaborations – LANL (FY23) (Part III)

Development of the SUPCRTNE and Summary of Thermodynamic Database Integration – LLNL (Part IV)

Surface Complexation/Ion Exchange Hybrid Model for Radionuclide Sorption to Clay Minerals (LLNL) (Part V)

TABLE OF FIGURES

Disposal in Argillite R&D and International Collaborations Activities – SNL (Part I)

Investigation of Coupled Processes in Argillite Rock: FY23 Progress – LBNL (Part II)

Argillite Disposal R&D and Argillite International Collaborations – LANL (FY23) (Part III)

Surface Complexation/Ion Exchange Hybrid Model for Radionuclide Sorption to Clay Minerals (LLNL) (Part V)

LIST OF TABLES

Disposal in Argillite R&D and International Collaborations Activities – SNL (Part I)

Investigation of Coupled Processes in Argillite Rock: FY23 Progress – LBNL (Part II)

Argillite Disposal R&D and Argillite International Collaborations – LANL (FY23) (Part III)

Development of the SUPCRTNE and Summary of Thermodynamic Database Integration – LLNL (Part IV)

REVISION HISTORY

Rev3	Draft	August 30, 2023

ACRONYMS

1D, 1-D	One Dimensional
2D, 2-D	Two Dimensional
3D, 3-D	Three Dimensional
0W, 1W, 2W, 3W	Zero, one, two, three water layers in the clay interlayer region
AI	Artificial Intelligence
ANDRA	Agence Nationale pour la Gestion Des Déchets Radioactifs (France)
ANL	Argonne National Laboratory
ARMA	American Rock Mechanics Association
BBM	Barcelona Basic Model
BGR	Bundesanstalt für Geowissenschaften und Rohstoffe (Germany)
BGS	British Geological Survey
BExM	Barcelona Expansive Model
BSE	Back-Scattered Electron
BSEI	Back-Scattered Electron Image
CASSM	Continuous Active Source Seismic Monitoring
CEC	Cation Exchange Capacity
CI	Cement–Opalinus Clay Interaction
CIEMAT	Centro de Investigaciones Energéticas, Medioambientales y Tecnológicas (Spain)
CNN	Convolutional Neural Networks
COx	Callovo-Oxfordian
CT	Computerized Tomography
DECOVALEX	DEvelopment of COupled Models and their VALidation against Experiments
DEM	Distinct Element Method
DFN	Discrete Fracture Network
DI	De-ionized Water
DL	Diffuse Layer
DOE	Department of Energy
DOE-NE	Department of Energy, Office of Nuclear Energy
DPC	Dual-Purpose Canister
DRZ	Disturbed Rock Zone
EBS	Engineered Barrier System

EDL	Electric Double Layer
EDS, EDX	Energy dispersive X-ray spectroscopy
EDZ	Excavated Disturbed Zone
EMP(A), EMPA	Electron Microprobe (Analysis)
EoS or EOS	Equation of State
EPA	Environmental Protection Agency
FAIR	Findable, Accessible, Interoperable, Reusable (FAIR)
FCRD	Fuel Cycle Research and Development
FCT	Fuel Cycle Technologies
FIB	Focused Ion Beam
FMDM or FMD	Fuel Matrix Degradation Model
FE	Full-Scale Emplacement Experiment
FEBEX	Full-scale Engineered Barriers Experiment
FEBEX-DP	Full-scale Engineered Barriers Experiment-Dismantling Project
FEP	Features, Events, and Processes
FO	Fiber Optical
FY	Fiscal Year
GCMC	Grand Canonical Monte Carlo
GDSA	Geologic Disposal Safety Assessment
GDSA-PA	Geologic Disposal Safety Assessment – Performance Assessment
GREET	Groundwater REcovery Experiment in Tunnel
GW	Gigawatt
GWB	Geochemist Workbench
GP	Gaussian Process
HC or H-C	Hydrological and Chemical
HEE	Half-Scale Heater Test (Mont Terri)
HLW	High-Level nuclear Waste
HM	Hydro Mechanical
HPC	High Performance Computing
HTO	Tritiated Water
HZDR	Helmholtz Zentrum Dresden Rossendorf
IAEA	International Atomic Energy Association

IC	Ion Chromatography
ICP	Inductively Coupled Plasma
IRSN	Institut de Radioprotection et de Sûreté Nucléaire
I-S	Illite-Smectite
ISC	Importance to the Safety Case
JAEA	Japan Atomic Energy Agency
JNC	Japan Nuclear Cycle Development Institute
LANL	Los Alamos National Laboratory
LASGIT	Large Scale Gas Injection Test
LBNL	Lawrence Berkeley National Laboratory
LCS	Low Carbon Steel
LPC	Low-pH Cement
L-SCIE	Lawrence Livermore National Laboratory-Surface Complexation/Ion Exchange
L-SURF	Lawrence Livermore National Laboratory-Speciation Updated Random Forest
LLNL	Lawrence Livermore National Laboratory
LSTM	Long Short-Term Memory
MC	Mechanical-Chemical
MEP	Mean Electrostatic Potential
MHM	Meuse/Haute-Marne
ML	Machine Learning
MS	Mass Spectroscopy
MMT	Montmorillonite
MT	Metric Ton
MTHM	Metric Tons Heavy Metal
Micro XR CT	Micro X-ray Computer Tomography
NAGRA	National Cooperative for the Disposal of Radioactive Waste
NBS	Natural Barrier System
NE	DOE-Nuclear Energy
NEA	Nuclear Energy Agency
NIST	National Institute of Standard and Technology
NMM	Numerical Manifold Method
NS	Natural (Barrier) System

NW	Nuclear Waste
OECD	Organization for Economic Co-operation and Development
OES	Optical Emission Spectroscopy
OPA	Opalinus Clay (rock)
OPC	Ordinary Portland Cement
P	Pressure
PA	Performance Assessment
Pa	Pascal pressure unit
PSI	Paul Scherrer Institute
PWR	Pressurized Water Reactor
QXRD	Quantitative X-ray Diffraction
R&D	Research and Development
RBSN	Rigid-Body-Spring Network
ReLU	Rectified Linear Unit
REV	Representative Elementary Volume
RFS-DSS	Rayleigh Frequency Shift-Distributed Strain Sensing
RF	Random Forest
RH	Relative Humidity
RNN	Recurrent Neural Networks
ROI	Region of Interest
RoIPool	Region of Interest Pooling
RPN	Region Proposal Network
SCIE	Surface Complexation Ion Exchange
SCM	Surface complexation model
SEM	Scanning Electron Microscopy
SFWST	The Spent Fuel Waste Science and Technology
SIMFIP	Step-Rate Injection Method for Fracture *In-situ* Properties
SKB	Swedish Nuclear Fuel Waste and Management Company
SNF	Spent Nuclear Fuel
SNL	Sandia National Laboratories
SS	Stainless Steel
STP	Standard Temperature and Presssure

T	Temperature
t	time
TC	Thermal and Chemical
TDB	Thermodynamic Database
TEM	Transmission Electron Microscopy
TF	Task Force
TH	Thermal and Hydrological
THM	Thermal-Hydrological-Mechanical
THMC	Thermal-Hydrological-Mechanical-Chemical
TM	Thermal-Mechanical
UFD	Used Fuel Disposition
UFDC	Used Fuel Disposition Campaign
URL	Underground Research Laboratory
WGW	Wakkanai Groundwater
WP	Waste Package
WRR	Water Rock Ratio
XRD	X-ray Diffraction
XRF	X-ray Fluorescence

Disposal in Argillite R&D and International Collaborations Activities – SNL (Part I)

1. Introduction

The DOE R&D program under the Spent Fuel Waste Science Technology (SFWST) campaign has made key progress in the application of modeling and experimental approaches towards the characterization of chemical and physical phenomena in engineered and natural barrier materials, providing crucial information to the safety assessment of nuclear waste disposition in deep clay/shale/argillaceous rock. Clay mineral stability and fluid/solid interactions at elevated temperatures can influence bentonite swelling/shrinkage phenomena in the clay barrier. The potential for direct disposal of dual-purpose canisters (DPCs; capacities of up to 32-PWR SNF assemblies) as a feasible, less costly, and safer alternative to re-packaging imposes high thermal loads to the development of deep geological disposal concepts. Therefore, high temperature conditions during the thermal period can affect long-term bentonite barrier performance.

Part I of the report is an update of SNL ongoing experimental and modeling work on bentonite barrier material described in Jové Colón et al. (2021, 2022, 2023) from international collaboration activities relevant to engineer barrier system (EBS) in deep geological argillite repositories. As noted in Jové Colón et al. (2021), work on international repository science activities such as FEBEX-DP and DECOVALEX19 is no longer continuing by the international partners. Nonetheless, research activities such as testing and material characterization on the collected sample materials. Descriptions of these underground research laboratory (URL) R&D activities are described in detail elsewhere (Birkholzer et al. 2019; Jové Colón et al. 2020, 2021) but will be described herein when deemed necessary. The current part of the report focuses on the following:

- Current international collaboration activities:
    - DECOVALEX2023: Modeling of bentonite saturation under isothermal and non-isothermal conditions using PFLOTRAN. TH modeling of a full-scale EBS heater test using the PFLOTRAN.
    - SKB Task Force (Task 12): Results of recent efforts on reactive-transport (HC) modeling of cement-bentonite interactions.
- Barrier material interactions modeling activities:
    - Reaction path modeling of ordinalry Portland cement (OPC) leaching (EPA 1313) test using EQ3/6. Updates to the 1-D reactive-transport model of OPC leaching (EPA 1315) test.
    - Molecular dynamics (MD) simulations H_2 interactions at clay interlayers. This modeling work exploit the application of metadynamics molecular simulations to evaluate the free energy landscape of H_2 intercalation into hydrated clay interlayers.
    - Effect of layer bending on water adsorption in expansive clays. Grand Canonical Monte Carlo (GCMC) simulations are used compare the energy required to bend clay layers to accommodate mixed hydration states in a single interlayer region relative to the energy barrier of an ideal planar interlayer.

The final stage of the DECOVALEX2023 Task D (full-scale engineered barrier system (EBS) experiment at the Honorobe URL) is currently focused on the thermal-hydrological (THM) modeling of laboratory-scale bentonite swelling and saturation experiments conducted under isothermal and non-isothermal conditions. TH modeling of a backfilled disposal gallery of the full-scale EBS experiment at the Horonobe URL site has been conducted for the time length of the heater test. The current focus of Sandia's work in DECOVALEX2023 Task D is on the TH modeling of bentonite saturation experiments and the full-scale EBS heater test.

The SKB Task Force (TF) Task 12 encompasses a benchmark problem on cement/bentonite (clay) interactions with various levels of complexity. The objective is to compare reactive-transport modeling approaches and results from different groups working towards the development of simulation tools to evaluate bentonite backfill behavior.

2. Molecular dynamics (MD) study on H_2 interactions at clay interlayers

2.1 Introduction

This section is a summary of the paper titled "Low Hydrogen Solubility in Clay Interlayers Limits Gas Loss in Hydrogen Geological Storage" by Ho et al. (2023) published in the journal Sustainable Energy and Fuels.

H_2 intercalation into clay interlayers is an important phenomenon in deep geological nuclear waste repository concepts, where H_2 can be generated from metal corrosion of nuclear waste canisters. Many experimental studies have focused on investigating H_2 adsorption onto dry clay (Bardelli, et al., 2014; Faybishenko, et al., 2022; Shaw and Shaw, 2015; Ziemiański and Derkowski, 2022). However, investigating H_2 interactions with clay in humid conditions is more relevant to nuclear waste disposal because water/moister is one of the reactants in the corrosion reactions. Under humid conditions, clay will adsorb water into the interlayers and open the interspacing that is wide enough to uptake other chemicals including gases. For example, in CO_2 geological sequestration, many studies have concluded that clay minerals can adsorb a considerable amount of CO_2 (Bowers, et al., 2017; Busch, et al., 2016). On the one hand, CO_2 adsorption in clay minerals may induce clay swelling that leads to closure of fractures in caprock, thus improving seal integrity. On the other hand, hydrated clay in contact with dry CO_2 might dehydrate (Schaef, et al., 2012; Schaef, et al., 2015), possibly leading to desiccation and crack formation that can potentially pose a risk for CO_2 leakage.

Compared to a CO_2 molecule, a H_2 molecule is smaller (kinetic diameters of H_2 and CO_2 are 2.89 and 3.30 Å (Kentish, et al., 2008), respectively). The quadrupole moment (13.4×10^{-40} C m^2) and polarizability (26.3×10^{-25} cm^3) of CO_2 (Walczak, et al., 2019) are higher than those for H_2 (2.1×10^{-40} C m^2 and 0.729×10^{-25} cm^3) (Buckingham, 1959; Iglauer, et al., 2021; Israelachvili, 2011). The question we address in this study is: How is H_2 intercalation different from that of CO_2 given the differences in the fundamental properties of these two gases?

2.2 Method

To answer question above, we first use metadynamics molecular dynamics (MD) simulations in LAMMPS package (Plimpton, 1995) to compare the free energy of H_2 intercalation into hydrated clay interlayers with the free energy of H_2 dissolution in bulk water. A detailed analysis of the relationship between the free energy profile and the clay layer structure illustrates the effect of H_2-water-clay molecular interactions on the intercalation process. We then use large-scale MD simulations to compare the solubility of H_2 in water confined in clay interlayers with that in bulk water. Finally, we compare the results obtained for H_2 with those published previously for CO_2 (Ho, et al., 2023).

We use the system in Figure 1 to investigate the intercalation of H_2 into the interlayer. Figure 1 represent a clay layer with patch-wise charge distribution. When applying periodic boundary condition in the z direction, water (red) is confined between two identical clay layers.

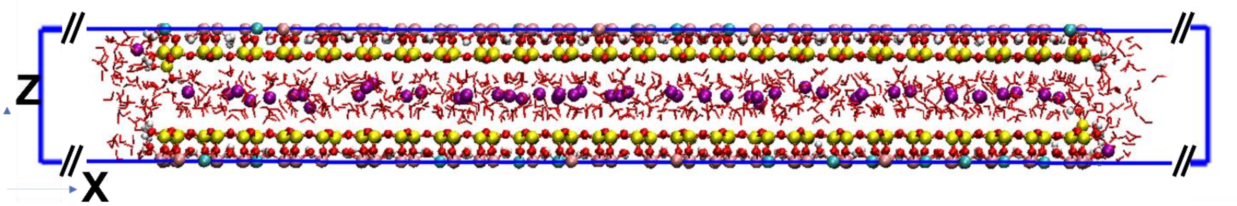

Figure 1. Water confined in two identical clay layers through applied periodic boundary condition. The simulation box size is 200×31.06×15 Å^3. The 104 Å long ribbon clay layer has 2916 atoms. There are 715 water molecules, including those at the clay edge, 1 H_2 molecule, and 52 Na^+ ions.

The method to build the clay layer in Figure 1 can be found in our previous work (Ho, et al., 2019). Briefly, a pyrophyllite layer was cleaved on the (0 1 0) face (Harvey, et al., 2019; Lavikainen, et al., 2015). The resultant broken bonds were fixed by adding –OH groups or –H atoms so that (i) each Si atom at the edge coordinates with 4 oxygen atoms and (ii) each edge Al atom coordinates with 5 oxygen atoms. In a solution, a 5-coordinated edge Al atom usually coordinates with a water molecule to complete its 6-coordinated configuration (Ho, et al., 2018; Ho, et al., 2017). After constructing the pyrophyllite layer with edges, we substituted some Al atoms in the octahedral sheet with Mg atoms to obtain the montmorillonite (MMT) layer with Mg:Al ratio of 0.75: 3.25. This substitution is subjected to two constraints. First, no substitution site is adjacent to another in the octahedral sheet (Loewenstein, 1954). Second, the Mg:Al ratio is smaller than 0.2 at the edge (Newton, et al., 2016). The distribution of Mg atoms in the Al octahedral sheet, which determines the charge distribution, is either patch-wise or random in our simulations (Figure 2). The negative charge due to the substitution is balanced by Na^+ ions in the interlayers. Enough water molecules are added into the interlayers to obtain the 1W or 2W hydration state.

Macroscopically, MMT is a hydrophilic material (i.e., water wets MMT surfaces) (Ho and Wang, 2021). Microscopically (e.g., at the molecular level), an MMT surface can have both hydrophobic sites (e.g., siloxane rings underlain by octahedral Al atoms) and hydrophilic sites (e.g., siloxane rings underlain by Mg atoms that substitute for Al atoms, and occupied by counter ions in the interlayers) (Ho, et al., 2022; Ngouana and Kalinichev, 2014). Simulation work also concluded that bare smectite surfaces (e.g., without the counter ions) are either hydrophobic or moderately hydrophilic. The macroscopically hydrophilic character of smectite surface is almost entirely due to charge balancing cations (Szczerba, et al., 2020).

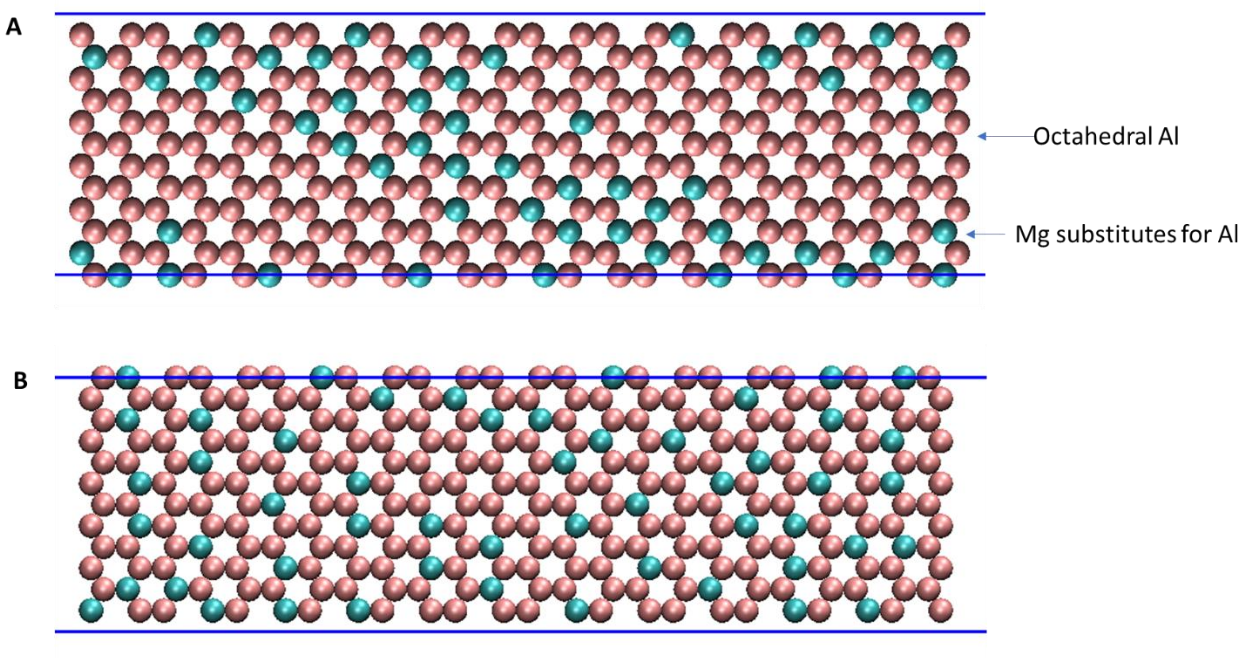

Figure 2. Patch-wise (A) and random (B) charge distributions in the octahedral sheet of a clay layer. Pink spheres are Al atoms, cyan spheres are the Mg atoms that substitute for Al atoms.

The Na-MMT layer/particle is simulated by the ClayFF force field (Cygan, et al., 2004), with additional Si-O-H and Al-O-H angle terms describing the edges (Pouvreau, et al., 2017; Pouvreau, et al., 2019). The interactions of Na^+ ions with bridging oxygen of surface (*ob* type in ClayFF force field) are also modified according to our previous work (Ho, et al., 2019). Water molecules are simulated using a flexible SPC water model (Teleman, et al., 1987), and Na^+ ion is modeled by the force field proposed by Dang and Smith (Smith and Dang, 1994). H_2 is simulated using a 3-sites (Lopez-Lazaro, et al., 2019) model that reproduces well the solublity of H_2 in water.

After selecting the 3-sites H_2 model, SPC water, and ClayFF force field, we need to ensure that the interaction between H_2 and clay layer is appropriate. We first perform the molecular dynamics simulation for the system including hydrogen molecules confined in the pyrophyllite nanopore (Figure 3, top left) using the using the Lorentz-Berthelot mixing rules $\varepsilon_{ij} = \sqrt{\varepsilon_{ii}\varepsilon_{jj}}$ and $\sigma_{ij} = (\sigma_{ii} + \sigma_{jj})/2$ for pair-wise interactions. We select pyrophyllite instead of MMT in this calculation because MMT is built from pyrophyllite structure with octahedral substitution. In an idea case we need to consider the interaction of H_2 with counterions (e.g., Na^+) and the Mg sites. However, with water molecules closely coordinate with Na^+ ions and accumulate near charge sites (Mg), H_2 will not interact directly with those sites. The simulation is performed in the NVT ensample with T= 300 K. Density profile (green line) of hydrogen in pyrophyllite nanopore is reported in Figure 3, bottom. We compare this density profile with that obtained from *ab initio* MD (AIMD) calculation using the model in Figure 3, top right. The AIMD calculation is performed using VASP (Kresse and Furthmüller, 1996). The exchange-correlation energy was calculated using GGA with the PBE parameterization (Perdew, et al., 1996). The interaction between valence electrons and ionic cores was described by the projector augmented wave

(PAW) method (Blöchl, 1994). The plane-wave cutoff energy for the electronic wavefunctions was set to 400 eV. Temperature is set at 300 K. The comparison of the density profile obtained from MD and AIMD indicates that the original interaction between H_2 and pyrophyllite does not reproduce the structure of H_2 in the pyrophyllite nanopore.

To better reproduce the H_2 density profile using MD simulation, we decide to modify the interaction parameter between H_2 and bridging oxygen atom of the pyrophyllite surface, i.e., the *ob* atom type in the CLAYFF force field. According to the Lorentz-Berthelot mixing rule the ε_{ij} and σ_{ij} for H atom and *ob* are 0.106464 kcal/mol and 0.306276 nm. We modify them to become 0.08 kcal/mol and 0.325 nm. The density profile obtained for the modified MD model (blue line, Fig 3, bottom) is comparable with the density profile obtained from AIMD simulation.

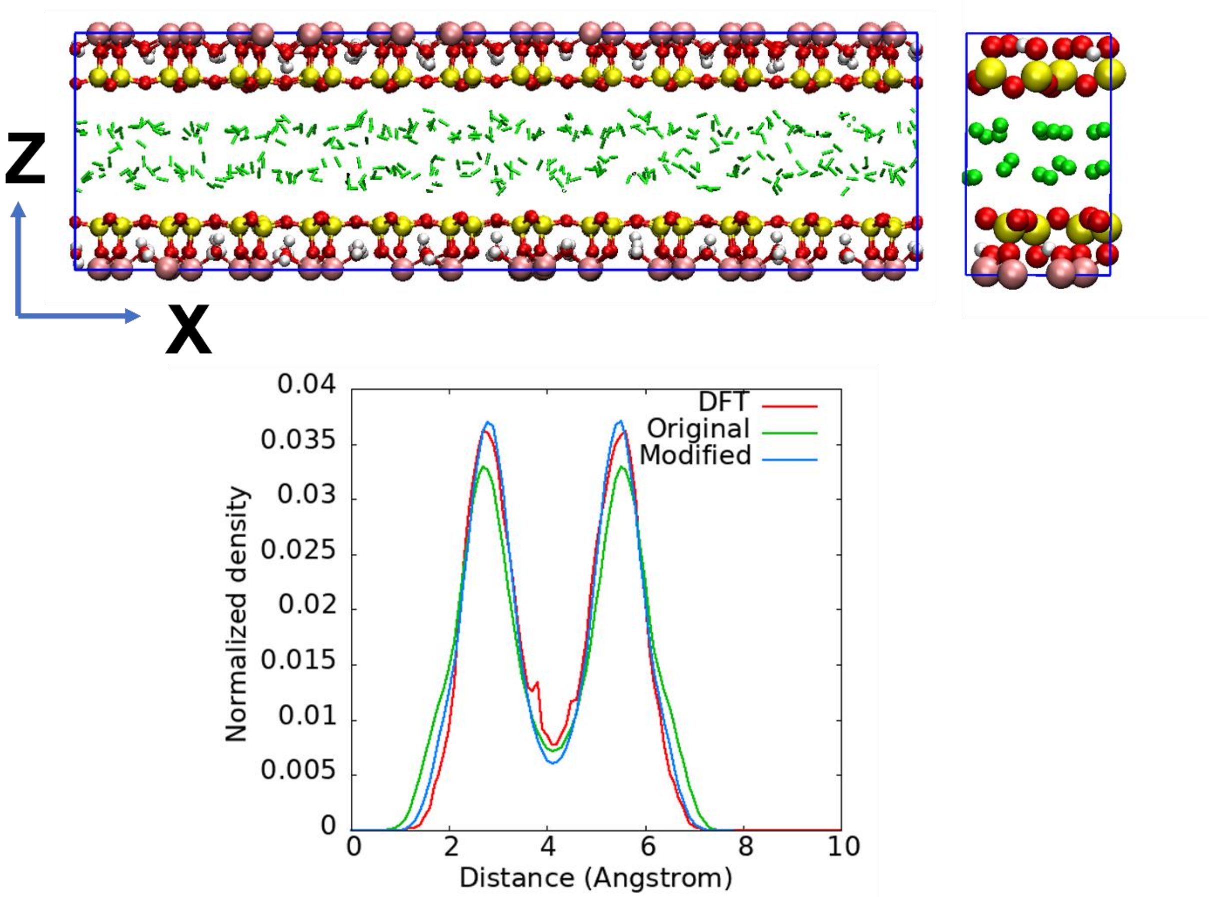

Figure 3. The MD (top left) and DFT (top right) models used to benchmark the interaction of H_2 with pyrophyllite. The simulation box size for DFT model is 5.16×8.96×15 Å^3, including a pyrophyllite layer and 10 hydrogen molecules. The MD model is 36 times larger than the DFT model. Density profile of H_2 in the pyrophyllite nanopore (bottom).

2.3 Results

In Figure 4A we present the system used to calculate the potential of mean force (PMF, i.e., the free energy landscape) of H_2 dissolution in bulk water. The system contains a H_2 molecule and bulk water (2025 molecules). The free energy landscape (Figure 4B) of moving a H_2 molecule from gas phase into water is calculated using well-tempered metadynamics MD simulations

(Barducci, et al., 2008; Laio and Parrinello, 2002). The results in Figure 4 indicate that the free energy of H_2 dissolution in bulk water is ~2.3 kcal/mol (i.e., the difference in the free energy between position 3 and position 1, Figure 4B) indicating that the dissolution process is highly unfavorable. For comparison, the dissolution of CO_2 molecule in bulk water (Figure 4B, reproduced from our previous work (Ho, et al., 2023)) is slightly unfavorable with a free energy of ~0.5 kcal/mol. The free energy profile for CO_2 also suggests that CO_2 molecule prefers to accumulate at the water/vacuum interface with a free energy of ~ -0.5 kcal/mol (i.e., the difference in the free energy between position 2 and position 1, Figure 4B). The high polarizability of CO_2 molecule is responsible for the favorable accumulation of CO_2 at the water/vacuum interface. H_2 does not tend to accumulate at the water/vacuum interface due to its low polarizability.

The primary goal of this study is to understand H_2 intercalation into swelling clay, e.g., montmorillonite (MMT). In Figure 5A, we provide a part of a simulation system used to calculate the free energy landscape of H_2 intercalation into hydrated clay interlayers. This system includes a MMT layer where an octahedral (O) Al-centered sheet is sandwiched between two Si-centered tetrahedral (T) sheets (i.e., TOT structure). We substitute some Mg atoms for Al atoms in the octahedral sheet to create two types of charge distributions: patch-wise and random. The structural charge is balanced by cations (Na^+) in the interlayers. Because the interlayer cations tend to adsorb water, MMT can swell to intercalate 1 (1W), 2 (2W), and more water layers.

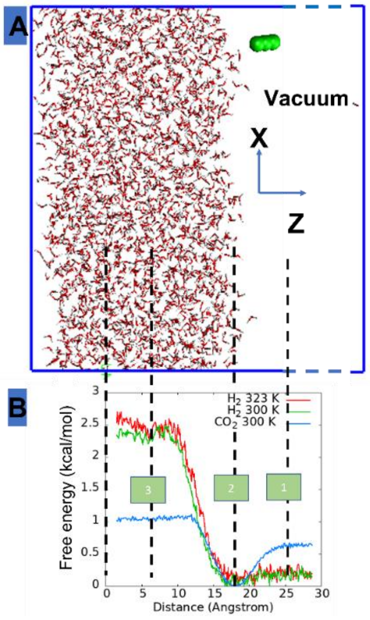

Figure 4. Simulation system (**A**) used to calculate the free energy landscape (**B**) of H_2 (green) dissolution in bulk water (red). The free energy profile is shown as a function of z positions of hydrogen molecule moving from vacuum (right) to bulk water (left). The molecular size is not to scale. There are 2025 water molecules and 1 H_2 molecule in a 50×50×70 $Å^3$ simulation box. The free energy landscape of H_2 dissolution is compared with that of CO_2 dissolution reported in our previous work. The black lines match the positions of gas molecule in the simulation box with the free energy profile.

During the PMF calculation, the H_2 molecule moves along the x direction, i.e., the reaction coordinate of the PMF is the x position of the H_2 molecule. The H_2 molecule is also restricted to move inside the blue region of the xy plane highlighted in Figure 5B. The free energy for 2W hydrated interlayer is shown in Figure 5C (red line). We also conduct the free energy calculation for 1W hydrated interlayer (Figure 5D), and the result is shown in Figure 5C (green line). For comparison, we reproduced the free energy profile for CO_2 (Figure 5E) from our previous work (Ho, et al., 2023).

In its intercalation into a 2W interlayer (red line, Figure 5C), the H_2 molecule has to move successively across the water/vacuum interface (position 1, Figure 5C), the pore opening (position 2), and the hydrophobic domain (i.e., from position 2 to position 4; there is no charge substitution in the hydrophobic domain), before it finally enters the hydrophilic region (beyond position 4) with increasing charge density (i.e., an increasing number of Mg atoms in the blue region in Figure 5B). Within the hydrophobic domain, the H_2 molecule experiences multiple minima (e.g., position 3, corresponding to the center of siloxane ring on the MMT surface) and maxima (e.g., position 4, corresponding to the rim of the siloxane ring). Overall, the free energy of H_2 accumulation at the minima (e.g., ~1.6 kcal/mol) is lower than the free energy of H_2 dissolution in bulk water (~2.3 kcal/mol), indicating that hydrophobic nanoconfinement enhances the H_2 accumulation at the siloxane ring center. Whereas in the hydrophilic region, the H_2 molecule experiences higher free energy (e.g., position 5) than it does in the hydrophobic region and also in bulk water. Overall, the H_2 intercalation into 2W interlayer is thermodynamically unfavorable with computed positive free energies. H_2 intercalation in the hydrophobic region is more favorable, compared to the intercalation into a hydrophilic region and dissolution in bulk water.

Reducing the interlayer d-spacing from 2W to 1W (green vs. red lines, Figure 5) doesn't seems to affect the intercalation in the hydrophobic region (e.g., the free energy at position 3 is comparable for 2W and 1W systems). However, this reduction seems to further inhibit the H_2 intercalation in the hydrophilic region (e.g., a higher free energy for 1W at position 5).

Through a comparison of the results for H_2 with those for CO_2 (Figure 5E), many differences are observed. For example, CO_2 accumulation in the hydrophobic region (e.g., position 3) is thermodynamically favorable. Reducing the d-spacing from 2W to 1W enhances the CO_2 intercalation into the hydrophobic domain. The free energy of CO_2 accumulation in the hydrophilic region is lower than the H_2 accumulation free energy at the same position (e.g., position 5). The CO_2 molecule also prefers to accumulate at the water/air interface (position 1).

We can image the dissolution of gas molecule into bulk water/confined water as follow: a cavity with a size of a gas molecule is created in water and then a gas molecule is inserted into that cavity and interacts with other species around it (Baldwin, 2012; Pollack, 1991). Because the H_2 molecule is smaller than the CO_2 molecule, the energy required to create a H_2-size cavity is lower than that required to create a CO_2-size cavity. In addition, the probability of a cavity formation in the hydrophobic regions is higher than the probability to form a cavity in the hydrophilic regions (Godawat, et al., 2009). In other words, due to its smaller size, H_2 would favor to dissolve in water, especially near hydrophobic surfaces. However, since the H_2 quadrupole moment and polarizability are much lower than those for the CO_2 molecule, H_2 interactions with other species are very weak thus hindering the H_2 molecule to dissolve in water. That is why H_2 dissolution in the hydrated clay nanopore is overall thermodynamically unfavorable; being less unfavorable in the hydrophobic region than in the hydrophilic region.

Since CO_2 interactions with other components are stronger, CO_2 dissolution in bulk/confined water can be thermodynamically favorable, especially in the hydrophobic region.

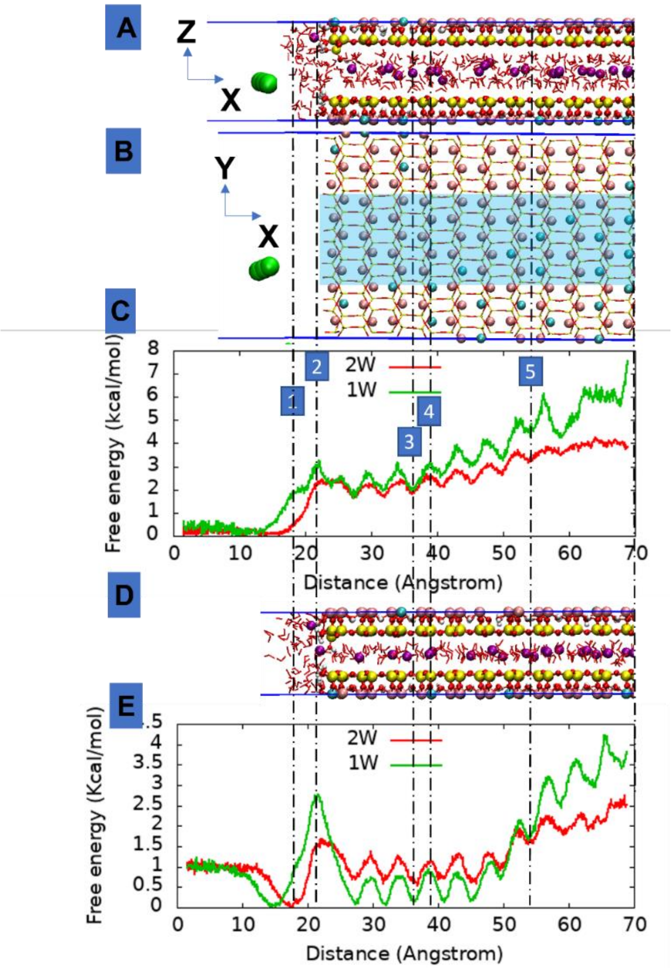

Figure 5. Side view of a part of the system used to calculate the free energy landscape of a hydrogen molecule (green) moving from vacuum into the 2W hydrated (water – red, Na^+ - purple) clay interlayer (**A**). Red, yellow, cyan, pink, and white are for O, Si, Mg, Al, and H of clay, respectively. The simulation box size is 200×31.06×15 $Å^3$. Top view of the siloxane rings (red - yellow) and octahedral Al (pink) and Mg (cyan) atoms of clay layer (**B**). Charge distribution in Figure 2B is patch-wise. During the PMF calculation, the hydrogen molecule is only allowed to move in the blue region highlighted in Figure 5B. The free energy profiles for H_2 intercalation from vacuum into 1W (green) and 2W (red) hydrated clay interlayers at 323 K (**C**). The black lines match the structure of clay layer with the PMF profiles. Side view of the 1W hydrated clay system (**D**); the simulation box size is 200×31.06×12.5 $Å^3$. d-spacing of interlayer is not allowed to change during the free energy calculation, i.e., d-spacing for 1W and 2W hydrated systems is fixed at 12.5 and 15 Å according to the experimental data (Ferrage, et al., 2005; Tamura, et al., 2000). The free energy profiles for CO_2 intercalation (**E**). The molecular size is not to scale.

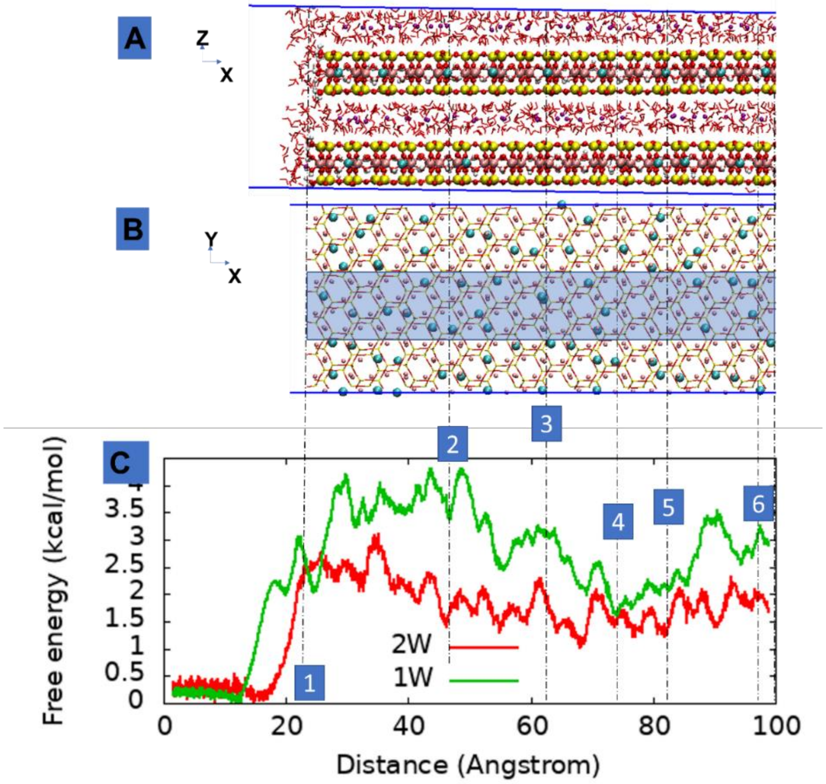

Figure 6. Side view of a complicated clay model used to calculate the free energy of a H_2 molecule moving from vacuum into the hydrated clay interlayer (**A**). The color code is similar with that in Figure 5. Top view of the siloxane rings and octahedral Al and Mg atoms of clay layers that are above and below an interlayer (**B**). During the free energy calculation, the H_2 molecule is only allowed to move into the bottom pores, and within the blue shaded region in Figure 6B. Free energy profile of a H_2 molecule moving from vacuum into 1W and 2W hydrated clay interlayer at 323 K (**C**). The black lines match the structure of clay layer with the PMF profile. The molecular size is not to scale.

The model in Figure 5 is simple: water is confined between two identical clay layers with a patch-wise charge distribution. This means that when a gas molecule is in the hydrophobic/hydrophilic domain, it will experience hydrophobic/hydrophilic effects from both clay layers above and below it. In Figure 6, we report the PMF results obtained from a more complicated clay model. The model in Figure 6A includes two clay layers that form two interlayers when applying periodic boundary condition in the z direction. The charge distribution in each clay layer is random. There is a possibility that a hydrophobic domain exists above a gas molecule and a hydrophilic domain exists below that gas molecule. This asymmetry occurs in addition to the symmetric cases in which a gas molecule (and water) is confined between two hydrophobic domains, or between two hydrophilic domains (e.g., Figure 5). The PMF calculation is carried out constraining the H_2 molecule to only enter the bottom pore. The H_2 molecule is also restricted to move only in the blue region on the xy plane in Figure 6B. The PMF in Figure 6C suggests an alternating minima-maxima pattern on the PMF profile, where the minima are at the center of the siloxane rings (e.g., positions 2, 4, and 5) and the maxima are at the rim of the rings (e.g., positions 3 and 6). Even though the charge distribution in each layer is random, we can still observe a small hydrophobic domain (with the size of about a few siloxane rings near position 4 and 5) that reduces the free energy of H_2 intercalation for both 2W and 1W when compared to the free energy of H_2 intercalation at other locations. Reducing the interlayer d-spacing from 2W to 1W (green vs. red lines, Figure 3C) seems to further inhibit H_2 intercalation.

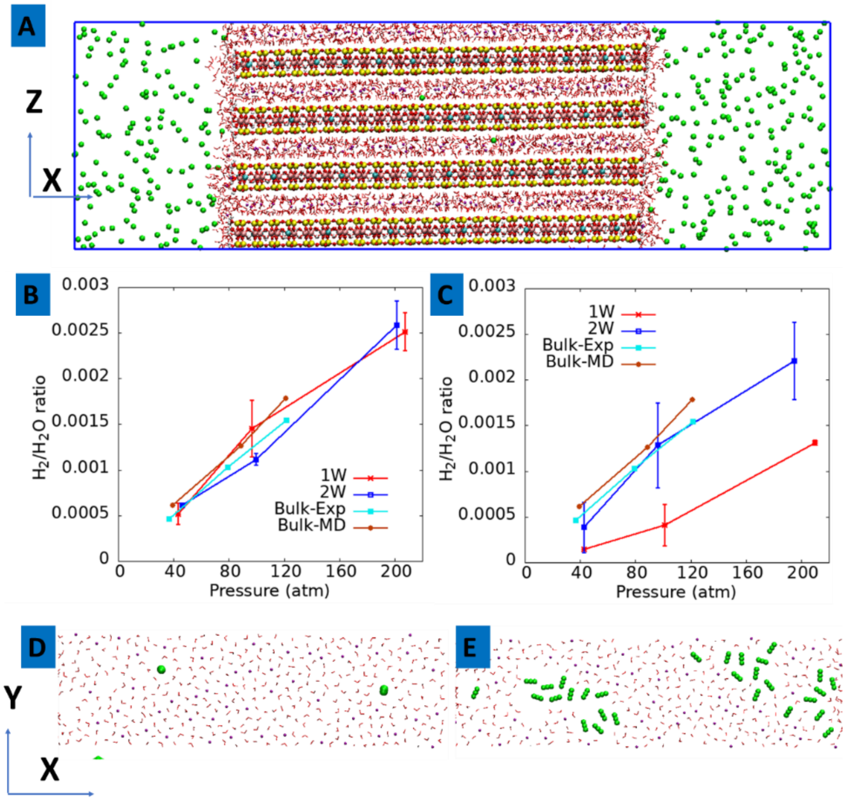

Figure 7. Simulation system (**A**) used to calculate H_2 solubility in water confined in clay interlayers. The simulation box size is 200×31.06×60 Å^3. There are 11664 clay atoms, 2888 water molecules, and 208 Na^+ ions. The number of H_2 molecules depends on pressure. The pressure is determined based on the density of H_2 in the region outside the hydrated clay structure. H_2/H_2O ratio inside the interlayers for patch-wise (**B**) and random (**C**) charge distributions. These results are compared with experimental data (cyan line) from reference(Chabab, et al., 2020) and our MD data for bulk water. Top (xy) view of intercalated H_2 (**D**) and CO_2 (**E**) with water and Na^+ ions in an 1W interlayer with patch-wise charge distribution. H_2 pressure for simulation of Figure D is 207 atm, and CO_2 pressure for simulation of Figure E is 61 atm.

The free energy results in Figure 5 and 6 suggest that H_2 accumulation near hydrophobic sites is less unfavorable than H_2 accumulation near hydrophilic sites. The actual amount of H_2 intercalated will be the average of the effect of hydrophobicity/hydrophilicity and gas pressure. To determine the amount of H_2 intercalated in the interlayers as a function of gas pressure we use the model depicted in Figure 7A. Hydrogen molecules can enter the interlayers through the edges in the x direction during the MD simulation (NVT ensemble) at a temperature of 323 K, relevant to subsurface storage conditions. The simulation in Figure 7A is conducted until the amount of H_2 in the interlayers reaches a constant value (e.g., 100 ns). The amount of H_2 in the interlayers as a function of H_2 pressure is reported in Figure 7B and C for both patch-wise and random charge distributions, respectively. The results indicate that the H_2/H_2O ratio in interlayers is comparable or smaller than the ratio in bulk water. Relative to CO_2, the amount of H_2 found in the interlayers is one to two orders of magnitude smaller. Our results also suggest that while CO_2 forms cluster and dries out water in the hydrophobic region, H_2 rarely forms a cluster in the interlayers even in the hydrophobic regions (Figure 7D and E). Note that the dehydration (Schaef, et al., 2012; Schaef, et al., 2015) due to CO_2 cluster formations potentially poses a risk for CO_2 leakage. Since H_2 cluster formation is not observed in the interlayers, the risk for H_2 leakage can be much lower.

2.4 Conclusions

In summary, we have used metadynamics molecular simulations to investigate the free energy landscape of H_2 intercalation into hydrated clay interlayers. The results indicate that H_2 intercalation is thermodynamically unfavorable. H_2 accumulation near hydrophobic sites is less unfavorable than accumulation near hydrophilic sites. H_2 solubility in confined water in the interlayers of swelling clay is comparable with H_2 solubility in pure water. Compared to CO_2, the amount of H_2 intercalated into hydrated interlayers is one to two orders of magnitude smaller. The results herein imply that H_2 pressure build up at the canister/EBS interface can be significant as H_2 intercalation is thermodynamically unfavorable and limited by water in the interlayers.

2.5 Future work

For FY24 we plan to investigate:

- The interaction of other products of canister corrosion reactions (e.g., Fe^{2+}) with clay.
- Also, continue to utilize MD simulations and Grand Canonical Monte Carlo (GCMC) to extract thermodynamics data regarding the clay hydration and dehydration.

3. Effect of layer bending on water adsorption in expansive clays

3.1 Introduction

Varying humidity conditions due to chemical or geologic processes in the near-field of waste packages could affect the structural properties of expansive clay phases in EBS or argillite host rock. Specifically, intracrystalline clay layers can undergo expansion or contraction in response to changes in relative humidity (RH). Since these changes could exert undue forces on waste forms, it is important to fully understand the hydration and dehydration processes of expansive clays at the molecular level.

Previously, a combined molecular dynamics (MD) simulation and experimental study of clay dehydration revealed a two-stage dehydration process (Ho, et al., 2022). During the first stage, experimental analyses indicates a rapid mass loss and partial reduction in *d*-spacing. According to the MD simulations, water molecules not coordinated to interlayer cations are lost during this first stage. The rate of mass loss and reduction in *d*-spacing is much slower during the second stage as waters coordinating interlayer cations are removed, accompanied by further reduction in *d*-spacing. This irregular water loss can result in localized bending of the aluminosilicate layers of the clay (Honorio, et al., 2018), particularly near particle edges. However, molecular simulation studies of expansive clays use planar (flat) models of clay layers based on time-averaged structures obtained from diffraction studies of related minerals (Drits, et al., 2012; Catti, et al., 1994).

The adsorption and desorption of water by expansive clays has been well studied using molecular simulation (Teich-McGoldrick, et al., 2015) and diffraction experiments (Ferrage, et al., 2010). These studies typically result in adsorption or desorption isotherms of water content (or *d*-spacing) as a function of water fugacity (RH). Recently, a comprehensive Grand Canonical Monte Carlo (GCMC) simulation study of water adsorption in Na-montmorillonite models predicted stable and metastable hydration states in good agreement with experiment (Brochard, 2021). However, the study only included standard models consisting of planar clay layers with one (1W), two (2W), or three (3W) water layers in the interlayer region. A previous MD study of transitions between these hydration states revealed that clay layers can assume bent configurations during these transitions (Ho, et al., 2019). Additionally, a theoretical study of the bending modulus of clay layers found that transitions between clay hydration states involve bending of the clay layers over length scales of a few nanometers (Honorio, et al., 2018).

Water adsorption profiles for interlayer regions associated with bent clay layers have not been included in previous simulation studies. Therefore we have begun a study to compare water adsorption isotherms in models composed of bent clay layers in mixed hydration states with isotherms of models consisting of planar clay layers and single hydration states (*i.e.*, 1W, 2W, or 3W). The effect of interlayer cation is included by comparing results for Na- and Ca-exchanged clays. Ultimately, we seek to compare the energy required to bend clay layers to accommodate mixed hydration states in a single interlayer region with the energy barrier between the ideal (planar) hydration states.

3.2 Methods

Hybrid MD-GCMC simulations were performed with the LAMMPS code (Thompson, et al., 2022) with modifications to allow for efficient sampling of water adsorption and desorption processes (Brochard, 2021). Simulation details are similar to those reported previously (Teich-McGoldrick, et al., 2015; Brochard, 2021), with the following exceptions. First, a larger supercell consisting of two clay layers and larger lateral dimensions (4 × 3 × 2 repeats in *a*, *b*, and *c*) was used to accommodate models with bent clay layers. Second, the models corresponded to mixed hydration states (e.g., 0W-1W, 1W-2W, 2W-3W) with the clay layers in either planar (flat) or bent configurations. Third, modified interaction parameters between interlayer Na^+ ions and the clay surface were used since these modifications resulted in a more realistic description of energy barriers between hydration states (Ho, et al., 2019). The *c*-dimension of each model system is the sum of the *d*-spacings of each single hydration state (Table 1). For example, the *c*-dimension for the 0W-1W models with Na^+ was 23.01 Å (9.97 Å + 13.04 Å). Each interlayer region included ten Na^+ or five Ca^{2+} ions to balance the negative charge on the clay layers.

Table 1. Interlayer spacings (Å) of hydration states used in the GCMC models.

	Interlayer cation	
Hydration state	**Ca^{2+}**	**Na^{+}**
0W	9.37	9.97
1W	11.71	13.04
2W	14.42	15.04
3W	17.91	17.38

Bent models were created by scaling the z-coordinate of atoms in each clay layer so that the *d*-spacing in each interlayer region varied from the lower hydration state to the higher hydration state (Figure 8). Fluid species (water and cations) were allowed to move during the MD steps with a thermostat temperature of 300 K. Water molecules were inserted or deleted with a GCMC algorithm, with 100 attempts performed for every 10 MD timesteps (1.0 fs). Separate simulations were performed for RH values from a nearly dry (5×10^{-7}% RH) to nearly saturated (95% RH) hydration states. The length of each simulation varied from 500 ps up to 800 ps, until a steady-state water loading was achieved.

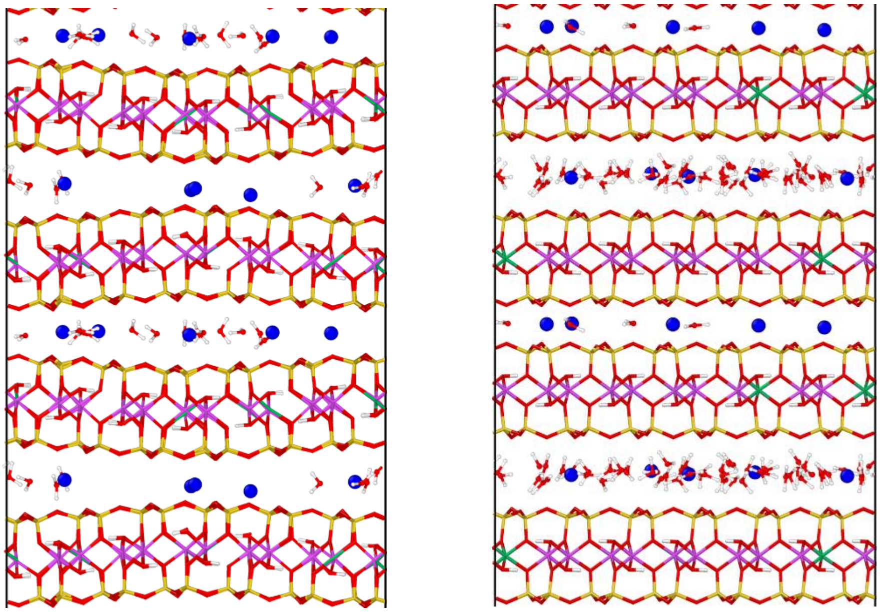

Figure 8. Simulation snapshots for the 0W-1W mixed hydration state of Ca-montmorillonite in bent (left) and flat (right) configurations. Clay layers are shown as sticks (Si = yellow, O = red, H = white, Al = magenta, Mg = green), with interlayer species as balls and sticks (Ca = blue). Two repeats of the simulation cell in *c* are shown so that both interlayer regions can be clearly seen.

3.3 Results

Water adsorption isotherms for each of the twelve model systems are shown in Figure 9. The main finding from the present work is that models with bent clay layers (representative of transition hydration states) show similar or identical water adsorption behavior to the standard models (flat clay layers with single hydration states). The presence of more strongly hydrating divalent Ca^{2+} ions in the interlayer results in slightly different isotherms between the bent and flat models. The bent model of 0W-1W Ca-montmorillonite has significantly lower water loading than the flat model at all RH values. A large portion of the bent interlayer region at the smallest *d*-spacing (0W) shows little or no adsorbed water, indicating that there is not enough accessible volume for a fluid-like layer of water to form.

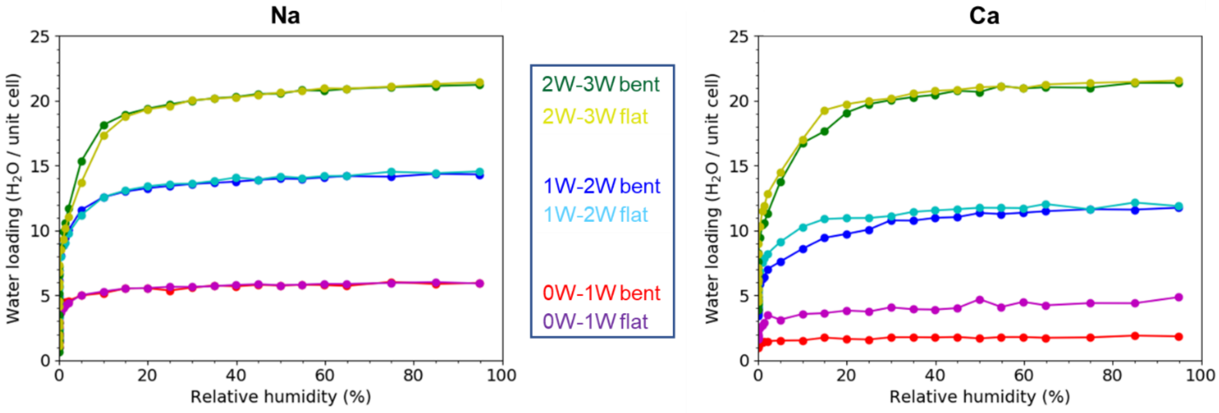

Figure 9. Water adsorption isotherms from MD-GCMC simulations at 300 K for mixed hydration states in bent and flat configurations.

Snapshots from the bent configurations of the 1W-2W and 2W-3W states are shown in Figure 10. Because all of the interlayer regions are accessible to water in these expanded states, the bent clay layers have little effect on water loading. However, isotherms for the Ca-montmorillonite models for these states show a more gradual increase in water loading at low RH. When Ca^{2+} ions are present in the interlayer, the curved clay surface has initial water binding sites that are slightly less favorable than those on the flat surface.

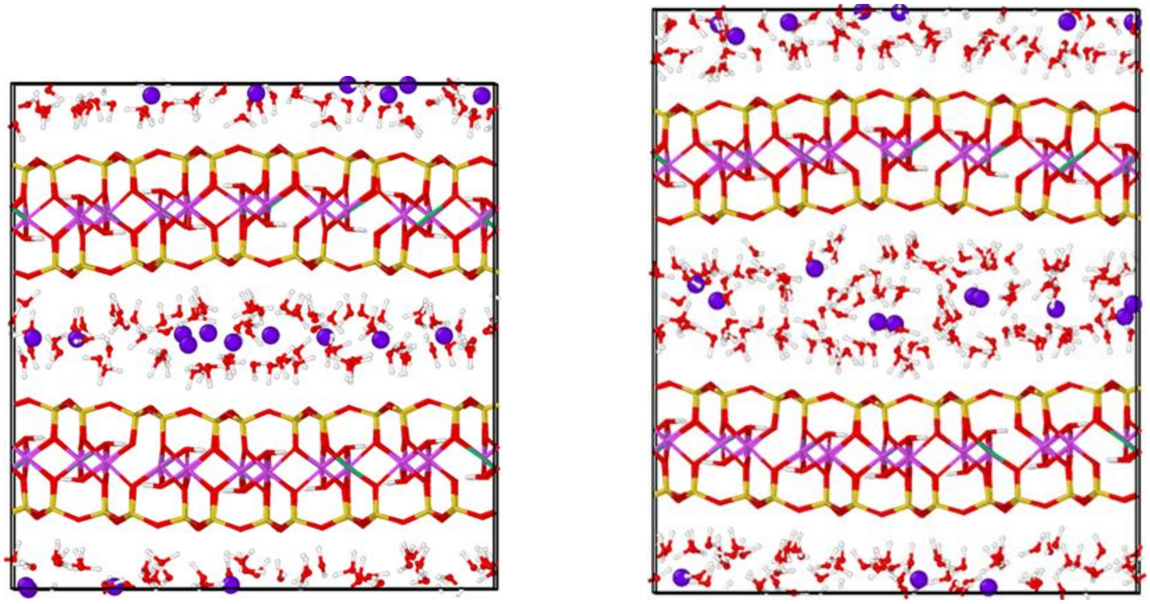

Figure 10. Simulation snapshots of bent clay configurations for the 1W-2W (left) and 2W-3W (right) mixed hydration states of Na-montmorillonite (Na^+ ions are purple).

Since the water loadings are obtained from equilibrium simulations, it is not possible to identify hysteresis in adsorption or desorption conditions due to metastable states. However, Brochard (2021) used a detailed analysis of pressures and free energies from extensive simulations to reveal such metastable states. Transitions between standard states during desorption (*e.g.*, 2W → 1W) occur at lower RH than the corresponding adsorption transitions (*e.g.*, 1W → 2W), in qualitative agreement with hysteresis behavior seen in diffraction studies (Berend, et al., 1995; Laird, et al., 1995).

3.4 Conclusions

The objective of this work is to evaluate water adsorption isotherms for expandable clay models corresponding to transitions between standard hydration states. Such transitions may cause undue forces in the near field of hydrated clays, so it is important to quantify these effects on clay phases in repository settings. This preliminary effort has established a method of creating model systems to explore the effect of layer bending on the thermodynamic and mechanical properties of expandable clays. Initial molecular simulation results indicate that configurations with bent clay layers show similar water adsorption behavior compared with standard hydration states with planar clay layers.

3.5 Future Work

Planned work for FY24 (and the remainder of FY23) include:

- MD simulations of the bent models at equilibrium water loadings will be performed to further characterize the structural, thermodynamic, and mechanical properties associated with transitions between the bent and flat configurations.

- In addition to verifying that the bent configurations are stable during unconstrained equilibrium simulation, geometries of the bent clay layer as well as corresponding mechanical properties will be determined.

3.6 References

Baldwin, R. L. Gas-liquid transfer data used to analyze hydrophobic hydration and find the nature of the Kauzmann-Tanford hydrophobic factor. *Proceedings of the National Academy of Sciences* **2012**, *109* (19), 7310-7313.

Bardelli, F.; Mondelli, C.; Didier, M.; Vitillo, J. G.; Cavicchia, D. R.; Robinet, J.-C.; Leone, L.; Charlet, L. Hydrogen uptake and diffusion in Callovo-Oxfordian clay rock for nuclear waste disposal technology. *Applied Geochemistry* **2014**, *49*, 168-177.

Barducci, A.; Bussi, G.; Parrinello, M. Well-Tempered Metadynamics: A Smoothly Converging and Tunable Free-Energy Method. *Phys Rev Lett* **2008**, *100* (2), 020603.

Berend, I., Cases, J.M., Francois, M., Uriot, J.P., Michot, L., Masion, A., and Thomas, F. (1995) Mechanism of Adsorption and Desorption of Water-Vapor by Homoionic Montmorillonites .2. The Li^+, Na^+, K^+, Rb^+ and Cs^+-Exchanged Forms. Clays Clay Miner., 43, 324-336.

Berend, I., Cases, J.M., Francois, M., Uriot, J.P., Michot, L., Masion, A., and Thomas, F. (1995) Mechanism of Adsorption and Desorption of Water-Vapor by Homoionic Montmorillonites .2. The Li^+, Na^+, K^+, Rb^+ and Cs^+-Exchanged Forms. *Clays Clay Miner., 43,* 324-336.

Blöchl, P. E. Projector augmented-wave method. *Physical Review B* **1994**, *50* (24), 17953-17979.

Bowers, G. M.; Schaef, H. T.; Loring, J. S.; Hoyt, D. W.; Burton, S. D.; Walter, E. D.; Kirkpatrick, R. J. Role of Cations in CO_2 Adsorption, Dynamics, and Hydration in Smectite Clays under in Situ Supercritical CO_2 Conditions. *The Journal of Physical Chemistry C* **2017**, *121* (1), 577-592.

Buckingham, A. D. Molecular quadrupole moments. *Quarterly Reviews, Chemical Society* **1959**, *13* (3), 183-214, 10.1039/QR9591300183.

Busch, A.; Bertier, P.; Gensterblum, Y.; Rother, G.; Spiers, C. J.; Zhang, M.; Wentinck, H. M. On sorption and swelling of CO_2 in clays. *Geomechanics and Geophysics for Geo-Energy and Geo-Resources* **2016**, *2* (2), 111-130.

Catti, M., Ferraris, G., Hull, S., and Pavese, A. (1994) Powder Neutron-Diffraction Study of 2M1 Muscovite at Room Pressurea nd at 2 GPa. European Journal of Mineralogy, 6, 171-178.

Chabab, S.; Théveneau, P.; Coquelet, C.; Corvisier, J.; Paricaud, P. Measurements and predictive models of high-pressure H_2 solubility in brine (H_2O+NaCl) for underground hydrogen storage application. *International Journal of Hydrogen Energy* **2020**, *45* (56), 32206-32220.

Cygan, R. T.; Liang, J. J.; Kalinichev, A. G. Molecular models of hydroxide, oxyhydroxide, and clay phases and the development of a general force field. *J Phys Chem B* **2004**, *108* (4), 1255-1266.

Drits, V.A., Guggenheim, S., Zviagina, B.B., and Kogure, T. (2012) Structures of the 2:1 Layers of Pyrophyllite and Talc. *Clays Clay Miner.*, *60*, 574-587.

Faybishenko, B.; Wang, Y.; Harrington, J.; Tamayo-Mas, E.; Birkholzer, J.; Jové-Colón, C. Phenomenological Model of Nonlinear Dynamics and Deterministic Chaotic Gas Migration in Bentonite: Experimental Evidence and Diagnostic Parameters. *Transport in Porous Media* **2022**, *141* (2), 585-606.

Ferrage, E.; Lanson, B.; Sakharov, B. A.; Drits, V. A. Investigation of smectite hydration properties by modeling experimental X-ray diffraction patterns: Part I. Montmorillonite hydration properties. *American Mineralogist* **2005**, *90* (8-9), 1358-1374.

Godawat, R.; Jamadagni, S. N.; Garde, S. Characterizing hydrophobicity of interfaces by using cavity formation, solute binding, and water correlations. *Proceedings of the National Academy of Sciences* **2009**, *106* (36), 15119-15124.

Harvey, J. A.; Johnston, C. T.; Criscenti, L. J.; Greathouse, J. A. Distinguishing between bulk and edge hydroxyl vibrational properties of 2 : 1 phyllosilicates via deuteration. *Chemical Communications* **2019**, *55* (24), 3453-3456, 10.1039/C9CC00164F.

Ho, T. A.; Coker, E. N.; Jové-Colón, C. F.; Wang, Y. Control of Structural Hydrophobicity and Cation Solvation on Interlayer Water Transport during Clay Dehydration. *Nano Lett* **2022**, *22* (7), 2740-2747.

Ho, T. A.; Criscenti, L. J.; Greathouse, J. A. Revealing Transition States during the Hydration of Clay Minerals. *J Phys Chem Lett* **2019**, *10* (13), 3704.

Ho, T. A.; Criscenti, L. J.; Greathouse, J. A. Revealing Transition States during the Hydration of Clay Minerals. *The Journal of Physical Chemistry Letters* **2019**, *10* (13), 3704-3709.

Ho, T. A.; Greathous, J. A.; Lee, A. S.; Criscenti, L. J. Enhanced Ion Adsorption on Mineral Nanoparticles. *Langmuir* **2018**, *34* (20), 5926-5934.

Ho, T. A.; Greathouse, J. A.; Wang, Y.; Criscenti, L. J. Atomistic Structure of Mineral Nano-aggregates from Simulated Compaction and Dewatering. *Sci Rep-Uk* **2017**, *7* (1), 15286.

Ho, T. A.; Wang, Y. Molecular Origin of Wettability Alteration of Subsurface Porous Media upon Gas Pressure Variations. *ACS Applied Materials & Interfaces* **2021**, *13* (34), 41330-41338.

Ho, T. A.; Wang, Y.; Rempe, S. B.; Dasgupta, N.; Johnston, C. T.; Xu, G.; Zwier, T. S.; Mills, M. Control of Structural Charge Distribution and Hydration State on CO_2 Intercalation into Expansive Clay Interlayers. *The Journal of Physical Chemistry Letters* **2023**.

Honorio, T., Brochard, L., Vandamme, M., and Lebee, A. (2018) Flexibility of nanolayers and stacks: implications in the nanostructuration of clays. *Soft Matter, 14*, 7354-7367.

Iglauer, S.; Abid, H.; Al-Yaseri, A.; Keshavarz, A. Hydrogen Adsorption on Sub-Bituminous Coal: Implications for Hydrogen Geo-Storage. *Geophysical Research Letters* **2021**, *48* (10), e2021GL092976.

Israelachvili, J. N. *Intermolecular and surface forces*; Academic Press, 2011.

Kentish, E. S.; Scholes, A. C.; Stevens, W. G. Carbon Dioxide Separation through Polymeric Membrane Systems for Flue Gas Applications. *Recent Patents on Chemical Engineering* **2008**, *1* (1), 52-66.

Kresse, G.; Furthmüller, J. Efficient iterative schemes for ab initio total-energy calculations using a plane-wave basis set. *Phys Rev B Condens Matter* **1996**, *54* (16), 11169-11186.

Laio, A.; Parrinello, M. Escaping free-energy minima. *Proceedings of the National Academy of Sciences* **2002**, *99* (20), 12562-12566.

Laird, D.A., Shang, C., and Thompson, M.L. (1995) Hysteresis in Crystalline Swelling of Smectites. *J. Colloid Interface Sci.*, *171*, 240-245.

Lavikainen, L. P.; Hirvi, J. T.; Kasa, S.; Schatz, T.; Pakkanen, T. A. Stability of dioctahedral 2:1 phyllosilicate edge structures based on pyrophyllite models. *Theoretical Chemistry Accounts* **2015**, *134* (9), 112.

Loewenstein, W. The distribution of aluminum in the tetrahedra of silicates and aluminates. *American Mineralogist* **1954**, *39* (1-2), 92-96. (acccessed 7/3/2022).

Lopez-Lazaro, C.; Bachaud, P.; Moretti, I.; Ferrando, N. Predicting the phase behavior of hydrogen in NaCl brines by molecular simulation for geological applications. *Bulletin de la Société Géologique de France* **2019**, *190* (1).

Newton, A. G.; Kwon, K. D.; Cheong, D.-K. Edge Structure of Montmorillonite from Atomistic Simulations. *Minerals* **2016**, *6* (2), 25.

Ngouana, B. F.; Kalinichev, A. G. Structural Arrangements of Isomorphic Substitutions in Smectites: Molecular Simulation of the Swelling Properties, Inter layer Structure, and Dynamics of Hydrated Cs-Montmorillonite Revisited with New Clay Models. *J Phys Chem C* **2014**, *118* (24), 12758-12773.

Perdew, J. P.; Burke, K.; Ernzerhof, M. Generalized Gradient Approximation Made Simple. *Phys Rev Lett* **1996**, *77* (18), 3865-3868.

Plimpton, S. Fast Parallel Algorithms for Short-Range Molecular-Dynamics. *J Comput Phys* **1995**, *117* (1), 1-19.

Pollack, G. L. Why Gases Dissolve in Liquids. *Science* **1991**, *251* (4999), 1323-1330.

Pouvreau, M.; Greathouse, J. A.; Cygan, R. T.; Kalinichev, A. G. Structure of hydrated gibbsite and brucite edge surfaces: DFT results and further development of the ClayFF classical force field with metal-O-H angle bending terms. *J. Phys. Chem. C* **2017**, *121*, 14757-14771.

Pouvreau, M.; Greathouse, J. A.; Cygan, R. T.; Kalinichev, A. G. Structure of Hydrated Kaolinite Edge Surfaces: DFT Results and Further Development of the ClayFF Classical Force Field with Metal–O–H Angle Bending Terms. *The Journal of Physical Chemistry C* **2019**, 11628–11638.

Schaef, H. T.; Ilton, E. S.; Qafoku, O.; Martin, P. F.; Felmy, A. R.; Rosso, K. M. In situ XRD study of Ca^{2+} saturated montmorillonite (STX-1) exposed to anhydrous and wet supercritical carbon dioxide. *Int. J. Greenh. Gas Control* **2012**, *6*, 220-229.

Schaef, H. T.; Loring, J. S.; Glezakou, V.-A.; Miller, Q. R. S.; Chen, J.; Owen, A. T.; Lee, M.-S.; Ilton, E. S.; Felmy, A. R.; McGrail, B. P.; et al. Competitive sorption of CO_2 and H_2O in 2:1 layer phyllosilicates. *Geochim Cosmochim Ac* **2015**, *161*, 248-257.

Shaw, R. P.; Shaw, R. P. The Fate of Repository Gases (FORGE) project. In *Gas Generation and Migration in Deep Geological Radioactive Waste Repositories*, Vol. 415; Geological Society of London, 2015; p 0.

Smith, D. E.; Dang, L. X. Computer-Simulations of Nacl Association in Polarizable Water. *J Chem Phys* **1994**, *100* (5), 3757-3766.

Szczerba, M.; Kalinichev, A. G.; Kowalik, M. Intrinsic hydrophobicity of smectite basal surfaces quantitatively probed by molecular dynamics simulations. *Appl Clay Sci* **2020**, *188*, 105497.

Tamura, K.; Yamada, H.; Nakazawa, H. Stepwise hydration of high-quality synthetic smectite with various cations. *Clay Clay Miner* **2000**, *48* (3), 400-404.

Teich-McGoldrick, S.L., Greathouse, J.A., Jové-Colón, C.F., and Cygan, R.T. (2015) Swelling Properties of Montmorillonite and Beidellite Clay Minerals from Molecular Simulation: Comparison of Temperature, Interlayer Cation, and Charge Location Effects. *J. Phys. Chem. C, 119*, 20880-20891.

Teleman, O.; Jonsson, B.; Engstrom, S. A Molecular-Dynamics Simulation of a Water Model with Intramolecular Degrees of Freedom. *Mol Phys* **1987**, *60* (1), 193-203.

Thompson, A.P., Aktulga, H.M., Berger, R., Bolintineanu, D.S., Brown, W.M., Crozier, P.S., in 't Veld, P.J., Kohlmeyer, A., Moore, S.G., Nguyen, T.D., Shan, R., Stevens, M.J., Tranchida, J., Trott, C., and Plimpton, S.J. (2022) LAMMPS - a flexible simulation tool for particle-based materials modeling at the atomic, meso, and continuum scales. *Comp. Phys. Commun., 271*, 108171.

Walczak, R.; Savateev, A.; Heske, J.; Tarakina, N. V.; Sahoo, S.; Epping, J. D.; Kühne, T. D.; Kurpil, B.; Antonietti, M.; Oschatz, M. Controlling the strength of interaction between carbon dioxide and nitrogen-rich carbon materials by molecular design. *Sustainable Energy & Fuels* **2019**, *3* (10), 2819-2827, 10.1039/C9SE00486F.

Ziemiański, P. P.; Derkowski, A. Structural and textural control of high-pressure hydrogen adsorption on expandable and non-expandable clay minerals in geologic conditions. *International Journal of Hydrogen Energy* **2022**, *47* (67), 28794-28805.

4. SKB Task 12: 1D Reactive-Transport Modeling of Cement-Bentonite Interactions

4.1 Introduction

The SKB Task Force (TF) Task 12 involves a benchmark problem on cement/bentonite (clay) interactions with various levels of complexity. The objective is to compare reactive-transport modeling approaches and results from participating groups working towards the development of simulation tools to evaluate barrier material interactions and backfill behavior. This task has evolved since it began last year and this report described the most recent modeling effort in response to those changes. Matteo et al. (2019) described 1-D PFLOTRAN reactive-transport simulations for the idealized case of cement-clay interactions with emphasis on the clay rock / cement interface. The role of barrier interfaces in seal performance and interactions with other barrier materials is crucial to the barrier isolation and containment behavior in deep geological nuclear waste repositories (Berner et al., 2013; Gaboreau et al., 2012; Kosakowski and Berner, 2013; Soler, 2012; Soler and Mader, 2010). The effects of porosity enhancement and reduction (e.g., clogging) due to mineral dissolution/precipitation have been the focus in various reactive-transport modeling efforts including benchmark test cases for computer code inter-comparisons efforts (Marty et al., 2015; Xie et al., 2015). The main purpose behind these computational reactive-transport modeling efforts lies in the complex coupling of geochemical interactions (kinetic vs. transport controlled) for the most part involving reactive diffusion phenomena in porous media (Marty et al., 2015). The extent to which these models capture relevant physico-chemical processes with enough realism and adequacy still needs to be examined and reconciled with the limited amount of available field and experimental laboratory data.

Leaching behavior of barrier materials whether engineered or natural provides key chemical and structural characterization data of (geo)chemical interactions at interfaces. Such data is useful in the evaluation and testing of reactive-transport models such as described in Matteo et al. (2019) for cement-clayrock interactions and those described for DECOVALEX19 Task C on the GREET URL experiment (Jové Colón et al. 2020) where kinetics (e.g., solid dissolution), transport length scale, and diffusion parameters can have an effect on the temporal change in measured solute concentrations. Similarly, modeling of cement-clay interactions and the potential chemical and physical changes occurring at the barrier interface could significantly impact mass fluxes and overall transport phenomena in the near-field environment.

The goal of the SKB TF (Task 12) is to evaluate and test reactive-transport models to represent interactions between backfill clay and cement barrier materials using a stylized benchmark problem with different levels of complexity and compare results with task participants. The test of computational tools will be based on comparisons between “blind predictions” or benchmarks between various modeling groups. This section will describe current efforts in Task 12 (Subtasks A and B) involving reactive transport simulations of a domain composed of concrete and MX-80 bentonite sharing an interface. Emphasis is given to results of Subtask A for evaluation of input parameter sensitivities and comparisons with results of other task participants. This work builds on efforts reported in FY22 (Jove-Colon et al., 2022). As such, the relevant text has been preserved. However, significant updates to the previously reported results are presented here due to key changes in the problem description as the task evolved from the past year.

4.2 Problem Details

The problems defined for Subtasks A and B comprise a rectangular domain of MX-80 bentonite and ordinary Portland cement (OPC) domain (see Figure 11) sharing an interface and allowed to interact for a period of 100,000 years. Both domains are fully saturated and each one is 1 m long. No-flux boundary conditions are applied to the 1-D problem on both domain ends. The domains are isothermal at 25°C and held at constant atmospheric pressure. The SKB task description originally defined a temperature of 15°C. However, this was changed afterwards by the task lead to 25 °C, consistent with our previous temperature definitions of thermodynamic data for reactions of aqueous, gas, and solid phases. In Subtask A, the concrete domain is defined as ordinary Portland cement (OPC), whereas in Subtask B, it is defined as low-pH cement (LPC). The initial porosity of the OPC concrete is 11%, and 13% for the LPC. The initial porosity of the bentonite is 42.3%. The compositions of the bentonite and cement phases and pore solution chemistries, and a list of potential secondary phases are also provided by the task description. It should be noted that the task doesn’t specify specific sources of thermodynamic data to be used in the simulations nor the choice of kinetic rate laws; these are left to the modeler's choice. Subtask A has three sub-cases; in each of these, the initial porewater chemistry of the cement is defined differently. In Case A1, pure water is allowed to equilibrate with the solid cement phases, with cation exchange turned on. In Case A2, a granite groundwater is used instead of pure water. In Case A3, the granite groundwater is used again, but cation exchange is turned off. The Task 12 team anticipates revising Subtask B in a similar way later in the year 2023.

4.2.1 Modeling Approach

PFLOTRAN, a massively parallel reactive-transport and flow simulator code (Lichtner et al. 2019) was used to conduct the 1-D diffusion, reactive transport simulations. The grid is discretized by using 190 grid cells for each of the two regions, for a total of 380 grid cells. Starting from the outside ends, the regions are composed of 90 cells having dimensions of 1×10-2 m wide, followed by 100 cells of 1×10^{-3} m wide nearest to the interface. Permeability is isotropic through the domains. The initial porosities for the MX080 bentonite and OPC are 42.3% and 11%, respectively. The permeability of the OPC is set to 2×10^{-18} m^2 and that of the bentonite is defined as 2.64×10^{-20} m^2. PFLOTRAN computes porosity and permeability changes based on variations in mineral solid volume fractions in the reactive-transport calculations. These parameters are summarized in Figure 11. No flux boundary conditions are applied to the 1-D problem at both domain ends.

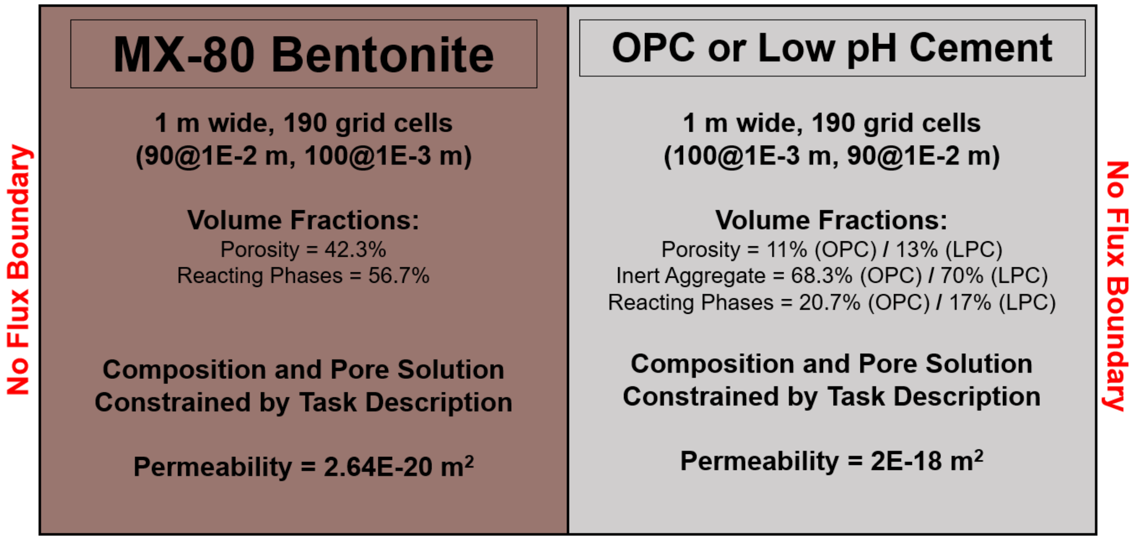

Figure 11. Schematic diagram describing the parameters of the 1D reactive-transport problem setup of SKB TF Task 12, Subtask A.

The thermodynamic database for solid and aqueous species is a modified version of the THERMODDEM database (Blanc, 2017; Blanc et al. 2012), with the addition of specific cement phases added from CEMDATA18 (Lothenbach et al., 2019). The solid phases considered for this problem and corresponding rate constants at 25 °C are listed in Table 2.

Table 2. Phases considered for the model of SKB TF (Task 12) Subtasks A and B along with corresponding rate constants for dissociation reactions.

Phase	Rate Constant (mol/m^2/sec)	Phase	Rate Constant (mol/m^2/sec)	Phase	Rate Constant (mol/m^2/sec)
Albite (low)	1E-14	Clinochlore	1E-14	Montmorillonite(HcCa)	1E-14
Amorphous Silica	3.2E-09	Clinoptilolite(Ca)	1E-14	Na_2O	1E-14
Analcime	1E-14	Clinoptilolite(Na)	1E-14	Phillipsite(Ca)	1E-14
Arcanite	1E-04	Epsomite	1E-07	Phillipsite(Na)	1E-14
Brucite	1E-14	Ettringite	1E-12	Portlandite	1E-08
CSH(0.8)	1E-14	Gypsum	2E-04	Quartz(alpha)	1E-13
CSH(1.2)	1E-14	Heulandite(Ca)	1E-14	Saponite(Ca)	1E-14
CSH(1.6)	2.75E-12	Heulandite(Na)	1E-14	Saponite(K)	1E-14
C_2S	5E-05	Hydrotalcite	1E-14	Saponite(Mg)	1E-14
C_3A	5E-05	Hydrotalcite(CO_3)	1E-14	Saponite(Na)	1E-14
C_3AH_6	1E-14	Illite(Al)	1E-14	Smectite(MX80)	1E-14
C_3S	5E-05	K_2O	1E-14	Straetlingite	1E-14
C_4AF	2E-05	Katoite	1E-14	Syngenite	1E-14
C_4AH_{13}	1E-14	Monocarboaluminate	1E-14	Thaumasite	1E-14
Calcite	1E-14	Monosulfoaluminate	1E-14	Thenardite	1E-04

The starting bentonite, OPC and LPC bulk solid and porewater compositions are as prescribed in the task problem (Tables 3 and 4, respectively). It should be noted that the initial pH used in Subtask A cases is 12.2, rather than 13.2 as defined in the task description due to simulation stability issues produced at high pH values. Also, Quartz(alpha) is considered as an inert phase in the mineral assemblage so its reactive surface area is set to zero.

Table 3. Initial reacting phase compositions in each domain for Subtasks A and B.

Phase	**Volume Fraction**	
	OPC	**Bentonite**
C_3S	0.58055	-
C_2S	0.09303	-
C_3A	0.02658	-
C_4AF	0.1265	-
Calcite	0.0094	-
Gypsum	0.04549	-
Na_2O	0.00417	-
K_2O	0.00428	-
Smectite (MX80)	-	0.577
Total	0.89	0.577

Cation exchange has also been implemented as prescribed in the task description. However, the task doesn't specify the exchanger phase and these were assumed in our model. In the bentonite, the selected exchanger phase is smectite (MX-80) with the exchangeable cations Na^+, Ca^{2+}, K^+, and Mg^{2+}. In the OPC, the exchanger phase is CSH (CSH(0.8) in the LPC; CSH(1.6) in the OPC) with the exchangeable cations Ca^{2+}, K^+, and Na^+. As an additional sensitivity test, Case A3 was run with and without cation exchange in the OPC whereas in the bentonite cation exchange was allowed in both scenarios. The task description provides cation exchanger composition parameters for the OPC and LPC phases such as CaX_2, K_2X_2, and NaX_2. These include logK values for each sorption reaction of the exchangeable species and cation exchange capacity (CEC) values. Similarly, cation exchanger composition parameters for the smectite phase in bentonite such as NaX, CaX_2, KX, and MgX_2 are also described by the task description.

Table 4. Pore solution compositions in each region of the Subtask A model.

Solute	Initial Solute Concentrations (mol/L or pH units)				
	Bentonite	OPC - A1	OPC - A2	OPC - A3	LPC
Al^{3+}	6.9E-10	2.8E-04	2.17E-04	3.87E-05	5.40E-02
Ca^{2+}	1.4E-02	1.65E-03	2.70E-03	4.43E-02	1.50E-03
Cl^-	1.4E-01	1E-10	1.39E-01	1.39E-01	1E-10
Fe^{2+}	1E-10	1E-10	1E-10	1E-10	1E-10
H_4SiO_4(aq)	1.8E-04	4.21E-05	2.89E-05	3.22E-06	1.80E-02
HCO_3^-	2.3E-03	1.98E-06	1.47E-06	2.04E-07	3.00E-06
K^+	1.5E-03	2.07E-01	2.51E-01	8.76E-04	1.10E-01
Mg^{2+}	6.9E-03	5.41E-10	7.62E-10	5.41E-09	6.60E-08
Na^+	2.3E-01	3.49E-02	7.4E-02	8.89E-02	1.80E-02
O_2(aq)	1E-10	1E-10	1E-10	1E-10	1E-10
SO_4^{2-}	6.5E-02	4.17E-04	2.89E-04	9.61E-06	2.90E-02
pH	7.33	12.2	12.2	12.2	10.3

4.3 Results

4.3.1 Subtask A

Selected results for key solute concentrations in Subtask A models are shown in Figures 12, 13, and 14. As previously noted, predicted pH and solute concentrations can exhibit significant changes with time, particularly in the vicinity of the interface, due to large differences in pore solution chemistry. The pH profiles in Figure 12 show the expected evolution of increasing pH with time within the bentonite domain. However, some of the Task Force participants remarked that the increase in bentonite pore solution pH with time was rather fast. The pore solution pH in the bentonite domain reaches values of ~11 to ~12 by 10 years of simulation. The adopted diffusion coefficient for all solutes value in the simulations is 1.4×10^{-9} m^2/s for Cases A1, A2, and A3. The effective diffusion coefficient is lower due to the scaling with porosity. Still, sensitivity analyses on the effect of diffusivity will be investigated in the future now that stable simulations capturing updates in porosity and permeability are possible.

Figures 13 and 14 show that spatio-temporal profiles for Ca and Si concentrations vary considerably at early times in the region close to the interface. Gypsum and brucite precipitation occur in the system, as well as the formation of cement phases such as ettringite and CSH(1.6). In all cases, similar solute concentrations in pore solutions in both the bentonite and cement domains is reached by ~100 to 1,000 years as the differences observed thereafter are relatively minor. The total Si concentration profiles (Figure 14) in the cement domain indicates the largest variation with time. Still, there was no large net change in porosity and permeability in either domain. Most of the relatively small porosity/permeability changes occur close to the interface in the cement domain. A key observation in this exercise is that having cation exchange present in the OPC had a minimal effect in the resulting spatio-temporal solute profiles for Case A3. The equilibrium pH in the system is above 12, however, few mineralogic changes occur in the bentonite. It is possible that mineral dissolution/precipitation rate constants in the current model, particularly at elevated pH, do not accurately capture the time-dependent response. It should be emphasized that some of the adopted dissolution rates for silicate phases (Table 2) are currently considered as "placeholders" until better constrained values are implemented. However, preliminary results of sensitivity analyses on reaction rates on key solids show that the effect on the spatio-temporal solute profiles may not be significant. An exception would be the reaction rates for phases such as ettringite and gypsum. Gypsum is the most active solid species close to the interface in both bentonite and cement domains.

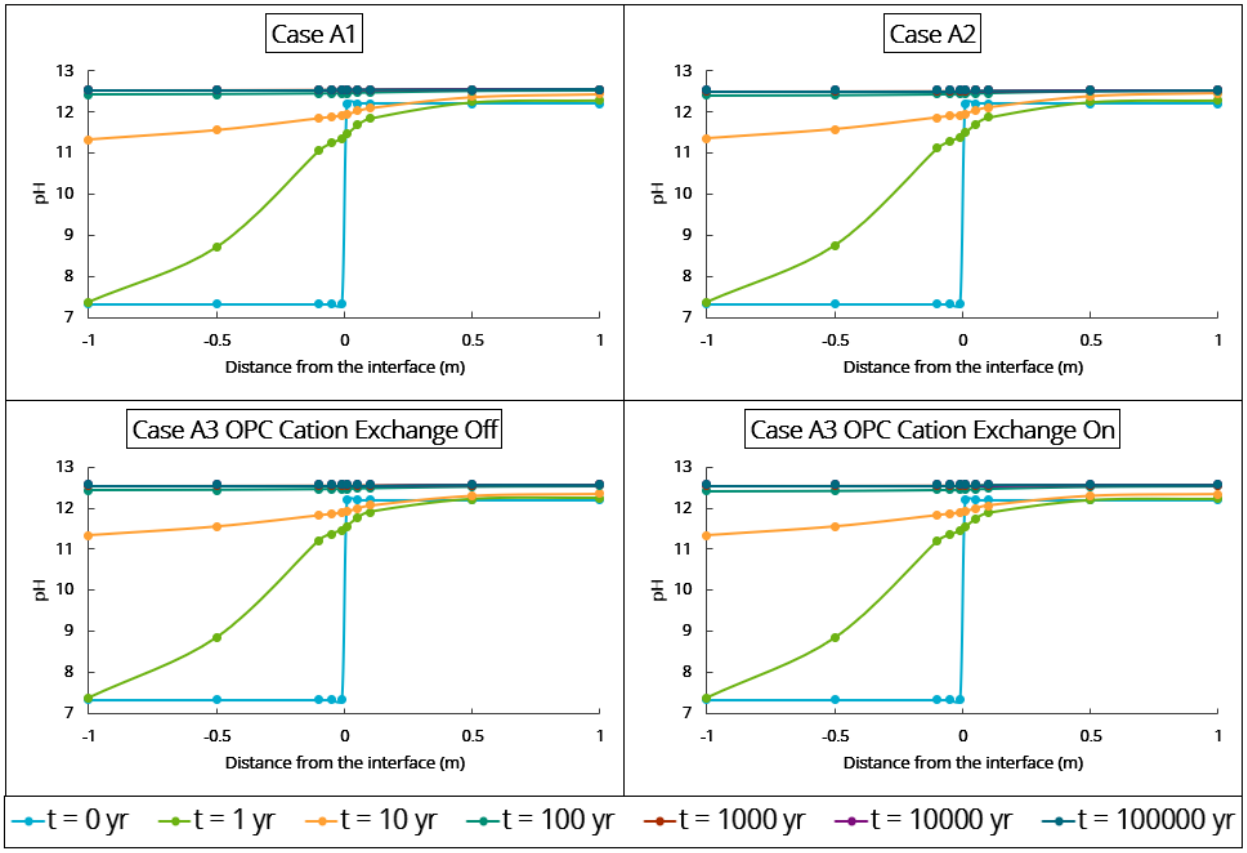

Figure 12. Spatio-temporal pH profiles for cases A1 through A3 (and variants of the latter) in Subtask A at selected times. Negative distances from the interface represent the bentonite region whereas positive values correspond to the OPC region. Zero distance represents the interface location (see text).

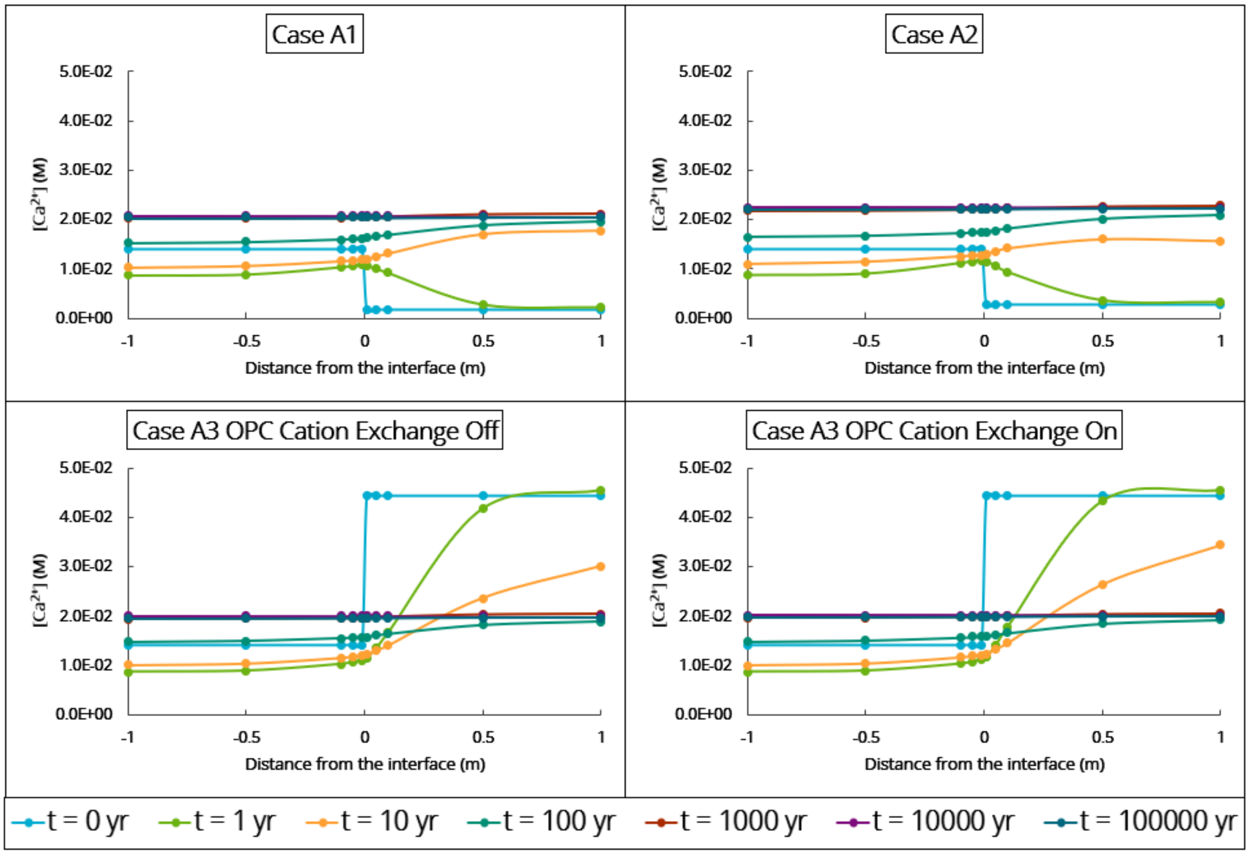

Figure 13. Concentration of Ca^{2+} in the Subtask A model system at selected times. Negative distances from the interface represent the bentonite region whereas positive values correspond to the OPC region. Zero distance represents the interface location.

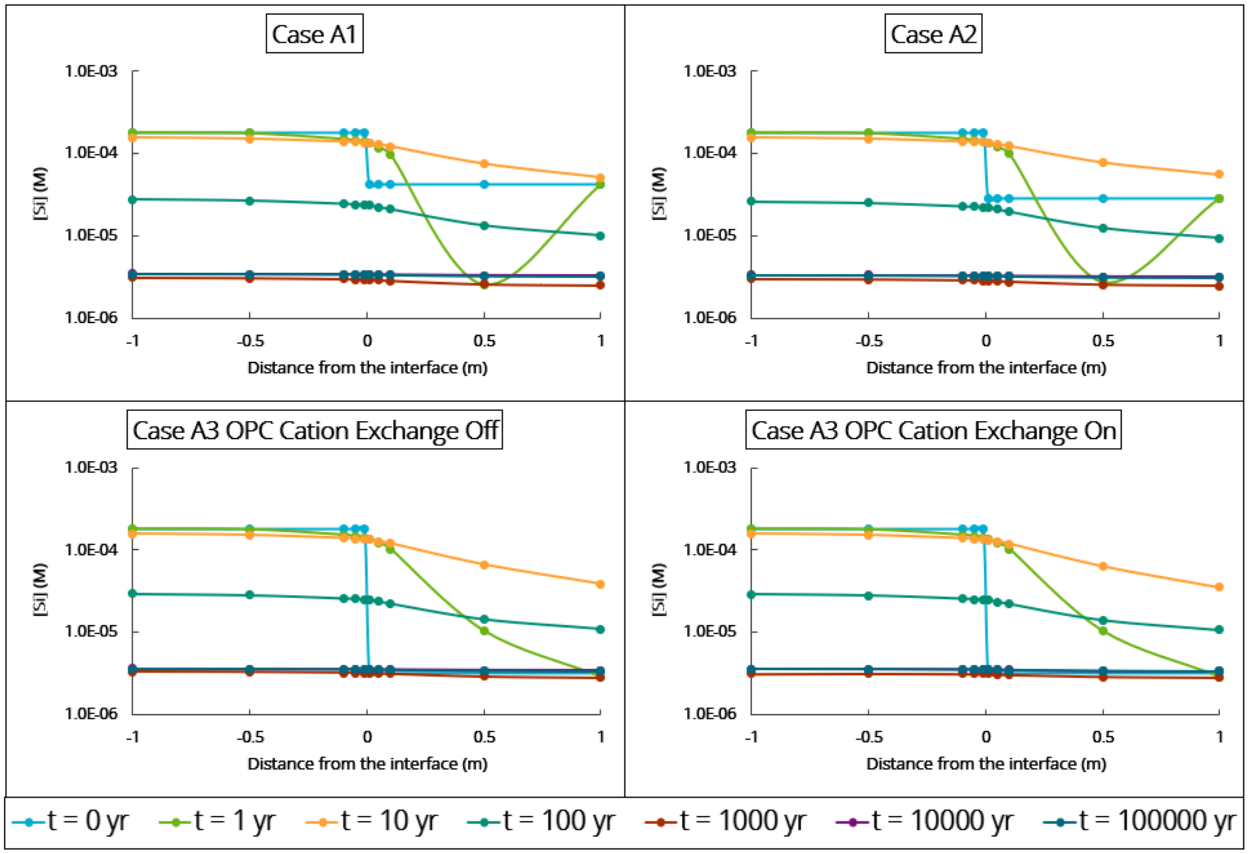

Figure 14. Concentration of total Si (computed as $H_4SiO_4(aq)$) in the Subtask A model system at selected times. Negative distances from the interface represent the bentonite region whereas positive values correspond to the OPC region. Zero distance represents the interface location.

4.3.2 Subtask B

This subtask is similar Subtask A with the key difference of low-pH cement (LPC) in the cement domain. Selected results for pH, porosity, and key solute concentration in Subtask B simulations are summarized in Figure 15. A key component in the LPC is amorphous silica which is absent in the OPC cement composition in Subtask A. The pH trend in this scenario varies markedly from Subtask A results in that its temporal change is noticeably different. The pH variation with time shows an initial increase, peaking at ~1 year and subsequently showing a continuous decrease reaching values comparable with those of the bentonite domain. This observation needs to be investigated further since it is not expected for the LPC pore solutions to attain such low pH values in the near-neutral region, even after long periods of time. Another difference from Subtask A results is the noticeable decrease in porosity in the LPC domain after 1 year of simulation time. The phase volume fractions with the largest changes in the LPC domain are Heulandite(Na) and amorphous silica. Total Ca and Si concentrations in the LPC domain also exhibit large variations with time up to ~100 years and subsequently stabilize to near constant values. These results are the product of stable simulations obtained recently. Therefore, more work is needed to look at these results in more detail and conduct sensitivity analyses to evaluate the effect of, for example, solid suppressions of secondary minerals (e.g., zeolites) and responses to silicate dissolution rates.

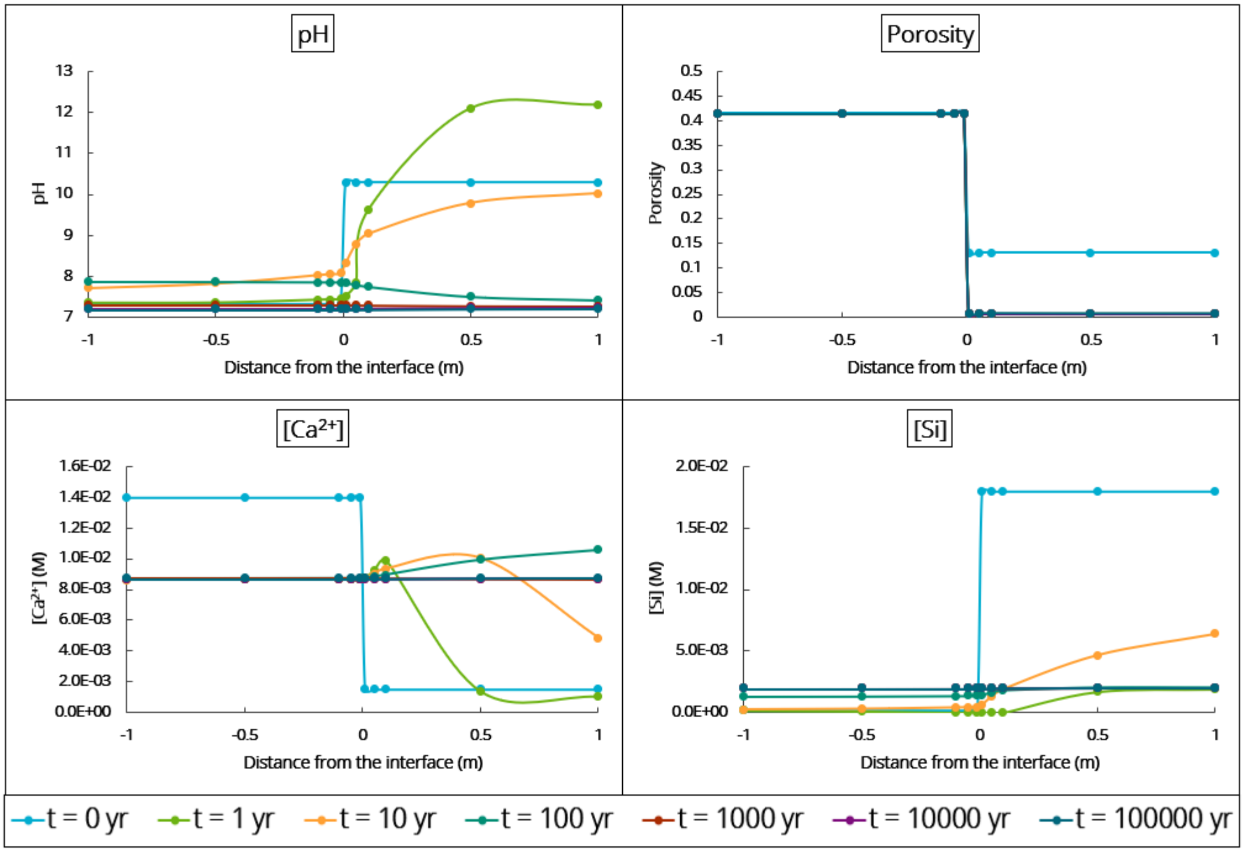

Figure 15. pH, porosity, and selected total solute concentrations in the Subtask B model system at selected times. Negative distances from the interface represent the bentonite region whereas positive values correspond to the OPC region. Zero distance represents the interface location.

4.4 Conclusions

The 1-D PFLOTRAN reactive transport model for Task 12 (Subtasks A and B) has evolved, with more recent modifications to the past year problem description, but it is still work in progress. Similar to results reported in FY22, current results of the "blind prediction" show a strong temporal dependence on changes in pore solution chemistry, particularly at early times up to ~100 years. The largest temporal differences in solute concentrations are in the cement domain. Moreover, the largest changes are focused in regions close to the interface between bentonite and cement, as expected. Such dynamic changes close to the interfacial region exert strong controls on the spatial distribution of secondary phase formation (e.g., gypsum), mostly in the cement domain. The recent updates in problem parameters yield an approximate steady-state or stable behavior in solute concentrations is achieved by ~1,000 years as the differences observed afterwards become relatively minor. The consideration of cation exchange in the model has minor effects on the overall solute concentration profiles. However, further evaluations and comparisons of these results and model implementation with other task participants is still ongoing.

4.4.1 Future Work

Further work for the remaining of FY23 and FY24 will focus on the role of input parameter sensitivities and their impact on simulation results. This will also include implementation of cases B1, B2, and B3 of Subtask B once these are made available by SKB TF lead. Additionally, we intend to shift our focus to Subtask C (unsaturated case) once Subtasks A and B have progressed to the desired level.

5. 1-D Reactive Transport Modeling of Ordinary Portland Cement (OPC) Leaching Experiments

5.1 Introduction

Cementitious materials are intrinsic to the engineered barrier system (EBS) of deep-geological nuclear waste repository design concepts. These materials are usually present as tunnel wall liners, shaft seals, and plugs. Given the relatively large amounts of cement material considered in these repository concepts, the interactions between cement pore fluids and other EBS components (e.g., bentonite) need to be evaluated as part of the long-term safety assessment. One aspect of this analysis is the model representation of cement leaching and its effect to the evolution of fluid chemistry, particularly at EBS material interfaces. Here we report results of a 1-D (diffusion-only) reactive transport model using the PFLOTRAN code for leaching of ordinary Portland cement (OPC) having a starting composition close to that of a CEM I cement. Experimental data used in calibrating the model was obtained for an OPC sample (height = 2.3 cm) at 30°C and 63 days following the EPA method 1315 (EPA, 2015) for leaching of monolithic and/or compacted granular materials. The experimental OPC leaching data was obtained from Dr. David Kosson, Dr. Chen Gruber, and Autumn Taylor from Vanderbilt University. This discussion provides updates on work presented in the milestone report for FY22 (Jove Colon et al., 2022), and as such, relevant text has been preserved.

5.2 Modeling Approach

5.2.1 Simulations of EPA Method 1315

The 1-D reactive transport simulations were conducted using PFLOTRAN, an open source, state-of-the-art massively parallel computer code capable of performing calculations for subsurface single- and multi-phase flow and reactive transport under (non)isothermal conditions. The code is designed for use on massively parallel or high-performance computing (HPC) platforms where efficient scalability becomes important for large coupled-process problems. Lichtner et al. (2013) provides details on PFLOTRAN simulation capabilities, reactive-transport formulations, and geochemical treatment of mineral-fluid interactions.

The THERMODDEM thermodynamic database (Blanc, 2017; Blanc et al., 2012; Blanc et al., 2006) was used in the simulations. Use of the most recent iteration of THERMODDEM results in some differences in formation reaction stoichiometries and reaction logK values for some cementitious phases (namely CSHs), relative to those used in previous work. The thermodynamic database was also complemented by the addition of cementitious solids from CEMDATA18 (Lothenbach et al., 2018), with corrections applied to previously entered stoichiometries.

The structured mesh discretization is defined by a rectangular geometry with dimensions consistent with those of the OPC sample in the leaching experiments (Figure 16). The solid monolith meshed domain is composed of 39 cells (bottom) and a single cell (top) for the leaching bath solution. The long top cell is used to accommodate an equivalent volume of leaching solution used in the experiments. No flow boundary conditions are imposed on the faces of the rectangular domain. Small pressure perturbations in the leaching solution upper "box" are allowed for some "mixing".

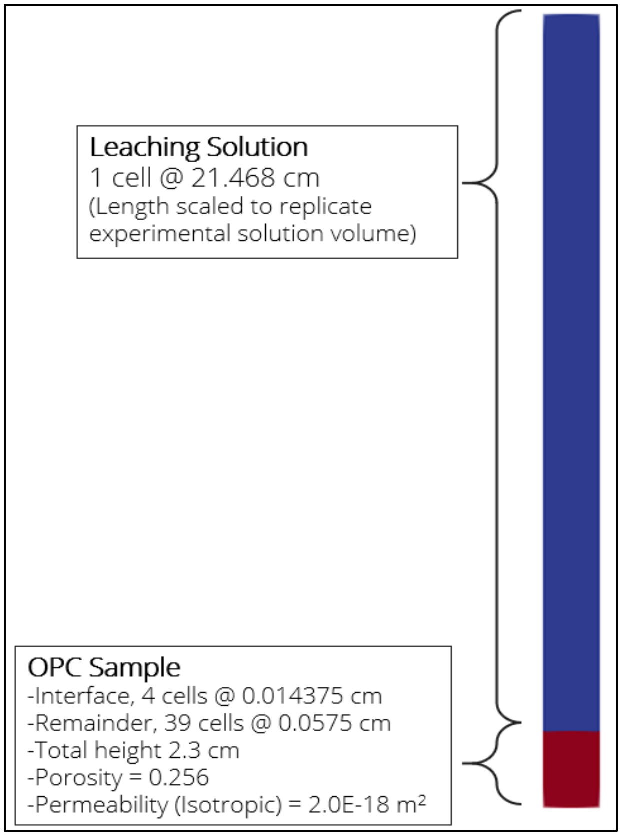

Figure 16. Mesh description of the solid OPC monolith (lower) and leaching solution (upper) domains along with dimensions of the rectangular domain.

Table 5 lists the starting phase assemblage in the modeled OPC and their corresponding volume fractions. This composition differs from that presented in the FY22 report. As previously mentioned, corrections were made to stoichiometries in the formation reactions of the cementitious phases. These corrections also necessitated adjustments to the initial volume fractions of C_2S and C_3S in the PFLOTRAN simulation. Additionally, the reactive surface area of C_2S was set to zero, to avoid the effect of this phase in the reactive transport calculation.

Table 5. Initial volume fractions of OPC monolith cement phases considered in the model.

Phase	Input Volume Fraction
$C_3AS_{0.41}H_{5.18}$	7.3%
$C_3FS_{0.84}H_{4.32}$	2%
Ettringite	5.4%
Portlandite	12.5%
Thenardite	0.9%
Arcanite	2.5%
Epsomite	1.4%
C_3S	12.1% (previously 10.1%)
C_2S	0% (previously 2%)
C_3A	8%
C_4AF	1%
CSH(1.2)	17.4%
Calcite	3.9%

In addition to the phases listed in Table 5, various secondary phases were allowed to form: amorphous silica, straetlingite, brucite, monosulfoaluminate (also known as monosulfate), gypsum, and syngenite. The porosity of the OPC is 25.6%, with an isotropic permeability of 2×10^{-18} m^2, and an assumed tortuosity of 0.8 (Table 6). The 1-D diffusion problem is isothermal at 25 ºC with a diffusion coefficient of 2.5×10^{-10} m^2/s. It is assumed that solubility effects due to the difference in temperature (25 ºC in the modeling vs. 30 ºC in the experiment) are negligible. Updates to permeability, tortuosity, and porosity at each time step were considered in the simulations.

Table 6. OPC monolith properties

Parameter	Value
Porosity	0.256
Tortuosity	0.8
OPC Density	1480 kg/m^3 *
Permeability (isotropic)	2.0E-18 m^2

* Derived from sample mass and dimensions.

Model calibration was performed by adjusting mineral reactive surface areas (RSAs) to fit the experimental data. Dissolution rate constants for all solids were constrained from literature values. The OPC was simulated as that of a CEM I cement composition having a solid phase assemblage representing 91 days of curing (Saillio et al., 2019). There is a range of volume fraction values for CEM I selected phases (e.g., C_3S) at given curing times that were adjusted to fit the temporal solute concentration profiles. The starting OPC pore solution chemistry is taken as a very dilute solution in all its components where the assumed HCO_3^- concentration is 1.0E-03 M having an initial pH 12. The dilute pore solution reacts rapidly in the initial steps of the simulation. The leaching solution (deionized (DI) water) was sampled/replenished at fixed time intervals and analyzed to quantify solute concentrations. These leachate solution or eluent chemistries at each renewal interval were obtained from Drs. Chen Gruber and David Kosson at Vanderbilt University. The initial (time zero) chemistry of leaching solution is taken as that of the leachate sampled after two hours of leaching. The leachate solution composition at subsequent times for each replenishment in the tank bath cell are that of a very dilute (or DI) water, except for HCO_3^- having a concentration of 2.0E-05 M.

5.2.2 Simulations of EPA Method 1313

In addition to the above-described PFLOTRAN reactive transport simulations, major solute concentrations of aqueous solutions from a different OPC leaching test were simulated using reaction path modeling with the geochemical modeling software package EQ3/6 (Wolery and Jarek, 2003). The goal of the reaction path simulation is to provide a relatively simplistic zero-D representation of the OPC leaching process mainly based on mass transfer relations between solids and solution, capturing the system feedbacks imposed by equilibria between reactant and secondary solid phases in the evolving solution chemistry. The experimental leaching tests were conducted following the EPA Method 1313 (EPA, 2012) to assess liquid-solid partitioning as a function of solution pH at conditions close to equilibrium. The solvents considered in this method are nitric acid (HNO_3) and potassium hydroxide (KOH) (EPA, 2012). Details of these OPC leaching experiments are given in Gruber et al. (2022). In the EQ3/6 reaction path model, solid OPC components are titrated into one kg of one molal nitric acid (HNO_3) solution. The reaction path calculations are performed as a batch-type closed system under isothermal conditions of 25 °C in a reaction progress mode (arbitrary kinetics). The thermodynamic database used is a modification of the Yucca Mountain Project (YMP) Pitzer database with the additions of cementitious phases from the CEMDATA18 database (Lothenbach et al., 2019). Two initial liquid to solid ratios (L/S) were used in the EPA 1313 leaching experiments: L/S=1 and L/S=10 mL/g-dry material. The EQ3/6 model used inputs that approximated to L/S=1 mL/g-dry material. The proposed OPC phase components from the PFLOTRAN reactive transport model described above were used as input (Table 3). The EQ3/6 simulation results of the EPA 1313 leaching experiments were also compared against those of the LeachXS/ORCHESTRA model reported by Vanderbilt University team (Gruber et al., 2022).

Table 7. Mineral phases allowed to form as exceptions to the suppressions constrains in EQ3/6 model.

Mineral Phases	
CSH(1.2)	Calcite
Portlandite	Thenardite
Ettringite	Arcanite
$C_3AS_{0.41}H_{5.18}$	Epsomite
$C_3FS_{0.84}H_{4.32}$	SiO_2(am)
C_3S	Gibbsite(am)
C_3A	INFCNA*
C_4AF	Brucite Gypsum

* The INFCNA phase has the composition $(CaO)_{1.25}(SiO_2)(Al_2O_3)_{0.125}(Na_2O)_{0.25}(H_2O)_{1.375}$

5.3 Results and Discussion

5.3.1 Simulations of EPA Method 1315 Test

The updated PFLOTRAN model of the 1315 experiment remains appropriate for the objectives of simulating cement leaching. As with previous results, there are moderate deviations from experimental data, however, the overall trends in the solute profiles have been replicated (Figures 17 and 18). Predicted Al and Si concentraions at t<400 hours and SO_4^{2-} concentrations at t>600 hours slightly differ from previous model results. However, as noted previously, the overall discrepancies in the predicted solute concentrations are considered reasonable given the nature of the experiment where multiple leachate solution batches (from periodic eluent renewals) are sampled at various times.

Previous observations still hold for the updated results. The overall pH trend is represented by the model except for deviations in the middle and final stages of the experiment. The predicted Si and Ca^{++} concentrations are also in good agreement with the experimental data. The temporal total Na and K concentrations indicate some discrepancies along the solute profile. The dependencies for Na anf K concentration are largely tied to the initial volume fractions of thenardite (Na_2SO_4) and arcanite (K_2SO_4) salts considered in the CEM I phase assemblage. Fitting the experimental SO_4 concentrations was challenging since changes in the relative amounts of ettringite along with other hydrous cementitious solids such as portlandite and CSH in the model exert strong spatial changes in porosity and permeability of the OPC domain.

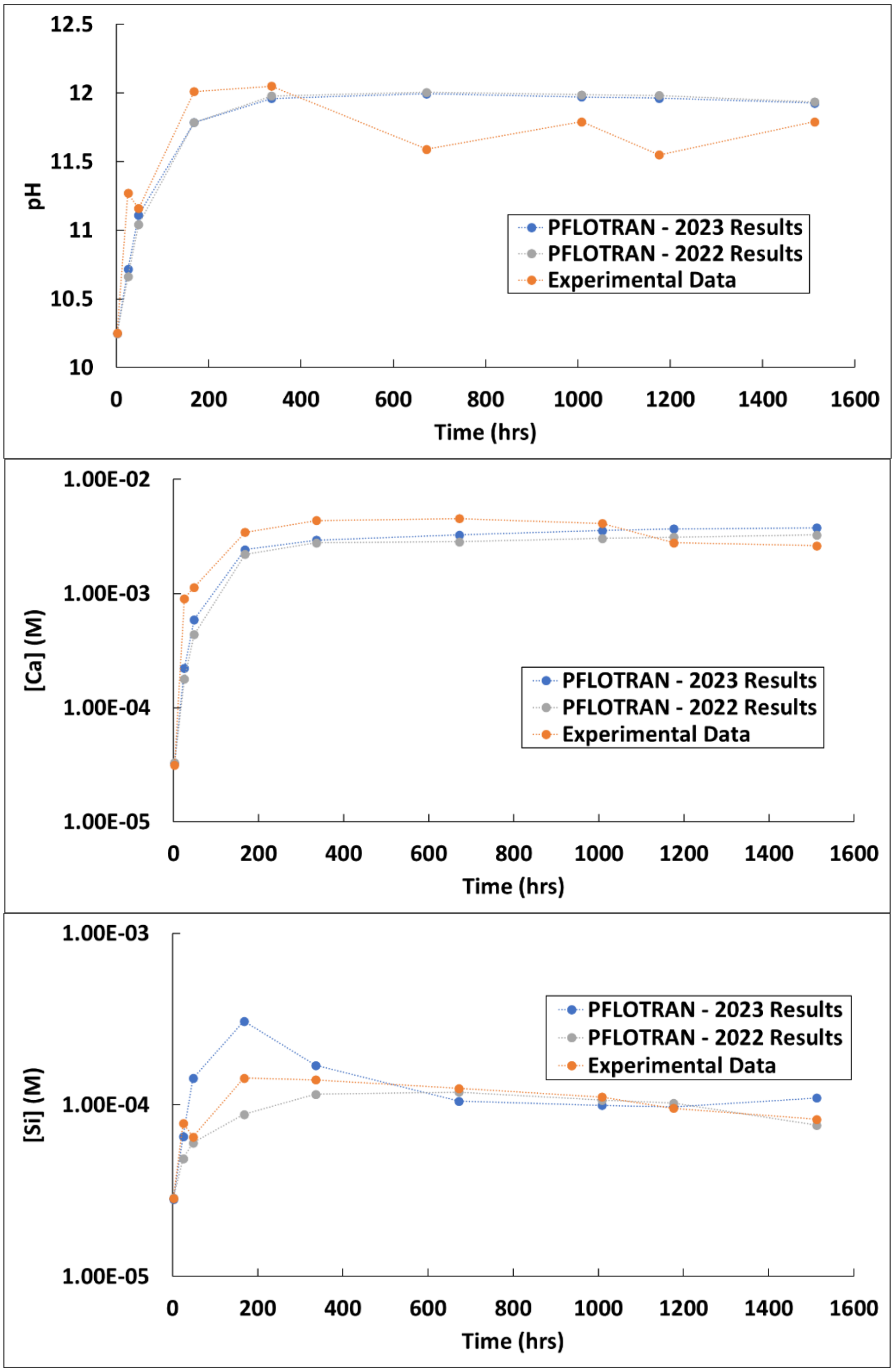

Figure 17. Temporal change of pH (upper panel), total Ca concentration (center panel), and total Si concentration (lower panel) in leachate solutions for the 1315 OPC leaching experiment.

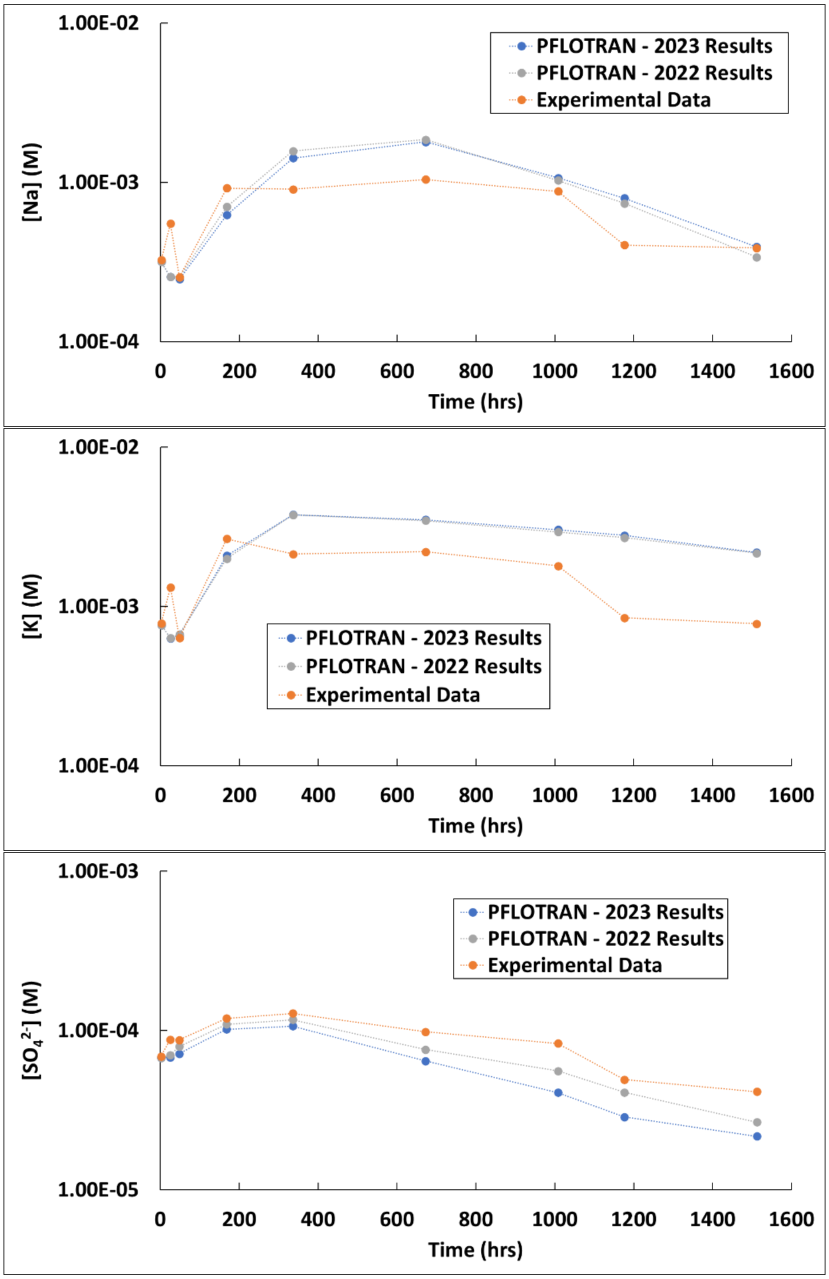

Figure 18. Temporal change of total Na (upper panel), total K concentration (center panel), and total SO_4 concentration (lower panel) in the leachate solutions.

5.3.2 Simulations of EPA Method 1313 Test

The simulation of the EPA 1313 OPC leaching test as a function of pH was successfully modeled by reaction path modeling using EQ3/6 (Figures 19 and 20). Overall, the simulated solute concentrations of major constituents closely mimics the trends in the experimental data but in some cases leading to some differences at pH>9. Though the input is set to a L/S=1 mL/g-dry, the reaction path model consistently represents the experimental data and the LeachXS/ORCHESTRA modeling results for L/S=10 mL/g-dry. The L/S ratio primarily affects the extent of reaction progress in the EQ3/6 simulation. That is, a model constrained with L/S=10 mL/g-dry would have less reactant mass that would be exhausted before reaching a high pH value relative to L/S=1 mL/g-dry. It would still, however, show the same trends up to where the final pH is reached. The final pH in the EQ3/6 simulation with L/S=1 is pH 12.

Some differences are predicted solute concentrations relative to the experimental data do exist in each case. Even so, these discrepancies are reasonable and may be caused by limitations from assumptions in the modeling approach. For example, consideration of the equilibrium assumption imposed at each titration step in the model whereas the experimental data may not necessarily reflect such condition. The concentration of Ca at pH=1 is not well predicted, however, the experimental data is well represented by the model from pH=4-12 (Figure 19). The Si concentration is nominally consistent with both experimental and VU model trends up to pH~10. However, the marked decrease trend in Si concentration at pH>10 diverges from the data. The total S concentration trend is captured by the model, but predictions at pH>9 somewhat deviate from the experimental data trend (Figure 20). The Al concentration profile shows some differences in terms of experimental values and overall VU model trends. We used this example to test the effect of solubility controlling solids for crystalline and amorphous gibbsite. The latter provides a closer representation of data trends as shown in the Figure 20. It should be noted that differences in thermodynamic data in the models can also contribute to these discrepancies.

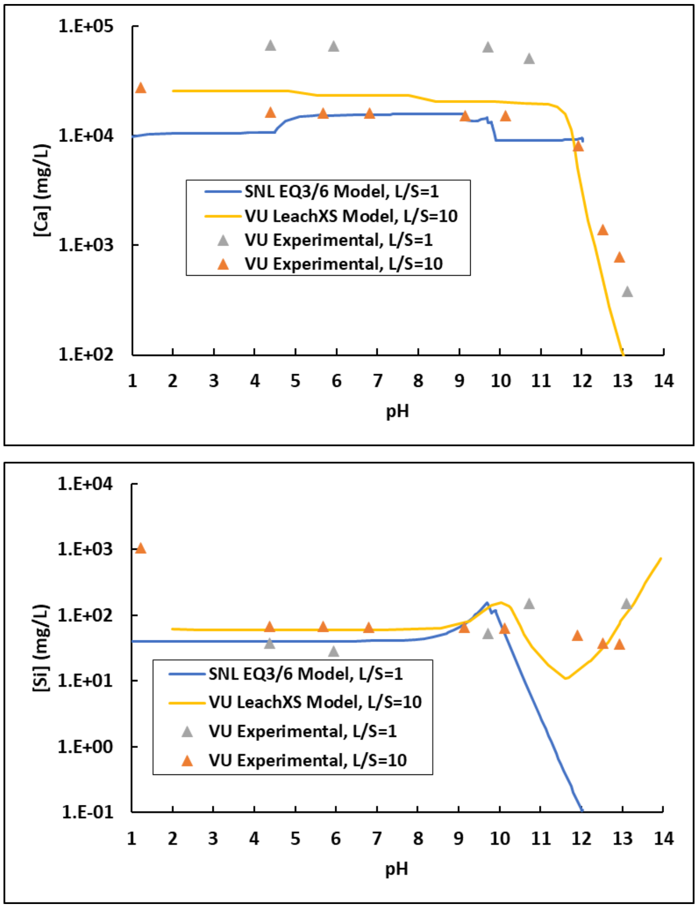

Figure 19. Temporal change of total Ca (upper panel) and total Si concentration (lower panel) in EQ3/6-simulated titration solutions. Symbols represent Vanderbilt University (VU) experimental data (Gruber et al., 2022).

Predictions of Mg concentrations (Figure 20) are in very good agreement with both experimental data and the VU model trends from Gruber et al. (2022). Brucite saturation is predicted by the model at pH≥9.4. This causes the decrease in Mg concentration above this pH value (Figure 5).

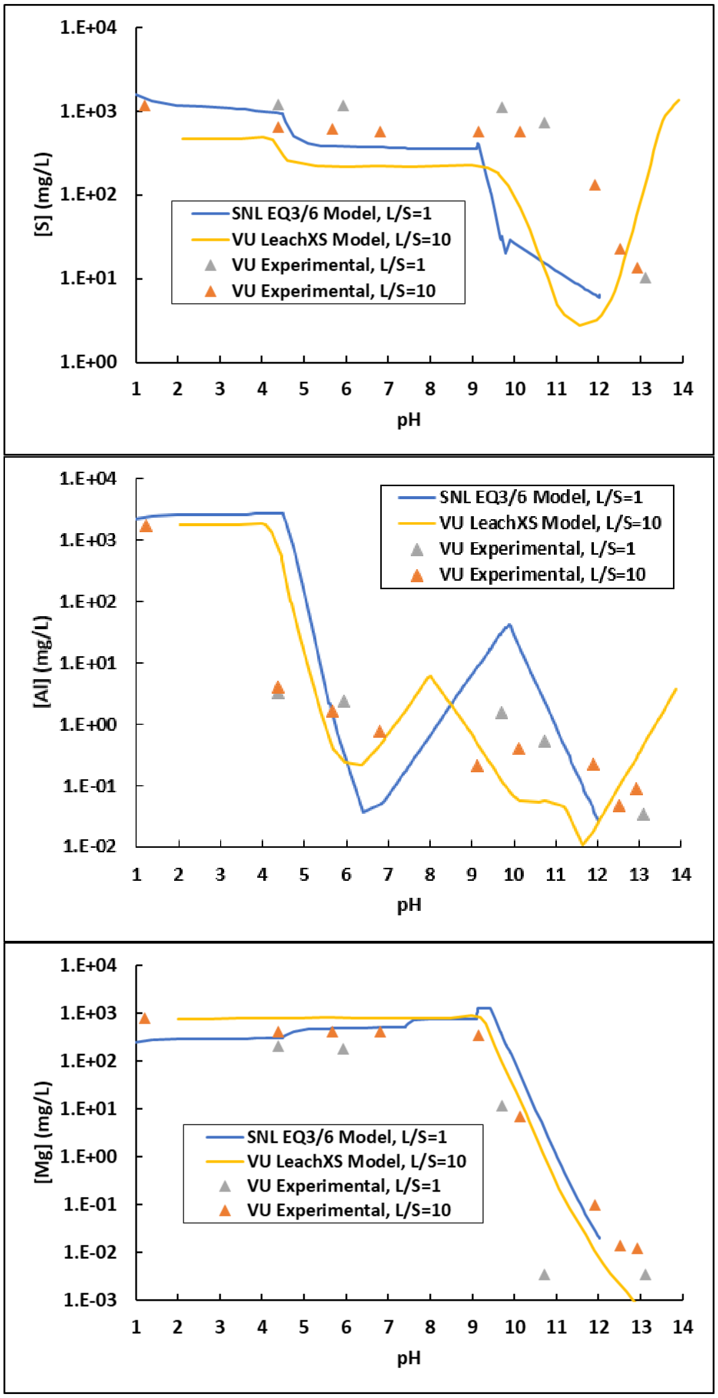

Figure 20. Temporal change of total S concentration (upper panel), total Al concentration (center panel), and total Mg concentration (lower panel) in EQ3/6-simulated titrations. Symbols represent Vanderbilt University (VU) experimental data (Gruber et al., 2022).

5.4 Conclusions

The PFLOTRAN 1-D reactive-transport model of the EPA 1315 OPC monolith leaching test provide good representations of the overall experimental leaching trends for temporal solute concentration profiles based on the major cement phase constituents and associated thermodynamic data. Similarly, the reaction path model representation of the EPA Method 1313 test for OPC leaching confirms that the cement phase assemblage developed from the PFLOTRAN simulations generate results that are in good agreement with experimental data. There are still some discrepancies between data and model(s), particularly in the high pH range. Nevertheless, this effort demonstrates the successful application of reaction path modeling to simulate a standardized OPC leaching tests. Furthermore, the results compare well with other modeling approaches developed to represent cement leaching tests. It also demonstrates that the assumption of mineral equilibria in controlling solution chemistry is applicable to cement systems for this type of test. This is important for model and data validation in assessments to evaluate barrier interactions involving cementitious materials in repository environments.

5.4.1 Future Work

The results of this 1-D reactive-transport simulation of OPC leaching will inform other simulations of cement-rock interaction studies. Planned FY24 activities include:

- Focus on reactive transport modeling of interfaces in shale/cement interactions. This will be done with further collaboration with Drs. D. Kosson and C. Gruber and their team at Vanderbilt University (VU).
- Investigate discrepancies in the reaction path model results of OPC leaching tests and associated leaching model.
- Explore model sensitivities to phase suppressions and phase thermodynamic data.

6. DECOVALEX2023 Task D: Modeling of the Step 1 S1-3 and S1-4 Experiments

Introduction

The DECOVALEX2023 Task D is described as the “Full-scale Engineered Barrier System Experiment at Horonobe URL (Underground Research Laboratory)” (Sugita 2022). The task is led by the Japan Atomic Energy Agency (JAEA) and is divided into two major steps. Step 1 involves modeling of the thermal-hydrological and mechanical characteristics of bentonite as an engineered barrier material. This step comprises modeling of four laboratory experiments conducted by the JAEA involving Kunigel V1 bentonite isothermal/non-isothermal saturation, swelling pressure, and free swelling tests. Experimental data have been provided to the participating teams by the JAEA for use in the modeling. In Step 2, the knowledge gained from Step 1 will be applied to build a 2-D multiphase transport model for the full-scale backfilled EBS experiment at the Horonobe URL (JNC, 2000). The Sandia National Laboratories (SNL) team has developed PFLOTRAN models for two of the Step 1 experiments (S1-3 and S1-4), in preparation for modeling Step 2. It should be noted that this is the last year for DECOVALEX2023 work activities and results from these will be documented in a final report.

6.1.1 Problem Details

Step 1 Experiment (S1-3): Infiltration Test

No new FY23 work was conducted on the modeling of the S1-3 experiment that generated new results. However, some updates will be presented in this section for completeness. A previous study of porous column infiltration tests has been conducted on bentonite from the in the Mont Terri in situ HE-E experiment (sand/bentonite mixture and bentonite pellets) to study hydration under ambient isothermal conditions (Villar et al., 2013). A test in this study used an experimental design similar to Task D experiment S1-3 but it experienced leak issues. The S1-3 infiltration test is the vertical saturation of a block of Kunigel V1 bentonite and silica sand for a period of about 30 days. The bentonite block is wetted from the bottom, and there is an air outlet at the top. The block is 50 mm tall. The wetting solution is either deionized water (DW) or 0.2 M NaCl aqueous solution as an analogue for dilute groundwater (GW). The system is isothermal at ambient conditions and modeled at 25°C. A schematic representation of the experimental setup is depicted in Figure 21. The parameter of interest in the simulated system is percent saturation, both as a function of time and as a function of distance along the sample.

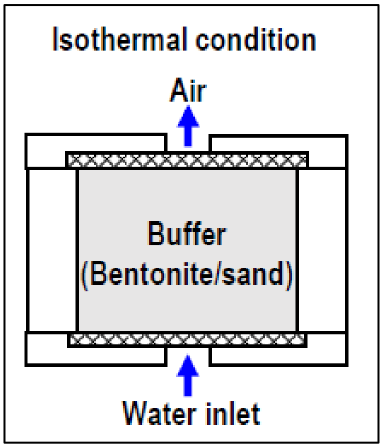

Figure 21. Schematic of the JAEA S1-3 experimental setup (Sugita, 2022).

Step 1 Experiment (S1-4): Temperature Gradient Moisture Diffusion Test

Previous studies on porous column tests have been conducted to study FEBEX bentonite hydration under non-isothermal conditions from 6 to 92 months (Villar et al., 2008a, b). These studies show that thermal gradients can drive changes bentonite water content and dry density throughout the column length. Such gradients can also affect permeability as well as swelling behavior (Villar et al. (2008b). It should be noted that the column experiment described in Villar et al., (2008a, b) involves water infiltration from the top which is different from Step 1 experiment S1-4 which has no fluid fluxes in the column. Nonetheless, the results of Villar et al., (2008a, b) provide key information on the hydration behavior of an unsaturated bentonite column with a thermal gradient.

The experiment S1-4 is an investigation of the thermal-hydrological behavior of a partially saturated bentonite block under an imposed temperature gradient. The block is encased in a jacket that creates an impermeable boundary around the sides. It’s assumed in our model that such jacketed configuration also prevents thermal fluxes. Copper plates are affixed to the top and bottom of the block and held at constant temperatures: 30°C at the top of the sample and 70 °C at the bottom of the sample. The block starts at either room temperature (20-25 °C) or 30°C, depending on the iteration of the experiment. The block is 10 cm tall, as shown in Figure 22. Models should assess 1-D transport of the porewater as a function of time over an 18-day period. The parameter of interest is percent water content, both as a function of time and as a function of distance along the sample. The measured data provided by the JAEA are water content and must be converted to saturation for the PFLOTRAN simulations.

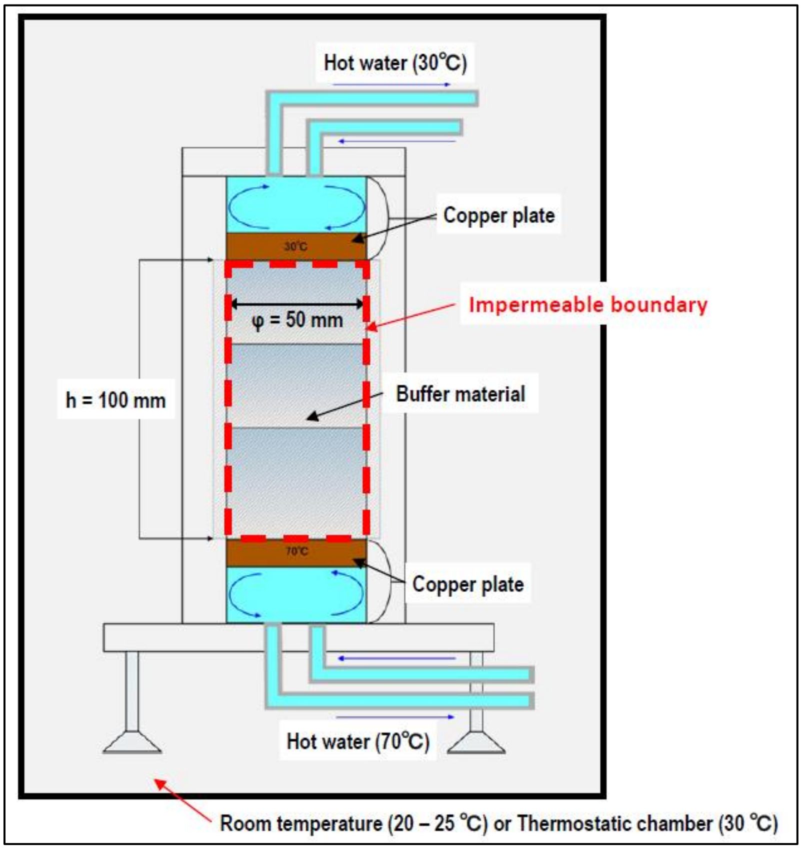

Figure 22. JAEA schematic of S1-4 experimental setup (Sugita, 2000).

Modeling Approach

PFLOTRAN simulation code

Computer simulations were done using the code PFLOTRAN, a massively parallel subsurface flow and reactive-transport code for hydrogeochemical applications (Lichtner et al, 2019). The code leverages thermal, hydraulic, and reactive transport capabilities with several input modes that allow for single- and multiphase flow in variably saturated porous media. The 1-D model uses PFLOTRAN's General Mode for thermal and hydraulic calculations of two-phase (liquid/gas) flow but no reactive transport (i.e., no chemical interactions) was considered in these simulations. Thermal conductivity can be specified as constant or as a function of liquid saturation. In these simulations, we adopted the default mode which computes thermal conductivities as a function of saturation based on input values for unsaturated (dry) and saturated (wet) end-members of the bentonite and sand sample. PFLOTRAN computes the water retention curve and relative permeabilities as a function of liquid saturation of the unsaturated porous domain. Additionally, anisotropic permeabilities can be specified as an input constraint depending whether the model is in 2D or 3D and the medium discretization.

Model Setup

S1-3 PFLOTRAN Simulation Setup

The simulated 1-D isothermal domain is made of Kunigel V1 bentonite and sand having 50 cells in the Z direction, where each cell is 1 mm tall for a total sample height of 50 mm. The water inlet was modeled as a saturation-driven fluid transport into porous bentonite and sand from a large liquid reservoir at the bottom of the sample. This reservoir is implemented as an inflow boundary condition under atmospheric pressure on the bottom face of the sample. The air outlet was modeled via an outflow boundary condition on the top face of the sample. All simulations were conducted at a temperature of 25 °C. The S1-3 model problem has been finalized and the following discussion is the same as that of the FY22 report (Jové Colón et al., 2022)

As stated previously, hese simulations do not account for chemical interactions between the pore solution and bentonite. That is, the potential for chemical reactions between bentonite and pore fluids that could lead to swelling are not considered as part of the bentonite saturation mechanism. Porosity is held constant at 32.8%. As such, a suitable mechanism that could control time-dependent saturation as well as account for the different behaviors of the two fluids was needed. To this end, heterogeneous permeability regions in the bentonite column were implemented and treated as an input variable that was constrained to fit the experimental data. The bentonite block was divided into two regions having different isotropic permeability. The size and permeabilities of these regions depend on the wetting fluid being modeled, which is either deionized water (DW) or groundwater (GW). These regions and permeabilities are depicted in Figure 23 and are listed in Table 8.

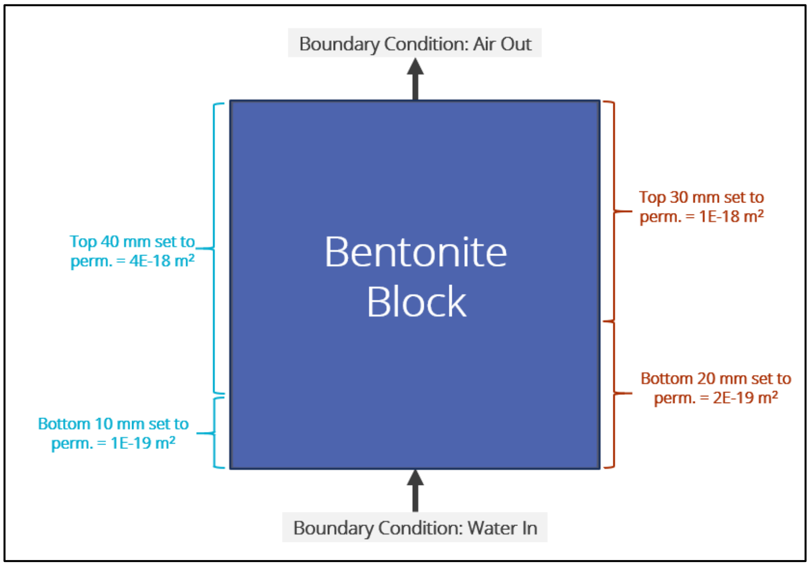

Figure 23. Schematic illustration of the PFLOTRAN 1-D simulation domain and boundary conditions for experiment S1-3. Permeabilities/regions for the distilled water case are depicted in blue (left) whereas those corresponding to the groundwater case are depicted in red (right). "Perm." refers to isotropic permeability.

Table 8. Case-dependent isotropic permeabilities according to sample regions.

Case	Region	Height (mm)	Permeability (m^2)
DW Case	Top	40	4E-18
	Bottom	10	1E-19
GW Case	Top	30	1E-18
	Bottom	20	2E-19

Two different initial saturation conditions were tested for both the GW and DW cases: heterogeneous and homogeneous. In the heterogeneous case, the bentonite was divided into ten regions where initial liquid saturation was set to represent temporal data obtained from the DW experiment (Table 9). In the homogeneous case, the entire block was assigned an initial liquid saturation of 33.4%, which is the average of the values used for the heterogeneous case. The saturation profiles are visualized in Figure 24. In all cases, a liquid residual saturation of 15% and a gas residual saturation of 0.1% were used. The van Genuchten saturation function implemented in PFLOTRAN (Lictner et al., 2020) was used with parameter values of M = 0.275 and α = 5.1E-7. A limitation of the model is that a saturation above 100% cannot be predicted, even though the experimental data indicates >100% saturation at later times. The measured saturation values above 100% is an artifact of the methodology used to quantify saturation in the samples. The relative permeability function is based on a combined Mualem-van Genuchten formulation (Lichtner et al. 2019; Mualem, 1976).

Table 9. Initial liquid saturations assigned to regions in heterogeneous saturation tests.

Region (Distance from the bottom of the sample)	Initial Liquid Saturation
0 mm - 5 mm	34%
5 mm - 10 mm	30%
10 mm - 15 mm	37%
15 mm - 20 mm	36%
20 mm - 25 mm	28%
25 mm - 30 mm	33%
30 mm - 35 mm	30%
35 mm - 40 mm	36%
40 mm - 45 mm	38%
45 mm - 50 mm	34%

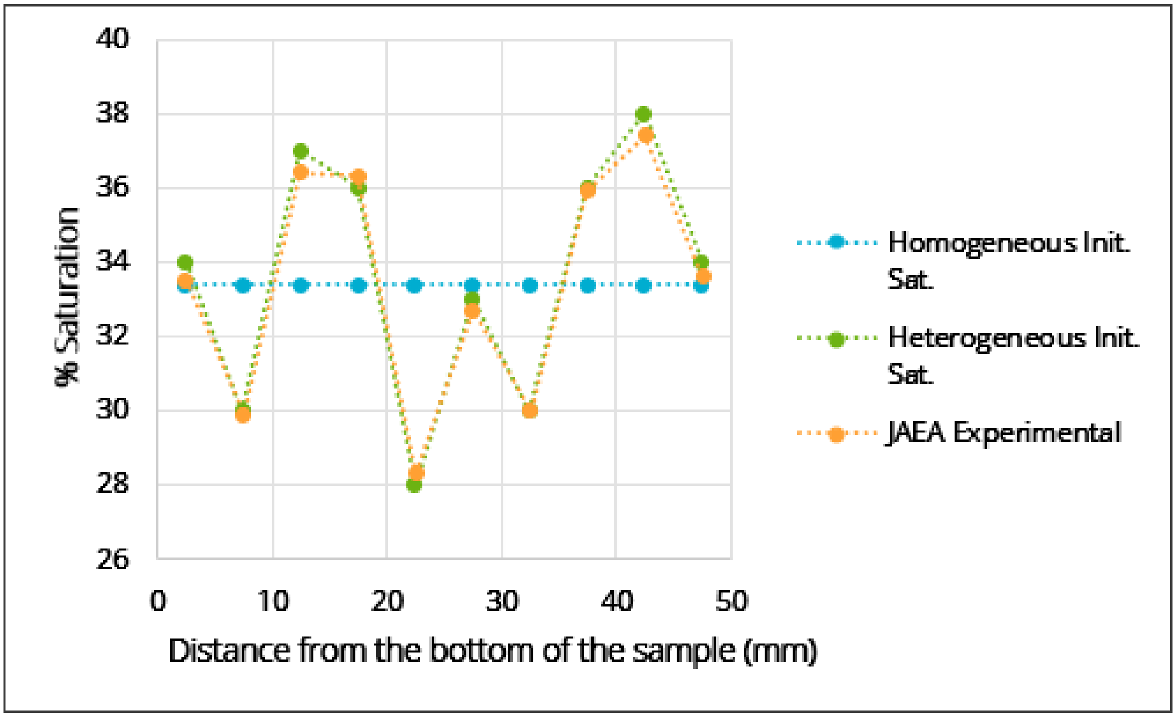

Figure 24. Initial saturation profiles for the homogeneous and heterogeneous cases.

S1-4 PLFOTRAN Simulation Setup

The modeled domain for this problem is 100 cells in the vertical (Z) direction, where each cell is 1 mm tall for a total sample height of 100 mm. The 1-D problem was modeled as a closed system saturation-driven transport. That is, all boundaries were constrained to have no mass or thermal fluxes. As with S1-3, the adopted saturation function was the van Genuchten formulation with M = 0.275 and α = 5.1E-7. Pressure is allowed to change with gradients in temperature across the simulated domain.

Key to this problem was the development of a temperature gradient along the vertical length of sample. The temperature gradient developed as a result of constant temperature boundary conditions on the top (30 °C) and the bottom (70 °C) faces of the sample. The considered thermal conductivity values for “dry” and “wet” bentonite having a dry density of 1.8 g/cm^3 are 0.798 and 1.94 W/m-K, respectively. The thermal conductivity values were provided by the JAEA to the task members. All other boundaries were set to have zero thermal flux. The bentonite domain had an initial temperature condition of 25 °C. See Figure 25 for schematic details of the problem setup.

The bentonite domain has initial uniform liquid saturation of 32%. This is approximated from an estimated water content of 10.5% and a constant porosity of 32.8% using the following equation (Eq. 1):

$$\frac{\%\,Water\ Content}{\%\,Porosity} * 100\% = \%\,Liquid\ Saturation \qquad (1)$$

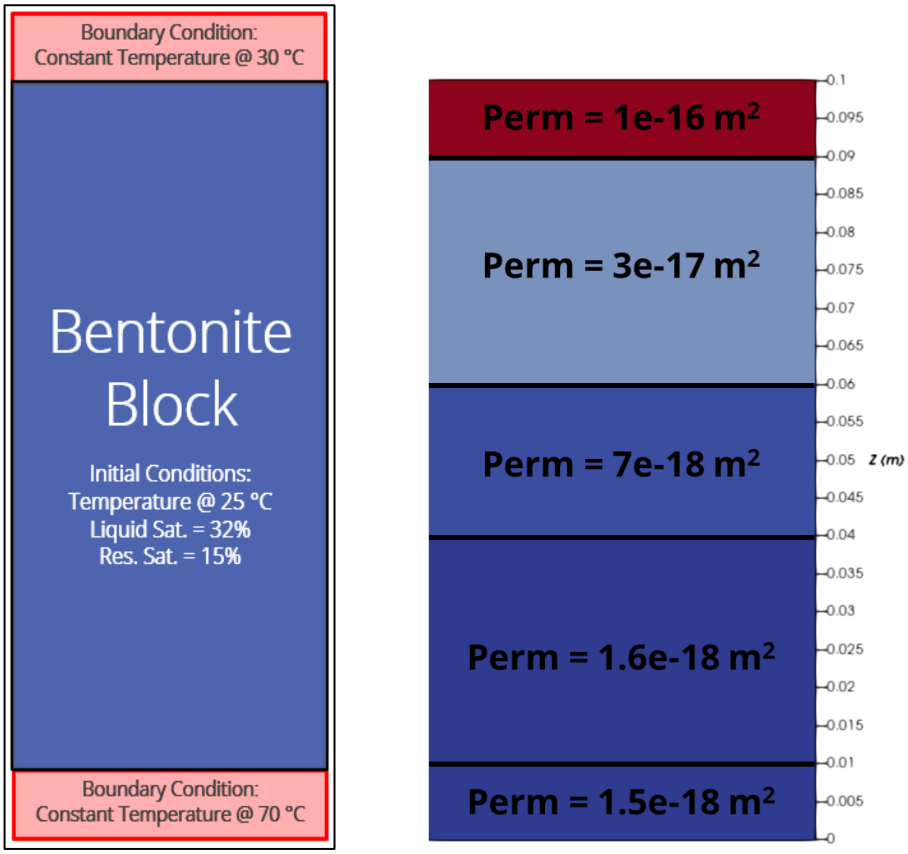

Figure 25. (Left panel) – schematic illustration of the non-isothermal PFLOTRAN 1-D simulation domain and boundary conditions for the experiment S1-4. (Right panel) – schematic diagram depicting the five permeability zones used in the model.

Water content will be assessed as an equivalent % liquid saturation, as the latter is a PFLOTRAN output. The liquid residual saturation was set to 15%. As with S1-3, these simulations do not account for the chemical and mechanical processes that occur in the sample during the saturation experiment (i.e., bentonite swelling). Permeability was again treated as an adjustable input parameter to fit experimental data. The previous model treated permeability as homogeneous throughout the whole sample domain. In this model iteration, permeability in the bentonite domain is divided into five zones (see Figure 25 – right panel).

Results

S1-3 Simulations

The results of the S1-3 DW tests are summarized in Figure 26. The PFLOTRAN 1-D model is successful in representing the saturation profiles of the S1-3 experiment in Kunigel V1 bentonite and sand, with both heterogeneous and homogenous initial saturation conditions. After 1 day of saturation time, the profiles of the PFLOTRAN model are similar to that of the experimental data, except for a discrepancy at 22.5 mm from the bottom of the sample. At 10 and 15 days, the simulations tend to overpredict saturation in the region between 10 and 40 mm from the bottom of the sample. However, this is improved at 30 days, with the only point of notable difference being the region near the top of the sample.

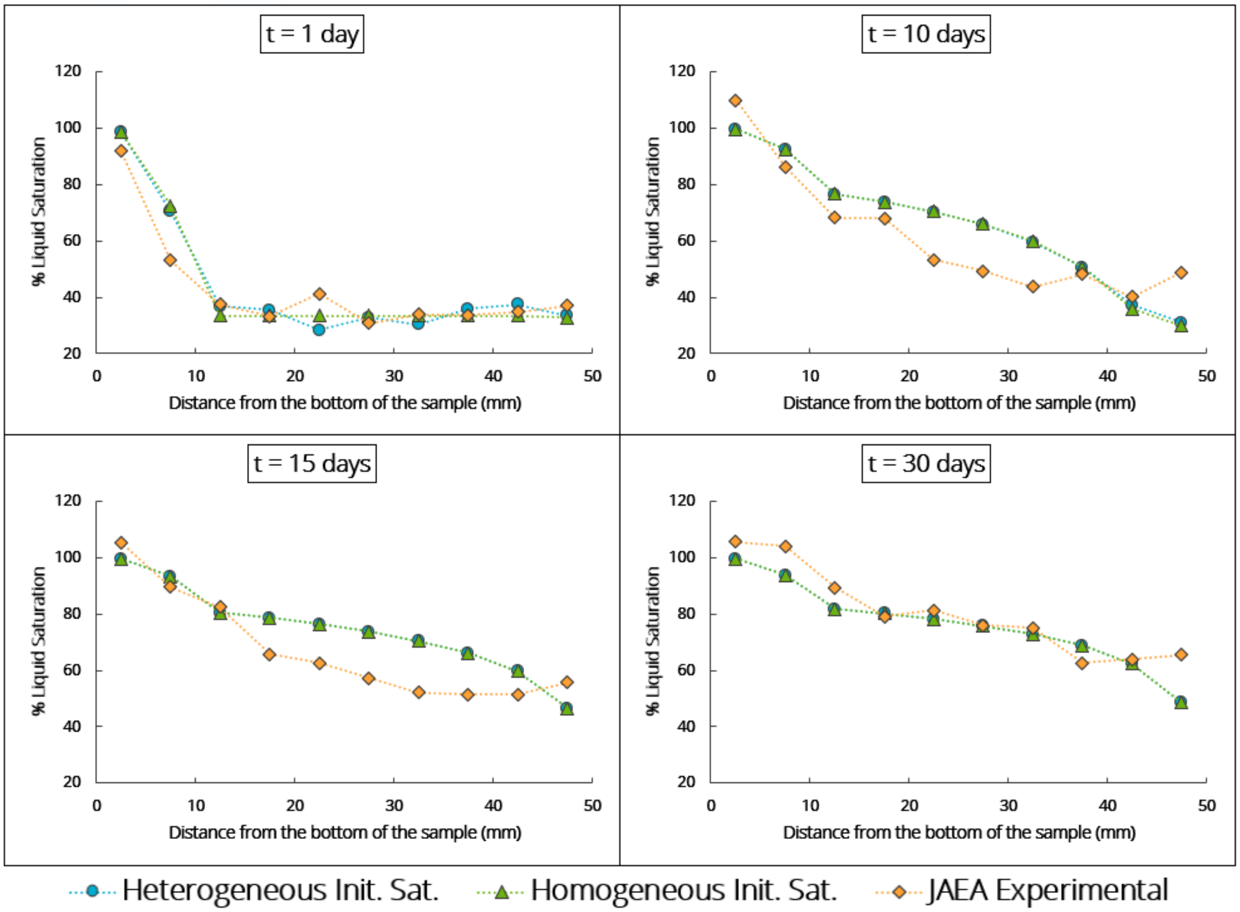

Figure 26. Saturation over distance profiles at after 1, 10, 15, and 30 days of saturation time, for the DW case. (Note: In the 10-, 15-, and 30-day plots, the plotted results for the homogeneous and heterogeneous cases are nearly identical.)

The results of the GW case are summarized in Figure 27. As with the DW case, after 1 day of saturation time, the profiles of the PFLOTRAN simulations are similar to that of the experimental data even when the model noticeably overpredicts saturation at 7.5 mm from the bottom of the sample. Discrepancies at 10 and 14 days persist as the PFLOTRAN simulations overestimate saturation closer to the bottom of the sample and underestimate closer to the top of the sample. As before, differences between simulations and experimental data are reduced at 30 days with the only notable departures occurring near the top and bottom of the sample.

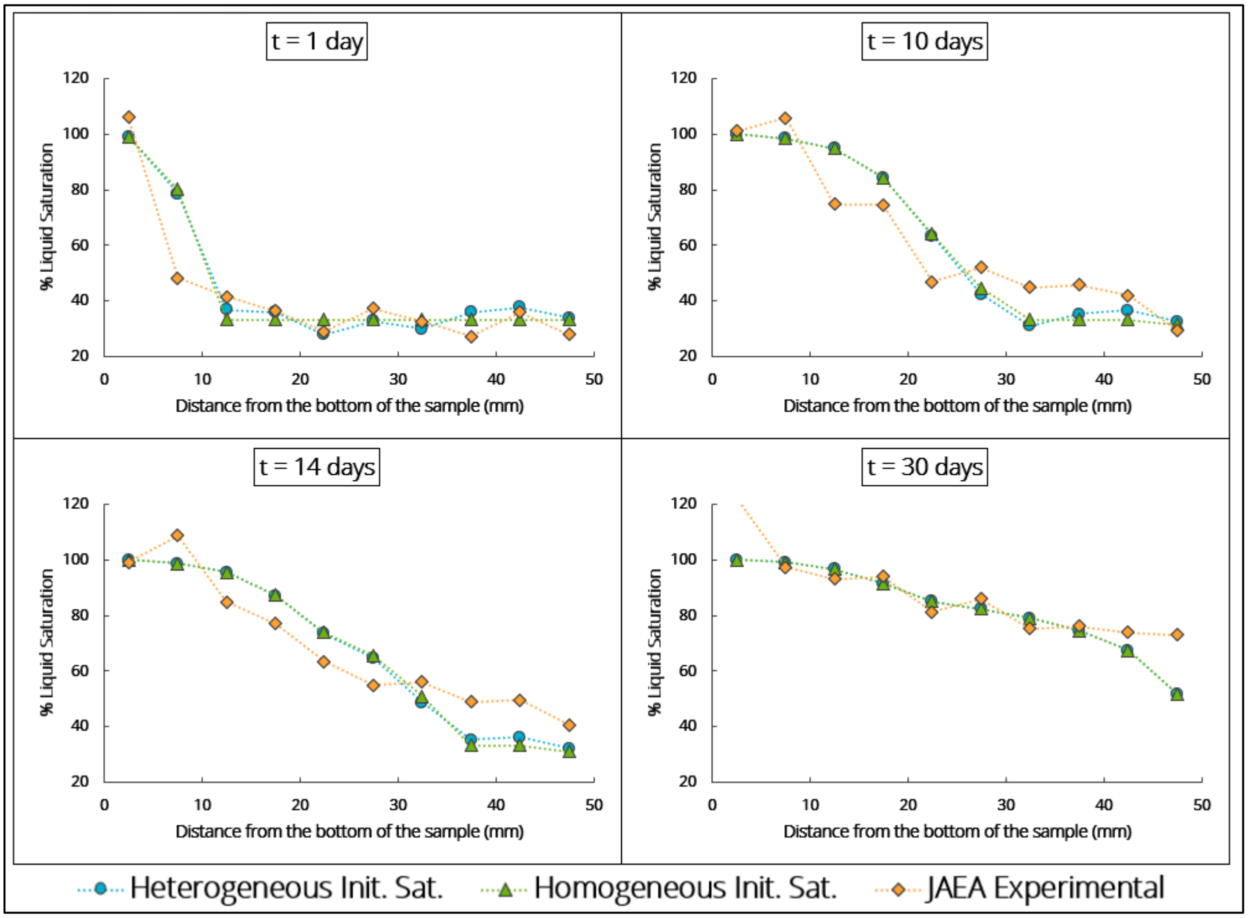

Figure 27. Saturation over distance profiles at after 1, 10, 14, and 30 days of saturation time, for the GW case. (Note: In the 30-day plot, the homogeneous and heterogeneous cases plot almost identically.)

Initial saturation profiles (homogeneous vs. heterogeneous) primarily affect predicted saturation profiles at early times. That is, the difference between model predictions made based on homogeneous vs. heterogeneous initial saturation decreases as simulated time increases. Figure 28 shows the largest difference among the homogeneous vs. heterogeneous initial saturation cases at any given time (arbitrary location along the sample). At any given time, the difference in predicted saturation between the two initial saturation profiles decreases and eventually drops well below 1%. Discrepancies are smaller at earlier times in the DW than in the GW simulations.

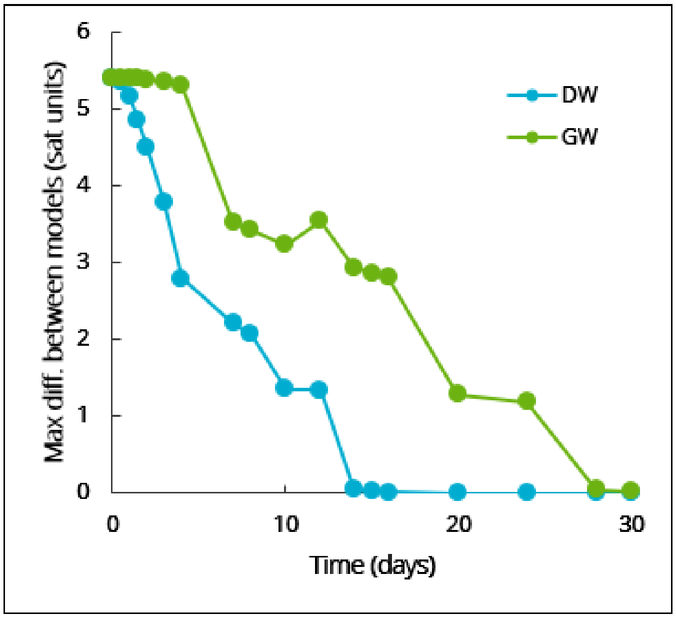

Figure 28. Maximum observed differences in predicted % (point) saturation at any sample location with time between simulations with homogeneous and heterogeneous initial saturation conditions.

S1-4 Results

The modeling results described in this section for experiment S1-4 are preliminary and as such are considered work in progress. The predicted temperature profile across the sample is approximately linear as seen in Figure 29. However, as the simulation progresses, slight deviations from linearity are observed within the bottom region of the sample closer to the heat source.

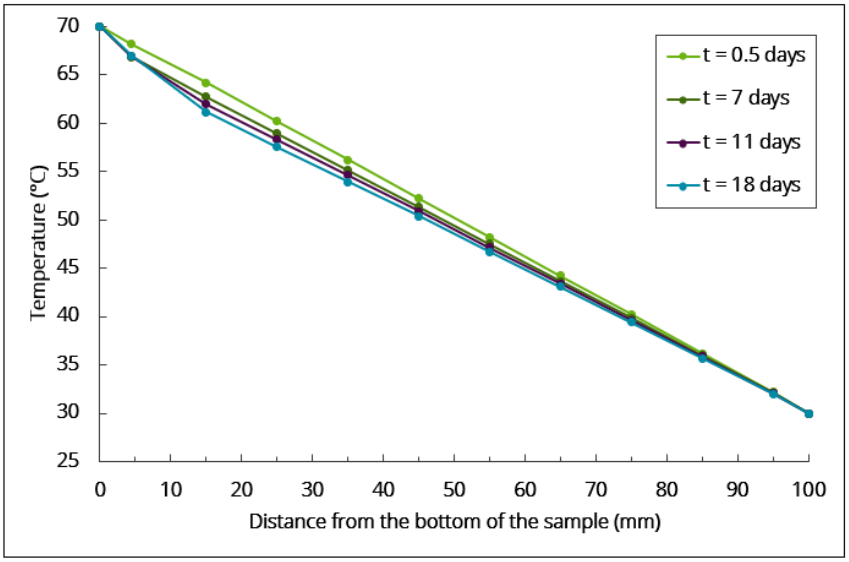

Figure 29. Temperature profile in the PFLOTRAN model of Experiment S1-4 where permeability was set to 5e-18 m^2.

As reported previously, the PFLOTRAN simulations using uniform permeabilities through the bentonite domain did not closely replicate the trends in liquid saturation observed in the S1-4 experimental data, particularly close to the bottom of the sample where it is hotter. For this reason, it was decided to divide the bentonite domain into five permeability zones as shown in Figure 25. An initial saturation of 34% is assumed in the current simulations, as opposed to 32% used in the previous report. Figure 30 shows the simulation results using stratified and homogenous permeabilities along with experimental data. The stratified permeability approach is better in representing some of the spatio-temporal trends at the top and bottom of the sample. However, more work is needed to achieve a better fit to the whole experimental data set. It is worth noting that the experimental observations of Villar et al. (2008a, b) show very similar sigmoidal or S-shape trends of water content data as a function of distance from the heated end. However, these experiments were conducted under different thermal and boundary conditions and with different column dimensions and bentonite material. Still, both experiments show similarly low levels of water content and/or liquid saturation near the heated end of the column, even with different boundary conditions. Villar et al. (2008b) also used a 1-D fully coupled thermal-hydrological-mechanical (THM) model to simulate the results of Villar et al. (2008a) for the bentonite hydration experiments.

Model predictions of liquid saturation using a uniform permeability tend to underpredict the S1-4 experimental data at the top of the sample (Figure 30). Achieving low saturations at early times near the bottom of the sample using either the stratified or uniform permeabilities is also difficult, even though a better match is obtained at later times. This is also indicative of the highly dynamic changes in saturation and relative permeabilities with time. Overall, the S-shape form of the saturation curve as a function of distance from the heated end as observed in the water content experimental data is predicted by the model for the simulated times. Parameter sensitivity evaluations on the van Genuchten and Mualem-van Genuchten formulations implemented in PFLOTRAN to represent water retention behavior are still ongoing. Preliminary observations of this sensitivity analysis indicate that changes in permeabilities in the stratified bentonite regions have a much larger effect on the resulting saturation profiles. Therefore, the analysis will focus on the behavior of relative permeabilities with time along with their corresponding regions in the column. The lack of mechanical effects in the model may be a limitation in predicting volumetric changes in the bentonite. This may be important in regions of high thermal loads as observed and analyzed by Villar et al. (2008a, b). Even with the “reduced order physics” in the current model, the overall bentonite saturation behavior is well represented under the thermal conditions and further work will determine if such porous medium heterogeneities captured by the stratified permeability approach leads to improvements of the model.

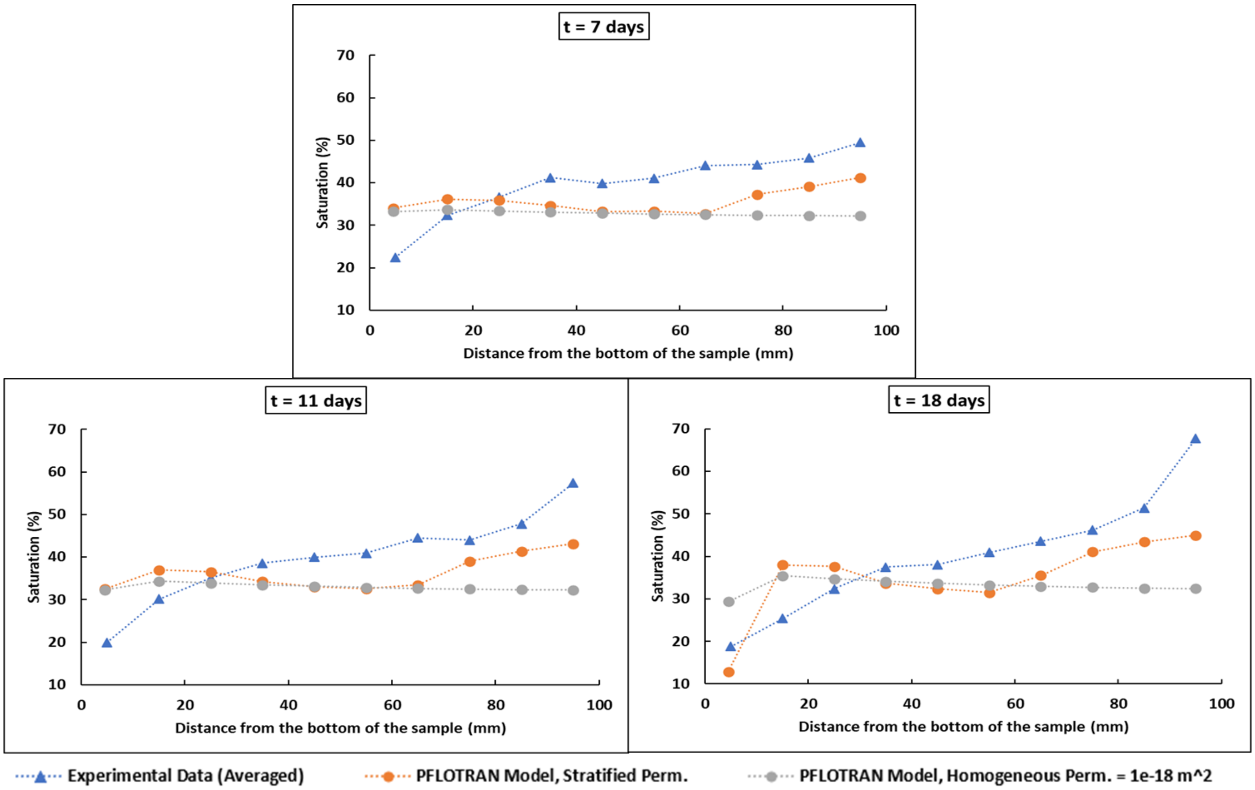

Figure 30. Saturation profiles for PFLOTRAN simulations of Experiment S1-4 using stratified permeabilities (shown in Figure 25) for 7, 11, and 18 days. These results are compared against the average of the experimental data and the case for homogeneous permeability through the domain.

Conclusions

The capability of a 1-D PFLOTRAN model to simulate the S1-3 bentonite saturation experiment has been demonstrated and validated against experimental data. Some work remains to refine 1-D PFLOTRAN simulations of the experiment S1-4 (still in progress) which include further evaluation of the stratified permeability approach to better fit the experimental data. For this effort, the DAKOTA software is being considered for optimization and sensitivity analysis of hydrological parameters. This analysis also involves sensitivities of water retention parameters and their effect on the prediction of material saturation and evolution of relative permeabilities. This is a dynamic non-isothermal problem that involves spatio-temporal variations in bentonite saturation which poses some challenges when fitting to experimental data. Further testing of PFLOTRAN capabilities will be done as part of DECOVALEX 2023 Task D contributions by the SNL team in the coming months. The DECOVALEX2023 project ends this year and SNL contributions will be documented in a final project report later this year.

7. DECOVALEX2023 Task D: Modeling of the Full-Scale EBS Experiment

Introduction

The deep geological nuclear waste disposal concept for Japan considers a high performance EBS with multibarrier safety functions (JNC, 2000a, b). The EBS design specifications and requirements for safety are described in JNC (2000b). The full-scale EBS test at Horonobe URL was active from January 15, 2015 until March 31, 2022, for approximately 2,632 days. The disposal concept for this heater test is that of a vertically-emplaced overpack containing two heaters surrounded by buffer barrier material composed of silica sand and Kunigel V1 bentonite. The region above the overpack emplacement zone was compacted / block backfill material made of a mix of bentonite and soil, lined with shotcrete and sealed with a concrete plug (see Figure 31). In addition to heating, the experiment also had controlled water inflow through a sand layer underneath the bentonite buffer material and within the backfill zones. Pressures, temperatures, and flow rates were recorded with sensors along the height of the canister and the surrounding bentonite region. Various physical parameters, such as total pressures (fluid + strain), temperature, and water potential were also provided.

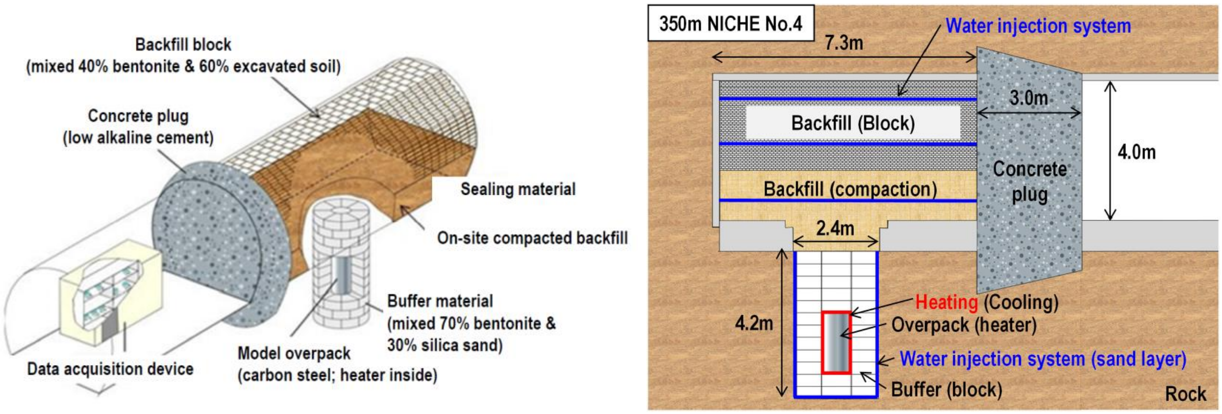

Figure 31. Schematics of the full-scale EBS experiment provided by the JAEA to the Task D modeling teams.

Modeling Approach

Computer simulations were done using PFLOTRAN, a massively parallel subsurface flow and reactive-transport code for hydrogeochemical applications (Lichtner et al, 2019). PFLOTRAN has thermal, hydrologic, and reactive transport capabilities, with several input modes that allow for single- and multiphase flow in variably saturated porous media.

The 2-D model uses PFLOTRAN's General Mode for thermal and hydrologic calculations of two-phase fluid flow. Reactive transport and chemical interactions were not considered in this model. The initial boundary conditions are Dirichlet for temperature. The model also assumes hydrostatic conditions for pressure in the Y direction and Dirichlet pressure in the X direction. Thermal conductivity is computed as a function of saturation based on input values for unsaturated and saturated states of each material. Permeability has been constrained to be constant and isotropic.

The water retention curve and relative permeabilities are computed as a function of liquid saturation. The van Genuchten model (van Genuchten, 1980) as implemented in the PFLOTRAN simulator is used to compute saturation in relation to capillary pressure (Eqs. 1-3; Lichtner et al., 2019, 2020):

$$S_e = (1 + (\alpha p_c)^n)^{-m} \qquad (1)$$

$$p_c = \frac{1}{\alpha}(S_e^{-1/m} - 1)^{1/n} \qquad (2)$$

$$S_e = \frac{S_l - S_{rl}}{1 - S_{rl}} \qquad (3)$$

Where S_e is effective saturation; α is the van Genuchten parameter with units of 1/pressure; p_c is capillary pressure; n and m are related constants; S_l is liquid saturation; and S_{rl} is residual liquid saturation. PFLOTRAN includes solver options to approximate capillary pressures at low saturations, either linearly or exponentially. Simulations shown herein use the exponential extrapolation.

The PFLOTRAN model domain is shown in Figure 32. The domain is composed of 185 cells in the X direction and 181 cells in Y direction, for a total of 33,485 cells. The overall domain size is 42.5 m by 42.1 m. The domain primarily consists of host rock surrounding the emplacement zone. This was done to avoid edge effects that could occur in response to the introduction of heat and water. Grid cells that make up host rock and some of the excavation damaged zone (EDZ) are larger than cells in the emplacement zone; larger cells are 40 cm by 40 cm, and smaller cells are 10 cm by 10 cm. (It should be noted that although this model is simulating 2-D flow, grid cell volume calculations require a nonzero Z dimension; this has been set to 5 m for all cells in the domain).

Sub-regions have been sized approximately to those given in the JAEA schematics. All areas within 0.5 m of the experiment region are treated as a high-permeability EDZ domain. Physical parameters for each material type were provided by JAEA. Where parameters were not provided, estimates were used. Input values to the model are shown in Tables 10 and 11.

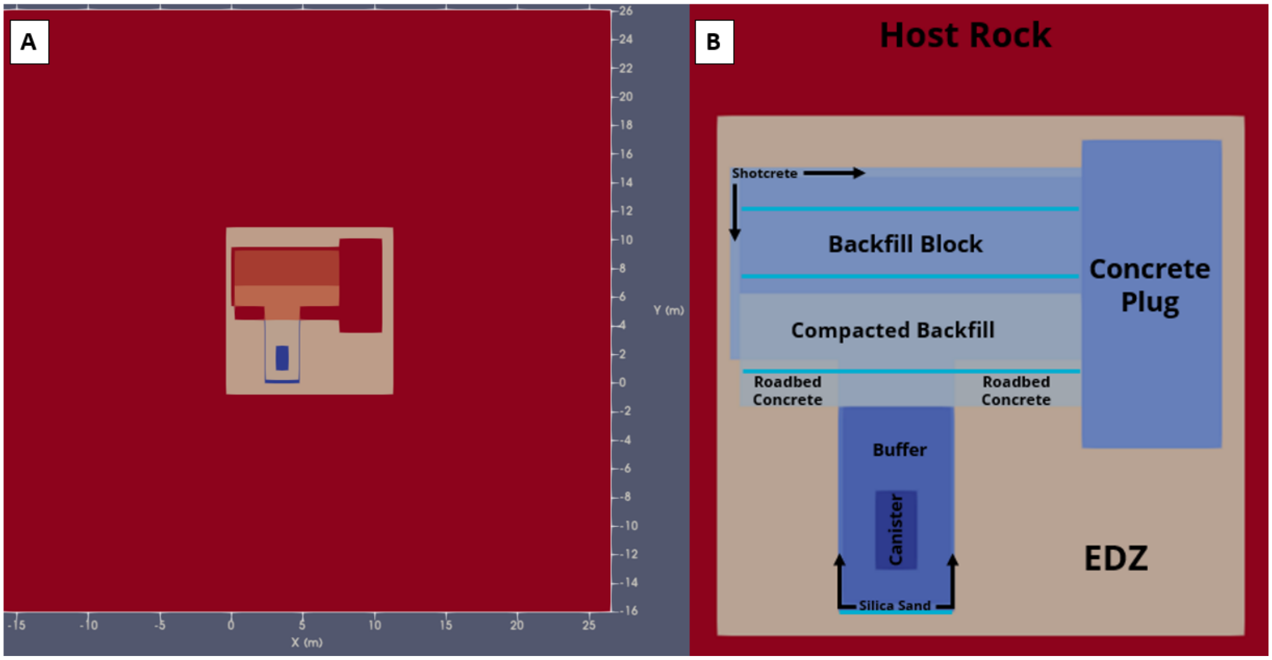

Figure 32. Step 2 PFLOTRAN model domain. (A) Overall PFLOTRAN model domain of Step 2, colored by initial saturation (red – 100%, blue – 0%). (B) Emplacement domain zones (solid blue lines indicate regions of water injection).

Table 10. Physical parameters of regions in the PFLOTRAN model of Step 2 of Task D.

Material	Initial Liquid Saturation	Porosity	Rock Density (kg/m^3)	Heat Capacity (J/kg-K)	Thermal Cond. Dry (W/K-m)	Thermal Cond. Wet (W/K-m)	Permeability (m^2)
Rock	1	0.416	1420	1270	0.579	1.237	7.5E-18
EDZ	0.6	0.416	1420	1270	0.579	1.237	1E-14
Compacted Backfill	0.8	0.538	1200	1647	0.224	1.273	3E-17
Backfill Block	0.91	0.46	1400	1437	0.339	1.463	1.76E-18
Roadbed Concrete	1	0.13	2280	1050	0.798*	2.56	9.32E-18
Shotcrete	0.99	0.328	2280	1050	0.798*	2.56	9.32E-18
Concrete Plug	1	0.13	2280	1050	0.798*	2.56	9.32E-18
Silica Sand	0	0.442	1400	1280	0.798*	2.04	1E-13
Buffer Material	0.58	0.328	1800	1135	0.798	1.94	2.81E-18
Overpack	0.01	0.001	1800	460	53	53	1E-30

*All data from or slightly modified from the JAEA data. Where dry thermal conductivities were not known, those of the buffer material were used as an estimate.

Table 11. van Genuchten water retention curve parameters adopted in the PFLOTRAN model of Step 2.

Material	m	α
Rock & EDZ	0.502	9.9E-03
All other materials	0.275	5.10E-07

The provided injection and power output data exhibit noisy behavior that required simplification. Some of the noise may be attributed to zero value measurements in the power data at certain times. Additionally, the provided flow and heating rates caused code run stability issues, including unrealistically high simulated pressures. As such, water injection rates and heating schedules were assumed based on simplified values constrained by the reported sensor data. The provided measurements are shown in Figure 33 and the simplified inputs are shown in Figure 34. Water inflow rates used in the model are much lower than those provided in the task description. Heating rates were modified to match thermocouple temperature measurements rather than using the power output data from the JAEA. The baseline used for comparisons to the EBS test were temperature readings halfway along the height of the overpack, corresponding to data from thermocouple TEOP004. Figure 35 shows the location of the thermocouples in the emplacement region and temperatures at TEOP004 over time.

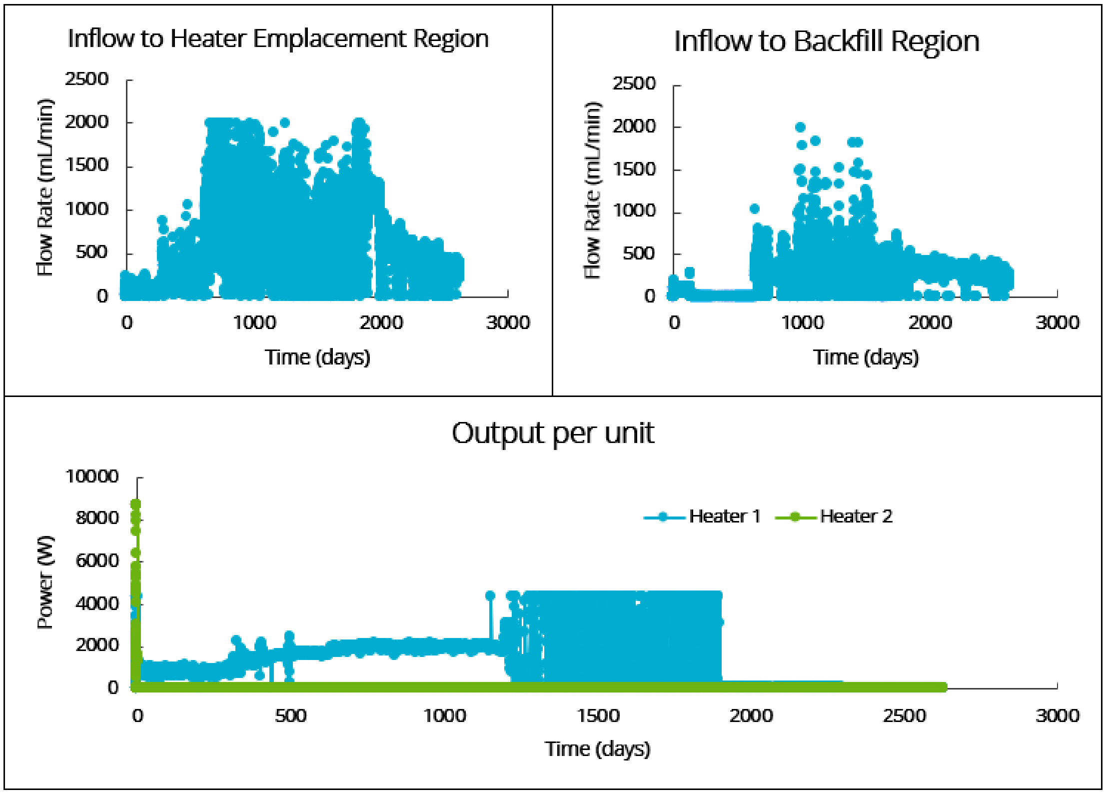

Figure 33. Experimental data for water inflow and power output in the full-scale EBS test.

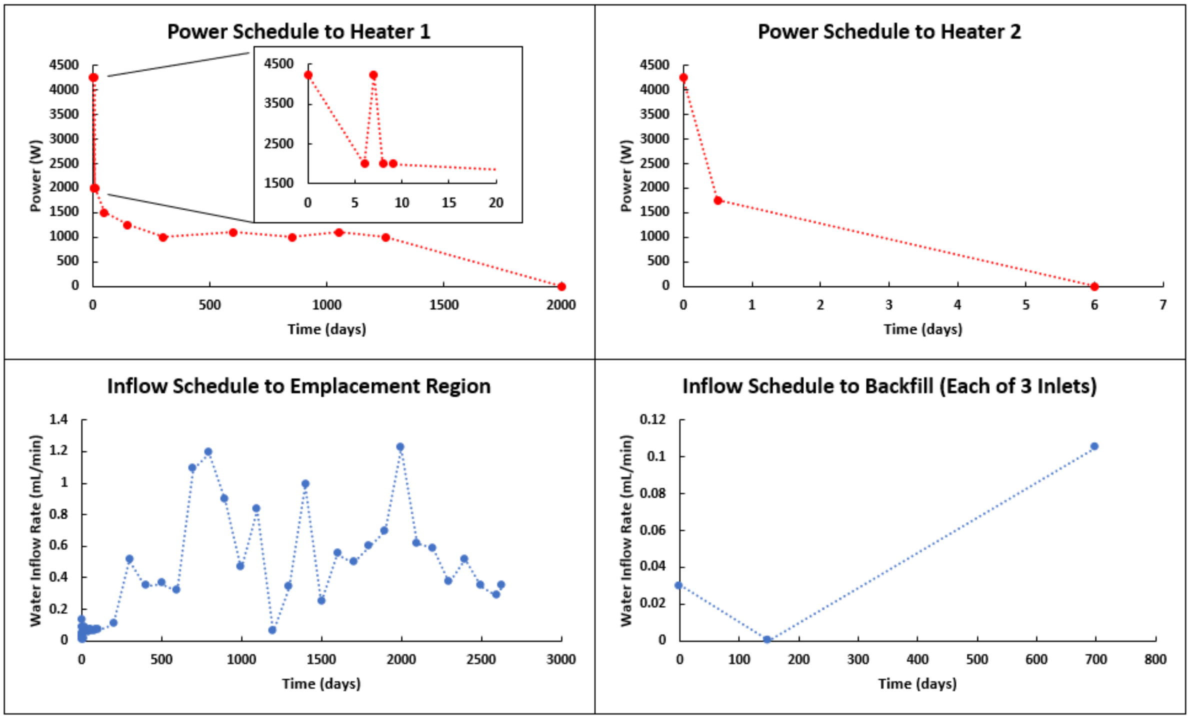

Figure 34. Simplified water inflow and power source time histories assumed in the model (dashed lines do not indicate continuity and are shown as a guide).

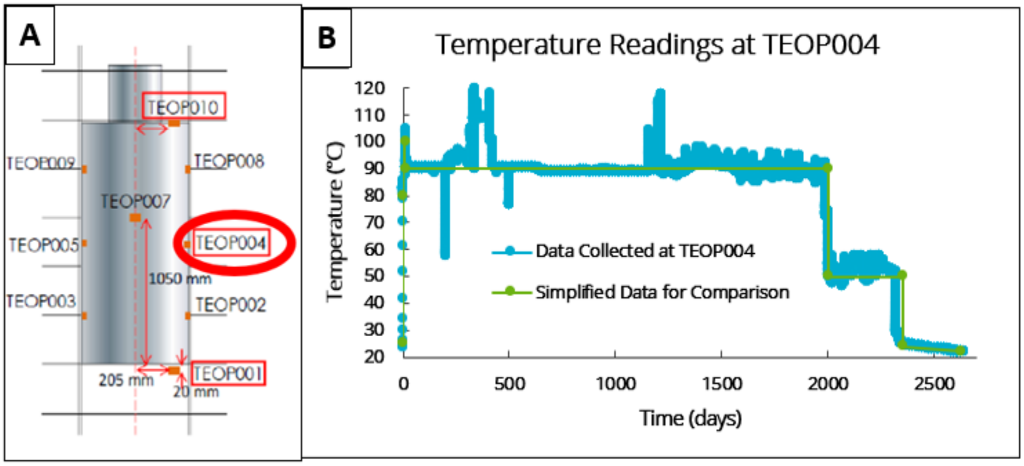

Figure 35. (A) Locations of thermocouples in the overpack region of the EBS Test. (B) Measurements of temperature at thermocouple TEOP400, used as a point of comparison against simulation data.

Discussion and Results

Simulated values of temperature immediately outside the overpack are summarized in Figure 36. The overall temperature trend has been approximately to within reasonable bounds of the sensor measurements. Notably, the current iteration of the PFLOTRAN simulation 1) is highly sensitive to oscillations in heater input and 2) does not successfully simulate up to the final time of t=2632 days and instead fails at t≈2468 days. The cause of this remains to be determined, however, it may be a result of an unstable system response to the steep decrease in temperature starting at t=2000 days. This sudden drop in temperature during this time is caused by the stepwise heater shutdown.

The JAEA does not provide saturation data for this heater test. However, water potential measurements (corrected during the DECOVALEX2023 meeting in Busan, Korea) in the backfilled domain are provided. These water potential measurements were not considered in this report but the corrected data will be evaluated when it becomes available. Total pressures measured by a sensor close to the canister are not expected to exceed ~1.8E+05 Pa over the course of the experiment. The liquid pressures in the simulation did not exceed 2.2E+05 Pa, which approximates the target pressure of~1.8E+05 Pa. However, a comparison of simulated liquid pressures and measured total pressures from the heater test is not entirely valid given the type of sensor used in the measurement.

Overall, the spatial and temporal evolution of saturation in the host-rock EDZ, bentonite buffer, and around the canister domains is driven by temperature. Starting from the heater and buffer region, the saturation front tends to move upwards concurrently with the saturation of the compacted and block backfill domains. This is expected given the injected water at these locations (Figure 32) and the buffer/backfill saturation behavior in these regions. Upon reaching high levels of saturation in the buffer/backfill regions, the saturation front tends to move towards the concrete plug domain. Figure 37 shows the initial and final saturation states of the model domain. As expected, the overall saturation behavior is strongly tied to the liquid pressure from the water injection system and with temperature. The simulation results also indicate that the model domain becomes highly saturated in ~700 to ~1000 days.

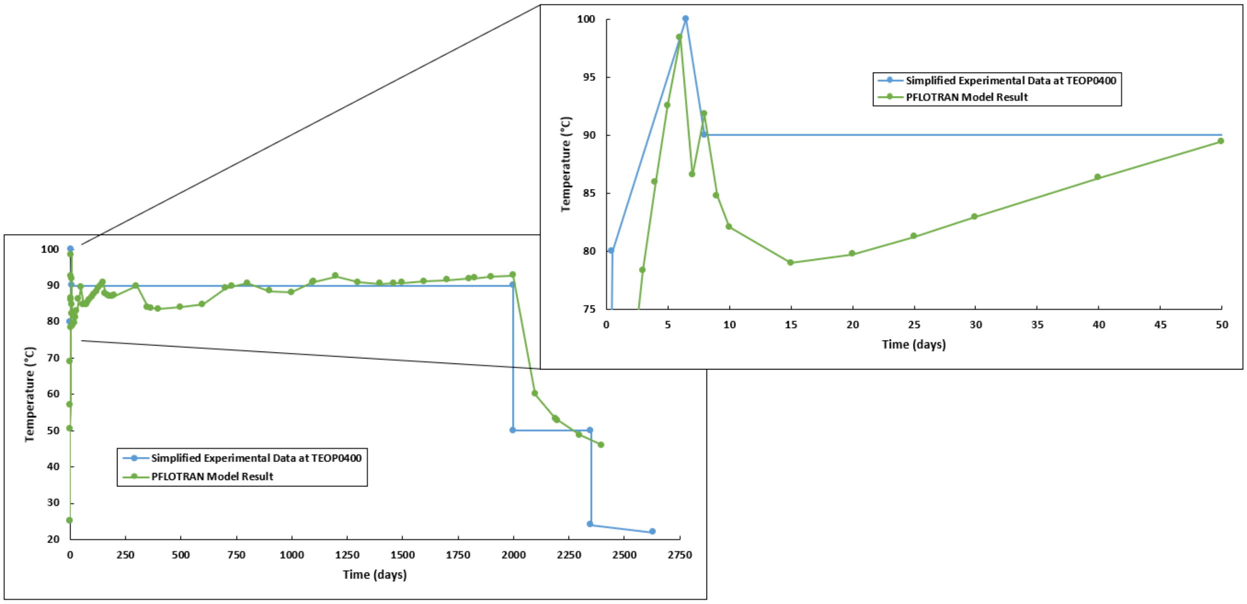

Figure 36. Simulated temperatures outside the overpack midpoint compared against simplified data from thermocouple TEOP0400.

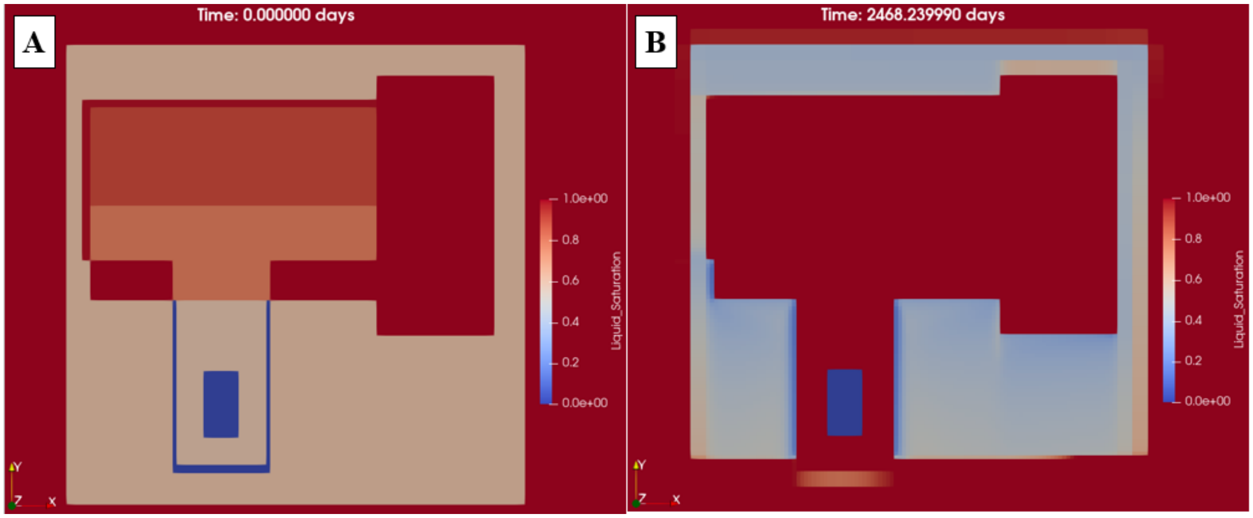

Figure 37. Initial (A) and final (B) liquid saturation in the domain predicted by the model. Blue indicates 0% saturation and red represents regions of high (~100%) saturation.

Concluding Remarks

PFLOTRAN 2-D simulations of the Full-Scale EBS Test at the Horonobe URL have made significant progress in representing key trends of this full-scale heater test experiment. Differences between 2-D flow simulations and the experiment still exist, but work is still ongoing towards the improvement of model predictions.

It should be recognized that the limitations of the 2-D mesh to represent the model domain necessitated modification of the experimental inputs to realistically characterize temperature observations. Additionally, PFLOTRAN is not currently able to simulate mechanical phenomena, such as bentonite swelling and related couplings that could affect porous media flow which limits the complete physical representation of the problem. Still, PFLOTRAN can model two-phase flow under non-isothermal conditions, which is a key aspect of fluid mass and heat transport in this problem. Expanding the model to a 3-D domain would be desirable to investigate the effects of inflow rates and temperature on saturation in a more realistic manner.

Future work

The simulations results discussed here are represent the final phase of the model refinement, as the final workshop of DECOVALEX2023 is scheduled for November 2023. Final iterations on this problem are expected to include some adjustments in the heating rate history and evaluating hydrologic parameter sensitivities.

FY24 activities (and the remainder of FY23) will include:

- Finalize PFLOTRAN model refinements and simulation tests.
- Development of the final report for DECOVALEX2023 along with the JAEA team.
- Determine which task(s) of DECOVALEX2027 (starting January 2024) are of interest to the disposal in argillite work package. Currently, two draft tasks appear to be well align with the interests of this work package: “Task D: ANALOG – Multiscale Long-term Radionuclide

Transport at Cigar Lake Uranium Ore Body" and "Task G: BaSiSS – Bentonite and Sand in Sealing Systems." Both tasks appear to involve modeling that could be done with PFLOTRAN and would be a suitable next step from the work done for DECOVALEX2023.

8. Summary and Conclusions

- **Molecular dynamics (MD) simulations of H_2 interactions and GCMC studies of H_2O adsorption at clay interlayers**
  - Metadynamics molecular simulations were used to investigate the free energy landscape of H_2 intercalation into hydrated clay interlayers. The results indicate that H_2 intercalation is thermodynamically unfavorable. This work has been published in the paper "Low Hydrogen Solubility in Clay Interlayers Limits Gas Loss in Hydrogen Geological Storage" by Ho et al. (2023) published in the journal *Sustainable Energy and Fuels*.
  - GCMC metthods were used to evaluate water adsorption isotherms for expandable clay models corresponding to transitions between standard hydration states. This effort has established a method of creating model systems to explore the effect of layer bending on the thermodynamic and mechanical properties of expandable clays.
- **SKB Task 12: 1-D Reactive-Transport Modeling of Cement-Bentonite Interactions**
  - Ongoing PFLOTRAN 1-D reactive-transport model for cement-bentonite interactions has evolved, with more recent modifications to the past year problem description and it is still work in progress.
  - Similar to results reported in FY22, current results of the "blind prediction" show a strong temporal dependence on changes in pore solution chemistry, particularly at early times up to ~100 years.
- **Reactive-Transport and Reaction Path Modeling of OPC Leaching**
  - Updates to the 1-D PFLOTRAN model of OPC cement leaching simulation of the EPA 1315 tests generate results that provide good representations of the overall experimental leaching trends for temporal solute concentration profiles based on the major cement phase constituents and associated thermodynamic data.
  - Reaction path model representation of the EPA Method 1313 test for OPC leaching confirms that the cement phase assemblage developed from the PFLOTRAN simulations generate results that are in good agreement with experimental data.

- **DECOVALEX2023 Task D: PFLOTRAN Modeling of the S1-3 and S1-4 Bentonite Saturation Experiments, and Full-Scale EBS Experiment at the Honorobe URL Site**

  - **S1-3 isothermal bentonite saturation:** The 1-D PFLOTRAN model can simulate the S1-3 bentonite isothermal saturation experiment whether initially homogeneous or heterogeneous conditions of initial saturation are considered.
  - **S1-4 non-isothermal bentonite saturation:** The refined 1-D PFLOTRAN model to simulate the S1-4 bentonite non-isothermal saturation experiment using a stratified permeability approach produced results that are in better agreement with test data.
  - **2-D modeling of the EBS Experiment at the Honorobe URL Site:** Successful simulations have been carried out through the heater test time history through modifications of test conditions to represent temperature profiles.

Future Work

Planned work focused on **MD and GCMC studies of clay interlayer interactions** and **modeling of leaching experiments** for FY24 (and the remainder of FY23):

- **MD studies of clay interlayer interactions**
  - Investigate the interactions of other products of canister corrosion reactions (e.g., Fe^{2+}) with clay.
  - MD simulations of the bent models at equilibrium water loadings will be performed to further characterize the structural, thermodynamic, and mechanical properties associated with transitions between the bent and flat configurations.

- **1-D Reactive Transport and Reaction Path Modeling of Ordinary Portland Cement (OPC) Leaching Experiments**
  - Focus on the EQ3/6 reaction path modeling towards resolving discrepancies between this and the VU model.

Planned work on international collaborations work for FY24 (and the remainder of FY23):

- **SKB TF (Task 12):** Continue 1-D PFLOTRAN reactive-transport modeling of cement-bentonite interactions of updated modeling constrains. Focus on subtask C for the unsaturated case.
- **DECOVALEX2023 Task D:** Finalize 1-D PFLOTRAN TH simulations of bentonite saturation experiments and 2-D TH simulations of the full-scale EBS heater test. This is the last year for the DECOVALEX2023 phase.

Other work to be considered in FY24:

- Geochemical modeling of LANL hydrothermal experiments on barrier materials. Some of this work is ongoing, specifically on the aqueous speciation at high temperatures of sampled solutions.
- Reaction path modeling of LANL hydrothermal experiments on barrier materials.

9. References

Berner, U., Kulik, D.A. and Kosakowski, G. (2013) Geochemical impact of a low-pH cement liner on the near field of a repository for spent fuel and high-level radioactive waste. Physics and Chemistry of the Earth, Parts A/B/C 64, 46-56.

Birkholzer, J., Faybishenko, B., Ajo-Franklin, J., Borglin, S., Dobson, P., Gilbert, B., Guglielmi, Y., Fox, P.M., Kim, K., Nico, P., Rutqvist, J., Sonnenthal, E., Xu, H., Wu, Y., Zheng, L., Caporuscio, F.A., Reimus, P., Viswanathan, H., Jove-Colon, C.F., Wang, Y., Kuhlman, K., Matteo, E., McMahon, K. and Zavarin, M. (2019) International Collaboration Activities in Different Geologic Environments, Spent Fuel Waste Science and Technology (SFWST) Deliverable M2SF-19LB010307012 (LBNL-2001239). Lawrence Berkeley National Laboratories (LBNL), Berkeley, CA USA, 356 pp.

Blanc, P. (2017) Thermoddem: Update for the 2017 version, Report BRGM/RP-66811-FR.

Blanc, P., Lassin, A., Piantone, P., Azaroual, M., Jacquemet, N., Fabbri, A. and Gaucher, A., (2012) Thermoddem: A geochemical database focused on low temperature water/rock interactions and waste materials. Applied Geochemistry, 27: 2107-2116.

Birkholzer, J., and Faybishenko, B. 2020. International Collaboration Activities in Geologic Disposal Research: FY20 Progress, Spent Fuel Waste Science and Technology (SFWST), Milestone Report, M2SF-20LB010307012, LBNL-2001353, Lawrence Berkeley National Laboratory, Berkeley, CA USA, 333 pp.

EPA, U.S. EPA. (2012) Liquid-solid Partitioning as a Function of Extract pH using a Parallel Batch Extraction Procedure. Environmental Protection Agency Method 1313, Service Center for Environmental Publications (NSCEP), Cincinnati, OH, USA, 28 pp.(https://www.epa.gov/sites/default/files/2015-12/documents/1313.pdf)

EPA, U.S. EPA. (2013) Method 1315, Mass Transport Rates of Constituents in Monolithic or Compacted Granular Materials Using a Semi-dynamic Tank Leaching Procedure National Service Center for Environmental Publications (NSCEP), Cincinnati, OH, USA, 36 pp. (https://www.epa.gov/sites/default/files/2015-12/documents/1315.pdf).

Gaboreau, S., Lerouge, C., Dewonck, S., Linard, Y., Bourbon, X., Fialips, C.I., Mazurier, A., Pret, D., Borschneck, D., Montouillout, V., Gaucher, E.C. and Claret, F. (2012) In-Situ Interaction of Cement Paste and Shotcrete with Claystones in a Deep Disposal Context. Am J Sci 312, 314-356.

Gruber, C., Steen, M., Brown, K.G., Delapp, R., Matteo, E.N., Klein-BenDavid, O., Bar-Nes, G., Meeussen, J.C., Ayers, J.C. and Kosson, D.S. (2022) Cement-carbonate rock interaction under saturated conditions: From laboratory to modeling. Cement Concrete Res 160, 106899.

JNC (2000a) H12: Project to Establish the Scientific and Technical Basis for HLW Disposal in Japan, Project Overview Report. Japan Nuclear Cycle Development Institute (JNC), Japan, p. 395 pp.

JNC (2000b) H12: Project to Establish the Scientific and Technical Basis for HLW Disposal in Japan (Supporting Report 2), Repository Design and Engineering Technology. Japan Nuclear Cycle Development Institute (JNC), Japan, 712 pp.

Jové Colón, C.F., Payne, C., Coker, E., Boisvert, L., Sanchez, A., Knight, A. and Hadgu, T. (2019) Argillite Disposal R&D International Collaborations interim report - 2019 (SAND2019-6731 R), Prepared for U.S. Department of Energy (DOE) Spent Fuel Waste Science and Technology (SFWST). Sandia National Laboratories, Albuquerque, New Mexico, 51 pp.

Jové Colón, C.F., Ho, T.A., Coker, E., Hadgu, T., Lopez, C. M., Sanchez, A., Kruichak, J.N., Mills, M.M., and Sanchez, A. (2020) International Collaborations Activities on Disposal in Argillite R&D: Characterization Studies and Modeling Investigations (SAND2020-14037 R), DOE Spent Fuel and Waste Science and Technologies (SFWST). Sandia National Laboratories, Albuquerque, New Mexico, 60 pp.

Jové Colón, C.F., Ho, T.A., Coker, E., Lopez, C.M., Kuhlman, K., Sanchez, A., Mills, M.M., Kruichak, J.N. and Matteo, E.N. (2021) International Collaborations Activities on Disposal in Argillite R&D: Characterization Studies and Modeling Investigations (SAND2021-6358 R), DOE Spent Fuel and Waste Science and Technologies (SFWST). Sandia National Laboratories, Albuquerque, New Mexico.

Jové Colón, C.F., Ho, T.A., Coker, E., Lopez, C.M., Kuhlman, K., Sanchez, A., Mills, M.M., Kruichak, J.N. and Matteo, E.N. (2022) International Collaborations Activities on Disposal in Argillite R&D: Characterization Studies and Modeling Investigations (SAND2022-10733 R), DOE Spent Fuel and Waste Science and Technologies (SFWST). Sandia National Laboratories, Albuquerque, New Mexico.

Jové Colón, C.F., Ho, T.A., Lopez, C.M., Sanchez, A., Coker, E., Kuhlman, K., Rutqvist, J., Guglielmi, Y., Hu, M., Sasaki, T., Yoon, S., Steefel, C.I., Tournassat, C., Mital, U., Luu, K., Wainright, H., Sauer, K.B., Caporuscio, F.A., Rock, M.J., Zandanel , A.E., Zavarin, M., Chang, E. and Han, S.-H. (2022) Evaluation of Nuclear Spent Fuel Disposal in Clay-Bearing Rock - Process Model Development and Experimental Studies, Spent Fuel Waste Science and Technology (SFWST) Deliverable M2SF-22SN010301072; SAND2023-03169R. Sandia National Laboratories, Albuquerque, New Mexico USA, p. 381 pp.

Kosakowski, G. and Berner, U. (2013) The evolution of clay rock/cement interfaces in a cementitious repository for low- and intermediate level radioactive waste. Phys Chem Earth 64, 65-86. Hisatake, K., Tanaka, S. and Aizawa, Y. (1993) Evaporation rate of water in a vessel. J Appl Phys 73, 7395-7401.

Lichtner, P. C., Hammond, G. E., Lu, C., Karra, S., Bisht, G., Andre, B., Mills, R. T., Kumar, J., & Frederick, J. M. (2020). PFLOTRAN User Manual, Technical Report (https://www.pflotran.org/).

Lichtner, P. C., et al. (2019). PFLOTRAN user manual: A massively parallel reactive flow and transport model for describing surface and subsurface processes. http://documentation.pflotran.org

Lothenbach, B., Kulik, D.A., Matshei, T., Balonis, M., Baquerizo, L. Dilnesa,B., Miron, G.D., Myers, R.J. (2019) Cemdata18: A chemical thermodynamic database for hydrated Portland cements and alkali-activated materials. Cement and Concrete Research 115: 472-506.

Marty, N.C.M., Bildstein, O., Blanc, P., Claret, F., Cochepin, B., Gaucher, E.C., Jacques, D., Lartigue, J., Liu, S., Mayer, K.U., Meeussen, J.C.L., Munier, I., Pointeau, I., Su, D., Steefel, C.I. (2015). Benchmarks for multicomponent reactive transport across a cement/clay interface. Computers and Geosciences 19: 635-653.

Matteo, E.N., Dewers, T.A., Jove Colon, C.F., Hadgu, T., Gruber, C., Steen, M., Brown, K., Delapp, R., Brown, L. and Kosson, D. (2019) FY19 Progress of EBS International Collaborations. Sandia National Laboratories; M4SF-19SN010308082; SAND2019-10787 R, Albuquerque, NM USA, p. 38 pp.

Mualem, Y. (1976) A new model for predicting the hydraulic conductivity of unsaturated porous media. Water Resources Research 12, 513-522.

Sassani, D., Birkholzer, J., Camphouse, R., Freeze, G. and Stein, E. (2021) SFWST Disposal Research R&D 5-Year Plan-FY2021 Update (SAND2021-12491R). Sandia National Labs. (SNL-NM), Albuquerque, NM (United States).

Soler, J.M. (2012) High-pH plume from low-alkali-cement fracture grouting: Reactive transport modeling and comparison with pH monitoring at ONKALO (Finland). Appl Geochem 27, 2096-2106.

Soler, J.M. and Mader, U.K. (2010) Cement-rock interaction: Infiltration of a high-pH solution into a fractured granite core. Geologica Acta 8, 221-233.

Sugita, Y. (2022) Task D Full-scale engineered barrier system experiment at Horonobe URL: Task introduction. DECOVALEX2023 5th Workshop, 25-29 April 2022. [Virtual meeting presentation]

van Genuchten, M.T. (1980) A Closed-form Equation for Predicting the Hydraulic Conductivity of Unsaturated Soils. Soil Sci Soc Am J 44, 892-898.

Villar, M.V., Fernández, A.M., Martín, P.L., Barcala, J.M., Gómez-Espina, R. and Rivas, P. (2008a) Effect of Heating/Hydration on Compacted Bentonite: Tests in 60-cm Long Cells, Informes Técnicos CIEMAT 1146. Madrid, Spain, 111 pp.

Villar, M., Sánchez, M. and Gens, A. (2008b) Behaviour of a bentonite barrier in the laboratory: experimental results up to 8 years and numerical simulation. Physics and Chemistry of the Earth, Parts A/B/C 33, S476-S485.

Villar, M.V. and Lloret, A. (2008c) Influence of dry density and water content on the swelling of a compacted bentonite. Appl Clay Sci 39, 38-49.

Villar, M.V. (2013) Long-term THM tests reports: Isothermal infiltration tests with materials from the HE-E (Deliverable - N°: D2.2-7.2) - CIEMAT Technical Report CIEMAT/DMA/2G210/07/2013, Long-term Performance of Engineered Barrier Systems PEBS. Centro de Investigaciones Energeticas, Medioambientales y Tecnologicas (CIEMAT), Madrid, Spain, 36 pp.

Xie, M.L., Mayer, K.U., Claret, F., Alt-Epping, P., Jacques, D., Steefel, C., Chiaberge, C. and Simunek, J. (2015) Implementation and evaluation of permeability-porosity and tortuosity-porosity relationships linked to mineral dissolution-precipitation. Computat Geosci 19, 655-671.

Investigation of Coupled Processes in Argillite Rock: FY23 Progress – LBNL (Part II)

1. Introduction

Clayey geological formations, such as shale and argillite, have been considered as potential host rocks for geological disposal of high-level radioactive waste (HLW) throughout the world because of their low permeability, low diffusion coefficient, high retention capacity for radionuclides, and capability to self-seal fractures. While fractures can occur in argillite and shale, these formations often demonstrate the tendency to self-seal fractures, reducing the effects of fractures on bulk permeability. Other favorable characteristics of argillite/shale are the strong sorptive behavior for many radionuclides, reducing conditions because of the lack of oxygen transport from the surface, and chemical buffering the effects of materials that could be introduced during repository construction and operation.

Related to research on argillite formations within the Spent Fuel and Waste Science and Technology (SFWST) Campaign, the focus is on repository-induced interactions of argillite host rock and an engineered barrier system (EBS) bentonite, which may affect the potential repository safety characteristics. This includes investigations of thermal-hydrological-mechanical-chemical (THMC) processes that occur because of repository construction and waste emplacement.

Within the SFWST program, Lawrence Berkeley National Laboratory (LBNL)’s work on argillite disposal research and development (R&D) started in 2010 by leveraging on previous experience on modeling of coupled thermal-hydrological-mechanical (THM) processes within domestic and international nuclear waste programs (Rutqvist et al., 2001; 2002; 2011). Much of this work has been dedicated to the development and validation of coupled THM simulators for modeling of near-field coupled processes. From a safety assessment perspective, near-field coupled processes are relatively short-lived, but could give rise to permanent changes, such as the formation of a thermally altered or a damaged zone around excavations, which could provide a pathway for transport of radionuclides if released from a waste package (Figure 1-1). For a repository hosted in clay-rock, the mechanical evolution and swelling of the protective buffer surrounding the waste package (often bentonite) are imperative to its functions, such as to provide long-term mechanical support to seal the Excavation Disturbed Zone (EDZ). At the same time, the mechanical evolution of the buffer is governed by complex coupled interactions of temperature and hydraulics, micro- and macro-structures of bentonite and the host rock. Currently, more advanced constitutive mechanical models are being applied, which, however, require a large number of input parameters to describe processes at different field scales. It is important to test and validate the models at a relevant field scale, in addition to verification and validation against independent analytical and numerical solutions and laboratory experiments.

Figure 1-2 illustrates a schematic representation of coupled THM processes at the repository scale, such as activation of faults or fractures, creation of new fractures due to thermal stress, and thermal pressurization. Thermal pressurization is a process of pressure increase due to thermal expansion of pore-fluids being trapped because of low permeability of a porous argillite host rock. Another potential cause of near field coupled THM processes is gas generation within the waste package, as well as seismic motion from a distant earthquake. The potential implication for repository performance related to the activation of faults includes creation of (permeable) flow paths, induced seismicity and a potential shear load on a waste canister.

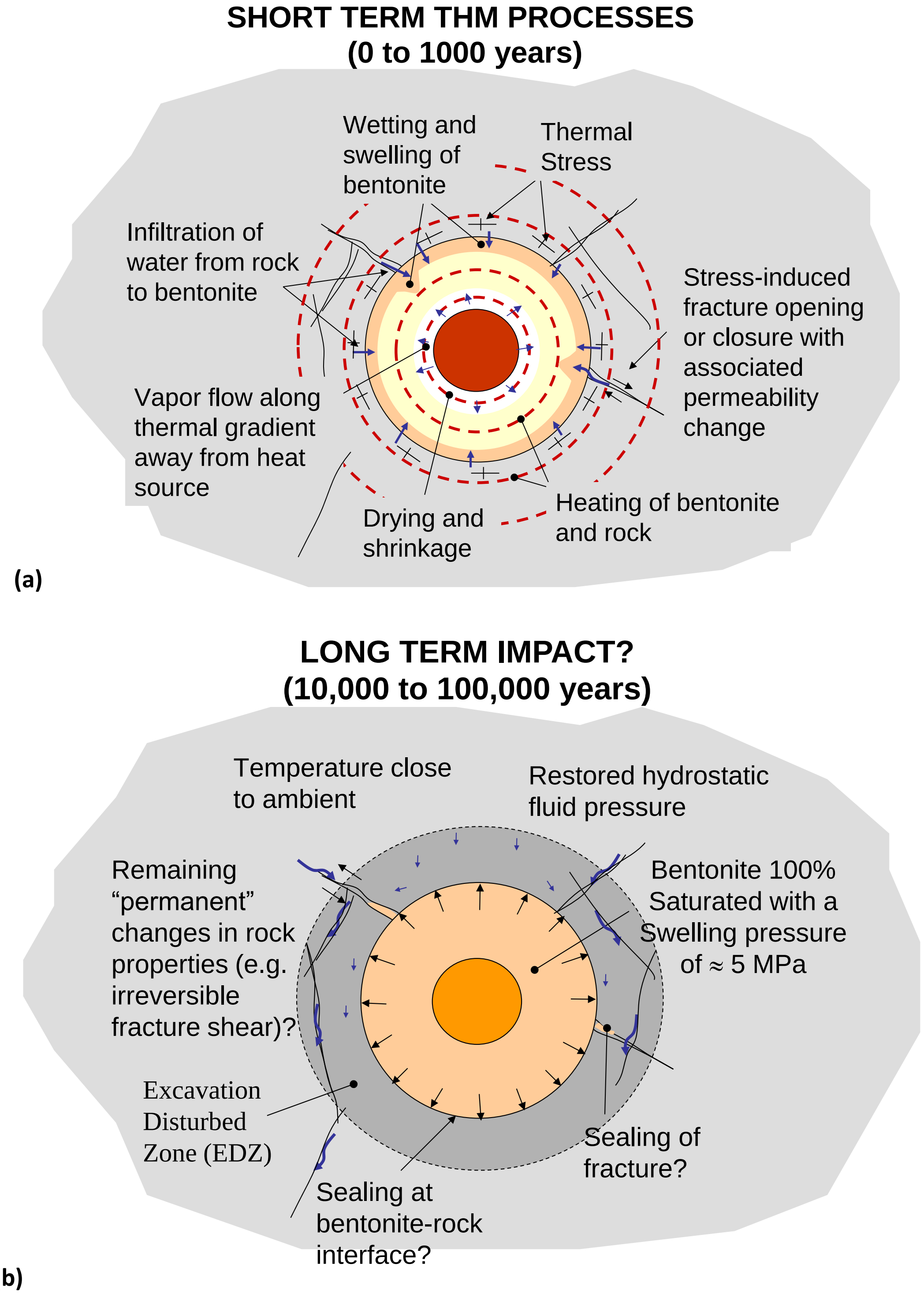

Figure 1-1. Schematic illustration of coupled THM processes driven by heat released from the waste package: (a) short-term THM processes, and (b) long-term impact of early time coupled THM processes.

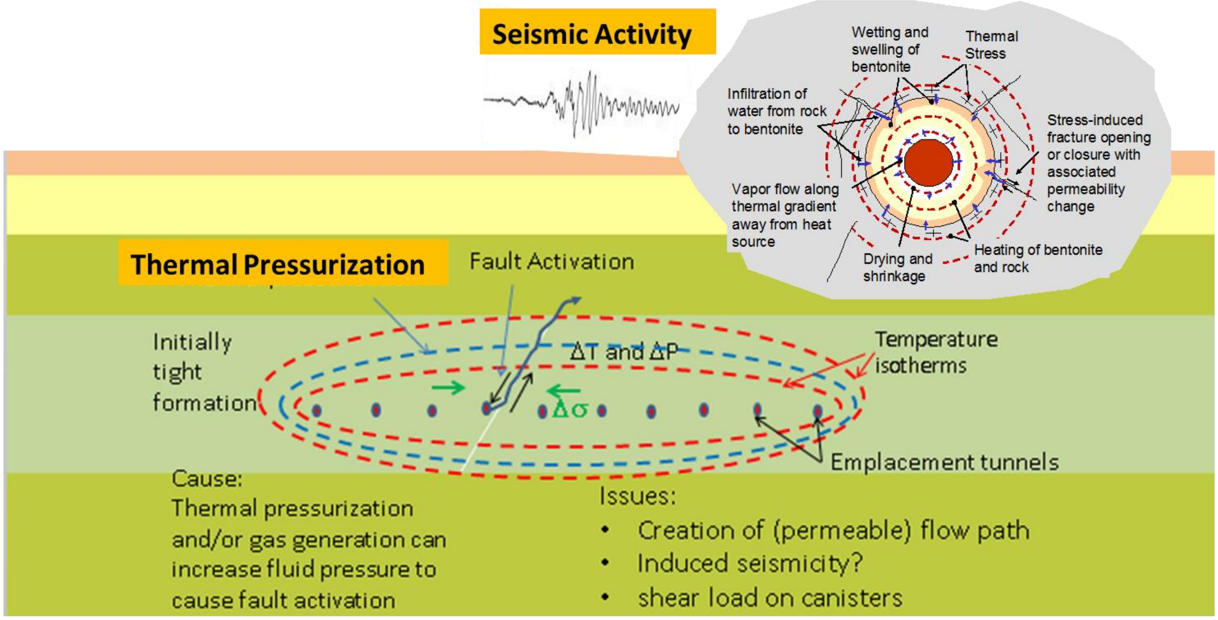

Figure 1-2. Schematic of coupled THM responses in a repository in the near field (upper right) and at the repository scale caused by heating, thermal pressurization and potential gas generation.

LBNL is developing and applying complementary coupled simulation approaches to model THM processes and in some cases extended modeling of coupled THMC processes. TOUGH-FLAC, based on linking LBNL’s TOUGH2 multiphase fluid flow simulator with the FLAC3D geomechanics code, provides an efficient continuum modeling approach with state-of-the-art constitutive models for bentonite and host rock (Rutqvist et al., 2002; Rutqvist, 2011; 2017). For rigorous modeling of the THM behavior of bentonite-based (swelling) buffer and backfill materials, the Barcelona Basic Model (BBM) and the Barcelona Expansive Model (BExM) have been incorporated into TOUGH-FLAC (Rutqvist et al., 2011; 2014b; Vilarrasa et al., 2016). Constitutive models to describe anisotropic THM behavior of shale rock have also been adapted along with models for shale creep (Sasaki and Rutqvist, 2021). For modeling THMC processes, similar sequential approach has been used linking the reactive transport simulator TOUGHREACT to FLAC3D (Zheng et al., 2014; Rutqvist et al., 2014; Xu et al., 2021). An enhanced TOUGH-FLAC version based on the updated software TOUGH3-FLAC3DV7 has been developed for faster simulations (Rinaldi et al., 2022). This model development has been accompanied by extensive testing, verification and validation, including participation within international collaborative projects, such as Development of Coupled Models and their Validation against Experiments (DECOVALEX).

Discrete fracture models, which are complementary to the continuum TOUGH-FLAC models, are also developed and applied within LBNL’s argillite repository work scope. This includes TOUGH-RBSN simulator, based on linking the TOUGH2 simulator with the Rigid-Body-Spring Network (RBSN) model, which enables for explicit modeling of discrete fractures and a fracturing process (Asahina et al., 2014; Kim et al., 2017; 2020; 2021). Another addition to this model development and applications is modeling of discrete fractured-porous media based on the Numerical Manifold Method (NMM) (Hu and Rutqvist, 2020a). This model has been applied for the analysis of fractured, granular and porous media at difference scales--from the micro-scale to macro-scale. The NMM is complementary to TOUGH-FLAC, because it can represent a complex fracture network more accurately and can be used to study underlying mechanics to understand the macroscopic behavior. The TOUGH-FLAC enables modeling of the evolution of the EBS, EDZ, and surrounding host rock at a larger scale. TOUGH-FLAC with appropriate constitutive models is also used to calculate the evolution of permeability and transport properties in the EDZ, which can then be used as input to future safety assessment models and the GDSA. The potential for activation for fault and creation of new flow paths resulting from the over pressure due to gas generation or thermal pressurization, as illustrated in Figure 1-2, are also part of coupled processes relevant to repository performance. TOUGH-FLAC is applied for model gas migration through the EBS and for potential gas fracturing of argillite. Another code applied for modeling fault activation is 3D Distinct Element Code (3DEC), based on the distinct element method (DEM).

Eventually, the research and models developed on coupled processes should be linked to the GDSA and performance assessment (PA). An approach for linking a coupled processes models to the GDSA could be to use detailed coupled THM process models to simulate near field of emplacement tunnels in different parts of a repository, for different features, events, and processes (FEPs) such as a nominal case or cases of extensive gas generation. The output from such modeling to the GDSA and PA model would be the following: (1) changes in flow properties (e.g., permeability and porosity) in the near-field, including the buffer and EDZ, and (2) inform PA about local flow created by coupled processes.

This document delivers milestone M3SF-23LB010301032 “Investigation of Coupled Processes in Argillite Rock” in the LBNL Argillite R&D Work Package (SF-23LB01030103) with input from the LBNL Argillite International Collaboration Work Package (Activity SF-23LB01030104). The activities addresses priorities related to Argillite Disposal R&D defined in the SFWST Disposal Research R&D 5-Year Plan (Sassani et al., 2021), including engagements in international activities (DECOVALEX-2023 and Mont Terri), integration of experimental and modeling activities of barrier material (engineered/natural) interactions at elevated temperatures for generic disposal concepts in argillite, and use of novel approaches to evaluate barrier material dynamic behavior and stability under repository conditions.

In Sections 2 (authored by Tsubasa Sasaki and Jonny Rutqvist), we present new results on the impact of time-dependent (creep) deformations, including results using a new anisotropic creep model. In Sections 3 and 4 (authored by Jonny Rutqvist and Tsubasa Sasaki), we present the results related to Task C and Task A of the DECOVALEX-2023 project, namely the Mont Terri Full-scale Emplacement (FE) Experiment, conducted at the Mont Terri Laboratory, Switzerland, modeling tasks related thermal and gas fracturing at the *in-situ* heater experiments at the Meuse/Haute-Marne (MHM) Underground Research Laboratory (URL) in Bure, France. Section 5 (authored by Jonny Rutqvist) presents LBNL’s activities focused on modeling gas migration in the EBS related to Task B of the international DECOVALEX-2023 project. Sections 6 (authored by Utkarsh Mital and Mengsu Hu with coworkers) present the results of application of machine learning (ML) for the analysis of data from field observations during fault activation experiments conducted at the Mont Terri Laboratory. Section 7 (Authored by Justin Cheng and Mengsu Hu with coworkers) presents the results of the application of ML for characterization of argillite structures from tunnels. Section 8 (authored by Yves Guglielmi) presents new field test and modeling results related to controlled fault activation experiments at the Mont Terri Laboratory.

Section 9 (authored by Carl Steefel and Christophe Tournassat) presents a status of modeling of the Cement–Opalinus Clay Interaction (CI) Experiment at the Mont Terri Laboratory. Finally, in Section 10, we provide a summary of the FY23 work as presented in this milestone report.

2. Modeling Shale Creep for the Long-Term Repository Performance

This section summarizes the progress on the modeling of shale creep for the long-term repository performance. The work is currently focused on evaluating the effect of shale creep on the evolution of stresses in the repository.

2.1 Introduction

It is known that the behavior of geological nuclear waste repositories is highly THM coupled, and, thus, it is crucial to incorporate each of the THM processes in the PA of the repository. The mechanical process is, in particular, time-dependent as formations creep (i.e., deform viscoelastically or viscoplastically) over a long time. However, formations such as shale possess inherent anisotropy due to the presence of bedding plane and it remains uncertain if/how the mechanical anisotropy of such formation affects the long-term behavior of geological repositories. Without understanding the anisotropy effect, it would not be possible to carry out robust PA of geological nuclear waste repositories, hence it is crucial to carefully examine such an effect. In this study, a THM coupled numerical modeling of a hypothetical geological repository was carried out to assess the effect of elastic and creep anisotropy of shale on the stress evolution of the repository for over 10,000 years. A new constitutive model for anisotropic creep was developed based on the power-law creep model and the anisotropic plasticity theory. The model parameters were calibrated against laboratory creep test results on shale with varied loading angle to the bedding plane. In order to assess the effect of elastic and creep anisotropy, three different shale cases were simulated: (1) isotropic elasticity and creep, (2) anisotropic elasticity and isotropic creep, and (3) anisotropic elasticity and creep. The results of these simulation cases along with a detailed description of the numerical model and an anisotropic creep model are provided in the rest of Section 2.

2.2 Numerical Modeling

The numerical model of a hypothetical geological nuclear waste repository was created with the TOUGH-FLAC simulator (Rinaldi et al., 2021) as shown in Figure 2-1. It consists of the formation, bentonite buffer, and canister. Only a ‘slice’ of the entire repository corresponding to a single disposal tunnel was modeled due to the symmetry, under which the displacements, fluid flow, and thermal flux across the horizontal boundaries are assumed to be nonexistent. The model was also assumed to be plane-strain in the tunnel axis direction (i.e., the out-of-plane component of the strain (and displacement) is zero), which makes this model a two-dimensional (2D) model. A time-varying thermal flux was specified for the canister elements as shown in Figure 2-2, which was used to simulate the decay heating of the nuclear waste and the corresponding temperature increase in the repository.

TOUGH-FLAC is a THM coupled simulator, in which multi-phase fluid flow and thermal transport are handled by the TOUGH3 simulator, whereas the mechanical calculation is implemented in FLAC3D. The detail of the multi-phase flow formulation is provided in our previous work (Sasaki and Rutqvist, 2021; 2022). The detail of the mechanical formulation is provided below.

The bentonite buffer was modeled with the BBM (Alonso et al., 1990) and its material properties are provided in our previous work (Rutqvist et al., 2011). The canister was modeled as an isotropic elastic material and its Young's modulus and Poisson's ratio were set to 200 GPa and 0.3, respectively.

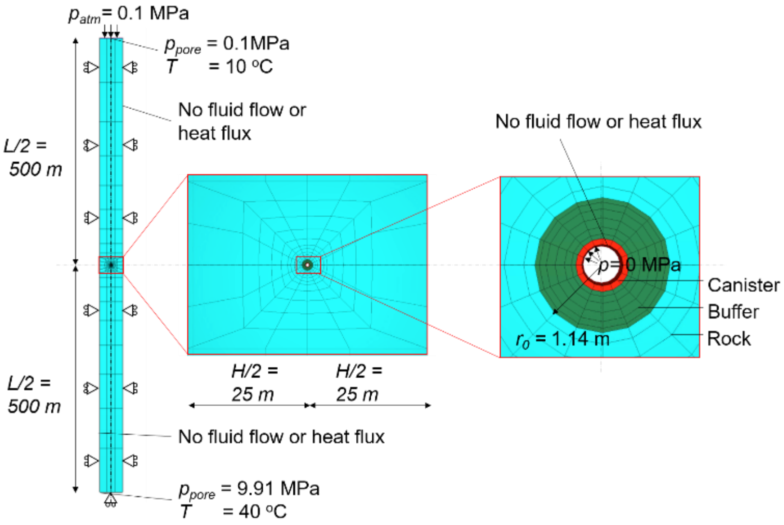

Figure 2-1. Geometry and boundary conditions of the TOUGH-FLAC model of a geological nuclear waste repository.

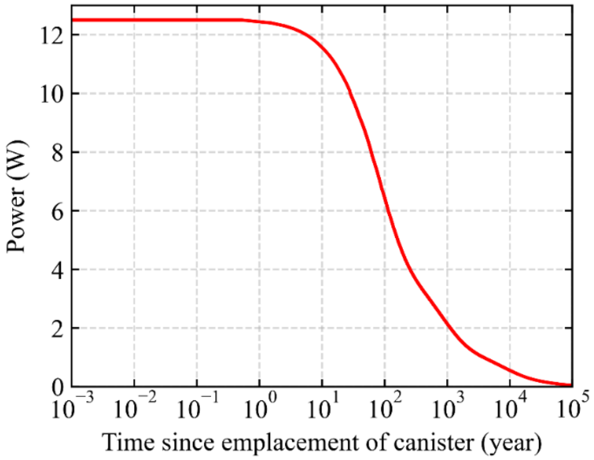

Figure 2-2. Decay heating of the nuclear waste modelled as time-varying thermal outflux from the canister.

2.3 Anisotropic Creep Model

The anisotropic creep model was developed so that the creep behavior of shale, which is inherently anisotropic due to the presence of bedding plane, can be captured more accurately than the isotropic creep model. The existing isotropic creep model that is often used for shale is the so-called power-law model or more formally known as the Norton-Bailey model (Bailey, 1935; Norton, 1929) or the Lemaitre-Menzel-Schreiner model (Lemaître, 1970; Menzel and Schreiner, 1977). The anisotropy of shale is caused by the bedding plane so it can be regarded as transverse isotropic. The equations below represent the transverse isotropic creep (i.e., viscoplastic) strain increments that are formulated based on the anisotropic plasticity theory (Hu, 1956; Murakami and Yamada, 1974):

$$\begin{pmatrix} d\epsilon_{11}^{c} \\ d\epsilon_{22}^{c} \\ d\epsilon_{33}^{c} \\ d\epsilon_{12}^{c} \\ d\epsilon_{23}^{c} \\ d\epsilon_{31}^{c} \end{pmatrix} = d\lambda \begin{pmatrix} \alpha_{11} & -\alpha_{11}/2 & -\alpha_{11}/2 & 0 & 0 & 0 \\ -\alpha_{11}/2 & \alpha_{22} & -(\alpha_{22}-\alpha_{11}/2) & 0 & 0 & 0 \\ -\alpha_{11}/2 & -(\alpha_{22}-\alpha_{11}/2) & \alpha_{22} & 0 & 0 & 0 \\ 0 & 0 & 0 & (3/2)\alpha_{44} & 0 & 0 \\ 0 & 0 & 0 & 0 & (2\alpha_{22}-1/2) & 0 \\ 0 & 0 & 0 & 0 & 0 & (3/2)\alpha_{44} \end{pmatrix} \begin{pmatrix} \sigma_{11} \\ \sigma_{22} \\ \sigma_{33} \\ \sigma_{12} \\ \sigma_{23} \\ \sigma_{31} \end{pmatrix} dt \tag{2.1}$$

where the coefficients were derived based on the isotropic power-law model as shown below ($\alpha_{11} = 1$)

$$d\lambda = m_1 A_1^{(1/m_1)} \left(\bar{\sigma}/\sigma_{ref}\right)^{(1-m_1)/m_1} \bar{\epsilon}^{-(1-m_1)/m_1} \tag{2.2}$$

$$\alpha_{22} = \left[(m_2/m_1)\left(A_2^{1/m_2}/A_1^{1/m_1}\right)\left(\left(\bar{\sigma}/\sigma_{ref}\right)/\bar{\epsilon}\right)^{(m_1-m_2)/m_1 m_2}\right]^{2m_2/(m_2+1)} \tag{2.3}$$

$$\alpha_{44} = (1/3)\left(-\alpha_{22} + \left[2^{(m_3+1)/m_3}(m_3/m_1)\left(A_3^{1/m_3}/A_1^{1/m_1}\right)\left(\left(\bar{\sigma}/\sigma_{ref}\right)/\bar{\epsilon}\right)^{(m_1-m_3)/m_1 m_3}\right]^{2m_3/(m_3+1)}\right) \tag{2.4}$$

where $\bar{\sigma}$ and $\bar{\epsilon}$ are an ‘effective’ deviatoric stress and creep strain, respectively, as shown below

$$\bar{\sigma} = \begin{bmatrix} (1/2)(\sigma_{11}-\sigma_{22})^2 + (\alpha_{22}-1/2)(\sigma_{22}-\sigma_{33})^2 \\ +(1/2)(\sigma_{33}-\sigma_{11})^2 + 3\alpha_{44}\sigma_{12}^2 + (4\alpha_{22}-1)\sigma_{23}^2 + 3\alpha_{44}\sigma_{31}^2 \end{bmatrix}^{1/2} \tag{2.5}$$

$$\bar{\epsilon} = \left(\epsilon_{total}^{c} + \epsilon_{shift}^{c}\right)/t_{ref} \tag{2.6}$$

where

$$\epsilon_{total}^{c} = \int d\bar{\epsilon} \tag{2.7}$$

$$
\begin{aligned}
d\bar{\epsilon} = \Big\{ & (1/(\alpha_{22} - 1/4)^2) \Big[(1/2)\big((\alpha_{22} - 1/2) d\epsilon_{11}^c - (1/2) d\epsilon_{22}^c\big)^2 \\
& + (\alpha_{22} - 1/2)\big((1/2) d\epsilon_{22}^c - (1/2) d\epsilon_{33}^c\big)^2 \\
& + (1/2)\big((1/2) d\epsilon_{33}^c - (\alpha_{22} - 1/2) d\epsilon_{11}^c\big)^2 \Big] \\
& + (4/3)\Big[{d\epsilon_{12}^c}^2/\alpha_{44} + {d\epsilon_{23}^c}^2/\big((4/3)\alpha_{22} - 1/3\big) + {d\epsilon_{31}^c}^2/\alpha_{44} \Big] \Big\}^{1/2}
\end{aligned}
\tag{2.8}
$$

Finally, A_1 and m_1, A_2 and m_2, A_3 and m_3 are the coefficients of the power law creep model obtained from the experiment by loading the specimen at 90°, 0°, and 45° degrees to the bedding, respectively. These coefficients characterize the strain-hardening power law creep, details of which are provided in Sasaki and Rutqvist (2022).

Assumptions:

The stress exponent $n = 1.0$

There is no effect of confining pressure on the creep strain and creep strain rate.

The principal axes of anisotropy form an orthogonal set and they do not rotate due to the accumulation of creep strain (i.e., material (initial) anisotropy >> strain-induced anisotropy).

Remark:

If $A_1 = A_2 = A_3 = A$, $m_1 = m_2 = m_3 = m$, and $\alpha_{22} = \alpha_{44} = 1.0$ are substituted into the above equations, the isotropic Norton-Bailey model is recovered along with

$$\bar{\sigma} = \sigma_{VM}/\sigma_{ref} \tag{2.9}$$

$$d\epsilon^c = \sqrt{(2/3) d\epsilon_{ij}^c : d\epsilon_{ij}^c} \tag{2.10}$$

The developed anisotropic creep model was calibrated against laboratory triaxial creep test results on shale in the literature (Li et al., 2020). The results of the calibration and the calibrated parameter values are provided in Figure 2-3 and Table 2-1, respectively. The simulation for the calibration was carried out with FLAC3D by loading one element in a principal direction (e.g., z-direction) while the other principal directions are applied with constant confining pressure (e.g., x-, y-direction). The direction of the bedding plane was set to three different values: 0 °, 45 °, or 90 °.

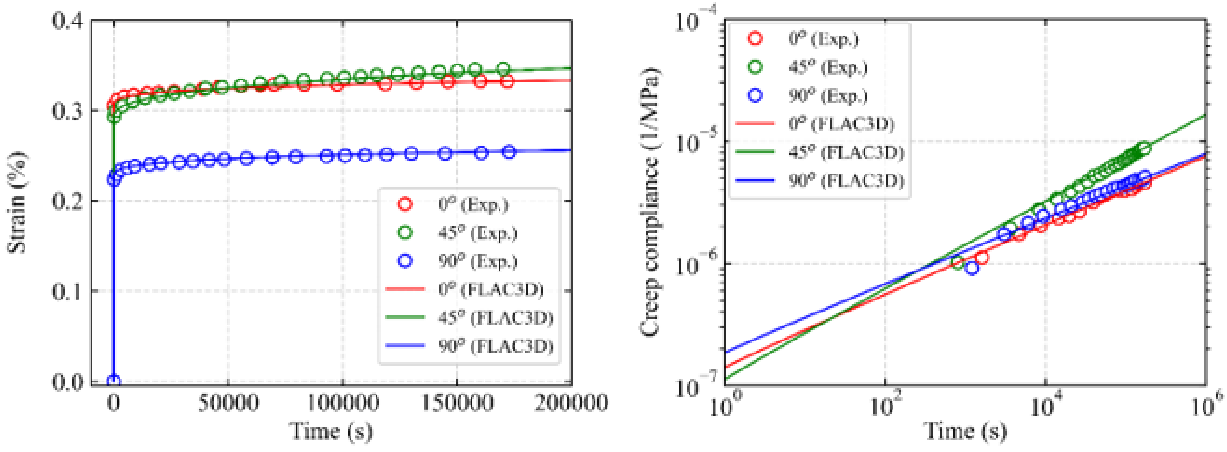

(a) (b)

Figure 2-3. Calibration results of the anisotropic creep model: (a) time vs. total axial strain; (b) log(time) vs. log(creep compliance).

Table 2-1. Calibrated parameter values of the anisotropic creep model.

Parameter	Isotropic elasticity & Isotropic creep	Anisotropic elasticity & Isotropic creep	Anisotropic elasticity & Anisotropic creep
Young's modulus normal to bedding plane (GPa)	19.7	19.7	19.7
Young's modulus normal to bedding plane (GPa)	19.7	26.7	26.7
Young's modulus parallel to bedding plane (GPa)	7.58	7.33	7.33
Shear modulus normal to bedding plane (GPa)	0.300	0.300	0.300
Poisson's ratio normal to bedding plane (-)	0.300	0.220	0.220
Poisson's ratio parallel to bedding plane (-)	$1.58\cdot10^{-13}$	$1.58\cdot10^{-13}$	$1.58\cdot10^{-13}$
Power-law coefficient normal to bedding plane, A_0 (s^{-1})	0.28	0.28	0.28
Power-law exponent normal to bedding plane, m_0 (-)	$1.58\cdot10^{-13}$	$1.58\cdot10^{-13}$	$1.40\cdot10^{-13}$
Power-law coefficient 45° to bedding plane, A_{45} (s^{-1})	0.28	0.28	0.33
Power-law exponent 45° to bedding plane, m_{45} (-)	$1.58\cdot10^{-13}$	$1.58\cdot10^{-13}$	$1.85\cdot10^{-13}$
Power-law coefficient parallel to bedding plane, A_{90} (s^{-1})	0.28	0.28	0.27
Power-law exponent parallel to bedding plane, m_{90} (-)	1.0	1.0	1.0
Power-law exponent, n (-)	1	1	1
Reference stress, σ_{ref} (Pa)	1	1	1
Reference time, t_{ref} (s)	$1\cdot10^{-6}$	$1\cdot10^{-6}$	$1\cdot10^{-6}$
Strain shift, ε_{shift} (-)	$1.0\cdot10^{-5}$	$1.0\cdot10^{-5}$	$1.0\cdot10^{-5}$
Linear thermal expansion coefficient (1/°C)			

2.4 Results

The THM coupled behavior of the repository during the decay heating of the nuclear waste was simulated over 10,000 years and the results were extracted at a number of data readout locations in the formation shown in Figure 2-4. Also, three different scenarios were simulated: (1) isotropic elasticity and creep case, (2) anisotropic elasticity and isotropic creep case, and (3) anisotropic elasticity and creep case. The bedding plane angle was set to 0^{o}. These three cases were simulated to elucidate the effect of elastic and creep anisotropy on the stress evolution of the repository relative to the case of elastic and creep isotropy.

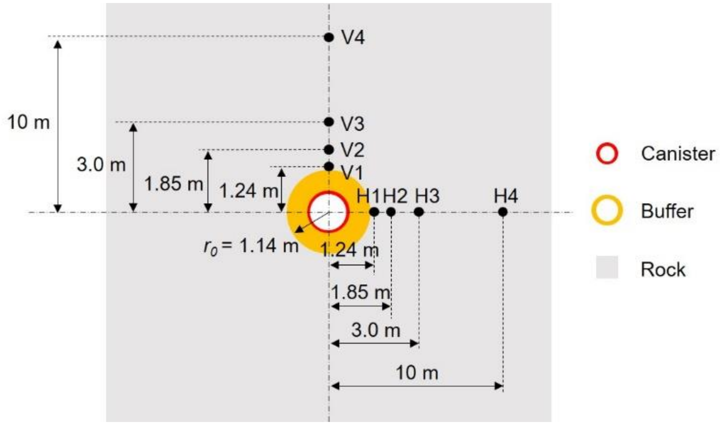

Figure 2-4. Data readout locations around the disposal tunnel in the repository model.

The calculated temperature, pore pressure, and liquid saturation in the formation are provided in Figure 2-5. It can be seen that the effect of elastic and creep anisotropy on these thermo-hydraulic (TH) variables is negligible, as the three curves (i.e., solid, dashed, and dotted curves) lie on top of each other at every data readout location.

Effective stresses in the formation are provided in Figure 2-6a. It was found that the elastic and creep anisotropy did not significantly affect the stress evolution as the maximum difference was approximately 10% for the circumferential effective stress at the V1 location at about 10 years, and the difference decreased toward the longer term (10,000 years). The deviatoric and mean effective stresses are provided in Figure 2-6b. The maximum difference was about 20% for the deviatoric stress at the H1 location at about 1 year, and the difference diminished toward the longer term. These results indicate that the effect of elastic and creep anisotropy on the stress evolution would become insignificant in the long term (> 10 years).

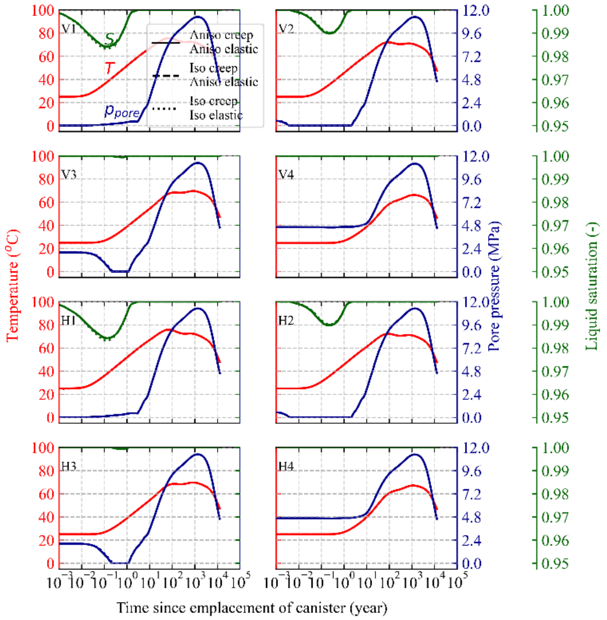

Figure 2-5. Temperature, pore pressure, and liquid saturation at the data readout locations around the disposal tunnel.

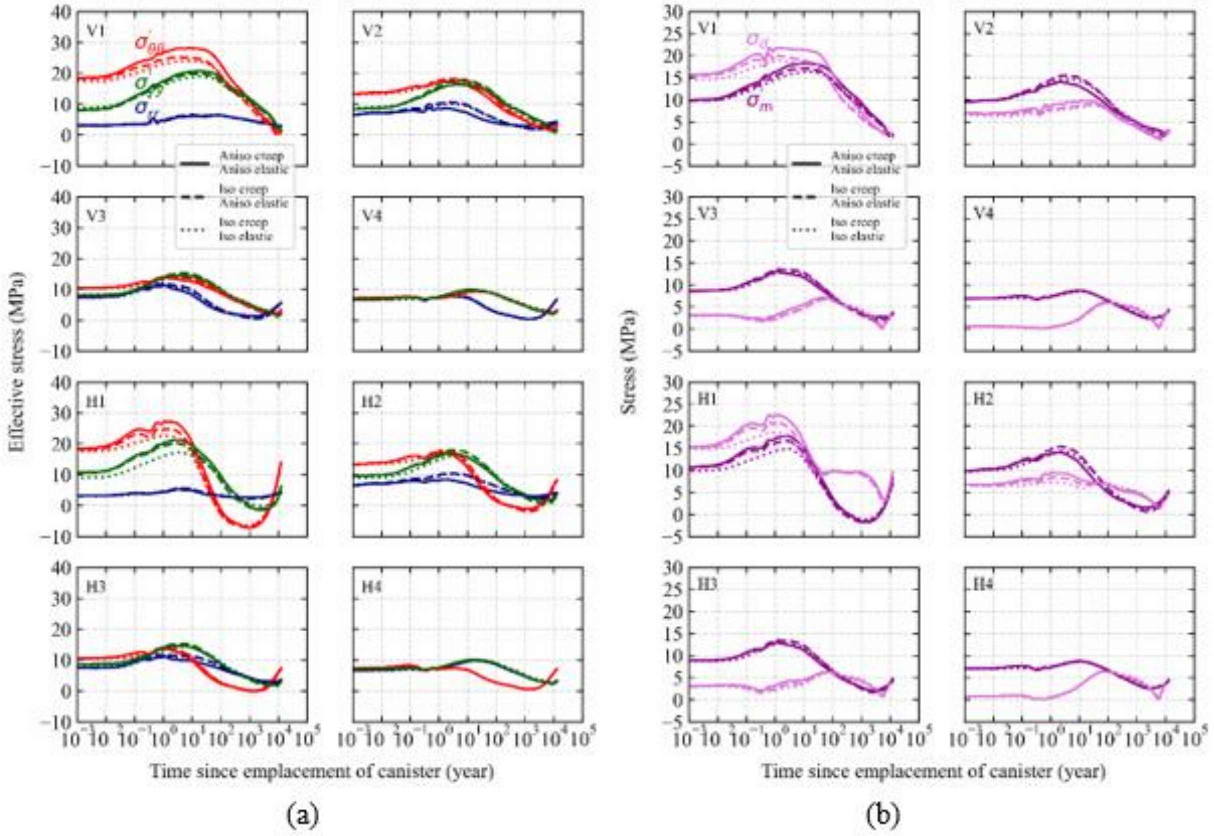

(a) (b)

Figure 2-6. Stresses at the data readout locations around the disposal tunnel: (a) radial, circumferential, and out-of-plane effective stresses; (b) deviatoric and mean effective stress.

The above claim was corroborated by assessing the spatial distributions of the stresses in the long term as shown in Figure 2-7. The spatial distributions are found similar between the examined three cases, indicating that the stresses at locations other than the data readout locations are also comparable between the three cases.

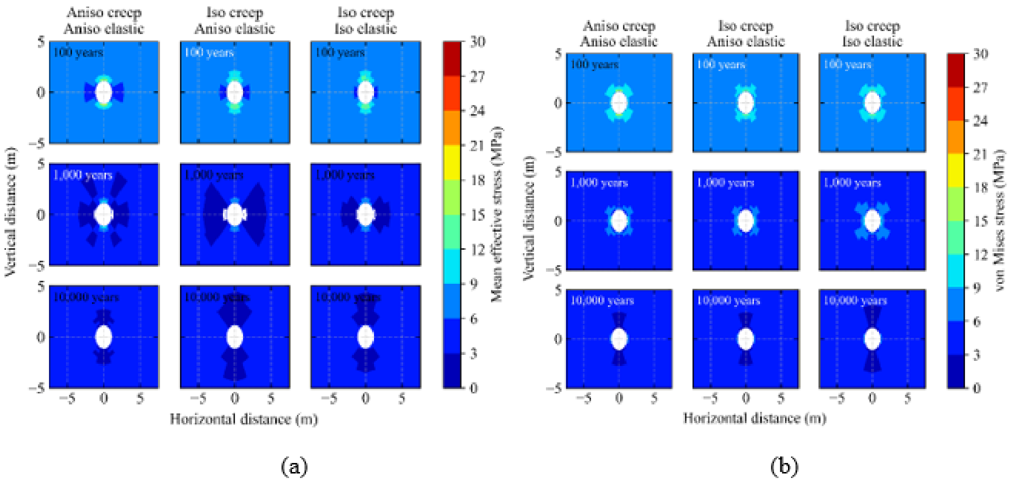

Figure 2-7. Stress distributions around the disposal tunnel: (a) mean effective stress; (b) deviatoric stress.

2.5 Summary and Future Plans

In this study, the numerical simulations of the long-term THM coupled behavior of a hypothetical geological nuclear waste repository were carried out using the TOUGH-FLAC simulator in order to assess the effect of elastic and creep anisotropy of the shale formation on the stress evolution of the repository. A new constitutive model for modeling anisotropic creep was developed based on the isotropic power-law creep model and the anisotropic plasticity theory. The anisotropic creep model was calibrated against laboratory triaxial test results on shale with varied bedding plane angles. It was found from the results of the present study that the stresses did not change significantly due to the elastic and creep anisotropy of shale relative to the case of elastic and creep isotropy in the long term (up to 10,000 years). Hence, it is claimed that the mechanical behavior of shale in the repository could be modelled with isotropic elastic and creep models without incurring significant errors. This indicates that the accuracy of the long-term PA of geological repositories in shale would not be compromised by ignoring the elastic and creep anisotropy of shale. It is noted, however, that the degree of anisotropy in the shale employed for the model calibration in this study appears to be weak, which suggests that the above claim would not be valid for shale with stronger anisotropy. Also, the anisotropy in terms of TH behaviors of shale was not considered in this study, which could have some impact on the results. Such anisotropy effects will be evaluated in a future study.

3. FE Experiment at the Mont Terri Site (DECOVALEX-2023)

In this section, we present the current status of LBNL’s modeling of the FE Experiment at Mont Terri and updated results of TOUGH-FLAC modeling. Because the FE Experiment at Mont Terri is now a task of the ongoing DECOVALEX-2023 project, this section is focused on a new model development and results associated with the DECOVALEX-2023 project.

3.1 Description and Status of the Mont Terri FE experiment

The Mont Terri FE experiment has been conducted by NAGRA, Switzerland, as an ultimate test for the PA of geologic disposal in Opalinus Clay (OPA), with focus on both the EBS components and the host-rock behavior. It is one of the largest and longest-duration heater tests worldwide, with focus on both the EBS components and the host-rock behavior. The FE experiment is being conducted in the side tunnel at Mont Terri, excavated along the claystone bedding planes, extending 50 m in length and about 2.8 m in diameter (Figure 3-1). Heating from emplaced waste is simulated by three heat-producing canisters of 1,500 W maximum power each. Temperature is expected to exceed 100°C, with a target temperature of 125° to 135°C at the inner part of the buffer. A sophisticated monitoring program has been implemented, including dense instrumentation of the bentonite buffer and host rock, and extensive geophysical monitoring.

The experiment provides data needed for the validation of THM coupling effects and processes taking place in the host rock, such as the emplacement tunnel temperature, saturation, and swelling pressure. The Mont Terri field scale experiment is used to achieve realistic temperature, saturation, and stress gradients. It will also be possible to test backfilling technology with granular bentonite, as well as lining technology with shotcrete, anchors, and steel ribs. Processes examined in the test cover many aspects of a repository evolution, such as criteria of desaturation of the EDZ during tunnel excavation and operation (including ventilation for about one year), as well as reconsolidation of the EDZ, resaturation, thermal stresses, and thermal pore-pressure increase after backfilling and heating (heating and a monitoring period for >10 years).

In 2011, a niche in front of the FE tunnel was constructed, following by a first phase of instrumentation of the rock mass surrounding the tunnel, using boreholes drilled from the niche. The FE tunnel was excavated by a road-header in 2012, following by instrumentation. The tunnel was kept open for a one-year ventilation period. This followed by emplacing the heaters, bentonite buffer, and a concrete plug, after which the heating was gradually turned on during the fall of 2014 and early 2015, with applying the full heat power of 1350 W at all three heaters (H1, H2, H3), starting on February 18, 2015 (Figure 3-2). The heating is expected to continue for at least 15 years, with continuous monitoring of THM processes in both the bentonite buffer and a surrounding rock. After over five years of the temperature at the heaters approached 130°C, and a relative humidity near the heaters in granular bentonite buffer stayed low at around 10% to 20%. Some wetting is also taking place at other parts of the buffer, at some locations reaching full saturation. No substantial swelling stress has yet been developed in the granular bentonite at this stage of the project.

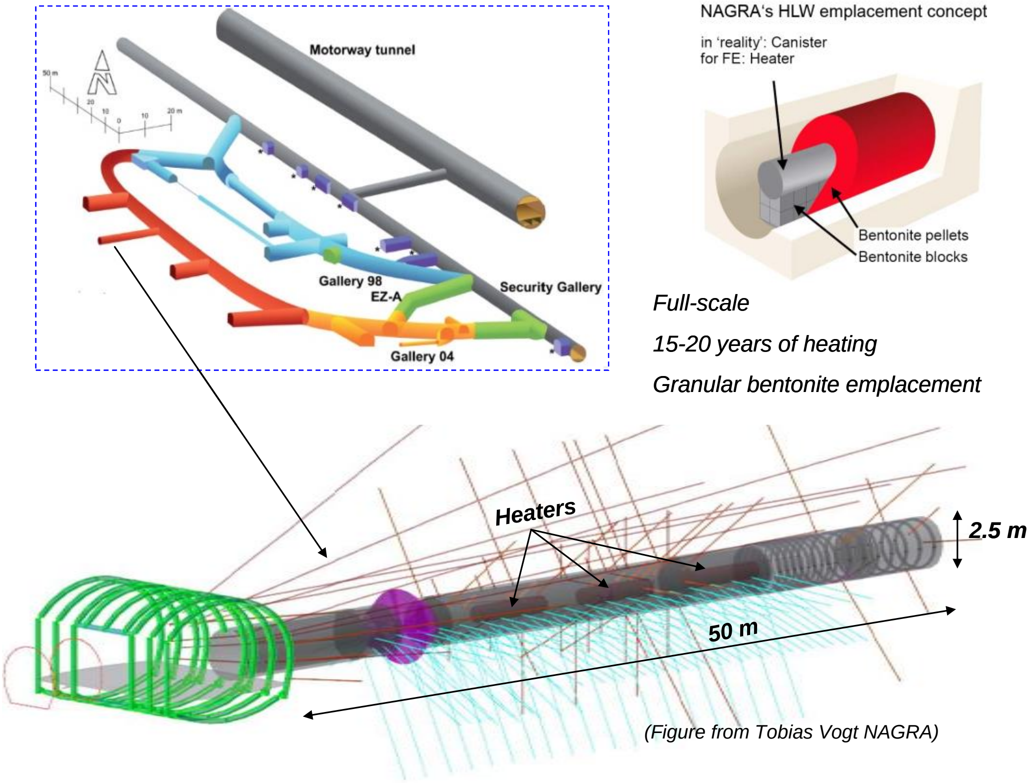

Full-scale

15-20 years of heating

Granular bentonite emplacement

(Figure from Tobias Vogt NAGRA)

Figure 3-1. Plan view of FE experiment setup and borehole layout.

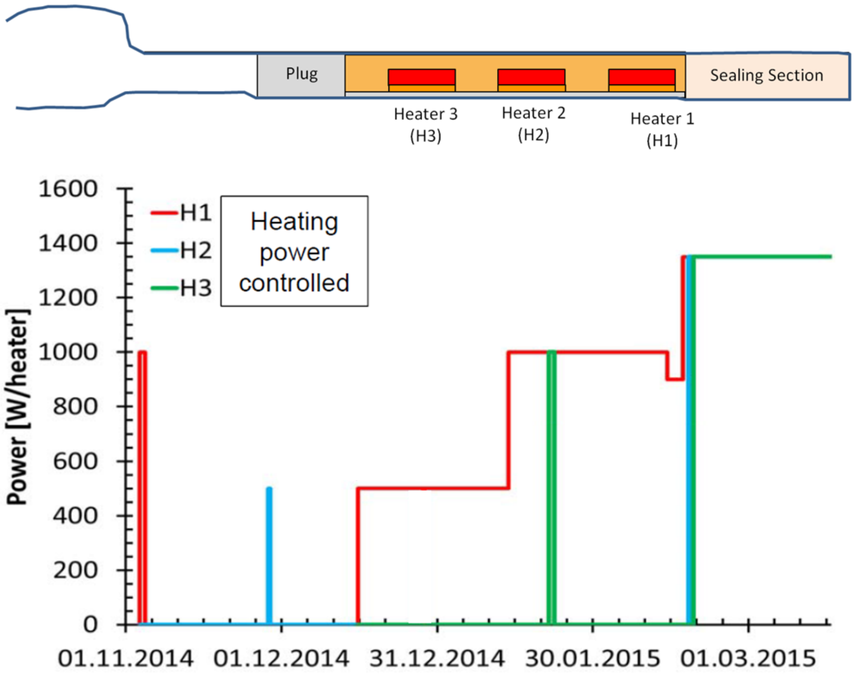

Figure 3-2. Heat power applied to H1, H2 and H3 during heater start-up at the Mont Terri FE experiment.

3.2 TOUGH-FLAC Model of the Mont Terri FE Experiment

For the FE experiment modeling, we have developed a conceptual model and a modeling approach based on the previous milestone reports by Rutqvist et al. (2022). In FY23, the FE modeling has continued along with the DECOVALEX 2023 tasks. The DECOVALEX-2023 project is at the stage of interpretative modeling and model calibration using field data up to 5 years of heating.

Using TOUGH-FLAC, the host rock is modeled taking into account anisotropic properties considering bedding planes of the OPA. To accurately model anisotropic thermal and hydrological behavior, we created a TOUGH2 inclined mesh. Anisotropic mechanical material behavior is simulated using available elastic anisotropic model in FLAC3D with parameters given by the DECOVALEX-2023 task. For the bentonite, we are not considering the mechanical behavior of the buffer as (a) no significant swelling stress has been developed at the experiment, and (b) the DECOVALEX-2023 project is focused on the THM processes in the host rock rather than on simulations of the bentonite buffer.

Figure 3-3 presents the 3D TOUGH-FLAC numerical grid used for modeling of the FE experiment. This model grid includes all material components used for modeling of the FE experiment, including the layered OPA host rock, EDZ, tunnel, three heaters, bentonite buffer, concrete liner, and a concrete plug. The following initial conditions for the model simulations were selected: 2 MPa pore-fluid pressure, 15°C temperature, and $\sigma_x = 4.5$ MPa, $\sigma_y = 2.5$ MPa, $\sigma_z = 6.5$ MPa for the host rock. Because the 2 MPa pore pressure does not represent hydrostatic conditions, the process is affected by the existing tunnel system. In our simulations, we first ran a simulation with an open tunnel at the atmospheric pressure for one year, creating a pressure drop and hydraulic gradient around the tunnel. Thereafter, we assumed instantaneous emplacement of the heater and the buffer to start the heating simulation. The outer boundary conditions for all the outer boundary edges of the model are fixed zero displacement and no heat or fluid transfer. Simulations indicate that these boundaries are being placed far enough from the heat source so that there is no effect of the outer boundaries.

The baseline thermal and hydraulic material properties for modeling the FE experiment are given in Table 3-1 as defined by the DECOVALEX-2023 task (Tatcher and Graupner, 2020).

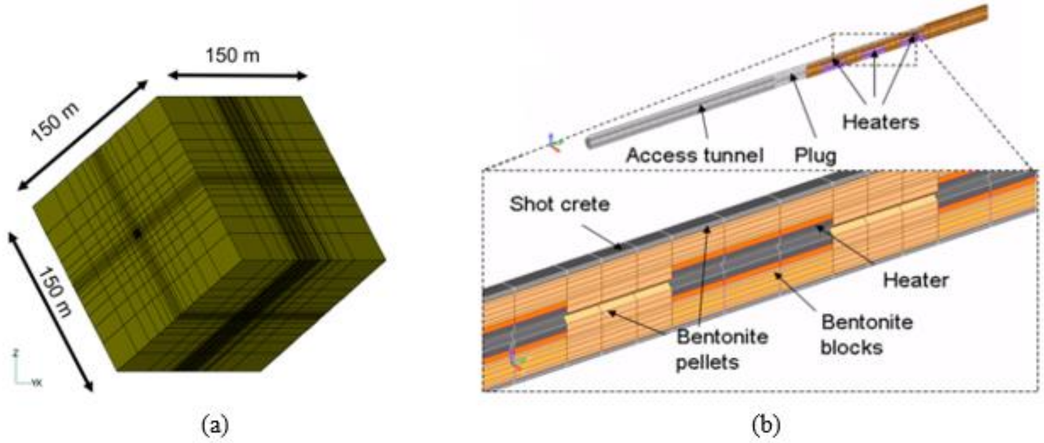

Figure 3-3. TOUGH-FLAC 3D numerical grid of the FE experiment: (a) Entire model, and (b) Materials and gridding of the EBS.

Table 3-1. Parameters used in modeling of the Mont Terri FE experiment defined in the DECOVALEX-2023 Task Description (Thatcher and Graupner, 2020)

Input parameters		Symbol	Unit	OPA[1]	GBM[3]	Bentonite blocks[4]	Concrete
Thermal parameters	Dry thermal conductivity parallel and perpendicular to bedding	$\lambda_{dry,\parallel}$	W/mK	2.4	0.35	0.26	0.1
		$\lambda_{dry,\perp}$	W/mK	1.3			
	Saturated thermal conductivity parallel and perpendicular to bedding	$\lambda_{sat,\parallel}$	W/mK	2.4	1.2	0.96	0.3
		$\lambda_{sat,\perp}$	W/mK	1.3			
	Solid specific heat capacity	c_s	J/kgK	995	800	800	750
Hydraulic parameters	Dry Bulk Density	ρ_{bulk}	kg/m^3	2340	1490	1690	1725
	Porosity	ϕ	-	0.13	0.331	0.331	0.25
	Intrinsic permeability	$k_{i,\parallel}$	m^2	5.0E-20	3.5E-20	1.0E-22	1.0E-19
		$k_{i,\perp}$		1.0E-20			
	Van Genuchten Entry Pressure	p_e	MPa	20.0	28.6	30	1
	van Genuchten n	n	-	2.5	2.0	1.67	1.49
	van Genuchten maximum water saturation	s_{max}	-	1.0	1.0	1.0	1
	van Genuchten residual water saturation	s_r	-	0.0	0.0	0.0	0.01
	Pore compressibility	c_{pore}	1/Pa	8.66E-10	1.05E-07	1.13E-07	1.40E-10
Mechanical parameters	Young's modulus	$E_\parallel$	MPa	8000	18	24	20000
		$E_\perp$		4000			
	Shear modulus	$G_\perp$	MPa	3500	-	-	-
	Poisson ratio	$\nu_\parallel$	-	0.35	0.35	0.2	0.15
		$\nu_\perp$		0.25			
	Linear thermal expansion	α_T	1/K	1.5E-05	3.0E-06	3.0E-06	1.5E-05
	Biot coefficient	α	-	1	1	1	1
Fluid parameters	Reference water density	ρ_{fluid_ref}	kg/m^3	1000			
	Fluid compressibility	c_{fluid}	1/Pa	4.65E-10			
	Linear thermal expansion water	α_w	Pa s	4.00E-04			
	Vapour diffusivity (vapour in air)	D_v	m^2/s	2.42E-05			

3.3 Simulation Results

In the updated simulations in FY23, we considered properties from previous modeling of Mont Terri Half-Scale (HEE) experiment. This experiment was simulated in DECOVALEX-2015. Among the properties used are the thermal properties of the bentonite as defined associated with the previous modeling of the HEE experiment (Figure 3-4). The properties for bentonite blocks, i.e., dry and wet thermal conductivity are quite different from baseline properties defined in Table 3-1. The thermal conductivity is higher in the updated properties in particular a dryer conditions. With these properties, some improvements were achieved in the modeling of the temperature evolution in the bentonite blocks below the heater (Figure 3-5).

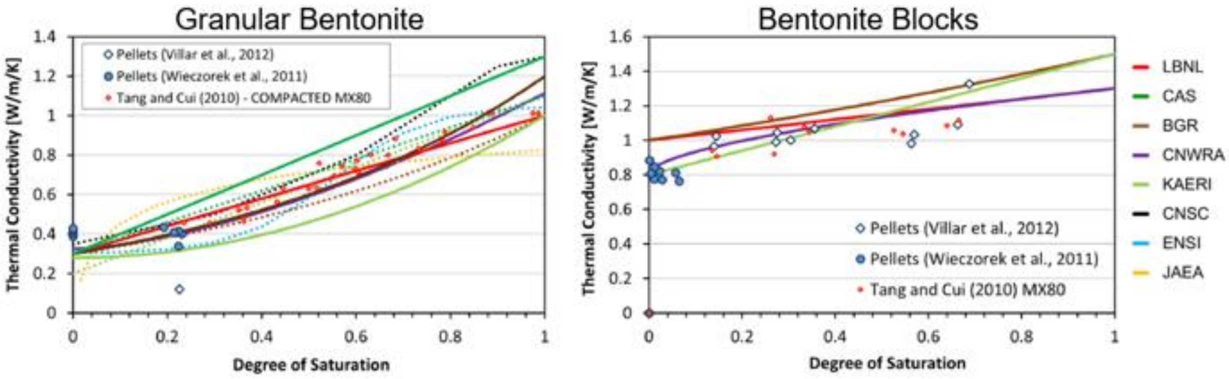

(a) (b)

Figure 3-4. Thermal conductivity of bentonite as used in modeling of the Mont Terri HEE experiment in DECOVALEX-2015 for: (a) granular bentonite and (b) bentonite blocks (Garitte et al., 2007).

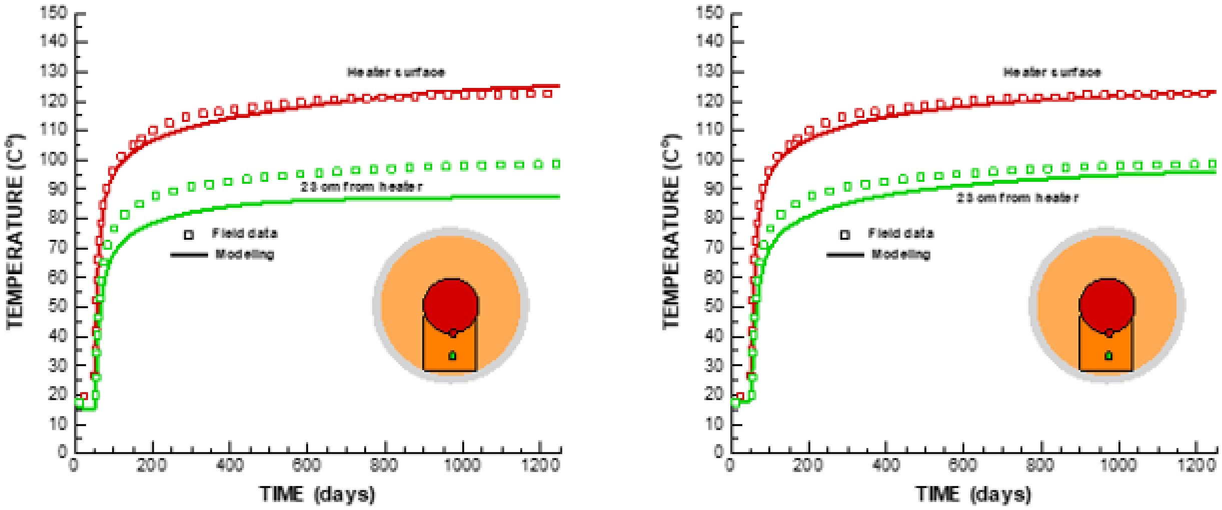

(a) (b)

Figure 3-5. Simulation results of temperature evolution in the bentonite blocks below the heater when considering: (a) old thermal conductivity bentonite block and (b) new update conductivity of bentonite blocks.

In DECOVALEX-2023 Task C, efforts are mostly focused on the THM responses in the host rock surrounding the buffer. In fact, it has been quite challenging for the teams to make a good prediction of the thermal pressurization and the pressure evolution in the host rock. In FY23, we have done extensive sensitivity studies in order to try to match the pressure evolution better. First, to better match the initial pressure at the start of heating, a model simulation was conducted considering an initial phase of the tunnel being open for one year. Moreover, a sensitivity study showed that the modeling had to consider a reduced permeability and increased fluid storage to avoid too much drainage into the tunnel. The increased fluid storage was modeled by increasing the pore-compressibility. The best overall match was by setting permeability to 5x10^{-20} m^2 (parallel bedding) and 1x10^{-21} m^2 (perpendicular bedding), while storage has to be increased by setting pore-compressibility to 2x10^{-9} Pa^{-1}. Using such parameters, a match between the modeling and field measurements is reasonable as shown in Figure 3-6, although there is room for further improvements. Such improvements will be part of future research.

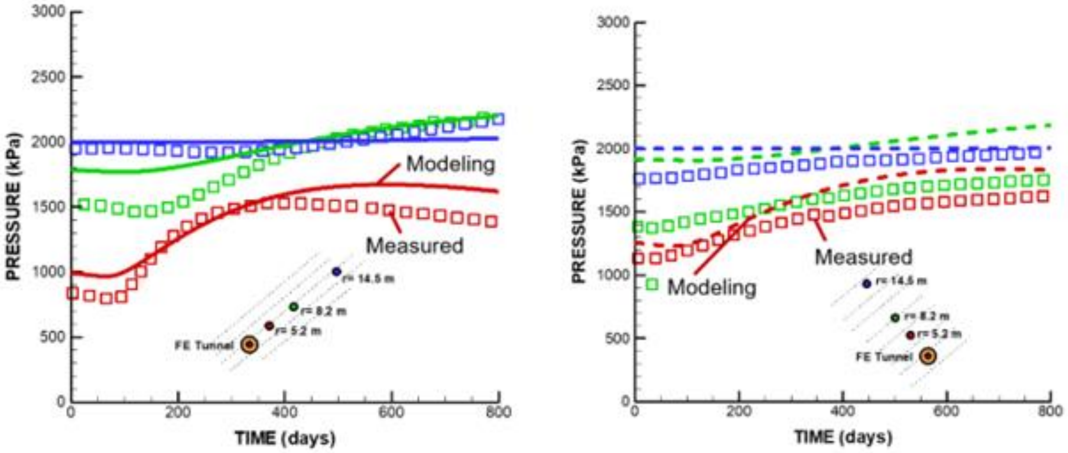

(a) (b)

Figure 3-6. Results of scoping calculation for thermal pressurization effects in the host rock for pressure monitoring points located (a) perpendicular to bedding, and (b) parallel to bedding of the tunnel.

3.4 Future FE Experiment Modeling

We have conducted several types of modeling of the Mont Terri FE experiment over the past few years including benchmarking, heating design modeling, model predictions and interpretative modeling. Currently, we are active in the DECOVALEX-2023 project, which provides additional code-to-code verifications. The model calibration is ongoing and we will try to improve by considering the concrete liner and EDZ that could have an impact on the pressure evolution especially in the near field. After completing the work with DECOVALEX-2023, we will then resume our regular Mont Terri project simulation of the field data going beyond five years. Finally, the work for Mont Terri project will focus in more detail on the evolution of the bentonite buffer and the stress in the bentonite buffer.

4. Modeling of Thermal and Gas and Fracturing at Bure in COx Claystone (DECOVALEX-2023)

In this section, we present the THM modeling results using iTOUGH related to thermal fracturing experiments conducted in Callovo-Oxfordian claystone (COx) at the MHM URL in Bure, France. The DECOVALEX-2023 Task A is divided into two subtasks: Task A.1 for thermal fracturing and Task A2 for gas fracturing. We mainly focus on performing a numerical analysis of thermal fracturing for Task A1. The objective of the heating experiment is to study thermal fracturing in the COx by reproducing the evolution of pressure, temperature, and stress in HLW repository. In this report, we present the results of 3D TH modeling of the CRQ experiment to better match the observed pore pressure and temperature changes.

4.1 CRQ Experiment

4.1.1 Experimental Setup

The CRQ experiment was conducted at the main level of the MHM URL, and its layout is presented in Figure 4-1. The experimental setup consists of ten 20 m long heater boreholes (diameter of 172 mm) labeled from CRQ1701 to CRQ1710. Heater boreholes were drilled horizontally from the GCS drift wall. CRQ1709 and CRQ1710 were installed approximately 0.8 m apart from each other and surrounded by the other eight heater boreholes. Heater devices were placed in each borehole at the last 10 m from the end of the boreholes. In the cross-section located 15 m from the GCS drift wall (section A), the peripheral boreholes are arranged in a way that approximately forms a square with a side of 3 m. This configuration has an objective to reach high pore pressures and minimize the hydraulic gradients inside the heated zone. Consequently, delaying the pore pressure dissipation, increasing tensile effective stresses, and having more probabilities of fracturing the COx. Given the heating design and the *in-situ* stress field at the level of the MHM URL, the fracture location is expected to be between the two central boreholes (CRQ1709 and CRQ1710) and the fracture is expected to be horizontal. A power/temperature regulation system controls the ten heater devices. The temperature along each heater casing was monitored by sensors. There were four multi-packer observation boreholes to monitor the THM response of the surrounding rock (CRQ1720-CRQ1723) for measuring pore pressure and temperature. CRQ1720-CRQ1723 with a diameter of 76 mm were equipped with five piezometer chambers each, associated with temperature sensors, and were only backfilled with resin the first 8 m from the GCS drift.

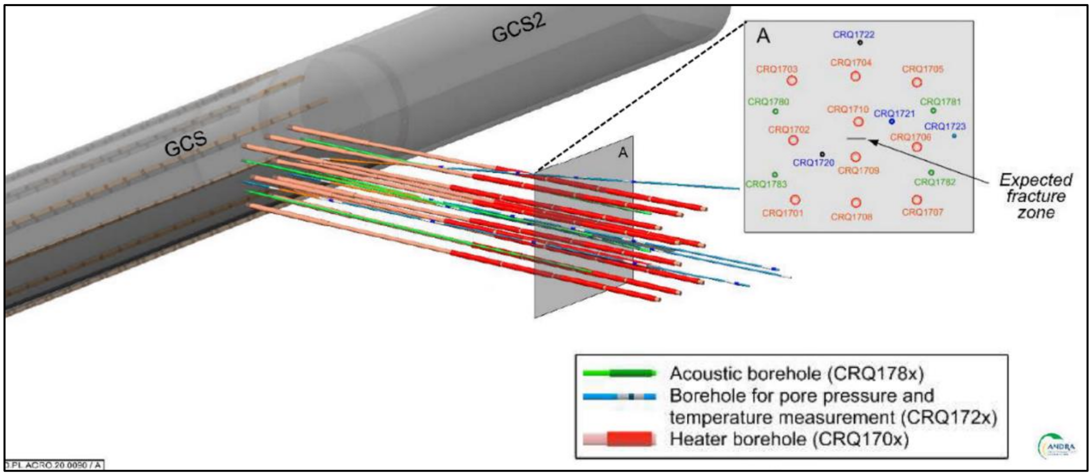

Figure 4-1. Layout of the CRQ experiment and section-A located at 15 m from the CGS drift wall.

The experiment had two heating phases separated by a cooling phase of about five months (Figure 4-2). The first cycle started on June 3, 2019, and lasted for two months without evidence of fracturing, so it was decided to stop the heating. The second cycle started on January 13, 2020, and lasted one month, until a few days after observing a sudden drop in pore pressure in two chambers located in the heated zone. The heater in CRQ1704 was damaged during the cooling phase; therefore, the second heating phase was heated only by the remaining nine heater devices.

	Date	Duration	
		Seconds	days
Begin GCS excavation	10/14/2010		
Phase 1		2.4978240E+08	2891
Begin borehole opening	9/13/2018		
Phase 2		2.3587200E+07	263
Begin 1st phase heating	6/3/2019		
Phase 3		1.9353600E+07	224
Begin 2nd phase heating	1/13/2020		
		3.6720000E+07	425
Finish measurement	8/1/2020		

Figure 4-2. The different phases of the CRQ experiment and their durations.

Figure 4-3 shows the heat power history, which was applied in all heater boreholes. The first heating phase was regulated by monitoring temperature in the heated zone, while the second heating phase was regulated in heat power to ensure a better control of temperature in the casing. During the second heating phase, the heat power was increased up to 2,220 W within a few hours, but it was rapidly reduced to 1,750 W, and then it was gradually reduced over the course of the experiment to prevent damage to the internal components of the heater devices.

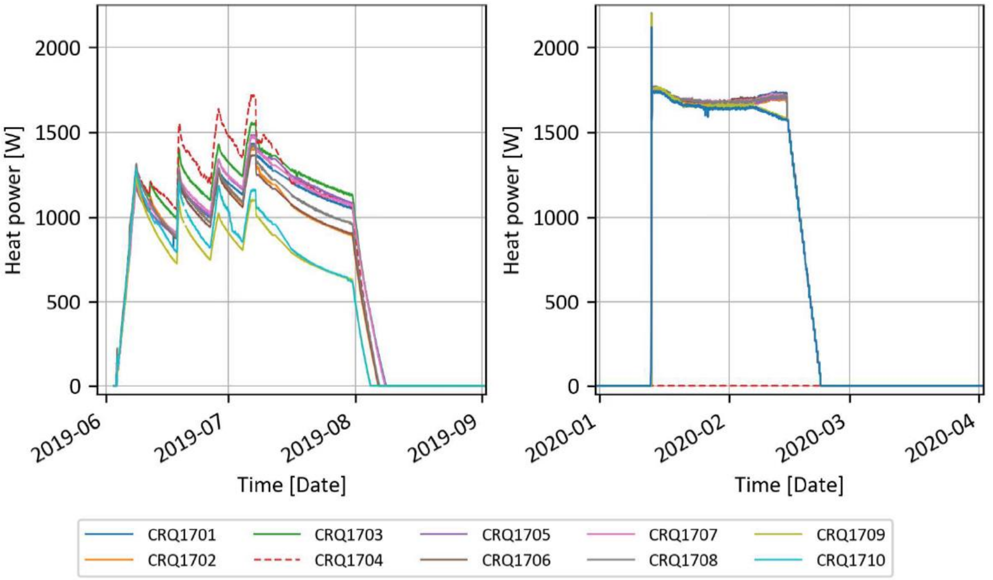

Figure 4-3. Heat power history of the CRQ experiment.

4.1.2 Description of a Numerical Model

A 3D modeling domain consists of a cube with a side length of 50 m, including the GCS drift with a diameter of 5.2 m, and the heater boreholes (CRQ1701 through CRQ1710) with a diameter of 0.172 m, as shown in Figure 4-4. The modeling domain includes the EDZ around GCS drift and heater boreholes to account for the potential longitudinal flow toward the GCS drift during heating phases.

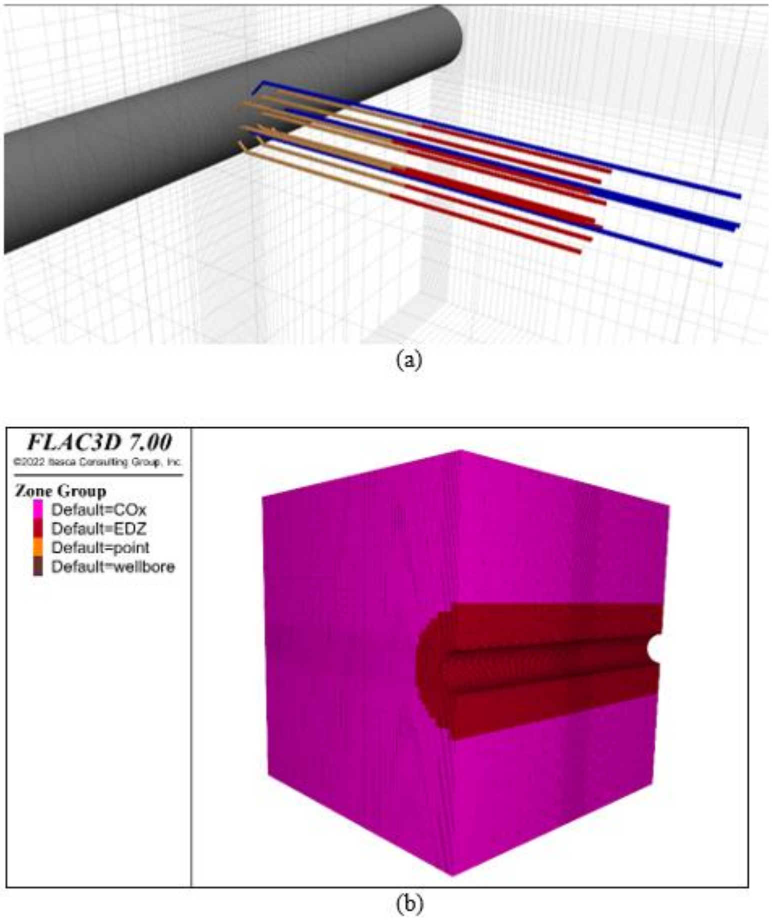

Figure 4-4. The 3D model of the CRQ experiment: (a) the monitoring and heater zones within the COx; (b) the EDZ and COx.

In this study, only the TH portions of the simulation were carried out with iTOUGH (i.e., no mechanical effects). The 3D domain shown in Figure 4-4b is used for visualization purposes only and no mechanical coupling was implemented, which will be simulated in a future study. The input parameter values for the iTOUGH TH simulation are listed in Table 4-1.

Table 4-1. The input parameter values of the CRQ experiment for the iTOUGH simulator.

Parameters	**Notation**	**COx**	**EDZ**	**Heater**
Density of solid grains	ρ_s	2770 kg/m3	2770 kg/m3	7850 kg/m3
Porosity	φ	0.18	0.18	0.18
Permeability (// to bedding)	Kwh	4 e-20 m^2	1 e-17 m^2	4 e-17 m^2
Permeability (ratio (⊥ to bedding)	Kwh	1.33 e-20 m^2		
Thermal conductivity (// to bedding)	λ_h	1.95 W/m/K	1.95 W/m/K	44 e3 W/m/K
Thermal conductivity (ratio (⊥ to bedding)	λ_v	1.28 W/m/K	1.28 W/m/K	1.28 W/m/K
Heat Capacity of solid phase	c_s	1000 J/kg/K	1000 J/kg/K	475 J/kg/K
Volumetric thermal expansion coefficient of solid phase	β_s	4.5 e-5 1/K	4.5 e-5 1/K	4.5 e-5 1/K

As was mentioned earlier, there were several different stages for the CRQ experiment (Figure 4-5). The first stage was the excavation stage, when the GCS drift with a diameter of 5.2 m was excavated, the second stage was the drilling of the heating boreholes, and the third stage was the heating stage.

In the excavation stage, a constant pore pressure of 100 kPa and temperature of 22°C were applied to the zones within the GCS drift, while the rest of the modeling domain was given the initial pressure and temperature of 4.7 MPa and 22°C, respectively. The gravity was not considered in modeling the excavation and the following stages. The following boundary conditions were assigned: the pressure and temperature of 4.7 MPa and 21°C were applied at the top boundary and of 4.7 MPa and 23°C at the bottom boundary, respectively. The side boundaries were specified with no fluid flow and heat flux. The modeling domain was then brought into equilibrium to calculate the initial TH conditions for the subsequent open borehole stage.

In the open borehole stage, permeability of the zones occupying the heating boreholes was altered; the permeability along the borehole was set to a high value of 10^{-4} m^2, whereas permeability in the other two orthogonal directions was set to 10^{-17} m^2. Permeability of the zones occupying the monitoring boreholes was set to the identical value to that of the intact COx (Table 4-1). The modeling domain was then brought into equilibrium with the same boundary conditions specified for the excavation stage.

In the subsequent heating stage, initial conditions for the pressure and temperature distributions were assigned from those obtained at the end of the previous stage. The heating boreholes were split into two portions: one is the length where the heater was embedded, and the other is along the remaining length of the borehole. Permeability of the zones corresponding to the heater length was set to 10^{-17} m^2, whereas that of the zones for the remaining length of the heating boreholes was set to zero (i.e., impermeable). As for the monitoring boreholes, permeability along the longitudinal direction was set to 10^{-14} m^2, whereas the permeability in the other orthogonal directions was set to 4×10^{-17} m^2. The longitudinal permeability of the monitoring borehole was set to the non-zero value to simulate the desaturation of the monitoring boreholes observed during the CRQ experiment. With the identical boundary conditions applied for the earlier stages, the temporal trend of heat source, shown in Figure 4-3, was applied for the heater zones to simulate the heating stage.

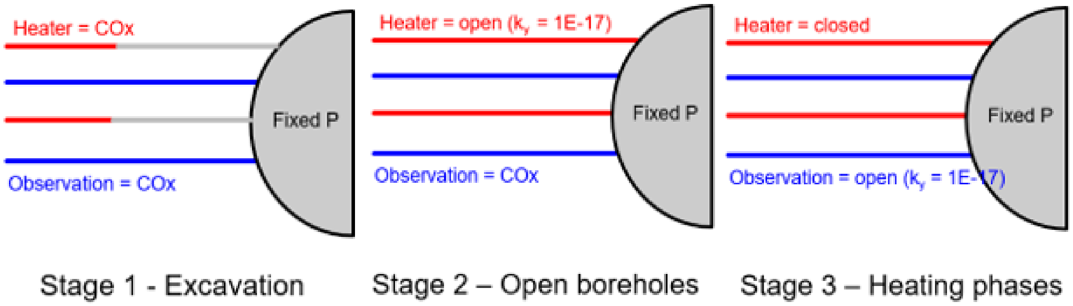

Figure 4-5. The three stages of the CRQ experiment.

4.1.3 Numerical Results

Figure 4-6 shows results of the 3D TH modeling of the CRQ experiment. At the end of the excavation stage (Figure 4-6a), the computed pore pressure distribution in the direction away from the GCS drift was compared against measured data, and it was found that they are in good match with each other. At the end of the following open borehole stage, the pore pressure decreased around the GCS drift and heater boreholes as shown in Figure 4-6b (note that the color within the GCS drift does not indicate pore pressure levels). In the heating stage, the pore pressure increased along with the temperature due to the heating of the boreholes (Figure 4-6c). More precise comparison of pore pressure and temperature at different locations along the monitoring boreholes are presented in the rest of this section.

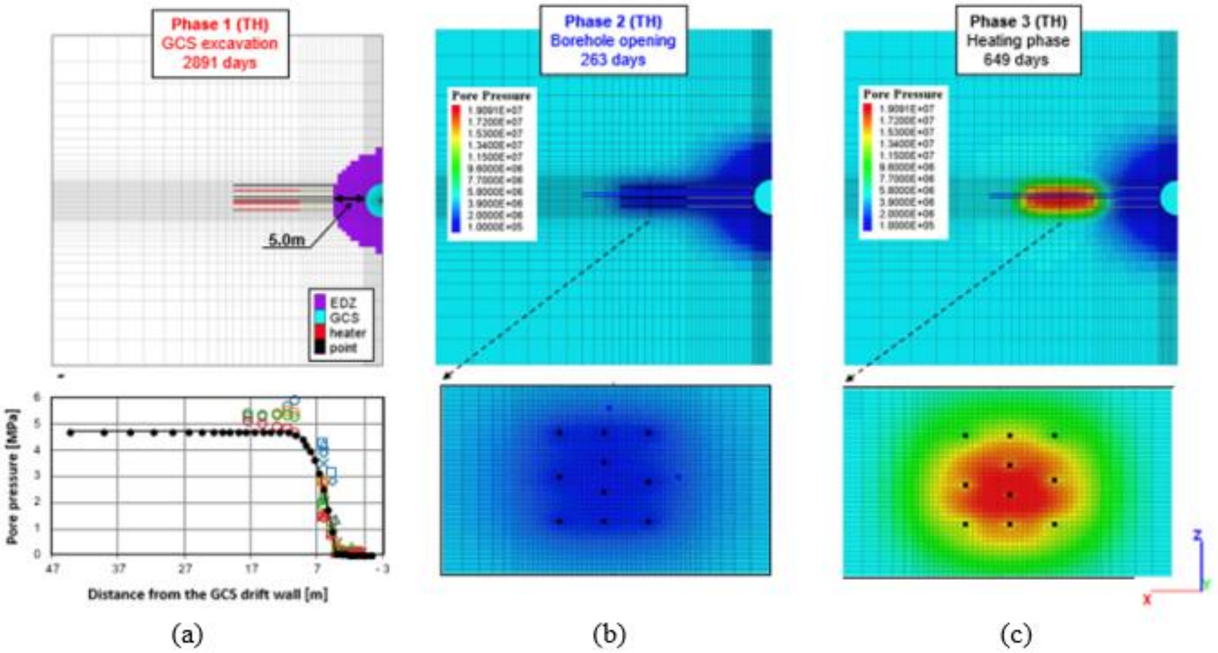

Figure 4-6. Simulated distributions of pore pressure at different stages of the CRQ experiment: (a) excavation stage; (b) open borehole stage; (c) heating stage.

Pore pressure and temperature are compared at three different locations along the monitoring boreholes as shown in Figure 4-7: 8 m, 15 m, and 25 m away from the GCS drift wall. Figures 4-8 and 4-9 show a comparison of pore pressure and temperature, respectively, at the 15 m location. Both pore pressure and temperature were in good match with the measured data. In particular, the desaturation (i.e., when pore pressure was decreasing to zero) at the 1720 and 1721 monitoring boreholes at the end of the first and second heating phases was accurately captured, which was not possible using the 2D model in the study in last year's FY22 report. This was made possible by assigning non-zero longitudinal permeability (10^{-14} m^2) to simulate leakage (i.e., desaturation due to imperfect packer sealing) along the monitoring boreholes. Also, the match for temperature improved relative to the previous 2D results, where the numerically computed temperature was slightly larger than the measured data. The improvement was enabled by assigning anisotropic thermal conductivity between the directions parallel and perpendicular to the bedding of COx.

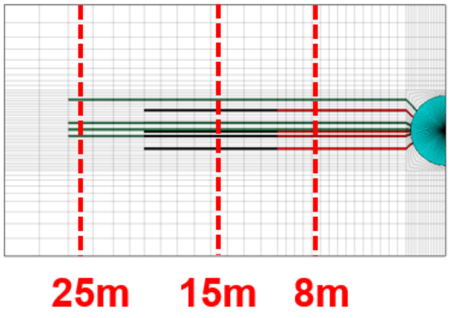

Figure 4-7. The location of the cross-section for pore pressure and temperature comparison.

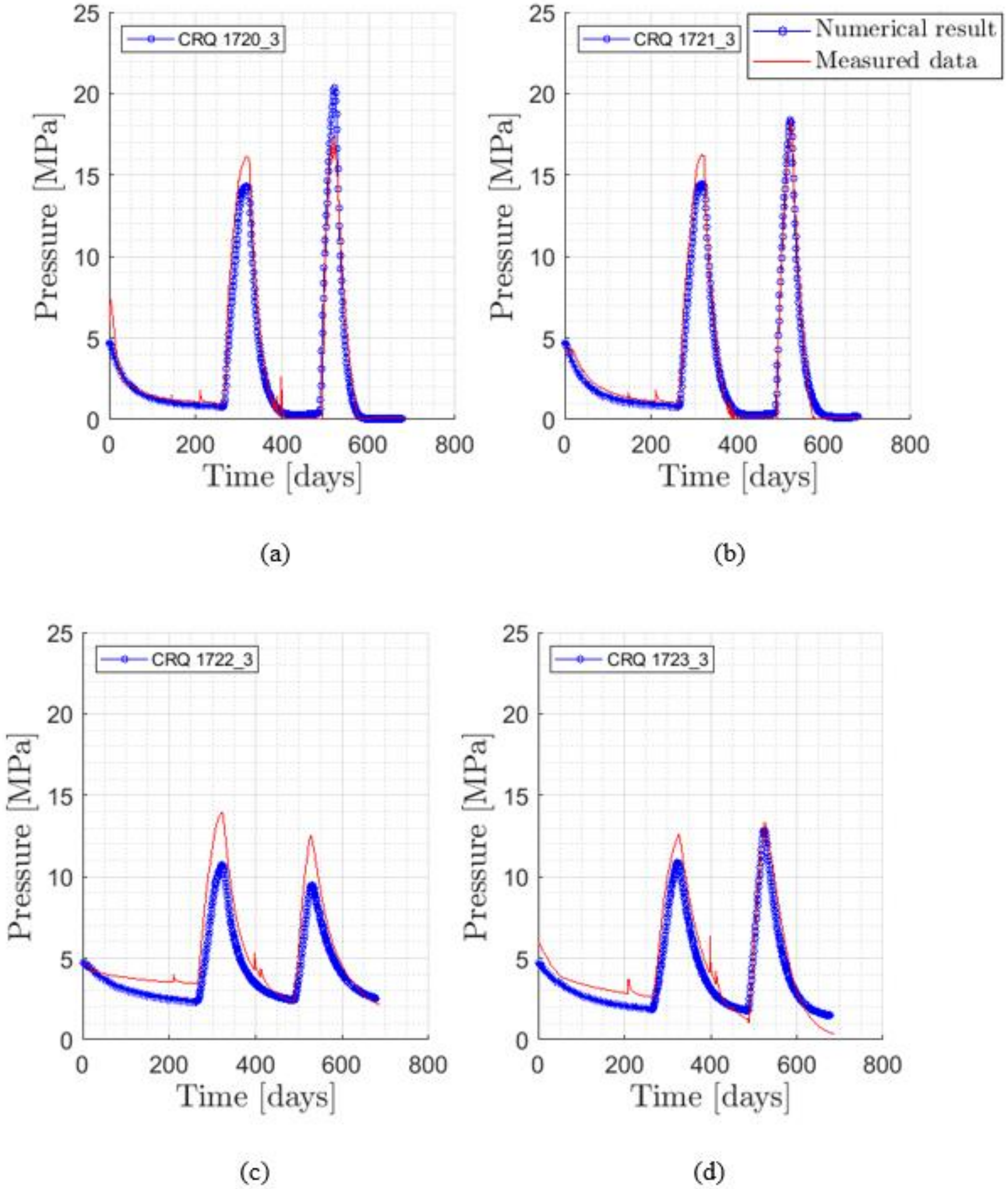

(a) (b)

(c) (d)

Figure 4-8. Comparison of measured and simulated pore pressure evolution 15 m away from the drift wall during the heating stage: (a) CRQ1720; (b) CRQ1721; (c) CRQ1722; (d) CRQ1723.

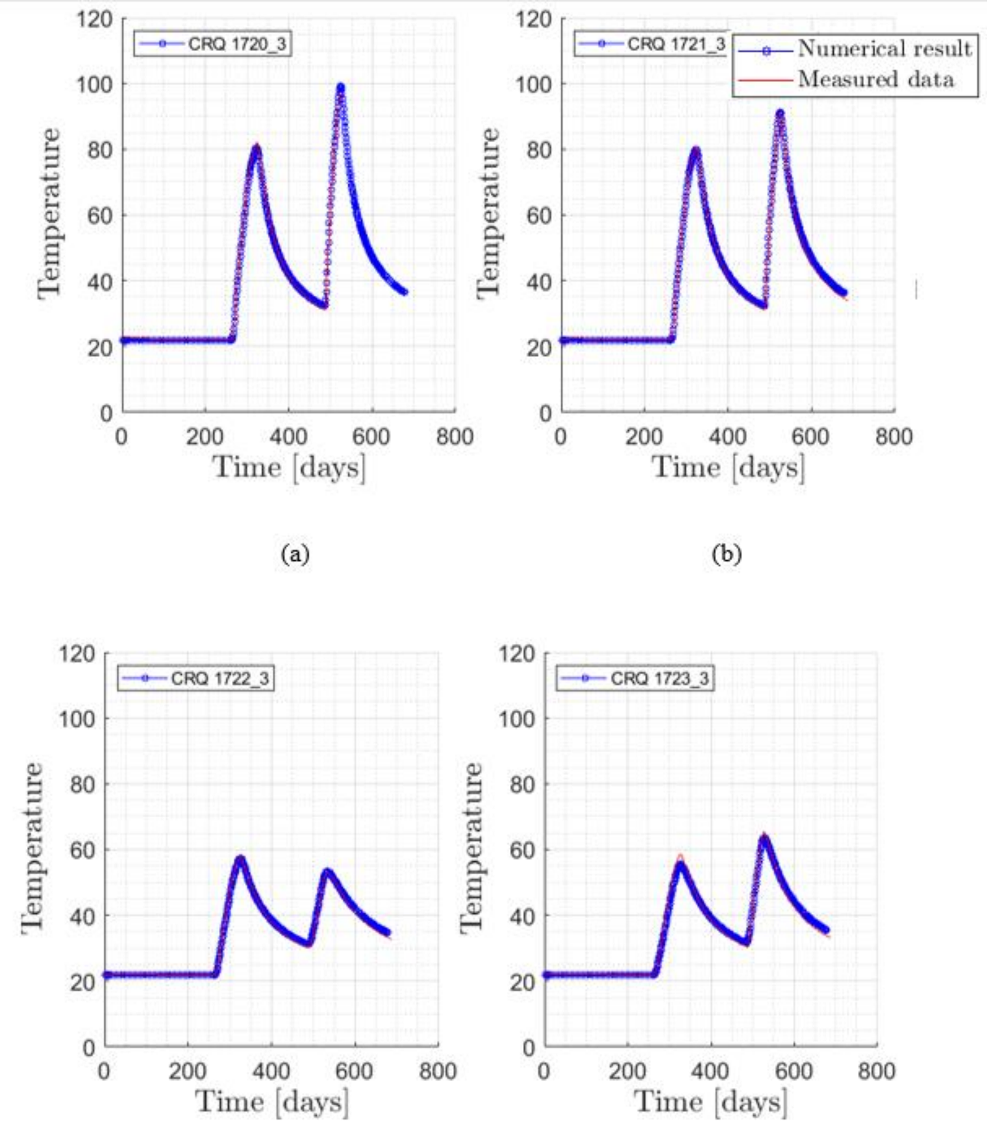

(a) (b)

(c) (d)

Figure 4-9. Comparison of measured and simulated temperature evolution 15 m away from the drift wall during the heating stage: (a) CRQ1720; (b) CRQ1721; (c) CRQ1722; (d) CRQ1723.

Figures 4-10 and 4-11 show a comparison of pore pressure and temperature at the 25 m location. It can be seen that although the match of temperature is good, the match of pore pressure is not (numerical results underestimate the measured pore pressure change). This suggests that the longitudinal permeability along the monitoring boreholes between the 15 m and 25 m locations is larger than what was assigned to the model (10^{-14} m^2). It is also possible that the mechanical effect such as porosity change had a significant effect on the measured pore pressure data.

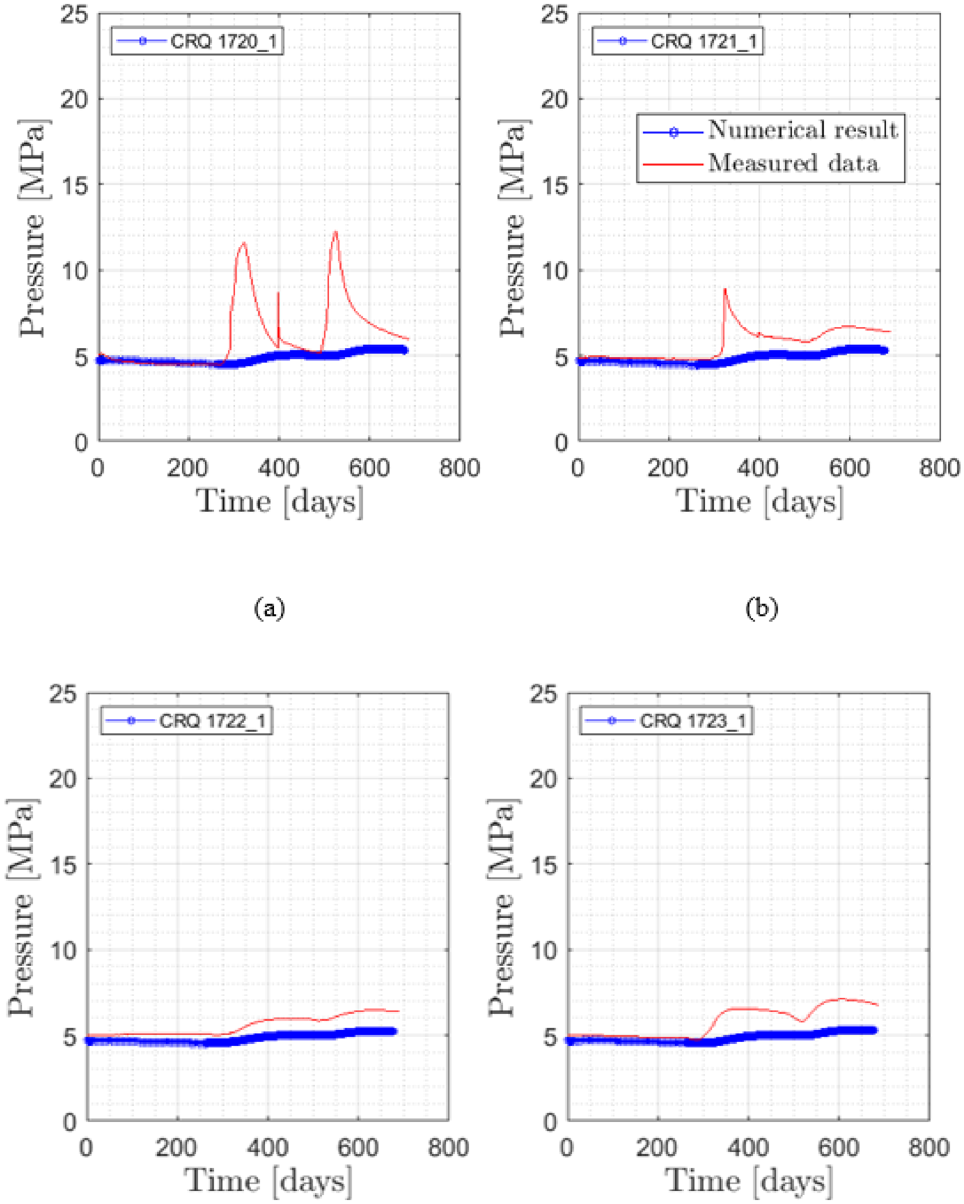

(a) (b)

(c) (d)

Figure 4-10. Comparison of measured and simulated pore pressure evolution 25 m away from the drift wall during the heating stage: (a) CRQ1720; (b) CRQ1721; (c) CRQ1722; (d) CRQ1723.

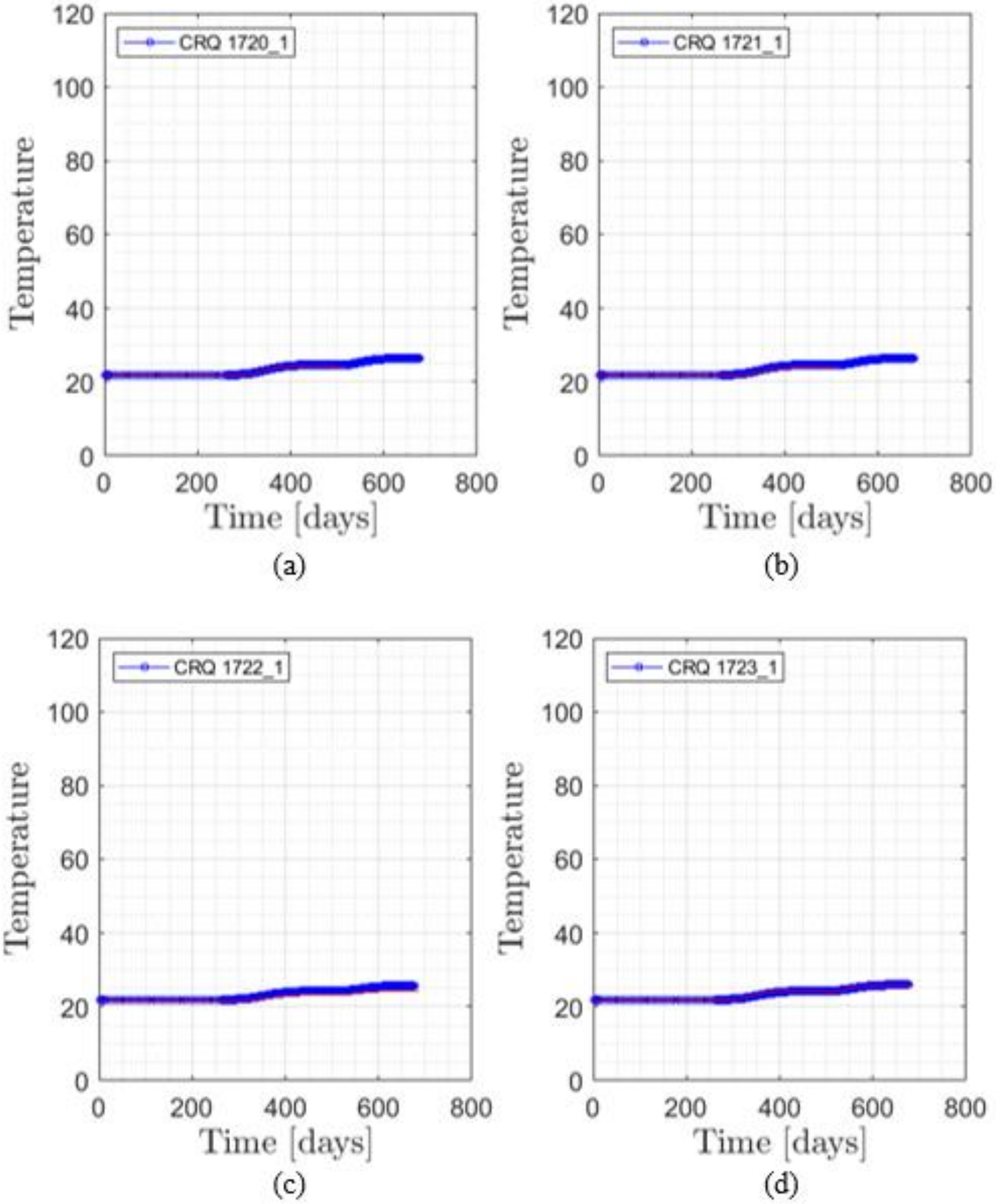

Figure 4-11. Comparison of measured (red) and simulated (blue) temperature evolution 25 m away from the drift wall during the heating stage: (a) CRQ1720; (b) CRQ1721; (c) CRQ1722; (d) CRQ1723.

Figures 4-12 and 4-13 show a comparison of pore pressure and temperature, respectively, at the 8 m location. The same mismatch for pore pressure was present at this location (whereas the match for temperature was good). The maximum error was over 100% at the peak pore pressure at the 1721 borehole (Figure 4-12b). Such a mismatch is probably related to the mechanical effect that was ignored in this study, as porosity reduction due to thermal compaction of COx during heating should increase pore pressure. Hence, in a future study, a coupled THM simulation of the CRQ experiment will be carried out with t TOUGH-FLAC simulator to incorporate the mechanical effect.

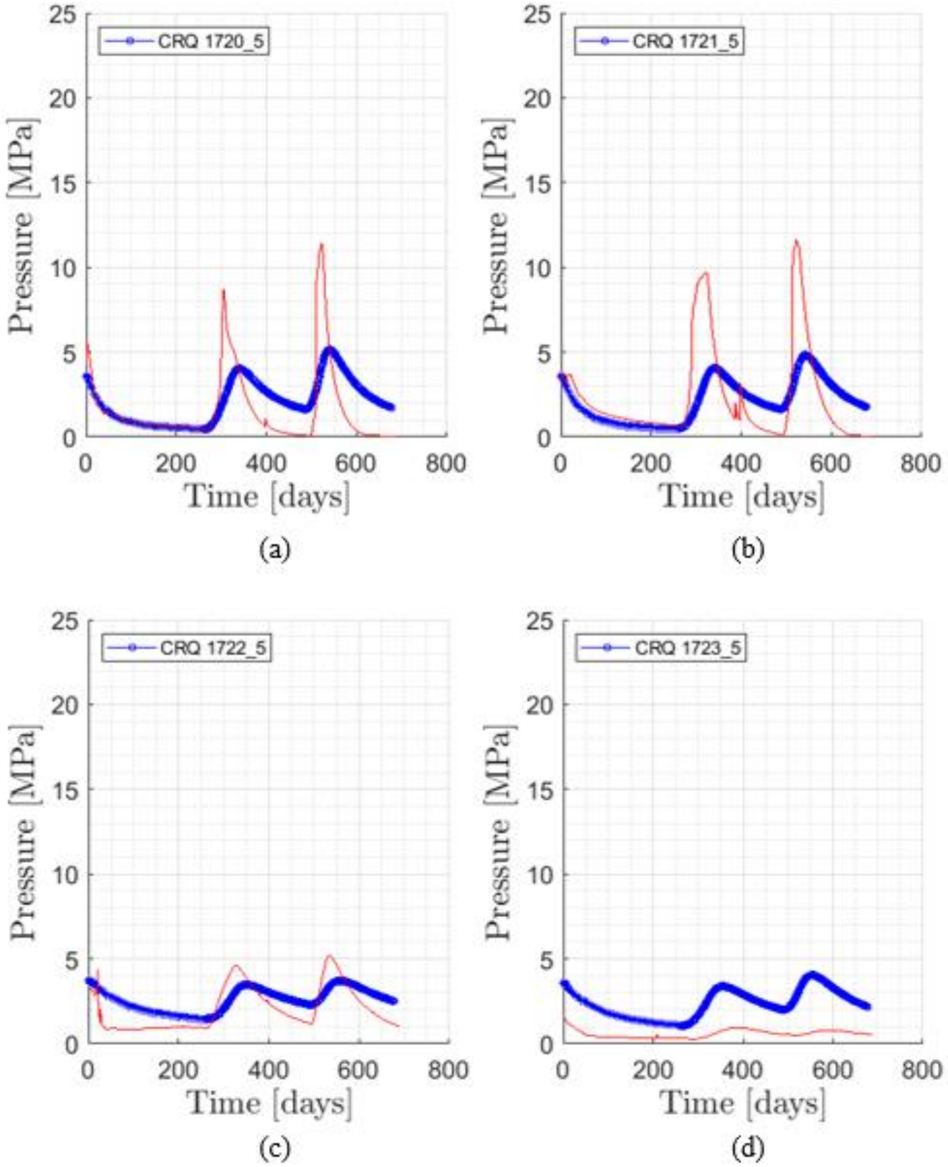

Figure 4-12. Comparison of measured (red) and simulated (blue) pore pressure evolution 8 m away from the drift wall during the heating stage: (a) CRQ1720; (b) CRQ1721; (c) CRQ1722; (d) CRQ1723.

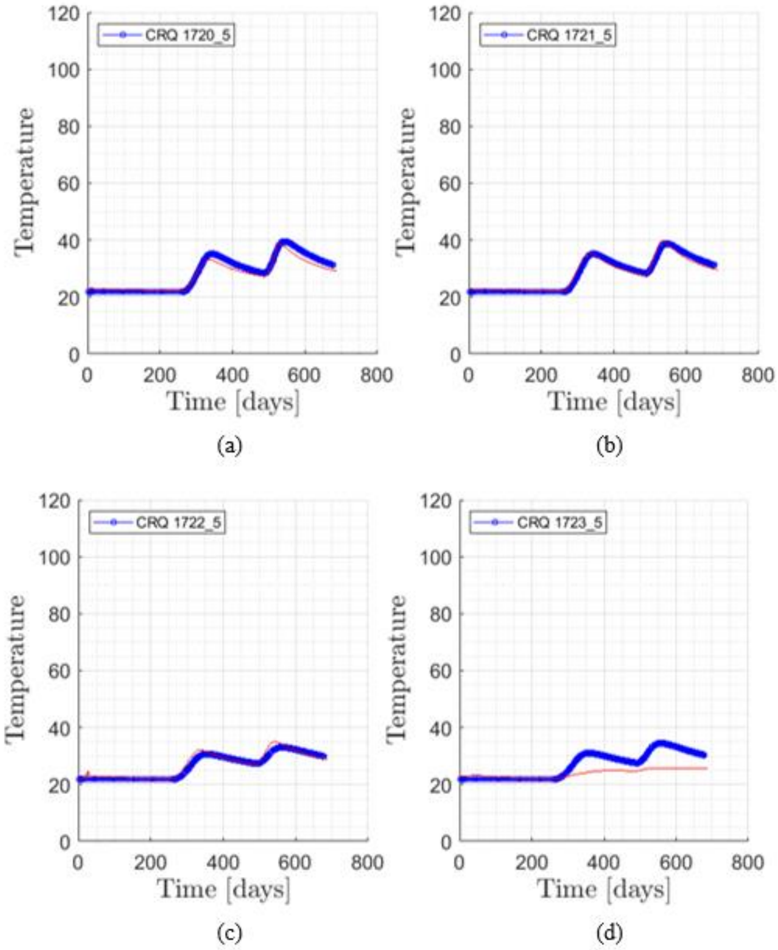

Figure 4-13. Comparison of measured (red) and simulated (blue) temperature evolution 8 m away from the drift wall during the heating stage: (a) CRQ1720; (b) CRQ1721; (c) CRQ1722; (d) CRQ1723.

4.3 Summary and Future work

In this study, a 3D TH modeling of the CRQ experiment was carried out using the iTOUGH software. Although the ultimate objective was to model thermal fracturing caused in HLW repositories, this study focused on capturing the measured pore pressure and temperature data in the CRQ experiment, as the pore pressure and temperature drive mechanical processes including thermal fracturing in HLW repositories. The previous 2D modeling was not able to capture the measured change in pore pressure and temperature because it ignored fluid flow and thermal flux in the direction parallel to the heating and monitoring boreholes. Results of this study using the 3D model showed that the measured change in pore pressure and temperature were better captured by including the 3D TH effects (e.g., non-zero longitudinal permeability along the boreholes and anisotropic thermal conductivity). The limitation of this study is that the mechanical coupling is ignored, such as mechanical stress-induced porosity change, and such a limitation is most likely the cause of the large error between the calculated and measured pore pressure changes at some locations along the monitoring boreholes. Thus, in a future study, a THM coupled simulation of the CRQ experiment will be carried out with the TOUGH-FLAC simulator to better match the measured pore pressure changes, and to simulate thermal fracturing observed in the CRQ experiment.

5. Modeling of Gas Migration in Clay (DECOVALEX-2023)

In this section we present the results of LBNL's activities aimed at modeling gas migration in clay related to Task B of the DECOVALEX-2023 project. The Task B of the DECOVALEX-2023 can be considered as a continuation of a similar task of the previous DECOVALEX-2019 Task A. Task B of DECOVALEX-2023 is led by scientists of the British Geological Survey (BGS). In FY22, LBNL conducted new simulations of a gas migration experiment as well as initial modeling of a Large-Scale Gas Injection Test (LASGIT) performed at the Äspö Hard Rock Laboratory, Sweden.

5.1 Gas Migration in Clay

Four primary phenomenological models describing gas flow, shown in Figure 5-1, can be defined as following: (1) gas movement by diffusion and/or solution within interstitial fluids along prevailing hydraulic gradients; (2) gas flow in the original porosity of the fabric, commonly referred to as viscocapillary (or two-phase) flow; (3) gas flow along localized dilatant pathways, which may or may not interact with the continuum stress field; and (4) gas fracturing of the rock similar to that performed during hydrocarbon stimulation exercises (Harrington, 2016).

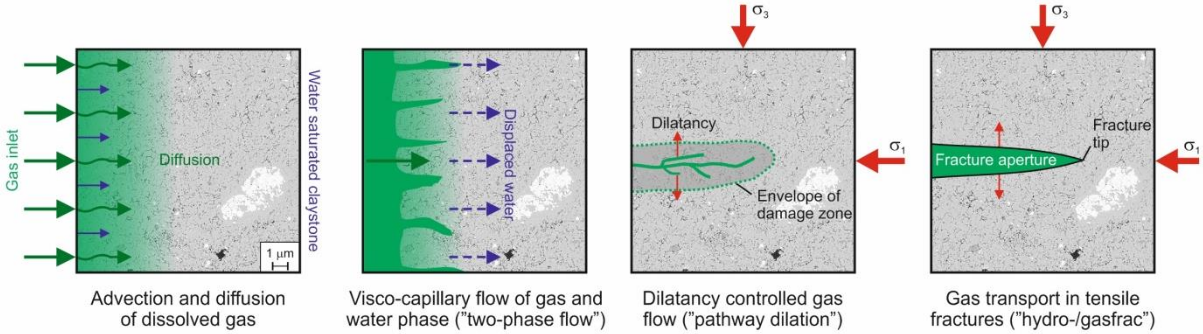

Figure 5-1. Conceptual models of gas flow (Harrington, 2016)

Studies on gas migration in clays (Horseman et al., 1999; 2004; Harrington and Horseman, 1999) indicate that classic concepts of porous medium two-phase flow are inappropriate and continuum approaches to modeling gas flow may be questionable, depending on the scale of the processes and resolution of the numerical model. However, the details of the dilatant mechanisms controlling gas entry, flow and pathway sealing are unclear. As such, development of new and novel numerical representations for the quantitative treatment of gas in clay-based repository systems is therefore required (Harrington, 2016).

LBNL explored two complementary approaches for modeling gas migration associated with DECOVALEX-2019:

- Continuum modeling approach using TOUGH-FLAC simulator (Rutqvist et al., 2011), and;

- Discrete fracture modeling approach using TOUGH-RBSN simulator (Kim et al., 2017).

The continuum approach is based on current developments and applications of TOUGH-FLAC for the modeling of long-term THM performance of nuclear waste repositories in clay host rocks. The TOUGH2 code and other continuum models have been used in the past to model gas migration in clay considering heterogeneous clay properties with pressure dependent permeability, but without considering geomechanical coupling (Senger and Marschall, 2008; Senger et al., 2014). The discrete fracture modeling approach is based on the TOUGH-RBSN simulator, in which the opening of grain boundaries for dilatant gas migration is modeled explicitly using a fracture mechanics approach. The TOUGH-RBSN provided the only discrete fracture model applied to gas migration in DECOVALEX-2019 (Kim et al., 2021; Tamayo-Mas et al., 2021). For DECOVALEX-2023 we focus on the application of the continuum approach to be able to model the field-scale LASGIT experiment and for potential upscaling to the repository scale.

5.2 TOUGH-FLAC Modeling of Gas Migration

The modeling approach that was first developed and applied in DECOVALEX-2019 and presently in DECOVALEX-2023 involves the following basic approach and material models:

- Multiphase (gas and liquid) flow;
- A linear poro-elastic model;
- A linear moisture swelling model; and
- A gas permeability model related to minimum effective compressive stress.

The linear poro-elastic model is based on the assumption of a linear elastic response, based on an effective stress law, and responding to the maximum phase pore pressure (either gas pressure for partially saturated media or liquid pressure for fully saturated media. The model is given by

$$\sigma' = \sigma - P^{\emptyset} \tag{5.1}$$

$$P^{\emptyset} = Max(P^l, P^g) \tag{5.2}$$

where P^{ϕ} is the pore pressure, and P^l *and* P^g are liquid and gas phase pressures, respectively.

The linear moisture swelling model implies a swelling strain as a function of liquid saturation, leading to a swelling stress, according to

$$\Delta\sigma_{sw} = 3K\Delta\varepsilon_{sw} = 3K\Delta S_l\beta_{sw} \tag{5.3}$$

where S_l is liquid saturation, and β_{sw} is the moisture swelling coefficient. These models have been used in the past for simplified modeling of bentonite behavior, and are described in Rutqvist et al. (2011). The applied gas permeability model considers a fracture-like behavior of permeability for dilatant flow paths (Figure 5-2). In this model, permeability is a non-linear function of the effective minimum compressive stress.

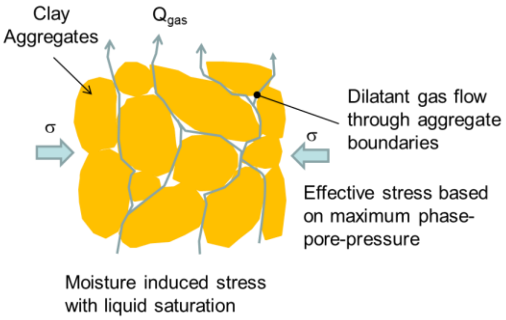

Figure 5-2. Conceptual model for dilatant gas flow through aggregate boundaries considered in a continuum model simulations using TOUGH-FLAC.

The van Genuchten (1980) capillary pressure model is used to define the water retention curve given by

$$P_c(S) = P_0\left([S^*]^{-1/\lambda} - 1\right)^{1-\lambda} \tag{5.4}$$

with $S^* = (S - S_{lr})/(1 - S_{lr})$. The following capillary pressure parameters are adopted for bentonite (Senger and Marschall, 2008): the capillary pressure parameter P_0=18 MPa, shape factor λ=0.45, and residual liquid saturation S_{lr}=0.01.

The relative permeability-saturation relationships of liquid and gaseous phases are parameterized using Corey's model as

$$\begin{gathered} k_{rl}(S) = \hat{S}^4 \\ k_{rg}(S) = m_g\left(1 - \hat{S}\right)^2\left(1 - \hat{S}^2\right) \end{gathered} \tag{5.5}$$

where $\hat{S} = (S - S_{lr})/\left(1 - S_{lr} - S_{gr}\right)$, and m_g is a multiplying factor for the enhanced gas permeability (Corey, 1954). The residual saturations S_{lr} and S_{gr} are provided to limit the mobility of the respective phase, i.e., both liquid and gaseous phases mobility can vary only in the range of $S = \left[S_{lr}, 1 - S_{gr}\right]$. The concept of an effective gas entry pressure, P_{ge}, is applied according to Senger and Marschall (2008). The concept is illustrated in Figure 5-3, where a residual gas saturation of S_{gr} = 0.11, which is a parameter of the gas relative permeability function) corresponds to the effective gas entry pressure P_{ge} = 10 MPa.

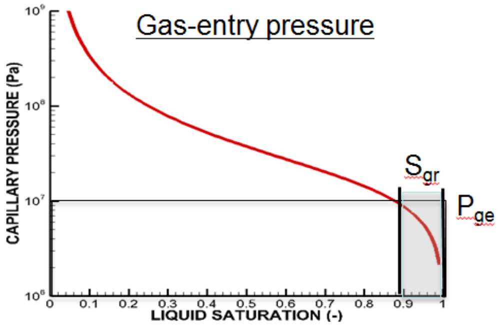

Figure 5-3. The concept of effective gas entry pressure used for the evaluation of the initial pressure response.

In the current simulations of the bentonite used in the laboratory experiment, the intrinsic permeability was set to a fixed value of $k = 3.4\times10^{-21}$ m^2 based on other independent laboratory tests as described in Tamayo-Mas et al. (2021). The gas permeability can increase more strongly with the gas saturation as well as a result of changes in effective stress. A relation between permeability and effective minimum compressive stress is shown in Figure 5-4 and simulates a fracture flow like behavior in each continuum element. First the permeability of an element is calculated as

$$k_{FC} = k_{matrix} + k_{fracture} = k_{matrix} + \frac{b_h^3}{12d} \tag{5.6}$$

where d is the element size and b_h is hydraulic conducting fracture aperture is calculated as

$$b_h = \frac{b_{h0}}{1+9\left(\frac{\sigma_n - p}{\sigma_{n,ref}}\right)} \tag{5.7}$$

where b_{h0} is a residual permeability maintained even at very high stress, σ_n is the stress normal to fracture plane, p = pore pressure, and $\sigma_{n,\,ref}$ is a reference stress. In this modeling, σ_n is assumed to be equal to the least compressive principal stress, and $\sigma_n - P$ would be the least compressive effective principal stress. The two parameters, $b_{h0} = 2.9\times10^{-6}$ m, and $\sigma_{n,ref} = 0.2\times10^6$ Pa, were determined by trial simulations to obtain the best possible match with experimental data.

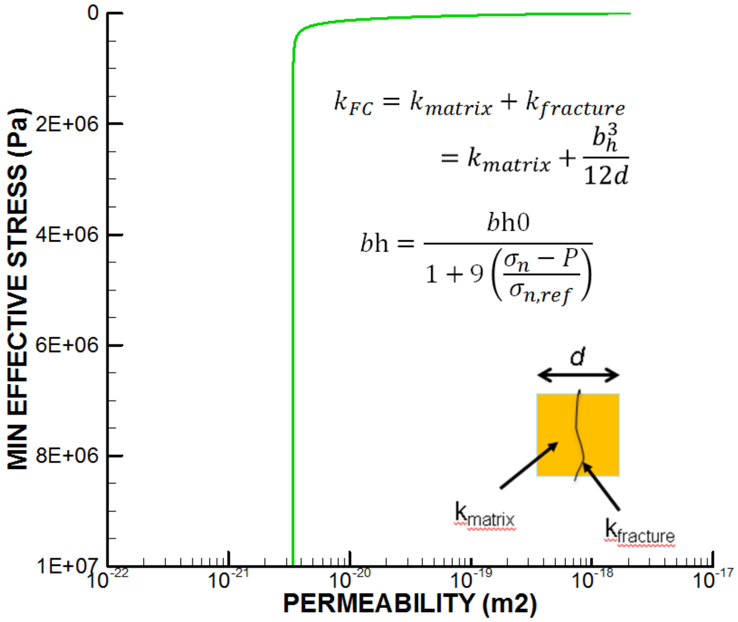

Figure 5-4. Relation between min effective stress and permeability used in numerical modeling.

5.3 Modeling 1D gas migration

LASGIT is a full-scale experiment based on the Swedish KBS-3 repository concept, examining the processes controlling gas and water flow in highly water-saturated compact buffer bentonite (Cuss et al., 2014). The experiment was conducted at a depth of 420 m in the Äspö Hard Rock Laboratory, Sweden (Figure 5-5). The installation phase of LASGIT was undertaken from 2003 to early 2005 and consisted of the design, construction and emplacement of the infrastructure necessary to perform the experiment. The experiment was initiated on February 1st, 2005, following the closure of the deposition hole.

The original aim of the LASGIT experiment was to perform a series of gas injection tests through water-saturated clay in a full-scale KBS-3 deposition hole (Cuss et al., 2014). In essence, the LASGIT experiment consists of three operational phases: an installation phase, a hydration phase and a gas injection phase. The initial hydration phase began on February 1st, 2005, with the closure of the deposition hole. A full-scale KBS-3 copper canister with iron insert was modified for the LASGIT experiment with thirteen circular filters of varying dimensions located on its surface in three separate arrays, to provide point sources for gas injection simulating potential (Figure 5-6).

The canister was surrounded by specially manufactured pre-compacted bentonite blocks, all of which had initial water saturations in excess of 95% (Cuss et al., 2010, 2014). In the engineering void between the pre-compacted bentonite rings and the rock-wall, bentonite pellets were used. As the bentonite system began to saturate these swelled to fill the construction gaps and form a seal around the canister.

The deposition hole, buffer and canister were equipped with instrumentation to measure the total stress, pore-water pressure and relative humidity in 32, 26 and 7 positions respectively (Figure 5-6). Additional instrumentation continually monitored variations in temperature and relative displacement of the lid.

In DECOVALEX-2023, the teams will model a gas test denoted Gas Test 4 performed at filter FL903 (Figure 5-6). The results of injection flow rate and injection pressure response is shown in Figure 5-7. A peak pressure of 6.2 MPa is close to the local swelling stress in the bentonite buffer. After the peak, the pressure the injection pressure drops sharply, followed by a more gradual pressure decline while injecting gas at the constant rate. The DECOVALEX-2023 models the gas injection and comparison will be conducted between simulated and measured responses of flow rate, pressure and stress at the different monitoring points.

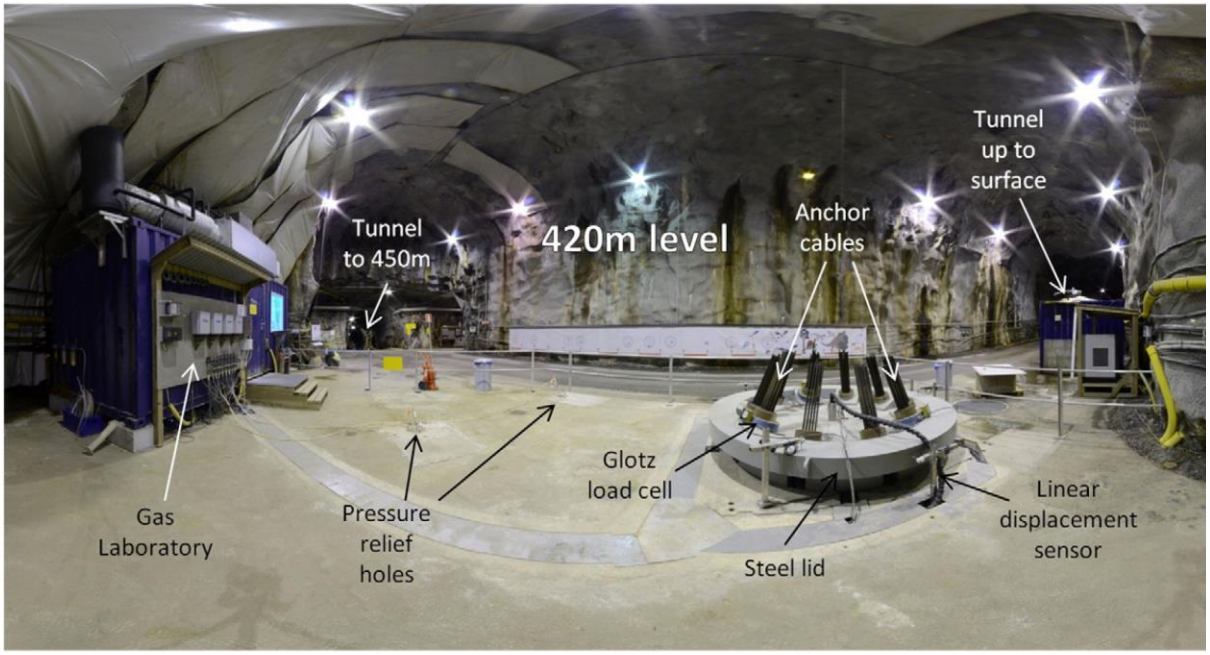

Figure 5-5. A panoramic view of the LASGIT test site located 420 m below ground at the Äspö Hard Rock Laboratory in Sweden (Cuss et al., 2014).

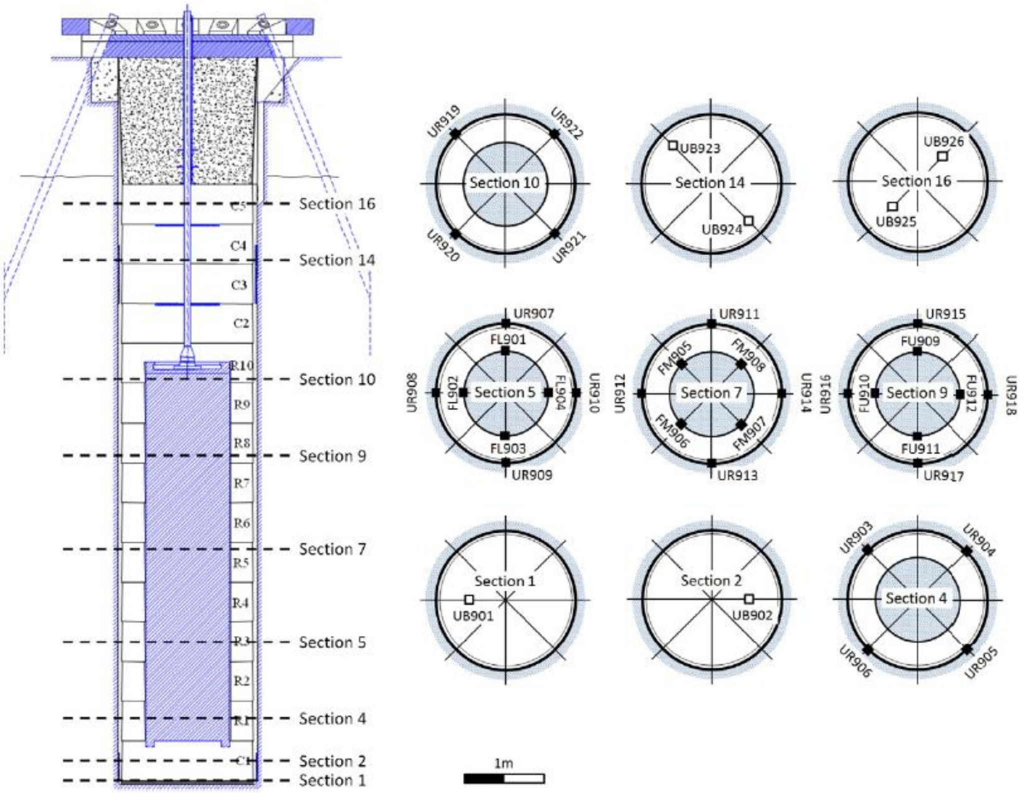

Figure 5-6. Schematic layout of the LASGIT experiment showing the locations of sensors (Cuss et al., 2014).

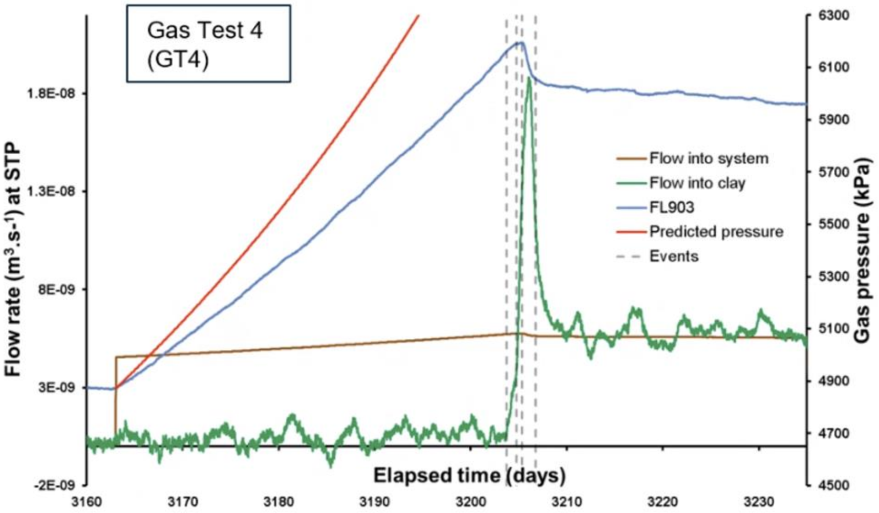

Figure 5-7. Injection pressure and flow rate during the Gas Test 4 at LASGIT (Cuss et al., 2022).

5.4 Modeling of LASGIT Test 4 Gas Injection

The modeling of the LASGIT Gas Test 4 was performed using TOUGH-FLAC with the same modeling approach and material model as in the previous modeling of the laboratory experiment. One addition in the modeling of the LASGIT was the consideration of interfaces between the canister and bentonite blocks, between individual bentonite blocks, and between the bentonite and host rock. In FY23, a full three-dimensional model has been developed as shown Figure 5-8. The interfaces have the same material model as listed above, including stress dependent gas permeability. The properties might be different from that of the blocks. For example, an interface between two blocks might be slightly more permeable than the blocks themselves. In this initial model the most attention is paid to the buffer.

The initial conditions in the model are:

- 100% liquid saturation
- Initial pressure 0.8 MPa
- Initial vertical stress 6 MPa
- Initial radial (and tangential) stress 5 MPa
- Initial temperature 15°C
- Initial pressure in injector 1.8 MPa

Figure 5-9 presents the simulation results of flow and pressure responses of the injection system. The injection element was initially filled with gas at a pressure of 1,868 kPa. Water was then injected into the gas filled injection element to compress the gas and raise the pressure according to the steps shown in the field. Because this is a half symmetric 3D model, only half of the injection filter and injection rate is modelled. The volume of the element was calibrated in order to achieve a good match with the field data. The calibrated volume was 2,000 mL for the half symmetric model. This means that the total injector volume was calibrated to 4,000 mL. This is slightly larger than the quoted 3,750 mL gas injection volume reported from the field.

After the initial sensitivity study, it was found that the properties listed in Table 5-1 could be used. The properties used for the bentonite block are those that were determined by previous modeling of laboratory gas migration experiments (Rutqvist et al., 2022). For the interface, further calibration was done to match the field data at LASGIT. The permeability of interface element was increased by one order of magnitude higher than for the bentonite blocks. Moreover, the residual gas saturation, $S_{gr,}$ was reduced from 0.11 to 0.05.

Figure 5-14 shows the gas flow and pressure response at the injection element. The simulated peak flow rate and the peak pressure in Figure 5-14 are similar to the measured peak flow rate and a peak pressure shown in Figure 5-12. Figures 5-15 and 5-16 depict how the gas propagates along the interfaces during more than hundred days after the initial gas breakthrough. The simulations are done for two different cases. In a based case shown in Figure 5-15, the basic properties as in Table 5-1 are used. However, some gas could penetrate into the first element of the blocks near an interface. For the case shown in Figure 5-16 it was assumed that the blocks were completely impermeable. In such a case the gas spread much further along the interfaces. Figure 5-17 shows a comparison of the simulation results of pressure changes for the two cases. In the case of completely impermeable blocks, a significant pressure change would occur at monitoring point PC902. Field measurements shows very small pressure changes in this point indicating that the base case with some penetration of gas into the blocks might be more realistic.

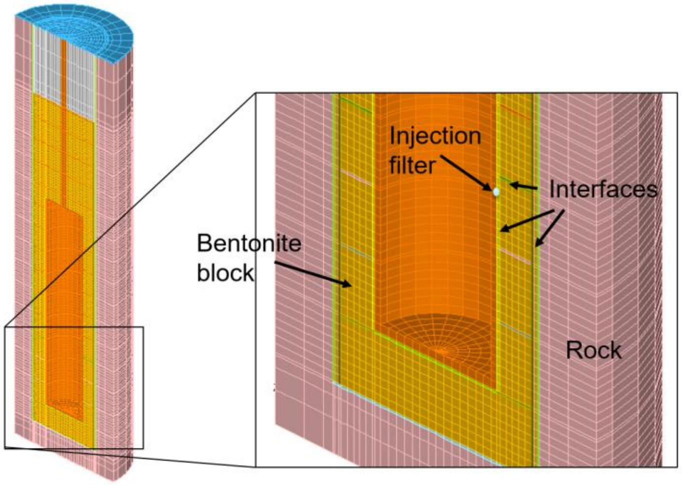

Figure 5-8. TOUGH-FLAC model of the LASGIT experiment for modeling Gas Test 4.

Table 5-1. Parameters used in modeling of gas injection Test 4 at LASGIT.

Meaning	**Symbol [units]**	**Bentonite blocks**	**Interfaces**	**Comments on source or calibration**
Elastic modulus	E [MPa]	307	307	Given in DECOVALEX Task Definition
Poisson's ratio	ν [-]	0.4	0.4	Given in DECOVALEX Task Definition
Porosity	ϕ [-]	0.44	0.44	Given in DECOVALEX Task Definition
Biot's coefficient	α [-]	1	1	Reasonable value for clay
Swelling coefficient	β_{sw} [-]	0.015	0.015	Calibrated from lab experiments (Rutqvist et al., 2022).
Max aperture for stress-k	bho [m]	$4.9\text{x}10^{-6}$	$4.9\text{x}10^{-6}$	Calibrated from lab experiment (Rutqvist et al., 2022).
Reference stress for stress-k	$\sigma_{n',ref}$ [MPa]	0.1	0.1	Calibrated from lab experiment (Rutqvist et al, 2022)
Intrinsic permeability	$[m^2]$	3.4e-21	3.4e-20	Given for blocks but increase 1 order for interfaces
Capillary pressure parameter Capillary scaling: P0	[MPa)	18	18	Fixed: Senger and Marschall (2008)
Capillary pressure parameter Shape factor: λ	[-]	0.45	0.45	Fixed: Senger and Marschall (2008)
Capillary pressure parameter Residual liquid saturation S_{lr}	[-]	0.01	0.01	Fixed: Senger and Marschall (2008)
Corey relative permeability. Residual liquid saturation S_{lr}		0.1	0.1	Fixed: Senger and Marschall (2008)
Corey relative permeability. Residual gas saturation S_{rg}		0.13	0.05	This parameter provides for gas entry pressure. For block calibrated from lab tests. For interface calibrated in this study.

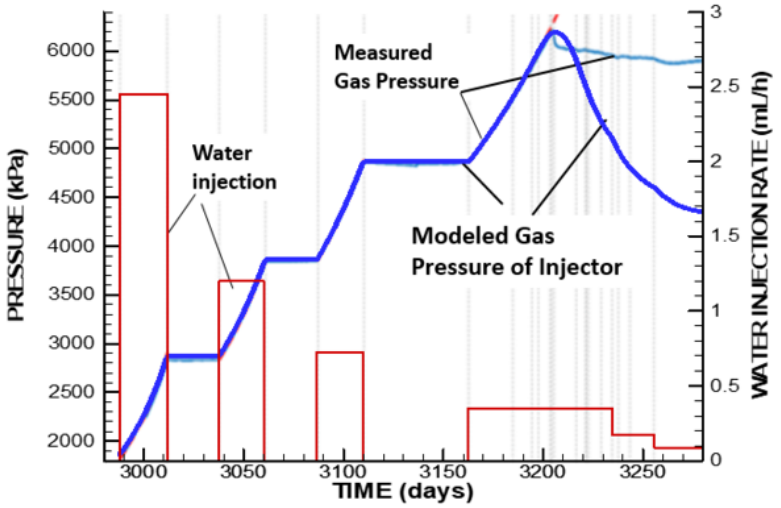

Figure 5-9. Simulation results for gas pressure of the injector (dark blue line) at the LASGIT experiment with comparison to the measured gas pressure (light blue line). The measure values of pressure plots behind the blue line of modeled gas pressure until peak pressure at about 3,200 days. The red line show water injection rates that are input into the TOUGH-FLAC simulations.

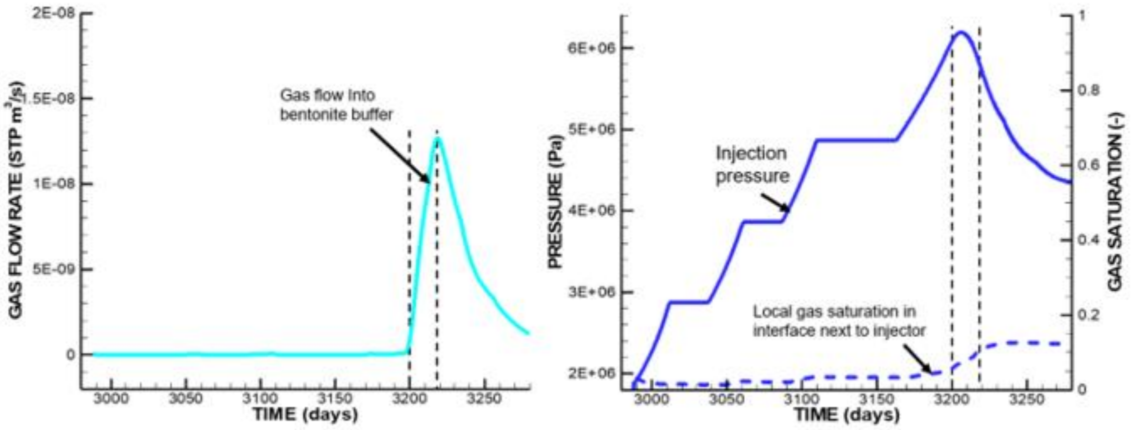

(a) (b)

Figure 5-10. TOUGH-FLAC modeling results of (a) injection rate, and (b) injection pressure and gas saturation evolution in the interface next to the modeled injector.

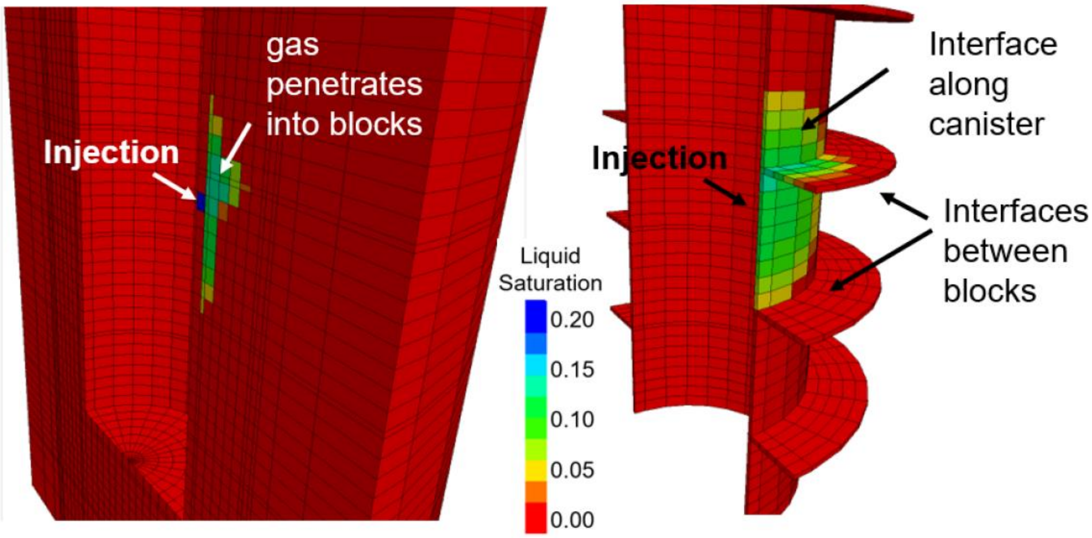

Figure 5-11. TOUGH-FLAC modeling results of pressure at 100 days after gas breakthrough (field experimental time = 3,300 days) for a base case with properties in Table 5-1.

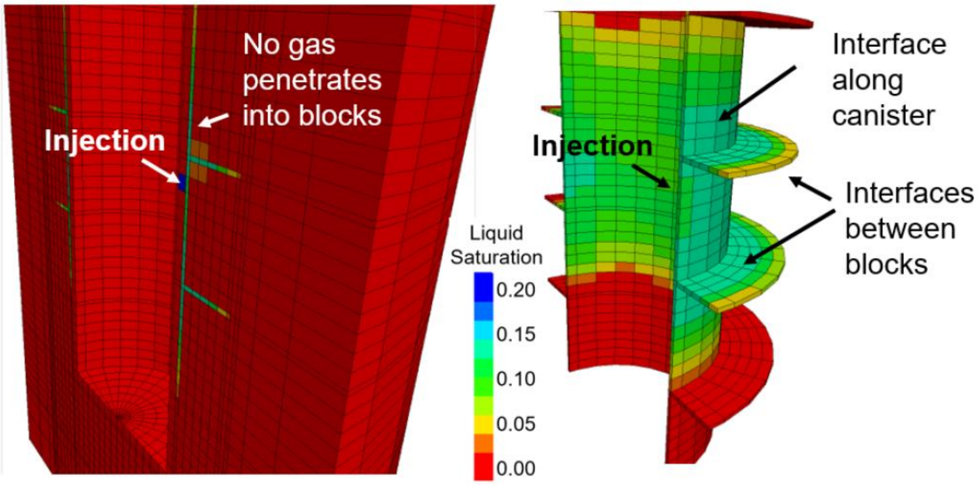

Figure 5-12. TOUGH-FLAC modeling results of pressure at 100 days after gas breakthrough (field experimental time = 3,300 days) for a case assuming impermeable bentonite blocks.

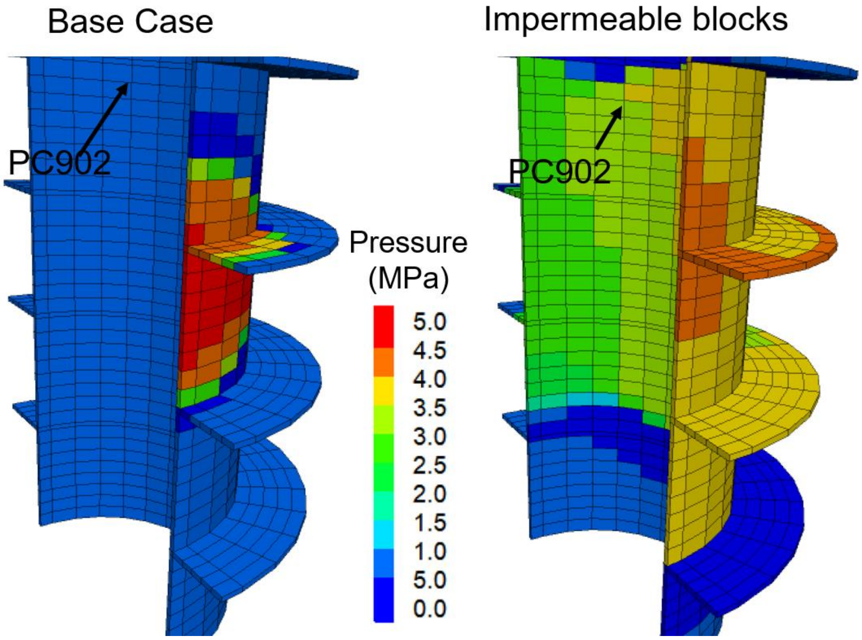

Figure 5-13. Comparison of pressure changes at 100 days above gas break through (3,300 days experimental time) for the base case and case of impermeable blocks.

5.5 Future Work on Gas Migration

The next step will be to conduct further model simulations on the full 3D model of the LASGIT, and to include a more detailed comparison to the experimental data and to the results of other modeling teams within the DECOVALEX-2023 project. Moreover, based on this material model that have been validated against LASGIT data, a model simulation of gas generation and gas migration at full scale repository tunnel will be performed.

6. Machine Learning of Fault Stability in Mont Terri

6.1 Introduction

Repository-induced interactions between the host rock and EBS may lead to reactivation of existing faults or fractures. This can result in an increase in permeability of the argillaceous host rock. It is important to understand how fluid pressure and stress changes can lead to fault reactivation to assess the long-term safety of HLW disposal. With this objective in mind, *in-situ* experiments of controlled fault activation have been conducted at the Mont Terri URL in Switzerland (Guglielmi et al., 2020, 2021). These experiments involve the injection of high-pressure synthetic pore water in a fault zone intersecting the OPA formation. Different types of monitoring techniques (e.g., active seismic systems, step-rate injection sensors, distributed acoustic sensors) are used to monitor the changes in pore pressure and fault displacements. In addition to characterizing the fault response, the rich quantity of data collected from these experiments motivates us to develop a new generation of predictive models capable of assessing the short- and long-term safety of the OPA as a potential host rock.

Numerical models that seek to predict the hydro-mechanical (HM) response of fault reactivation require a robust formulation to capture the rapid and strong coupling between the fluid flow and deformation (including the fault slip). In addition, the complex 3D fault geometry, material composition, and nonlinear and discontinuous shearing behavior of a fault are challenging to capture with a general constitutive law in a numerical model. To overcome such limitations of numerical modeling, ML provides an alternate yet powerful modeling framework. In contrast to the above physics-based models, ML models do not require prior information about physical constraints or constitutive relationships. By learning from sufficient data, ML can predict physical changes in time and space without explicitly solving coupled physical processes. The *in-situ* fault activation experiments at Mont Terri provide a large quantity of data from diverse sources. However, ML on such datasets has never been attempted. In this study, we take this opportunity to develop novel ML approaches to predict the HM response of a fault.

In this chapter, we use a ML approach to model fault response due to high-pressure synthetic pore water injection. ML approaches are increasingly being used in earth science applications (Mital et al., 2020; Hu et al., 2021; e.g., Dwivedi et al., 2022; Mital and Andrade, 2022). To make predictions based on sequences of data, we utilize long short-term memory (LSTM) networks. LSTM networks possess the ability to extract temporal dependencies in data, making them an ideal candidate to analyze and predict the sequence of pore fluid injection, fault slip, fluid pressure dissipation, and the cycling of such a sequence. Since their invention, LSTMs have been used extensively in problems such as speech recognition, language modeling, language translation and image captioning. In earth sciences, LSTM networks have been used in applications such as rainfall-runoff modeling, earthquake detection, and landslide modeling (e.g., Kratzert et al., 2018; Yang et al., 2019; Wang et al., 2020). The proliferation of ML applications has been aided by the advent of open-source libraries such as TensorFlow and PyTorch, which make it straightforward to implement increasingly complex ML architectures.

The goal of this work is to develop a model that can generate the evolution of pore pressures and fault displacements in response to fluid injection. We start by training a model on a few injection cycles and then evaluating its ability to generate the response for subsequent injection cycles. In doing so, we investigate whether a ML model can reproduce key HM processes of fault response: such as peaks in pore pressure and displacement during fluid injection, and decays in pore pressure and displacement during injection shut-in. We develop a methodology that can be used to train LSTM models to reliably generate the HM response of a fault when subjected to fluid injection.

Section 6.2 begins by presenting a brief description of the fault slip data used in this work. This is followed by a brief overview of LSTM networks that are used to model the fault response (Section 6.2.2). We then describe the model setup, which clearly describe the model inputs and outputs, as well as the steps needed to reliably capture fault response (Section 6.2.3). We then summarize our approach for model evaluation (Section 6.2.4) and our experimental design (Section 6.2.5). Thereafter, we present the results of our predictive model, and discuss the importance of carefully training a model. Finally, we conclude by presenting a summary of the current work along with some future directions. As far as notations are concerned, boldface lower-case variables correspond to vectors (e.g., $\boldsymbol{b}$), and boldface upper-case variables correspond to matrices (e.g., $\boldsymbol{W}$).

6.2 Data and Methods

6.2.1 Mont Terri Fault Slip FS-B Experiment Data

In this work, we utilize data from the Mont Terri Fault Slip FS-B experiment. The FS-B experiment was designed to study the integrity of a faulted caprock and involved seismic imaging of fluid flow and stress variations during six constant flowrate pore water injections directly in the fault zone. A detailed description of the FS-B experiment along with its instrumentation can be found in Guglielmi et al. (2021). Here, we only describe the data obtained via a SIMFIP probe (Step-Rate Injection Method for Fracture In-Situ Properties, Guglielmi et al., 2014) installed in the injection borehole. The SIMFIP probe monitors the relative displacement between the hanging wall and footwall of the Main Fault, in addition to pore pressure and injection flowrate.

The FS-B experiment took place on November 21, 2020. Six injections were conducted at constant flowrates 2 l/min (injection 1), 6 l/min (injection 2), and ~10 l/min (injections 3, 4, 5, 6; Figure 6-1). Injections 1-5 were 10 minutes long while Injection 6 was 20 minutes long. Instantaneous increase in pressure and displacements were observed with injection pressure increase (Figure 6-1). During injection shut-in periods, which were about 45 to 90 minutes long, slow decays in pressure and displacements were observed following an initially rapid decline. Note that the sampling frequency of the data was 0.5-1 kHz. For this work, the data were down-sampled to 2 Hz. The resultant time-series of injection and response was about 9 hours (or 16,000 time steps) long.

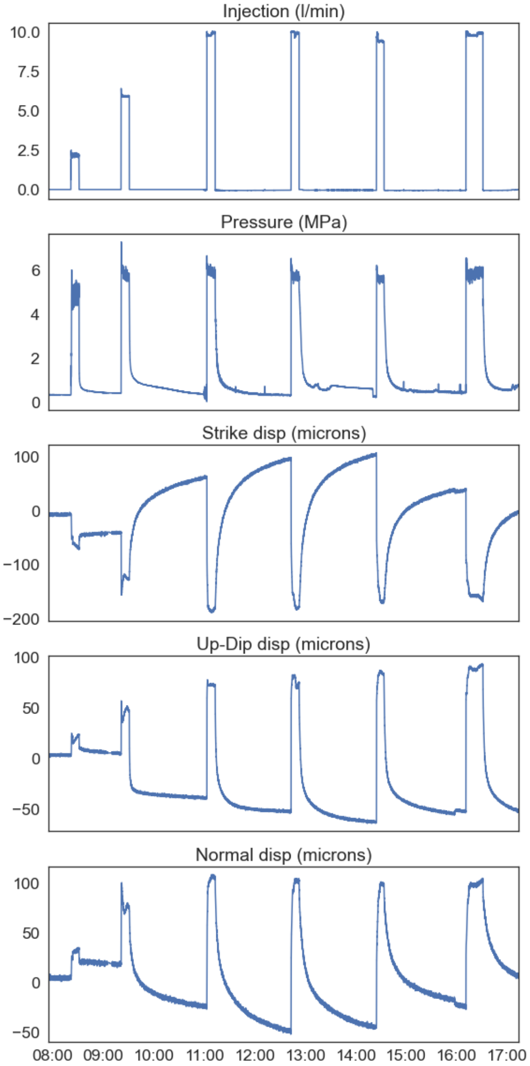

Figure 6-1. Injection borehole data obtained via SIMFIP probe (Guglielmi et al., 2021).

It is important to highlight some salient features of the fault response (Guglielmi et al., 2021). Cycle 1 is characterized by the onset of fault rupture or fracture opening. The flow rate was kept low to induce a gradual progression of fault slip. Cycle 2 involved an increase in flow rate which was accompanied by an increase in permeability and dilation of the fault. Cycle 3 involved the formation of a hydraulic connection between the injection borehole and a neighboring borehole (not shown). As fluid was now leaking in the fault zone, the injection flow rate was not increased for subsequent cycles. Cycles 4, 5, 6 were characterized by an increasing dilatant behavior of the fault, where causing irreversible displacements, which became larger with each successive cycle.

Long Short-Term Memory (LSTM) Networks

LSTM networks (Hochreiter and Schmidhuber, 1997) belong to a family of neural networks, called recurrent neural networks (RNNs), that process sequential data. A neural network consists of a collection of nodes, or ‘neurons’, which are grouped into three types of layers: input layer, hidden layer(s), and output layer. The conceptual basis of an RNN is formed using a feedforward neural network, which is schematically represented in Figure 6-2a. The nodes in the input layer consist of model input, while nodes in the output layer report the model output.

Each node in the hidden layer(s) and the output layer takes in all the nodes from the preceding layer as inputs and produces a single output by computing a weighted sum. For any layer after the input layer, given an n-dimensional input vector $\boldsymbol{x}$, the output is expressed as:

$$\hat{\boldsymbol{y}} = F(\boldsymbol{W}\boldsymbol{x} + \boldsymbol{b}) \tag{6.1}$$

where $\boldsymbol{W}$ is a weight matrix (unique to each layer), $\boldsymbol{b}$ is a bias vector, and F is an activation function (such as sigmoid or tanh) whose purpose is to introduce non-linearity in the computation. $\hat{\boldsymbol{y}}$ approximates the true output $\boldsymbol{y}$**.** If our input consists of a sequence of data given by $\left(\boldsymbol{x}^{(1)}, \boldsymbol{x}^{(2)}, \boldsymbol{x}^{(3)}, \dots, \boldsymbol{x}^{(k)}\right)$, then the above formulation will result in a sequence of outputs $\left(\hat{\boldsymbol{y}}^{(1)}, \hat{\boldsymbol{y}}^{(2)}, \hat{\boldsymbol{y}}^{(3)}, \dots, \hat{\boldsymbol{y}}^{(k)}\right)$, where $\hat{\boldsymbol{y}}^{(t)}$ is the output corresponding to input $\boldsymbol{x}^{(t)}$. Each input can be thought of an n-dimensional vector, with the superscript t corresponding to the position in the sequence.

If the input sequence comprises a time series, then the output $\hat{\boldsymbol{y}}^{(t)}$ will depend on not just $\boldsymbol{x}^{(t)}$, but also on all the past input values $\left(\boldsymbol{x}^{(1)}, \boldsymbol{x}^{(2)}, \boldsymbol{x}^{(3)}, \dots, \boldsymbol{x}^{(t-1)}\right)$. The formulation in Equation (6.1) is not capable of accounting for this dependency since it can consider input only from the current time step t. This motivates the use of RNNs, schematically represented in Figure 6-2b. Each RNN cell takes in two inputs: (i) $\boldsymbol{x}^{(t)}$, the input at time step t, and (ii) $\boldsymbol{h}^{(t-1)}$, the hidden state at the previous time step.

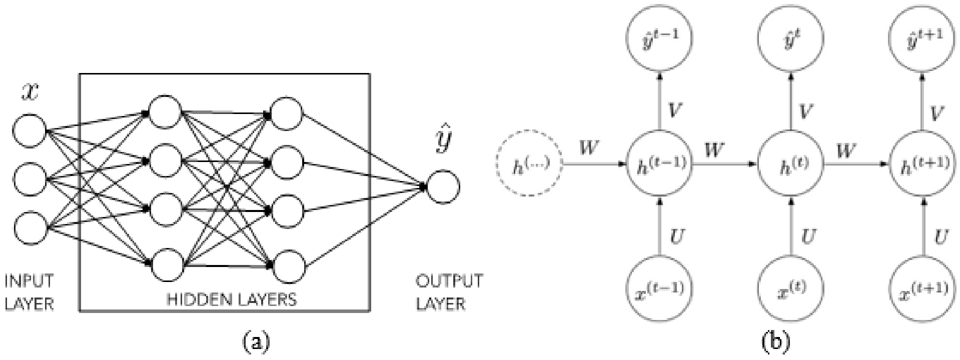

Figure 6-2. (a) Schematic of various layers in a feed-forward neural network; (b) Schematic of an RNN (Goodfellow et al., 2016).

In an RNN cell, the output for each time step t is computed as follows:

$$\boldsymbol{h}^{(t)} = \tanh\left(\boldsymbol{b} + \boldsymbol{W}\boldsymbol{h}^{(t-1)} + \boldsymbol{U}\boldsymbol{x}^{(t)}\right) \tag{6.2}$$

where $\boldsymbol{h}^{(t)}$ is the hidden state vector at time step t, $\boldsymbol{b}$ is a bias vector, and $\boldsymbol{U}$, $\boldsymbol{W}$ are weight matrices. The output of the RNN cell at each time step is then fed into a fully connected layer to produce the final output $\hat{\boldsymbol{y}}$ of the network**:**

$$\hat{\boldsymbol{y}}^{(t)} = F\left(\boldsymbol{d} + \boldsymbol{V}\boldsymbol{h}^{(t)}\right) \tag{6.3}$$

where $\boldsymbol{d}$ is a bias vector, and $\boldsymbol{V}$ is a weight matrix. For a regression problem, the activation function F is taken to be the identity function (i.e., $F(\boldsymbol{z}) = \boldsymbol{z}$).

The above RNN maps an input sequence to an output sequence of the same length. It is also possible to design an RNN that reads an entire sequence and produces a single output corresponding to the final time step. In the latter scenario, at the intermediate time steps, only the hidden states are computed while the output values are discarded.

A shortcoming of the RNN design presented above is its inability to learn long-term dependencies. RNNs suffer from a “vanishing gradient” problem which makes it difficult for them to capture dependencies in sequences of length greater than 10 or 20 (Bengio et al., 1994). An effective solution to this problem involves the use of “gated RNNs”, the most popular of which is the LSTM network.

Figure 6-3 shows the schematic of an LSTM cell. At a given time step, an LSTM cell takes in three inputs: (i) $\boldsymbol{x}^{(t)}$, the input vector at time step t, (ii) $\boldsymbol{h}^{(t-1)}$, the hidden state vector at the previous time step, and (iii) $\boldsymbol{c}^{(t-1)}$, the cell state vector at the previous time step. $\boldsymbol{x}^{(t)}$ and $\boldsymbol{h}^{(t-1)}$ are used to compute the following four quantities:

$$\boldsymbol{f}^{(t)} = \sigma\left(\boldsymbol{b_f} + \boldsymbol{U_f}\,\boldsymbol{x}^{(t)} + \boldsymbol{W_f}\,\boldsymbol{h}^{(t-1)}\right) \tag{6.4}$$
$$\boldsymbol{i}^{(t)} = \sigma\left(\boldsymbol{b_i} + \boldsymbol{U_i}\,\boldsymbol{x}^{(t)} + \boldsymbol{W_i}\,\boldsymbol{h}^{(t-1)}\right) \tag{6.5}$$
$$\boldsymbol{o}^{(t)} = \sigma\left(\boldsymbol{b_o} + \boldsymbol{U_o}\,\boldsymbol{x}^{(t)} + \boldsymbol{W_o}\,\boldsymbol{h}^{(t-1)}\right) \tag{6.6}$$
$$\tilde{\boldsymbol{c}}^{(t)} = \tanh\left(\boldsymbol{b_c} + \boldsymbol{U_c}\,\boldsymbol{x}^{(t)} + \boldsymbol{W_c}\,\boldsymbol{h}^{(t-1)}\right) \tag{6.7}$$

where $\boldsymbol{f}^{(t)}$ is the forget gate vector, $\boldsymbol{i}^{(t)}$ is the input gate vector, $\boldsymbol{o}^{(t)}$ is the output gate vector, and $\tilde{\boldsymbol{c}}^{(t)}$ is an intermediate cell state. $\boldsymbol{b_f}$, $\boldsymbol{b_i}$, $\boldsymbol{b_o}$, $\boldsymbol{b_c}$ are bias vectors and $\boldsymbol{W_f}$, $\boldsymbol{W_i}$, $\boldsymbol{W_o}$, $\boldsymbol{W_c}$ are weight matrices. σ refers to the sigmoid function. The cell state $\boldsymbol{c}^{(t)}$ is then computed with the help of the forget gate and the input gate vectors as follows:

$$\boldsymbol{c}^{(t)} = \boldsymbol{f}^{(t)} \odot \boldsymbol{c}^{(t-1)} + \boldsymbol{i}^{(t)} \odot \tilde{\boldsymbol{c}}^{(t)} \tag{6.8}$$

where $\odot$ refers to the Hadamard product (i.e., element-wise multiplication) of two vectors. Finally, the hidden state vector $\boldsymbol{h}^{(t)}$ is computed using the output gate vector and cell state vector:

$$\boldsymbol{h}^{(t)} = \boldsymbol{o}^{(t)} \odot \tanh \boldsymbol{c}^{(t)} \tag{6.9}$$

At time step t, each LSTM cell outputs the cell state vector $\boldsymbol{c}^{(t)}$ and the hidden state vector $\boldsymbol{h}^{(t)}$. The hidden state vector can then be used to compute the output $\hat{\boldsymbol{y}}^{(t)}$ as shown in Equation (6.3). LSTMs have been shown to capture long-term dependencies more effectively then basic RNNs because a higher order temporal interpolation is obtained by combining Equations (6.4)- (6.9). The use of various gates along with the cell state vector allows for a dynamic time scale of integration that can change based on the input sequence. (Goodfellow et al., 2016).

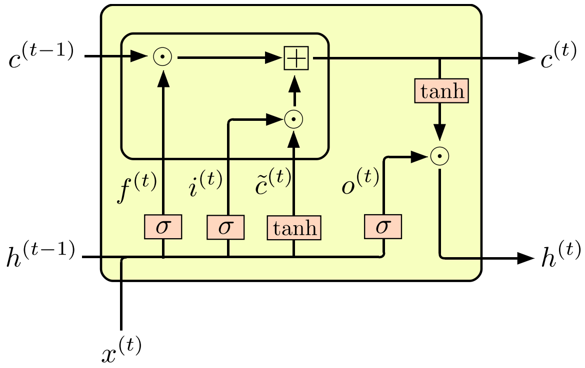

Figure 6-3. Schematic of an LTSM cell.

The various bias vectors and weight matrices are determined during the training process s, which is designed to minimize the mean-squared error between the predicted output ($\hat{\boldsymbol{y}}$) and the true output ($\boldsymbol{y}$). The gradients of the loss function (i.e., mean-squared error) are computed using the back-propagation algorithm, and the weights and biases are updated using the Adam optimization algorithm.

6.2.3 Model Setup

Injecting high-pressure fluid can lead to fault slip by decreasing the shear strength of a fault due to reduction of effective stress. Herein, we developed a model that can output the HM behavior of a fault (as characterized by evolution of pore pressure and displacements) in response to fluid injection. In the current work, we focused our efforts on response near the injection borehole.

In order to model pore pressure and fault displacements (normal, strike, and up-dip) at a given time step, we considered injection at the current time step and the previous $n-1$ time steps. In addition, we also considered pore pressure and displacements from the previous n time steps. Incorporating a lag (of n time steps) enables the model to capture temporal dependencies in data. In functional terms, our model can be expressed as:

$$\left(P^{(t)}, \boldsymbol{\delta}^{(t)}\right) = g\left(I^{(t,t-1,\dots,t-n+1)}, P^{(t-1,t-2\dots,t-n)}, \boldsymbol{\delta}^{(t-1,t-2\dots,t-n)}\right) \tag{6.10}$$

where I refers to the injection flow, P refers to the pore pressure, $\boldsymbol{\delta}$ refers to the three-dimensional vector of displacements (normal, strike, and up-dip) and g is the function learnt by the LSTM model. We use $I^{(t,t-1,\dots,t-n+1)}$ as a shorthand for $(I^{(t)}, I^{(t-1)}, \dots, I^{(t-n+1)})$, $P^{(t-1,t-2\dots,t-n)}$ as a shorthand for $(P^{(t-1)}, P^{(t-2)}, \dots, P^{(t-n)})$, and $\boldsymbol{\delta}^{(t-1,t-2\dots,t-n)}$ as a shorthand for $(\boldsymbol{\delta}^{(t-1)}, \boldsymbol{\delta}^{(t-2)}, \dots, \boldsymbol{\delta}^{(t-n)})$. The superscript (e.g., (t)) refers to the time step. Equation 6.10 shows that for a given time step t, the model input consists of five sets of time series, while the model output consists of four scalar predictions. The length of each input time series, or the lag, is n. (see below for details on n).

The function g (which is a collection of weights and biases) is learnt by minimizing the mean-squared error between the modeled and true output. The gradients of the loss function (i.e., mean-squared error) were calculated using back-propagation (Rumelhart et al., 1986), and the weights (and biases) were updated using the Adam optimization algorithm (Kingma and Ba, 2017).

Training vs. Generation

After training, the model is evaluated by generating fault pore pressure and displacements in response to fluid injection, with one significant departure from the training procedure. During generation, the model outputs are fed back into the model as part of the input for the next time step, unlike in training where the actual values of pore pressure and displacements are used. This can propagate prediction errors from early to later time steps. To ensure that our training produces a robust model, we adopted several measures as described in the following sections.

Setting the LSTM Lag n

When building an LSTM network, lag is an important hyper-parameter to consider and refers to the number of time steps used to predict the output. Put differently, lag refers to the length of the input sequence over which an LSTM captures dependencies. A value of lag that is too small may prohibit the network from capturing enough information about the past to make an accurate prediction, while a value of lag that is too large may lead to over-fitting and poor generalization. In the FS-B experiment, injections 1-5 were about 10 minutes long. The injections were followed by shut-in periods during which an initially rapid decline in pressure and displacement was followed by a slow decay. The period of rapid decline lasted less than 10 minutes. Therefore, we picked a lag of 20 minutes to capture most of the time-dependent behavior of the fault during and after an injection. Since our data was downsampled to a frequency of 2 Hz, a lag of 20 minutes corresponded to 600 time steps. We demonstrate the limitations of choosing a small value of lag in Section 6.3.

Calibrating the LSTM Cell Dimension

Another important hyper-parameter is the LSTM cell dimension, also referred to in literature as “LSTM units”. The LSTM cell dimension refers to the dimension of the hidden state vector $\boldsymbol{h}$ (as shown in Equations 6.3 and 6.9), which is the same as the dimensions of other vectors associated with an LSTM cell (as shown in Equations 6.4- 6.8). The LSTM cell dimension influences the complexity of relationships that can be learnt by the network. Generally, a higher cell dimension facilitates complexity but comes with added computational cost and a potential for overfitting. A lower cell dimension facilitates simplicity and lower computational cost but could lead to underfitting. For the FS-B experiment, we trained a suite of models whose cell dimensions were varied manually, and observed that cell dimensions of around 25, 30, 35 were the most optimal. It is worth noting that similar cell dimensions have been found to be optimal in the context of rainfall-runoff modeling (Kratzert et al., 2018). We also demonstrate how the model performance could be adversely affected if the cell dimension is too large.

Weight Optimization: Learning Rate Reduction

The learning rate determines the rate at which the weights (and biases) of a neural network are updated during the training process. A high learning rate can lead to faster convergence. This is especially useful during the early stages of training as the neural network weights are far from their optimal values. However, as the training progresses and model weights start converging, a high learning rate could cause the optimizer to overshoot and oscillate near the global minimum. Therefore, we reduced the learning rate by a factor of 2 every time the improvement in loss function plateaued.

No Validation Set During Training

Our objective is to train a model on the first few injection cycles and evaluate its ability to generate pore pressure and fault displacement response for subsequent cycles. In a ML framework, it is a common practice to set aside a subset of data (called validation set) which is used to estimate the model's ability to generalize to new unseen data. The validation set is typically also used to make decisions about choosing hyperparameters and reducing the learning rate. This suggests setting aside an injection cycle for validation. However, the various cycles elicit distinct responses from the fault, as the fault evolves with each successive injection cycle. This limits the selection of an initial validation set that can be used to reliably assess model performance throughout the experiment.

6.2.4 Model Evaluation

In lieu of using a validation set, we evaluated the generative ability of a model using an injection cycle that was also for training. Our objective here was to evaluate the impact of all the above measures (Section 6.2.3) on model development. As the cycle generated during the evaluation phase was also used for training, the generated response should closely match the true response. Discrepancies between the generated and true response would point to a lack of robustness of the model.

6.2.5 Experimental Design

Our model architecture comprised of an input layer, an LSTM layer, and a fully-connected layer which produced the final output. To highlight the impact of all the above measures (Section 6.2.3), we trained a model on injection cycles 1-3, and generated the response to injection cycle 4. Although we considered additional combinations of cycles (which highlight different aspects of our model), we describe the results of the above combination for brevity.

6.3 Results and Discussion

6.3.1 Network Architecture

Table 6-1 shows the final architecture of the model that performs best in our study. As stated earlier, we used a lag of 600. We observed that an LSTM cell dimension of 25 was the most optimal. Finally, we show the performance of our best performing set of parameters that incorporated all the above steps.

Table 6-1. Network architecture for the best performing model.

Layer type	Output shape
Input	(600, 5)
LSTM	25
Fully connected (output)	4

6.3.2 A Small Value of Lag Hampers Predictions During Shut-In

Figure 6-4 shows the model limitations when the value of lag is too small. Here, we trained a model by selecting a lag of 100, and with other parameters otherwise identical to Table 6-1. At the onset of injection, the peak pressure is slightly over-predicted, but otherwise the response is well captured during the injection period. However, there are significant errors in the model response during the shut-in period. Interestingly, we observe that the predicted response diverges from the true values at approximately time step 400, which corresponds to 100 time steps (or the lag value) into the shut-in period. This is a clear indication that a memory of more than 100 time steps is needed to accurately model the decay. Near time step 600, which is about 300 time steps in the shut-in period, the predictions flatten out, suggesting a complete memory loss for the model.

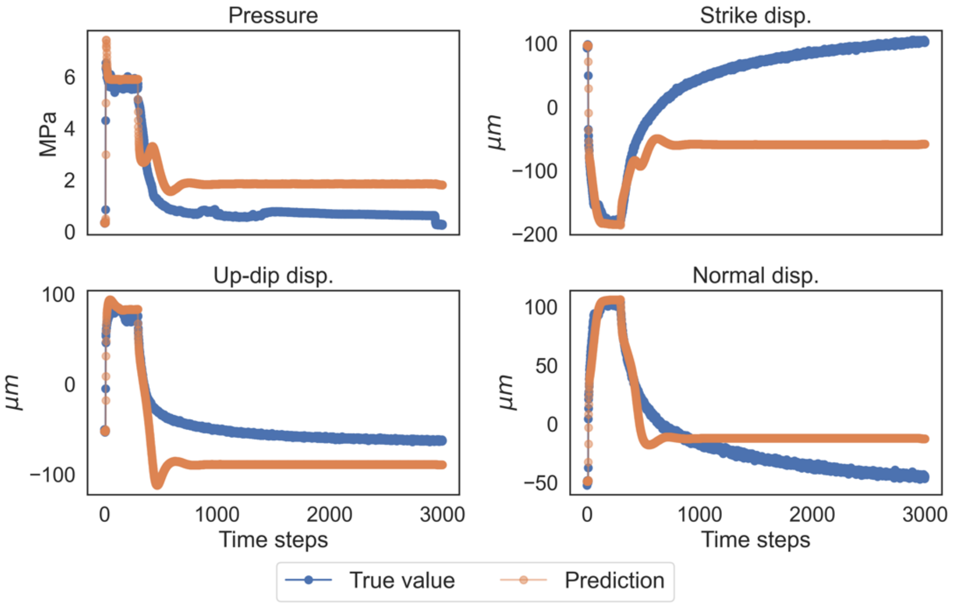

Figure 6-4. Predictive capability of the LSTM model declines when the value of lag is small (100 in this case).

6.3.3 A High Value of Cell Dimension May Lead to Overfitting

Figure 6-5 shows the adverse impact of choosing a value of cell dimension that is too large. Here, we trained a model by selecting a cell dimension of 200, and otherwise identical to Table 6-1. Once again, we observe that the model can accurately predict the response during the injection period, while the shut-in period is characterized by oscillations that suggest a model that may be overly complex. We observe that the predicted response diverges from the true values at approximately time step 900, which corresponds to 600 time-steps (or the lag value) into the shut-in period. The oscillations suggest that the model may have been overfit to the training data.

6.3.4 A Constant Learning Rate Limits Learning

Figure 6-6 considered the network architecture described in Table 6-1. However, the learning rate is not reduced during the training process. We used the default learning rate of 0.001. We note that despite this limitation, the model generates significantly improved responses during the shut-in period (compared to Figures 6-4 and 6-5). It is interesting to note that the Adam optimizer adapts the learning rate during the training process by considering the mean and variance of gradients during earlier time steps. This means that as the global minimum of the loss function is approached, the rate at which the neural network weights are updated automatically slows down. However, there are still limitations to how well the trained model can generate the shut-in response. This suggests that the built-in reduction in learning rate by the optimizer may not be sufficient. It may be beneficial to manually reduce the learning rate once the learning plateaus. We also observed that not reducing the learning rate caused the optimizer to oscillate which likely hampered its ability to reach the global minimum (learning curve not shown for brevity).

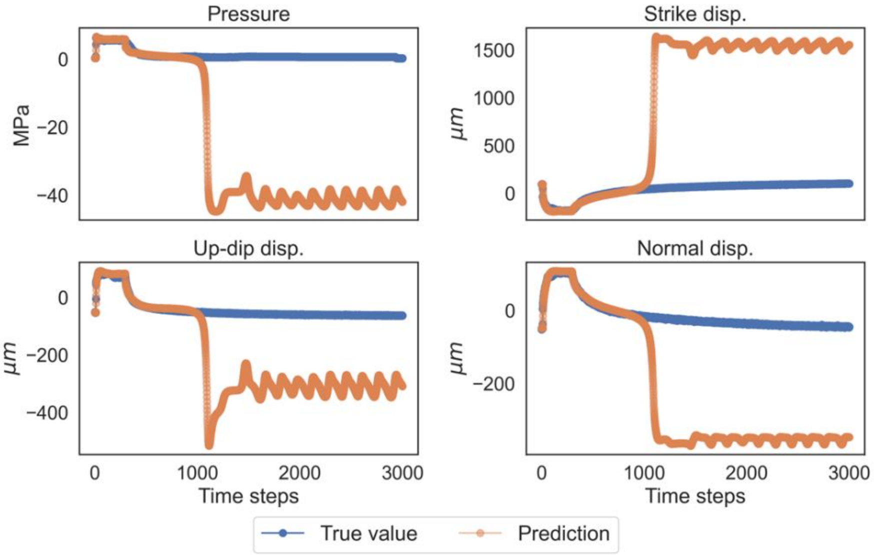

Figure 6-5. Predictive capability of the LSTM model is adversely impacted when the value of LSTM dimension is too large (200 in this case).

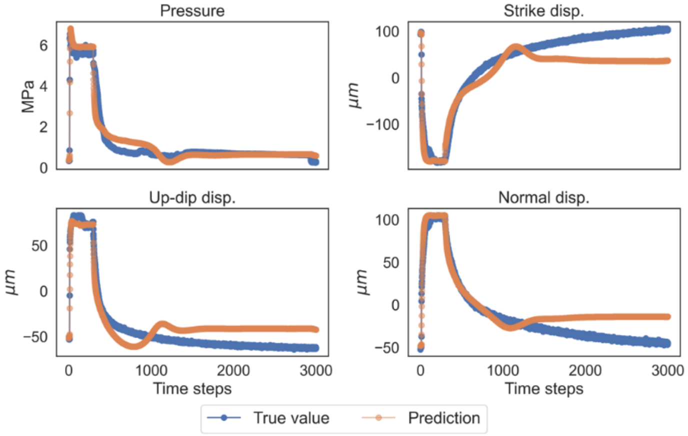

Figure 6-6. Predictive capability of the LSTM model is compromised when the learning rate is held constant.

6.3.5 Using a Validation Set Limits Learning

Figure 6-7 shows how the predictive ability of a model is compromised if a validation set is used during the training process. The model setup was otherwise identical to Table 6-1. Since the architecture was otherwise kept constant, the validation set was used to make decisions about when the learning rate should be reduced. Once again, we observe that the main challenge involves predicting the shut-in response. The results are especially striking since cycle 4 was used as a validation set. A priori, we would expect that since we are generating response for the same cycle that was used for validation, the predictions should be very close to the true values. A likely reason for this seemingly non-intuitive observation is the fact that the fault response during cycle 4 is distinct from fault response during cycles 1-2. As discussed in Section 6.2.3, the validation set should be representative of data in the training set. Therefore, by assessing its performance against cycle 4 during training, the model is not able to accurately learn all the characteristics of fault response. We also observe that reduction in the overall loss value is hampered by the use of a validation set (not shown here for brevity).

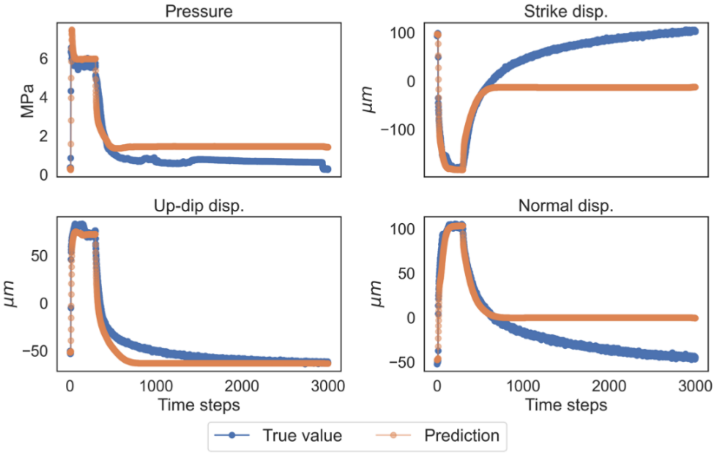

Figure 6-7. Predictive capability of the LSTM model is compromised when a validation set is used during the training process.

6.3.6 Best Performing Model: Putting It All Together

Figure 6-8 shows the generated response using a model that incorporates all the steps described in Section 6.2.3. The model captures the fault response both qualitatively and quantitatively. At the onset of injection, the peak pressure is slightly over-predicted. However, the displacements are captured accurately throughout the injection period. Prediction of the response during the shut-in period, which proved to be the most challenging aspect for our modeling process, displayed significant improvements. The evolution of pressure, strike and normal displacements very closely matched the true response. There is a small under-prediction in the decay of up-dip displacement, which is accompanied by smaller under-predictions in the decay of strike and normal displacements. This suggests that the model is slightly over-estimating the magnitude of irreversible shear. This discrepancy could be attributed to the fact that a hydraulic connection formed with a neighboring borehole at the end of cycle 3, which affects fault response during cycle 4 (Guglielmi et al., 2021). This information is not provided to the ML model.

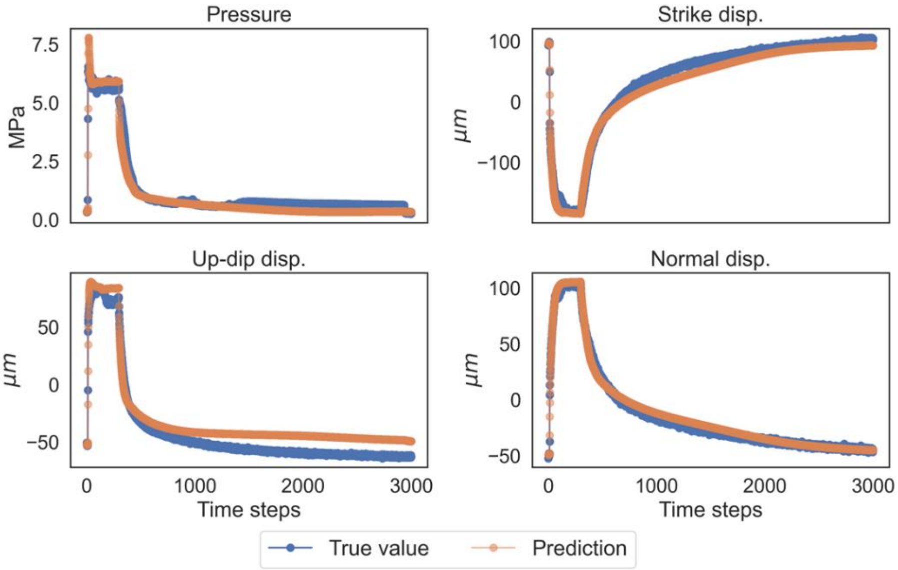

Figure 6-8. Results of our LSTM model for predicting fault response for cycle 4 when trained on cycles 1-3.

6.4 Summary and Future Directions

We developed a ML model based on Long-short term memory (LSTM) networks that can predict changes in pore pressure and fault displacements in response to injection of high-pressure fluid. We utilized data from the Mont Terri Fault Slip FS-B experiment, conducted in November 2020. The results of this study demonstrated that various steps are necessary to develop a model that can accurately model pore pressure and displacement during both the injection and the shut-in period. In general, we observed that modeling the decaying fault response during the shut-in period is especially challenging if the model is not trained properly. It is important to: (1) set an appropriate value of lag; (2) calibrate the LSTM cell dimension; (3) reduce learning rate when the learning plateaus, and (4) avoid using a validation set if it not representative of data in the training set.

However, the responses of injection cycles 5 and 6 are quite different from those of the earlier cycles, thus requiring additional dataset or training techniques. Additional work will explore modeling these cycles, as well as the development of a model that could model fault response away from the injection borehole. Such developments may require us to not only incorporate data from other boreholes, but also consider a physics-informed neural network. Important physics-based constraints may involve consideration of diffusion equations that govern fluid flow along a fault.

In FY23, we have built on the preliminary ML framework that was first introduced in FY22 and have developed a model that is capable of modeling pore pressure and displacements in response to fluid injection. The main achievements can be summarized as:

- We refined an LSTM framework that can model pore pressure and normal displacement in response to fluid injection in the fault.
- We developed a recipe for training that is necessary to ensure that the model can generate injection-induced fault response accurately.

For FY24, our plans will involve expanding the scope of the current modeling efforts which can be summarized as follows:

- We will assess the ability of our modeling framework to predict the HM response when the fault is more dilative.

- We will explore the development of a framework that can predict fault response some distance away from the injection borehole.

7. Recognizing Faults and Multiscale Geologic Features in Mont Terri Using ML

7.1 Introduction

Fractures, faults, interfaces, and textures with mineral compositions are features in geological formations that may play key roles in the Earth's evolution and in human's engineering activities for recovering energy and storing gas or waste in the Earth. For the design of a nuclear waste repository that is 400-800 meters below the ground surface, it is challenging to predict or measure fractures, faults, and their evolution as a result of excavation. Specifically, excavating repository drifts or access tunnels into fractures/faults at acute angles may lead to deep rock mass damage related to large tunnel caving/overbreak on the order of 1–3 tunnel diameters. Consideration of these damage zones are not only critical for the short-term stability of an excavation in OPA shale but also could reduce the integrity of the geological barrier, thus affecting long-term safety. In low-permeability clay shales, failure can be initiated due to excavation and the damage of the geological barrier may occur progressively over decades to thousands of years driven by THM coupled processes and deterioration of tunnel support systems. Thus, it is important to identify these geological features and their changes to ensure both short-term and long-term safety of a repository (Ziegler and Loew, 2021).

Identifying geological features and their changes from field observations can be very challenging. First, the scales of fractures and faults can be marginal, which makes it challenging to train and predict a uniform pattern for fractures. This is a unique feature that is observed from the field that is distinguished from a laboratory test where the scale is limited, and boundary effects may play a role. Secondly, at the scale of a meter-wide borehole, fractures and faults are often thin zones and sometimes may be invisible in a borehole image, as shown in Figure 7-1. Thirdly, these thin lines, which are formed as a result of intergranular or intragranular damage, may be very challenging to distinguish from other features such as textures of the rock and breakout or damage zones. Lastly, the number of images and the resolution of images that are obtained from the field are uncertain. In some cases, one may not be able to obtain a sufficient number of high-resolution images to tell when and where progressive or sudden damage occurs. More often, a well-trained geologist needs to process a great number of images (tens of thousands of images) from the field, such as in the Mont Terri tests (Ziegler and Loew, 2021).

Figure 7-1. Unwrapped image of the Mont Terri URL borehole (0.6 m in diameter).

Convolutional neural network (CNN) is one of the deep learning approaches that has been widely applied to image recognition (Simonyan and Zisserman, 2015; Babhulgaonkar et al., 2020; Rabbani et al., 2020). In recent years, more research has been conducted to apply such models in the Earth sciences. CNN has been successfully applied for recognizing pore structures and mineral types in laboratories where the geometric features are at the same scale. However, applying CNN to recognize complicated multiscale features with almost invisible thin fractures from tens of thousands of images has never been attempted.

In this section, we will present results of multiscale features recognition from the Mont Terri data by using two different CNN models. We will first introduce the Mont Terri experiments and the data. Then we will introduce the fundamentals of CNN, and the two different CNN models that are used for recognizing multiscale features. These introductions include the structure of each model and our approach of making use of each. Finally, we will show results of image recognition by using these two different CNN models in combination.

It is important to note that this work was a result of an LBNL “Ingenuity” project— NEXT-GEN NUCLEAR WASTE DISPOSAL INTERNSHIP, which aims to inspire and train the next generation to conduct research on nuclear waste disposal starting from spending a summer working with LBNL scientists. This ML study was performed by the first author-- undergraduate student Justin Cheng, who was awarded an internship from the LBNL Ingenuity project. The project also involves an international collaboration between Swisstopo and LBNL—the former provided a large number of raw images from Mont Terri, which lay the basis for this ML study.

7.2 The Mont Terri Experiment and Data

The progressive failure experiment aims to image and identify structurally-controlled damage evolution in faulted OPA shale in a 1:5 scale *in-situ* experiment at the Mont Terri URL (Ziegler and Loew, 2021). The experiment is conducted in a 0.6- meter-wide and 12.9-meter-long central experiment borehole, representing a repository drift at 1:5 scale, and six monitoring boreholes. The unsupported experiment and cased monitoring boreholes measure a rock mass that contains different degrees of tectonic fracturing and a major fault zone delineated by using high-resolution (0.2 mm) optical imaging. The experiment borehole’s relative air humidity (RH) and temperature are set to mimic open and closed drift phases-- in a first phase the RH was set to approximately 65%, and in a second phase the RH is increased naturally by re-saturation of the closed borehole. The evolution of rock mass damage is monitored by manifold techniques, which use novel photogrammetric surveys of the experiment borehole, active seismic and electrical resistivity single-hole and cross-hole tomographic imaging, as well as recordings of pico-seismicity, aimed at exploring and localizing macro- and microscopic damage propagation evolving in the crown of the experiment borehole. A more detailed description of the technical setups and processing techniques were provided by Ziegler and Loew (2021) and Ziegler et al. (2022).

When the experiment is in the ventilation phase, desaturation and suction can strengthen the rock surrounding the experiment borehole. On the other hand, desiccation can lead to fracturing. During the re-saturation phase, the rock strength decreases, potentially leading to more damaged areas. To capture these, additional fiber optic strain sensors were planned installed to monitor fracture displacements along the borehole wall to compare with photogrammetric data.

The results show that 24 tectonic structures were identified along the experiment borehole from unwrapped borehole wall images (Ziegler et al., 2021). The major fault zone is rich in scaly clay, and also includes a few mm thick dark layers of fault gouge that have a slightly different orientation from the average orientation of the fault zone (Figure 7-2).

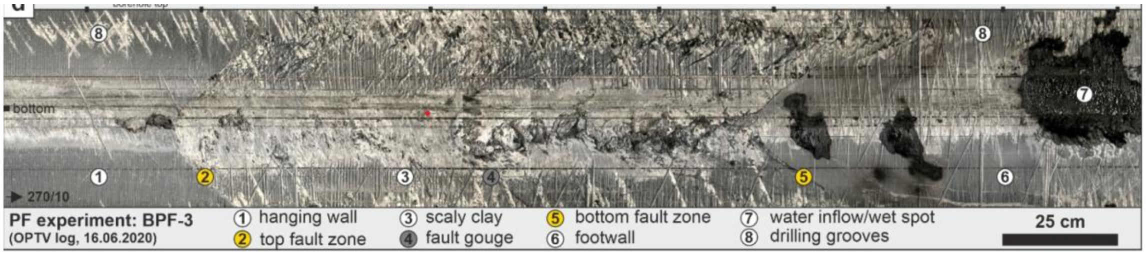

Figure 7-2. Unrolled optical borehole wall image of BPF-3 showing details of the rock mass structure surrounding the major fault zone (Ziegler et al., 2022).

It was observed that borehole breakouts occurred rapidly during the drilling of the experiment borehole (BPF-7) in likely saturated rock and then increased in size only slowly during the desaturation phase (Sutter, 2021). Moreover, time-lapse borehole wall images show ongoing displacements in damage zones and offsets along some tectonic faults, i.e., progressive failure. Within the first five weeks after drilling and the start of the ventilation, new sets of tensile fractures were formed. The first set follows the orientation of bedding planes. The second set is roughly perpendicular to the borehole axis or dips steeply (>70°) toward NE in some parts of the borehole. Sutter (2021) identified about 570 open fracture traces with a cumulative length of 24 m on the unrolled borehole wall image of October of 2020, and maximum numbers of traces of about 5,460 and 5,500 fractures (and cumulative lengths of 127 m and 128 m) on images of November of 2020. Later images between December of 2020 and April of 2021 showed a slightly decreasing number of visibly open fractures from about 5,400 to 4,890 and decreased cumulative fracture lengths from 125 m to 118 m. The observations suggest that the ventilation process leads to the formation of shrinkage cracks that form and propagate soon after the start of the ventilation. The reduction of the number and cumulative lengths of fractures seen later may indicate HM processes causing fracture closure, e.g., as part of borehole convergence.

7.3 Methodology

Because the geological features (such as discrete thin fractures, borehole breakouts, and scaly clay textures) are geometric features at different scales, we use two different models to identify these multiscale features. We use the U-Net model to segment individual fractures, while we use the Mask R-CNN to segment borehole breakouts.

7.3.1 CNN for Image Recognition

Deep neural networks make use of multiple layers of different types of functions to establish a highly nonlinear (or discontinuous) propagation of information from the input and output. The general hypothesis of a deep neural network can be expressed as:

$$\left\{\begin{array}{c} \mathbf{y} = \mathbf{a}^{[l]} = g^{[l]}\left({\boldsymbol{\theta}^{[l]}}^{\mathbf{T}}\mathbf{a}^{[l-1]}\right) \\ \mathbf{a}^{[l-1]} = g^{[l-1]}({\boldsymbol{\theta}^{[l-1]}}^{\mathbf{T}}\mathbf{a}^{[l-2]}) \\ \vdots \\ \mathbf{a}^{[1]} = g^{[1]}\left({\boldsymbol{\theta}^{[1]}}^{\mathbf{T}}\mathbf{x}\right) \end{array}\right. \tag{7.1}$$

where the superscript l refers to the total number of layers of a neural network. In Equation (7.1), the hypothesis may involve a number of layers of linear or nonlinear algebraic transformation functions g in different layers. If $l = 2$ (only two layers), and if $g(z) = z$, this neural network is simplified as a linear regression problem. If $l = 2$ and if g is a sigmoid function, this neural network is simplified as a classification problem.

In most cases, however, the purpose of introducing multiple layers is to introduce additional orders for enhanced approximation, which is achieved when multiple layers are combined. These layers include an input layer, several hidden layers, and an output layer. Therefore, such enhanced approximation is realized as Equation (7.1), which functions like a propagation from the bottom to the top row. With an increased number of layers, the function becomes highly nonlinear. Solving $\boldsymbol{\theta}$ in each layer is challenging. Thus, back-propagation is used to solve $\boldsymbol{\theta}$ from the output layer to the input layer. Embedded in the steps of a typical ML routine, a neural network consists of a forward propagation routine to construct the hypothesis and a back-propagation routine to approximate the $\boldsymbol{\theta}$ until convergence is achieved.

In the field of image recognition where images are represented by pixels, the input data is represented as a tensor, i.e., image height x image width x color depth. Different types of CNN have been developed to accommodate different types or sizes of data. Figure 7-3 shows a CNN that consists of several layers to classify rock matrix and fractures from an image. In this CNN, different layers can be used to realize higher-order approximation and matrix transformation with multiplication of a number of different functions. These layers include convolutional, rectified linear unit (ReLU), normalized exponential (softmax), pooling, and fully connected layers.

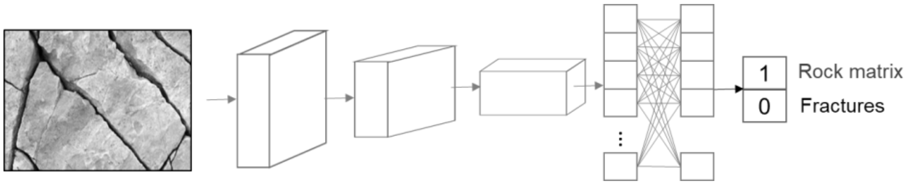

Figure 7-3. CNN for recognizing rock matrix and fractures.

7.3.2 U-Net CNN for Image Segmentation

In order to learn and predict the thin fractures, a simplified end-to-end convolutional neural network based on U-Net architecture was used (Ronneberger et al., 2015). Image segmentation is the process of partitioning a digital image into multiple segments, a set of pixels, based on specified criteria. The granularity level provided by the image segmentation technique can help us better delineate objects of interest in the image (Blaschke et al., 2004). To develop a simplified U-Net neural network for image segmentation, the number of convolutional layers and features were reduced within each layer to save memory and computational time while still preserving good performance in prediction.

The U-Net consists of four encoder blocks and four decoder blocks (Figure 7-4). As the image is encoded, its size shrinks and the number of filters grows. The filters help the model to detect spatial patterns. Decoding the model does the opposite: the image size grows and the number of filters reduces as the model uses the previously encoded information to create a high-resolution segmentation mask. Skip connections are also utilized to transfer information directly from the encoder side to the decoder side of the architecture.

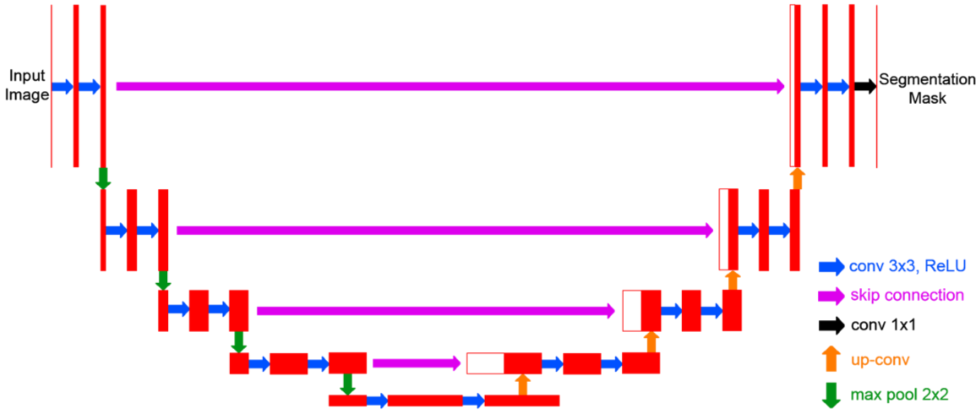

Figure 7-4. U-Net architecture for image segmentation.

7.3.3 Mask R-CNN for Image Segmentation

When attempting to efficiently identify a number of mm-thick fractures as a result of borehole breakout or reginal failure from a m-scale images, it becomes overly expensive to use toolsets such like U-Net. Thus, we made use of a ML toolset named Mask R-CNN (He et al., 2017).

Region-based CNN (R-CNN) approaches including Mask R-CNN utilizes bounding boxes across the object regions, which then evaluates convolutional networks independently on all the Regions of Interest (ROI) to classify multiple image regions into the proposed class.

An improved version of R-CNN is Fast R-CNN. Fast R-CNN splits image segmentation with two stages: (1) Region Proposal Network (RPN)-- a Neural Network that proposes multiple objects that are available within a particular image, and (2) Fast R-CNN, which extracts features using RoIPool (Region of Interest Pooling) from each candidate box and performs classification and bounding-box regression. RoIPool is an operation for extracting a small feature map from each RoI in detection.

On top of R-CNN, Mask R-CNN was developed as state-of-the-art in terms of image segmentation and instance segmentation. While Faster R-CNN has 2 outputs for each candidate object-- a class label and a bounding-box offset, Mask R-CNN outputs the object mask in addition. The mask output is distinct from the class and box outputs, requiring the extraction of a much finer spatial layout of an object. Mask R-CNN is an extension of Faster R-CNN and works by adding a branch for predicting an object mask (Region of Interest) in parallel with the existing branch for bounding box recognition.

The Mask R-CNN generates a bounding box, confidence level, and segmentation mask for each instance of an object that it detects in an image (Figure 7-5). To do this, it first passes the raw image through a backbone neural network that extracts features. These features are then passed to the region proposal network (RPN), which proposes candidate object bounding boxes known as regions of interest (ROIs). Features are then extracted from each ROI individually using ROIAlign. Finally, the individual features are passed along to the head layers, which classify the enclosed object, refine the boxes, and create a binary mask for each ROI.

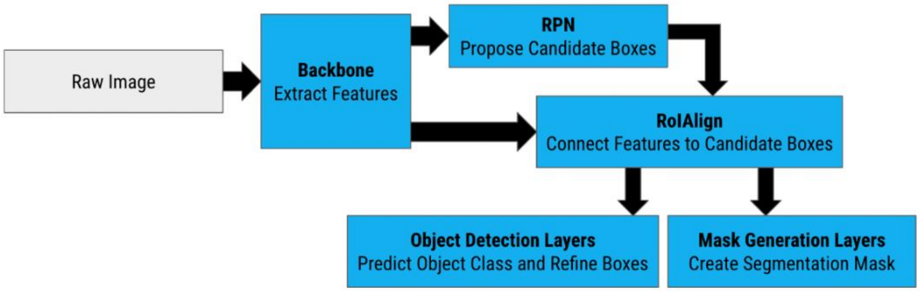

Figure 7-5. Mask R-CNN architecture for image segmentation.

7.4 Results

We extracted the data of 45 borehole surface images from the PF experiment at the Mont Terri URL (Ziegler et al., 2022). We trained the U-Net model on three images for 30 epochs using a sparse categorical cross entropy loss function and the Adam optimizer (Kingma and Ba, 2014). We tested the model on the 42 images withheld from training and a large, unwrapped borehole wall model. To train the Mask R-CNN model, we first loaded weights pretrained on MS COCO (Lin et al., 2014). Then we froze all layers except head layers and trained for one epoch. Finally, we trained on all layers for two epochs but reduced the learning rate by a factor of ten to help the model converge. A small size for the training data was selected to accelerate the training process. Future work will explore the effect of a larger training set.

To evaluate our models, we used: Dice score $= \frac{2*\text{True Positive}}{2*\text{True Positive}+\text{False Positive}+\text{False Negative}}$. This metric ranges from 0% to 100%, with 100% denoting perfect accuracy. Dice scores vary, but generally 70% is regarded as good and 80% is excellent (Wu et al., 2021).

The results of prediction of fractures at multiple scales are shown below.

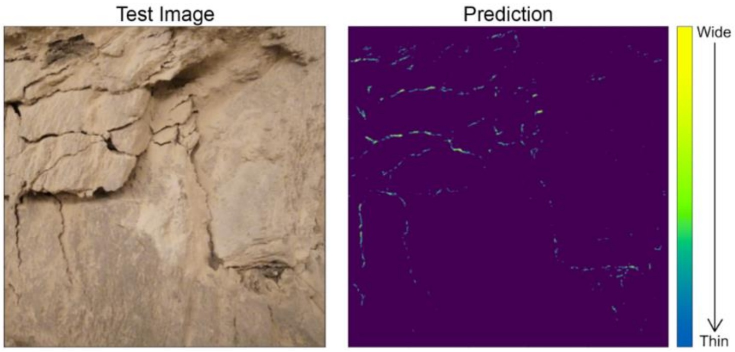

Figure 7-6. U-Net fracture segmentation prediction on a test image with a heterogeneous fracture network. Image size approximately 25 cm × 25 cm.

Figure 7-6 shows the result of thin fracture recognition in a 25 cm × 25 cm domain using U-Net. We can see that the geometric patterns of fractures, including the very thin fractures, are all captured. In addition, the color scheme ranges from yellow to blue, with yellow indicating a wide aperture and blue with a thin aperture. This color information could be used in future studies to calculate permeability changes in thin fractures and complex fracture networks.

In Figure 7-7, we show the fractures (blue lines) that are recognized from an unwrapped large borehole wall image. Comparing the thickness of the fractures with the overall dimension of the image, we show that it is efficient and accurate to use U-Net to recognize a large number of densely intersecting fractures from a borehole image—this is a tedious and time-consuming task even for a well-trained geologist.

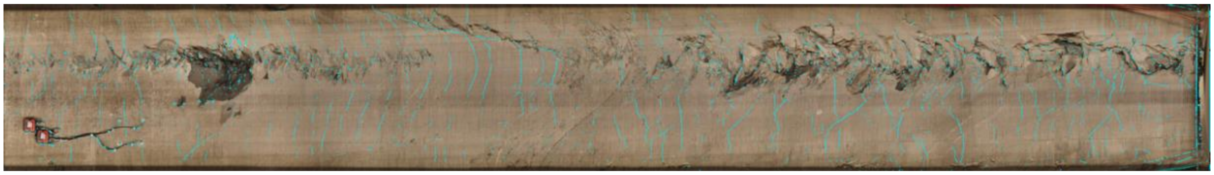

Figure 7-7. U-Net fracture prediction on large, unwrapped borehole wall image.

As illustrated before, U-Net may not be the most efficient to identify zones (i.e., clustered features) such as a zone of borehole breakout. We use Mask R-CNN to predict zones of damage as shown in Figure 7-8. In Figure 7-8, we show the results of the prediction of borehole wall damage zones on two test images. The red closed-shaped areas are the identified damage zones. We see that the prediction of the clustered damage zones is acceptable except in the case of individual thin fractures—these appear to be geometric features at a different scale in these two images. In the future, we will apply this Mask R-CNN model to images at larger scales to identify borehole breakouts and damages zones at the tunnel-scale image (such as shown in Figure 7-7).

Figure 7-8. Mask R-CNN prediction of borehole wall damage zones (red) on two test images.

Overall, our U-Net model achieved an average dice score of 81.4% and our Mask R-CNN model scored 77.7%. Thus, both models also perform well when tested with withheld data.

7.5 Summary and Perspectives

Automatically recognizing multiscale geologic features (such as fractures, faults, rock textures and damage zones) and detecting their changes can be very useful to quantify potential damage evolution and fault reactivation, thereby providing early warning signs of progressive and dynamic failure such as fracturing, borehole breakout, and induced seismicity. However, it is challenging to automatically recognize fractures, faults, textures, and damage zones from field observation because multiscale features may be present in a single geological formation.

In this study, we made use of two different CNN models and created two ML pipelines to automatically and accurately identify these multiscale features by using images that were obtained from the Mont Terri PF tests. We used a U-net model to recognize discrete thin fractures and used a Mask R-CNN model to recognize clustered features such as damage zones. We obtained average dice scores of 81.4% and 77.7% for U-Net and Mask R-CNN respectively. Additional interactions with geologists are necessary to estimate if statistically predicting about 80% of the fracture traces is accurate enough to predict the dynamic failure mechanisms affecting OPA (and other rocks), over time.

The main achievements of FY23 can be summarized as:

- We achieved auto-detection of multiscale features (including fractures/faults, fracture networks, and borehole breakouts) from images of Mont Terri using different ML algorithms.
- We trained U-Net CNN to segment and recognize thin fractures and fracture networks. The color scales that are recognized by U-Net CNN can be used for calculating spatially variable apertures and permeability of the thin, discrete fractures.
- We trained Mask R-CNN to predict zones (e.g., a borehole breakout zone)– a feature that is at a larger scale than individual fractures.
- We achieved dice scores of 81.42% and 77.66% for U-Net and Mask R-CNN predictions, respectively. These suggest that both models can learn, detect, and delineate geologic features at different scales from borehole images.

This work was a result of an LBNL Ingenuity internship project. The project also involves an international collaboration between Swisstopo and LBNL— Swisstopo provided a large number of raw images from Mont Terri, which lays the basis for this ML study.

In FY24, we will extend this work in the following directions:

- We will use the results of U-Net prediction to calculate the permeability change of each fracture within a fracture network over time.
- We will extend this work to predict the dynamic changes (location, trace length, aperture) of multiscale features over time and track the movement of such features to infer the slip of visible and hidden faults.

8. Short- to Long-Term Hydromechanical Response of Faults and EDZ in Argillite Host Rock

In this Section we report the results of the Mont Terri fault activation experiments that are of cross-cut interest related to several DOE program offices as well as international consortia. The section is written by Yves Guglielmi, and included work with main collaborators: C.Hopp, V.Rodriguez-Tribaldos, F.Cappa, J.Ajo-Franklin (and his PHD student Tanner Shadoan), P.Cook, F.Soom, T.Wood and M.Robertson, who are all affiliates of the LBNL. We thank C.Nussbaum and his team (Swisstopo, Mont Terri), G.Armand and his team (ANDRA, Bure), A.P.Rinaldi and A.Zappone (ETHZ, Switzerland) for their multiple interactions with the LBNL team.

8.1 Introduction

Repository-induced effects such as creation of an EDZ, gas generation and thermally-induced pore pressure perturbations, may result in the reactivation of pre-existing fractures, faults or bedding planes within the host rock and consequent permeability increase. Understanding such reactivation due to pressure and stress changes, the possible formation of permeable pathways, and their potential long-term sealing is critical in assessing the performance of radioactive waste repositories in shale formations. In 2015, a fault activation experiment was conducted by injecting high-pressure synthetic pore water in a fault zone intersecting the Opalinus Clay formation at a 300 m depth in the Mont Terri URL (Switzerland). In 2018, a new experiment started with the permanent installation of a new sensor to monitor long term coupled fault pore pressure and three-dimensional displacements. The key concluding points from these experiments are:

- Complex opening and slip was measured on the fault at fluid activation pressures close to the normal stress applied on the fault,
- High transmissivity flow paths developed at least temporarily and “local” (on a scale of meters) to the injection under high pressure injection, and their development was conditioned by rupture propagation within the fault zone,
- Fault reactivation and leakage produced mainly aseismic movements and a limited number of small magnitude seismic events,
- When injection pressure dropped, an instantaneous mechanical closing of the fault was observed. Nevertheless, a residual hydraulic permeability was measured. Since 2015, the pressure in the ruptured patch slowly increased but did not fully recover,

remaining ~0.45 MPa below its initial value. This may highlight slow sealing of the activated fault patch.

In 2019, significant pore pressure changes coupled to fault displacements were triggered by ongoing excavation work for a new Mont Terri gallery ~40 to 50 m away from the fault, at distances significantly farther than a few tunnel diameters. We observed that because the Main Fault and more typically shale faults display an architecture with a limited fractured damage zone, there was no stain gradient developing from the high deforming core toward the intact rock. Indeed, peaks in shear strain localize at the top and bottom sharp interfaces between the fault core and the intact rock.

In November 2020, a new fluid injection experiment was conducted with a much larger monitoring array than the 2015 experiment, including time lapse seismic imaging of fault leakage and movements.

In **Section 8.2**, we describe in detail the key result from this experiment, which is one of the first continuously observed time lapse imaging of a shale fault leakage propagation.

In **Section 8.3** we analyze in details the mechanism of fault permeability increase during activation and the long term decrease following activation. We show that the most significant permeability increase is tightly coupled to fault rupture. We then describe fault hydromechanical response following activation through the analysis of a unique dataset of hydraulic tests and continuous measurements spreading over one year. We finally propose a new fault sealing constitutive law tuned on this dataset.

In **Section 8.4**, we explore the link between the fault zone c leakage and the time-lapse seismic imaging conducted during the FS-B experiment. We show that changes in p-waves' velocities are related to fault normal displacements exceeding 50 micrometers. Overall, we explore the reasons for the observed directional propagation of fault leakage. We build a fully couple hydromechanical model where we keep the fault hydromechanical properties unchanged but vary the stresses inside and at model boundaries. We observe that stress gradient as small as 0.01 MPa/m are enough to drive the leakage in a given direction. Finally, we discuss what could be the reasons for such calculated stress gradients by comparing the far field effects of topography and gallery excavation.

In **Section 8.5**, we analyze in details the variety of microseismic events produced by the 2015 fault activation experiment conducted at Mont Terri. We show that some types of events clearly correlate with slip on the activated fault while other may reveal more local mode 1 openings. Thus, microseismicity even if it is in general scarce in such rate-strengthening clay material may help inform on what type of deformation mechanism is involved during a fault or a fracture zone reactivation, with clear potential implications to defining different types of loss of integrity.

In **Section 8.6**, we show the first measurements done after a volume of intact argillite has been heated to about 90°C at the site of Bure (ANDRA, France). We conducted four SIMFIP hydromechanical tests: two tests were in the heated volume, one test was outside in the intact rock, and test was outside in the excavation damage zone. An interesting preliminary result is that the hydromechanical response of the heated volume tests looks similar to the excavation damage zone test one.

In **Section 8.7**, we summarize the key conclusions from this year's current work and work perspectives.

8.2 Influence of Fault Asperities on Activation and Leakage – Results from the Mont Terri Fault Activation Experiments

An asperity is considered a key area on a fault where the higher friction may significantly redistribute the slip during fault rupture and earthquakes (Lay et al., 1982). Indeed, earthquake rupture is in general considered to initiate with the failure of an asperity (https://www.sciencedirect.com/topics/engineering/asperity). It has been shown that there is a tight coupling between slip on a complex fault topography and internal fault deformation (Sagy et al., 2009; Kim et al., 2004). In addition, asperities may impact fluid flow path evolution and fault hydraulic permeability variation at rupture (Rinaldi et al., 2016) although there is still little direct observation of HM coupling in fault asperities at field scale. Here we show direct observations of fault asperities influencing fault seismic rupture and leakage during the 2020 Mont Terri fault activation experiment. In Section 8.2.1, we reconstruct the fault three-dimension geometry using GOCAD software, highlighting a wavy fault surface geometry. In Section 8.2.2, we compile the full stress tensor measurements conducted at 11 borehole sections in and off the fault and discuss the effect of asperities on fault normal and shear stress variability. In Section 8.2.3, we describe that fault leakage flowpath and induced seismic event location during the 2020 fluid injection experiment have been constrained by the distribution of fault asperities.

8.2.1 Fault Zone Geological Model

The FS-B experiment instrumented volume of about 70 m x 70 m x 70 m is centered on the Mont Terri Main Fault zone (Switzerland). The volume is instrumented with 23 boreholes, creating a unique fault-testing field laboratory, monitored permanently by a large array of instruments including local and distributed strain measurements, pore pressure measurements, passive acoustic and seismic events detection and active seismic imaging. Here we first analyzed boreholes logs and cores to identify the coordinates of the top and the bottom of the Main Fault. Then, we used GOCAD software to interpolate top and bottom fault surfaces (Figure 8-1). The borehole data and the Main Fault geological mapping were done by the Swisstopo engineers at the Mont Terri laboratory level, using the Discrete Smooth Interpretation method to constrain the two surfaces.

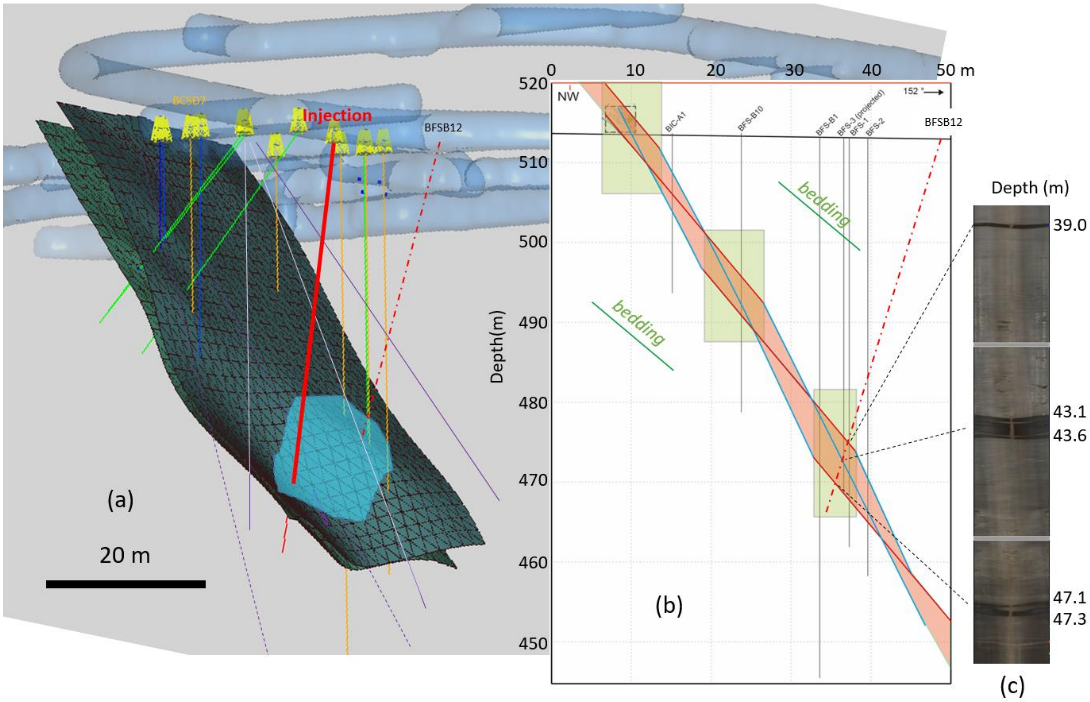

Figure 8-1. Main Fault Top and Bottom surfaces. (b) Geological cross section showing the schematic internal structure of Asperities. (c) Post 2021 injection experiment coring through the Main Fault showing three wet zones corresponding to preferential flow paths created during the experiment.

Result show that the Main Fault zone displays spatial strike, dip and thickness variations respectively N040°-to-N075°, 40-to-65° SE and 1 to 6 m (Figure 8-1a). Moreover, the fault displays asperities oriented N070 and dipping 30-40° NE. Asperities wave length is about 15-18m. Asperities correspond to thick zones inside the Main Fault (Figure 8-1b). These zones are composed of fault gouge, shear bands, meso-scale folds, microfolds, numerous fault planes and apparent undisturbed parts. Large amounts of "scaly" fabric that form an anastomosing network of polished surfaces where clay-rich rock splits into progressively smaller flakes are observed. The larger amounts of scaly clay are observed in the asperities where they are interpreted as a product of brittle-ductile strain in locked positions such as relay zones linking shear bands (green rectangles in Figure 8-1b). Core observations show that almost all of the fault planes strike and dip belong to the same directional family. This family belongs to the Jura deep decollement structures (Nussbaum et al., 2011). The Main Fault rupture may have occurred in at least three successive phases:

- Initiation of failure more or less favored by shearing along the OPA bedding anisotropy (red faults in Figure 8-1b). Schematically, red faults can be seen as en-echellon faults created under a thrust faulting regime with intercalated relay zones (green rectangles)

- Creation of the thrust faulting ramp and the Mont Terri anticline. This is inducing the tilting of the initially horizontal faults to N030-50°SE, and the creation of N046-70°SE faults preferentially in the relay zones.

- Final “stretching” of the fault zone during the late anticline folding installation.

In summary, the observed asperities of the top and bottom Main Fault surfaces result from the complex bulk evolution of deformations in the fault zone. Our approach shows that it is possible to identify these fault surface heterogeneities from field measurements. It also shows that there is a close and complex link between these surface undulations and the internal fault zone deformation. This result is of importance when considering the best way to model fault asperities either as geometrical or rheological heterogeneities.

8.2.2 Stress Heterogeneity

Here we computed the stress state from 11 tests conducted in and around the fault zone during the 2015, 2020 and 2021 experiments. This work is finalizing the work initiated in last year report. We used the protocol described in the 2022 report. First, we isolated the fault slip vector measured with a SIMFIP probe, which was produced by the activation test (Table 8-1). We then estimated the optimal reduced stress tensor orientation by matching a calculated slip vector to the measured one. Slip is calculated using the Wallace-Bott’s hypothesis, i.e., slip direction on the fault plane is consistent with the direction of the resolved shear stress on the plane (Table 8-2). Then we estimated the principal stress magnitudes using ratio between principal stresses, and estimated the vertical stress and stress normal to the activated plane at the test depth.

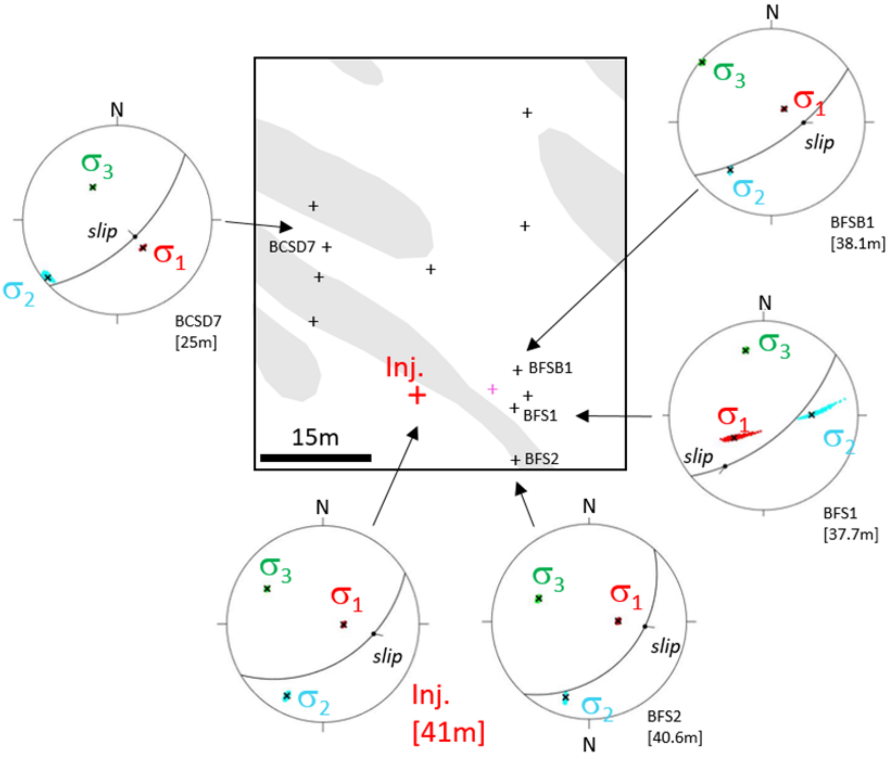

Figure 8-2. Stress tensor estimated from SIMFIP tests conducted across the Main Fault. Central figure is a front view of the fault top surface with the light grey patches where the surface dip angle is >65° (crosses are the intersections between boreholes and the fault surface). Tensor’s orientation is plotted in stereographic lower hemisphere projection with the local fault surface orientation and slip vector (Colored dots show all possible solutions to explain both fault activation pressures and measured slip vectors. Black crosses correspond to the mean stress values).

Figure 8-2 shows a high consistency between stress orientations deduced from tests conducted at different locations and at different times. All slip vectors display roughly the same left-lateral displacement with some orientation variations with the local orientation of the Main Fault surface. The maximum principal stress is subvertical to inclined to the NE, the intermediate principal stress trends SW-NE, and the minimum principal stress is NW-SE. Variability of principal stress direction is ±20°.

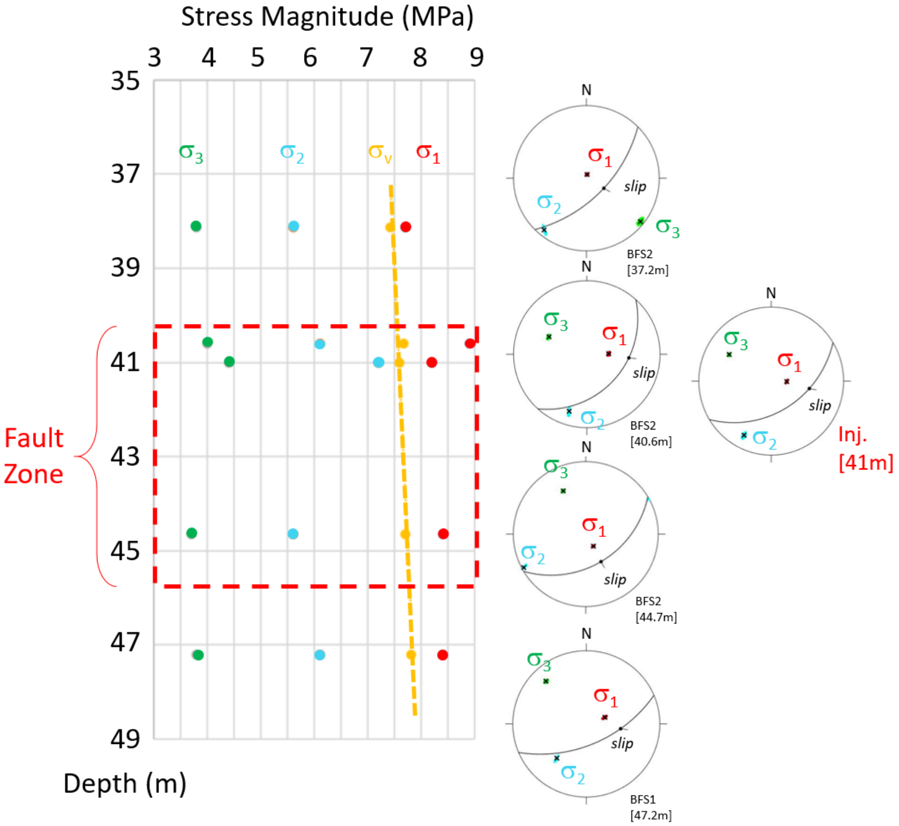

Figure 8-3. Variations of stress tensor with depth. Left graph shows the variation of the principal stresses and of the vertical stress magnitude with depth. On the right, stereoplot shows variations of the tensor's orientation at different depths.

Figure 8-3 shows that stress tensor orientation and magnitude do not seem to be altered by the fault zone (points in the dashed red rectangle and stereoplots at BFS2 40.6 and 44.7 m and Inj. 41 m depths). Variability of the mean principal stress magnitudes is ±2 MPa.

Table 8-1. Compilation of SIMFIP tests used for stress tensor estimation at Mont Terri.

Borehole	Activated Fault plane		Slip vector		Initial Formation Pressure	Fault Opening Pressure	*Shut-in* or ISIP pressure	Activation Mechanism
	dd (°)	da(°)	Dd	da	(MPa)	(MPa)	(MPa)	
BFSB2 2020 Exp.	148.7	44.7	100.8256	33.5750	1.4	6.0	4.8-5.1	Strike slip with normal component and opening **Seismic event**
BFSB1 2020 Exp.	145.1	65.3	91	51.8895	1.0	~2	-	Strike slip with Normal component preceding hydraulic connection to injection **Seismic events (2)**
CSD7 2020 Exp.	135.8	61.0	-46.9	-60.973	1.0	-	-	Reverse slip
BFS2 Test 37.2m 2015 Exp.	135	60	140	59.9053	1.4	3.63		Normal (A1A2)
BFS2 Test 37.2m 2015 Exp.	135	60	120	59.1325	1.4	5.01		Normal with slight strike slip (A7A8)
BFS2 Test 40.6m 2015 Exp.	132	36	95	30.1241	1.4	3.45	5.5	Strike slip with normal component (vector u3 in Guglielmi et al., 2020)
BFS2 Test 44.65m 2015 Exp.	149	43	151	42.9826	1.4	3.34		Normal Between anchors (C2 A9A10)
BFS1 Mon 37.7m 2015 Exp.	140	61	217	22.0884	1.0	3.93	-	Strike slip with normal component (vector V4m in Guglielmi et al., 2020) **Seismic event**
BFS1 Mon 37.7m 2015 Exp. Autre faille possible	167	63	217	51.5968	1.0	3.93	-	
BFS1b Mon 37.7m 2015 exp.	140	61	287	-56.5378	1.4	0.45	-	Strike slip with reverse component preceding the hydraulic connection with injection
BFS1 Test 47.2m 2015	157	58	98	39.4965	1.4	4.37		Normal with strike slip component. Activated frac. Above anchors (A7A8)

Static friction coefficient 0.375 (Cappa et al., 2022), dd = dip direction da = dip angle

Table 8-2. Stress tensor estimated in and around the Mont Terri Main Fault.

Borehole	σ_1			σ_2			σ_3			σ_v	σ_n
	dd1(°)	da1(°)	mag1(MPa)	dd2(°)	da2(°)	mag2(MPa)	dd3(°)	da3(°)	mag3(MPa)	(MPa)	(MPa)
BFSB2 2020 Exp.	83.2	63.7	8.2	211.7	17.1	7.2	307.9	19.4	4.4	7.59	5.4
BFSB1 2020 Exp.	44.2	67.9	7.7	220.5	22.1	5.6	311.0	1.3	3.8	7.42	4.5
CSD7 2020 Exp.	137.5	44.7	10.49	228.4	0.9	7.7	319.3	45.3	3.8	7.15	4.0
BFS2 37.2m (A1A2) 2015 Exp	228.7	56.4	7.5	43.4	33.5	7.0	135	2.5	5.3	7.4	4.5
BFS2 37.2m (A7A8) 2015 Exp	8.3	84.0	7.4	219.2	5.1	6.0	128.9	3.0	5.3	7.4	5.78
BFS2 40.6m 2015 Exp.	89.0	56.8	8.9	197.3	11.7	6.1	294.4	30.6	4.6	7.66	5.5
BFS2 44.65m 2015 Exp.	147.7	67.7	8.4	241.7	1.7	5.6	332.3	22.2	3.7	7.7	4.5
BFS1 37.7m 2015 Exp.	232.7	47.6	8.3	89.2	36.3	7.5	344.7	18.9	3.9	7.5	4.0
BFS1 N77-63° 37.7m 2015 Exp.	258.7	70.5	7.8	92.6	19.0	5.5	1.1	4.4	3.7	7.5	4.5
BFS1b 37.7m 2015 exp.	126.2	43.4	11.2	228.0	12.2	7.6	330.1	44.1	3.6	7.42	4.0
BFS1 47.2m 2015 Exp.	70.3	60.2	8.4	220.5	26.4	6.1	317.0	12.8	3.8	7.8	4.7

Finally, we used the stress tensor estimated in the BFSB2 2020 SIMFIP test (Table 8-2) to calculate the effects of the Main Fault surface asperities on the normal and tangential stress variations (Figure 8-4). It clearly appears that asperities induce 1-to-2 MPa variations in stresses magnitudes, and generate sharp stress gradients perpendicular to the asperities dip direction.

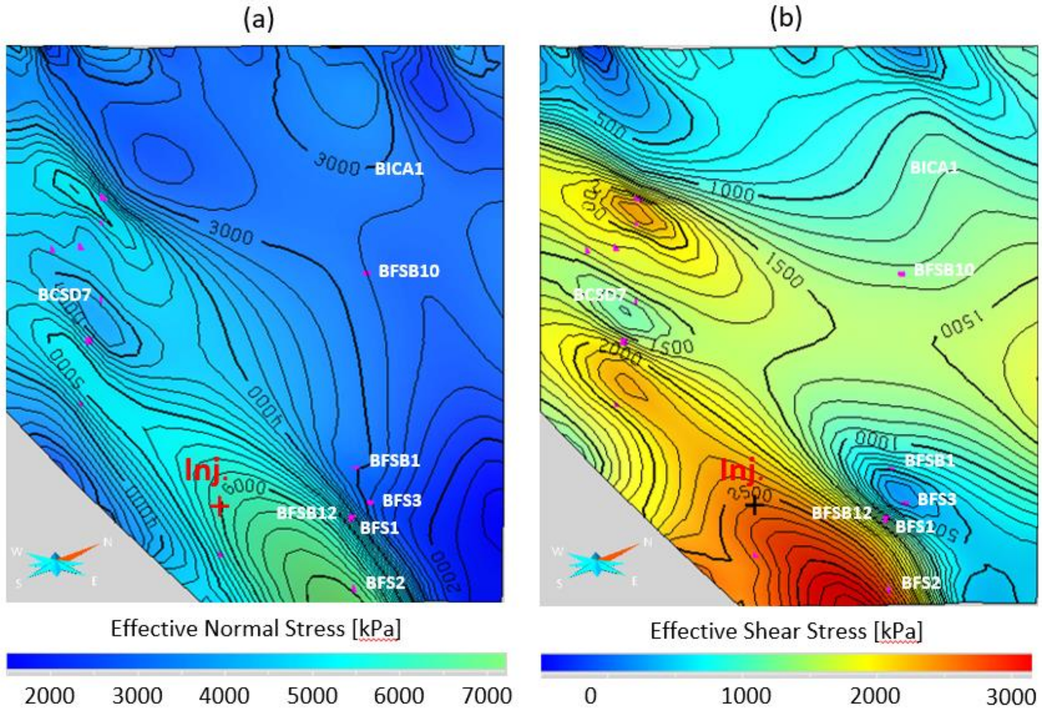

Figure 8-4. Influence of fault asperities on normal (a) and tangential (b) stress to the fault top surface (isolines were calculated by projecting the BFSB2 stress tensor on the fault surface in GOCAD).

8.2.3 Fault Asperity Control on Fault Rupture and Leakage

We used the results from the 2020 fault activation experiment to further explore the potential impact of asperities on fault activation and leakage. The 2020 Mont Terri fault activation experiment setting was described in last year’s report. Several constant flowrate injections were conducted respectively of 5, 8 and 10 l/min for 10 minutes each. Pressure at the injection section across the top Main Fault surface increased to a maximum of 6.2 MPa until a leakage flow path developed along the fault in the NE direction (Figure 8-5a). At the third injection cycle, a hydraulic connection occurred with borehole BFSB1 located 18 m away from the injection. It was associated with a 2 MPa pressure increase in the fault at this point.

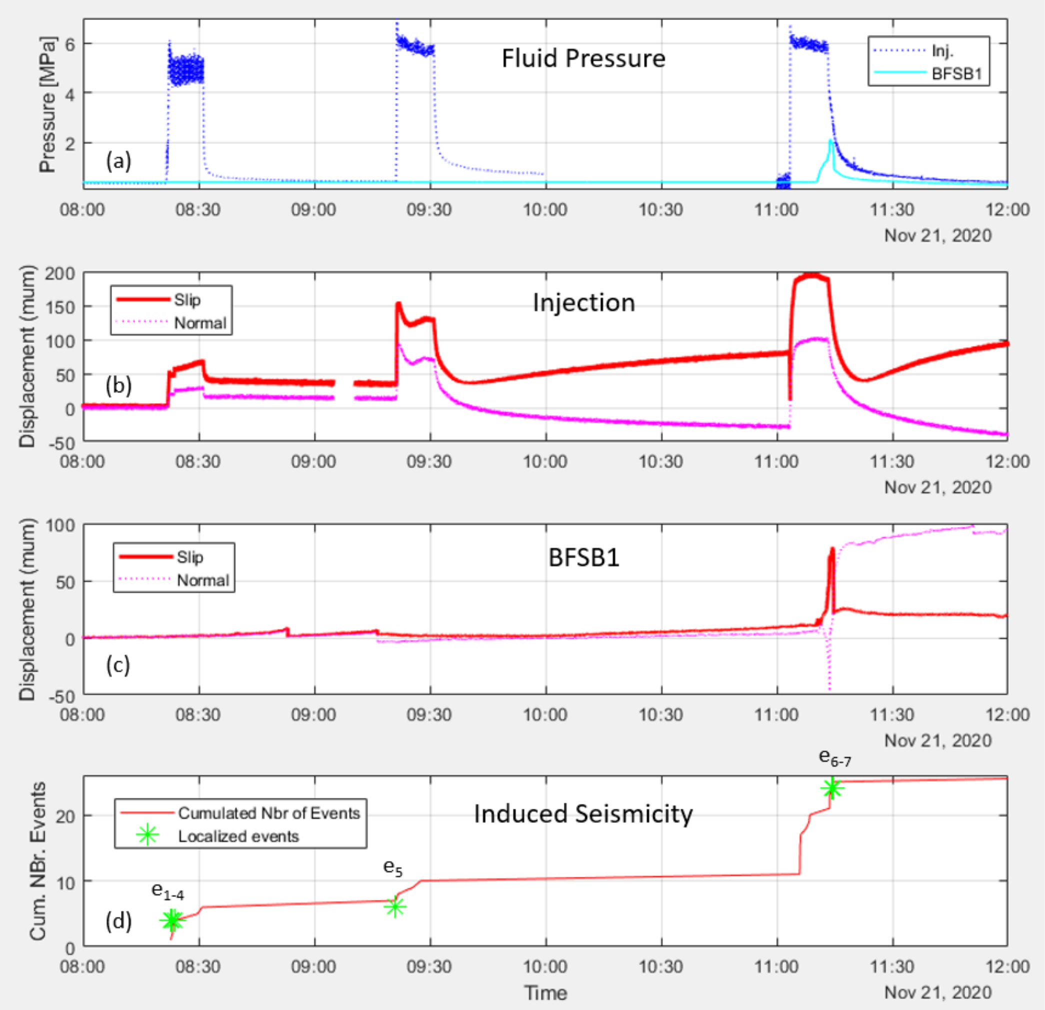

Figure 8-5. Fault HM and seismic response at injection and BFSB1 monitoring point: (a) pore pressure; (b) and (c) slip and opening at Injection and BFSB1; and (d) cumulated number of seismic events (red curve) and localized main events (green stars).

About 200 and 80 microns fault slip and 150 and 100 microns normal displacement were measured, respectively, at Injection well and at BFSB1 (Figure 8-5b,c). At injection, slip and normal opening follow pressure variations. There is a fast dilatant slip response of the fault to the fast pressure increase. After the first injection, there is a constant residual slip and opening respectively of 45 and 20 microns (Figure 8-5b). After the second and the third injection periods, this residual slip was slowly increasing with time while a slow closing was observed. This may be related to slow fluid diffusion in the fault zone. At BFSB1, a slow slip and normal opening were activated starting during cycles and continuing between cycles (Figure 8-5c). This was associated to a slight pore pressure decrease of 10^{-4} and $4x10^{-4}$ MPa during cycles 1 and 2, respectively.

Two compacting slip events occurred at 8:53 and 9:16:25. At cycle 3, there was first an acceleration of the slow slip and opening. When pore pressure started increasing slip acceleration continued while a sharp fault closing was measured. Finally, a sharp back slip and a large opening occurred while pore pressure dropped at 79 seconds after the injection stopped. After cycle 3, there was a persistent and complex slow opening trend. A compacting slip event was observed at 11:51.

The complex response observed at pressure increase related to the complex fluid diffusion into the asperity. Posttest coring showed three wet zones (Figure 8-1c) proving that several fractures opened and leaked within the asperity. We hypothesize that the opening of one of these fractures located below the top Main Fault surface (were the BFSB1 displacement sensor was set) induced the compression and the measured closing. Moreover, this increased the pressurization and accelerated the slip on the top Main Fault surface. Pore pressure release at injection point mainly controls back slip. Normal closing at injection might control fault drainage and the dissipation of the pressurized patch that keeps fault dilating away from injection point.

25 seismic events were recorded and 7 events could be located with a ±1 m accuracy (Figure 8-6), all being associated to the injection periods (Figure 8-5d). During the experiment, the pressurized patch could also be located by using a Continuous Active Seismic Monitoring system (see description in last year's report and dashed lines in Figure 8-6). The patch is not detected at cycle 1. Then, the patch is migrating North-Eastward and up-dip along the fault (corresponding to the patch extension to the upper right side of the fault fron view in Figure 8-6a). Seismic events correlate well with the maximum slip periods measured at injection during cycles 1-2 and at BFSB1during cycle 3. Events e1-4 are several meters away from injection where no pressurization is detected. Event 5 is outside the limits of the pressurized patch associated to injection period 2 (dark dashed curve in Figure 8-6a). Events 6-7 are at the injection patch front and close to BFSB1. This shows that fault movements in the pressurized patch may be mainly aseismic or may produce a very small magnitude seismicity that could not be localized.

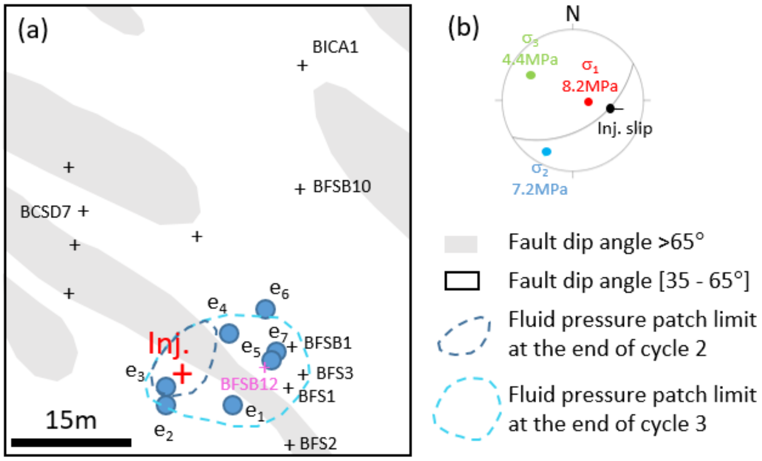

Figure 8-6. Localization of seismic events on the fault: (a) fault surface front view with seismic events e1-7 located (dashed curves show the limits of the pressurized patch after injections 2 and 3); (b) stereo plot lower hemisphere projection of slip event and stress tensor at injection associated to seismic event e4 (about the same slip was recorded at BFSB1 associated to seismic events 6-7, see Table 8-1 and Figure 8-2 for more details).

Another observation is that events all localize outside the large >65° fault dip angle zone that figures the fault asperity (grey patch in Figure 8-6a). We then used the stress tensor estimated from the inversion of slip at injection (Figure 8-6b) to calculate the tendency to slip on the undulated top Main Fault surface (Figure 8-7a, see details in Section 8.2.2). It appears that seismic events are located in fault areas where the slip tendency is above 0.3 because given the stress tensor's orientation the >65° dipping side of the asperities is less prone to slip than the <65° side. Moreover, Figure 8-7b shows that the pressurized patch developed towards a low fault normal stress area, along a sharp stress gradient corresponding to the >65° dipping side of the asperities.

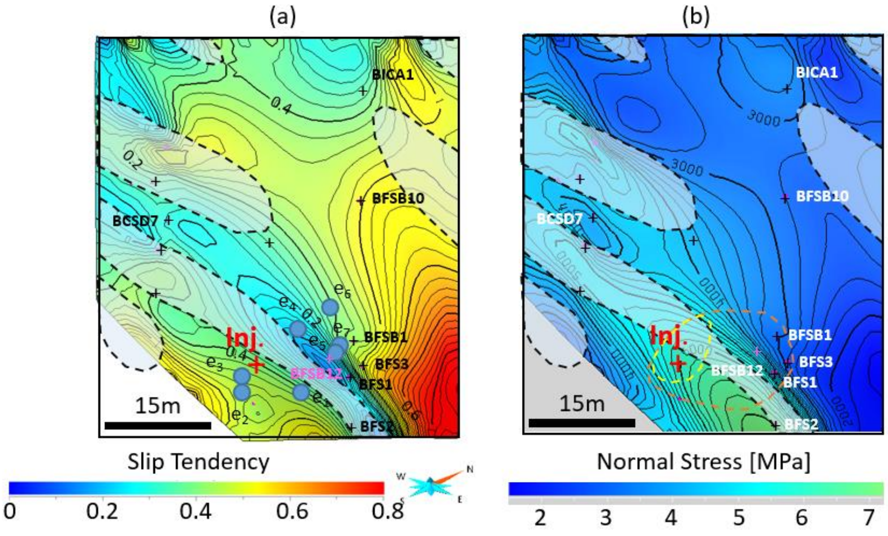

Figure 8-7. Influence of asperities on seismic slip and fault leakage. (a) Localization of seismic events induced by injection on a slip tendency map of the fault top surface, and (b) Localization of the pressurized patch limit on a map of the fault normal stress.

8.2.4 Conclusion and Implications

We showed that fault slip surface geometry is connected to the fault zone architecture, which resulted from the multi-phased faulting history. The Mont Terri Main Fault has elongated asperities correlated with variations in thickness of granular-like layers of "scaly clay" where brittle and ductile deformation has occurred. These observations are in good accordance with observations on other fault zones (Sagy et al., 2009; Smith, 1977; Johnson and Fletcher, 1994). We observed two roles played by the asperities:

A geometrical role. Asperities provide a fault surface dip variability of about 30° that generates stress heterogeneity and stress gradients. The first implication is that some zones of the surface display a larger tendency to slip than others. We observe that seismicity localized in these zones. The second implication is that the normal stress on the surface also varies and leakage flow paths preferentially develop towards the lower normal stress patches.

A rheological HM role. For the first time to our knowledge, we measured a compacting slip associated to a seismic event. The possible mechanism is that multiple flow paths open in the bulk of the fault zone generating compacting slip on the fault surface and fluid expelled. Compacting slip and fluid expelled may increase the potential for slip rate acceleration and induced seismicity.

Therefore, this work shows how fault slip and leakage is related to fault surface geometry and its relation to bulk fault zone structure. The way the geometry and structure interact together dictate the amount of slip and leakage that can be produced in response to a given fault zone THM loading. In a host rock, one proxy to characterize fault potential reactivation may be to estimate the localization and thickness of scaly clay material.

8.3 Numerical Modeling of Fault Activation

8.3.1 Fault Activation in the Context of Nuclear Waste Repository

Fault activation may be induced associated with deep geological nuclear waste disposal, especially in low permeability rock, where thermally driven fluid pressure increases (thermal pressurization) and pressure increases due to gas generation could be significant. In the case of storage in OPA, the maximum temperature increase in host rock at short distance from the canister is in general expected to be 75°C-100°Cx. At laboratory scale and in saturated undrained conditions, a ~8MPa pore pressure increase due to an increase in temperature of 30°-60°C is observed on intact OPA samples (Zhang et al., 2017). It is explained by the larger increase in fluid volume with respect to the volumetric thermal expansion of the clay. In addition, Zhang (2018) showed that temperature below 90°C may accelerate volumetric creep rates probably by reducing viscosity and friction of bound water-films between solid clay particles. The same observations are made on clay bearing fault gouges where friction is decreasing with elevated temperature, eventually driving the faults to seismic instability at temperatures >100°C in some cases (Ashman et al., 2022). Nevertheless, there are very few laboratory data on the effects of temperature of shale fault gouge strength evolution.

At field scale, previous HE-D heating experiment in intact OPA showed that an increase of temperature leads to an increase in pore pressure on the order of 0.1MPa/°C (Wileveau, 2005). Using TOUGH-FLAC numerical simulator and OPA THM properties, Urpi et al. (2019) calculated that the combined stress transfer effect of thermoelastic and poroelastic stress could reactivate a fault located at a lateral distance of hundreds of meters from a repository site. Eyinla and Oladunjoye (2021) showed that cooling of a reservoir fault at *in-situ* temperature of 70°C and a 1.8 km depth by injecting fluids at 50°C can produce a contraction of the fault significant enough to induce larger rupture and longer slip than a decoupled isothermal case. In addition, depending on the fault orientation toward stress, the THM case can trigger fault rupture where the HM isothermal case will not. In summary, temperature plays a major role in the mechanical behavior of clay rich materials and there is a lack of data about the THM response of clay faults at relevant field scale.

The Mont Terri fault slip experiments showed that the initially impermeable Main Fault can be reactivated by a 4-5 MPa water injection into the fault. This is in good accordance with the local stress tensor. Fault HM rupture was characterized by accelerating creep up to ~10 µm/s preceding a 4 order magnitude permeability increase respectively from 10^{-17} to 10^{-13} m^2 (Guglielmi et al., 2021; Cappa et al., 2022 and Figure 8-5). A 40°C temperature increase in the host rock close to the fault could potentially increase the fault pore pressure from ~0.8MPa to 4.8MPa. Given the Mont Terri experiment results, this could activate the fault.

In Section 8.3.2, we implemented a creep law in 3DEC software to better describe the fault rupture potentially evolving from aseismic fault creep to seismic rapid slip. In Section 8.3.3, we continued using the fully coupled numerical approach to analyze the role of asperities on fault displacement and leakage previously described in Section 8.2.

8.3.2 Modeling Fault Slip Evolution from Creep to Seismic Slip

We model a fluid injection with fault displacements over a single fault plane using the 3DEC v.7.0 (Itasca Consulting Group, 2020). The code allows us to resolve, in a single simulator, the interaction between fluid flow with two-way HM coupling, fault opening and slip on a planar fault intersecting impervious elastic rock (i.e. shale).

The model uses the cubic law to describe the coupling between fluid flow, pressure and the hydraulic aperture change:

$$\vec{\mathrm{Q}} = -\frac{\mathrm{b_h^3 \cdot w}}{12\mu_f}\overrightarrow{\nabla \mathrm{P}} \tag{8.1}$$

where $\vec{\mathrm{Q}}$ is the flow rate vector (m^3/s), $\overrightarrow{\nabla \mathrm{P}}$ is the fluid pressure gradient (Pa/m), μ_f is the viscosity of fluid (Pa.s), w is the fault width (m), and b_h is the hydraulic aperture (m), which can vary both as a function of the change in effective normal stress ($\Delta\sigma_n'$, total normal stress minus fluid pressure), and dilation caused by shear slip. Then, the hydraulic aperture is linked to the permeability (k in m^2) as follows:

$$b_h = b_{ho} + \frac{\Delta\sigma_n'}{k_n} + \Delta u_s \cdot \tan\psi, \text{ and } k = \frac{b_h^2}{12} \tag{8.2}$$

where b_{ho} (m) is the initial aperture at zero normal stress, k_n is the fault stiffness (Pa/m), Δu_s (m) is the shear slip increment, and ψ is the dilation angle (°). Dilation occurs only as the fault slips. Assuming smooth fault surfaces (i.e., no roughness), the hydraulic aperture is linked to permeability, k, (m^2) as follows:

$$\mathrm{k} = \frac{\mathrm{b_h^2}}{12} \tag{8.3}$$

The fluid pressure in the deformable fault follows a diffusion equation:

$$\frac{\delta p}{\delta t} = \frac{{b_h}^2 K_f}{12\mu_f}\nabla^2 \mathrm{p} - \frac{K_f}{b_h}\frac{\delta b_h}{\delta t} \tag{8.4}$$

where K_f is the fluid bulk modulus (Pa) and t is the time. Thus, the change in pressure is a result of fluid flow (the first term in equation 4) and mechanical deformation (the second term in equation 4).

The DEM is used to calculate displacements along the fault and rotations of rock blocks that surrounds it. On the fault, linear stress-displacement relations govern the elastic motions, in both the parallel and perpendicular directions.

Fault slips according to two modes: (1) aseismic, slow creep, and (2) seismic, rapid slip. Fault creep obeys to a viscoelastic behavior based on a creep formulation combining a Power law and a Kelvin law in series (Figure 8-8). The transient Kelvin component of the rheology is considered to be dominant at short timescales, while the Power component dominates at long timescales (Jaeger and Cook, 1979). This allows to model both the primary and secondary creep commonly observed in laboratory experiments. The creep phases occur during periods separating two seismic slips.

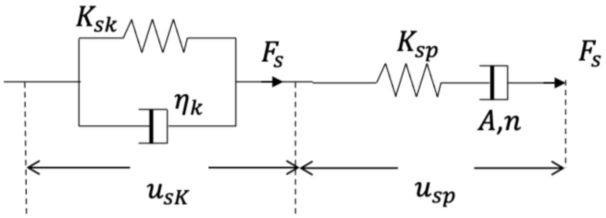

Figure 8-8. Schematic of the fault creep model with Kelvin and Power laws in series (η_k = Kelvin viscosity, K_{sK} = Kelvin shear modulus, F_s = shear force, A_c = contact area, u_{sK} = shear displacement due to Kelvin section, A and n = Power law constants, K_{sp} = shear stiffness, u_{sp} = shear displacement due to Power section).

Seismic slip initiates based on the Mohr-Coulomb failure criterion ($\tau = \mu \cdot \sigma_n'$, where τ is the shear stress at which slip initiates, σ_n' is the effective normal stress equal to the normal stress acting on fault minus the fluid pressure) (Jaeger et al., 2009). The evolution of fault friction during sliding is calculated with the linear slip-weakening law (Ida, 1972):

$$\mu = \begin{cases} \mu_s - (\mu_s - \mu_d)\frac{D}{\delta_c} & D < \delta_c \\ \mu_d & D > \delta_c \end{cases} \tag{8.5}$$

where μ_s and μ_d are the static and dynamic friction coefficients, respectively, and d_c is the critical slip distance over which friction decreases as a function of the amount of slip (D). After a slip event, no healing is considered over the short duration of the modeled injection experiment.

To test the new fault slip model programmed in this study, we have developed a simple spring-slider example in 3D (Figure 8-9). This example is conventionally used in geophysics to explain fault slip and friction evolution against data collected in the laboratory and the field.

As expected, results show cycles of stress accumulation and phases of frictional weakening and healing (Figure 8-10). This results in slow fault creep and fast slip as predicted in the theory (Figure 8-11). This result provides a degree of confidence that our approach is correctly implemented. Shape of the calculated shear displacement curve (blue curve in Figure 8-11) can be compared with the experimental curve during injection cycle 3 at borehole BFSB1 as described in Section 1.2 (Figure 8-5c).

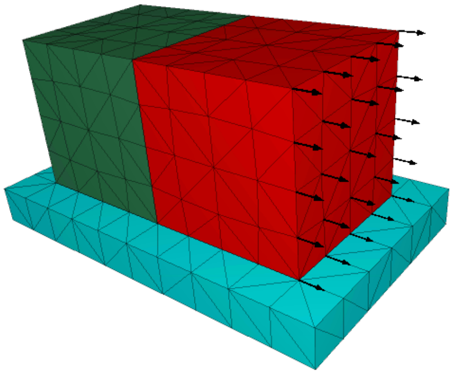

Figure 8-9. Spring-slider model with a fixed base (blue), a spring (red) and a slider (green). The spring is loaded at a horizontal velocity of 10^{-9} m/s (black arrows).

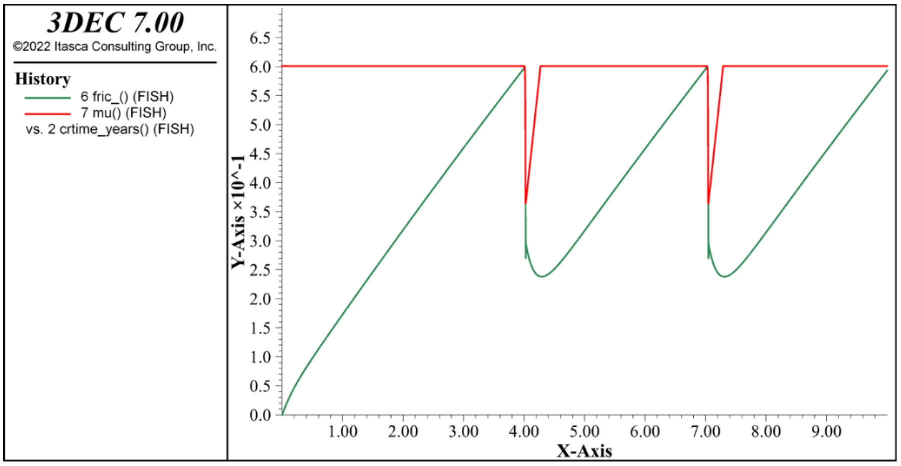

Figure 8-10. Comparison between the evolution of the friction coefficient (μ; red) and the frictional strength (shear stress/normal stress; green). The duration of frictional healing after a rapid slip is 6 months in this example.

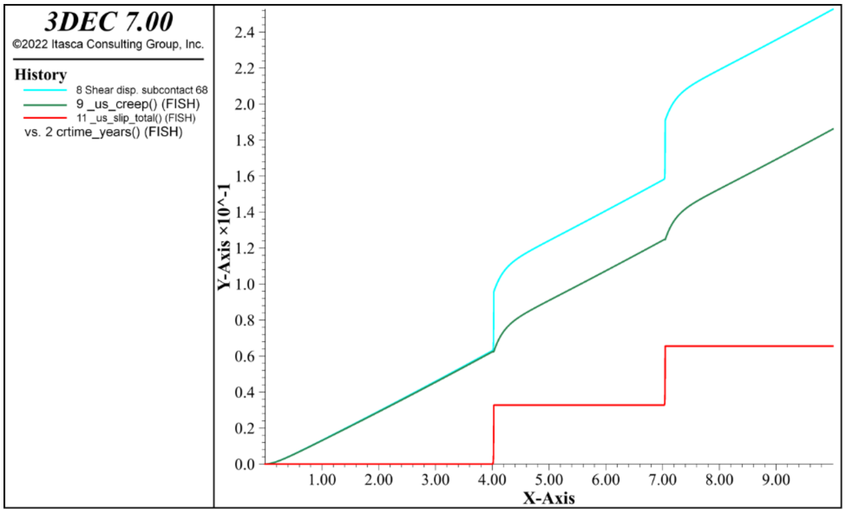

Figure 8-11. Calculated fault slip (blue) with phases of slow creep (green) and rapid slip (red).

8.3.3 Modeling the Mont Terri Fault Activation

The model aims to simulate the *in-situ* experiment of fault activation caused by fluid injection at 340 m depth in the low permeability shales with $k \sim 1 \times 10^{-18}$ to 1×10^{-21} m^2 (Wenning, 2020) within the Mont Terri URL. As described in Section 8.2, this experiment allowed the observation of fluid flow and rupture growth during a series of injections separated by repose periods. The internal structure of the fault zone, its physical properties and the geology of the host rock were extensively characterized in previous works (Nussbaum et al., 2011; Nussbaum et al., 2017; Guglielmi et al., 2020a,b; Orellana et al., 2019). Latest work presented in Section 8.2 highlights the influence of fault asperities on fault slip and leakage flow path propagation.

Here we explore the effects of three different fault zone geometries on the fault mechanical response (Figure 8-12). The models geometry (~50 m × ~50 m × ~50 m) is a cube intersected with the fault (Figure 8-12).

- A simple planar surface with a dip angle of 60° and a dip direction of 140°,
- A combination of multiple fault planes to figure the effects of bulk fault zone response. Dip direction and dip angle of the fault planes are in accordance with the ones in Figure 8-1b cross section,
- An undulated surface with asperities. Here we figure an average dip direction/dip angle 140°/60° fault surface with asperities oriented N070 and dipping 30-40° NE. Asperities create 30° variations of the fault surface dip angle in accordance with field observations.

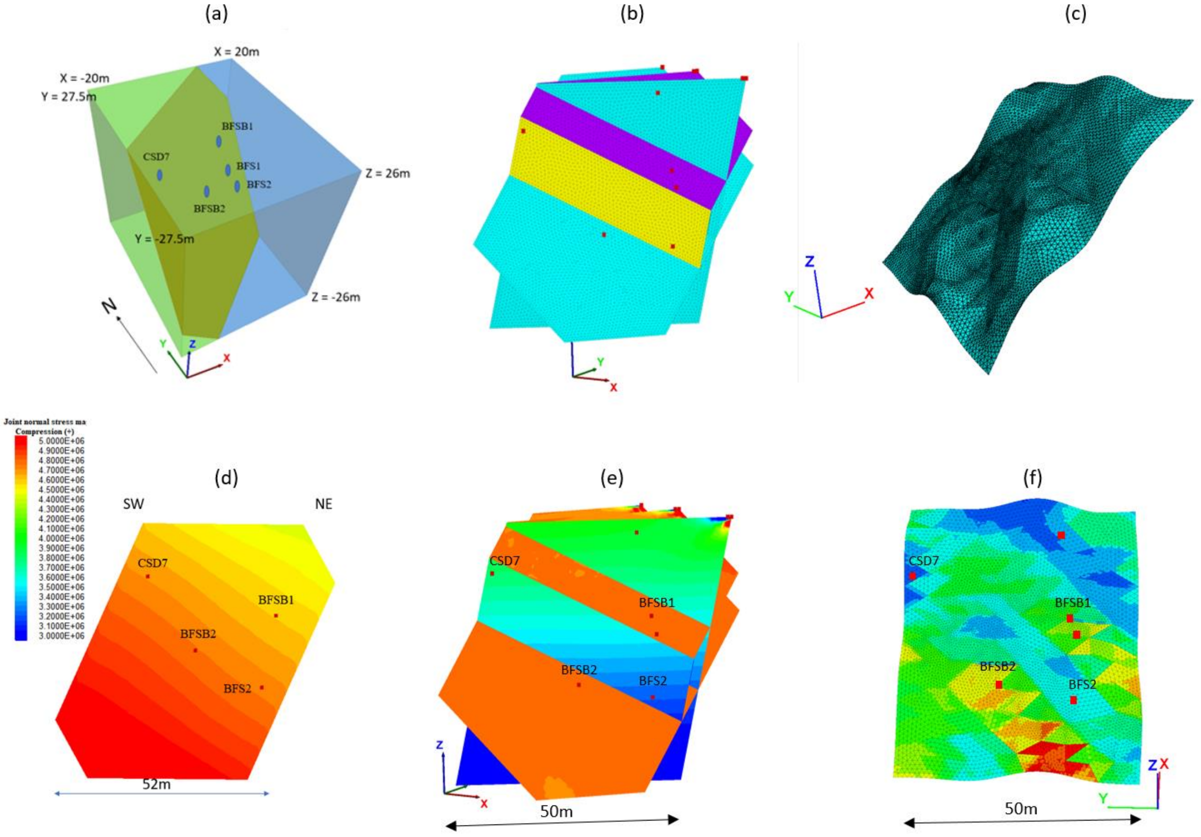

Figure 8-12. Different fault zone numerical models: (a) single plane fault; (b) multiple faults; (c) fault surface with asperities; (d) to (f) calculated normal stress variations on the three a-to-c fault models.

The remote principal stress (σ_1 = 7.00 MPa, σ_x = 5.38 MPa, σ_y = 5.67 MPa, σ_{xy} = 0.44 MPa) and fluid pressure (P_o = 1.4 MPa) applied at the model boundaries and resolved on the fault planes are constant. These values of stress and HM properties (Table 8-3) were estimated *in-situ* at the depth of experiments (Guglielmi et al., 2020a-b and Section 1.2), using a combination of geological data, borehole HM measurements, and modeling.

At the injection point BFSB2, the initial effective normal stress and shear stress acting on the fault were estimated at ~5.0 ± 0.3 MPa, and ~ 0.75 ± 0.3 MPa, respectively. Figures 8-12d,e,f show the variations of the initial effective normal stresses acting on the fault depending on the fault model. In the single plane case, the stress gradient is "artificially" created by applying a $\sigma_{xy} = 0.44$ MPa shear stress. We showed in previous work (see FY22 results) that it is the best way to match the observed NE flowpath's growth (see Figure 8-6a for the mapping of the flowpath limits on the fault surface). In the multiple fault planes model, sharp contrasts were calculated depending on planes orientation versus stress. The 70° dipping planes display a lower normal stress than the 50° dipping planes. In the fault surface with asperities (model *f*), transitions in normal stresses between <65° and >65° asperities were smoother than in the purely discontinuous model *e* (note that some patches of normal stress are influenced by the meshing of the surface topography and will be adjusted in the next studies). Moreover, models e and f show that asperities generate much larger stress variations on the fault that what is "needed" in the single plane model to match the measurements.

Table 8-3. Hydraulic and mechanical parameters for rock and fault.

Parameter	**Value**	**Units**
Young's modulus of rock *(K)*	8	GPa
Poisson coefficient of rock *(G)*	0.28	(-)
Rock density (ρ_r)	2450	kg/m^3
Fault elastic stiffness (k_n, k_s)	70	GPa/m
Initial friction coefficient (μ_s)	0.6	(-)
Residual friction coefficient (μ_d)	0.4	(-)
Critical slip distance (d_c)	150	µm
Initial cohesion (c_o)	0.1	MPa
Residual cohesion (c_r)	0	MPa
Tensile strength (T_0)	0.1	MPa
Kelvin viscosity (η_k)	10^{16}	Pa.h
Kelvin shear stiffness (K_{sK})	1	GPa/m
Power law constant (a)	10^{-16}	(-)
Power law constant (n)	1.1	(-)
Power law shear stiffness (K_{sp})	70	GPa/m
Initial hydraulic aperture (b_{ho}) at failure initiation	10	µm
Dilation angle (ψ)	2.5	Degree
Initial fluid pressure (P_o)	0.5	MPa
Fluid Bulk modulus (K_w)	2	GPa
Fluid density (ρ_f)	1000	kg/m^3
Fluid viscosity (μ_f)	0.001	Pa.s

After the initialization of the background stress and fluid pressure conditions, a fluid injection was modeled as a point source in the fault. Figure 8-13 presents the hydraulic loading path in a diagram of injected flowrate as a function of time. Three injection cycles (569 s, 585 s and 589 s, respectively) spaced with repose periods (300 s; voluntarily taken shorter to optimize the computation time) are simulated. The injected flowrates were 2.2, 3.6 and 8.58 l/min, respectively. The total time of injection was 2,600 seconds. The fluid pressure, displacements and stress were monitored over the fault plane and at selected points corresponding to the position of injection and monitoring points during the experiment (BFSB2, BCSD7, BFSB1). In addition, changes in hydraulic and frictional fault parameters are also calculated.

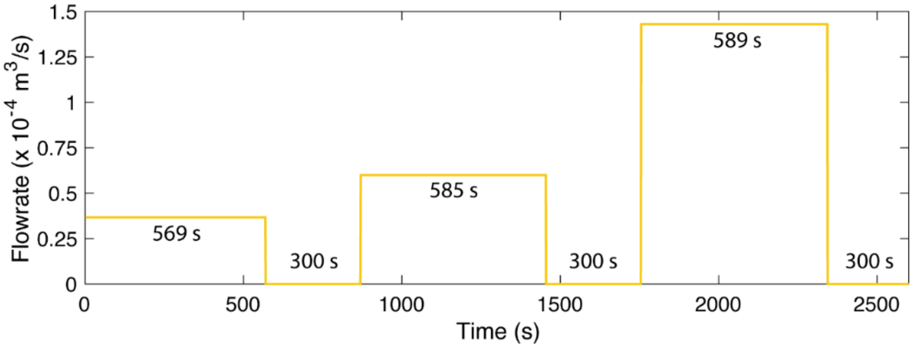

Figure 8-13. Hydraulic loading applied at injection (BFSB2 in Figure 8-12): flowrate versus time. The time indicated on each injection cycle and repose period corresponds to the duration of each phase. The injected flowrates are 2.2, 3.6 and 8.58 l/min, respectively.

Based on the previous study of Cappa et al. (2022), we used a model with fluid flow occurring in the activated parts in shear failure of the fault plane, and preventing flow from occurring in the remaining elastic parts. An adaptive time stepping scheme was employed with a time step of 0.1 second during the repose periods without injection (i.e., flowrate is equal to zero) and a reduced time step comprised between 10^{-4} and 10^{-2} second during the phases of maximum injected flowrate.

The modeling results show that a typical simulation lasts about 18 hours to model the entire loading sequence. Figure 8-14 shows the calculated change in fluid pressure, fault slip and opening at the end of the third injection cycle in the single fault plane case (Figure 8-12a). We first compare a model with a σxy = 0.44 MPa shear stress that create a stress gradient on the plane in addition to gravity (Figure 8-12d) with a model with σ_{xy} = 0 MPa shear stress where the only gradient is due to gravity. The model with additional σ_{xy} = 0.44 MPa shear stress allows to reproduce a fluid flow and pressurized area in the preferential easterly direction observed by the geophysical imaging. Indeed, the model without σxy calculates a HM connection between injection and BCSD7 which never happened in the field. However, the spatial distribution and magnitude of fluid pressure over the fault (Figure 8-14) and the range of calculated displacements (Figure 8-14d,e,f) show some differences with observations (compare for example Figure 8-14f with Figure 8-15d) that need more in-depth investigation with others simulations and parametric study. Here we show that the direction of this channel is likely due to the initial state of stress with an influence of the deviatoric component and a horizontal gradient. Figure 8-14 also indicates that the slipping patch develops in the pressurized area highlighting the effect of shear-induced dilation.

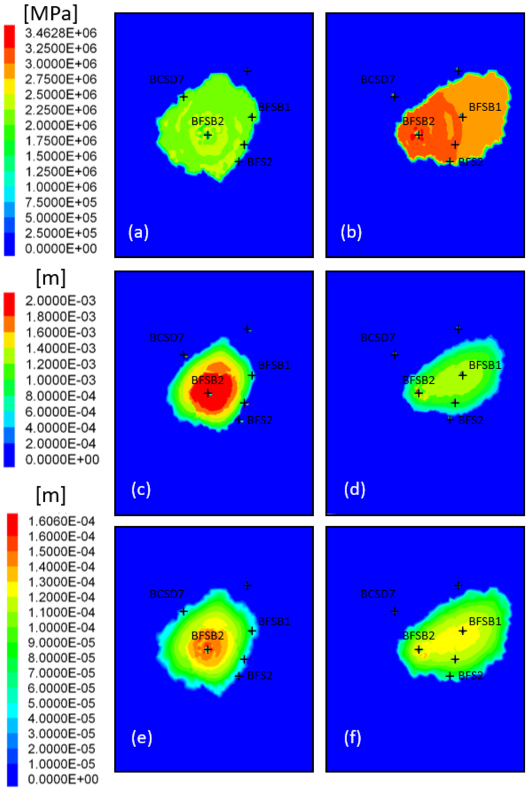

Figure 8-14. Calculated change in fluid pressure (a, b) and fault slip displacements (c-f) at the end of the third injection cycle for the single fault plane case (see text).

Figures 8-15a,b compare the fault normal displacement induced by flowpath growth in the multiple faults and in the single fault plane models. In the multiple faults model, we get a NE flowpath propagation with σ_{xy} = 0 MPa shear stress. This shows that the fault internal architecture is influencing fault HM behavior as well as flow channeling. The multiple faults model is highlighting two factors:

- Flowpath preferentially develops in 70° dipping faults. It appears to be stopped eventually by 50° dipping faults when the flowpath fluid pressure is too small to significantly reduce the effective normal stress and hydraulically open the fault.
- Some flowpaths may develop at fault intersections.

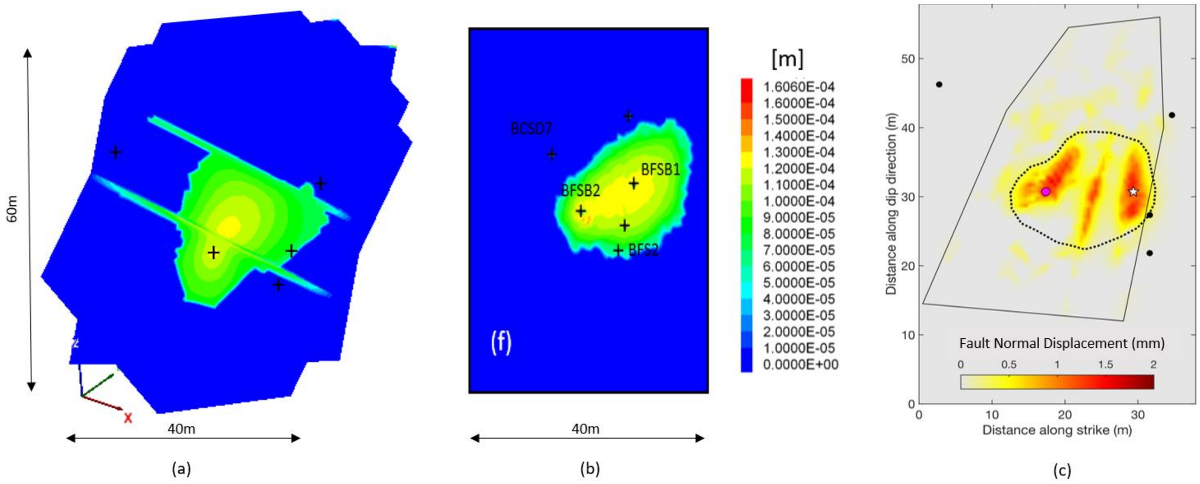

Figure 8-15. Calculated normal displacement induced by flowpath growth in: (a) the multi-fractures fault zone, (b) the single plane fault zone and (c) estimated from p-waves travel times changes measured in the field.

8.3.4 Conclusions and Perspectives

The series of 3D HM models of the Mont Terri experiment performed in 2020 allowed for calculation of the fluid pressure during three cyclic injections at constant flow rate. We have introduced a new algorithm that allowed for modeling both aseismic creep and seismic slip in a single simulator together with evolution of fault permeability and friction. The results showed that a small initial deviatoric stress gradient and a rupture-driven permeability evolution are two necessary conditions to reproduce the fluid leakage in the preferential north-easterly direction along the fault observed by geophysical imaging. We obtained a reasonable match between the calculated shape of the fluid pressure perturbation and the observed shape of p-wave velocity change. This gives a degree of confidence that our model is well adapted to reproduce complex fluid flow and slow deformation in an initially low permeability fault in shale host rock.

Although more work is needed on this research path, interestingly, a small stress gradient is sufficient to propagate rupture and fluid leakage in a preferential direction. This has implications for the design of monitoring techniques of fluid leakage in a faulted host rock and its integrity. Our numerical results highlight that the association of repeated high-resolution seismic imaging with controlled active sources together with local measurements of fluid pressure and deformation in boreholes provide useful data for understanding fluid leakage in host rock.

Work described in Section 8.3 of this report highlighted that fault topography is characterized by asperities, and that these asperities act as geometrical heterogeneities and rheological complexities. Asperity at the fault surface is also tightly coupled to bulk fault zone heterogeneity. How this fault geometry influences the hydraulic, mechanical and seismic responses to the fluid injection is unknown and need to be explored. In the continuation of this work, we will first finalize the HM modeling of the fault asperity model (Figure 8-12c). Then, the next step will be to mix a fault zone geometry with a major slip surface with asperities bounding an internal multiple faults zone.

8.4 Comparison of Fault and Fracture Response for Different Loading Scenarios

8.4.1 Distributed HM Response Close and Away from a Gallery

We compared the Mont Terri Main Fault distributed HM response to a local pressurization induced by water injection with fault response close to a gallery wall while this gallery is re-saturated. In both cases, we conducted time lapse monitoring of fault zone deformation with an extremely high spatial resolution of about 10 cm using fiber optic cables cemented behind the casing of boreholes entirely crosscutting the Main Fault in FS experiments and clamped to the gallery wall in PF experiments (Figures 8-16 and 8-17). Distributed strain changes affecting the rock along the boreholes are detected on the fiber based on the principle of Rayleigh Frequency Shift Distributed Strain Sensing (RFS-DSS, Ugueto et al., 2021). The strain changes are correlated to high spatial resolution fault geology characterized by a continuous X-ray micro-CT scanning of the borehole cores in FS, and to a high-resolution gallery wall photogrammetry in PF (Figures 8-16a and 8-17; Ziegler and Loew, 2021). In addition, pore pressure and temperature were monitored every ~0.5 m across the entire fault zone section in FS (Figure 8-16b). Long-term, structurally-controlled damage evolution, as is targeted in the PF experiment involving high-resolution resistivity and seismic tomographies, as well as extremely high-resolution photogrammetric assessment of the experiment borehole (Ziegler and Loew 2021), are compared with fiber-based strain data to damage and fault creep under different boundary conditions (i.e., desaturated and resaturated rock mass). Note that the PF experiment borehole also dissected the Main Fault zone and its hanging wall and footwall.

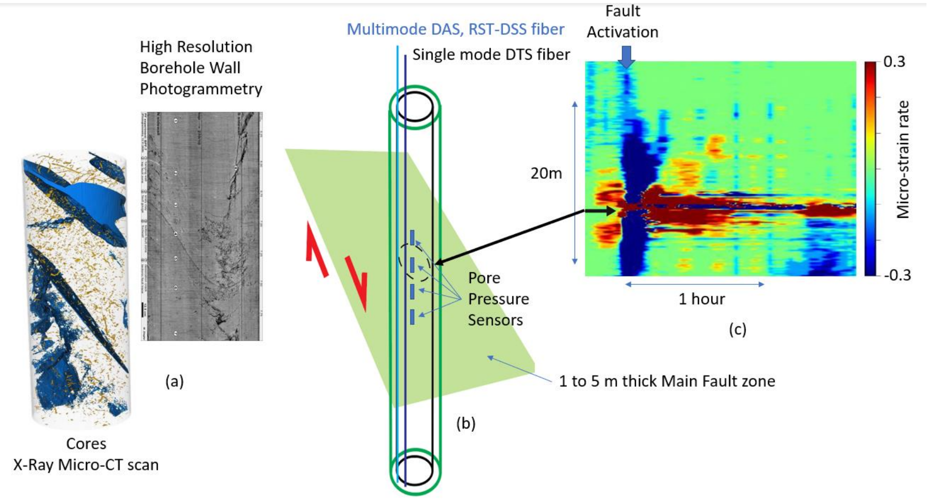

Figure 8-16. (a) High resolution fault zone mapping (CT scan example and BPF-7 experiment borehole unwrapped photogrammetric model showing the Main Fault zone). (b) Fiber optic monitoring of distributed strains and temperatures across the fault zone. Fibers are cemented behind casing in FS boreholes. Some pressure sensors monitor pore pressure every 0.5 m in the fault zone. Inside casing allows deploying other types of instruments or to eventually repeat logging such as full waveform acoustics. (c) Example of a RFS-DSS monitoring of strain rates across the Mont Terri Main Fault during one of the FS-B injection experiments. Multiple opening of fault zone structures seems to occur within the fault and through time (red color). Part of these signals seem to vanish after 1 hour injection but some complex residual areas seem to remain.

Figure 8-17 shows how RFS strains distribute across the Main Fault in borehole BFSB1 during the 2021 FSB activation (red curve in Figure 8-17a) and one year after in December 2022 (brown dashed curve in Figure 8-17a). BFSB1 was affected by the Main Fault activated rupture that was initiated by water injection in borehole BFSB2 located 18 m away along fault strike (Figure 8-17c). Figure 8-17b shows a geological log of BFSB1 that has been restored from the integration of optical log data and continuous micro-CT scans of the fault cores. In addition to the RFS fibers, local three-dimensional displacement sensors allow capturing movements on some of the main faults within the 6 m thick fault zone.

During activation (red curve in Figure 8-17a), RFS shows a localized extension characterized by positive 100 to 250 µstrain at about 40 m depth in the middle of the Main Fault zone. These correspond to a major contact between a fault and a scaly clay lens. Above and below, RFS show compression characterized by negative strains affecting the entire thickness of the fault zone intersected by BFSB1 borehole. RFS displays negative and positive peaks. Most of them appear to match with local faults. The negative peak at 38.5 m depth corresponds to a local 80 µm reverse slip on a fault with dip direction and dip angle respectively of 145.1° and 65.3°. Interestingly, all the local displacement sensors set in the fault are in contraction zones and display such reverse compacting slip. One year after the 2021 activation, the RFS cumulated strain is about 20 µstrain (brown dashed curve in Figure 8-17a). This means that most of the stain produced during the 2021 activation has not recovered although pore pressure measurements show a clear hydraulic closing of the fault following activation.

To summarize, RFS data combined with local displacement and pore pressure measurements allow refining the Main Fault HM response during and after activation. Interpretation is still in progress but it seems that the 6 m thick fault zone behaves as brittle with local slip on pre-existing faults and ductile in bulk scaly clay volumes. Take away message at this point could be that leakage is thus possible on localized brittle structures inside such shale fault zones. More refined RFS temporal measurements coupled with pore water pressure and chemistry monitoring will help better constrain this shale fault HM conceptual model in the next experiments.

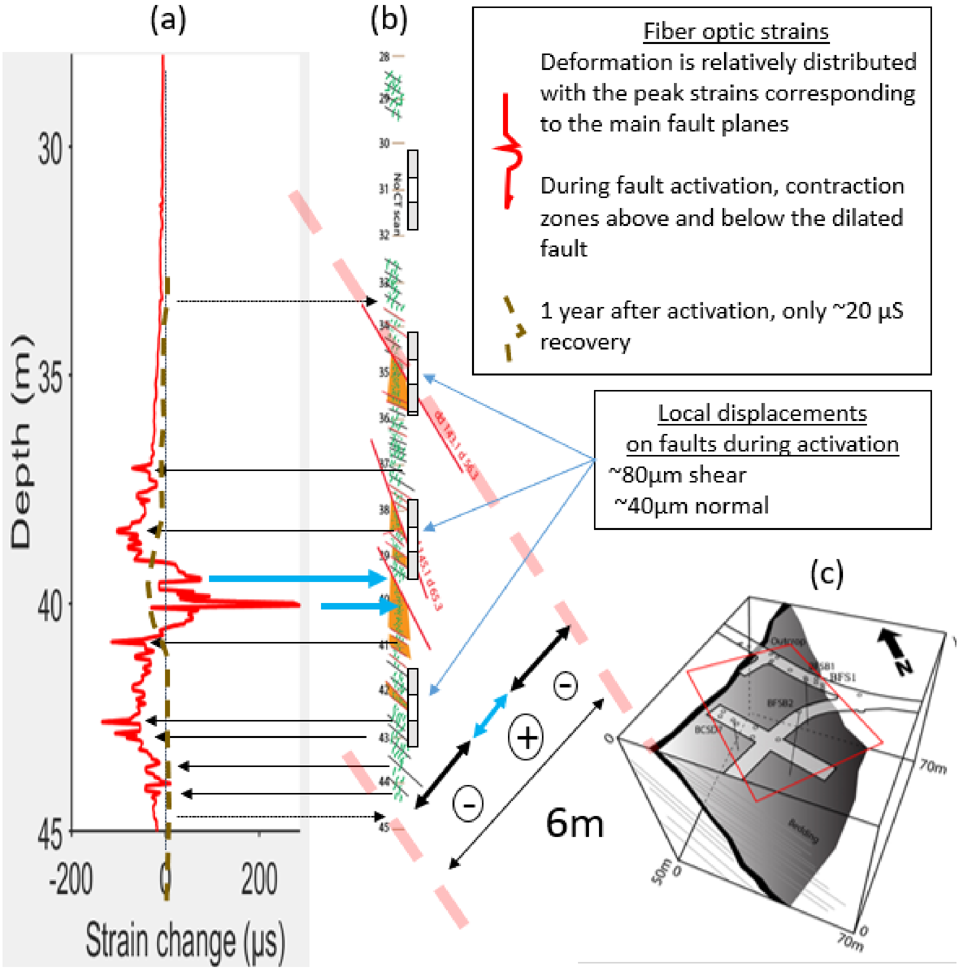

Figure 8-17. RFS strain distributed across the Main Fault during and after the 2021 FSB activation experiment: (a) RFS strain distributes along borehole BFSB1; (b) fault geological log and location of the three-dimensional displacement sensors; (c) localization of BFSB1 and BFSB2 injection boreholes.

Figure 8-18 (lower right) shows the fiber installation in the PF gallery. Five separate optical fiber loops were installed and fixed pointwise. The fibers span over sections with intact, lower-frequency, and higher-frequency discrete tectonic fault planes, as well as over the Main Fault zone containing at this location mostly scaly clay and a distinct gouge layer. Two RFS measurements were conducted before stopping the experiment borehole ventilation. Then, three additional RFS measurements were conducted after stopping ventilation while the relative humidity inside the tunnel increasing naturally (Figure 8-18 lower left). RFS showed significant 200-to-400 µ strains distributed along the open wall tunnel (Figure 8-18 top right). Extension zones characterized by positive strain variations display larger variation magnitude than negative strains. The link between distributed strains localization and the evolution of the tunnel wall features deduced from photogrammetric and geophysical methods will be carried out in the coming months.

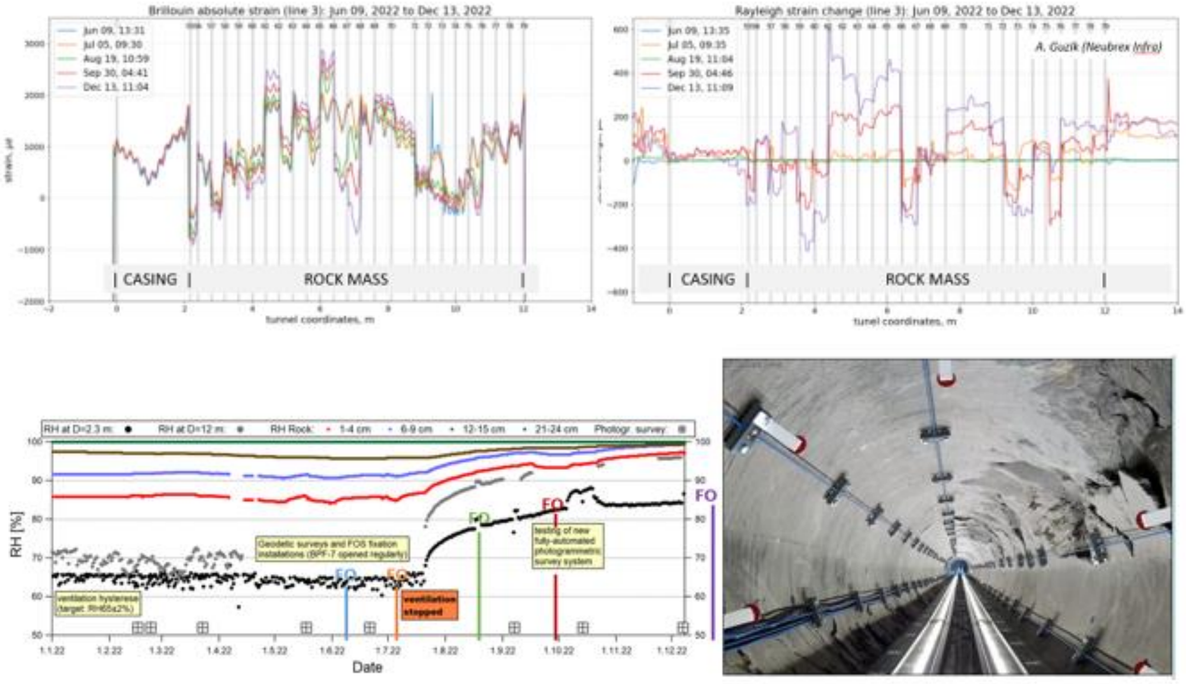

Figure 8-18. Top: Distributed fiber-optical (FO) strain measurements along the PF tunnel wall (work in progress). Lower left: Time localization of the FO measurements before and after the resaturation start. Lower right: Position of 5 optical fibers clamped lines that are used for distributed strain monitoring.

8.4.2 ANDRA Intact Rock Heated Volume Post-Experiment HM Response

The experiment designed by ANDRA (France) aimed at studying the potential thermo-hydrofracturing of the COx layer induced by thermal heating from the nuclear waste around the repository site. In the low permeable clay layers, temperature elevation could induce both a total stress and a pore pressure variation high enough to fracture the rocks. ANDRA has designed a heater experiment to study the mode(s) of thermo-hydrofracturing as a function of the state of stresses and rock heterogeneous properties. ANDRA performed two heating tests, respectively from June to September 2019 and from January to March 2020. The rock temperature was raised to a maximum of about 80° C and 95°C, while formation pore pressure increased to about 16 to 18MPa. During the second heating cycle, a pore pressure dropped from 1.25 to 1.175 MPa, which was observed on February 12, 2020. This pressure event was suspected to relate to the creation of a thermal hydrofracture (HF) in the near field of the pressure measurement borehole.

After the heating tests, from October 12 to 22, 2021, we conducted SIMFIP HM tests in the ANDRA's URL of Bure. Last year's report describes the SIMFIP tests operations and Figure 8-19 shows the details of the SIMFIP probe used in the test.

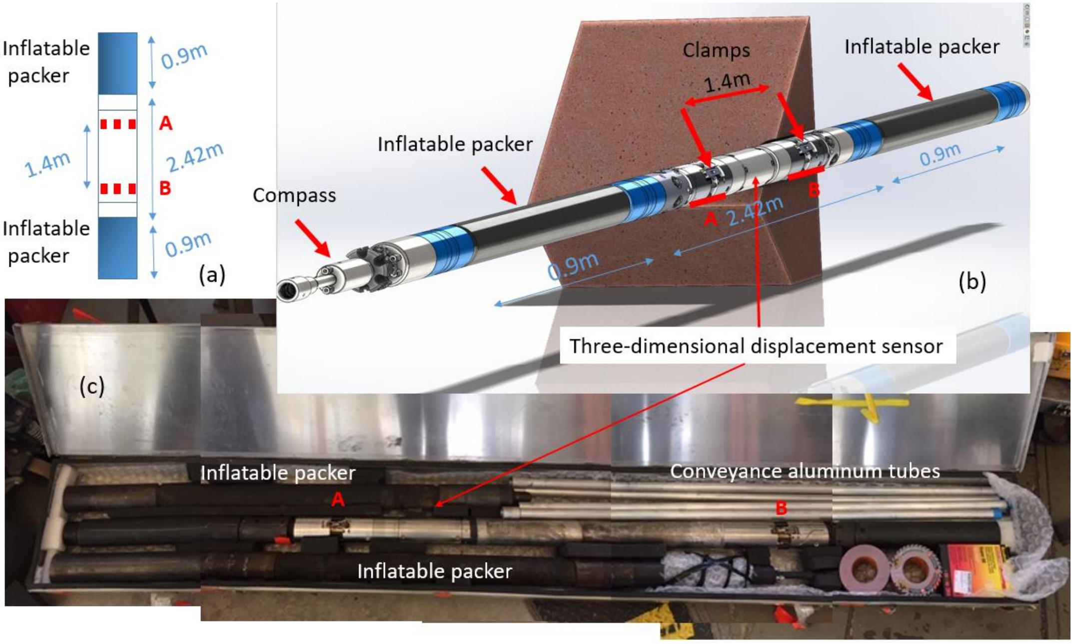

Figure 8-19. SIMFIP probe prepared for the ANDRA tests: (a) schematic plan of the probe showing length of packers, injection interval and distance between the two clamping zones (A and B); (b) Solidworks view of the SIMFIP probe; (c) photo of the probe prepared for the ANDRA experiment into its box before shipment to France.

The testing borehole CRQ1724 displays a dip direction and a dip respectively N239.734° and -5.288°. Borehole length and diameter respectively are 27m and 101mm. The borehole was drilled in order to explore the effects of heating a 3m x 3m x 10m volume roughly located between 10m and 20m away from the gallery wall (Figure 8-20 and Table 8-4). Four SIMFIP tests were conducted, Test 1 in intact rock outside the heated volume and away from the gallery EDZ, Tests 2 and 3 inside the heated volume, and Test 4 outside the heated volume in the gallery EDZ. The test protocol was detailed in FY22 report, and the same test protocol was applied to the 4 tests.

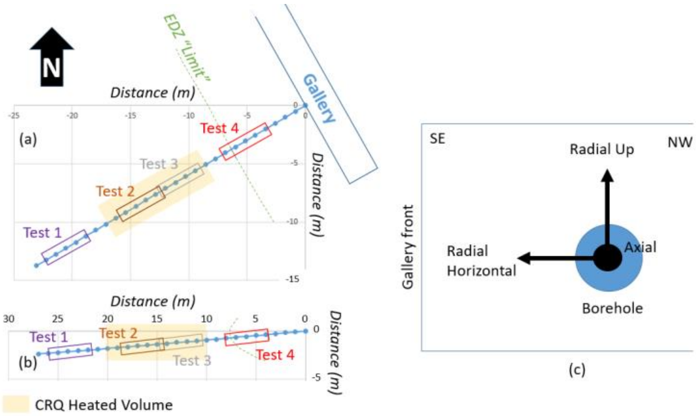

Figure 8-20. SIMFIP testing locations at the CRQ Heated Volume: (a) plan view of experiment setting; (b) vertical cross section along the borehole orientation; (c) orientation of the SIMFIP displacement components in the borehole coordinates (schematic view from a position looking at the gallery wall and the borehole mouth).

Table 8-4. SIMFIP tests geology.

Test #	Interval Depth (m)	Position relative to the CRQ heated volume	Local Geology
1	[21.78 – 26]	outside	Intact rock A thin and non-linear tensile fracture at the borehole top observed on the borehole video
2	[14.4 – 18.6]	inside	Mode 1 fractures parallel to core axis between 16.4 and 16.6m. Same observation on the borehole video where the tensile fracture looks offset and thicker compared to test 1 interval.
3	[10.43 – 14.65]	inside	High density of thin fractures sub-parallel to the core axis (there is a small angle between fractures dip and core axis). On cores, this zone of thin and dense fracturation extends from 11.66 to about 13.41m On borehole video, the tensile fracture is more complex than in tests 1 and 2. It is thicker and it is offset by many short fractures not cutting the entire borehole.
4	[3.9 – 8.1]	outside	On cores, many shear fractures fully cutting the sample are observed between about 4 and 6m, indicating the onset of the EDZ. On the borehole video, the first EDZ fractures are located at 7.2m. The borehole walls are hardly damaged over more than 50% of the borehole diameter. A borehole “washout” is observed at 4.57 and 3.87m.

Test 1 was considered as the reference test since it was located outside the heated volume in intact argillite rock. We conducted six injection cycles (Figure 8-21): 5 SRT cycles 1.1 to 1.5, and one constant flowrate cycle 1.6. Cycle 1.1 showed transient chamber pressure variations at relatively low pressures of about 6.1 MPa. We, thus, increased the packer pressure before conducting the following cycles in order to check if leakage was real into the formation or along the packer. After doing that, we found a clear pressure decay initiating at pressure step of 10.3MPa during cycle 1.3 (de period in Figure 8-21). This value fluctuated at cycles 1.4 and 1.5 where pressure decays were observed at steps respectively of 9.9 and 14.1 MPa (gh and kl periods in Figure 8-21). These fluctuations might reveal the complex propagation of a small hydraulic fracture away from the borehole nearfield. During cycle 1.6, an inflexion is observed in the pressure at about 13.5 MPa, while injection is constant at 1.2 l/min (*uv* period in Figure 8-21). Thus, these cycles displayed a fracturing pressure varying between 9.9 and 14.1 MPa.

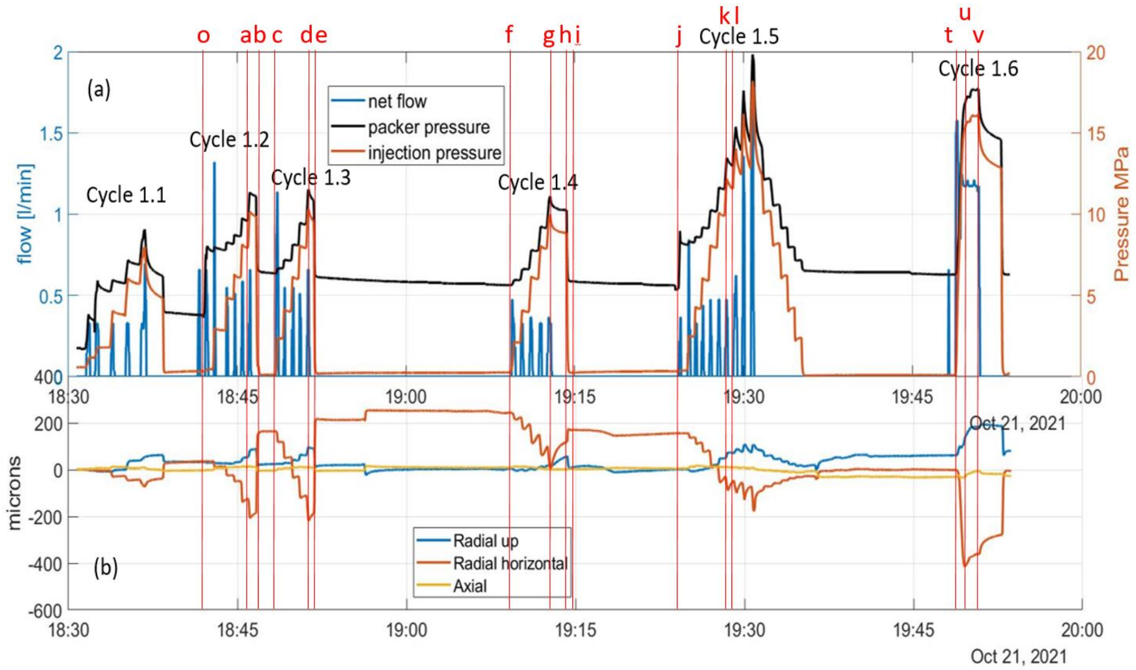

Figure 8-21. Test 1 SIMFIP pressure-displacement variations: (a) Chamber pressure, Packer pressure and Flowrate variations versus time; (b) Borehole Radial up, radial horizontal and axial displacements of the upper SIMFIP anchor (see Figure 8-18a for the probe anchoring system and Figure 8-19c for the local SIMFIP orientation in the borehole).

The displacements were mainly radial, with an amplitude of 130, -406 and 26 microns, respectively for the radial up, radial horizontal and axial components. There was a clear correlation between displacements variations and chamber pressure increase. At the end of the tests, a residual displacement was observed on the radial up and the vertical components mainly. We then rotated the displacements into the geographic origin and plotted the *oa* to *uv* periods as vectors in a stereographic lower hemisphere projection (Figure 8-22, vectors correspond to the difference between the displacement coordinates at the two limits of the given period).

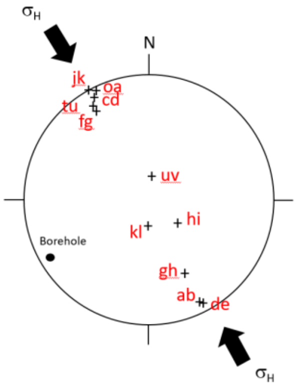

Figure 8-22. Test 1 key displacement vectors (lower hemisphere stereographic projection, vectors temporal location during the test can be seen in Figure 8-20).

Below the fracturing pressure, vectors display mainly a sub-horizontal N155° trend that was parallel to the regional maximum horizontal stress σH (see for example vectors *oa*, *ab*, *bc*, *fg*, *jk*, and *tu* in Figure 8-22). Above the fracturing pressure, vector progressively migrated from sub-horizontal to sub-vertical from cycle 1.4 (vectors *gh* and *hi*) to cycle 1.6 (vector *uv* in Figure 8-22). A first interpretation would be that at fracturing pressure, a sub-horizontal fracture was created, inducing a sub-vertical displacement.

We then did the same vector picking in all the tests. In Figure 8-23, we only plotted the vectors measured above the fracturing pressure (Figures 8-23b,c,d). There was a rotation of displacement vectors between Test 1 and the other tests. Tests 2 and 3 in the heated volume roughly displayed the same displacement as Test 3 set at the limit of the EDZ. If we consider an average EDZ fracture orientation (dashed semicircle in Figure 8-23e), the measured displacement highlights that the fracture was reactivated in shear. This is consistent with the fact that in the conceptual EDZ model in Figure 8-23a these orange fractures were created by failure in shear in this part of the EDZ. These fractures are thus be favorably oriented to reactivate in dilatant slip under the local stress state. Unfortunately, we have poor geological information about Tests 2 and 3, except that these tests were conducted in the heated volume initially selected outside the EDZ in intact host rock. We hypothesize that fractures with some similar orientation as in EDZ may have also been reactivated in shear in these test intervals. This could then show that the heating created favorable stress/strain conditions for failure in shear, may be by extending the EDZ far away from its average preheating depth from gallery wall.

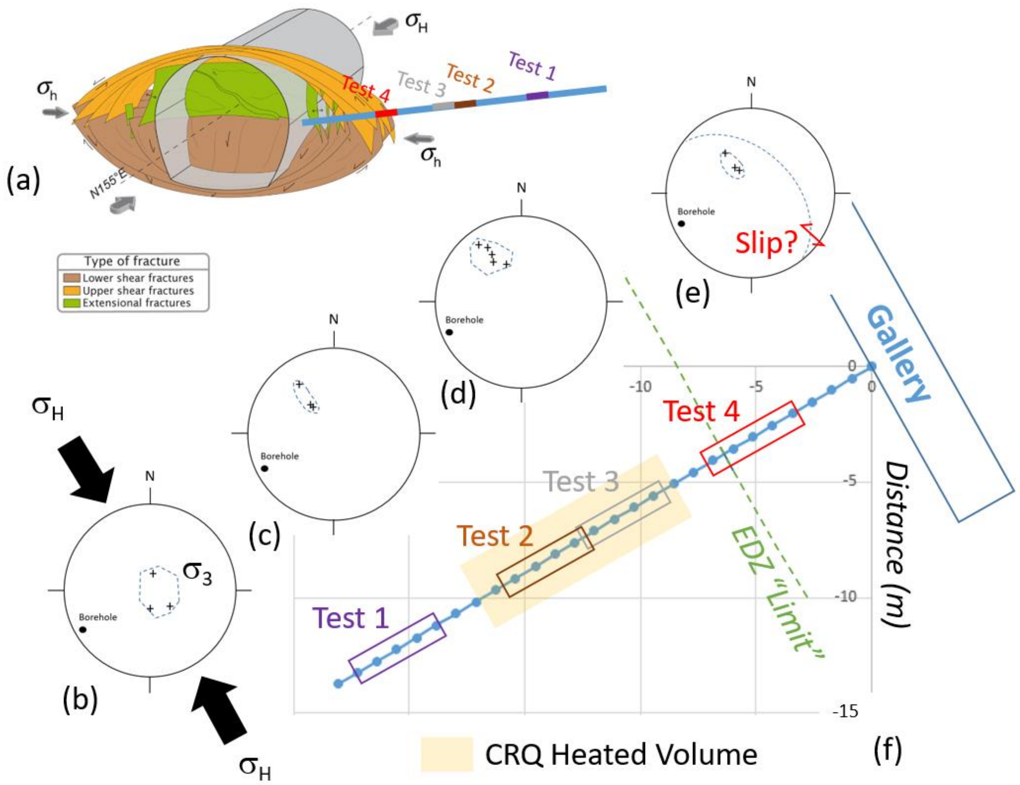

Figure 8-23. Displacement vectors measured above the fracturing pressure: (a) conceptual view of the EDZ at Bure site from de La Vaissiere et al. (2015); (b) to (e) displacement vectors (lower hemisphere stereographic projection); (f) map view of gallery and SIMFIP tests location.

Finally, our current analysis of post-heating SIMFIP tests at the ANDRA heater experiment in Bure highlight an unexpected rotation of displacements and fracture activation pressures in the heated volume, which was initially considered as intact rock away from the gallery EDZ. The intact rock interval (Test 1) displayed the highest 9.9 to 14.1 MPa leaking pressure, and vertical displacement that were consistent with a sub-horizontal HF. This is consistent with the regional stress tensor's orientation and magnitude. The other three intervals display a leaking pressure around 6.9 to 7.8 MPa, and about the same range of borehole displacement magnitudes that could be related to dilatant slip on pre-existing EDZ or heating-induced fractures.

8.5 Conclusions and Perspectives

In argillite faults, significant permeability increases appear tightly coupled to slip, thus, to rupture in shear. Nevertheless, we show in this report the geometric and rheological role of fault asperities that favor stress heterogeneity and local gradients that drive the mode of reactivation from dilatant shear to mixed shear-opening. Asperities also drive the direction of flowpaths development roughly perpendicular to the asperity's orientation.

In parallel, we have implemented a creep law in 3DEC software to better figure fault HM activation from slow dilatant creep to fast seismic slip. This model will be applied to the Mont Terri fault displacement measurements in the coming months.

We continued analyzing the SIMFIP tests done in the volume heated by ANDRA at the Bure URL. Key result is that the tests done in the heated volume give a pressure-displacement response that looks like the test in the gallery EDZ. This makes us suggest that the heating may have increased the EDZ volume.

The work perspectives until the end of FY23 are the following:

- Continue the HM modelling of fault asperities,
- Apply the implemented creep law to Mont Terri field data,
- Inverse the ANDRA displacement/pressure measurements into stress tensor's orientation and magnitude,
- Continue the distributed strain monitoring and comparison of fault response close and far from the gallery wall at Mont Terri, and
- Start designing a fault heating experiment at Mont Terri.

9. Progress Report on Modeling of CI-D Experiment at Mont Terri

The objective of this modeling task is the predictive simulation of hydro-chemical coupling occurring during the *in-situ* CI-D experiment at Mont Terri. In addition to providing understanding of the CI-D field experiment and the coupled processes relevant to nuclear waste repository disposal, we will benchmark and improve our multi-dimensional software CrunchClay in the process. The primary objective of the CI-D experiment is to understand how such parameters as diffusivity, permeability, and reactivity change as a result of the high pH cement and OPA interaction. Porosity change affecting diffusivity is of primary interest. With the CrunchClay code, we are able to consider electrostatic effects on ion transport (anion exclusion and cation enrichment), since these processes are expected to impact the reactivity of the overall system.

Current Capabilities in CrunchClay

CrunchClay represents an evolving branch of the code CrunchTope/CrunchFlow (Steefel et al., 2015) that considers electrostatic effects associated on transport (Tournassat and Steefel, 2019; Tournassat et al., 2020; Steefel and Tournassat, 2021; Tournassat and Steefel, 2021). The electrostatic effects on transport include those associated with the development of a diffusion potential as captured by the Nernst-Planck equation, and the formation of a diffuse layer (DL) bordering negatively charged clay particles within which partial anion exclusion occurs. The model is based on a dual continuum formulation that accounts for DL and bulk water pore space, providing a more flexible framework than that is found in the classical mean electrostatic potential (MEP) models. The DL model is obtained by volume averaging ion concentrations in the Poisson-Boltzmann equation. The model also includes longitudinal transport of solutes within the DL continuum. The calculation of transport within the bulk and DL porosity is based on a new formulation for the Nernst-Planck equation that averages diffusion coefficients and accumulation factors at grid cell interfaces (Tournassat et al, 2020).

9.1.1 MEP Model

Since the numerical solution of the Poisson-Boltzmann equation requires a fine discretization close to charged surfaces to resolve the DL, it is not practical for larger scale (>cm) domains. To be usable at the continuum scale, the Poisson-Boltzmann equations need to be upscaled in some fashion. An upscaling approach based on the MEP model has been discussed extensively in the literature (Tournassat and Steefel, 2019). The model assumes that the mean concentration in the DL, $\overline{C_{i,DL}}$ can be obtained by integrating over the DL volume in the Poisson-Boltzmann equation. This allows us to scale to a mean electrical potential, ψ_m, that applies to the DL volume, V_{DL}:

$$\overline{C_{i,DL}} = \frac{1}{V_{DL}} \iiint_{DL} z_i C_{i,0} \exp\left(\frac{-z_i \mathrm{F} \psi_{DL}(x,y,z)}{\mathrm{R}T}\right) \mathrm{d}x\mathrm{d}y\mathrm{d}z \approx C_{i,0} \exp\left(\frac{-z_i \mathrm{F} \psi_M}{\mathrm{R}T}\right) \tag{9.1}$$

The MEP can then be determined from the charge balance between the charged mineral surface (including the Stern layer) and the DL:

$$\sum_i z_i \mathrm{F} \overline{C_{i,DL}} = \sum_i z_i \mathrm{F} C_{i,0} \exp\left(\frac{-z_i \mathrm{F} \psi_M}{\mathrm{R}T}\right) = -Q_{DL} \tag{9.2}$$

where Q_{DL} is the volumetric charge that must be balanced in the DL (Tournassat and Steefel, 2019).

9.1.2 Dual Continuum Representation of Pore Space

A more general and flexible representation of the pore space can be provided using a dual continuum approach (Tournassat and Steefel, 2019). In this model, the pore space is divided into two compartments, one corresponding to bulk water that is electrically neutral, and a second that is not electrically neutral and that is subject to the MEP required to balance the surface charge in the pores. As we shall see, the volume of the compartment subject to the MEP need not be strictly the same as the actual DL volume. A schematic representation comparing the Poisson-Boltzmann equation and the dual continuum model for a case involving a sodium chloride solution is shown in Figure 9-1.

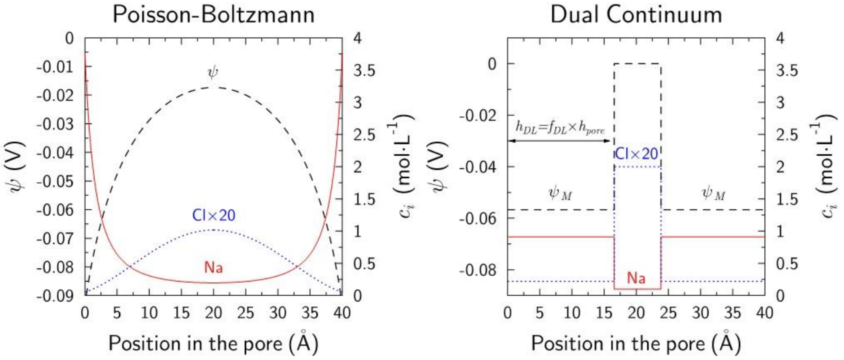

Figure 9-1. Comparison of the Poisson-Boltzmann distribution and that predicted by the dual continuum model of Tournassat and Steefel (2019), a refinement of the MEP model.

Defining the fraction of the pore space subject to the MEP, f_{DL} as:

$$f_{DL} = \frac{V_{DL}}{V} \tag{9.3}$$

we can transform Equation (9.2) so that the charge balance is applied over the entire pore (Tournassat and Steefel, 2019):

$$\sum_i z_i \mathrm{F} \overline{c_{i,pore}} = \left(1 - f_{DL}\right) \mathrm{F} \sum_i z_i c_{i,0} + f_{DL} \mathrm{F} \sum_i z_i c_{i,0} \exp\left(\frac{-z_i \mathrm{F} \psi_M}{\mathrm{R}T}\right) = -Q_{DL} \tag{9.4}$$

The fraction f_{DL} can be adjusted to be consistent with theoretical Poisson-Boltzmann predictions or with experimental results. As pointed out by Tournassat and Steefel (2019), this refinement of the MEP model does not necessarily imply that electrically neutral bulk water exists in the center of a pore—the Poisson-Boltzmann equation in Figure 9.1 shows that in fact, the electrical double layers (EDLs) from either side of the pore overlap in this case, so no electroneutral water is actually present. The objective of the dual continuum is to capture the average concentration that is consistent with the Poisson-Boltzmann prediction. The fixed charge of the mineral surface may be modified by adsorption in the Stern layer. In this case, the charge in the DL balances both the fixed mineral surface charge and the accumulation of ions in the Stern layer. In practice, both the fraction of the pore volume that is considered to be affected by the MEP, f_{DL}, and the DL charge can be adjusted to achieve the best fit with the available data. Alternatively, the sorption of ions in the Stern layer can be calculated independently using a surface complexation model (Steefel et al., 2015).

The volume of the DL, V_{DL}, can be defined as a multiple of the Debye length and the surface area of the clays:

$$V_{DL} = \alpha_{DL} \lambda_D S \tag{9.5}$$

where α_{DL} is an empirical multiplying factor. These modifications make it possible to simulate many systems more accurately than is possible with the classical MEP model (Tournassat and Steefel, 2019).

Returning to the Nernst-Planck equation and neglecting convection, we can develop a general form that is applicable to both compartments in the dual continuum (bulk water and DL) model described above and that accounts for ion mobility in porous media:

$$J_i = -u_i^{pm} C_{i,0} A_i \nabla \mu_i - u_{EP,i}^{pm} C_{i,0} A_i \nabla \psi_e \tag{9.6}$$

where ψ_e is the electrical potential in the fluid and as a result of a diffusion potential or external electric field, and not the MEP (Tournassat and Steefel, 2019). A_i is an accumulation factor defined by:

$$C_i = C_{i,0} A_i \tag{9.7}$$

The value of accumulation factor, A_i, is defined for both the DL and bulk water as, respectively:

$$\begin{aligned} A_i &= \exp\left[-z_i \frac{F\psi_m}{RT}\right] &&: \text{ Diffuse Layer} \\ A_i &= 1 &&: \text{ Bulk} \end{aligned} \tag{9.8}$$

where it should be noted that $A_i = 1$ for the bulk water because the electrical potential = 0. Defining the chemical and electrophoretic mobilities for porous media to include the tortuosity, τ_i, and porosity, ϕ:

$$\begin{aligned} u_i^{pm} &= \phi\tau_i \frac{D_{i,0}}{RT} \\ u_{EP,i}^{pm} &= \phi\tau_i z_i F \frac{D_{i,0}}{RT} \end{aligned} \tag{9.9}$$

Equation (9.6) then becomes:

$$J_i = -\phi\tau_i D_{0,i} A_i \nabla C_i - \phi\tau_i D_{0,i} C_i A_i \nabla \ln \gamma_i - \phi\tau_i \frac{z_i F}{RT} D_{0,i} C_i A_i \nabla \psi_e \tag{9.10}$$

In the case where there is no electrical current and thus no net flux of charge,

$$\sum_i J_i = 0 = -\sum_i \left(\phi\tau_i D_{0,i} C_{i,0} A_i \nabla \ln\left(\gamma_i C_{i,0}\right) + \phi\tau_i \frac{z_i F}{RT} D_{0,i} C_i A_i \nabla \psi_e \right) \tag{9.11}$$

which leads to (Tournassat and Steefel, 2019):

$$\nabla \psi_e = \frac{-\sum_i \phi\tau_i D_{i,0} z_i C_{i,0} A_i \nabla \ln\left(\gamma_i C_{i,0}\right)}{\sum_k \phi\tau_k \frac{z_k^2 F}{RT} D_{k,0} C_{k,0} A_k} \tag{9.12}$$

This result makes it possible to write the diffusive flux without the gradient in the electrical potential:

$$J_i = \phi\tau_i D_{0,i} C_{i,0} A_i \nabla \ln\left(\gamma_i C_{i,0}\right) + \phi\tau_i z_i D_{0,i} C_{i,0} A_i \frac{-\sum_j \tau_j D_{0,j} z_j C_{j,0} A_j \nabla \ln\left(\gamma_j C_{j,0}\right)}{\sum_k \tau_k z_k^2 D_{0,k} C_{k,0} A_k} \tag{9.13}$$

This form in which the electrical potential is eliminated in the diffusion potential term was used in these simulations.

9.1.3 Extension to 3D

To simulate the CI-D experiment at Mont Terri, it was necessary to develop a full 3D treatment of the system, since there is no symmetry that can be made use of there. We extended the loops and the geometry to 3D in the new version of CrunchClay (referred to as CrunchClay-MPI)

9.1.4 MPI Implementation

Extension to 3D requires that the overall calculation speed be improved while efficiently managing the memory allocation. The code is parallelized using the implementation of MPI in the PETSc (the Portable, Extensible Toolkit for Scientific Computation) from Argonne National Laboratory (Balay et al, 2022). The implementation has been completed and successfully tested on a laptop equipped with multicore processors and Windows OS. Then, it was migrated on Linux to make it possible to model very large systems on HPC user facilities.

D-Axisymmetric and 3D Simulations of CI-D Experiment at Mont Terri

The objective of the work in this project is to develop a predictive understanding of the coupled processes determining the evolution of the CI-D experiment at Mont Terri. The field campaign consisted of a number of boreholes, beginning with BCl-6, that placed cement within the OPA. The key objective of the field experiment and associated modeling is to understand the long-term interaction of the cement with the OPA. The latest borehole is angled from Gallery 98 and has the objective of overcoring the interaction zone between the cement (OPC) and the OPA.

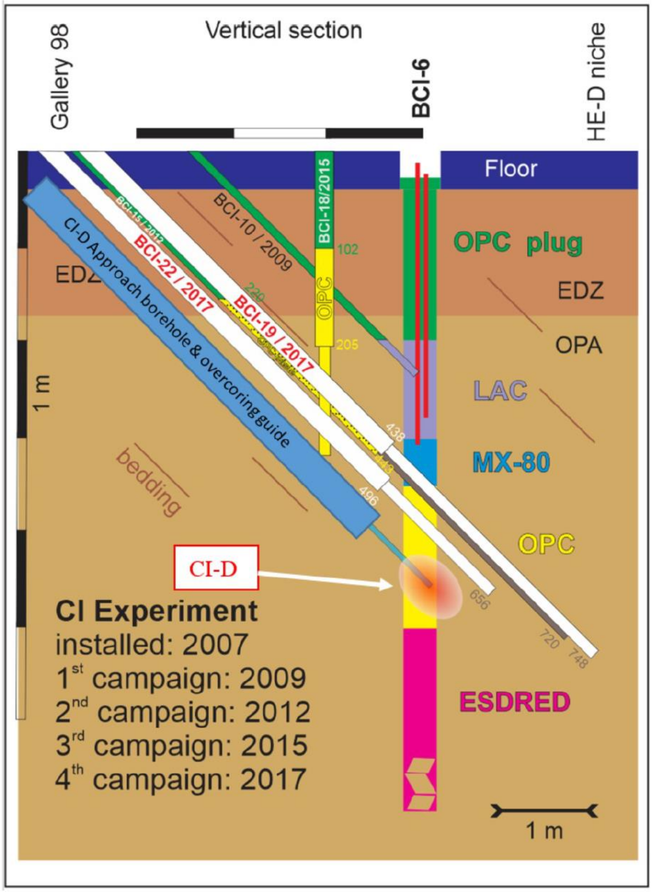

Figure 9-2. Schematic illustration of CI-D field experiment at Mont Terri. The CI-D overcoring borehole is approaching the zone of long-term interaction between OPC and the OPA. Note that the bedding within the OPA is parallel to the overcoring borehole, and at an angle of about 45° from the contact with the cement plug. Information from the overcoring is expected to be available in the Fall of 2023.

Earlier boreholes were used to set a recirculation system into the borehole that could be used for injection of uncharged tracers (tritiated water, HTO) and the isotopologue of the anion chloride, ^{36}Cl (Figure 9-3). To make use of the data from the recirculation system, and to consider the asymmetry and the anisotropy of the system, a 3D model was built (Figure 9-4), so that the bedding of OPA was parallel to the *z*- and *y*-axis. 3D calculations were compared to 1D-radial and 2D-axisymmetric calculations in which the concrete material was the only material surrounding the borehole.

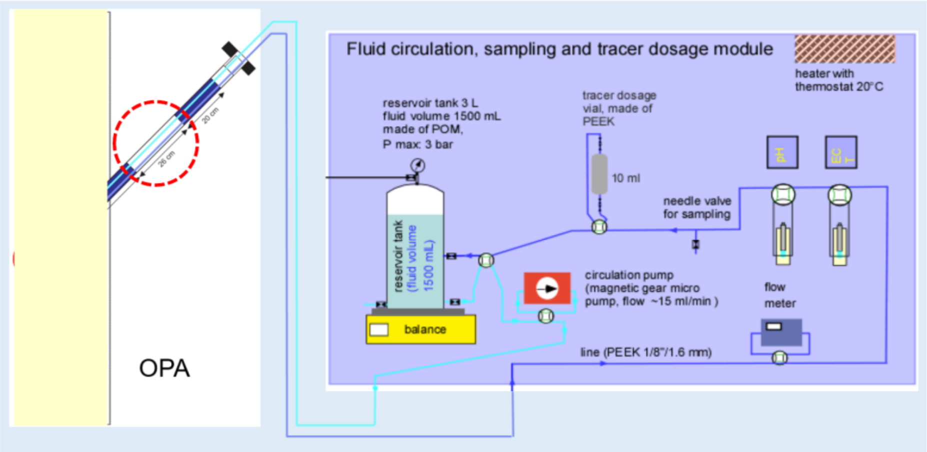

Tracers: ^{3}H, ^{36}Cl

Water tracer and anion (conservative, electrostatic effect)

Tracer	Activity conc.	LL	Activity (1.5 L)	LA (1.5 L)
^{3}H (HTO)	$2 \cdot 10^5$ Bq/kg	2	$3 \cdot 10^5$ Bq	0.001
^{36}Cl	$4 \cdot 10^4$ Bq/kg	40	$6 \cdot 10^4$ Bq	0.06

LL: clearance limit / Befreiungsgrenze; LA: licensing limit / Bewilligungsgrenze

Figure 9-3. Schematic illustration of fluid circulation, sampling, and tracer dosing system in the Cl-D experiment at Mont Terri.

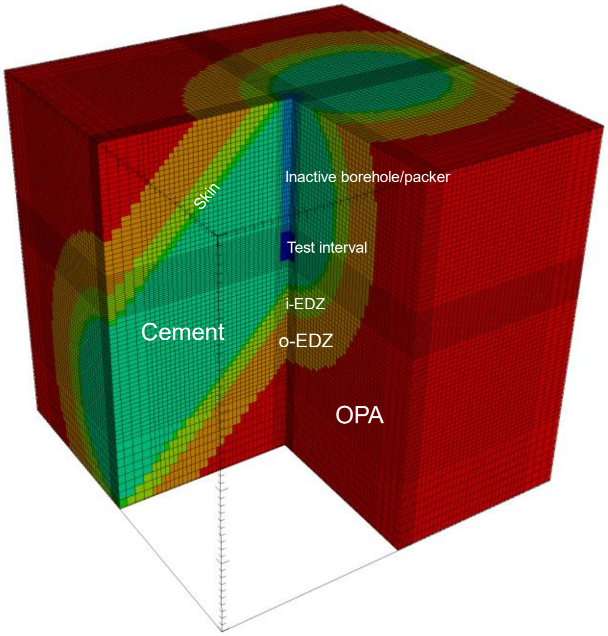

Figure 9-4. Geometry of the simulation grid. Dimensions are 1 m × 1 m × 1 m. Grid size dimensions are 5 mm, 1.25 cm or 2.5 cm. The total number of cells is 592,704 including boundary cells (not represented here). The simulation domain is truncated to show the position of the different materials. The porosity and thus the volume in the test interval (0.194 dm^3) was increased to 7.73 dm^3 to match the volume of the circulating water (1.5 dm^3).

9.3 Comparison of the 3D Simulations with 1D-Radial and 2D-Axisymmetric Simulations

1D-radial and 2D-axisymmetric simulations were carried out with only concrete material around the test interval.

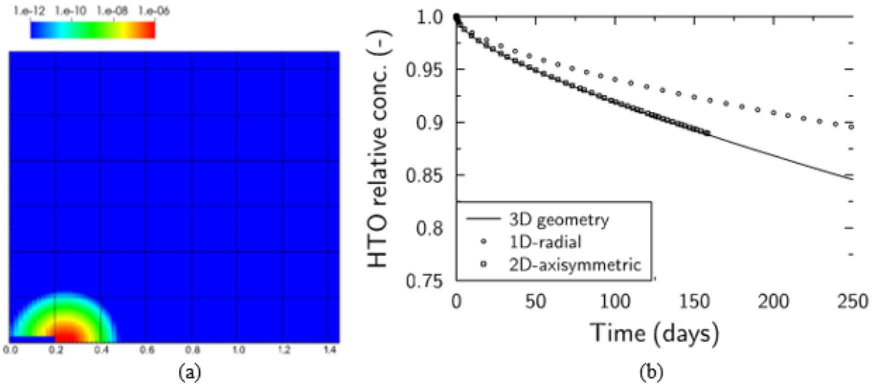

Figure 9-5. (a) 2D-axisymmetric simulation results (100 days; distances are given in meters on the x-axis; same scale for the y-axis); (b) comparison of 3D, 1D-radial, and 2D-axisymmetric simulation results for HTO concentration as a function of time in the test interval.

The comparison of 3D and 2D-axisymmetric simulation results shows that HTO concentration evolution in the test interval was entirely controlled by the concrete transport properties during the first year of the experiment. A 1D-radial simulation is not correct to reproduce the geometry of the experiment, even in the first 100 days of the experiment. Diffusion parameters of the concrete can be fitted with a less computing-demanding 2D-axisymmetric geometry.

Table 9-1. Concrete diffusion parameter estimation.

Zone	**Bulk Porosity**	**EDL Porosity**	**Kd HTO**	**Kd Cl-**
Borehole	7.73	1.0E-05	0.0	0.0
Cement+Skin	0.14	1.0E-08	0.1	0.4
OEDZ	0.015	0.135	0.0	0.0
OPA	0.015	0.135	0.0	0.0

We considered a concrete porosity of $\varepsilon = 0.14$ and a K_D value of 0.1 L kg^{-1} for HTO (Nedyalkova et al., 2021). The tortuosity of the concrete was adjusted to $\tau = 0.12$ to fit the measured concentrations in the test interval as a function of time up to 350 days (**Error! Reference source not found.**). The corresponding effective diffusion coefficient was $D_e = 3.6\ 10^{-11}$ m^2 s^{-1}. We kept the same tortuosity and porosity parameters for chloride, and we adjusted the K_D value to fit the measured ^{36}Cl concentrations. A K_D value of 0.4 L kg^{-1} yielded an acceptable fit of the data up to 350 days and was in agreement with experimental K_D values obtained on aged cement matrices (Nedyalkova et al., 2021).

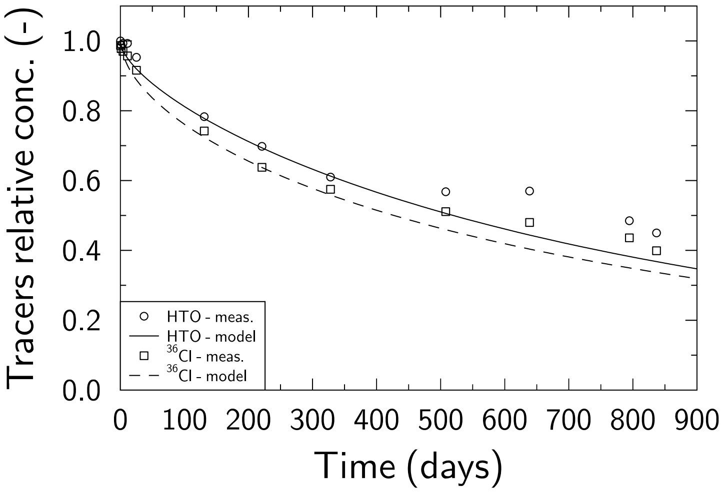

Figure 9-6. 2D-axisymmetric simulation of HTO and ^{36}Cl diffusion.

Table 9-2. Initial conditions for three zones, including fracture (higher porosity zone), cement (OPC), and OPA.

Component	Borehole	Cement	Skin	OEDZ	Opalinus Clay
pH	13.63	13.63	13.63	7.30	7.30
Na^+	676	676	676	281	281
Ca^{2+}	2.49	2.49	2.49	19.0	19.0
Cl^-	41.0	41.0	41.0	284	284
SO_4^{2-}	0.8	0.8	0.8	17.2	17.2
Tracer	0.001	0.0	0.0	0.0	0.0

Table 9-3. Self-diffusion coefficients for chemical species considered in simulations. Molecular diffusion is calculated using the Nernst-Planck equation (Steefel et al, 2015; Tournassat and Steefel, 2019a).

Chemical Species	Diffusion Coefficient $\left(\mathrm{m}^2 \cdot \mathrm{s}^{-1}\right)$
H^+	9.31×10^{-9}
Na^+	1.30×10^{-9}
Ca^{2+}	0.79×10^{-9}
Cl^-	2.10×10^{-9}
SO_4^{2-}	1.07×10^{-9}
Tracer	2.15×10^{-9}

Table 9-4. Tortuosity values in *X*, *Y*, and *Z* for various zones in simulation. OPC is cement, while OPA refers to the Opalinus clay with typical values, and distinct outer and inner disturbed zones. The borehole chamber is open to the recirculation system (thus the high tortuosity value to capture well-mixed conditions), while the borehole itself is sealed. Note the higher tortuosity values in the *Z* and *Y* coordinate directions parallel to the bedding in the OPA.

Zone	**TortuosityX**	**TortuosityY**	**TortuosityZ**
Borehole Chamber	10.0	10.0	10.0
Borehole	$1\text{x}10^{-11}$	$1\text{x}10^{-11}$	$1\text{x}10^{-11}$
OPC	0.05	0.05	0.05
OPC Skin	0.05	0.05	0.05
OPA	0.07	0.21	0.21
OPA Outer Disturbed Zone	0.14	0.42	0.42
OPA Inner Disturbed Zone	0.14	0.42	0.42

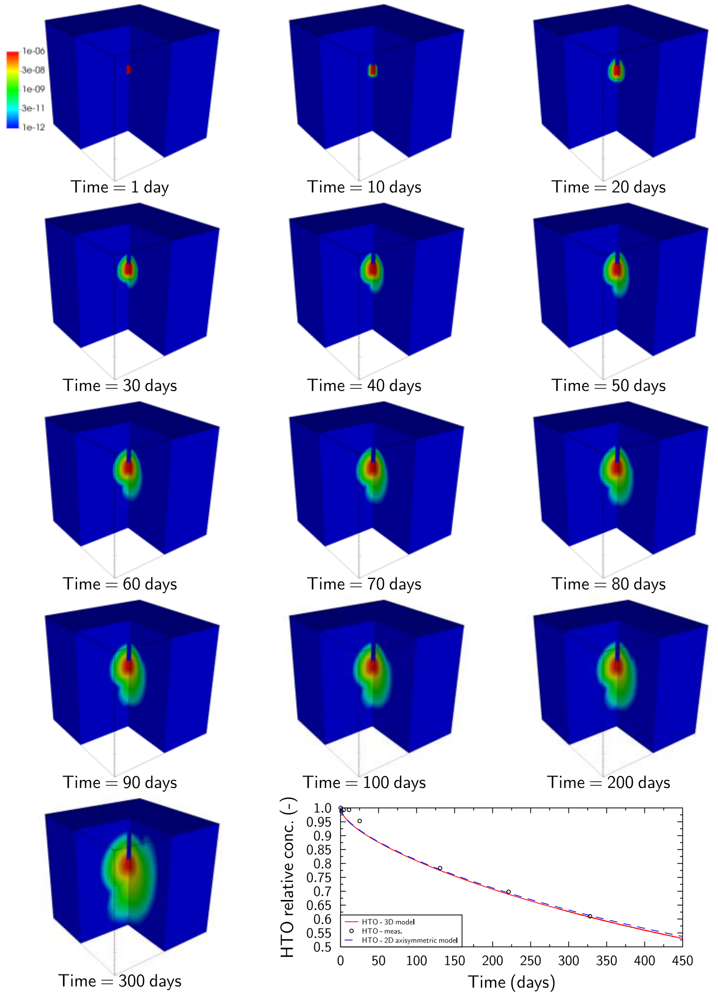

Figure 9-7. 3D contour plots of HTO (uncharged solute) out to 300 days, borehole chemistry out to 450 days. The plume is almost completely located within the isotropic cement, so the anisotropy of the OPA has yet to have a significant effect.

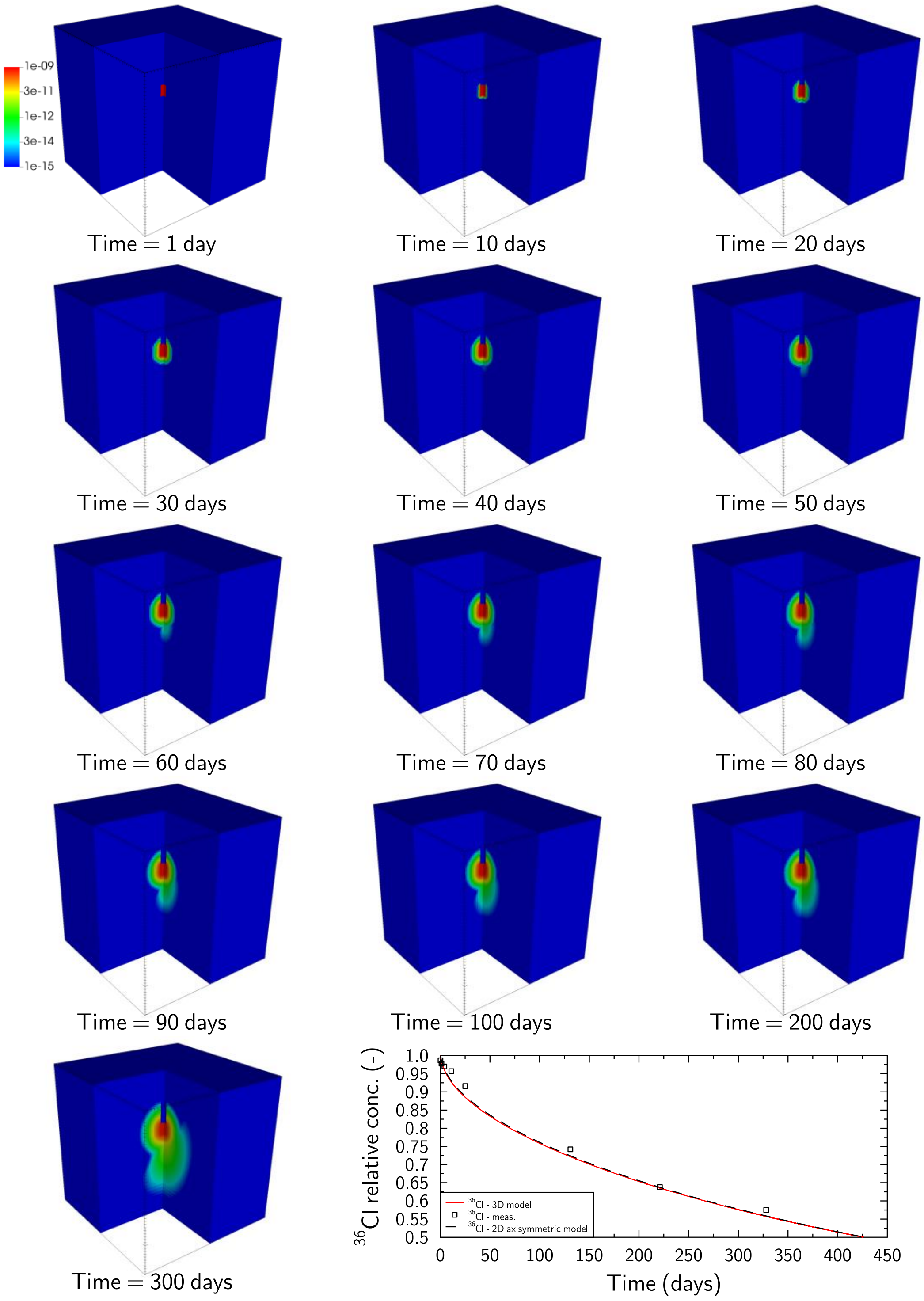
Time = 1 day
Time = 10 days
Time = 20 days
Time = 30 days
Time = 40 days
Time = 50 days
Time = 60 days
Time = 70 days
Time = 80 days
Time = 90 days
Time = 100 days
Time = 200 days
Time = 300 days

Figure 9-8. ^{36}Cl out to 300 days, borehole chemistry out to 450 days. The plume is almost completed located within the isotropic cement, so the anisotropy of the OPA has yet to have a significant effect. The more rapid drawdown of the Cl compared to the HTO is due to sorption of the chloride in the cement, resulting in a loss to the borehole.

3D contour plots of HTO and ^{36}Cl in Figures 9-7 and 9-8, respectively, indicate that the loss of ^{36}Cl from the borehole is more rapid. This is due to the sorption of ^{36}Cl in the cement (K_d = 0.4 l/kg) as compared to the HTO. Neither is impacted by the properties of the OPA, since the leading edge of the plume is only just approaching the cement-Opalinus Clay contact. Longer simulation times will be required.

9.4 Summary and Future Work on CI-D Experiment at Mont Terri

In this section we have briefly described the progress in simulating the CI-D diffusion test at Mont Terri. 1D radial and 2D-axisymmetric models that included only the cement were used to estimate diffusion coefficients in the cementitious material. Only the 2D-axisymmetric model gave good results. A 3D model has been developed and applied to simulating tracer transport out to 450 days and results were compared favorably with the 2D-axisymmetric model. These simulations make use of the full dual continuum model in CrunchClay in which electrostatic effects in the EDL are resolved, although these effects are not readily apparent in the simulations because of the limited duration of the simulation time--the plume does not extend significantly into the OPA by this time. Additional runs will be needed to extend it to full time scale of the experiment. In the coming period, we will consider a more comprehensive reaction network in which cement and cement-clay interactions are included. This will allow us to compare directly to the results of the overcoring of the cement-claystone interface expected to be completed in early 2024.

10 years of cement-clay interactions will be calculated prior to tracer diffusion. The focus will be to include a full treatment of cement chemistry, along with the interaction between the concrete and the OPA. This will make it possible to simulate the influence of this preliminary phase on the porosity evolution in the system, and thus on the diffusivity of the materials, especially at interfaces (skin, EDZ). The overcoring of the cement-Opalinus Clay is expected to be completed in early 2024 and the simulation results can then be compared to the observations made on overcore samples.

We will then restart the simulation with the addition of the borehole and the tracer injection. The extension of the simulation time so as to reach the time of the CI-D experiment will bring in the effects of anion exclusion, cation enrichment, and diffusion anisotropy in the OPA, although no significant influence on the evolution of the tracer concentration in the borehole is expected. The geometry of the tracer plume in the OPA will be influenced though. If available, tracer data in overcore samples will be compared to the simulation results.

10. Summary of FY23 Progress and Future Work

In FY23, LBNL work on coupled processes in argillite rock has continued with a broad research portfolio, including model development, validations, and applications, along with fundamental studies of argillite and bentonite-based buffer materials. Summaries and future work have been provided in Sections 2 through 9 of this report. Below is a brief summary of performed and future work related to the current LBNL Argillite R&D and Argillite International Collaboration work packages:

- As presented in Section 2, LBNL continued investigating the effect of shale-creep on the long-term performance of an argillite repository. This year, the creep model was extended to consider anisotropic creep. The analysis showed that the results of long-term repository performance considering anisotropic creep was not significantly different from the results when considering isotropic creep. However, the degree of anisotropy in the shale employed in this study appears to be weak, which suggests that the above claim would not be valid for shale with stronger anisotropy. Such stronger anisotropy effects will be evaluated in FY24.
- As described in Sections 3, 4, and 5, LBNL's scientists have been participating in three DECOVALEX-2023 tasks that include coupled processes model validation against experiments and necessary model developments. These tasks are:
    - Task A on thermal and gas fracturing at MHM URL in France,
    - Task B related to gas migration in clay, and
    - Task C related to THM response around the Mont Terri FE Experiment.

The 6th and 7th Workshops of DECOVALEX-2023 have been held in FY23, and included a comparison and discussion of modeling results obtained by international modeling teams. In FY23, much of the work have been focused on modeling with comparison to actual field experimental data obtained from the field experiments at Mont Terri and MHM URLs on Argillite, and from the LASGIT at the Äspö Hard Rock Laboratory. The DECOVALEX-2023 and will end and documented in journal publications and plans for DECOVALEX-2027.

- As presented in Section 6, LBNL continued a task directed toward developing a ML model to predict the HM behavior of a fault in response to high-pressure fluid injection. We utilized data from the Mont Terri Fault Slip FS-B experiment. In FY23, we have built on the preliminary ML framework that was first introduced in FY22 and have developed a model being capable of modeling pore pressure and displacements in response to fluid injection. The main achievements can be summarized as:
- We refined an LSTM framework that can model pore pressure and normal displacement in response to fluid injection in the fault.
- We developed a recipe for training that is necessary to ensure that the model can generate injection-induced fault response accurately.

For FY24, we plan to expand the scope of the current modeling efforts which can be summarized as follows:

- Assess the ability of our modeling framework to predict the HM response when the fault is more dilative, and
- Explore the development of a framework that can predict fault response away from the injection borehole.
- LBNL has launched a new task on the use of ML for automatically recognizing multiscale geologic features (such as fractures, faults, rock textures and damage zones) scanned from a borehole, using data from Mont Terri URL. We used a U-net model to recognize discrete thin fractures and used a Mask R-CNN model to recognize clustered features such as damage zones. We obtained average dice scores of 81.4% and 77.7% for U-Net and Mask R-CNN respectively. This work was a result of an LBNL Ingenuity internship project. The project also involves an international collaboration between Swisstopo and LBNL. Swisstopo provided a large number of raw images from Mont Terri, which lays the basis for this ML study. In FY24, we will extend this work in the following directions:
    - Use the results of U-Net prediction to calculate the permeability changes of each fracture within a fracture network over time, and
    - Extend this work to predict the dynamic changes (location, trace length, aperture) of multiscale features over time and track the movement of such features to infer the slip of visible and hidden faults.
- LBNL scientists in collaboration with international scientists have achieved substantial progress in the study of short- to long-term HM response in argillite host rock through new field studies at Mont Terri and Bure URLs. The work at Mont Terri fault activation experiments have led to new in-sights into the mechanisms for the creation of fast flow paths, followed by the longer-term sealing, involving stress relaxation, creep and swelling. The geometric and rheological role of fault asperities are being investigated with detailed modeling. At Bure, new experiments have been conducted on the effects of thermal pressurization in intact shale, with *in-situ* HM testing flowing a TH fracturing experiment. In FY24, we expect to continue HM modeling of fault asperities and conduct a fault heating experiment in which thermal pressurization could activate the fault.
- LBNL has in FY23 continued work on concrete-clay interfaces involving modeling the Cement–Opalinus Clay Interaction (CI-D) experiment at the Mont Terri URL, with the focus on understanding the reaction-induced porosity, permeability, and diffusivity changes in both the cement and the OPA as a result of their interaction. In FY23, a 3D model has been developed and applied to simulating tracer transport out to 450 days and results were compared favorably with the 2D-axisymmetric model. We are also going to develop a more comprehensive reaction network in taking into account cement and cement-clay interactions, and will compare these results to the data obtained from overcoring of the cement-claystone interface, which expected to be completed in early 2024.

LBNL’s plans for future work in FY24 as described above are aligned with priorities defined in the SFWST Disposal Research R&D 5-Year Plan (Sassani et al., 2021), including engagements in international activities (e.g., DECOVALEX-2023 and Mont Terri), integration of experimental and modeling activities of barrier material (engineered/natural) interactions at elevated temperatures for generic disposal concepts in argillite, and use of novel approaches to evaluate barrier material dynamic behavior and stability under repository conditions.

11. Acknowledgements

This work was supported by the Spent Fuel and Waste Science and Technology Campaign, Office of Nuclear Energy, of the U.S. Department of Energy under Contract Number DE-AC02-05CH11231 with Lawrence Berkeley National Laboratory.

12 References

Ajo-Franklin, J. B., Thomas Daley, Belinda Butler-Veytia, John Peterson, Yuxin Wu, Bob Kelly, and Susan Hubbard. (2011). Multi-level continuous active source seismic monitoring (ML-CASSM): Mapping shallow hydrofracture evolution at a TCE contaminated site, SEG Expanded Abstracts 30, 727.

Alonso, E. E., Gens, A., & Josa, A. (1990). A constitutive model for partially saturated soils. Géotechnique, 40(3), 405–430. https://doi.org/10.1680/geot.1991.41.2.273

Angelier, J. (1979). Determination of the mean principal directions of stresses for a given fault population. Tectonophysics, Volume 56, Issues 3-4, T17-T26.

Apted, M., and Ahn, J. (2010). Geological Repository Systems for Safe Disposal of Spent Nuclear Fuels and Radioactive Waste (1st Ed.). Woodhead Publishing. https://www.elsevier.com/books/geological-repository-systems-for-safe-disposal-of-spent-nuclear-fuels-and-radioactive-waste/apted/978-1-84569-542-2

Asahina, D., Houseworth, J.E., Birkholzer, J.T., Rutqvist, J., and Bolander, J.E. (2014) Hydro-mechanical model for wetting/drying and fracture development in geomaterials, Computers & Geosciences, 65, 13–23.

Ashman, I. and Faulkner, D. (2022). Temperature affects the frictional stability of experimental claybearing fault gouges. EGU22-8011, https://doi.org/10.5194/egusphere-egu22-8011. EGU General Assembly 2022.

Axen GJ. Pore pressure, stress increase, and fault weakening in low-angle normal faulting. J. Geophys. Res. 97, 8979–8991. 1992.

Babhulgaonkar, S., Hu, M., Luu, K., Derakhshandeh, Z., & Rutqvist, J. (2020). Machine learning of fracture morphology and growth in geological media: Preliminary study. In International Conference on Coupled Processes in Fractured Geological Media: Observation, Modeling, and Application (CouFrac), Seoul, Korea.

Bailey, R. W. (1935). The Utilization of Creep Test Data in Engineering Design. Proceedings of the Institution of Mechanical Engineers, 131(1), 131–349.

Balay, S., Abhyankar, S., Adams, M.F., Brown, S., Brown, J., Brune, P.,Buschelman, K., Constantinescu, E.M., Dalcin, L., Dener, A., V. Eijkhout, W.D. Gropp, V. Hapla, T. Isaac, P. Jolivet, D. Karpeev, D. Kaushik, M.G. Kneply, F. Hong, S. Kruger, D.A. May, L. Curman

McInnes, R.T. Mills, L. Mitchell, T. Munson, J.E. Roman, K. Rupp, P. Sana, J. Sarich, B.F. Smith,, S. Zampini, H. Zhang, J. Zhang. 2022, PETSc Web Page, https://petsc.org/

Bechthold, W., Rothfuchs, T., Poley, A., Ghoreychi, M., Heusermann, S., Gens, A., & Olivella, S. (1999). Backfilling and sealing of underground repositories for radioactive waste in salt (BAMBUS Project). https://op.europa.eu/en/publication-detail/-/publication/49ae90df-e3a6-4bd5-b55e-e505a9a15753.

Belytschko, Ted, and Tom Black. 1999. "Elastic Crack Growth in Finite Elements with Minimal Remeshing." International Journal for Numerical Methods in Engineering 45(5):601–20.

Bengio, Y., P. Simard, and Frasconi, P. (1994), Learning long-term dependencies with gradient descent is difficult, IEEE Trans. Neural Netw., 5, no. 2, 157–166.

Benge, M., Lu, Y., Katende, A., Rutqvist, J., Crandall, D., Haecker, A., King, G., Joseph, B., Radonjic, M., Bunger, A., Berkeley, L., Energy, N., Resources, C., & Engineering, G. E. K. (2021). Connecting Geomechanical Properties with Potential for Proppant Embedment and Production Decline for the Emerging Caney Shale , Oklahoma. Unconventional Resources Technology Conference. https://doi.org/10.15530/urtec-2021-1234.

Binder. G., Titov, A., Tamayo, D., Simmons, J., Tura, A., Byerley, G., Monk, G. Time delays from stress-induced velocity changes around fractures in a time-lapse DAS VSP. 88th Annual International Meeting, SEG, Expanded Abstracts, 5328–5332.

Blanco-Martín, L., Rutqvist, J., Battistelli, A., & Birkholzer, J. T. (2018). Coupled Processes Modeling in Rock Salt and Crushed Salt Including Halite Solubility Constraints: Application to Disposal of Heat-Generating Nuclear Waste. Transport in Porous Media, 124(1), 159–182.

Blanco-Martín, L., Rutqvist, J., & Birkholzer, J. T. (2015). Long-term modeling of the thermal-hydraulic-mechanical response of a generic salt repository for heat-generating nuclear waste. Engineering Geology, 193, 198–211.

Blanco-Martín, L., Wolters, R., Rutqvist, J., Lux, K. H., & Birkholzer, J. T. (2015). Comparison of two simulators to investigate thermal-hydraulic-mechanical processes related to nuclear waste isolation in saliferous formations. Computers and Geotechnics, 66, 219–229.

Blaschke, T., Burnett, C., & Pekkarinen, A. (2004). Image segmentation methods for object-based analysis and classification. Remote sensing image analysis: Including the spatial domain, 211-236.

Bossart, P., Meier, P. M., Moeri, A., Trick, T., & Mayor, J. C. (2002). Geological and hydraulic characterisation of the excavation disturbed zone in the Opalinus Clay of the Mont Terri Rock Laboratory. Engineering Geology, 66(1–2), 19–38.

Bott, M.H.P., 1959. The mechanics of oblique slip faulting. Geol. Mag. 96, 109–117.

Braun, P. (2019) Thermo-hydro-mechanical behavior of the Callovo-Oxfordian claystone: Effects of stress paths and temperature changes. Thesis, Université Paris-Est, 2019.

Cappa, F., Guglielmi, Y., Nussbaum, C., De Barros, L. and J. Birkholzer (2022). Fluid migration in low-permeability faults driven by decoupling of fault slip and opening. Nat. Geosci. 15, 747–751 (2022).

Cappa, F., Guglielmi, Y., Nussbaum, C., Birkholzer, J. On the Relationship between Fault Permeability Increases, Induced Stress Perturbation, and the Growth of Aseismic Slip During Fluid Injection. Geophysical research letters, Volume45, Issue20, 28 October 2018, Pages 11,012-11,020.

Cappa, F., Scuderi, M.M., Collettini, C., Guglielmi, Y., Avouac, J.P. Stabilization of fault slip by fluid injection in the laboratory and in situ. Science Advances, 13 Mar. 2019, EAAU4065.

Chen, T., Lapusta, N., 2009. Scaling of small repeating earthquakes explained by interaction of seismic and aseismic slip in a rate and state fault model. J. Geophys. Res. Solid Earth 114. https://doi.org/10.1029/2008JB005749

Conil, N., Vitel, M., Plua, C., Vu, M. N., Seyedi, D., and Armand, G. (2020). In Situ Investigation of the THM Behavior of the Callovo-Oxfordian Claystone. Rock Mechanics and Rock Engineering, 53(6), 2747–2769.

Corey, A.T. (1954). The Interrelation Between Gas and Oil Relative Permeabilities, Producers Monthly, 38-41.

Cundall, P.A., and Strack. O. 1979. “A Discrete Numerical Model for Granular Assemblies.” Geotechnique 29(1):47–65.

Daley, T.M., Ajo-Franklin, J.B., and Doughty, C. (2011) Constraining the reservoir model of an injected CO2 plume with crosswell CASSM at the Frio-II brine pilot. Int J Greenhouse Gas Control. 2011; 5:1022–1030.

Das, I., and Zoback, M.D., 2013. Long-period, long-duration seismic events during hydraulic stimulation of shale and tight-gas reservoirs—Part 1: Waveform characteristics LPLD events: Waveform characteristics. Geophysics 78, KS107–KS118.

Davi, R., O’Brien, G.S., De Barros, L., Lokmer, I., Bean, C.J., Lesage, P., Mora, M.M., and Soto, G.J., 2012. Seismic source mechanisms of tremor recorded on Arenal volcano, Costa Rica, retrieved by waveform inversion. J. Volcanol. Geotherm. Res. 213–214, 1–13.

De Barros, L., Guglielmi, Y., Rivet, D., Cappa, F., and Duboeuf, L., 2018. Seismicity and fault aseismic deformation caused by fluid injection in decametric in-situ experiments. Comptes Rendus Geosci. 350, 464–475.

De Barros, L., Daniel, G., Guglielmi, Y., Rivet, D., Caron, H., Payre, X., Bergery, G., Henry, P., Castilla, R., and Dick, P., 2016. Fault structure, stress, or pressure control of the seismicity in shale? Insights from a controlled experiment of fluid-induced fault reactivation. J. Geophys. Res. Solid Earth 121, 4506–4522.

Degiacomi, A., Nicollier, T., Maeder, P., Schefer, S., Steffen, T., Theurillat, T., and Ziegler M. (2022). FS-E Experiment: Installation of fibre optic sensors in borehole BPF-7. Installation report. Mont Terri Technical Note TN2023-03. 18 pp.

De La Vaissiere, R., Armand, G., and Talandier J. (2015). Gas and water flow in an excavation-induced fracture network around an underground drift: A case study for radioactive waster repository in clay rock. Journal of Hydrology 521, 141-156.

Dieterich, J. H. (1979) Modeling of rock friction experimental results and constitutive equations, J. Geophys. Res., 84, 2161–2168.

Donzé, F., and Magnier S.A. 1995. Formulation of a 3-D Numerical Model of Brittle Behaviour. Geophysical Journal International 122(3):790–802.

Duriez, J., Scholtès, L., and Donzé F.J. (2016). Micromechanics of Wing Crack Propagation for Different Flaw Properties. Engineering Fracture Mechanics 153:378–98.

Dwivedi, D., U. Mital, B. Faybishenko, B. Dafflon, C. Varadharajan, D. Agarwal, K. H. Williams, C. Steefel, and S. Hubbard, (2022). Imputation of Contiguous Gaps and Extremes of Subhourly Groundwater Time Series Using Random Forests, J Mach Learn Model Comput, 3, no. 22, 1–22.

Eaton, D., van der Baan, M., Tary, J.-B., Birkelo, B., Spriggs, N., Cutten, S., and Pike, K. (2013). Broadband microseismic observations from a Montney hydraulic fracture treatment, northeastern BC, Canada. CSEG Rec. 1150, 1250.

Eyinla, D.S., Oladunjoye, M.A. (2021). Controls of fault geometry and thermal stress on fault slip modes: Implications for permeability enhancement and injection-induced seismicity, Petroleum Research, Volume 6, Issue 4, Pages 392-407, ISSN 2096-2495.

Eyre, T.S., Eaton, D.W., Garagash, D.I., Zecevic, M., Venieri, M., Weir, R., Lawton, D.C., (2019). The role of aseismic slip in hydraulic fracturing–induced seismicity. Sci. Adv. 5, eaav7172.

Faulkner, D.R., Rutter, EH. (2001). Can the maintenance of overpressured fluids in large strike-slip fault zones explain their apparent weakness? Geology, 29, 503–506.

Fu, Y., Bai, L., Zhao, S., Zhang, X., Jin, Y., and Cheng, Y. (2018) Simulation of reactive mixing behaviors inside micro-droplets by a lattice Boltzmann method. Chemical Engineering Science, 181, 79-89.

Garagash, D.I., and Germanovich, L.N. Nucleation and arrest of dynamic slip on a pressurized fault, J. Geophys. Res., 117, B10310. 2012.

Gens, A., and Alonso, E. E. (1992). A framework for the behaviour of unsaturated expansive clays. Canadian Geotechnical Journal, 29(6), 1013–1032.

Goodfellow, I., Y. Bengio, and A. Courville, 2016, Deep Learning, MIT Press.

Guglielmi, Y. et al., (2021). Imaging leakage associated to a caprock fault activation: results from the fault slip experiment in Mt-Terri Opalinus Clay analogue caprock (Switzerland), in CCP4 2021 Annual Report.

Guglielmi, Y., Christophe Nussbaum, Frédéric Cappa, Louis De Barros, Jonny Rutqvist, Jens Birkholzer (2021). Field-scale fault reactivation experiments by fluid injection highlight aseismic leakage in caprock analogs: Implications for CO2 sequestration, International Journal of Greenhouse Gas Control, Volume 111, 103471,ISSN 1750-5836.

Guglielmi, Y., Birkholzer, J., Rutqvist, J., Jeanne, P., and Nussbaum, C. (2017) Can Fault Leakage Occur Before or Without Reactivation? Results from an in Situ Fault Reactivation Experiment at Mont Terri. Energy Procedia, 114, 3167–3174.

Guglielmi, Y., Cappa, F., Avouac, J.-P., Henry, P., and Elsworth, D. (2015a) Seismicity triggered by fluid injections induced aseismic slip. Science, 348(6240), 1224–1226.

Guglielmi, Y., Elsworth, D., Cappa, F., Henry, P., Gout, C., Dick, P., and Durand, J. (2015b) In situ observations on the coupling between hydraulic diffusivity and displacements during fault reactivation in shales. J. Geophys. Res., 120, 7729–7748.

Guglielmi, Y., F. Cappa, H. Lançon, J. B. Janowczyk, J. Rutqvist, C. F. Tsang, and J. S. Y. Wang, 2014, ISRM Suggested Method for Step-Rate Injection Method for Fracture In-Situ Properties (SIMFIP): Using a 3-Components Borehole Deformation Sensor, Rock Mech Rock Eng, 47, no. 1, 303–311.

Guglielmi, Y., Cappa, F., Lancon, H., Janowczyk, J. B., Rutqvist, J., Tsang, C.F., and Wang, J.S.Y. (2013) ISRM Suggested Method for Step-Rate Injection Method for Fracture In-Situ Properties (SIMFIP): Using a 3-Components Borehole Deformation Sensor. In the ISRM suggested methods for rock characterization testing and monitoring: 2007-2014 (pp. 179–186). Springer International Publishing.

Guglielmi, Y., Nussbaum, C., Jeanne, P., Rutqvist, J., Cappa, F., Birkholzer, J. Complexity of fault rupture and fluid leakage in shale: Insights from a controlled fault activation experiment. Journal of Geophysical Research: Solid Earth, 125, e2019JB017781. 2020a.

Guglielmi, Y., Nussbaum, C., Jeanne, P., Rutqvist, J., Cappa, F., and Birkholzer, J. (2020a) Complexity of fault rupture and fluid leakage in shale: Insights from a controlled fault activation experiment. Journal of Geophysical Research: Solid Earth, 125, e2019JB017781.

Guglielmi, Y., Nussbaum C., Rutqvist, J., Cappa F., Jeanne, P., and Birkholzer, J. (2020b) Estimating perturbed stress from 3-D borehole displacements induced by fluid injection in fractured or faulted shales, Geophys. J. Int., 221, 1684-1695.

Guglielmi, Y., J.Birkholzer, J.Ruqvist, P.Jeanne, C.Nussbaum, 2016, Can fault leakage occur before or without reactivation? Results from an in situ fault reactivation experiment at Mt Terri, Greenhouse Ga Control Technologies 13th International Conference (Lausanne, Switzerland, Nov. 14-18 2016).

Guglielmi, Y., C., Nussbaum, F., Cappa, L., De Barros, J., Rutqvist, J., Birkholzer (2021). Field-scale fault reactivation experiments by fluid injection highlight aseismic leakage in caprock analogs: Implications for CO2 sequestration. International Journal of Greenhouse Gas Control, Volume 111, 2021, 103471, ISSN 1750-5836.

Guglielmi, Y., Nussbaum, C., Jeanne, P., Rutqvist, J., Cappa, F., & Birkholzer, J. (2020). Complexity of fault rupture andfluidleakageinshale:Insightsfrom a controlled fault activation experiment. Journal of Geophysical Research: Solid Earth, 125, e2019JB017781.

Guglielmi, Y., Cappa, F., Lançon, H., Janowczyk, J.B., Rutqvist, J., Tsang, C.F., Wang, J.S.Y., 2014. ISRM Suggested Method for Step-Rate Injection Method for Fracture In-Situ Properties (SIMFIP): Using a 3-Components Borehole Deformation Sensor. Rock Mech. Rock Eng. 47, 303–311.

Hagin, P. N., & Zoback, M. D. (2010). Inverting for creep strain parameters of uncemented reservoir sands using arbitrary stress-strain data. 44th US Rock Mechanics Symposium - 5th US/Canada Rock Mechanics Symposium. https://onepetro.org/ARMAUSRMS/proceedings-abstract/ARMA10/All-ARMA10/ARMA-10-171/119372.

Haimson, B.C. and F.H.Cornet (2003). ISRM Suggested Method for rock stress estimation – Part 3: hydraulic fracturing (HF) and/or hydraulic testing of pre-existing fractures (HTPF). International Journal of Rock Mechanics & Mining Sciences 40, 1011-1020.

Harrington, J. (2016) Specification for DECOVALEX-2019: Task A: modElliNg Gas INjection ExpERiments (ENGINEER). Ref: BGS-DX-v3.

Harrington, J.F., and Horseman, S.T. (1999) Gas transport properties of clays and mudrocks. In: Muds And Mudstones: Physical And Fluid Flow Properties (eds A.C.Aplin, A.J. Fleet, and J.H.S. Macquaker). Geological Society of London, Special Publication No. 158, 107-124.

Hazzard, James F., R. Paul Young, and S. C. Maxwell. 2000. “Micromechanical Modeling of Cracking and Failure in Brittle Rocks.” Journal of Geophysical Research: Solid Earth 105(B7):16683–97.

Hu, L. W. (1956). Studies on Plastic Flow of Anisotropic Metals. Journal of Applied Mechanics, 23(3), 444–450.

He, K., Gkioxari, G., Dollár, P., Girshick, R. (2017). Mask R-CNN. 2017 IEEE International Conference on Computer Vision (ICCV), 2980-2988. https://dxoi.org/10.1109/ICCV.2017.322

Herrmann, J., Rybacki, E., Sone, H., & Dresen, G. (2020). Deformation Experiments on Bowland and Posidonia Shale—Part II: Creep Behavior at In Situ p c–T Conditions. Rock Mechanics and Rock Engineering, 53(2), 755–779.

Hochreiter, S., and J. Schmidhuber, 1997, Long Short-Term Memory, Neural Computation, 9, no. 8, 1735–1780.

Horseman, S.T., Harrington, J.F., and Sellin, P. (1999) Gas migration in clay barriers. Engineering Geology, Vol. 54, 139-149.

Horseman, S.T., Harrington, J.F., and Sellin, P. (2004) Water and gas flow in Mx80 bentonite buffer clay. In: Symposium on the Scientific Basis for Nuclear Waste Management XXVII (Kalmar), Materials Research Society, Vol. 807. 715-720.

Hu, H., Li, A., Zavala-Torres, R., 2017. Long-period long-duration seismic events during hydraulic fracturing: Implications for tensile fracture development. Geophys. Res. Lett. 44, 4814–4819.

Hu, M., and Rutqvist, J. (2020a) Numerical manifold method modeling of coupled processes in fractured geological media at multiple scales. Journal of Rock Mechanics and Geotechnical Engineering 12(4): 66681.

Hu, M. and Rutqvist, J. (2020b). "Microscale Mechanical Modeling of Deformable Geomaterials with Dynamic Contacts Based on the Numerical Manifold Method." Computational Geosciences 24(5):1783–97.

Hu, M., J. Rutqvist, and C. I. Steefel, 2021, Mesh generation and optimization from digital rock fractures based on neural style transfer, Journal of Rock Mechanics and Geotechnical Engineering, 13, no. 4, 912–919.

IAEA. (2003). Scientific and Technical Basis for the Geological Disposal of Radioactive Wastes. https://www.iaea.org/publications/6568/scientific-and-technical-basis-for-the-geological-disposal-of-radioactive-wastes

Itasca Consulting Group. (2020). FLAC3D — Fast Lagrangian Analysis of Continua in Three-Dimensions, Ver. 7.0. https://www.itascacg.com/software/FLAC3D.

Jaeggi, D., Laurich, B., Nussbaum, C., Schuster, K., Connolly, P. Tectonic structure of the ''Main Fault'' in the Opalinus Clay, Mont Terri rock laboratory (Switzerland). Swiss J Geosci. 2017.

Jeanne, P., Guglielmi, Y., Rutqvist, J., Nussbaum, C., Birkholzer, J. Permeability variations associated with fault reactivation in a claystone formation investigated by field experiments and numerical simulations. Journal of Geophysical Research: Solid Earth, 123, 1694–1710. 2018.

Jeanne, P., Y. Guglielmi, J. Rutqvist, C. Nussbaum & J. Birkholzer (2017). Field characterization of elastic properties across a fault zone reactivated by fluid injection, J. Geophys. Res. Solid Earth, 122, 6583–6598.

Johnson, A. M., and R. C. Fletcher (1994), Folding of Viscous Layers: Mechanical Analysis and Interpretation of Structures in Deformed Rock, Columbia Univ. Press, New York.

Julian, B.R., 1994. Volcanic tremor: Nonlinear excitation by fluid flow. J. Geophys. Res. Solid Earth 99, 11859–11877.

Kingma, D. P., Ba, J. (2014). Adam: A Method for Stochastic Optimization. Proceedings of the 3rd International Conference on Learning Representations (ICLR), https://doi.org/10.48550/arXiv.1412.6980

Kumar, A., Zorn, E., Hammack, R., Harbert, W., 2017. Long-period, long-duration seismicity observed during hydraulic fracturing of the Marcellus Shale in Greene County, Pennsylvania. Lead. Edge 36, 580–587.

Jung, Y., Shu Heng Pau, G., Finsterle, S., & Doughty, C. (2018). TOUGH3 User's Guide. https://tough.lbl.gov/assets/files/Tough3/TOUGH3_Users_Guide_v2.pdf,

Kakurina, M., Guglielmi, Y., Nussbaum, C., & Valley, B. (2019). Slip perturbation during fault reactivation by a fluid injection. Tectonophysics, 757, 140–152.

Kakurina, M., Guglielmi, Y., Nussbaum, C., & Valley, B. (2020). In situ direct displacement information fault reactivation during fluid injection. Rock Mechanics and Rock Engineering, 53, 4313–4328.

Katende, A., Rutqvist, J., Benge, M., Seyedolali, A., Bunger, A., Puckette, J. O., Rhing, A., & Radonjic, M. (2021). Convergence of micro-geochemistry and micro-geomechanics towards understanding proppant shale rock interaction: a Caney shale case study in southern Oklahoma, USA. Journal of Natural Gas Science and Engineering, 96.

Kratzert, F., D. Klotz, C. Brenner, K. Schulz, and M. Herrnegger, 2018, Rainfall–runoff modelling using Long Short-Term Memory (LSTM) networks, Hydrol. Earth Syst. Sci., 22, no. 11, 6005–6022.

Kim, Y. S., D. C. P. Peacock, and D. J. Sanderson (2004), Fault damage zones, J. Struct. Geol., 26, 503 – 517.

Kim, K., Rutqvist J. and Birkholzer J. (2020) Lattice modeling of excavation damage in argillaceous clay formations: Influence of deformation and strength anisotropy. Tunneling and Underground Space Technology, 98, 2020.

Kim, K., Rutqvist, J., Harrington, J.F., Tamayo-Mas, E., and Birkholzer, J.T. (2021) Discrete dilatant pathway modeling of gas migration through compacted bentonite clay. International Journal of Rock Mechanics and Mining Sciences. 137, 104569 (2021).

Kim, K., Rutqvist, J., Nakagawa, S., and Birkholzer, J. (2017) TOUGH-RBSN simulator for hydraulic fracture propagation within fractured media: Model validations against laboratory experiments, Computers & Geosciences, 108, 72–85.

Kingma, D. P., and J. Ba, 2017, Adam: A Method for Stochastic Optimization, arXiv:1412.6980 [cs].

Kratzert, F., D. Klotz, C. Brenner, K. Schulz, and M. Herrnegger, 2018, Rainfall–runoff modelling using Long Short-Term Memory (LSTM) networks, Hydrol. Earth Syst. Sci., 22, no. 11, 6005–6022.

Kumar, A., Zorn, E., Hammack, R., Harbert, W., 2017. Long-period, long-duration seismicity observed during hydraulic fracturing of the Marcellus Shale in Greene County, Pennsylvania. Lead. Edge 36, 580–587.

Lemaître, J. (1970). Sur la détermination des lois de comportement des matériaux élasto-visco-plastiques. In Office national d'études et de recherches aérospatiales (Vol. 135). https://books.google.com/books/about/Sur_la_détermination_des_lois_de_compor.html?id=iFq0nAEACAAJ.

Li, C., Wang, J., & Xie, H. (2020). Anisotropic creep characteristics and mechanism of shale under elevated deviatoric stress. Journal of Petroleum Science and Engineering, 185(December 2018), 106670.

Lin, T. Y., Maire, M., Belongie, S., Hays, J., Perona, P., Ramanan, D., ... & Zitnick, C. L. (2014). Microsoft coco: Common objects in context. In Computer Vision–ECCV 2014: 13th European Conference, Zurich, Switzerland, September 6-12, 2014, Proceedings, Part V 13 (pp. 740-755). Springer International Publishing.

Lay, T., H. Kanamori, and L. Ruff (1982), The asperity model and the nature of large subduction zone earthquakes, Earthquake Prediction Res., 1, 3 – 71.

Lee, Heekwang, and Seokwon Jeon. 2011. "An Experimental and Numerical Study of Fracture Coalescence in Pre-Cracked Specimens under Uniaxial Compression." International Journal of Solids and Structures 48(6):979–99.

Li, Y., & Ghassemi, A. (2012). Creep behavior of Barnett, Haynesville, and Marcellus shale. 46th US Rock Mechanics / Geomechanics Symposium, 641–647. https://onepetro.org/ARMAUSRMS/proceedings-abstract/ARMA12/All-ARMA12/ARMA-2012-330/120741.

Li, C., Li, Z., Peng, Z., Zhang, C., Nakata, N., Sickbert, T., 2018. Long-Period Long-Duration Events Detected by the IRIS Community Wavefield Demonstration Experiment in Oklahoma: Tremor or Train Signals? Seismol. Res. Lett. 89, 1652–1659.

Lengliné, O., Boubacar, M., Schmittbuhl, J., 2017. Seismicity related to the hydraulic stimulation of GRT1, Rittershoffen, France. Geophys. J. Int. 208, 1704–1715.

Liang, Z., Chen, Z., & Rahman, S. S. (2020). Experimental investigation of the primary and secondary creep behaviour of shale gas reservoir rocks from deep sections of the Cooper Basin. Journal of Natural Gas Science and Engineering, 73(September 2019), 103044.

Martin, C.D., Lanyon, G.W. (2003). Measurement of in-situ stress in weak rocks at Mont Terri Rock Laboratory, Switzerland. International Journal of Rock Mechanics and Mining Sciences. Volume 40, Issues 7–8, October–December 2003, Pages 1077-1088.

Marchesini, P., J.B. Ajo-Franklin, T.M. Daley. In-Situ Measurement Of Velocity-Stress Sensitivity Using Crosswell Continuous Active-Source Seismic Monitoring (CASSM), Geophysics 82 (5), 1-27. 2017.

Menzel, W., & Schreiner, W. (1977). Zum geomechanischen Verhalten von Steinsalz verschiedener Lagerstätten der DDR. Teil II: Das Verformungsverhalten. Neue Bergbautechnik, 7(8), 565–574. https://scholar.google.com/scholar_lookup?title=Zum geomechanischen Verhalten von Steinsalz verschiedener Lagerstätten der DDR. Teil II%3A Das Verformungsverhalten&journal=Neue Bergbautechnik&volume=7&pages=565-574&publication_year=1977&author=Menzel%2CW.

Mital, U., and J. E. Andrade, 2022, Bridging length scales in granular materials using convolutional neural networks, Comp. Part. Mech., 9, 221–235.

Mital, U., D. Dwivedi, J. B. Brown, B. Faybishenko, S. L. Painter, and C. I. Steefel, 2020, Sequential Imputation of Missing Spatio-Temporal Precipitation Data Using Random Forests, Front. Water, 2, 20.

Moës, Nicolas, John Dolbow, and Ted Belytschko. 1999. “A Finite Element Method for Crack Growth without Remeshing.” International Journal for Numerical Methods in Engineering 46(1):131–50.

Murakami, S., & Yamada, Y. (1974). Effects of hydrostatic pressure and material anisotropy on the transient creep of thick-walled tubes. Int. J. Mech. Sci., 16, 145–160.

Nedyalkova, L., Tits, J., Bernard, E., Wieland, E., & Mäder, U. (2021). Sorption Experiments with HTO, 36-Cl, 125-I and 14-C Labeled Formate on Aged Cement Matrices Retrieved from Long-term In-situ Rock Laboratory Experiments. Journal of Advanced Concrete Technology, 19(7), 811–829.

Neuzil, C. (1082). On conducting the modified “slug” test in tight formations. Water Resources Research 18(2):439-441.

Nielsen, Michael A. 2015. Neural Networks and Deep Learning. Vol. 25. Determination press USA.

Niu, F., Silver, P.G., Daley, T.M., Cheng, X., Majer, E.L. Preseismic velocity changes observed from active source monitoring at the Parkfield SAFOD drill site, Nature, 454, 204-208. 2008.

Nopola, J. R., & Roberts, L. A. (2016). Time-dependent deformation of Pierre Shale as determined by long-duration creep tests. 50th US Rock Mechanics / Geomechanics Symposium, 584–591. https://onepetro.org/ARMAUSRMS/proceedings-abstract/ARMA16/All-ARMA16/ARMA-2016-508/126299.

Norton, F. H. (1929). Creep of Steel at High Temperatures. McGraw-Hill. https://archive.org/details/creepofsteelathi00nort/page/66/mode/2up?ref=ol&view=theater

Nussbaum, C., Bossart, P., Amann, F., Aubourg, C., 2011. Analysis of tectonic structures and excavation induced fractures in the Opalinus Clay, Mont Terri underground rock laboratory (Switzerland). Swiss J. Geosci. 104, 187–210.

Nutt, M. (2012) Used Fuel Disposition Campaign Disposal Research and Development Roadmap (FCRD-USED-2011-000065 REV1), U.S. DOE Used Fuel Disposition Campaign.

Orellana, L.F., Scuderi, M.M., Collettini, C., Violay, M., 2018. Do scaly clays control seismicity on faulted shale rocks? Earth Planet. Sci. Lett. 488, 59–67. https://doi.org/10.1016/j.epsl.2018.01.027

Rutledge, J.T., Phillips, W.S., Mayerhofer, M.J., 2004. Faulting induced by forced fluid injection and fluid flow forced by faulting: An interpretation of hydraulic-fracture microseismicity, Carthage Cotton Valley gas field, Texas. Bull. Seismol. Soc. Am. 94, 1817–1830.

Rumelhart, D. E., G. E. Hinton, and R. J. Williams, 1986, Learning representations by back-propagating errors, Nature, 323, no. 6088, 533–536.

Thoeny, R. (2022). FLAC3D Modelling - Hydro-mechanical modelling of multi-scale rock mass behavior and pore pressure evolution around underground excavations of the Mont Terri Rock Laboratory. Internal note from NAGRA (Switzerland).

Park, J.W., Guglielmi, Y., Graupner, B., Rutqvist, J., Taehyum, K., Park, E.-S., Changsoo, L. Modeling of fluid injection-induced fault reactivation using coupled fluid flow and mechanical interface model. International Journal of Rock Mechanics and Mining Sciences. 132. 104373. 10.1016/j.ijrmms.2020.104373. 2020.

Pedregosa, Fabian, Gaël Varoquaux, Alexandre Gramfort, Vincent Michel, Bertrand Thirion, Olivier Grisel, Mathieu Blondel, Peter Prettenhofer, Ron Weiss, Vincent Dubourg, Jake Vanderplas, Alexandre Passos, David Cournapeau, Matthieu Brucher, Matthieu Perrot, and Édouard Duchesnay. 2012. "Scikit-Learn: Machine Learning in Python." Journal of Machine Learning Research 12:2825–30.

Perera, Roberto, Davide Guzzetti, and Vinamra Agrawal. 2021. "Graph Neural Networks for Simulating Crack Coalescence and Propagation in Brittle Materials." ArXiv:2107.05142 [Cond-Mat].

Pyrak-Nolte, L. J., Myer, L. R. and N.G.W. Cook. Journal of Geophysical Research, volume: 95 issue: (B6), pages: 8617-8638. 1990.

Rabbani, A., Babaei, M., Shams, R., Da Wang, Y., & Chung, T. (2020). DeePore: A deep learning workflow for rapid and comprehensive characterization of porous materials. Advances in Water Resources, 146, 103787.

Renard, P. (2017). Hytool: an open source matlab toolbox for the interpretation of hydraulic tests using analytical solutions. The Journal of Open Source Software 2 (19);441.

Rice, JR. Fault stress states, pore pressure distributions, and the weakness of the San Andreas fault. In Fault mechanics and transport properties in rocks (eds B Evans, T-F Wong), pp. 475–503. London, UK: Academic Press. 144, 39-58. 1992.

Rinaldi A.P., Rutqvist J., Luu K., Blanco-Martín L., Hu M., Sentís M.L., Eberle L., and Kaestli P. TOUGH3-FLAC3D: a modeling approach for parallel computing of fluid flow and geomechanics. Computational Geosciences. 26, 1563–1580 (2022). https://doi.org/10.1007/s10596-022-10176-0.

Antonio P. Rinaldi, Luca Urpi, Dimitrios Karvounis (2016), Effects of asperity distribution on fluid flow and induced seismicity during deep geothermal exploitation. Energy Procedia 97, 470 – 477.

Ronneberger, O., Fischer, P., Brox, T. (2015). U-Net: Convolutional Networks for Biomedical Image Segmentation. International Conference on Medical Image Computing and Computer-Assisted Intervention, 234-241. https://doi.org/10.1007/ 978-3-319-24574-4_28

Rostami, Shahin, and Ferrante Neri. 2017. “A Fast Hypervolume Driven Selection Mechanism for Many-Objective Optimisation Problems.” Swarm and Evolutionary Computation 34:50–67.

Rutledge, J.T., Phillips, W.S., Mayerhofer, M.J., 2004. Faulting induced by forced fluid injection and fluid flow forced by faulting: An interpretation of hydraulic-fracture microseismicity, Carthage Cotton Valley gas field, Texas. Bull. Seismol. Soc. Am. 94, 1817–1830.

Rutqvist J. Coupled Thermo-Hydro-Mechanical Behavior of Natural and Engineered Clay Barriers. In Tournassat, Steefel, Bourg and Bergaya editors. Natural and Engineered Clay Barriers. Elsevier. pp. 329-255 (2015).

Rutqvist, J., Börgesson, L., Chijimatsu, M., Kobayashi, A., Nguyen, T. S., Jing, L., Noorishad, J., and Tsang, C.-F. (2001) Thermohydromechanics of partially saturated geological media – Governing equations and formulation of four finite element models. International Journal of Rock Mechanics and Mining Sciences, 38, 105-127.

Rutqvist, J., and Tsang, C.-F. (2002) A study of caprock hydromechanical changes associated with CO2-injection into a brine formation, Environmental Geology, 42, 296–305.`

Rutqvist, J., Ijiri, Y, and Yamamoto, H. (2011) Implementation of the Barcelona Basic Model into TOUGH-FLAC for simulations of the geomechanical behavior of unsaturated soils. Computers & Geosciences, 37, 751–762.

Rutqvist, J. (2011) Status of the TOUGH-FLAC simulator and recent applications related to coupled fluid flow and crustal deformations. Computers & Geosciences, 37, 739–750.

Rutqvist, Jonny, Zheng, L., Chen, F., Liu, H. H., & Birkholzer, J. (2014). Modeling of coupled thermo-hydro-mechanical processes with links to geochemistry associated with bentonite-backfilled repository tunnels in clay formations. Rock Mechanics and Rock Engineering, 47(1), 167–186. https://doi.org/10.1007/s00603-013-0375-x

Rutqvist, J. (2015). Coupled Thermo-Hydro-Mechanical Behavior of Natural and Engineered Clay Barriers. In C. Tournassat, C. Steefel, I. Bourg, & F. Bergaya (Eds.), Natural and Engineered Clay Barriers (pp. 329–355). Elsevier. https://www.elsevier.com/books/natural-and-engineered-clay-barriers/tournassat/978-0-08-100027-4.

Rutqvist, J., Kim, K., Xu, H., Guglielmi, Y., and Birkholzer, J. (2018) Investigation of Coupled Processes in Argillite Rock: FY18 Progress. Prepared for U.S. Department of Energy, Spent Fuel and Waste Disposition, SFWD-SFWST-2018-000XXX, LBNL-2001168, Lawrence Berkeley National Laboratory.

Rutqvist J., Guglielmi Y., Hu M., Sasaki T., Deng H., Li P., Steefel C., Tournassat C., Xu H., Babhulgaonkar S., Birkholzer J. Investigation of coupled processes in argillite rock: FY21 progress. Prepared for U.S. Department of Energy, Spent Fuel and Waste Disposition, LBNL-2001402, Lawrence Berkeley National Laboratory (2021).

Rutqvist J, Guglielmi Y, Xu H., Tian Y., Zarzycki P., Deng H., Li P, Hu M, Steefel C., Nico P, Borglin S, Fox P, Sasaki T., Birkholzer J. Investigation of coupled processes in argillite rock: FY20 progress. Prepared for U.S. Department of Energy, Spent Fuel and Waste Disposition, LBNL-2001324, Lawrence Berkeley National Laboratory (2020).

Rutqvist J, Guglielmi Y., Kim K., Xu H., Deng H., Li P., Hu M., Steefel C., Gilbert B., Rinaldi A., Nico P., Borglin S., Fox P., Birkholzer J. Investigation of coupled processes in argillite rock: FY19 progress. Prepared for U.S. Department of Energy, Spent Fuel and Waste Disposition, LBNL-2001202, Lawrence Berkeley National Laboratory (2019).

Rutqvist, J. (2017) An overview of TOUGH-based geomechanics models. Computers & Geosciences, 108, 56–63.

Rutqvist, J. (2020). Thermal management associated with geologic disposal of large spent nuclear fuel canisters in tunnels with thermally engineered backfill. Tunnelling and Underground Space Technology, 102(April), 103454.

Rutter, E.H. & Hackston, A. On the effective stress law for rock-on-rock frictional sliding, and fault slip triggered by means of fluid injection. *Philosophical Transactions of the Royal Society of London*, **375**, 10.1098/rsta.2016.0001 (2017).

Rivet D., De Barros L., Guglielmi Y., Cappa F., Castilla R. and Henry P. Seismicity velocity changes associated with aseismic deformations of a fault stimulated by fluid ibnjection. Geophys. Res. Lett., 43, 9563-9572. 2016.

Rybacki, E., Herrmann, J., Wirth, R., & Dresen, G. (2017). Creep of Posidonia Shale at Elevated Pressure and Temperature. Rock Mechanics and Rock Engineering, 50(12), 3121–3140.

Sagy, A., and E. E. Brodsky (2009), Geometric and rheological asperities in an exposed fault zone, J. Geophys. Res., 114, B02301.

Sasaki, T., & Rutqvist, J. (2021). Estimation of stress and stress-induced permeability change in a geological nuclear waste repository in a thermo-hydrologically coupled simulation. Computers and Geotechnics, 129 (October 2020), 103866.

Sasaki, T., & Rutqvist, J. (2022). Effects of time-dependent deformation of shale on the integrity of a geological nuclear waste repository. International Journal of Rock Mechanics and Mining Sciences, 158(December 2021), 105206.

Sassani, D., Birkholzer, J., Camphouse, R., Freeze, G. and Stein, E. (2021). SFWST Disposal Research R&D 5-Year Plan – FY2021 Update. Prepared for U.S. Department of Energy, Spent Fuel and Waste Disposition, Prepared for U.S. Department of Energy Spent Fuel and Waste Science and Technology (SFWST) Sandia National Laboratories, Albuquerque, New Mexico.

Saxena, N., Mavko, G., Zoback, M., Hofmann, R., & Braunsdorf, N. (2015). Joint estimation of acoustic properties, creep, and stress relaxation in organic-rich shales. SEG New Orleans Annual Meeting, 3053–3057.

Schwarzer, Max, Bryce Rogan, Yadong Ruan, Zhengming Song, Diana Y. Lee, Allon G. Percus, Viet T. Chau, Bryan A. Moore, Esteban Rougier, Hari S. Viswanathan, and Gowri Srinivasan. 2019. "Learning to Fail: Predicting Fracture Evolution in Brittle Material Models Using Recurrent Graph Convolutional Neural Networks." Computational Materials Science 162:322–32.

Scholtès, Luc, and Frédéric-Victor Donzé. 2013. "A DEM Model for Soft and Hard Rocks: Role of Grain Interlocking on Strength." Journal of the Mechanics and Physics of Solids 61(2):352–69.

Scuderi, M.M. et al. Frictional stability and earthquake triggering during fluid pressure stimulation of an experimental fault. *Earth Planet. Sci. Lett.* **477**, 10.1016/j.epsl.2017.08.009 (2017).

Scuderi, M.M., Collettini, C., 2018. Fluid Injection and the Mechanics of Frictional Stability of Shale-Bearing Faults. J. Geophys. Res. Solid Earth 123, 8364–8384.

Senger R., Romero, E., Ferrari, A., and Marschall, P. (2014) Characterization of gas flow through low-permeability claystone: laboratory experiments and two-phase flow analyses. Norris, S., Bruno, J., Cathelineau, M., Delage, P., Fairhurst, C., Gaucher, E. C., Ho¨hn, E. H., Kalinichev, A., Lalieux, P. & Sellin, P. (eds) Clays in Natural and Engineered Barriers for Radioactive Wast Confinement. Geological Society, London, Special Publications, 400, http://dx.doi.org/10.1144/SP400.15.

Senger, R., and Marschall, P. (2008) Task Force on EBS / Gas Transport in Buffer Material, Nagra Arbeitsbericht NAB 08-24.

Silver, P.G., Daley, T.M., Niu, F., Majer, E.L. Active source monitoring of crosswell seismic travel time for stress induced changes, Bulletin of Seismological Society of America, v97, n1B, p281-293. 2007

Simonyan, K., & Zisserman, A. (2014). Very deep convolutional networks for large-scale image recognition. arXiv preprint arXiv:1409.1556.

Smith, R. B. (1977), Formation of folds, boudinage, and mullions in non-Newtonian materials, Geol. Soc. Am. Bull., 88, 312– 320.

Sone, H., & Zoback, M. D. (2011). Visco-plastic properties of shale gas reservoir rocks. 45th US Rock Mechanics / Geomechanics Symposium. https://onepetro.org/ARMAUSRMS/proceedings-abstract/ARMA11/All-ARMA11/ARMA-11-417/120373

Sone, H., & Zoback, M. D. (2014). Time-dependent deformation of shale gas reservoir rocks and its long-term effect on the in situ state of stress. International Journal of Rock Mechanics and Mining Sciences, 69, 120–132.

Stanley, Kenneth O., and Risto Miikkulainen. 2002. "Evolving Neural Networks through Augmenting Topologies." Evolutionary Computation 10(2):99–127.

Steefel, C.I., Appelo, C.A.J., Arora, B., Jacques, D., Kalbacher, T., Kolditz, O., Lagneau, V., Lichtner, P.C., Mayer, K.U., Meeussen, J.C.L. and Molins, S., 2015. Reactive transport codes for subsurface environmental simulation. Computational Geosciences, 19(3), pp.445-478.

Steefel, C.I. and C. Tournassat (2021) A model for discrete fracture-clay rock interaction incorporating electrostatic effects on transport. Computational Geosciences 25 (1): 395-410.

Sutter, E. 2021. Progressive failure and deformation analysis of a large-diameter experiment borehole. B.Sc. thesis, Department of Earth Sciences, ETH Zurich, 40 pp.

Tamayo-Mas, E, Harrington, J.F., Brüning, T., Shao, H., Dagher, E.E., Lee, J., Kim, K., Rutqvist, J., Kolditz, O., Lai, S.H., Chittenden, N., Wang, Y., Damians, I. and Olivella, S. (2021) Modelling advective gas flow in compact bentonite: lessons learnt from different numerical approaches. International Journal of Rock Mechanics and Mining Sciences. 139, 104580.

Tary, J.-B., Van der Baan, M., Eaton, D.W., 2014. Interpretation of resonance frequencies recorded during hydraulic fracturing treatments. J. Geophys. Res. Solid Earth 119, 1295–1315

Thatcher K., and Graupner B. (2020). DECOVALEX 2023 Task C Specification: THM modelling of the FE experiment Quintessa. Document Id: QDS-1612F-TaskC-specification. Version: 1.

Thomas, H. R., Vardon, P. J., & Cleall, P. J. (2014). Three-dimensional behaviour of a prototype radioactive waste repository in fractured granitic rock. Canadian Geotechnical Journal, 51(4), 246–259.

Tournassat, C., & Steefel, C. I. (2015). Ionic transport in nano-porous clays with consideration of electrostatic effects. Reviews in Mineralogy and Geochemistry, 80(1), 287-329.

Tournassat, C., & Steefel, C. I. (2019). Reactive transport modeling of coupled processes in nanoporous media. Reviews in Mineralogy and Geochemistry, 85(1), 75-109.

Tournassat, C., & Steefel, C. I. (2021). Modeling diffusion processes in the presence of a diffuse layer at charged mineral surfaces: a benchmark exercise. Computational Geosciences, 25(4), 1319–1336.

Tournassat, C., Steefel, C. I., & Gimmi, T. (2020). Solving the Nernst-Planck equation in heterogeneous porous media with finite volume methods: Averaging approaches at interfaces. Water resources research, 56(3), e2019WR026832.

Tsang, C.-F. (1987). Introduction to coupled processes. In C.-F. Tsang (Ed.), Coupled processes associated with nuclear waste repositories (pp. 1–6). Academic Press. https://www.elsevier.com/books/coupled-processes-associated-with-nuclear-waste-repositories/tsang/978-0-12-701620-7

Tsang, C. F., Bernier, F., & Davies, C. (2005). Geohydromechanical processes in the Excavation Damaged Zone in crystalline rock, rock salt, and indurated and plastic clays - In the context of radioactive waste disposal. International Journal of Rock Mechanics and Mining Sciences, 42(1), 109–125.

G. A. Ugueto, M. Wojtaszek, S. Mondal, A. Guzik, D.Jurick, G. Jin. (2021). New Fracture Diagnostic Tool for Unconventionals: High-Resolution Distributed Strain Sensing via Rayleigh Frequency Shift during Production in Hydraulic Fracture Test 2. Unconventional Resources Technology Conference (URTeC) DOI 10.15530/urtec-2021-5408.

Urpi, L., Rinaldi, A. P., Rutqvist, J., & Wiemer, S. (2019). Fault stability perturbation by thermal pressurization and stress transfer around a deep geological repository in a clay formation. Journal of Geophysical Research: Solid Earth, 124, 8506–8518.

van Genuchten, M.T. (1980) A closed-form equation for predicting the hydraulic conductivity of unsaturated soils. Soil. Sci. Soc. Am. J., 44, 892-898.

Vaswani, A., N. Shazeer, N. Parmar, J. Uszkoreit, L. Jones, A. N. Gomez, Ł. Kaiser, and I. Polosukhin, 2017, Attention is All you Need, in Long Beach, CA, USA.

Viesca, R. C., and J. R. Rice. Nucleation of slip-weakening rupture instability in landslides by localized increase of pore pressure, J. Geophys. Res., 117, B03104. 2012.

Vilarrasa, V., Rutqvist, J., Blanco-Martin, L., and Birkholzer, J. (2016) Use of a dual structure constitutive model for predicting the long-term behavior of an expansive clay buffer in a nuclear waste repository.

Wallace, R.E., 1951. Geometry of shearing stress and relation to faulting. J. Geol. 59, 118–130.

Wang, H.F. Theory of Linear Poroelasticity, 287 pp., Princeton Univ. Press. (2000).

Wang, Y. (2011) Research & Development (R&D) Plan for Used Fuel Disposition Campaign (UFDC) Natural System Evaluation and Tool Development, U.S. DOE Used Fuel Disposition Campaign.

Wang, Q., Y. Guo, L. Yu, and P. Li, 2020, Earthquake Prediction Based on Spatio-Temporal Data Mining: An LSTM Network Approach, IEEE Trans. Emerg. Topics Comput., 8, no. 1, 148–158.

Wileveau, Y. (2005). THM behaviour of host rock (HE-D experiment): Progress report September 2003–October 2004, Part 1 Mont Terri Technical Report TR 2005-03. Wabern, Switzerland: Federal Office of Topography (Swisstopo).

Wileveau Y, Su K, Ghoreychi M. A heating experiment in the argillites in the Meuse/Haute-Marne Underground research laboratory. In: The 11th International Conference on Environmental Remediation and Radioactive Waste Management. Bruges; 2-6 September 2007:939–944.

Wynants-Morel, N., Cappa, F., De Barros, L., Ampuero, J.-P., 2020. Stress Perturbation From Aseismic Slip Drives The Seismic Front During Fluid Injection In A Permeable Fault. J. Geophys. Res. Solid Earth 125, e2019JB019179.

Wong, L. N. Y., and H. H. Einstein. 2009. “Systematic Evaluation of Cracking Behavior in Specimens Containing Single Flaws under Uniaxial Compression.” International Journal of Rock Mechanics and Mining Sciences 46(2):239–49.

Wu, Z., and Wong L.N.Y. 2012. “Frictional Crack Initiation and Propagation Analysis Using the Numerical Manifold Method.” Computers and Geotechnics 39:38–53.

Wu, M., et al. (2021). Development and Evaluation of a Deep Learning Algorithm for Rib Segmentation and Fracture Detection from Multicenter Chest CT Images. Radiology: Artificial Intelligence, 3(5).

Xu H., Zheng L., Rutqvist J., and Birkholzer J. Chemo-Mechanical behavior of bentonite in nuclear waste disposal based on the Barcelona expansive model. Computers and Geotechnics 132, 103968 (2021).

Yang, B., K. Yin, S. Lacasse, and Z. Liu, 2019, Time series analysis and long short-term memory neural network to predict landslide displacement, Landslides, 16, no. 4, 677–694.

Yamaji, A. (2003). Are the solutions of stress inversion correct? visualization of their reliability and the separation of stresses from heterogeneous fault-slip data. Journal of Structural Geology, 25(2):241–252, 2003.

Yu, Chi-Hua, Chang-Yan Wu, and Markus J. Buehler. 2022. “Deep Learning Based Design of Porous Graphene for Enhanced Mechanical Resilience.” Computational Materials Science 206:111270.

Yu, L., Weetjens, E., Sillen, X., Vietor, T., Li, X., Delage, P., Labiouse, V., & Charlier, R. (2014). Consequences of the thermal transient on the evolution of the damaged zone around a repository for heat-emitting high-level radioactive waste in a clay formation: A performance assessment perspective. Rock Mechanics and Rock Engineering, 47(1), 3–19.

Zappone, A., Rinaldi, A.P., Grab, M., Wenning, Q.C., Roques, C., Madonna, C., Obermann, A.C. , Bernasconi, S.M., Brennwald, M.S., Kipfer, R., Soom, F., Cook, P., Guglielmi, Y., Nussbaum, C., Giardini, D., Mazzotti, M. and Stefan Wiemer. Fault sealing and caprock integrity for CO2 storage: an in situ injection experiment. Solid Earth, 12, 319–343. 2021.

Zecevic, M., Daniel, G., Jurick, D., 2016. On the nature of long-period long-duration seismic events detected during hydraulic fracturingOn the nature of LPLD events. Geophysics 81, KS113–KS121.

Zhang, C.-L., Conil, N., & Armand, G. (2017). Thermal effects on clay rocks for deep disposal of high-level radioactive waste. Journal of Rock Mechanics and Geotechnical Engineering, 9(3), 463–478.

Zhang, C.L. (2018). Thermo-hydro-mechanical behavior of clay rock for deep geological disposal of high-level radioactive waste, Journal of Rock Mechanics and Geotechnical Engineering, Volume 10, Issue 5, Pages 992-1008, ISSN 1674-7755.

Zhang, Q., Fink, R., Krooss, B., Jalali, M., & Littke, R. (2021). Reduction of shale permeability by temperature-induced creep. SPE Journal, 26(2), 750–764.

Zhang, X.-P., and Wong L.N.Y. (2011). “Cracking Processes in Rock-Like Material Containing a Single Flaw Under Uniaxial Compression: A Numerical Study Based on Parallel Bonded-Particle Model Approach.” Rock Mechanics and Rock Engineering.

Zheng, H., and Xu D.. (2014). “New Strategies for Some Issues of Numerical Manifold Method in Simulation of Crack Propagation.” International Journal for Numerical Methods in Engineering 97(13):986–1010.

Zheng L., Rutqvist J., Liu H.-H., Birkholzer J.T. and Sonnenthal E. Model evaluation of geochemically induced swelling/shrinkage in argillaceous formations for nuclear waste disposal. Applied Clay Science, 97–98, 24–32 (2014). https://doi.org/10.1016/j.clay.2014.05.019.

Ziegler, M., Loew S. (2021). PF-Experiment: Installation and first data. Mont Terri Technical Note 2020-37, 15 pp.

Ziegler, M., Low, S. (2021). Mont Terri PF Experiment: Progressive Failure of Structurally-Controlled Overbreaks - Site characterisation and in-situ experiment installations. ENSI Research and Experience Report, ENSI-AN-11061, 291-299.

Ziegler, M., Furche, M., Beilecke, T., Obermann, A., Loew, S. (2022). Progressive failure of a repository drift in clay shale (PF experiment, Mont Terri Project). RFP 2022, June 20-24, Flatrock, NC, USA.

Zoback, M.D., Kohli, A., Das, I., McClure, M., 2012. The importance of slow slip on faults during hydraulic fracturing stimulation of shale gas reservoirs, in: SPE Americas Unconventional Resources Conference. OnePetro

Argillite Disposal R&D and Argillite International Collaborations – LANL (FY23) (Part III)

1. Argillite Disposal R&D

1.1 Introduction

The United States Department of Energy Spent Fuel and Waste Disposition program is investigating reference cases in multiple host rock types for the geologic disposal of spent nuclear fuel and waste. This report presents experimental results on engineered barrier system (EBS) interactions at elevated temperature and pressure in an argillite host rock formation. The generic disposal concept in argillaceous rock (shale) includes a waste package encapsulated in a bentonite clay barrier formed of pellets or compressed blocks that is emplaced in a horizontal tunnel and lined with a form of concrete (often shotcrete or pre-formed concrete blocks) (Figure 1). The bentonite barrier's function relies on the physical and chemical properties of swelling clay minerals (i.e., smectite), which are the main mineralogical components of bentonite (Dohrmann et al., 2013; Pusch, 1979; Sellin and Leupin, 2013). Smectite has unique swelling properties that 1) maintain in-drift pressure, 2) have the ability to seal cracks and fractures that may develop, and 3) retard the infiltration of fluid from the surrounding wall rock that may interact with the waste package (Pusch et al., 2015; Sellin and Leupin, 2013). Smectite and other clay minerals may also act to attenuate actinide migration through sorption on clay mineral surfaces (Higgo, 1987; Sellin and Leupin, 2013; Singh and Um, 2023). However, there remain large uncertainties regarding the long-term stability of bentonite at potential repository conditions, particularly under prolonged periods of high thermal loads in the presence of highly concentrated infiltrating groundwater solutions.

The U.S. DOE is interested in exploring repository concepts at higher temperatures than have been considered by foreign programs, to assess the potential impacts of disposing of waste packages with higher thermal loads. For example, dual-purpose canisters (DPCs) that are primarily designed for storage and transportation may contain up to 37 spent-fuel assemblies (37 pressurized-water reactors (37-PWR)). In contrast, many European concepts are limited to four spent fuel assemblies (4-PWR) (Hardin et al., 2015; Pusch, 2009). The closer packing of spent fuel assemblies within these DPCs has the potential to generate a greater amount of heat radiating into the EBS and host rock in a disposal scenario. Thermal modeling calculations have shown that the surface of a DPC containing 37-PWR (60 gigawatt-days per metric ton burnup) has the potential to reach 400 °C in a repository hosted in argillaceous rock (under 50-year decay storage with 100-year ventilation, 20 m package spacing, and an unsaturated bentonite thermal conductivity = 0.60 W/m-K; Hardin et al., 2015) (Figure 2).

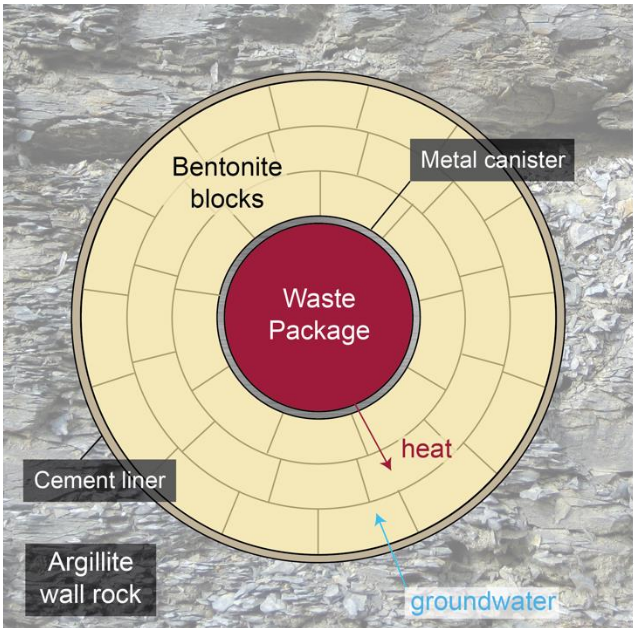

Figure 1. Schematic of a generic engineered barrier system concept in argillite host rock. Bentonite blocks surround a waste canister emplaced in a horizontal tunnel lined with cement.

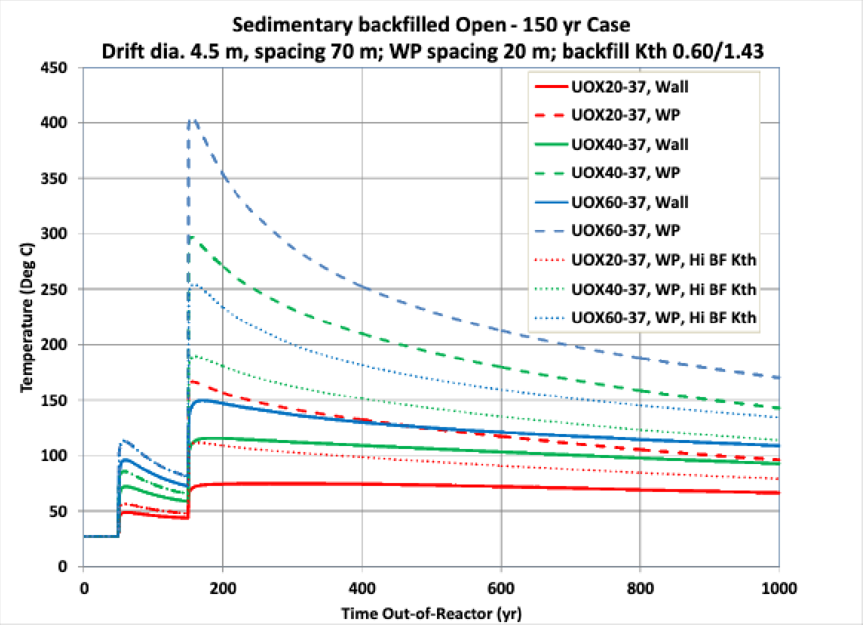

Figure 2. Calculated temperatures for various burnup levels (e.g., OUX20) of spent nuclear fuel 37-PWR at the repository drift wall (wall) and waste package surface (WP) in a backfilled sedimentary rock-hosted repository. The calculations include 50 years of decay storage and 100-year ventilation time. Waste package spacings and drift dimensions are listed on the figure. Thermal conductivity of the bentonite is either 0.60 W/m-K (unsaturated bentonite) or 1.43 W/m-K (fully hydrated bentonite). From Hardin et al. (2015).

Cementitious materials will likely make up a large component of the underground repository. Interaction between cement, bentonite, and steel will therefore likely occur at elevated temperature and pressure and in the presence of water. Experiments in FY22 included comparisons of the effects of 1) uncured ordinary Portland cement (OPC) powder, 2) cured OPC chips, and 3) low-pH cement with 50 wt.% silica fume replacement on bentonite mineral and geochemical properties at temperatures of 200 to 300 ºC.

Overall, the hydrothermal experiments conducted at Los Alamos National Laboratory in FY23 aimed to develop concepts related to the function of EBS in the high-temperature isolation of spent fuel and waste in argillite host rock. Our work on bentonite interaction with Opalinus Clay in experimental hydrothermal systems was developed in the FY17, FY18, and FY19 reports and was published by Cheshire et al. (2014) and Sauer et al. (2020). The FY23 report will focus on our current experimental tests in argillite including: 1) the effects of different cement compositions on bentonite stability and Opalinus Clay mineralogy and 2) clay-steel interface mineralization and growth rates in systems with and without cement.

1.2 Background

1.2.1 Wyoming Bentonite in EBS Applications

Bentonite barrier performance in the EBS relies on the physical and chemical properties of the mineral components. The bentonites investigated for potential barrier usage are largely selected for a high content of clay minerals, particularly the smectite mineral, montmorillonite. Smectite minerals act as a critical part of most EBS designs because of their aforementioned swelling properties, as well as their sorption potential and high cation exchange capacity (CEC) that may act to retard radionuclide transport. Mineralogical changes to the bentonite EBS materials that affect swelling and CEC of smectites are then a primary concern for long-term EBS functionality. Heating events pose a particular concern to the efficacy of bentonite barriers when potentially concurrent with groundwater infiltration. Under dry conditions, bentonite mineral assemblages may be stable to over 350 °C (Wersin et al., 2007); however, many geologic repository designs consider sitting below the local water table to promote anoxic conditions. Water-saturated conditions combined with elevated temperatures (> 100 °C) may provoke hydrothermal alteration of smectite minerals (Cheshire et al., 2014; Ferrage et al., 2011; Mosser-Ruck et al., 2010). The reduction of swelling capacity of smectite responsive to heating events – driven by the formation of non-swelling clays, cementation of smectite lamellae caused by silica precipitation, and/or recrystallization to other mineral phases (e.g., zeolites) – is believed to a potentially significant risk to the isolation capability of bentonite buffers (Pusch et al., 1998).

Previous experimental studies have characterized smectite mineral transformations over a wide range of repository temperatures (i.e., ~25–300 °C) (Cheshire et al., 2014; Guillaume et al., 2003; Hofmann et al., 2004; Madsen, 1998; Meunier et al., 1998). The reduction of swelling capacity of montmorillonite, the main swelling clay species comprising bentonite, may be due dominantly to the formation of non-swelling clays (specifically illite, $K(Al,Mg,Fe)_2(Si,Al)_4O_{10}[(OH)_2]$) (Wersin et al., 2007). For example, in experimental systems where K+ was reacted with bentonite, the formation of non-swelling, K^+-rich, collapsed layer smectite and/or illite was observed (Cheshire et al., 2014; Kaufhold and Dohrmann, 2010; Mills et al., 2023; Mosser-Ruck et al., 1999). Silica release also occurs, as illustrated by the following generalized reaction:

$$\text{Na-montmorillonite} + K^+ + H^+ \rightarrow \text{illite} + SiO_{2\,(aq)} + Na^+ + Mg^{2+} + H_2O \quad (1)$$

Low availability of K^+ and/or silica saturation in the infiltrating solution may then act to limit illitization (Cheshire et al., 2014; Pusch and Madsen, 1995; Savage et al., 2019). For example, in targeted experiment studies of bentonite systems reacted with NaCl solutions, montmorillonite structural alteration was not observed (Cheshire et al., 2014; Kaufhold and Dohrmann, 2009) in comparison to experiments in a K^+-rich environment (Kaufhold and Dohrmann, 2010).

Zeolite formation within bentonite EBS material has also been reported (Cheshire et al., 2014, 2013; Ferrage et al., 2011; Mosser-Ruck et al., 2016, 2010). Zeolites may form by dissolution of precursor zeolites (e.g., clinoptilolite) under silica-saturated conditions (Cheshire et al., 2014, 2013) or clay-mineral reactions (Mosser-Ruck et al., 2016). Dissolution of clinoptilolite, which makes up roughly 13% of the Wyoming bentonite used in this study, and precipitation of analcime may result in a slight volume loss within the bentonite barrier (Cheshire et al., 2014).

1.2.2 Opalinus Clay

The URL and international research project Mont Terri in Switzerland is sited in the Opalinus Clay argillaceous rock which is considered the preferred host rock for repository siting in Switzerland (Bossart et al., 2017; Wieczorek et al., 2017). The high clay content of the argillaceous rock confers low permeability, high sorption potential for radionuclides, and crack-sealing properties to the formation (Bossart and Milnes, 2017; Bossart and Thury, 2008). Laboratory-based experimental studies as well as site-specific experiments at Mont Terri have targeted the mineralogical and chemical evolution of Opalinus Clay under various conditions to inform generic performance evaluations of argillite as a repository host rock.

Laboratory-scale experiments have evaluated the interaction of high pH fluids and Opalinus Clay at ambient (Adler et al., 1999; Taubald et al., 2000) and elevated temperatures (90–200 °C) (Chermak, 1992; Honty et al., 2012) temperatures. At higher temperatures (150–200 °C) and elevated pH, the formation of analcime, vermiculite, and Na-rectorite was observed within powdered Opalinus Clay (Chermak, 1992).

Observations from long-term, full-scale, in situ demonstrations at the Mont Terri URL also provide insight into cement-bentonite interactions in the natural environment, including potential effects on groundwater geochemistry, host-rock properties, and hydrologic processes. In situ EBS experiments at the Mont Terri underground research laboratory in Opalinus Clay are in progress (HE-E, up to 140 °C; Wieczorek et al., 2017; FE, up to 150 °C; Müller et al., 2018) (Müller et al., 2018; Wieczorek et al., 2017).

1.2.3 Cement Materials

Cementitious materials such as shotcrete, cast-in-place cements, and/or preformed cement blocks are necessary elements of repository infrastructure and provide ground support to maintain drift integrity and prevent collapse. Traditional ordinary Portland cement (OPC) interactions with water may have a significantly impact the repository system through the dissolution of portlandite ($Ca(OH)_2$), alkali-rich phases, calcium silicate hydrate (CSH) minerals, and other reactive components of the cement (e.g., sulfates). Cement-water reactions then have the potential to release significant amounts of OH^- and Ca^{2+} into the groundwater migrating into the EBS system, leading to increase in pore water pH in the bentonite buffer, montmorillonite dissolution, and the formation of secondary mineral phases (e.g., Ca-zeolites, CSH phases, feldspars).

Laboratory-scale studies of bentonite-cementitious material interactions and bentonite stability in highly alkaline environments have been researched for a variety of conditions (Balmer et al., 2017; Chen et al., 2019; Cuevas et al., 2006; Dolder et al., 2014; Fernández et al., 2009a, 2009b, 2006; Karnland, 1997; Karnland et al., 2007; Kaufhold et al., 2020; Kaufhold and Dohrmann, 2009; de la Villa et al., 2001;Wieland et al., 2017). Experiments below ~100 ºC showed that the reaction of bentonite in contact with cement and alkaline porewaters over even relatively short timescales (~months to 1–2 years) result in the formation of secondary phases and changes to clay swelling behavior. 16-month experiments with MX-80 Wyoming bentonite and pH = 12.8–13.7 solutions at 40 ºC resulted in minor illite and chlorite formation, cristobalite dissolution and quartz precipitation, and CSH mineral and CSH gel formation (Karnland, 1997). Column tests with FEBEX bentonite and alkaline solutions reacted at 60 ºC for 6 to 12 months resulted in alteration concentrated in a 2.0 to 2.5 mm reaction front, which included brucite, chlorite, Mg-smectite, and minor zeolite formation and montmorillonite dissolution (Fernández et al., 2009b). A comparative study of 40 different bentonites in contact with Portland cement powder at 80 ºC for three months showed that the presence of reactive silica in bentonite helped to stabilize clay minerals (Kaufhold et al., 2020). In aggregate these experimental results demonstrate the potential for montmorillonite dissolution, and for zeolite, feldspar, and CSH mineral formation near the bentonite-cement interface within a thin alteration zone that expands with increasing temperature (Cuevas et al., 2006).

The potential for significant and wide-ranging geochemical and mineralogical effects of bentonite-cement interaction has led repository programs to implement a pH limit for cement porewater (e.g., B, pH < 11). The pH limit is achievable using low-pH cements that replace traditional cement components (e.g., limestone aggregate) with siliceous materials (e.g., fly ash and silica fume) resulting the reduced abundance of portlandite in the cured product and a lower Ca/Si ratio in the CSH minerals (Calvo et al., 2010; Lothenbach et al., 2011). Experiments reacting montmorillonite-bearing clay with cement porewater at ambient temperatures suggested little alteration would be expected on short timescales (up to 5 months) (Pusch et al., 2003). Long-term in-situ experiments at the Mont Terri URL also characterized the co-alteration of Opalinus Clay with different types of cements (ESDRED cement (as described by (Lothenbach et al., 2014; Verstricht, 2009) and low-alkali cement, as well as OPC) for up to five years in ambient conditions. Mäder et al. (2018) reported that both ESDRED cement and OPC experienced decalcification and potentially decreased porosity at the Opalinus clay-cement interface, although overall alteration was reported as minimal for both materials. The second low-alkali cement tested also experienced Ca leaching, as well as increased porosity at the interface in both the cement and Opalinus Clay phases (Jenni et al., 2014; Lerouge et al., 2017).

1.2.4 Waste Canister Materials

In general, the metal waste canister overpack (likely carbon steel) in a shale-hosted repository will be expected to corrode over time (Guo et al., 2020; Kursten et al., 2004a, 2011). The steel will corrode at the bentonite buffer interface in the presence of oxygen according to one of the following reactions (aerobic corrosion) (Kursten et al., 2004b):

$$4\ Fe^{o} + 3\ O_2 \rightarrow 2\ Fe_2O_3 \qquad (2)$$

$$2\ Fe + 2\ H_2O + O_2 \rightarrow 2\ Fe(OH)_2 \qquad (3)$$

In the presence of oxygen, the ferrous hydroxide in the second reaction can corrode further (Kursten et al., 2004b):

$$4\ Fe(OH)_2 + 2\ H_2O + O_2 \rightarrow 4\ Fe(OH)_3 \qquad (4)$$

$$4\ Fe^o + 6\ H_2O + 3\ O_2 \rightarrow 4\ Fe(OH)_3 \qquad (5)$$

If ferrous oxides or hydroxides are formed by the corrosion potential exceeding equilibrium (Eq. 2), a resistant oxide film will precipitate on the metal surface. The oxide film will act as a protective coating against further corrosion in the effect called passivation. At lower pH, the “passive” oxide films can break down from interaction with H+ and other reactive species (Kursten et al., 2004b). The same study also reviewed differences in passivation behaviors of different types of steel. Stainless steel may form more corrosion-resistant films of chromium oxy-hydroxide that resultantly slow the corrosive reaction described in Eq. 3, whereas carbon steel forms a less resilient film composed of a mixture of Fe(II) and Fe(III) oxy-hydroxides (Eq. 4 and 5). Passive films overlaying carbon steel may more easily be broken down by chloride corrosion than on stainless steel (Kursten et al., 2004b). Stainless steel corrosion then tends to be highly localized (i.e., pitting corrosion, stress corrosion) while carbon steel presents more general/uniform corrosion (Smart et al., 2011).

1.2.4.1 Corrosion at the Steel-Bentonite Interface

Effects of bentonite buffer materials on steel corrosion at the bentonite-steel interface have been extensively studied at ambient and elevated temperatures (Carlson et al., 2007; De Combarieu et al., 2007; El Mendili et al., 2015, 2014; Kaufhold et al., 2015; Kaufhold and Dohrmann, 2016; Madsen, 1998). Previous work by (Smailos et al., 2003) experimentally tested corrosion potentials of various steels and alloys in the presence of oxidizing clay-water solutions. These authors demonstrated an increased potential for corrosion (pitting) at stainless steel surfaces with increasing chloride concentrations which was further enhanced by high concentrations of sulfate (> 200 mg L^{-1}). Hydrothermal studies conducted at lower temperatures (80 °C) for over 10 years showed minor formation of iron oxides and decreases to CEC in bentonite within 1 mm of the steel-bentonite interface in one type of bentonite, indicating that the type and extent of alteration out from the steel-bentonite barrier is driven in part by the type of bentonite (Ishidera et al., 2008). Complementary results of a study on the effect of occluding minerals on steel corrosion suggested that montmorillonite in contact with steel may interact with the steel surface to slow general corrosion, although transport through pores in the interfacing mineral layer may still promote localized corrosion (Jeannin et al., 2010). These examples among many illustrate the interconnected nature of evolving solution chemistries, bentonite alteration, and steel corrosion, and underline the need for specific studies that isolate alteration products and solution chemistry evolution in specific environments.

Previous experiments conducted at LANL characterizing mineral precipitation at the steel-bentonite interface have focused on the effect of Opalinus Clay groundwater and wall rock on bentonite-steel co-alteration and have been described in Caporuscio et al. (2015; 2017; 2018; 2019) and (Cheshire et al., 2018). These studies describe a layered alteration sequence observed on the surface of steel coupons included in Wyoming bentonite-only experiments. In general, an oxide layer formed directly at the surface of steel coupons. An Fe-saponite layer also formed at the steel-clay interface distal to the oxide layer. Concurrent with Fe-saponite formation, sulfides precipitated from the sulfide-bearing fluids near the steel interface. The thickness of the Fe-rich phyllosilicate minerals perpendicular to the SS surface ranged from 9 to 44 µm. There was no significant change in the precipitation thicknesses between three different temperature profiles at 300 °C (ramped to 300 °C, cooling from 300 °C, and isothermal).

1.2.4.2 Corrosion at the Steel-Cement Interface

Studies have documented decreasing corrosion rates correlated with increasing pH for both stainless and carbon steels (Kursten et al., 2004b; Smart et al., 2011); for example, corrosion rates for low-carbon steel reacted with cement have been shown to be 5 times higher at pH 7 than at pH 13 (Kursten et al., 2004b). A common layer at the steel-cement interface is “laitance,” a weak, easily crumbled layer consisting of cement and fine aggregates. This laitance can act as a controlling factor for the rate of corrosion of steel in cement and has exhibited the ability to limit diffusion of chloride species. In cases where calcium hydroxides precipitate, they can reduce pitting corrosion by buffering the local acidification caused by corrosion product hydrolysis (Smart et al., 2006).

2. Methods

2.1 Hydrothermal Experiments

Experiments were conducted using a Dickson-type, gold cell autoclave system as designed by (Seyfried et al., 1987). Experimental design using the reactors at LANL is described in (Cheshire et al., 2014; Sauer et al., 2020; Zandanel et al., 2022): briefly, reactions were conducted in closed flexible gold reaction cells fixed within a 500 mL confined reactor and surrounded by an annulus of DI water that controlled pressure within the reaction cell (Seyfried et al., 1987). Fluid samples were collected from inside the reaction cell during each experiment by means of an exit tube fitted with a sampling valve. In contact with ambient laboratory conditions the samples were equilibrated to bench conditions (~25 °C, 1 atm) within minutes; precipitation of solid phases was not observed during fluid cooling. Fluid samples collected before, during, and after experiments measured pH and a filtered (0.22 µm syringe filter) aliquots were prepared for anion (ion chromatography - IC) and cation (ICP-OES, ICP-MS) analysis. All aliquots were stored in polytetrafluoroethylene vials at 1 °C before analysis.

Experiments completed in FY23 combined synthetic Opalinus Clay groundwater (GW) with Wyoming bentonite (80%) and Opalinus Clay (20%) heated isothermally to 150 °C and reacted for 4 or 8 weeks (EBS-35A and EBS-35B, respectively; Table 1) to evaluate any controlling influence of a generic wall rock on the solution chemistry and resulting bentonite alteration. Additionally, one experiment containing Wyoming bentonite-only (EBS-36) was reacted 150 °C for 8 weeks. Our work on bentonite interaction with Opalinus Clay in experimental hydrothermal systems was initially developed in 2016 and presented in FY17, FY18, FY19, and FY20 reports, as well as published in (Cheshire et al., 2014) and (Sauer et al., 2020). Experiments FY21 and FY22 focused on reactions between Wyoming bentonite ± Opalinus Clay with other barrier materials including different steel and cement materials, detailed in Section 2.2.1 (Materials). Parameters for all experiments discussed in this report are included in Table 1.

Table 1. Parameters for experiments completed in FY23 and experiments from previous years that have new analytical results collected in FY23. All experiments were run at 150 MPa. Abbreviations: GW=Opalinus Clay groundwater; OC=Opalinus Clay; WB=Wyoming bentonite: OPC=ordinary Portland cement; LpHC=experimental low-pH cement; WRR=water-rock ratio (by mass). Detailed information on reactants is included in Section 1.3.4 below.

Exp. ID	FY	Reactants	Temp (°C)	Run Time	GW (g)	OC (g)	WB (g)	Cement (g)	Steel (g)	Fe (g)	FE_3O_4 (g)	WRR
EBS-30	FY21	WB+OC +OPC +316SS	200	8 weeks	104	2.1	6.4	2.1	5.1	0.50	0.50	9:1
EBS-31	FY21	WB+OC +OPC +304SS	200	8 weeks	131	2.1	6.1	2.1	4.7	0.50	0.50	12:1
EBS-32	FY22	WB+OC +OPC +LCS	200	8 weeks	139	2.2	6.5	2.2	5.8	0.50	0.50	12:1
EBS-33	FY22	WB +LpHC	200	9 weeks	153		12.6	3.2		0.59	0.59	9:1
EBS-34	FY22	WB+OC +LpHC	200	9 weeks	110	2.3	6.9	2.3		0.43	0.43	9:1
EBS-35A	FY23	WB+OC	150	4 weeks	147	3.1	12.3			0.58	0.58	9:1
EBS-35B	FY23	WB+OC	150	8 weeks	114	2.4	9.4			0.44	0.44	9:1
EBS-36	FY23	WB	150	8 weeks	163		15.3			0.58	0.58	10:1

2.2 Materials

2.2.1 Materials used in experiments completed in FY23

Wyoming bentonite. Previous experiments used an unprocessed Wyoming bentonite provided by Bentonite Performance Minerals LLC from Colony, Wyoming, U.S.A. It is composed dominantly of Na-montmorillonite (general composition: $Na_{0.33}(Al,Mg)_2(Si_4O_{10})(OH)_2 \cdot nH_2O$), lesser clinoptilolite and feldspar, and minor biotite, pyrite, quartz, opal, and sulfide minerals. The QXRD results from unheated bentonite are presented in Table 3.

Opalinus Clay. Opalinus Clay is a thinly laminated, dark gray shale with a dry density of 2.2 to 2.4 g cm-3 and water content of 6.5 to 8.0%, dominantly composed of clay minerals, with lesser carbonates and silicates. Other minerals present include calcite, ankerite, dolomite, quartz, and biotite. Well-preserved pyrite also occurs, primarily as < 2 µm octahedral crystals in fractures and/or along bedding planes. Na^+ is the dominant exchangeable cation in the Opalinus clay followed by Ca^{2+}, Mg^{2+}, K+, and Sr^{2+} (Pearson et al., 2003).

Opalinus Clay used in this study was sourced from the Mont Terri Underground Rock Laboratory in Canton Jura, northern Switzerland. The rock used was from the shaley facies of Opalinus Clay at Mont Terri (drill core BFE-A10) and was exposed to air (i.e. oxidizing conditions) before the experiment. QXRD performed on these samples showed the rock to be composed of mixed illite, smectite, and illite-smectite (24%), kaolinite (17%), calcite (16%), chlorite (9%), mica (7%), K-feldspar (6%), and plagioclase (3%), with minor dolomite and pyrite (Table C-1in Caporuscio et al., 2023). Illite and smectite are reported together here due to the difficulty of quantifying these mineral phases when they are mixed. SEM analyses showed calcite primarily occurs as pocket filling agglomerates, exemplifying layered structures with alternating calcite and clay layers (Figure 3).

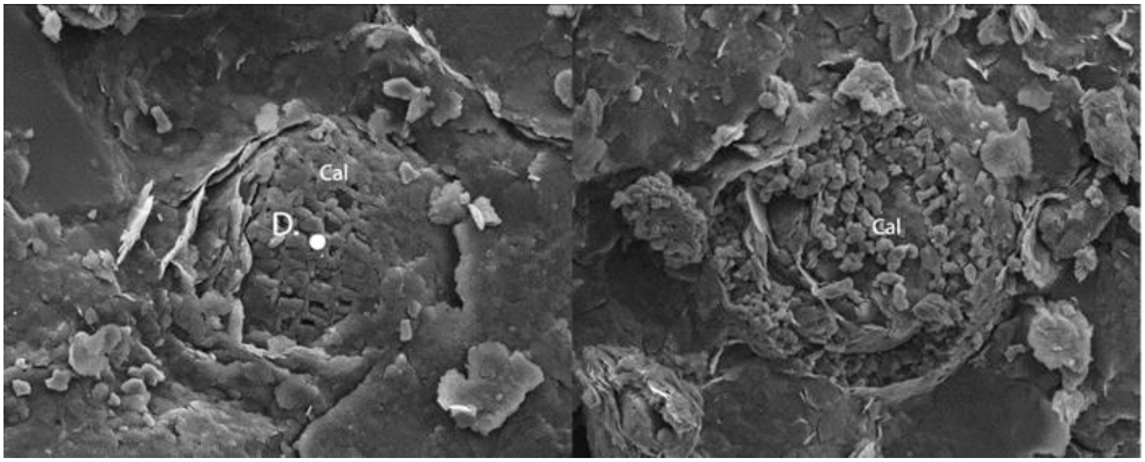

Figure 3. SEM images of unheated Opalinus Clay. [Left] Biogenic calcite (Cal) filling a pocket with in the Opalinus Clay matrix. [Right] Disturbed pocket-filling calcite showing layered structure with alternating calcite and clay layers.

Opalinus Clay synthetic groundwater. A solution selected to approximate the pore water found in the Mont Terri Opalinus Clay as reported by Pearson et al. (2003) as Na-Cl brine with pH ~7.5. As synthesized based on measurements from the Opalinus clay formation, the solution chemistry is targeted to be in equilibrium with the exchangeable cations of the clay phase of the Opalinus Clay. The target initial solution chemistry is reported in Table 2.

Table 2. Solution composition for synthetic Opalinus Clay solution modeled after data reported from the Mont Terri site (Pearson et al., 2002) used in the Opalinus Clay experiments and Los Alamos Municipal tap water. The Los Alamos Municipal tap water was used in the curing of the ordinary Portland cement. Note that while the solutions were not analyzed for carbonate species, the initial formulation includes ~165 mg L^{-1} HCO_3^{2-} in the form of $NaHCO_3$ (n.m. indicates that the analyte was not measured).

	Synthetic Opalinus Clay GW	**LANL Tap Water**
Species	**mg L^{-1}**	**mg L^{-1}**
Ca^{2+}	426	9.62
Cl^-	6470	24.7
HCO_3^{2-}	~165 (n.m)	n.m.
K^+	225	2.04
Na^+	3846	12.8
Si	1	35.4
SO_4^{2-}	998	6.93
Sr^{2+}	0.16	0.045
TDS	12153	n.m.
pH	7.50	6.61

2.2.2 Additional materials used in experiments completed in FY21, FY22

Ordinary Portland cement. Chips consisting of 100% OPC and Los Alamos municipal tap water (Table 2) were mixed according to API standards and cured for at least 28 days. Major mineral phases observed in the XRD pattern of OPC chips include portlandite ($Ca(OH)_2$), belite (Ca_2SiO_4), alite (Ca_3SiO_5), and brownmillerite ($Ca_2(Al,Fe)_2O_5$).

Low-pH cement. An experimental low-pH cement product was included as a reactant in EBS-33 and -34. Low-pH cement cylinders were developed and manufactured at Vanderbilt University using Type I/Type II cement powder (LafargeHolcim, USA), 50 wt.% silica fume replacement, and 2 wt.% Glenium (superplasticizer). A 0.6 water to binder ratio was used. The samples were cured for six months at 30 ºC and were at 100% relative humidity at the time of sample preparation.

316SS. (NIST SRM 160b) is an iron alloy primarily with 18.37 wt.% Cr, 12.35 wt.% Ni, 2.26 wt.% Mo, 1.619 wt.% Mn, 0.5093 wt.% Si, and 0.175 wt.% Cu.

304SS. Stainless steel with a higher Cr:Ni ratio compared to 316SS. Primarily iron alloy with 18 wt.% Cr, 8 wt.% Ni, < 2 wt.% Mn, < 1 wt.% Si, < 0.045 wt.% P, and < 0.03 wt.% S, and < 0.08 wt.% C.

Low carbon steel (LCS). A steel product composed largely of Fe with ~0.2 wt.% C, 0.9 wt.% Mn, < 0.04 wt.% P, and < 0.05 wt.% S.

3. Results

3.1 Aqueous Geochemistry

Aqueous geochemistry tables can be found in Appendix B-1 of Caporuscio et al. (2023) report LA-UR-23-27280. Major cation and anion analytical results are included for all previous FY experiments discussed in this report and for the three experiments EBS-35A, -35B, and -36 completed in FY23. Bench pH as measured at the time of the experiments is reported for all experiments completed in previous years discussed in this report and for those completed in FY23 (EBS-34A, -35B, and -36).

3.1.1 pH

All experiments began with a near neutral pH at 25 ºC of ~7.4 (Figure 4). In the experiments with cured OPC cement chips (EBS-30, EBS-31, and EBS-32; 200 ºC), pH values decreased to ~6 within the first two weeks of experiment time before gradually increasing to values between 6 and 7 by the end of the experiments. In EBS-31, pH initially increased in the first week to just > pH 9 before the decrease to ~6. The pH then gradually increased similarly to EBS-30 and -32, staying within pH 6-7. The two experiments containing low-pH cement (EBS-33 and -34) both experienced an increase in pH to > 9 in the first week followed by a decrease to pH ~6 in the second week. The pH in both experiments then increased until approaching an apparent steady-state pH of ~8 after approximately 1000 h of experimental time.

In the experiments completed in FY23 reacting WB and Opalinus Clay at lower temperatures, pH reached an apparent steady-state value of ~6 within two weeks of reaction time in all experiments. The pH initially increased in the first week during the 4-week experiment, EBS-35A; in the 8-week experiments no such initial pH increase was observed.

Though there are variances in steady-state pH values and trends in different experiments, we note that an initial sharp increase then decrease in pH was observed in several experiments with different reactants and heated to different temperatures. Specifically, this trend was observed in experiments EBS-31 with WB, Opalinus Clay, steel, and cured OPC chips reacted at 200 ºC; EBS-33 and -34 that reacted low-pH cement with WB ± Opalinus Clay at 200 ºC; and in EBS-35A that included bentonite and Opalinus Clay with no cement reactants reacted at 150 ºC.

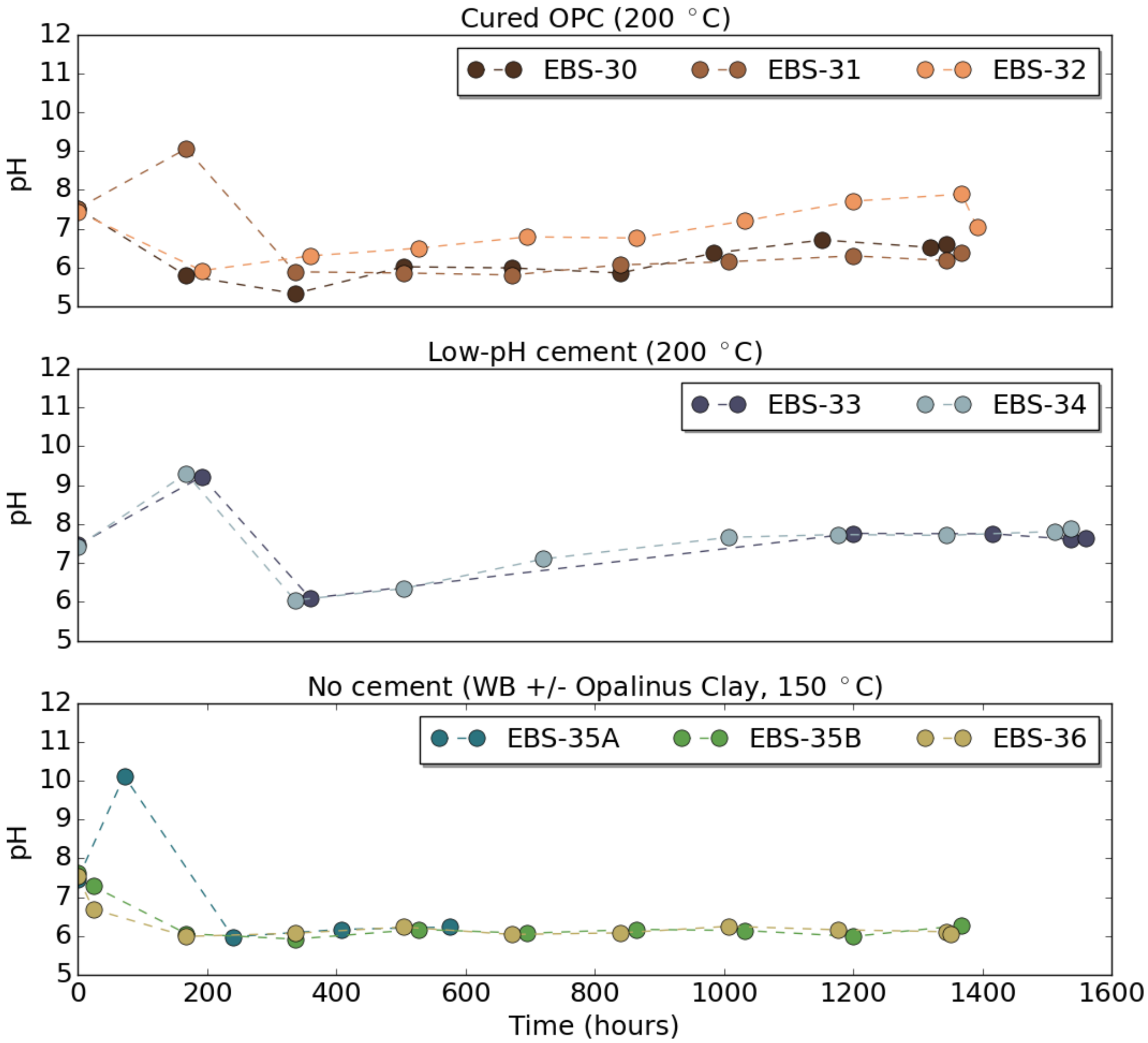

Figure 4. Bench pH (measured at 25 °C) throughout the experimental durations of experiments EBS-30 through EBS-36.

3.1.2 Silica

In all experiments, silica cocnentrations increased from the initial concentrations in the synthetic Opalinus Clay GW (Figure 5). In experiments with cured OPC (EBS-30, -31, and -32), silica increased to concentrations of ~300 mg L^{-1} by the end of the experiments (Figure 5). Silica concentrations also increased in the two experiments that reacted cured, low-pH cement; in EBS-33, silica concentrations appeared to plateau at ~100 mg L^{-1} after an increase to ~150 mg L^{-1} in the first week of sampling, although the mechanical difficulties that prevented sampling between weeks 3 and 7 of the experimental time prevented observation of any fluctuations in the aqueous chemistry during this time. The silica concentrations in EBS-34, however, fluctuate initially before increasing to ~400 mg L^{-1} at ~1400 hours until the end of the experiment.

Initial results from EBS-34A completed in FY23 reacting WB and Opalinus Clay at 150 ºC had SiO_2 increasing from the initial solution throughout the 4-week experiment duration and had not come to a steady-state concentration. SiO_2 concentrations in samples from EBS-35B also followed an increasing trend throughout the experimental duration except for decreased concentration (from > 200 to < 100 mg L^{-1}) in the last sample before experiment termination. In contrast, the measured SiO_2 concentration in EBS-36 increases for the first three weeks of reaction time to ~212 mg L^{-1} before decreasing again throughout the experimental duration.

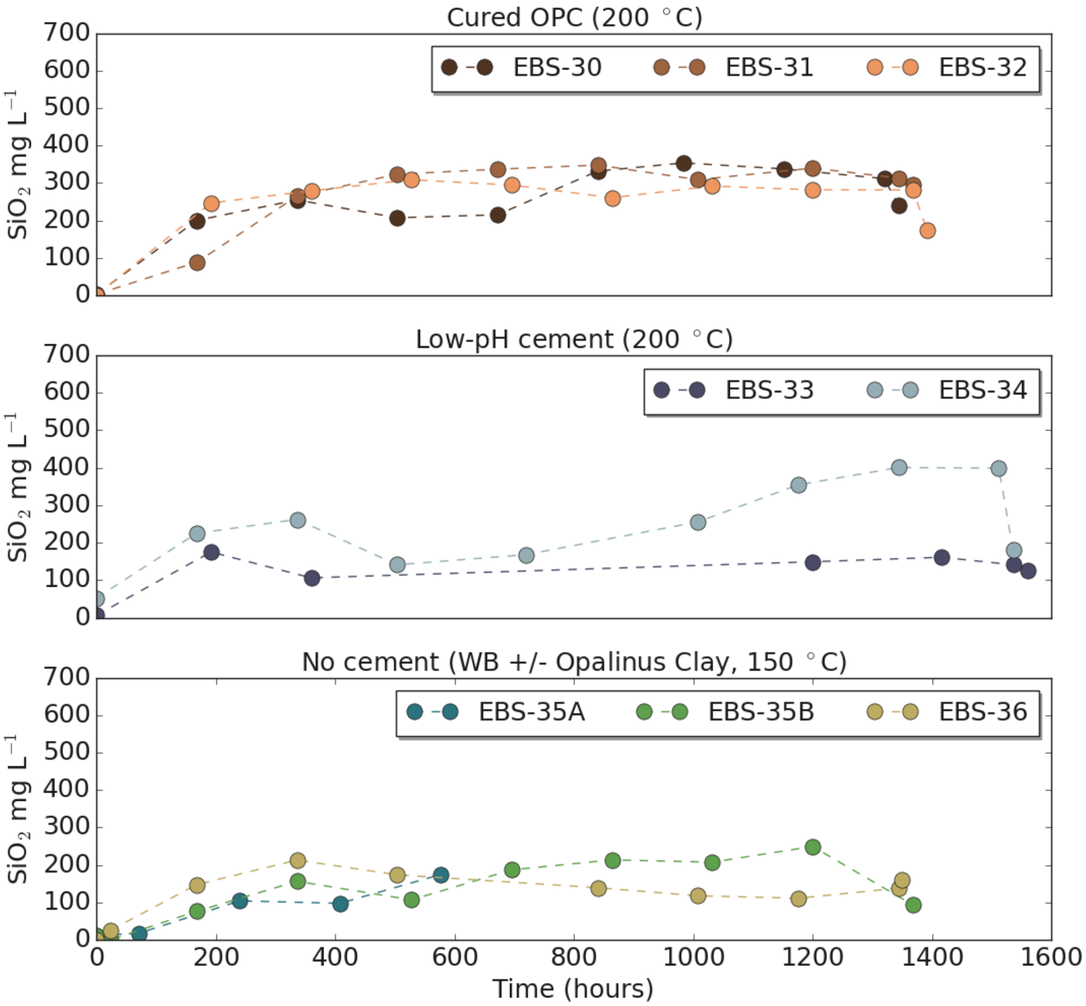

Figure 5. SiO_2 concentrations (measured as Si) throughout the experimental durations of experiments EBS-30 through EBS-36.

3.1.3 Aluminum and Magnesium

In all experiments regardless of reactants or temperature, Al concentrations remained constant at or below near detection limits (< 0.032 mg L-1 for experiments in FY21 and 22; < 0.016 mg L^{-1} for experiments run in FY23). In experiments with OPC (EBS-30 through -32), Mg concentrations decreased to < 50 mg L^{-1} within the first week, then continued to gradually decrease throughout the remainder of the experiments without reaching a steady-state. The two experiments with low-pH cement (EBS-33 and -34) also experienced an initially gradual decrease in Mg concentration and reached a steady-state concentration of < 1 mg L^{-1} after 1000 to 1200 hours of reaction time. All experiments conducted at 200 °C had final Mg concentrations of less than 1 mg L^{-1}. In EBS-35A (150 °C), Mg concentrations decreased from an initial concentration of ~200 mg L^{-1} to a final concentration of ~62 mg L^{-1} and did not reach a steady-state concentration. Mg concentrations in EBS-35B and -36 also decrease throughout their experimental durations, from the initial concentrations ~200 mg L^{-1} to ~20 mg L^{-1} in EBS-35B and ~45 mg L^{-1} in EBS-36 (Appendix B-1 of Caporuscio et al., 2023, Tables B11 through B16).

3.1.4 Potassium, Sodium, and Calcium

In the OPC cement chip experiments EBS-30 and EBS-31, sodium and potassium concentrations followed a decreasing trend, whereas in the OPC cement chip experiment (EBS-32) potassium decreased slightly over the experimental duration while sodium concentrations remained relatively stable. In both low-pH cement chip experiments EBS-33 and -34, sodium concentrations remained relatively stable while potassium concentrations decreased continuously during the experimental duration.

In the experiments completed in FY23, concentrations of all of potassium, sodium, and calcium had minor differences in trends between the experiments. Potassium concentrations initially decreased then increased over the remaining experimental durations in EBS-35B and -36 and decreased slightly before maintaining an apparent steady-state concentration ~170 mg L^{-1} for the experimental duration barring an anomalously high concentration in the penultimate sample (Figure 6). Sodium concentrations increased throughout the experimental durations of all three experiments, from ~3780 to ~4160 mg L^{-1} after 4 weeks of reaction in EBS-35A and increasing to ~4700 mg L^{-1} in EBS-35B and -36 after 8 weeks (Figure 7).

In the experiments conducted at 200 °C reacting cured OPC (EBS-30, -31, and 34) and experiments run at 200 ºC reacting low-pH cement (experiments EBS-33 and -34), calcium concentrations decreased from the initial solution chemistry within the first week. In those experiments, the Ca concentrations remained relatively stable around 150 mg L^{-1} through their reaction times before increasing in the “quench” samples collected after the experiments were completed and cooled to bench conditions (~25 °C, ~0.1 MPa). In the experiments executed in FY23 at 150 ºC (EBS-35A, -35B, and -36), calcium concentrations decreased from the initial solution concentration of ~430 mg L^{-1} before reaching an apparent steady-state. The steady-state Ca concentration in the experiments conducted at 150 °C remained elevated compared to the experiments run at 200 °C and did not increase in solution after quench (Figure 8).

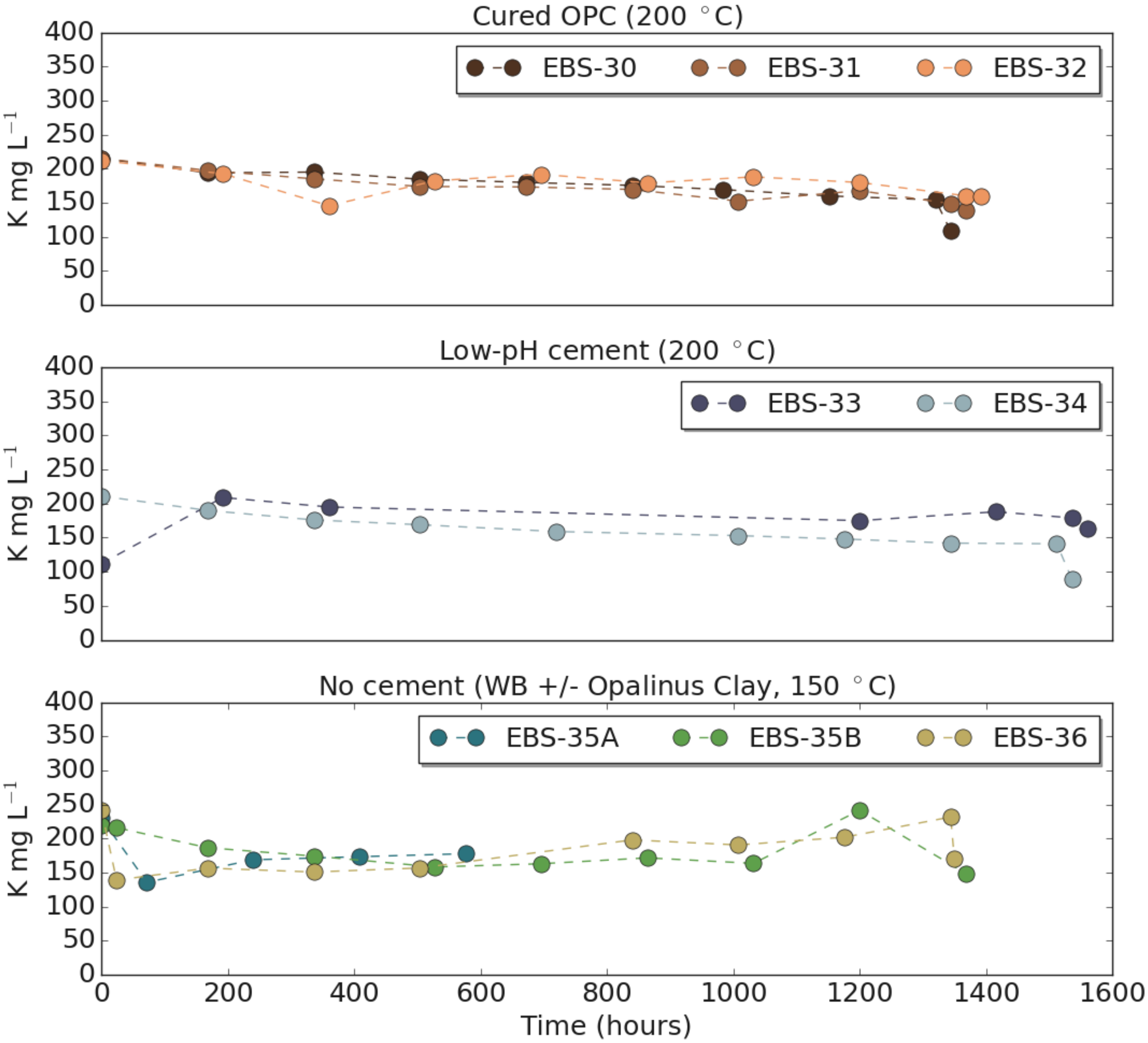

Figure 6. Potassium concentrations throughout the experimental durations of experiments EBS-30 through EBS-36.

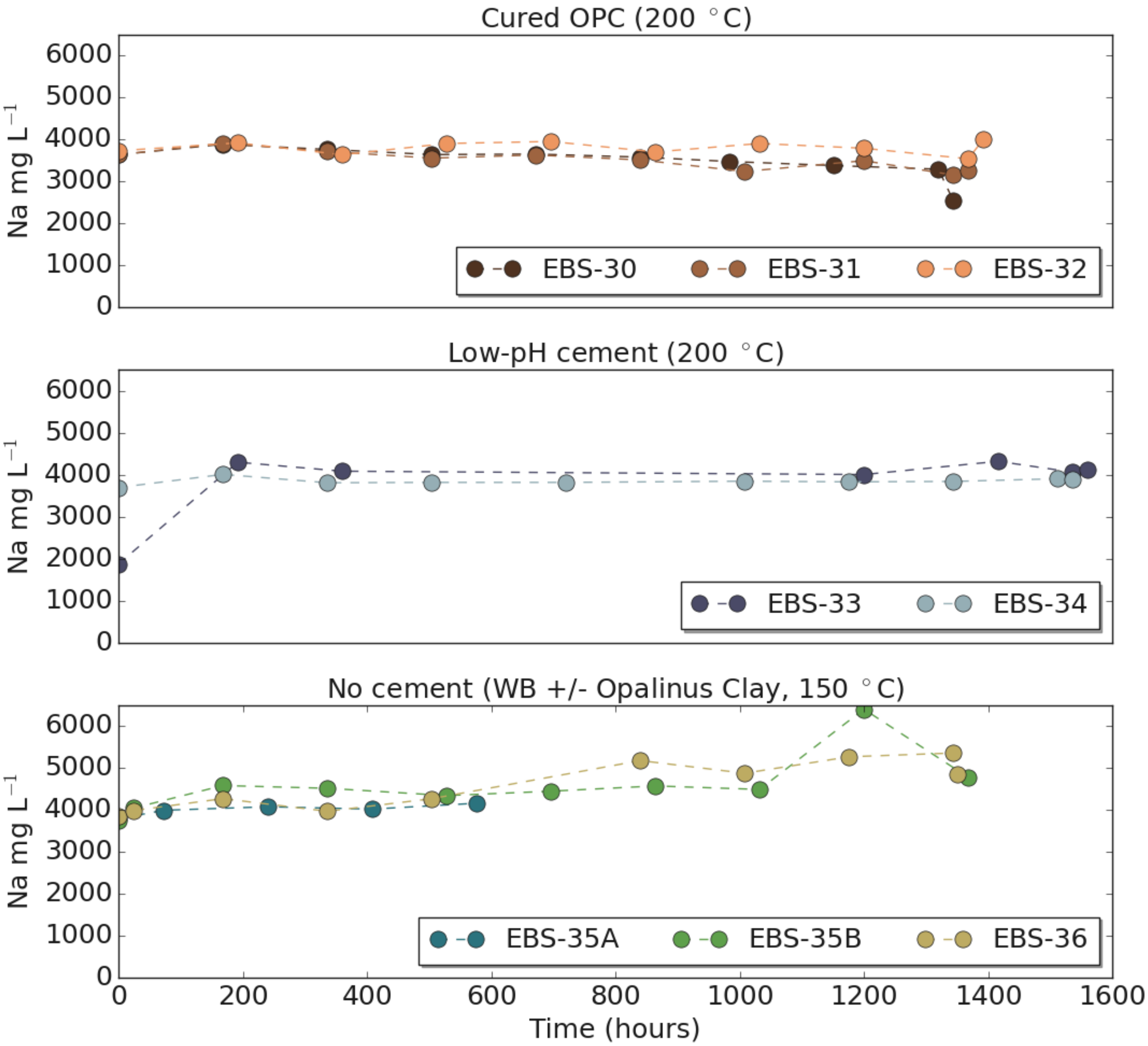

Figure 7. Sodium concentrations throughout the experimental durations of experiments EBS-30 through EBS-36.

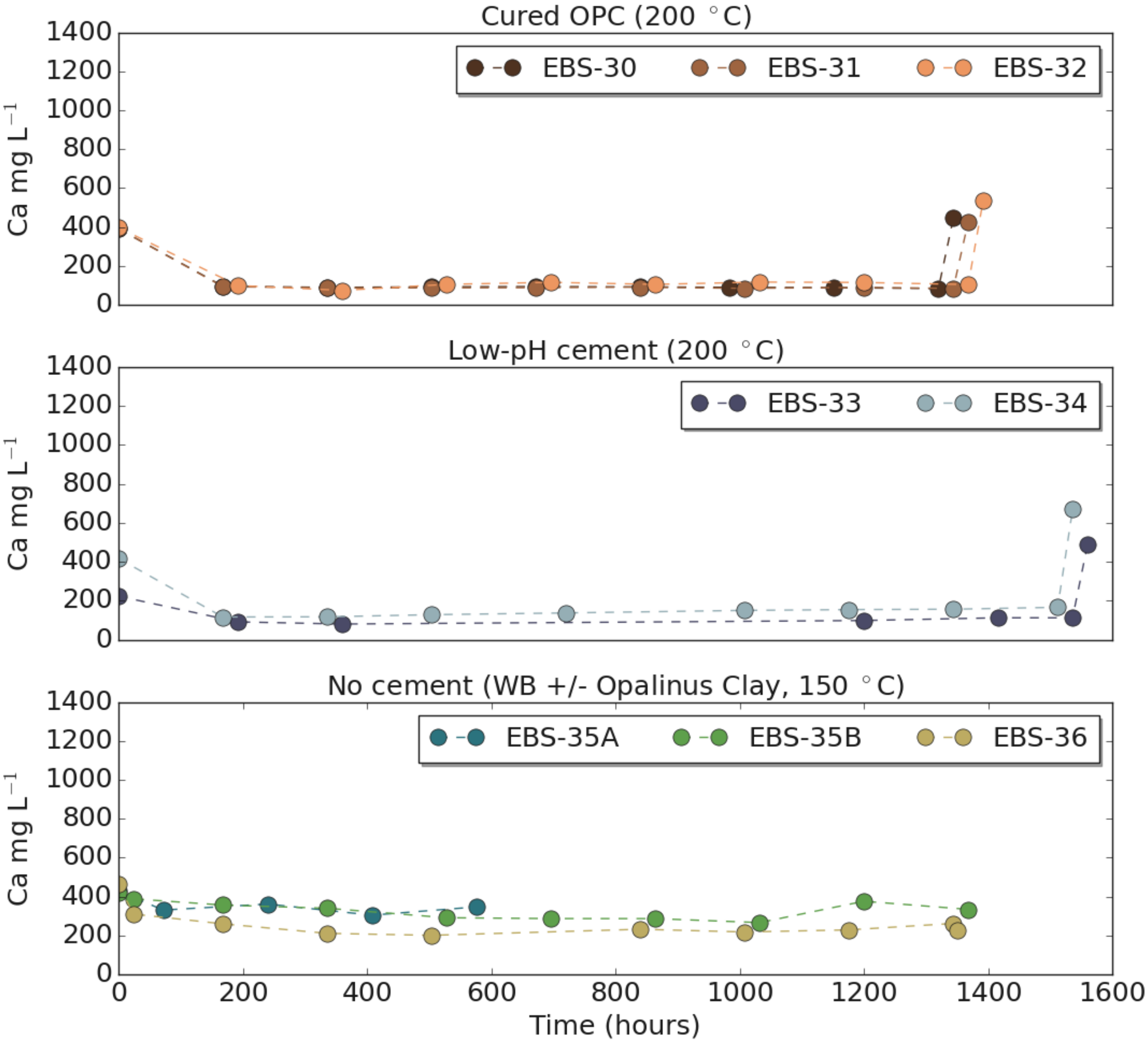

Figure 8. Calcium concentrations throughout the experimental durations of experiments EBS-30 through EBS-36.

3.1.5 Chloride

In the experiments with cured OPC cement chips (EBS-30, -31, and -32), chloride concentration values generally decreased to ~5000 mg L^{-1} by the end of the experiment. In the experiments with low-pH cement chips (EBS-33 and -34). Cl$^-$ behaved conservatively, remaining at a relative steady-state at ~6000 mg L^{-1}. In contrast, Cl$^-$ concentrations in the low-temperature experiments completed in FY23 increase slightly throughout the 8-week experiments (EBS-35B and -36), from an initial concentration of ~6500 to final concentrations of ~7000 mg L^{-1}. No trend of increase or decrease in chloride concentration was evident from the data collected over the 4-week experiment (EBS-35A), given the short time span and few samples collected. In the 8-week experiments EBS-35B and -36, Cl$^-$ concentrations increased slightly over the experimental durations (Figure 9).

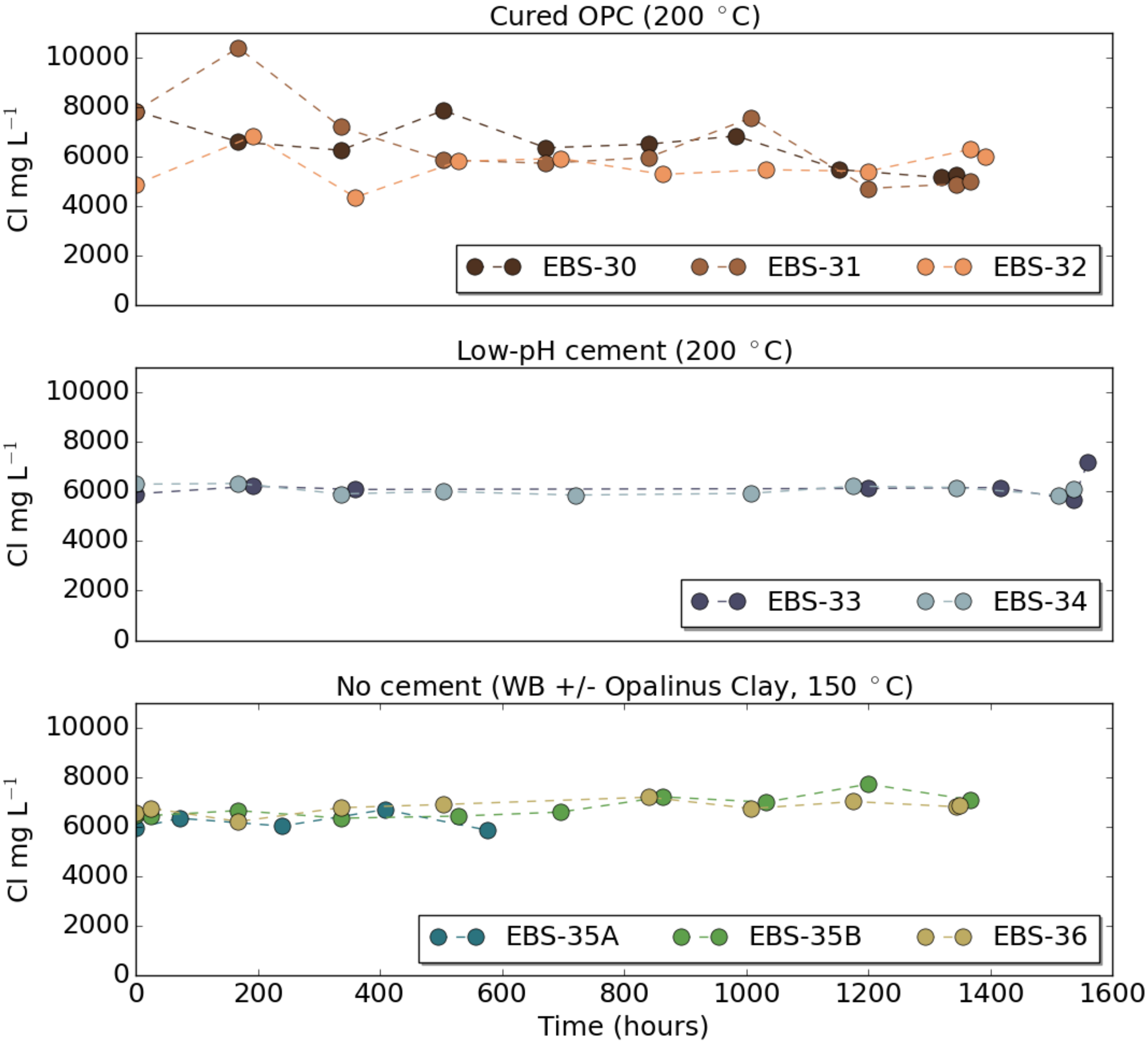

Figure 9. Chloride concentrations (measured as Cl$^-$) throughout the experimental durations of experiments EBS-30 through EBS-36.

3.1.6 Sulfate

In each of the cured OPC and low-pH cement chip experiments (EBS-30 through -34) reacted at 200 °C, sulfate decreased within the first week and generally remained around 150 mg L^{-1}. In all experiments, sulfate concentrations were highest in the initial and final quench samples, collected at 25 °C (Figure 10). In EBS-35A (WB and Opalinus Clay reacted at 150 °C; completed in FY23), sulfate concentration decreased over the 4-week duration. In contrast, sulfate concentrations remained relatively stable throughout the 8-week durations of EBS-35B and -36. Quench samples from the 150 °C experiments completed in FY23 also did not have sulfate concentrations that were higher than the last samples taken before quench in any of those experiments.

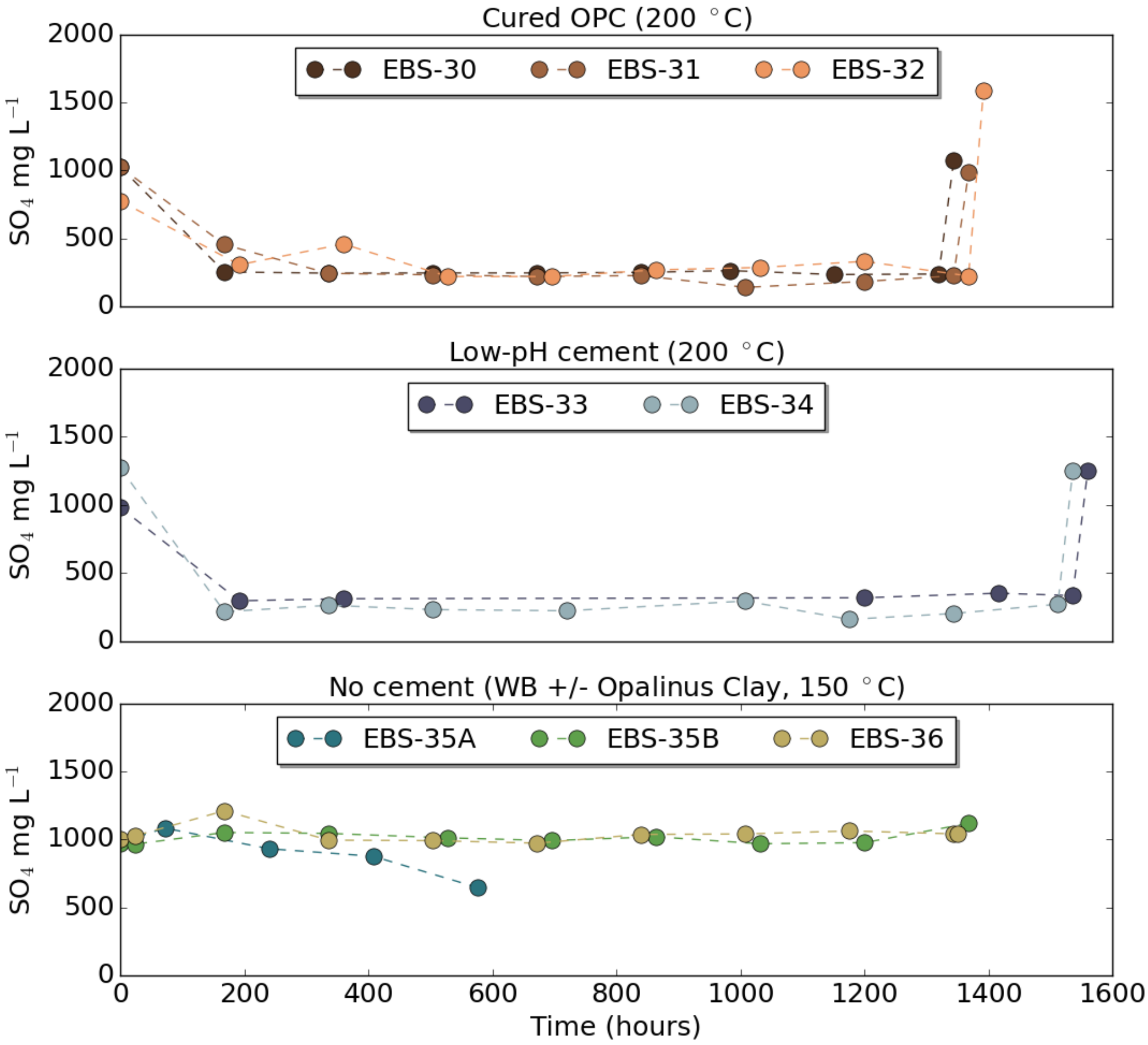

Figure 10. Sulfate concentrations (measured as SO_4^{2-}) throughout the experimental durations of experiments EBS-30 through EBS-36.

3.2 X-Ray Fluorecence (XRF) Analyses

Previous years' results

The XRF analyses for bulk rock oxide chemistry were performed on unreacted starting materials and bulk reaction products (Appendix D, Table D-1, Caporuscio et al. (2023)).

The Wyoming bentonite + Opalinus Clay + cured OPC chip experiments (EBS-30 to -32) only differed in the stainless-steel type used. Measured weight percent oxide values were consistent between the three experiments. There were only slight variations in Fe_2O_3 and loss of ignition (LOI). In comparison to the starting mixture chemistry, weight percent CaO decreased.

The XRF results for the Wyoming bentonite ± Opalinus Clay + low-pH cement chip experiments (EBS-33 and -34) varied in the measured weight percent oxide values due to the absence of

Opalinus Clay in EBS-33. Compared to unreacted Wyoming bentonite, EBS-33 had increased CaO and Fe_2O_3 with decreased SiO_2 and Al_2O_3. EBS-34, compared to the calculated 80:20 Wyoming bentonite to Opalinus Clay XRF, mostly differed in Fe_2O_3 due to the addition of an Fe°/Fe_2O_3 redox buffer to the experiment.

FY23 results

The Wyoming bentonite + Opalinus Clay (EBS-35A & -35B, four and eight weeks respectively) experiments varied from the unreacted material most noticeably in the Fe_2O_3 content due to the addition of redox buffers. Between the two experiments, the four-week experiment had a slight increase in Na_2O, whereas the eight-week experiment experienced an increase in MgO (Appendix D, Table D-2, Carporuscio et al. 2023).

The XRF results from the 150 °C Wyoming-only experiment are consistent with that of the unreacted Wyoming bentonite. The only major difference is the increase in Fe_2O_3, like all the previous experiments, from the addition of redox buffers.

3.3 Quantitative X-Ray Diffraction (QXRD)

Previous years' results

QXRD results from the solid phases of EBS-30 to EBS-32 (excluding cement: see Methods Section 2.2.1) show that the reaction of cured OPC chips resulted in modest alteration to the clay matrix at 200 °C (Figure 11, Table C-1 1in Caporuscio et al., 2023). Combined smectite + illite + smectite-illite comprised 59 to 78 wt.% of the reacted samples, and the patterns indicate that mixed layer phases are not abundant (i.e., the prominent peak at 6° 2 theta). Detailed clay mineral XRD analyses are presented in the following section (3.5) that support this observation. Zeolite minerals, CSH minerals, and amorphous material were also identified (Figure 11).

QXRD results from experiments with low-pH cement chips (EBS-33 and EBS-34) indicate that newly formed phases in the reaction products were dominantly of the clintoptilolite-heulandite solid solution series. Clay mineral bulk abundance is 54 wt.% and 67 wt.% in the two experiments.

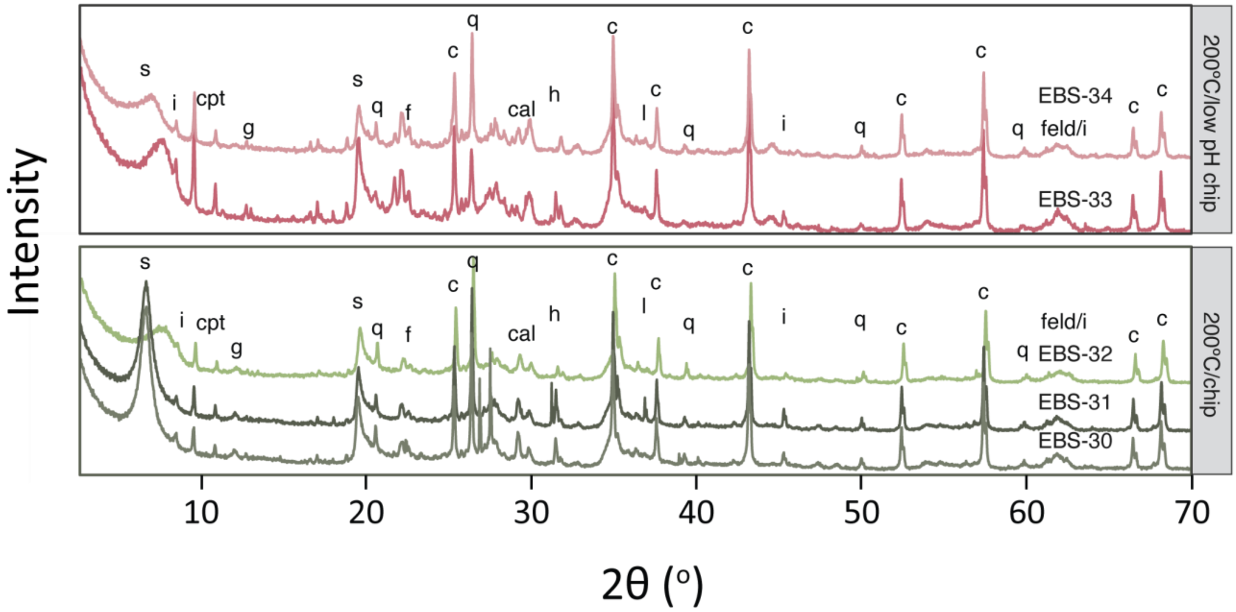

Figure 11. QXRD pattern of the bulk post-reaction products from the cement experiments. Peaks corresponding to corundum (c), smectite (s), illite (i), clinoptolite (cpt), calcite (cal), quartz (q), garronite (g), feldspar (f/feld).

FY23 results

QXRD results from the bulk reaction product mineralogy from the unreacted Wyoming bentonite and the EBS experiments for FY23 are shown in Table 3 and Figure 12.

In the experiments with Wyoming bentonite and Opalinus Clay (EBS-35A and -35B), new phases in the reaction products are magnetite and halite, most likely from the addition of buffers and from the saline synthetic groundwater, respectively. The reacted Wyoming bentonite + Opalinus Clay experiments had a reduction of clinoptilolite, mica, and kaolinite/chlorite when compared to the unreacted results. Conversely, the reacted products had a greater amount of the feldspar and plagioclase fractions. These differences may be explained by sample variation in the Wyoming bentonite and/or Opalinus Clay.

The QXRD results from EBS-36 (Wyoming bentonite-only at 150 °C) also had the additional phases of magnetite and halite from the buffer and synthetic groundwater, respectively, like the previous EBS-35 experiments. Compared to the unreacted Wyoming bentonite, there was a slight decrease in the smectite content with an increase in the mica fraction. All other differences are likely due to sample variation in the Wyoming bentonite.

Table 3. Quantitative X-Ray Diffraction (QXRD) results of the unreacted starting materials and the post-reaction products from experiments completed in FY23.

	WB 80 : OPA 20	**EBS-35A**	**EBS-35B**	**Wyoming Bentonite**	**EBS-36**
Non-Clay					
Quartz	4.5	4.8	5.4	1.5	3.2
Feldspar	2.4	2.7	3.0	0.7	0.9
Plagioclase	9.4	12.0	9.0	6.2	3.3
Pyrite	0.5	0.4	0.8	0.2	
Calcite	4.0	1.3	0.4		
Halite		0.9	0.9		1.7
Clinoptilolite	7.1	3.3	6.9	13.0	12.2
Cristobalite	3.6	0.8	0.5	1.5	2.7
Magnetite		3.8	3.7		2.6
Amorphous	4.0	5.3	2.7		5.7
Clay					
Smectite + Illite + Smectite-Illite	57.3	59.5	62.1	71.0	60.2
Mica	4.6	1.9	2.4	3.8	6.3
Kaolinite/Chlorite	2.7	3.4	2.2	2.0	1.2
SUM	**99.7**	**100.0**	**100.0**	**100.0**	**100.0**

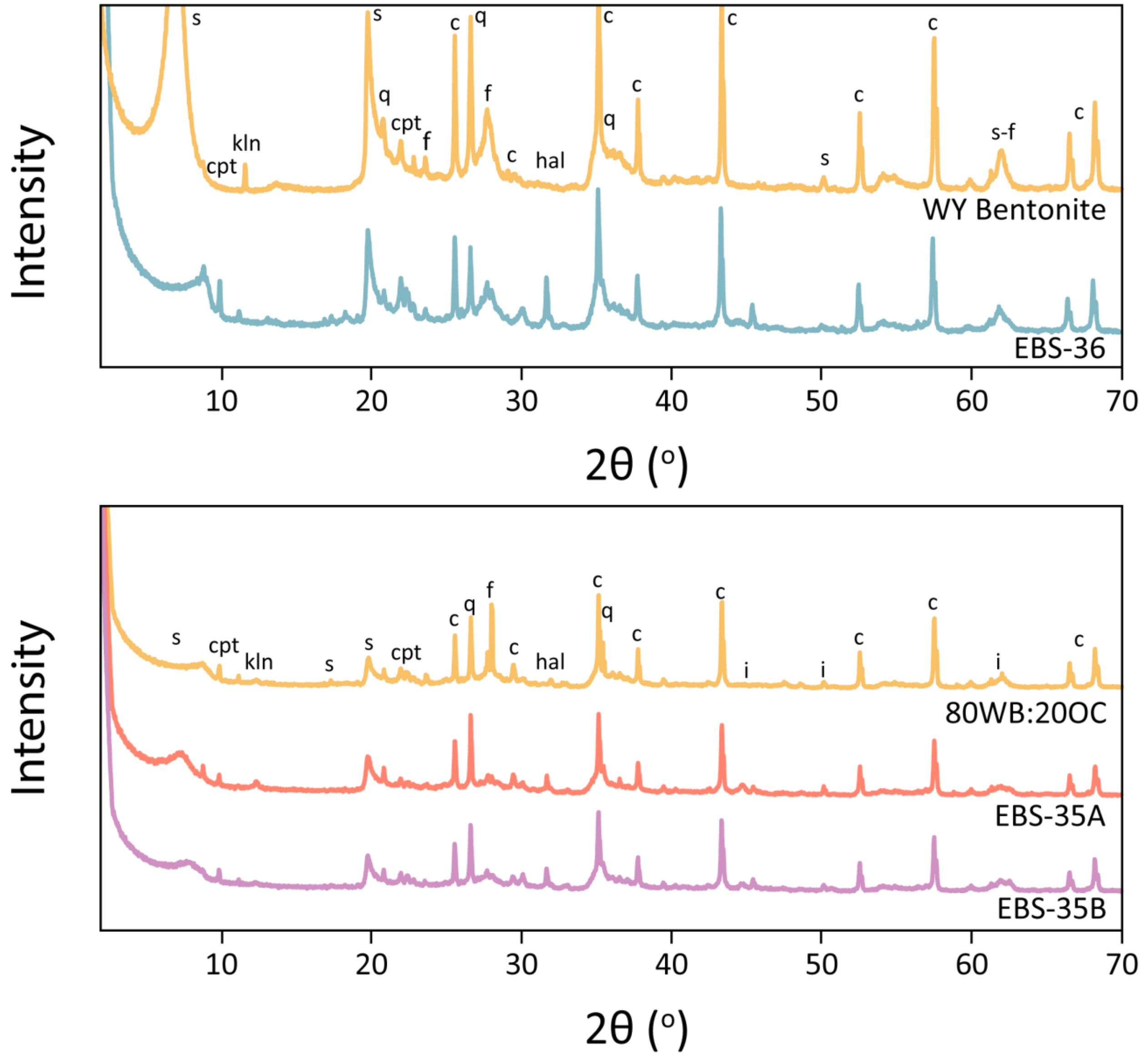

Figure 12. QXRD pattern of the bulk post-reaction products from the cement experiments. Peaks corresponding to corundum (c), smectite (s), illite (i), clinoptolite (cpt), halite (hal), quartz (q), feldspar (f), kaolinite (kln).

3.4 Clay XRD

Previous years' results

The clay fractions of EBS-30, EBS-31, and EBS-32 show slight shifts in ethylene glycol-saturated smectite peak positions, indicating a decrease in swelling capacity (Table 4). Interlayered illite is only detected in EBS-30, in which 1 to 5% interlayered illite is indicated by the difference between the 002 and 003 glycolated smectite peaks.

In the low-pH cement experiments (EBS-33 and EBS-34), smectite peaks similarly do not show significant shifts in position. The formation of ~1% illite interlayers is indicated in EBS-33.

Other secondary mineral peaks (e.g., zeolite, CSH) are not observed in the clay fraction XRD patterns for either cement chip type. Calcite is observed in the < 2 µm fraction of all samples.

Table 4. Glycolated smectite (GS) peak positions for the < 2 µm clay fraction separated from the Opalinus Clay–Wyoming bentonite experiments (EBS -30 to -34). Expandability and %illite (%I) were calculated based on the difference in position between the 002 and 003 glycolated smectite peaks.

EG-smectite	**001**		**002**		**003**		**002/003**	**1**	**2**	**3**	
Sample	**d (Å)**	**2θ**	**d (Å)**	**2θ**	**d (Å)**	**2θ**	**Δ 2θ**	**%Exp**	**%Exp**	**%Exp**	**%I**
WY Bentonite	17.0	5.2	8.5	10.4	5.7	15.7	5.3	100	102	103	0
OPC Chip											
EBS-30	16.7	5.3	8.4	10.5	5.6	15.8	5.3	96	87	98	1-5
EBS-31	16.8	5.3	8.5	10.5	5.6	15.7	5.3	99	101	101	0
EBS-32	16.8	5.3	8.4	10.5	5.6	15.8	5.3	99	100	101	0
Low-pH Cement Chip											
EBS-33	16.9	5.2	8.5	10.4	5.6	15.7	5.3	98	99	100	1
EBS-34	16.6	5.3	8.4	10.5	5.6	15.8	5.3	100	102	102	0

1: %Exp = 973.76 – 323.45Δ + 38.43Δ2 – 1.62Δ3 (Eberl et al., 1993)

2: %Exp = 1517.8 – 548.49Δ + 68.35Δ2 – 2.90Δ3 (Eberl et al., 1993)

3: %Exp = 766.01 – 194.10Δ + 12.924Δ2 (Moore and Reynolds, 1997)

FY23 results

Peak positions from EBS-35A through -36 are similar to those of the ethylene glycol-saturated smectite peaks of unreacted Wyoming bentonite (Table 5, Figure 13). The calculated expandabilities, based on the difference between the d002 and d003 peaks, from these samples show an increase in clay expansion in EBS-35B. In comparison, EBS-35A and -36 show slightly lower expandabilities.

Table 5. Glycolated smectite (GS) peak positions for the < 2 µm clay fraction separated from the Opalinus Clay–Wyoming bentonite experiments (EBS -35A, -35B, and -36). Expandability and %illite (%I) were calculated based on the difference in position between the 002 and 003 glycolated smectite peaks.

EG-smectite	**001**		**002**		**003**		**002/003**	**1**	**2**	**3**	
Sample	**d (Å)**	**2θ**	**d (Å)**	**2θ**	**d (Å)**	**2θ**	**Δ 2θ**	**%Exp**	**%Exp**	**%Exp**	**%I**
WY Bentonite	17.0	5.2	8.5	10.4	5.7	15.7	5.3	100	102	103	0
EBS-35A	5.24	16.85	10.44	8.47	15.70	5.64	26.64	3.34	5.26	100	102
EBS-35B	5.22	16.91	10.42	8.48	15.64	5.66	26.66	3.34	5.22	102	104
EBS-36	5.24	16.86	10.40	8.50	15.68	5.65	26.24	3.39	5.28	99	100

1: %Exp = 973.76 – 323.45Δ + 38.43Δ2 – 1.62Δ3 (Eberl et al., 1993)

2: %Exp = 1517.8 – 548.49Δ + 68.35Δ2 – 2.90Δ3 (Eberl et al., 1993)

3: %Exp = 766.01 – 194.10Δ + 12.924Δ2 (Moore and Reynolds, 1997)

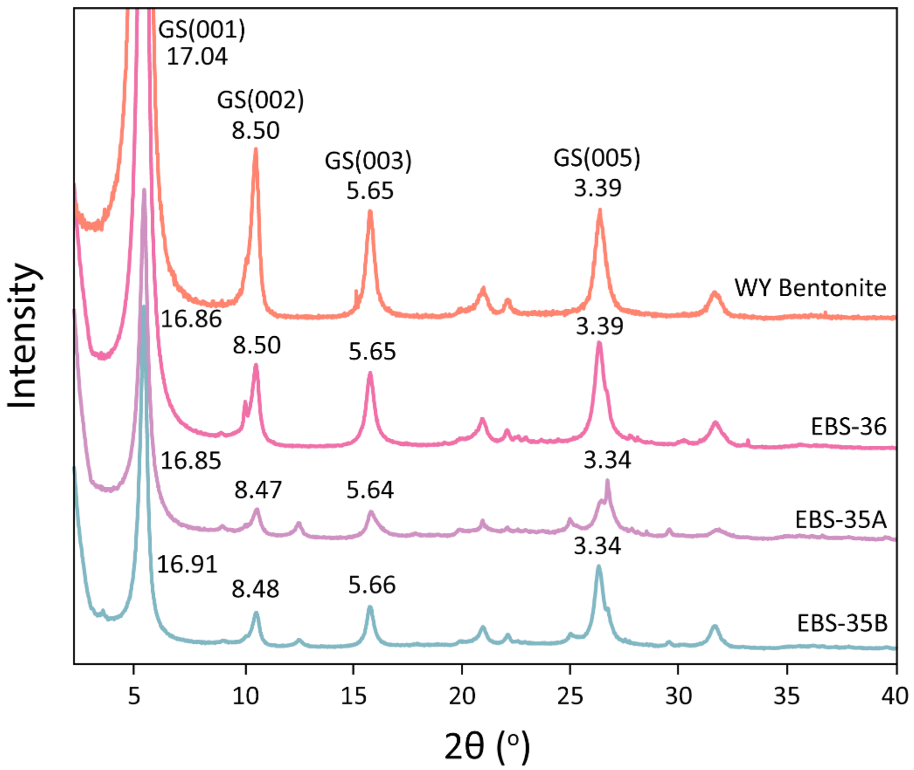

Figure 13. XRD patterns of the oriented and ethylene glycol saturated < 2 µm clay fraction from the clay groundmass of the FY23 experiments to unheated Wyoming bentonite.

3.5 Cement Chip XRD

Previous years' results

The surfaces of cement reacted in EBS-30 through -32 (OPC chips) and in EBS-33 and -34 (low-pH cement) chips were analyzed with XRD (Figures 14 and 15, respectively). Unreacted OPC and low-pH cement chips were also analyzed by XRD as a comparison. The resulting patterns show that mineral reactions occurred at the chip surface, consistent with other chemical analyses (specifically SEM-EDS). The unreacted OPC chip is characterized by portlandite with calcite and belite (calcium silicate mineral). The reacted OPC chip patterns are dominated by calcite with lesser smectite and hydrated CSH minerals (Figure 14). The mineralogy of the unreacted low-pH cement chip is characterized by riversideite and calcite with brownmillerite, silicon dioxide and anhydrite. The low-pH cement, reacted in EBS-33 and -34, showed riversideite and calcite with silicon dioxide still present with the addition of zeolite and smectite (Figure 15).

FY23 results

No experiments completed in FY23 used cement as a reactant.

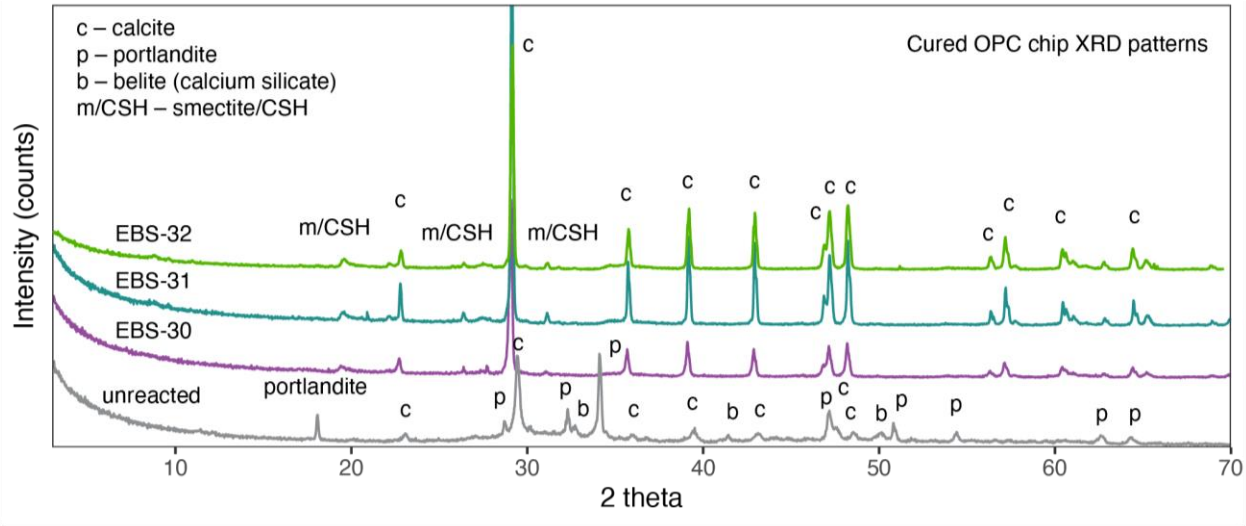

Figure 6 XRD pattern on the unreacted and reacted OPC chip from EBS-30 through -32.

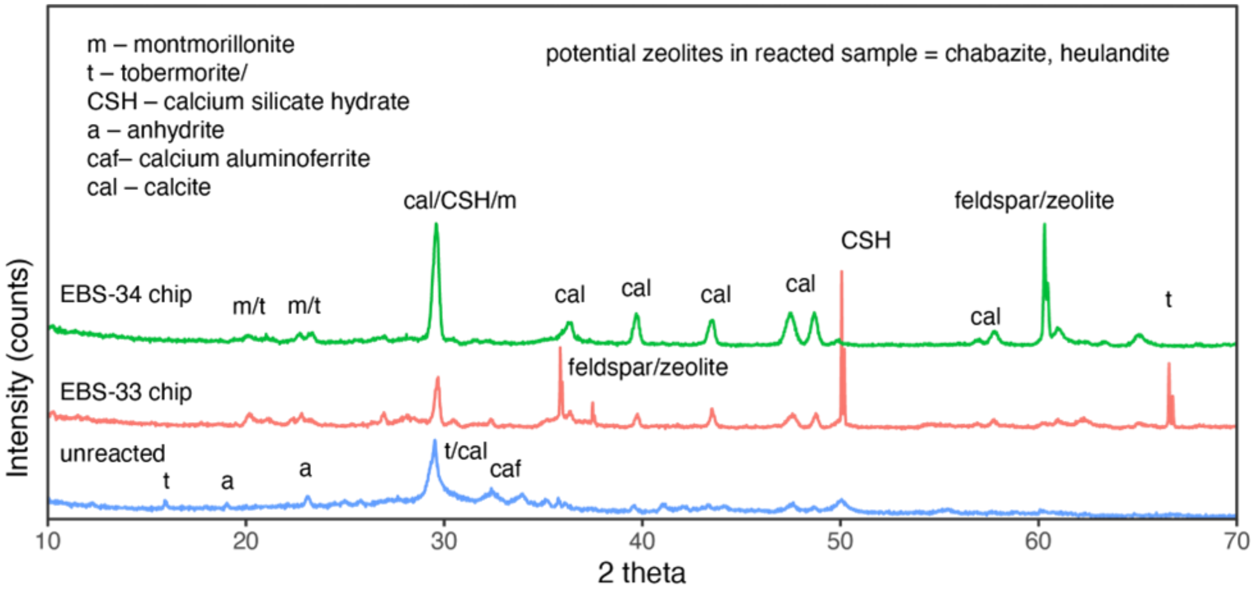

Figure 15. XRD patterns of the surfaces of the unreacted and reacted (EBS-33 and EBS-34) low-pH cement chips.

3.6 EMP

Previous years' results

Solid reactants from experiments completed in previous years were analyzed by EMP in FY23 to isolate quantitative chemistries of reaction products. Thin sections were prepared from clay and cement reactants, and epoxy mounts were prepared for metal (steel) reactants. Focus was placed on reaction products formed at the interfaces between reactants (i.e., at the steel-clay or cement-clay boundaries). Data reduction and interpretation is ongoing and will be included and discussed in the FY24 report.

FY23 results

EMP analyses on samples from experiments completed in FY23 will be performed in FY24.

3.7 SEM-EDS

Previous years' results

EBS-30 through EBS-32 reacted WB with OPC and three different types of steel (316SS in EBS-30; 304SS in EBS-31; and LCS in EBS-32). The smectite from the WB matrix as reacted in all experiments was largely preserved and exhibited a foily texture (Figure 16a). Minor calcite (secondary) and plagioclase phenocrysts were also found embedded in the smectite (for example, EBS-31 in Figure 16b). A spherical mineral, chemically consistent with a lime or CSH phase, was also observed sporadically throughout the WB matrix reacted in EBS-31. Gypsum or anhydrite was observed, as illustrated here in the WB matrix reacted in EBS-32 (Figure 16c). The OPC chips reacted in all experiments were identified to be heterogeneously coated with C(A)SH gel, calcite (as shown in Figure 16d-f), and minor smectite. SEM-EDS analyses also identified similar types of minerals and alteration products at the surface of the three different types of steel reacted in EBS-30 through 32. The surface of the 316SS reacted in EBS-30 was coated with smectite with large gypsum crystals (~100-300 µm in length, Figure 16g), and Fe-saponite was observed on the steel coupon (Figure E-4). Fe-saponite also formed a honeycomb texture on the 304SS steel from EBS-31, and (Fe,Cr,Ni) oxides were identified directly adjacent to the steel. Minor amounts of smectite were also observed at the steel surface (Figure 16). The LCS reacted in EBS-32 was covered in an Fe-saponite mat (Figure 16) with minor amounts of a platy, randomly oriented growth of Fe-oxide on portions of the surface (Figure 16). Comparisons between the types of steel alteration and steel-bentonite interface mineralization are discussed at length in (Cheshire et al., 2014; Sauer et al., 2022).

EBS-33 and -34, completed in FY22, reacted WB with the low-pH cement material described in Section 2.2.1. Characterizations of the WB matrix as reacted in these experiments were similar to those of the WB reacted in EBS-30 through EBS-32, described above. SEM images collected of the bentonite matrix reacted in EBS-33 show a predominantly smectite-rich matrix with minor plagioclase and calcium carbonate. Smectite dominated the clay-bentonite matrix observed in the SEM images. In the WB matrix reacted in EBS-34, clinoptilolite was additionally noted in clusters along with minor anhydrite. The cement surfaces of the low-pH cement pucks reacted in both EBS-33 and -34 were coated with smectite intermixed with lesser amounts of calcite. Intact silica fume spheres were observed to be encapsulated in the surface of the cement puck after reaction in EBS-33, along with patches of CSH spheres (Figures E-14A, Appendix E, Caporuscio et al. 2023). The cement puck reacted in EBS-34 also had smectite preserved at the surface, along with lesser amounts of calcite and anhydrite embedded in the clay or directly on the cement surface (Figure E-16A).

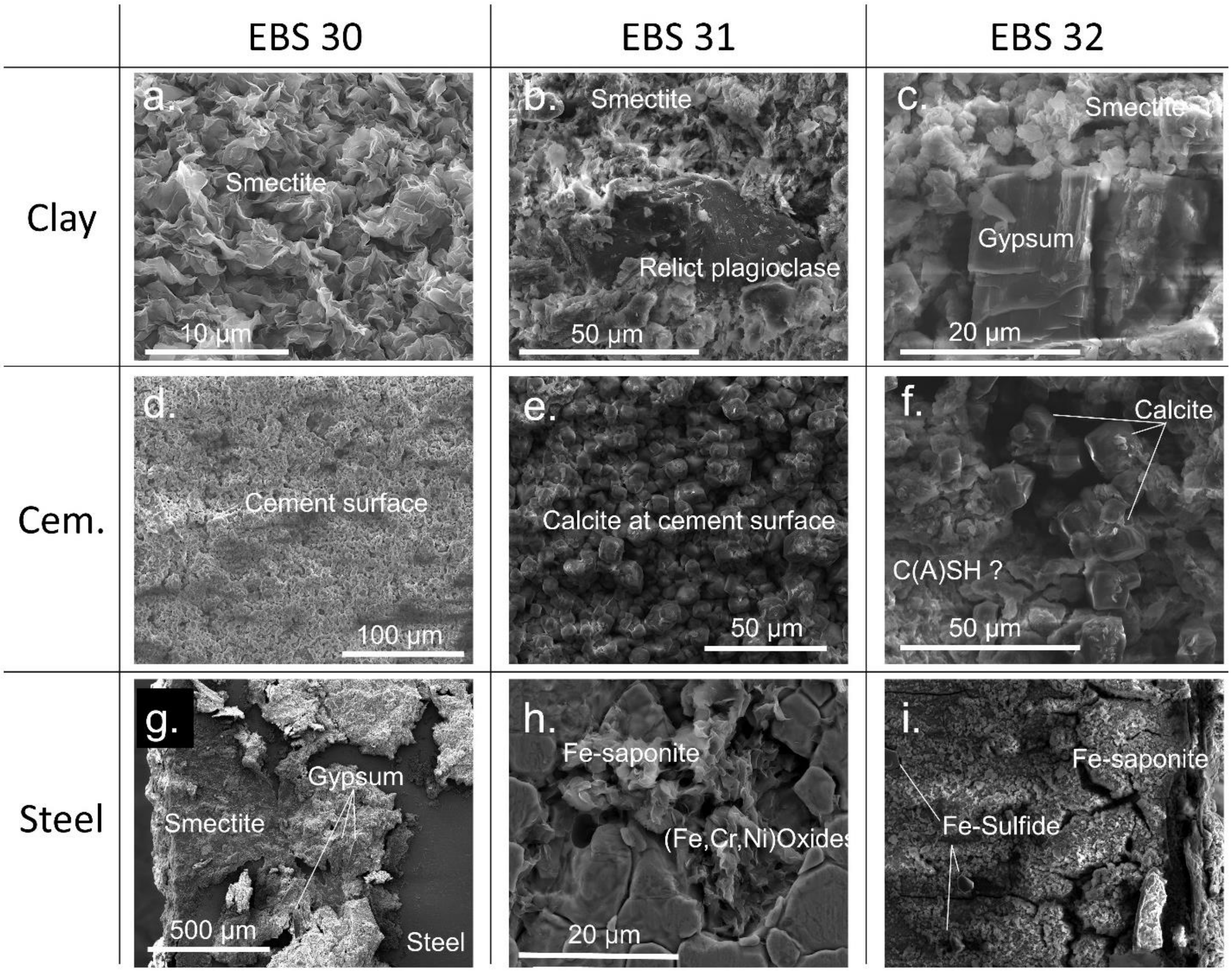

Figure 16. SEM micrographs of illustrating alteration of the solid reactants from experiments EBS-30 through -32. a-c show the minimal impact of hydrothermal conditions on the bentonite matrix. a. EBS-30: foily smectite texture after reaction; b. EBS-31: relict plagioclase embedded in the smectite matrix; c. EBS-32: gypsum formed in the smectite matrix. d-e show the OPC surfaces after reaction in each of the three experiments. g-i show the steel surfaces after reaction in each experiment, where g. shows the surface of 316SS reacted in EBS-30 and coated with bentonite matrix and gypsum crystals; h. images of Fe-clay (saponite) and (Fe,Cr,Ni) oxide alteration products at the surface of 304SS reacted in EBS-31; and i. shows the surface of LCS reacted in EBS-32 coated in Fe-saponite and Fe-sulfide alteration products. Where labeled, gypsum was identified through SEM-BSE characterization and may be anhydrite (c and g).

FY23 results

Bentonite reacted in EBS–35A had a foily texture in the matrix (Figure 17) and SEM-EDS results showed chemical composition ranges within the range compositions of unreacted WB. The same was true of the bentonite matrix reacted in EBS-35B and EBS-36. SEM analysis of the clays reacted in EBS-35A, EBS-35B, and EBS-36 also revealed few alteration products distinctive to the hydrothermal interaction of the WB with Opalinus Clay at 150 °C. After all experiments, we observed foily textures of smectite minerals in the bentonite matrix (Figure 17a-c) with isolated relict minerals. The bentonite matrices included very few isolated, apparently secondary products (specifically isolated pyrrhotite and possible evaporite (NaCl) minerals identified embedded in the bentonite matrix reacted in EBS-35B, Figure E-19B).

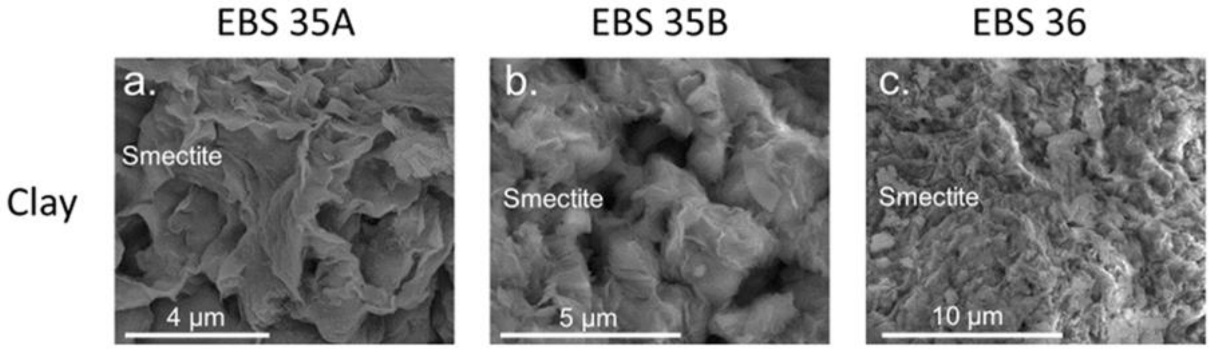

Figure 17. Foily texture of bentonite reacted at 150 °C. a. Smectite reacted in EBS-35A; b. Smectite reacted in EBS-35B; c. smectite reacted in EBS-36.

4. Discussion

Experiments discussed in this report are designed to characterize hydrothermal reactions of EBS materials with the synthetic Opalinus Clay groundwater solution. The anticipated results included dissolution and precipitation or re-precipitation of minerals in the solid phase and corresponding fluctuations in the solution chemistry. The solution used in these experiments was selected to emulate water in equilibration with the Opalinus Clay at in-situ conditions, and as such evolved to a new steady-state chemistry during interaction with the EBS reactants included in the reaction cells and with heating to an elevated temperature. The inclusion of cured Wyoming bentonite and cement reactants resulted in aqueous chemistry trends reflective of the chemistry of and stability of those reactants. In addition, specific experimental temperatures (200 or 150 °C) also affected the observed aqueous geochemistry changes. Notable implications of these factors on selected aqueous geochemistry trends over the experimental durations are detailed below.

4.1 Aqueous Geochemistry

4.1.1 pH

The pH values (as measured at bench conditions, 25 ºC and 0.1 MPa) in experiments EBS-30, -31, and -32 that reacted OPC chips at 200 ºC had an increasing trend over time from pH ~6 to pH ~6.5-8. Increases in pH are expected from the equilibration of ordinary Portland cements with water, as is introduced in detail in the Introduction (Section 1.1). Portlandite dissolution as a driver of increased pH is corroborated by the decreased portlandite in the XRD pattern of the reacted mixture (Figure 11). The initial rapid increase in solution pH to ~9.5 is interpreted to be caused by rapid initial dissolution of Portlandite on interaction with water and heating. The pH evolution in experiments reacting low-pH cement chips at 200 ºC (EBS-33 and -34) was very similar to that of the OPC cement chip experiments, especially EBS-31 (Figure 4). Specifically, in the sample taken one week after experimental conditions were met, pH increased to > 9 (from the initial groundwater solution pH of ~7) before decreasing to pH ~6, then steadily increased again until reaching an apparent steady state pH of ~7.5 after ~1200 hours. We note that the pH values of the samples collected from the bulk solution in these experiments do not necessarily reflect that of the pore water within or contacting the cements; however, the counterintuitive effect on bulk solutions is notable because of the interest in using low-pH cement as a cement medium that develops lower porewater pH than traditional ordinary Portland cements.

Measured pH from the three experiments completed in FY23 indicate that solution in contact with WB and Opalinus clay stabilizes at circumneutral pH conditions at 150 ºC. The pH-buffering effect of WB is anticipated to be the reason for the decreased pH after the initial increase seen in the results from the OPC and low-pH cement alteration experiments.

4.1.2 Silica Saturation

Silica saturation is known to be a major factor in the hydrous alteration of EBS materials (Smyth, 1982; Bish and Aronson, 1993; Neuhoff and Ruhl, 2006; Cheshire et al., 2014). Evaluating saturation with respect to selected silicate minerals shows groupings based on the reactants in the experiments at 200 ºC (EBS-30, -31, and -32). The OPC experiments appeared to reach a steady-state silica concentration after 1000 hours of reaction time as opposed to the low-pH cement experiments (Figure 5). The OPC experiments also have higher silica concentrations that approach thermodynamic stability with respect to quartz compared to their low-pH counterparts. It is notable that the low-pH cement has a higher silica content than that of the OPC chip; however, solutions interacting with the low-pH cement chips do not have higher rates of silica increase or higher silica concentrations after 1000 hours as compared to the OPC experiments.

The difference in silica saturation between EBS-33 and -34 may indicate the input of Opalinus Clay wall rock in controlling the solution chemistry and specifically silica concentrations. EBS-33 is the sole cement experiment that excluded Opalinus Clay as a reactant and thus can be directly compared to the EBS-34 experiment, which is identical except for the inclusion of Opalinus Clay as a reactant. Without the controlling influence of the mineral assemblage in the Opalinus Clay, the mineral assemblage in the low-pH cement appears to approach a different steady-state silica concentration even as the bulk solutions in the experiments are at similar pH. This highlights the need for more analyses of mineral reaction pathways specific to hydrous alteration of low-pH cements and their controlling influence on local solutions, especially at elevated temperatures.

4.1.3 Quench Reactions

Geochemical conditions in the experiments described here were designed to explore disequilibria of the system with respect to the same reactants at bench conditions. For this reason, cooling and depressurizing the experiments to bench conditions at experiment termination may cause changes to the solid assemblage even over the brief (<8 hour) quench periods of our experiment design. The depressed concentrations of Ca and SO_4^{2-} during the duration of the experiments completed at 200 ºC, compared to that of the initial solution chemistry and quench samples, is interpreted as evidence of calcium sulfate formation in the experiments that then partially dissolved during quench. Minor amounts of gypsum and anhydrite were identified by SEM in the clay matrix and at the steel surfaces of select experiments. Anhydrite was also identified at the low-pH cement chip surfaces from surface XRD. From the aqueous chemistry evidence, we posit that these phases were more abundant in the reaction cell before the quench.

Comparing the trends observed in the 200 ºC experiments to those heated to 150 ºC gives additional insight. Specifically, the steady-state Ca and SO_4^{2-} concentrations in the lower-temperature experiments (EBS-35A, -35B, and -36) were not substantially depressed compared to the concentrations in the initial fluid chemistry and were not increased in the quench samples from those experiments. No calcium sulfate minerals were identified in the matrix by SEM-EDS or XRD. Combined, these results suggest that during a heating event, formation of calcium sulfates responsive to decreased stability at elevated temperature will be largely reversible during cooling. Extensive formation of anhydrite is not expected to occur at heating events of 150 ºC, and back-reactions that dissolve anhydrite formed at higher temperatures (~200 ºC) may occur at continued elevated temperatures (~150 ºC) and before the system returns to ambient temperatures. Below ~130 ºC, calcium concentrations are expected to be controlled by calcite solubility (Figure 18) which will drive continued dissolution of calcium sulfate phases by depressing the bulk calcium concentrations with respect to the solubility of calcium sulfates, especially high-temperature phases such as anhydrite.

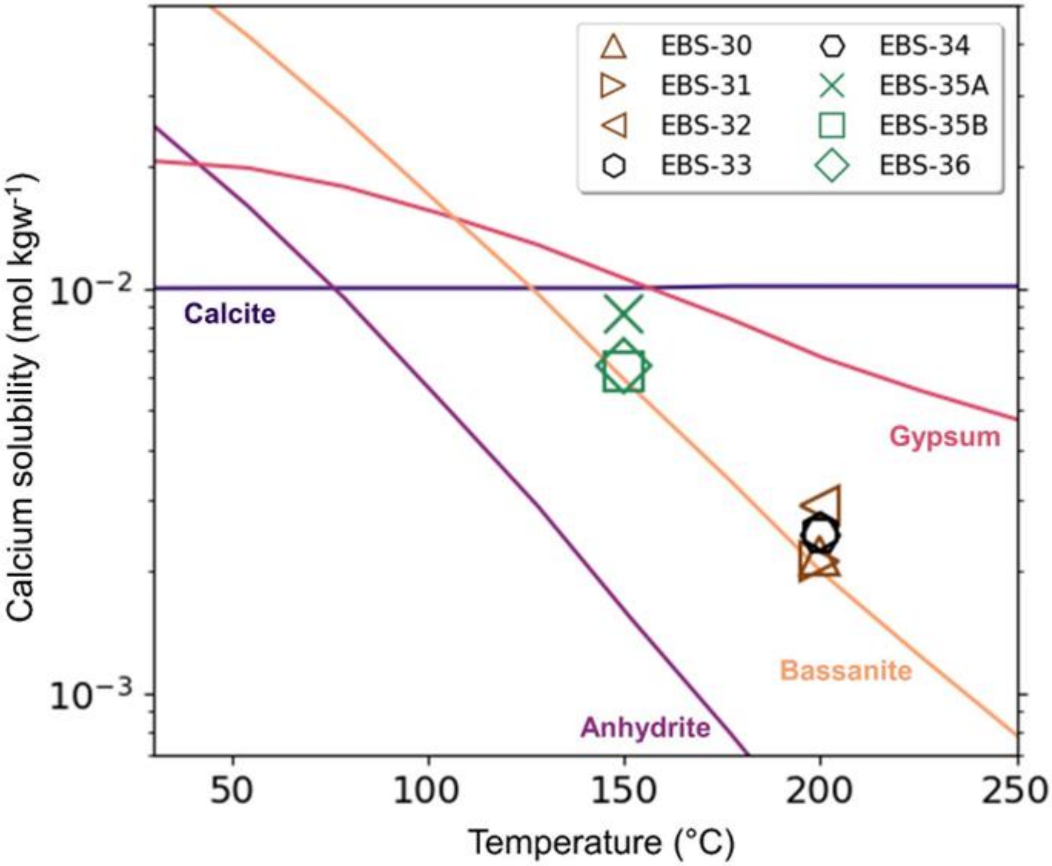

Figure 18. Calcium solubility (in moles per kilogram water). Curves indicate the calcium concentration in thermodynamic equilibrium selected minerals of interest (calcite and calcium sulfate minerals anhydrite, bassanite, and gypsum) at the pH and background electrolyte conditions of the initial fluid chemistry Opalinus GW. Areas above a curve indicate calcium oversaturation with respect to that mineral, and areas under a curve indicate undersaturation. Markers indicating calcium concentrations for each experiment are from the first samples collected after 1000 hours of reaction time (brown → OPC chips; black → low-pH cement chips; green → no cement). The marker plotted for EBS-35A is the concentration of the last sample before experimental failure at ~580 hours.

4.2 Cement Alteration

In the experiments that included cured OPC chips (EBS-30 through -32), the reacted OPC chip surface was predominately calcite with smectite and hydrated calcium silicate minerals (CSH), a change from portlandite with calcite and belite on the unreacted OPC surface. The carbonation of calcium hydroxide to calcium carbonate occurs from the following well known reaction:

$$Ca(OH)_2 + CO_2 + H_2O \rightarrow CaCO_3 + 2H_2O \qquad (6)$$

The carbonation of the calcium hydrate, portlandite, to calcium carbonate, calcite, causes the cement to lose alkalinity and subsequently lowers the pH of the cement and the aqueous solution (Figure 4). In addition, the volume change from this mineral transition may help to fill pore space in the cement resulting in a lower porosity.

The low-pH cement chips included in EBS-33 and -34 still retained the riversideite, calcite, and silicon dioxide observed on the unreacted low-pH cement chips, but the reacted cement chip had zeolites and smectite instead of brownmillerite and anhydrite. The results from the physical alteration of the low-pH cement experiment were part of a collaboration with Vanderbilt University (VU) and will be discussed in their future publications. No experiments completed in FY23 at lower temperatures included cement as a reactant.

4.3 Steel Corrosion

EBS-30 through EBS-32 reacted WB with OC, OPC, and three different types of steel (316SS in EBS30; 304SS in EBS31; and LCS in EBS32). These three experiments were replicates in pressure, temperature, WRR, and reactants except for the steel type, allowing analysis of the effect of steel type on alteration of interfacing minerals as well as an illustration of the effect of Opalinus Clay/Wyoming bentonite-controlled environment on the steel alteration. In general, the different types of steel used in the three experiments did not have different overall impacts on the fluid chemistry, the surrounding clay matrix, or on alteration of the OPC.

The steel acted as a substrate for new mineral growth in response to corrosion. New mineral growth was spatially restricted to ~< 50 µm rinds on the surface of the reacted coupon. Common to all three steel types was the formation of Fe-saponite. The distribution of Fe-saponite on the surface of the steel coupons, however, was discontinuous, and sometimes only non-Fe enriched smectite was observed. Fe-saponite forms by the congruent dissolution/oxidation of steel (Eq 7) and reaction with the smectite component of bentonite (Eq 8). The reaction for stainless steel follows:

Stainless steel dissolution

$$Fe_{1.22}Cr_{0.37}Ni_{0.22} \rightarrow 1.22\ Fe^{2+} + 0.37\ Cr^{+} + 0.22\ Ni^{2+} + 3.99\ e^{-} \qquad (7)$$

Smectite evolution

$$Fe^{2+} + Ni^{2+} + Cr^{3+} + H_2S_{\ (aq)} + (Na,K,Ca)_{0.33}(Al_{1.67},Fe^{3+}{}_{0.20},Mg_{0.13})Si_4O_{10}(OH)_2\ \text{(smectite)} \rightarrow$$

$$(Fe,Ni,Cr)_9S_8\ \text{(pentlandite)} + (Na, K, Ca)_{0.33}Fe3(Si_{3.67},Al_{0.33})O_{10}(OH)_2\ \text{(Fe-saponite)} \qquad (8)$$

Accessory minerals and alteration products vary some between steel types, suggesting that steel composition may have minor effects on mineralization reactions. On 316SS, Fe sulfides and Cr oxides were common at the steel-bentonite interface as viewed in cross section, whereas in 304SS, iron sulfides, CaO, and some (Fe,Cr,Ni) oxides were identified in SEM images (Figures

E-4, -8, and -12, Appendix E, Caporuscio et al. 2023). Minerals identified on the surface of LCS include pyrrhotite, discontinuous layers of iron oxides, iron chlorides, and CaO (Figure E-12). Cr-oxides did not form on the surface of the LCS, since Cr is not an alloying element in LCS. The heterogeneous distribution of new mineral growth and alteration products suggests that alteration reactions reflect highly localized chemical environments. Other minerals identified on the steel-bentonite interface are likely derived from the bentonite clay matrix (plagioclase, biotite, apatite) or precipitated directly from the synthetic groundwater solution (halite, gypsum/anhydrite).

4.4 Clay Alteration

The clay fraction in experiments that contained cured OPC chips and low-pH cement chips had less evidence of mineralogical alteration than in the experiments with uncured OPC powder described in previous annual reports (i.e., Caporuscio et al., 2021; Sauer et al., 2022). For example, the combined smectite + illite + smectite-illite comprised 59 to 78 wt.% of the cement chip experiment versus 16 to 30 wt.% in the 200 ºC experiments containing uncured cement powder. Further, the patterns indicate that mixed layer phases were more abundant in the clay phases of experiments reacted with uncured cement powder. In addition, there was less zeolite, CSH minerals, and amorphous material observed in the QXRD results with the addition of the cement chip in comparison to uncured OPC powder. The difference in QXRD results of repeated experiments discussed in this and previous results give a quantitative view of the alteration that could be expected from introducing uncured cement in a generic argillaceous repository.

Low-temperature effects on Wyoming bentonite and Opalinus Clay demonstrated the stability of montmorillonite at 150 ºC. The smectite + illite + smectite-illite wt.% remained unchanged in the Wyoming bentonite + Opalinus Clay experiments, remaining around 60 wt.%. The Wyoming bentonite-only experiment saw a slight decrease in the combined smectite + illite + smectite-illite but may be attributable to composition differences in the starting material. In addition, the mineral structure was unaffected with the clay expandabilities similar to the unreacted Wyoming bentonite and the peak position suggest there is no interlayered illite present. The circum-neutral pH values of the system likely favor montmorillonite stability (Sauer et al., 2020).

5. Conclusions

The work in FY23 was designed to further develop concepts of bentonite alteration during a high-temperature event in an argillite-hosted repository. Three 4- to 8-week experiments (EBS-35a, EBS-35b, and EBS-36) were completed reacting Wyoming bentonite ± Opalinus clay wall rock in a synthesized Opalinus clay groundwater solution at 150 ºC. Characterization was completed for experiments run during FY21 and FY22, and started for the experiments finished this FY. This report presents new results and interpretations from our series of experiments with Opalinus Clay, Wyoming bentonite, steel, and cements (EBS-30 through EBS-34).

Concepts developed include:

- Bentonite stability in an argillaceous host rock at temperatures from 150-200 ºC.
- Findings that montmorillonite was stable over the experimental time period (4 to 8 weeks) at 150 °C in the circumneutral pH values and low bulk system K^+ aqueous concentrations expected in the environment of EBS systems.
- Recrystallization of montmorillonite to illite was not observed.

Future research will emphasize the following areas:

- Thermodynamic and kinetic modeling of the evolution of bentonite alteration at 150-200 °C and comparison to experimental results
- Studies of host rock alteration at low temperatures to evaluate influence on system chemistry.
- Conduct investigation into the physical properties of Fe-saponite and other mineral products observed at the steel-bentonite interface.

6. Argillite International Collaborations – Honorobe URL Research

6.1 Introduction

In 2000, Japan initiated a 20-year investigation on deep geologic disposal of high-level radioactive waste. Led by the Japan Nuclear Cycle Development Institute (JNC) and later the Japanese Atomic Energy Agency (JAEA), this effort has investigated disposal in both crystalline and argillite rock types. The first underground research laboratory (URL) was emplaced in a crystalline rock type located in Mizunami, Gifu, and a second URL emplaces in an argillite rock type located in Horonobe (Hokkaido). Recent full-scale experimental designs were presented at the DECOLOVEX 2023 meeting (JAEA, 2021).

In FY20, LANL compiled a literature review of the Japanese URL approach (Caporuscio et al., 2020). This overview presented literature focused on four main points: 1) regional geology of the western coastal plain of Hokkaido, northern Japan; 2) lithology of the Wakkanai and Koetoi Formations, the target URL repository horizon; 3) regional structural geology, such as faults and large-scale structures; 4) the water chemistry of the URL area. These points can be briefly summarized as follows:

1. Regional geology surrounding the Horonobe URL consists of a Quaternary alluvium and terrace deposit (Figure 19) overlying Tertiary and Cretaceous sedimentary rocks deposited in the Mesozoic Tenpoku Basin. Target horizons of the URL are the Wakkanai Formation that consists of mixed sandstone and mudstone and the overlying Koeti Formation which is dominantly diatomaceous mudstone (Ishii et al., 2010; Kunimaru et al., 2010).
2. The lithology of target horizons of the URL are the Wakkanai Formation that consists of mixed sandstone and mudstone and the overlying Koeti Formation which is dominantly diatomaceous mudstone (Ishii et al., 2010; Kunimaru et al., 2010). The marine diatomaceous deposits in particular contain highly siliceous sediments (Iijima and Tada, 1981).
3. The regional structural geology is dominated by several north-south trending anticlinal structures and two recognized fracture features (Kunimaru et al., 2010). The inactive Omagari Fault (reverse) is also in the URL vicinity, trending northwest to southeast, and was active until the early Quaternary period (Milodowski et al., 2004).
4. Hydrogeologic studies conducted for over ten years characterized groundwater samples from wells and pore waters extracted from cores. Analyses were focused on samples collected from the Wakkanai and Koetoi formations in the region of the Horonobe URL. Vertical and lateral salinity gradients have been attributed to the dilution of fossil

seawater followed by diagenetic water rock interactions. Vertical salinity trends suggest that shallow groundwaters are Na-HCO_3-rich fresh water while deeper groundwaters are saline and NaCl-dominated (Hama et al., 2007).

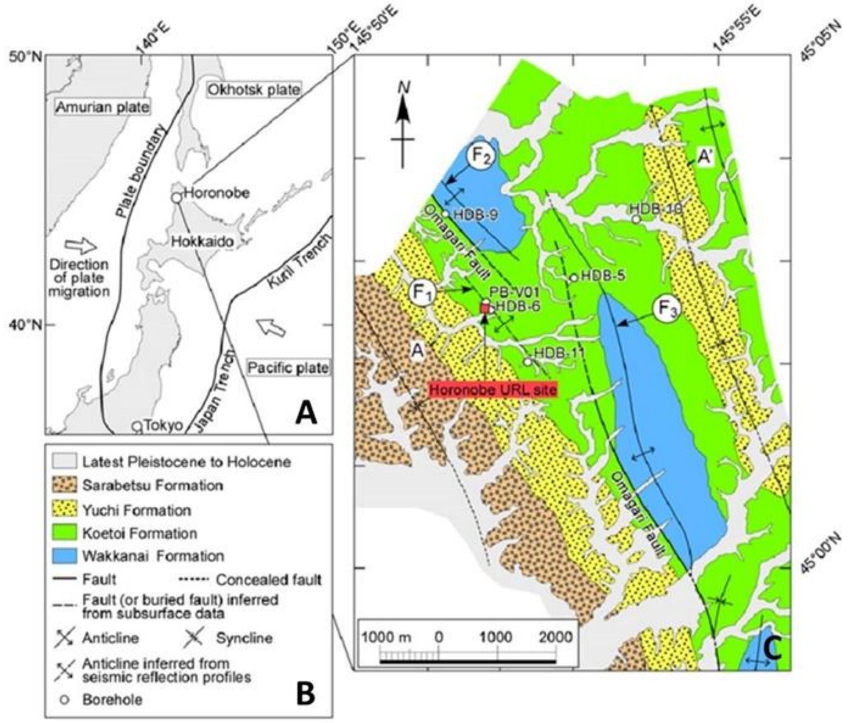

Figure 19. [A] Plate boundaries and directions of plate movement in relation to the Horonobe URL modified from (Wei and Seno, 1998). [B-C]. Geological map of the Horonobe area adapted from (Ishii et al., 2010). Labels indicate borehole locations.

Operational activities pursued at the Horonobe URL were detailed in (Fujita et al., 2011). The Horonobe URL is not considered a candidate for repository siting; rather, the URL is being used to evaluate engineered technology for barriers in an in-situ environment (Nakata et al., 2018; Ota et al., 2011). The full-scale test includes heater experiments (Fujita et al., 2011; JAEA, 2023) with multiple phases of heating and groundwater injection (Figure 20; JAEA, 2021). Complementary thermal-hydrological-mechanical-chemical models based on physical properties of the Horonobe URL and heat from waste packages indicate the potential for increased permeability of the rock near the disturbed zone of excavation, and potential for permeability decrease following waste disposal (Ogata et al., 2020).

Work completed at LANL in FY22 and FY23 comprised elevated-temperature laboratory experiments to simulate the full-scale EBS test that is currently underway at the Horonobe URL. These hydrothermal experiments characterized the alteration of Kunigel bentonite, considered a suitable bentonite buffer material (Kohno et al., 2018; Xiang and Wang, 2019), saturated with a synthetic Wakkanai groundwater. The results provide a counterpoint to the argillite R&D study described in Sections 1-5 and indicate the diversity of reactions that may occur in different argillaceous environments specific to the brine chemistry and buffer materials.

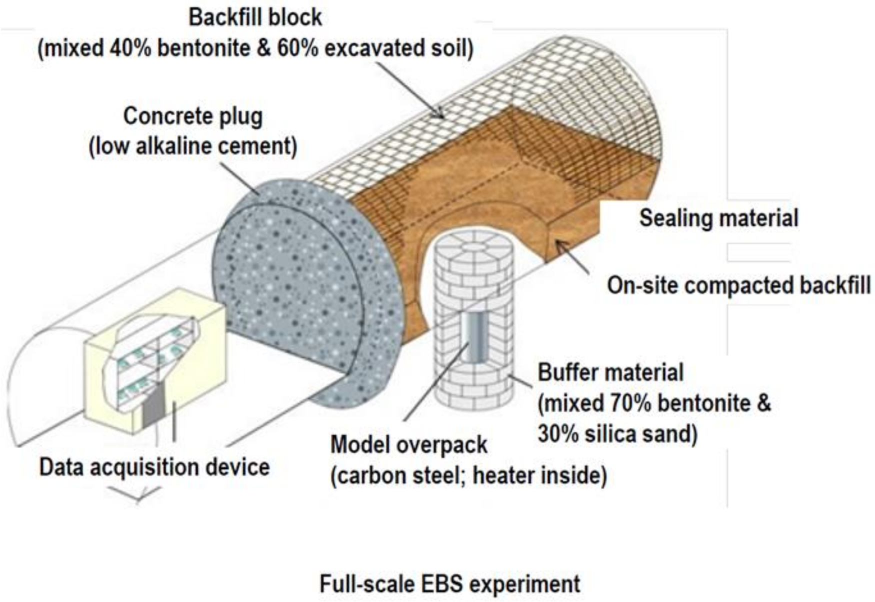

Figure 20. Simplified depiction of the full-scale EBS experiment at the Horonobe URL (JAEA, 2021).

6.2 Methods

6.2.1 Hydrothermal Experiments

One experiment completed in FY22 (HNB-1) reacted a Kunigel bentonite (powder) with a synthetic Wakkanai groundwater (WGW) at 150 °C. Two additional experiments in FY23 (HNB-2 and HNB-3) reacted Kunigel bentonite (powder) with WGW: HNB-2 additionally included LCS as a reactant and was reacted at 200 °C; HNB-3 reacted the Kunigel bentonite at 150 °C. All experiments had a WRR of 9:1 and were reacted for 8 weeks. Initial parameters for all experiments are included in Table 6.

Experiments completed in this set were conducted using the pressurized gold-cell system as described in Section 2.1 (Argillite R&D materials) that allowed sampling of the fluid phases (gas and liquid) directly from the reaction cell while maintaining experimental pressure and temperature. Fluid chemistries were monitored by aqueous samples extracted weekly during and after the experiment. Unreacted Kunigel and post-reaction solid products were characterized by XRD and SEM-EDS. Solid and aqueous phase characterization methods are reported in Appendix A of Caporuscio et al. (2023).

Table 6. Parameters for experiments completed in FY23 and experiments from previous years that have new analytical results collected in FY23. Abbreviations: WGW=Wakkanai groundwater; LCS=low carbon steel; WRR=water-rock ratio (by mass).

Exp. ID	FY	Reactants	Temp (°C)	Run time	WGW (g)	Kunigel (g)	LCS (g)	Fe (g)	Fe_3O_4 (g)	WRR
HNB-1	FY22	Kunigel	200	8 weeks	144	14.88		0.56	0.56	9:1
HNB-2	FY23	Kunigel +LCS	200	8 weeks	109	11.29	5.05	0.42	0.42	9.1
HNB-3	FY23	Kunigel	150	8 weeks	100	10.16		0.38	0.38	9.1

6.2.2 Materials

Kunigel V1 bentonite. The finely powdered bentonite (~63 µm grain size) used in this present study was provided by Kunimine Kogyo Co., Ltd., Japan. It is composed dominantly of Na-montmorillonite (general composition: $Na_{0.33}(Al,Mg)_2(Si4O_{10})(OH)_2 \cdot nH_2O$) and quartz/chalcedony with lesser calcite, dolomite, zeolites and feldspar, and minor sulfide minerals. The QXRD results from unheated bentonite are presented in Table 9.

Low carbon steel (LCS). A steel product composed largely of Fe with ~0.2 wt.% C, 0.9 wt.% Mn, < 0.04 wt.% P, and < 0.05 wt.% S.

Wakkanai Groundwater (WGW). A synthetic groundwater composition was developed from water chemistry reports of the Horonobe area published by (Hama et al., 2007) and summarized in Caporuscio et al. (2020). From the 14 relevant water analyses we downselected to include only water analyses from the target Wakkanai Formation that were greater than 300 meters in depth. The resulting seven analyses were then averaged to produce a “synthetic” Wakkanai groundwater (Table 7).

Table 7. Target WGW composition, based on an average of seven groundwater samples from the Wakkanai formation with an average depth of 393 m. All values (excluding pH) are in mg L^{-1}.

	pH	Na	K	Ca	Mg	Si	Fe	Cl	Br	I	SO_4	HCO_3
Synthetic Wakkanai Groundwater	7.5	2968	59.7	77.7	50.6	26.0	0.58	3759	13.4	12.4	3.5	1605

6.3 Results

Experimental reactants were analyzed to isolate changes in the solid and liquid fractions of the experiments, respectively. Quench samples were collected from within the reaction cell after the experiment was cooled and were exposed to air during that sample. Solid reactants were also exposed to air during quench and drying. The experiment HNB-3 had fully saturated bentonite in the reaction cell but no separated liquid fraction available to collect a quench sample.

6.3.1 Aqueous Geochemistry

6.3.1.1 *Experiments run at 200 °C*

The two experiments run at 200 °C (HNB-1 and HNB-2) had relatively stable solution chemistry throughout the duration of the experiments (Figures 21 and 22). In all experiments, the pH decreased within the first two weeks of experimental time from ~7.5 to a relative steady-state pH of ~6.5. Na, Cl, Ca, and K all remained within 10% of their concentrations in the initial WGW solution (Figures 21 and 22; Appendix B-2 of Caporuscio et al. 2023). SO_4 and SiO_2 concentrations both increased from the WGW. SO_4 concentrations increased during the first three weeks, from ~17 mg L^{-1} in the initial WGW to a maximum concentration of 166 mg L^{-1} and 119 mg L^{-1} in HNB-1 and HNB-2, respectively. After the initial increase, SO_4 concentrations decreased slowly throughout the remainder of the experimental time in both HNB-1 and HNB-2. SiO_2 concentrations increased from ~26 mg L^{-1} in the starting solution to maximum concentrations of ~300 mg L^{-1} in both HNB-1 and HNB-2.

Abrupt decreases in SiO_2 concentrations were observed in samples from both experiments. In HNB-1 the decreased SiO_2 concentrations in the samples collected between 600-1000 hours of experimental time are not accompanied by deviations from steady-state concentrations of any other analytes; the cause is under evaluation. In HNB-2, the decreased SiO_2 concentration in the sample collected at 100 hours (Figures 21 and 22) is interpreted as an error in sample handling or analyses as no similar decreases were apparent in the anion analyses or in the cation analyses of unfiltered replicate samples (Appendix B-2 of Caporuscio et al. 2023).

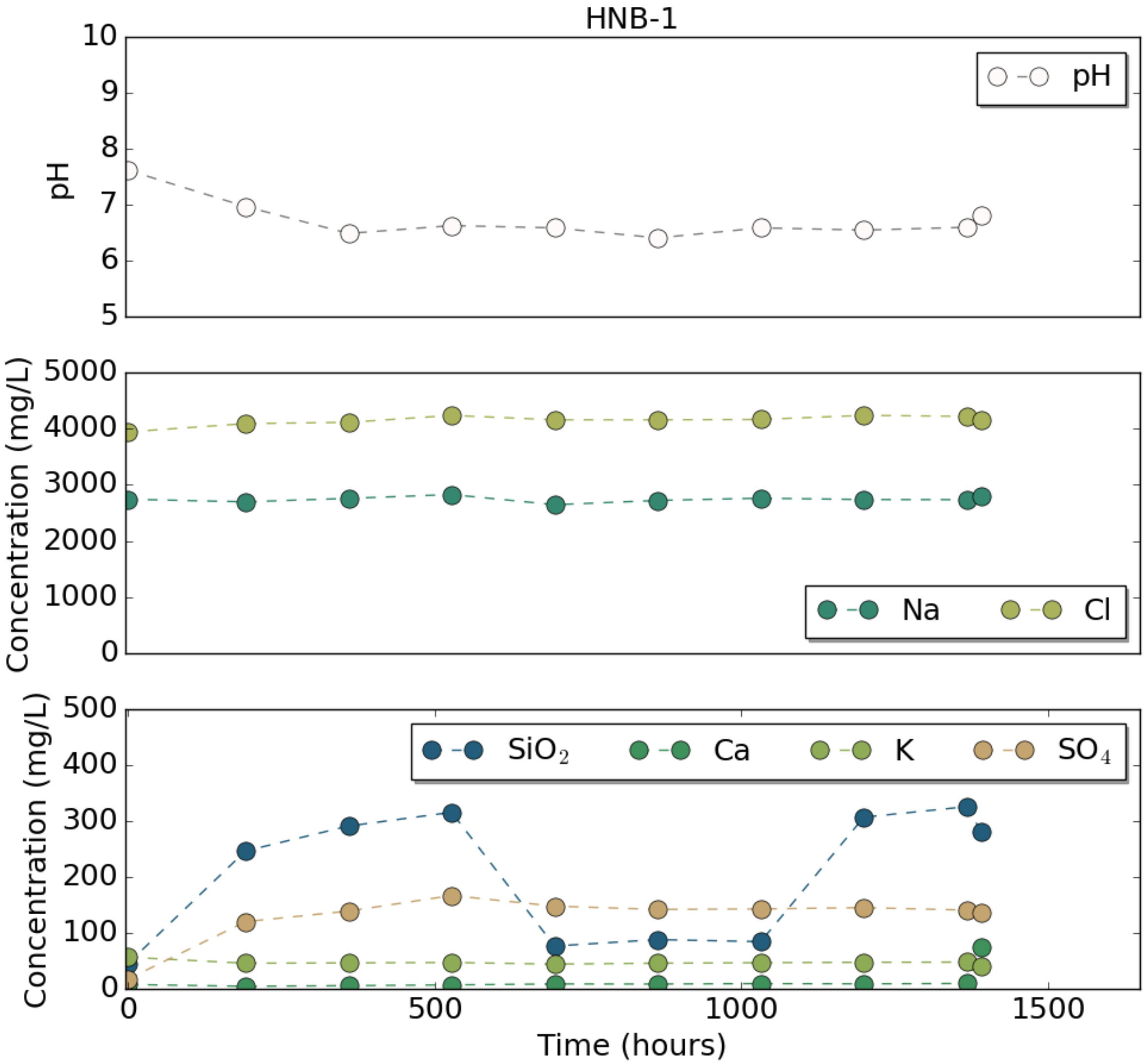

Figure 7 Fluid chemistry results from HNB-1. pH indicates pH at bench conditions.

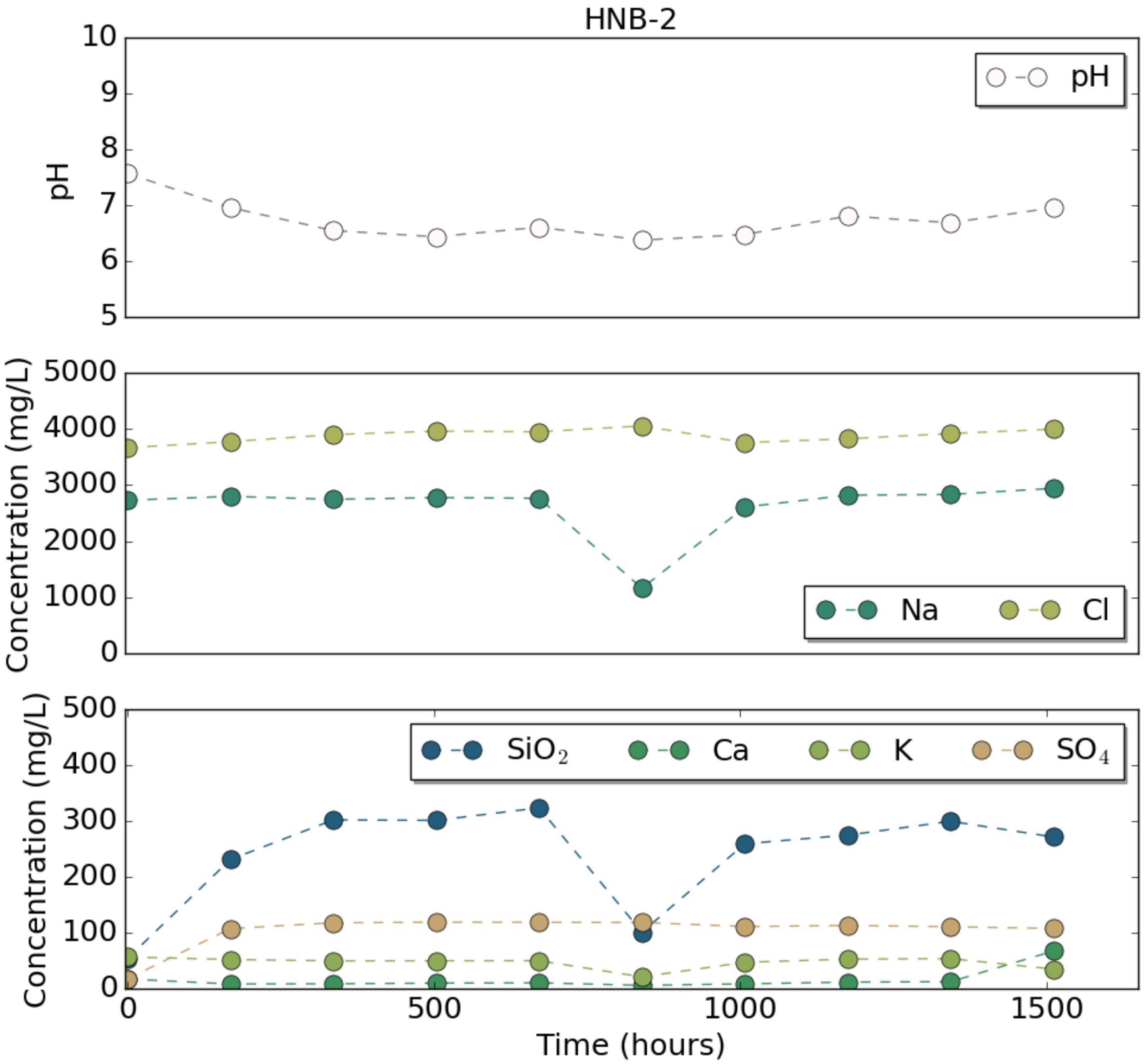

Figure 22. Fluid chemistry results from HNB-2. pH indicates pH at bench conditions.

6.3.1.2 *Experiments run at 150 °C*

Results from the experiment run at 150 °C (HNB-3) similarly showed a decrease in pH within the first two weeks. Within the first week there was a transient increase in pH, from the initial pH ~7.5 to just greater than pH 8, before decreasing to a relatively stable pH value of ~6.5 for the remainder of the experiment time (Figure 23). In contrast to the results from HNB-1 and -2, Na and Cl concentrations increased slightly throughout the course of the experiment. Specifically, concentrations appeared to be at a steady state until ~4 weeks (~600 hours) of experiment time, then increased slightly. This increase was also observed in the concentrations of SiO_2 and SO_4^{2-} (Figure 23 and Appendix B-1 of Caporuscio et al. 2023). Starting at 5 weeks of experimental time (~780 hours), a change in color was observed in the sampled solution from clear to a yellowish tint. Suspended solids were observed in the final sample collected before experiment quench at 8 weeks (~1080 hours).

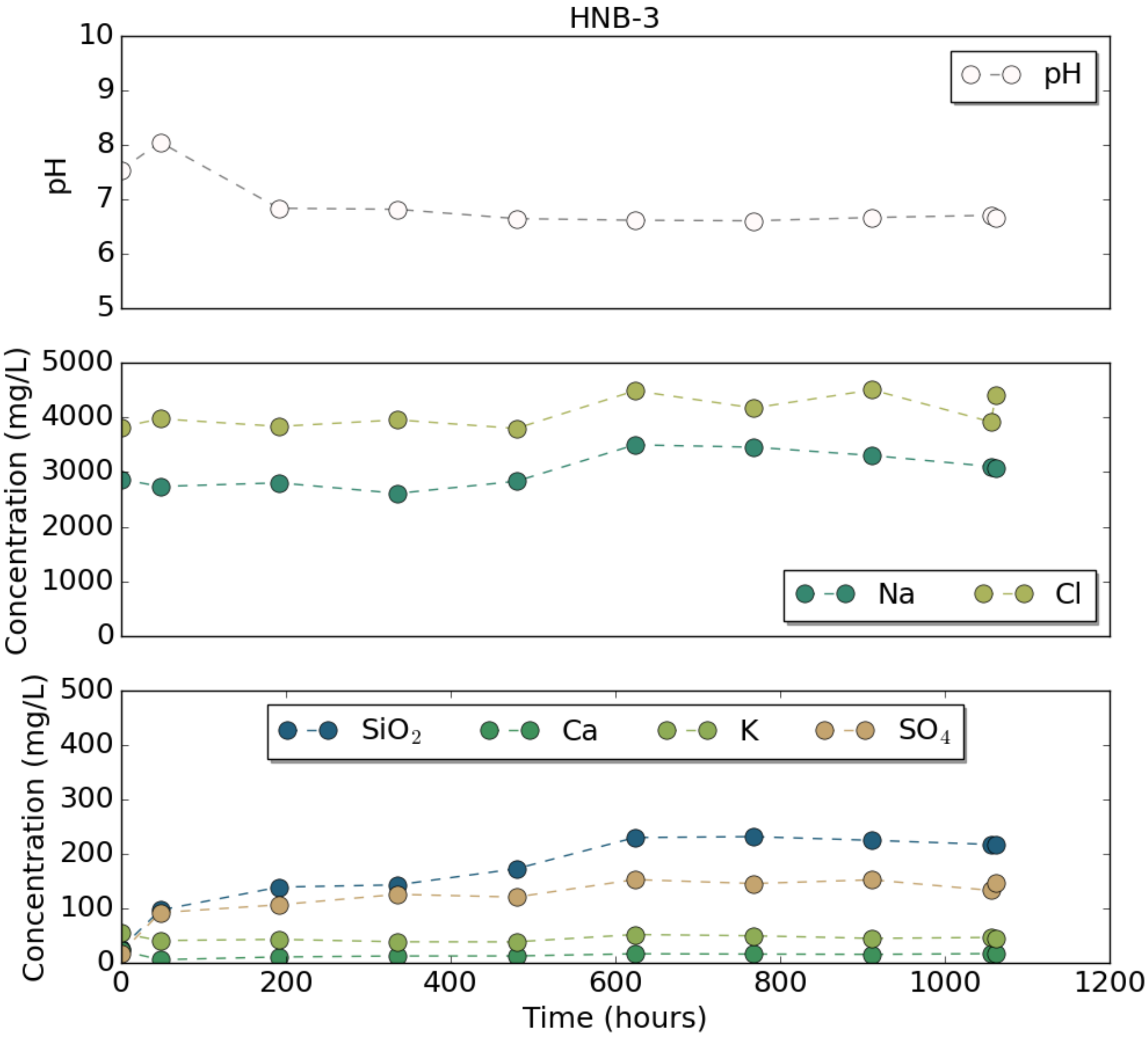

Figure 23. Fluid chemistry results from HNB-2. pH indicates pH at bench conditions.

6.3.2 X-Ray Fluorescence (XRF) Analyses

XRF analyses for bulk rock oxide chemistry were performed on unreacted Kunigel bentonite and the bulk reaction product from HNB-1 (Table 8).

There was a slight decrease of Al_2O_3, SiO_2, and loss on ignition in the reacted Kunigel bentonite from all the experiments compared to the unreacted Kunigel bentonite. Fe_2O_3 increased from the unreacted Kunigel bentonite to the reacted product because of the addition of redox buffers. The Na_2O showed a minor increase in the reacted bentonites.

Table 8. X-Ray Fluorescence (XRF) analyses of unreacted Kunigel bentonite and post-reaction results from the HNB experiments. Values are in weight percent.

Oxide (wt.%)	Unreacted Kunigel bentonite	HNB-1	HNB-2	HNB-3
Na_2O	2.51	3.58	3.07	3.25
MgO	2.11	1.98	1.94	1.80
Al_2O_3	13.56	12.46	12.29	12.11
SiO_2	70.24	63.64	64.02	63.29
P_2O_5	0.05	0.07	0.07	0.04
K_2O	0.44	0.44	0.43	0.41
CaO	2.31	2.17	2.11	2.15
TiO_2	0.18	0.34	0.34	0.39
MnO	0.08	0.11	0.12	0.11
Fe_2O_3	2.01	9.32	10.42	9.74
BaO	0.13	0.12	0.12	0.11
LOI	6.35	5.68	4.95	6.51

6.3.3 Quantitative X-ray Diffraction (QXRD)

QXRD results from the bulk reaction product mineralogy from the unreacted Kunigel bentonite and the HNB experiments are shown in Table 9 and Figure 24. The results indicate that new phases in the reaction products are magnetite and halite, most likely from the addition of redox buffers and from the saline synthetic groundwater, respectively. The change in the existing mineral fractions is likely due to sample variation in the Kunigel bentonite.

Table 9. Quantitative X-Ray Diffraction (QXRD) results of the unreacted Kunigel bentonite and the post-reaction products from the HNB experiments.

	Kunigel	HNB-1	HNB-2
Non-Clay			
Quartz	32.1	35.5	32.5
Cristobalite	2.9	0.7	1.0
Feldspar	2.4	7.4	8.3
Calcite	1.0	4.0	2.8
Clinoptolite	1.2	0.9	0.8
Heulandite	3.1	2.4	1.4
Pyrite	0.4	0.5	0.0
Maghemite	2.1		
Buffers		4.4	3.4
Halite		1.2	1.2
Amorphous	1.4	2.9	5.0
Clay			
Smectite + Illite + I/S	53.5	40.0	43.6
SUM	**100.0**	**100.0**	**100.0**

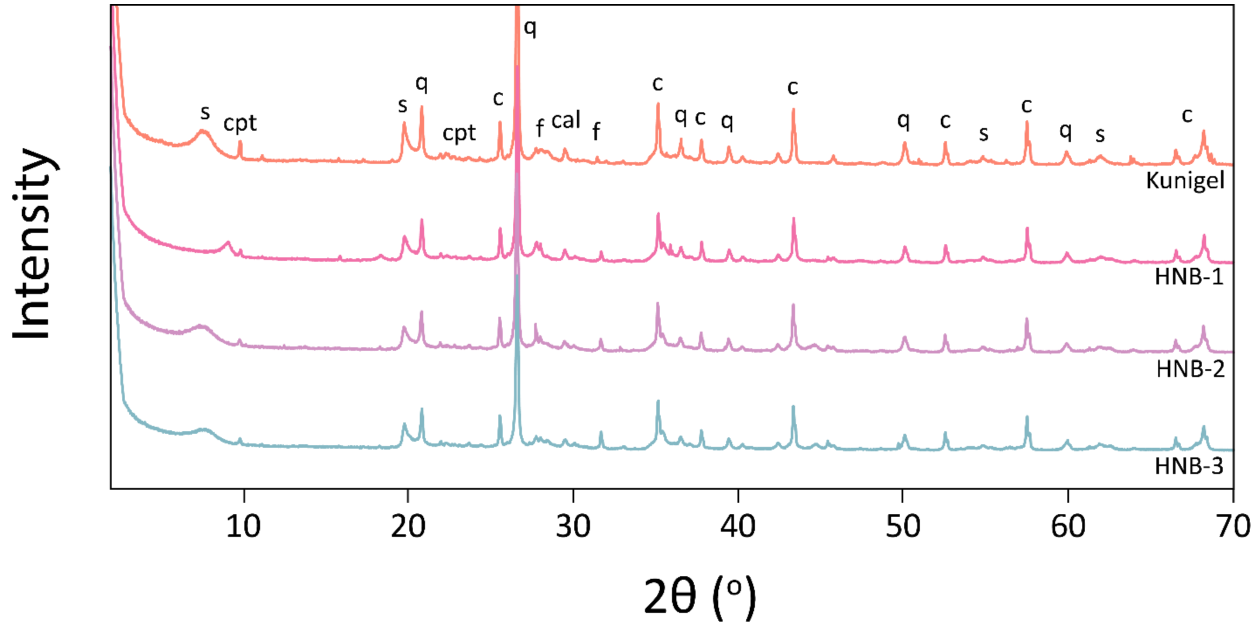

Figure 24. QXRD pattern of the unreacted Kunigel and the bulk reaction product from HNB-1. Peaks corresponding to corundum (c), smectite (s), clinoptolite (cpt), calcite (cal), quartz (q), feldspar (f).

6.3.4 Clay X-ray Diffraction (XRD)

The starting montmorillonite in the Kunigel bentonite was a Na-montmorillonite. Clay XRD results are reported in Table 10 and Figure 25. The clay fraction of the HNB-1 and -2 experiment experienced little alteration with only a slight shift in the ethylene glycol-saturated smectite peak positions. Small amounts of interlayered illite (1–5%) may be indicated by the spacing between the d002 and d003 peaks of the ethylene glycol-saturated pattern. This amount increased slightly with hydrothermal treatment (1–5%). HNB-3 also experienced a small amount of alteration with slight shift in the ethylene glycol-saturated smectite peak positions. However, no illite was detected at 150 °C compared to the unreacted Kunigel bentonite and HNB-1 and -2.

Table 10. Glycolated smectite (GS) peak positions for the < 2 μm clay fraction separated from the HNB experiments. Expandability and %illite (%I) were calculated based on the difference in position between the 002 and 003 glycolated smectite peaks.

EG-smectite	**001**		**002**		**003**		**002/003**	**1**	**2**	**3**	
Sample	**d (Å)**	**2θ**	**d (Å)**	**2θ**	**d (Å)**	**2θ**	**Δ 2θ**	**%Exp**	**%Exp**	**%Exp**	**%I**
Kunigel Bentonite	5.32	16.60	10.54	8.39	15.86	5.58	26.68	3.34	5.32	97	98
HNB-1	5.32	5.32	5.32	5.32	5.32	5.32	5.32	5.32	5.32	5.32	5.32
HNB-2	16.59	16.59	16.59	16.59	16.59	16.59	16.59	16.59	16.59	16.59	16.59
HNB-5	10.60	10.60	10.60	10.60	10.60	10.60	10.60	10.60	10.60	10.60	10.60

1: %Exp = 973.76 – 323.45Δ + 38.43Δ2 – 1.62Δ3 (Eberl et al., 1993)

2: %Exp = 1517.8 – 548.49Δ + 68.35Δ2 – 2.90Δ3 (Eberl et al., 1993)

3. %Exp = 766.01 – 194.10Δ + 12.924Δ2 (Moore and Reynolds, 1997)

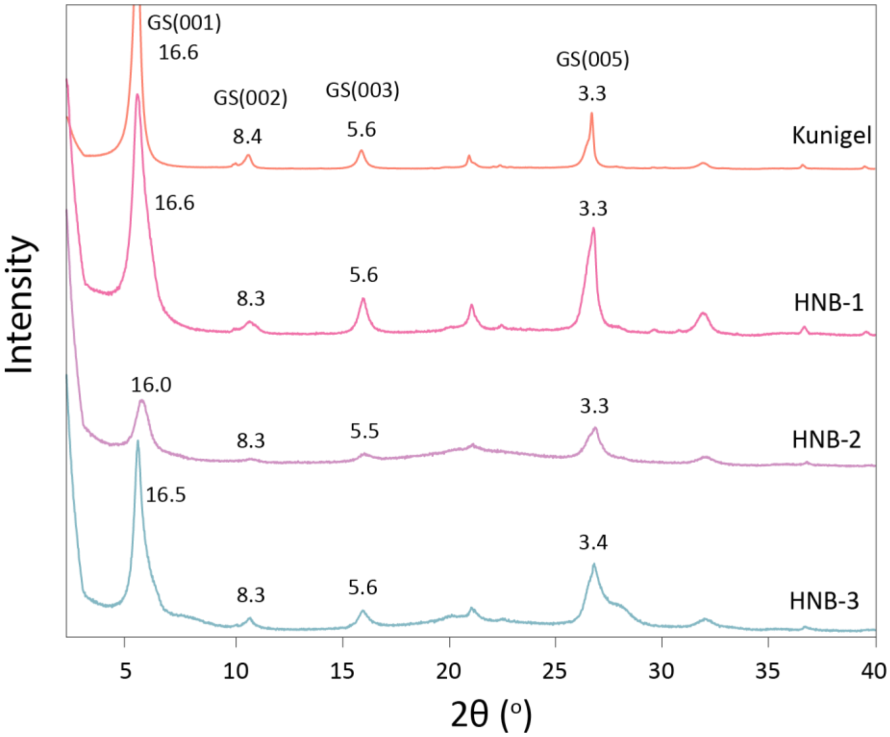

Figure 25. XRD patterns of the oriented and ethylene glycol saturated < 2 μm clay fraction from the clay groundmass reacted in HNB-1 through -3 compared to unheated Kunigel bentonite.

6.3.5 Scanning Electron Microscopy Energu Dispersive Spectroscopy (SEM-EDS)

Kunigel bentonite unreacted. The unreacted Kunigel shows a Na-rich montmorillonite with flaky edges with quartz throughout (Figure E-21B of Caporuscio et al., 2023). In addition, the samples contained minor amounts of plagioclase and pyrite (Figure E-21A of Caporuscio et al., 2023). All figures referenced to Appendix E in this section are given in Caporuscio et al. (2023).

HNB-1. SEM images of the reacted Kunigel bentonite show a Na-rich smectite matrix with minor pyrite, feldspar, SiO_2, and salt (Figure E-22).

HNB-2. The reacted Kunigel bentonite shows Na-rich smectite with a flaky texture along with minor plagioclase (Figures E-23). SEM images of the LCS exhibit Fe-saponite interlaced with Fe-sulfide. The iron content in the saponite increases with increasing proximity to LCS. The Fe-sulfide crystals – most likely pyrrhotite – are monoclinic and largely appear in clusters (Figure E-24A). Minor calcite was also observed (Figure E-24B).

HNB-3. The images of the reacted Kunigel bentonite heated at 150 °C shows a foily, Na-rich smectite with minor SiO_2, pyrite, and apatite (Figure E-25).

6.4 Discussion and Conclusions

The results from the three completed experiments discussed here suggest that Kunigel bentonite in the presence of the Wakkanai groundwater solution as used here was relatively stable and did not undergo extensive alteration, even at elevated temperatures. QXRD results indicate a preferential loss of non-clay silicates (quartz, feldspars, clinoptilolite) and sulfides (pyrite) compared to the clay phase. This was further corroborated by an increase in silica and sulfate concentrations in solution over the experimental duration. As silica increased and then reached a quasi-steady state concentration at ~330 mg/L, saturation with solid SiO_2 (quartz) additionally approached saturation, indicating that the dissolution of these phases may have occurred early in the experiment and slowed as the solution approached equilibrium with respect to solid SiO_2. Apparent formation of 5% illite interlayers within the smectite was identified in the 200 °C experiments (HNB-1 and -2) by clay XRD (Table 10), but not in the 150 °C experiment (HNB-3). These results indicate that the Kunigel bentonite may quickly approach a quasi-steady state chemistry in contact with similar solutions to the synthesized Wakkanai formation groundwater with minimal alteration and may experience even less alteration in lower water-rock ratios, as may be encountered from saturation during emplacement in a repository.

That the evolution of solution chemistry uniquely showed an increase of several solutes after ~4 weeks (~600 hours) of reaction time may be attributable to experimental parameters rather than a specific reaction mechanism at 150 °C. While all experiments began with initially identical WRR, masses of solid and liquid reactants were different between each experiment depending on limitations such as the sizes of the different gold cells used for experiments (Table 6). As the sample volume collected at each sampling event remains relatively unchanged between experiments, WRR may evolve differently over the course of different experiments. It is notable that the HNB-3 had the smallest initial mass of solution in the reaction cell and had a decreased WRR at 4 weeks to ~ 6.5:1. Bentonites also have been shown to have decreased water retention capacity at increased temperatures (Ye et al., 2012). Decreased water retention may have resulted in slightly increased water availability in the higher-temperature experiments than can be expected in lower-temperature experiments with similar water-bentonite ratios by mass and less water available for sampling at lower temperatures. These factors potentially led to the sampling of water from within the porewater solution of the saturated bentonite, which is expected to have a slightly different fluid chemistry than that of the bulk solution. That samples may have been collected from HNB-3 from within this saturating solution is additionally evidenced by the change in color of the samples collected during the run, the suspended solids visible in the final sample collected before experiment quench, and the lack of separated liquid phase in the reaction cell after cooling (Results, Section 2.3). The correlation between lower WRR and increased concentrations of Cl and Na was also noted in previous experiments EBS-23 and-24, reported in Sauer et al. (2022).

Alteration at the boundary of a low-carbon steel included with Kunigel showed significant formation of an Fe-sulfide phase (likely pyrrhotite) and Fe-saponite at the steel surface. The Fe-content of the clay decreased with increasing distance from the steel surface, suggesting that the effects of steel corrosion on the Kunigel bentonite are highly localized and restricted to the steel-bentonite interface. Cross section SEM images are needed to ascertain the thickness of the LCS-bentonite alteration rim. The S in the Fe-sulfide phase formed likely reflects a reaction between pyrite in the Kunigel bentonite and the LCS which also contains ~0.05 wt.% S. Alternatively, the Fe-sulfide phases may have formed from a reaction between the SO_4 in the synthetic groundwater and the LCS, however, the aqueous SO_4 concentration did not decrease over the course of the experiment.

6.4.1 Future Work

FY24 experiments will:

- Expand the experimental dataset on hydrothermal alteration of Kunigel bentonite in Wakkanai synthetic groundwater at elevated temperature, with possible addition of a generic agillaceous wall rock and other EBS materials of interest.
- The results from HNB-1 through HNB-3 and future experiments will additionally be compared to any future finalized reports from in-situ experiments conducted at the Horonobe URL.

7. References

Adler M, Mäder U, Waber HN. High-pH alteration of argillaceous rocks: an experimental study. Schweiz Miner Petrogr Mitt 1999;79:445–54.

Balmer S, Kaufhold S, Dohrmann R. Cement-bentonite-iron interactions on small scale tests for testing performance of bentonites as a barrier in high-level radioactive waste repository concepts. Appl Clay Sci 2017; 135:427–36.

Bossart PJ, Jaeggi D, Nussbaum C. Experiments on thermo-hydro-mechanical behaviour of Opalinus Clay at Mont Terri rock laboratory, Switzerland. J Rock Mech Geotech Eng 2017; 9:502–10.

Bossart PJ, Milnes AG. Mont Terri Rock Laboratory, 20 Years: Two Decades of Research and Experimentation on Claystones for Geological Disposal of Radioactive Waste 2017.

Bossart PJ, Thury M. Mont terri rock laboratory project: programme 1996 to 2007 and results. Federal Office of Topography Swisstopo; 2008.

Calvo JG, Hidalgo A, Alonso C, Luco LF. Development of low-pH cementitious materials for HLRW repositories: Resistance against ground waters aggression. Cem Concr Res 2010; 40:1290–7.

Carlson L, Karnland O, Oversby VM, Rance AP, Smart NR, Snellman M, et al. Experimental studies of the interactions between anaerobically corroding iron and bentonite. Phys Chem Earth Parts ABC 2007;32:334–45.

Caporuscio FA, Cheshire MC, Palaich S, Norskog K, Jové Colón C. Argillite Disposal R&D-LANL 2015. Summary of baseline experiments for generic repository engineered barriers. (FY 2015). (FCRD-UFD-2015-000356, LA-UR-15-26110). Los Alamos National Lab. (LANL), Los Alamos, NM (United States) 2015.

Caporuscio FA, Norskog K. Disposal Overpack and Waste Package Options – LANL Petrographic descriptions of FEBEX Section 49 - Dismantlement Phase operation. (SFWD-SFWST-2017-000116, LA-UR -17-28576) Los Alamos National Lab. (LANL), Los Alamos, NM (United States) 2017.

Caporuscio, FA, Sauer, KB, Houser L. Rock, M. Argillite R&D and International Collaborations – LANL. (SF-18LA01030102 Rev.2/SF-18LA01030106, LA-UR-18-27277) Los Alamos National Lab. (LANL), Los Alamos, NM (United States) 2018.

Caporuscio FA, Sauer KB, Rock M. Argillite Disposal R&D – LANL (FY19). (SF-19LA01030801/SF-19LA01030805, LA-UR-19-24397). Los Alamos National Lab. (LANL), Los Alamos, NM (United States) 2019.

Caporuscio FA, Sauer KB, Rock MJ, Kalintsev A, Migdissov A, Alcorn CD. Engineered Barrier System R&D and International Collaborations–LANL (FY20): Spent Fuel and Waste Disposition. Los Alamos National Lab (LANL), Los Alamos, NM (United States); 2020.

Caporuscio, F.A., Rock, M.J., Zandanel , A.E. and McKanna, A.J. Argillite Disposal R&D and Argillite International Collaborations - LANL (LA-UR-23-27280), Spent Fuel and Waste Disposition (SFWD) Program; Consolidated Report Deliverables M3SF-23LA010301011 and M3SF-23LA010301021. Los Alamos National Lab., Los Alamos, NM (United States); 2023.

Chen Y, Sun Z, Cui Y, Ye W, Liu Q. Effect of cement solutions on the swelling pressure of compacted GMZ bentonite at different temperatures. Constr Build Mater 2019; 229:116872.

Chermak J. Low temperature experimental investigation of the effect of high pH NaOH solutions on the Opalinus Shale, Switzerland. Clays Clay Miner 1992; 40:650–650.

Cheshire MC, Caporuscio F, Jové-Colón C, McCarney M. Alteration of clinoptilolite into high-silica analcime within a bentonite barrier system under used nuclear fuel repository conditions. Int High-Level Radioact Waste Manag 2013 IHLRWM Albuq NM 2013.

Cheshire MC, Caporuscio FA, Jové-Colón C, Norskog KE. Fe-saponite growth on low-carbon and stainless steel in hydrothermal-bentonite experiments. J Nucl Mater 2018; 511:353–66.

Cheshire MC, Caporuscio FA, Rearick MS, Jové-Colón C, McCarney MK. Bentonite evolution at elevated pressures and temperatures: An experimental study for generic nuclear repository designs. Am Mineral 2014; 99:1662–75.

Cuevas J, De La Villa RV, Ramírez S, Sánchez L, Fernández R, Leguey S. The alkaline reaction of FEBEX bentonite: a contribution to the study of the performance of bentonite/concrete engineered barrier systems. J Iber Geol 2006; 32:151–74.

De Combarieu G, Barboux P, Minet Y. Iron corrosion in Callovo–Oxfordian argilite: From experiments to thermodynamic/kinetic modelling. Phys Chem Earth Parts ABC 2007; 32:346–58.

Dohrmann R, Olsson S, Kaufhold S, Sellin P. Mineralogical investigations of the first package of the alternative buffer material test–II. Exchangeable cation population rearrangement. Clay Miner 2013; 48:215–33.

Dolder F, Mäder U, Jenni A. Stability of bentonite under high-pH conditions 2014.

El Mendili Y, Abdelouas A, Chaou AA, Bardeau J-F, Schlegel M. Carbon steel corrosion in clay-rich environment. Corros Sci 2014; 88:56–65.

El Mendili Y, Abdelouas A, Karakurt G, Chaou AA, Essehli R, Bardeau J-F, et al. The effect of temperature on carbon steel corrosion under geological conditions. Appl Geochem 2015; 52:76–85.

Ewing RC. Long-term storage of spent nuclear fuel. Nat Mater 2015; 14:252–7.

Fernández R, Cuevas J, Mäder UK. Modelling concrete interaction with a bentonite barrier. Eur J Mineral 2009a; 21:177–91.

Fernández R, Cuevas J, Sánchez L, de la Villa RV, Leguey S. Reactivity of the cement–bentonite interface with alkaline solutions using transport cells. Appl Geochem 2006;21:977–92.

Fernández R, Mäder UK, Rodríguez M, Vigil De La Villa R, Cuevas J. Alteration of compacted bentonite by diffusion of highly alkaline solutions. Eur J Mineral 2009b; 21:725–35.

Ferrage E, Vidal O, Mosser-Ruck R, Cathelineau M, Cuadros J. A reinvestigation of smectite illitization in experimental hydrothermal conditions: Results from X-ray diffraction and transmission electron microscopy. Am Mineral 2011;96:207–23.

Fujita T, Taniguchi N, Maekawa K, Sawada A, Makino H, Sasamoto H, et al. Horonobe Underground Research Laboratory project. Synthesis of phase 1 investigation 2001-2005, 2011; Geologic Disposal Research.

González-Santamaría DE, Angulo M, Ruiz A, Fernández R, Ortega A, Cuevas J. Low-pH cement mortar-bentonite perturbations in a small-scale pilot laboratory experiment. Clay Miner 2018;53:237–54.

González-Santamaría DE, Fernández R, Ruiz AI, Ortega A, Cuevas J. Bentonite/CEM-II cement mortar INTERFACE EXPERIMENTS: A proxy to in situ deep geological repository engineered barrier system surface reactivity. Appl Geochem 2020;117:104599.

Guillaume D, Neaman A, Cathelineau M, Mosser-Ruck R, Peiffert C, Abdelmoula M, et al. Experimental synthesis of chlorite from smectite at 300 C in the presence of metallic Fe. Clay Miner 2003;38:281–302.

Guo X, Gin S, Frankel GS. Review of corrosion interactions between different materials relevant to disposal of high-level nuclear waste. Npj Mater Degrad 2020;4:34.

Hama K, Kunimaru T, Metcalfe R, Martin A. The hydrogeochemistry of argillaceous rock formations at the Horonobe URL site, Japan. Phys Chem Earth Parts ABC 2007; 32:170–80.

Hardin E, Hadgu T, Clayton DJ. Cavern/Vault Disposal Concepts and Thermal Calculations for Direct Disposal of 37-PWR Size DPCs. Sandia National Lab.(SNL-NM), Albuquerque, NM (United States); 2015.

Higgo J. Clay as a barrier to radionuclide migration. Prog Nucl Energy 1987;19:173–207.

Hofmann H, Bauer A, Warr LN. Behavior of smectite in strong salt brines under conditions relevant to the disposal of low-to medium-grade nuclear waste. Clays Clay Miner 2004;52:14–24.

Honty M, Wang L, Osacký M, Uhlík P, Czímerová A, Madejová J. Experimental interactions of the Opalinus Clay and Boom Clay with various repository relevant solutions at 90 C under closed conditions. Appl Clay Sci 2012;59:50–63.

Iijima A, Tada R. Silica diagenesis of Neogene diatomaceous and volcaniclastic sediments in northern Japan. Sedimentology 1981; 28:185–200.

Ishii E, Funaki H, Tokiwa T, Ota K. Relationship between fault growth mechanism and permeability variations with depth of siliceous mudstones in northern Hokkaido, Japan. J Struct Geol 2010;32:1792–805.

Ishidera T, Ueno K, Kurosawa S, Suyama T. Investigation of montmorillonite alteration and form of iron corrosion products in compacted bentonite in contact with carbon steel for ten years. Phys Chem Earth Parts ABC 2008;33:S269–75.

JAEA. Research details: Research and development on geological disposal. Horonobe Undergr Res Cent 2023.

JAEA. Presentation at DECOVALEX-2023 3rd Workshop, April 23-30, 2021 2021.

Jeannin M, Calonnec D, Sabot R, Refait P. Role of a clay sediment deposit on the corrosion of carbon steel in 0.5 mol L− 1 NaCl solutions. Corros Sci 2010;52:2026–34.

Jenni A, Mäder U, Lerouge C, Gaboreau S, Schwyn B. In situ interaction between different concretes and Opalinus Clay. Phys Chem Earth Parts ABC 2014;70:71–83.

Karnland O. Cement/bentonite interaction. Results from 16 month laboratory tests. Swedish Nuclear Fuel and Waste Management Co.; 1997.

Karnland O, Olsson S, Nilsson U, Sellin P. Experimentally determined swelling pressures and geochemical interactions of compacted Wyoming bentonite with highly alkaline solutions. Phys Chem Earth Parts ABC 2007;32:275–86.

Kaufhold S, Dohrmann R. Distinguishing between more and less suitable bentonites for storage of high-level radioactive waste. Clay Miner 2016;51:289–302.

Kaufhold S, Dohrmann R. Stability of bentonites in salt solutions: II. Potassium chloride solution—Initial step of illitization? Appl Clay Sci 2010;49:98–107.

Kaufhold S, Dohrmann R. Stability of bentonites in salt solutions| sodium chloride. Appl Clay Sci 2009;45:171–7.

Kaufhold S, Dohrmann R, Ufer K. Determining the extent of bentonite alteration at the bentonite/cement interface. Appl Clay Sci 2020;186:105446.

Kaufhold S, Hassel AW, Sanders D, Dohrmann R. Corrosion of high-level radioactive waste iron-canisters in contact with bentonite. J Hazard Mater 2015;285:464–73.

Kohno M, Nara Y, Kato M, Nishimura T. Effects of clay-mineral type and content on the hydraulic conductivity of bentonite–sand mixtures made of Kunigel bentonite from JapanMasanori Kohno et al. Effects of clay mineral type and content on hydraulic conductivity. Clay Miner 2018; 53:721–32.

Kunimaru T, Ota K, Alexander WR, Yamamoto H. Groundwater/porewater hydrochemistry at Horonobe URL. Data freeze 1. Preliminary data quality evaluation for boreholes HDB-9, 10 and 11 2010.

Kursten B, Druyts F, Macdonald D, Smart N, Gens R, Wang L, et al. Review of corrosion studies of metallic barrier in geological disposal conditions with respect to Belgian Supercontainer concept. Corros Eng Sci Technol 2011;46:91–7.

Kursten B, Smailos E, Azkarate I, Werme L, Smart N, Marx G, et al. Corrosion evaluation of metallic HLW/spent fuel disposal containers-review 2004a.

Kursten B, Smailos E, Azkarate I, Werme L, Smart N, Santarini G. COBECOMA, State-of-the-Art Document on the Corrosion Behaviour of Container Materials, European Commission. 2004b.

Landolt D, Davenport A, Payer J, Shoesmith D. A review of materials and corrosion issues regarding canisters for disposal of spent fuel and high-level waste in Opalinus Clay 2009.

Lange L, Hills C, Poole A. Preliminary investigation into the effects of carbonation of cement-solidified hazardous wastes. Environ. Sci. Technology 1996; 30: 25-30.

Lerouge C, Gaboreau S, Grangeon S, Claret F, Warmont F, Jenni A, et al. In situ interactions between opalinus clay and low alkali concrete. Phys Chem Earth Parts ABC 2017;99:3–21.

Lothenbach B, Rentsch D, Wieland E. Hydration of a silica fume blended low-alkali shotcrete cement. Phys Chem Earth Parts ABC 2014;70:3–16.

Lothenbach B, Scrivener K, Hooton R. Supplementary cementitious materials. Cem Concr Res 2011;41:1244–56.

Mäder U, Jenni A, Lerouge C, Gaboreau S, Miyoshi S, Kimura Y, et al. 5-year chemico-physical evolution of concrete–claystone interfaces, Mont Terri rock laboratory (Switzerland). Mont Terri Rock Lab. 20 Years, Springer; 2018, p. 309–29.

Madsen F. Clay mineralogical investigations related to nuclear waste disposal. Clay Miner 1998;33:109–29.

Meunier A, Velde B, Griffault L. The reactivity of bentonites: a review. An application to clay barrier stability for nuclear waste storage. Clay Miner 1998;33:187–96.

Mills MM, Sanchez AC, Boisvert L, Payne CB, Ho TA, Wang Y. Understanding smectite to illite transformation at elevated (> 100° C) temperature: Effects of liquid/solid ratio, interlayer cation, solution chemistry and reaction time. Chem Geol 2023;615:121214.

Milodowski A, Barnes R, Bouch J, Kemp S, Wagner D. Characterisation of fractured rock and fracture mineralisation in Horonobe Boreholes HDB-6, HDB-7 and HDB-8: Final Report. Br Geol Surv Rep CR04251 2004.

Mosser-Ruck R, Cathelineau M, Baronnet A, Trouiller A. Hydrothermal reactivity of K-smectite at 300 degrees C and 100 bar; dissolution-crystallization process and non-expandable dehydrated smectite formation. Clay Miner 1999;34:275–90.

Mosser-Ruck R, Cathelineau M, Guillaume D, Charpentier D, Rousset D, Barres O, et al. Effects of temperature, pH, and iron/clay and liquid/clay ratios on experimental conversion of dioctahedral smectite to berthierine, chlorite, vermiculite, or saponite. Clays Clay Miner 2010;58:280–91.

Mosser-Ruck R, Pignatelli I, Bourdelle F, Abdelmoula M, Barres O, Guillaume D, et al. Contribution of long-term hydrothermal experiments for understanding the smectite-to-chlorite conversion in geological environments. Contrib Mineral Petrol 2016;171:1–21.

Müller HR, Garitte B, Vogt T, Köhler S, Sakaki T, Weber H, et al. Implementation of the full-scale emplacement (FE) experiment at the Mont Terri rock laboratory. Mont Terri Rock Lab 20 Years Two Decades Res Exp Claystones Geol Dispos Radioact Waste 2018:289–308.

Nakata K, Hasegawa T, Oyama T, Ishii E, Miyakawa K, Sasamoto H. An evaluation of the long-term stagnancy of porewater in the Neogene sedimentary rocks in northern Japan. Geofluids 2018;2018:1–21.

Ogata S, Yasuhara H, Kinoshita N, Kishida K. Coupled thermal–hydraulic–mechanical–chemical modeling for permeability evolution of rocks through fracture generation and subsequent sealing. Comput Geosci 2020; 24:1845–64.

Ota K, Abe H, Kunimaru T. Horonobe Underground Research Laboratory project. Synthesis of phase I investigation 2001-2005. 2011; Geoscientific Research.

Pearson F, Arcos D, Bath A, Boisson J, Fernandez A, Gäbler H, et al. Mont Terri Project–Geochemistry of Water in the Opalinus Clay Formation at the Mont Terri Rock Laboratory. Reports of the Federal Office for Water and Geology (FOWG) Geology Series No. 5 2003.

Pusch R. Geological storage of highly radioactive waste: current concepts and plans for radioactive waste disposal 2009.

Pusch R. Highly compacted sodium bentonite for isolating rock-deposited radioactive waste products. Nucl Technol 1979;45:153–7.

Pusch R, Kasbohm J, Knutsson S, Yang T, Nguyen-Thanh L. The role of smectite clay barriers for isolating high-level radioactive waste (HLW) in shallow and deep repositories. Procedia Earth Planet Sci 2015;15:680–7.

Pusch R, Madsen FT. Aspects on the illitization of the Kinnekulle bentonites. Clays Clay Miner 1995;43:261–70.

Pusch R, Takase H, Benbow S. Chemical processes causing cementation in heat-affected smectite-the Kinnekulle bentonite 1998.

Pusch R, Zwahr H, Gerber R, Schomburg J. Interaction of cement and smectitic clay—theory and practice. Appl Clay Sci 2003;23:203–10.

Sauer K, Caporuscio F, Rock M, Cheshire M, Jové-Colón C. Hydrothermal Interaction of Wyoming Bentonite and Opalinus Clay. Clays Clay Miner 2020;68:144–60.

Sauer KB, Caporuscio FA, Rock M, Zandanel AE. Argillite Disposal R&D and Argillite International Collaborations – LANL. 2022.

Savage D, Wilson J, Benbow S, Sasamoto H, Oda C, Walker C, et al. Natural systems evidence for the effects of temperature and the activity of aqueous silica upon montmorillonite stability in clay barriers for the disposal of radioactive wastes. Appl Clay Sci 2019;179:105146.

Sellin P, Leupin OX. The use of clay as an engineered barrier in radioactive-waste management– a review. Clays Clay Miner 2013;61:477–98.

Singh BK, Um W. Application of Clay Materials for Sorption of Radionuclides from Waste Solutions. Minerals 2023;13:239.

Smailos E, Azkarate I, Kursten B, Marx G, Cunado M. Long-term performance of candidate materials for HLW/spent fuel disposal containers. FZKA; 2003.

Smart N, Fennell P, Rance A, Winsley R, Reddy B, Kursten B. Experimental studies of the effect of irradiation on the anaerobic corrosion of carbon steel in relation to the Belgian supercontainer concept. vol. 12, EDP Sciences; 2011, p. 02003.

Smart N, Naish C, Pritchard A. Corrosion principles for the assessment of stainless steel radioactive waste containers. Serco Rep 2006.

Taubald H, Bauer A, Schäfer T, Geckeis H, Satir M, Kim J. Experimental investigation of the effect of high-pH solutions on the Opalinus Shale and the Hammerschmiede Smectite. Clay Miner 2000;35:515–24.

Verstricht J. The ESDRED project: Engineering studies and demonstration of repository designs 2009.

de la Villa RV, Cuevas J, Ramírez S, Leguey S. Zeolite formation during the alkaline reaction of bentonite. Eur J Mineral 2001;13:635–44.

Wersin P, Johnson L, McKinley I. Performance of the bentonite barrier at temperatures beyond 100 C: A critical review. Phys Chem Earth Parts ABC 2007;32:780–8.

Wieczorek K, Gaus I, Mayor JC, Schuster K, García-Siñeriz J-L, Sakaki T. In-situ experiments on bentonite-based buffer and sealing materials at the Mont Terri rock laboratory (Switzerland). Swiss J Geosci 2017;110:253–68.

Wieland E, Mader U, Lothenbach B, Jenni A, Bernard E. Mechanisms and modelling of waste-cement and cement-host rock interactions. Phys Chem EARTH 2017;99:1–2.

Xiang G, Wang Y. A Prediction Method for Swelling Deformation of Bentonite and Its Sand-Mixtures in Salt Solution, Springer; 2019, p. 551–7.

Ye, WM, et al. Investigation on compression behaviour of highly compacted GMZ01 bentonite with suction and temperature control. Nuclear Engineering and Design; 2012 p.11-18.

Development of the SUPCRTNE and Summary of Thermodynamic Database Integration – LLNL (Part IV)

1. Introduction

This part of the report summarizes research conducted at Lawrence Livermore National Laboratory (LLNL) within the Disposal in Argillite media R&D activity. LLNL is leading efforts in the development of thermodynamic databases in support of the Spent Fuel and Waste Science Technology (SFWST) program. In this effort, SUPCRTNE is being developed as the primary engine for thermodynamic database development in support of geologic disposal of high-level nuclear waste. As used here, "SUPCRT" refers to both a computer program and its supporting database. Additional letters or numbers refer to specific variants (SUPCRT92, Johnson et al., 1992; SUPCRTBL, Zimmer et al., 2016; and SUPCRTNE). A SUPCRT database contains the data required to calculate the thermodynamic properties of solid, gas, and aqueous species over a wide range of temperature and pressure. Normally SUPCRT is used to create a higher-level data base that directly supports modeling and simulation codes such as EQ3/6, GWB, PHREEQC, and PFLOTRAN.

SUPCRTNE replaces SUPCRT92 (Johnson et al., 1992), on which it is based. SUPCRT92 was originally intended to support calculations of rock/water interactions pertinent to natural systems. Its slop98.dat data file was largely lacking the species and data for radionuclides of interest to radioactive waste disposal (uranium being an exception). SUPCRT92 was earlier used on the Yucca Mountain Project (Wolery and Jove-Colon, 2007) to generate what data it could (minerals and related aqueous species). However, most of the necessary radionuclide data were treated in a series of spreadsheets, not added to slop98.dat and run through SUPCRT92. This sufficed owing to the low temperatures and pressures considered for the Yucca Mountain Repository ($T \leq 90^{\circ}C$, $P \sim 1$ bar). Our current plan is to run all thermodynamic data through SUPCRTNE to cover a wide range of temperatures and pressures for possible future repository scenarios. Using the "full might" of SUPCRT (requiring the necessary supporting data; see Johnson et al., 1992), the addressable temperatures and pressures (up to about 1000ºC and 1000 MPa) exceed values likely to be required for geologic disposal of radioactive waste in the earth's crust.

An important goal of present work is to adhere to applicable international standards. The International Association for the Properties of Water and Steam (IAPWS, see iapws.org) is an entity that sanctions models for the calculation of water properties. SUPCRT92 uses a model (actually two used in combination) that is now obsolete. IAPWS presently sanctions the model of Wagner and Pruss (2002), known as IAPWS-95. It is technically superior to older models in dealing with conditions at and near the critical point of water. We previously developed a computer code called H2OI95 to evaluate the IAPWS-95 model, and a form of this has been developed as the water properties module used in SUPCRTNE.

In the new work, we are following the thermochemical standards established by CODATA (Cox et al., 1989), which have been adopted by the Organization for Economic Cooperation and Development/Nuclear Energy Agency (OECD/NEA, hereafter "NEA") in the development of a lengthy and continuing project to provide high quality thermodynamic data for radionuclide elements and other elements pertinent to radioactive waste disposal. For a full description of the NEA thermodynamic data project, see the NEA's website: https://www.oecd-nea.org/jcms/pl_22166/thermochemical-database-tdb-project. NEA is expanding the set of key data beyond those provided by CODATA. We consider the NEA recommendations for key thermodynamic data to be the new international standard, as other players including NBS/NIST, the JANAF tables, the U.S. Geological Survey, and CODATA, all once active in this area, have effectively left the field. See Wolery and Jove Colon (2017) for a history and summary of past efforts to develop key thermodynamic data.

When the Yucca Mountain data base was developed, data for the rock-forming minerals and related aqueous species were obtained using SUPCRT92, and data for most radionuclide species were taken from the NEA volumes then available. Data for still more needed species were obtained from a variety of sources, each with generally more limited content. In general, it was only possible to address some obvious inconsistencies among the data. We are building the SUPCRTNE data base centering on the NEA radionuclide data, which are now more abundant. We then want to ensure maximum consistency of other data with the NEA thermochemical standard.

The mineral data associated with SUPCRT92 (slop98.dat) were largely developed by Helgeson et al. (1978) in a pioneering effort to exploit high temperature phase equilibrium data. Their work inspired a series of efforts by others to develop similar “mineralogic/petrologic” data sets, all using various optimization techniques to extract the desired data and incorporating the increasingly available experimental data (see Wolery and Jove Colon (2017) for references). None of these efforts, however, made it into SUPCRT until Zimmer et al. (2016) included the mineral data set of Holland and Powell (2011) into SUPCRTBL. Here our interest is also in the Holland and Powell data set (hereafter HP11) as a replacement for the Helgeson et al. (1978) data set, which in addition to being outdated is known to have errors (see Wolery and Jove Colon, 2017). An important issue must be addressed. How consistent is the HP11data set with the NEA data set, and what can be done to eliminate or at least minimize any inconsistencies?

All codes, data files, and spreadsheets produced by this project will be made available for download as open source products. Historical and new versions of thermochemical databases will be included in several formats for use by the SFWST-relevant codes (PFLOTRAN, PHREEQC, EQ3/6, GWB, etc.). Some of our products (e.g., H2OI95) are presently available for download from GitHub. GitHub is now favored by LLNL for distributing open source codes (LLNL has its own section on GitHub).

We are also developing a project web page with ancillary web pages from which our products can be downloaded (hosted on the Seaborg Institute resources webpage: https://seaborg.llnl.gov/resources). This will provide an alternative to GitHub that will be more geochemist friendly. Also, GitHub is oriented toward distribution of software. Our own web site will be able to handle distribution of other items including spreadsheets. The project web page will expand on the current LLNL web page that provides download of EQ3/6 and its existing thermodynamic databases and include both thermodynamic and surface complexation modeling codes and databases in one location.

2. FY23 Activities

For FY23 most of our effort has focused on adjusting the Holland and Powell (2011) mineral data set for consistency with the NEA data set. This is the subject of a paper by Wolery, Jove Colon, and Zavarin entitled “On Combining Two Internally Consistent Thermodynamic Databases of Geochemical Interest,” to be submitted by the end of this fiscal year. As the title implies, we assume that both the HP11 data set and the NEA dataset are each internally consistent. This is something of a working assumption, though internal consistency is claimed for both data sets. The work in this area, including the documentation in this paper, was significantly expanded from what was originally planned. Consequently, other originally planned work (e.g., testing of SUPCRTNE) was consequently deferred to FY24 or scaled back (e.g., production of data base files).

We believe that the HP11 data set is internally consistent, based upon their methodology and attention to detail. This includes their documentation of excluded input data, which we consider a necessary feature to avoid future problems. They do not, however, present a convenient summary of what we would call key data. Nor do they relate such to any national or international standard. To find their key data, one must look through the table for their full data set (which is intended to support their modeling code THERMOCALC). In some instances, as will be noted below, one must dig deeper. The NEA data set is considered internally consistent owing to its adoption of a defined set of key data (mostly in its data tables for "auxiliary species) and a rigorous process for developing the whole data set. There is an upcoming issue in that NEA may alter its recommended key data values in an upcoming "Ancillary Data" volume.

The approach is to focus on comparing key data values. These key data values are the standard entropies (S^o) of the chemical elements in their standard reference forms at 298.15K and 1 bar, and the standard enthalpies of formation (ΔH_f^o) and entropies (S^o) of key binary species (mostly oxides such as CaO, MgO, SiO_2, and Al_2O_3) at the same reference temperature and pressure. Essentially these give the standard enthalpy of formation (ΔH_f^o) and standard entropy of formation (ΔS_f^o), and thus define the standard Gibbs energy of formation ($\Delta G_f^o = \Delta H_f^o - T\Delta S_f^o$), where T is the absolute temperature, 298.15K for standard reference conditions. The theory is this. If the enthalpy and entropy values (and Gibbs energy values) for two components, say CaO and SiO_2 match up for two data sets, then there should be little to no inconsistency within a data set for a species composed from them (say $CaSiO_3$). Note that the key species that must be used cannot be just the chemical elements, as they have no enthalpy information (ΔH_f^o being zero by definition).

Thus, we can use calculated differences (NEA - HP11) for CaO and SiO_2 as adjustment coefficients. Applied to CaO and SiO_2, the data for these taken from HP11 would be converted to match the data from NEA. The enthalpy and entropy adjustments would be applied to the HP11 data for $CaSiO_3$, accounting for stoichiometry and considering $CaSiO_3$ compositionally as $CaO.SiO_2$. The resulting data for $CaSiO_3$ represents the HP11 adjusted to the NEA thermochemical standard. We would expect this to differ little from the actual NEA data for $CaSiO_3$, were such to exist, which it does not, as the relevant experimental data would likely mostly if not exactly overlap. Note that in this adjustment process, the elemental entropy data from HP11 would simply be replaced by the corresponding NEA data.

There is limited overlap between the species in the HP11 and NEA data sets. That is why it is so important to combine them. However, this limited overlap constrains our ability to further test the adjustment methodology. In adjusting the HP11 data for consistency with the NEA data set, we are not "correcting" the HP11 data. The HP11 data are just fine on their own, for example as they are used in Holland and Powell's own THERMOCALC modeling code. All we are doing here is adjusting them to the NEA thermochemical standard. Also, the HP11 data (original and adjusted) lead to the same calculated values of Gibbs energies, enthalpies, and entropies of reactions.

The presumption here is that compositionally more complex species are related to less complex species which eventually link to the binary species and the reference elemental forms. In truth, there are some subtleties. For one, the actual development of data for a complex species might be tied to more than one kind of binary species (e.g., NaCl in place of Na_2O). For example, reacting Na metal with oxygen gives Na_2O, but reaction of Na metal with chlorine gas gives NaCl. We would hope to use an adjustment coefficient for NaCl that is consistent with one for Na_2O, but thoroughly justifying such a thing may require a deep examination. This leads to a larger question, which is, what is internal consistency and how do you demonstrate it. There are two ways to approach this. One is to show that data are derived from other data in a consistent process. This could be termed “consistency by development.” The other is to show that two sets of data independently derived do together produce results that closely match experimental results. This might be termed “consistency by demonstration.” In our view, this is valid but perhaps weaker.

The Holland and Powell (2011) overall model consists of three parts: rock-forming minerals (the “minpet” part), melt species, and aqueous species. What we are here interested in is just the “minpet” part. It exemplifies “consistency by development.” We do not consider the melt model, as sites chosen for geologic disposal of nuclear waste are unlikely to include locations where melt (magma) is anticipated. The aqueous species model is limited in composition and appears mainly intended for very high temperature scenarios where aqueous liquid might separate from melt. We are following a more extensive aqueous model that is far more appropriate for our area of intended application. Thus, we have not proposed adjustments for the Holland and Powell melt or aqueous data, though that could certainly be done.

In an earlier part of our study in FY22, we looked at assigning adjustment coefficients to individual chemical elements. Initially these were the metals from metal oxides (e.g., Ca from CaO). An adjustment coefficient for oxygen (O) was indeterminate and taken as zero. This approach works for a large subset of the HP11 data. However, attempts to determine an adjustment coefficient for O itself showed inconsistent results. Using Fe_2O_3 and Fe_3O_4 (using data on the NEA side from volume 13b, Lemire et al., 2020) gave a fine-looking result. Using $CO_{2(g)}$ and $CO_{(g)}$ also gave a fine-looking result. However, it was not the same result. Further analysis showed that no consistent correction factor for O can exist. One can only define such a thing for a given redox pair. Essentially, one must use oxide (or other types) of binary components (e.g, H_2O, CaO, SiO_2, Fe_2O_3, FeO, CO_2, CO). Although one could refer to chemical elements by oxidation state (e.g., Fe(II), Fe(III)), even that falls apart when non-oxide components such as NaCl must be considered.

An overall picture of the proposed adjustments to the HP11 “minpet” data is shown in Table 1. Out of 23 component species, straightforward adjustments are possible for only 12. In order to determine an adjustment factor it is first necessary to calculate a difference for a component between the two data sets. For this to work there must be data for a component in both data sets, which is not always the case. For example, the NEA data set lacks data for NiO, MnO, Cr_2O_3, CuO, Cu_2O, and $CaSO_4$ (the only S(VI) species in HP11; SO_3 would have been preferred). However, if an inconsistency cannot be quantified, there is no need for a correction. Note that this situation might change if, for example, the NEA released a manganese volume.

Table 1. Proposed adjustments to HP11 data.

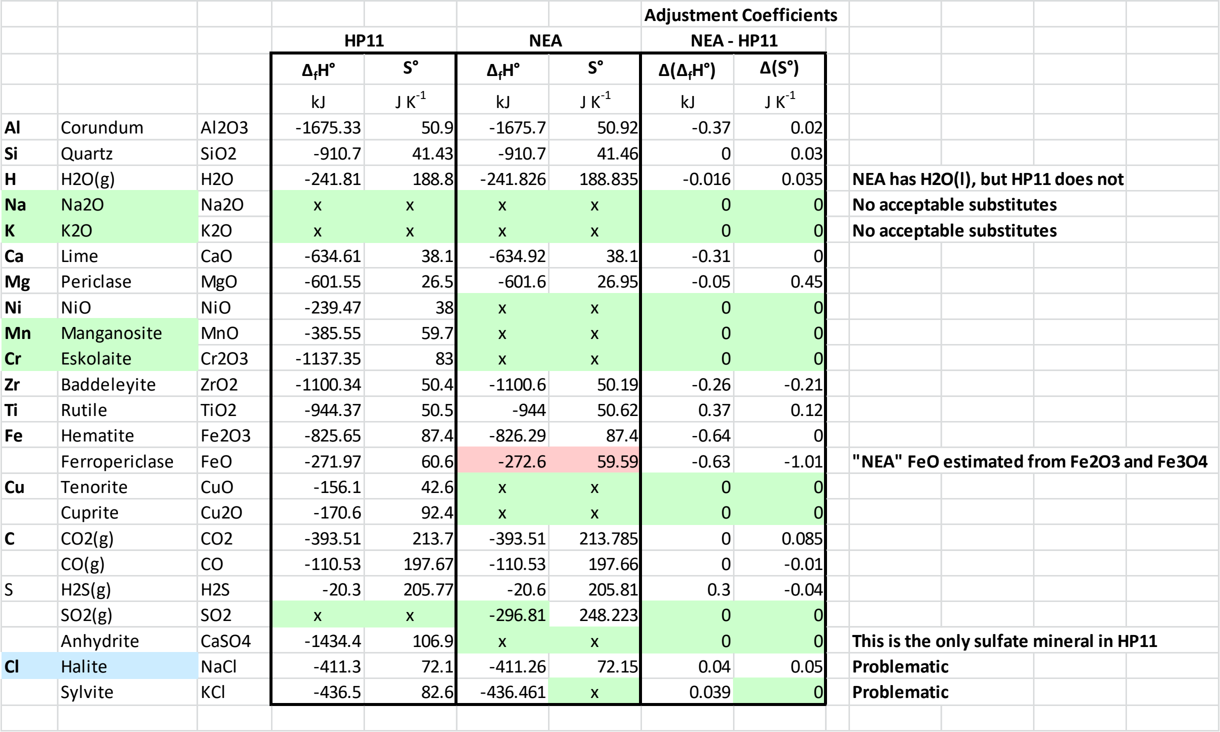

							Adjustment Coefficients		
			HP11		NEA		NEA - HP11		
			$\Delta_f H°$	S°	$\Delta_f H°$	S°	$\Delta(\Delta_f H°)$	Δ(S°)	
			kJ	J K^{-1}	kJ	J K^{-1}	kJ	J K^{-1}	
Al	Corundum	Al2O3	-1675.33	50.9	-1675.7	50.92	-0.37	0.02	
Si	Quartz	SiO2	-910.7	41.43	-910.7	41.46	0	0.03	
H	H2O(g)	H2O	-241.81	188.8	-241.826	188.835	-0.016	0.035	**NEA has H2O(l), but HP11 does not**
Na	Na2O	Na2O	x	x	x	x	0	0	**No acceptable substitutes**
K	K2O	K2O	x	x	x	x	0	0	**No acceptable substitutes**
Ca	Lime	CaO	-634.61	38.1	-634.92	38.1	-0.31	0	
Mg	Periclase	MgO	-601.55	26.5	-601.6	26.95	-0.05	0.45	
Ni	NiO	NiO	-239.47	38	x	x	0	0	
Mn	Manganosite	MnO	-385.55	59.7	x	x	0	0	
Cr	Eskolaite	Cr2O3	-1137.35	83	x	x	0	0	
Zr	Baddeleyite	ZrO2	-1100.34	50.4	-1100.6	50.19	-0.26	-0.21	
Ti	Rutile	TiO2	-944.37	50.5	-944	50.62	0.37	0.12	
Fe	Hematite	Fe2O3	-825.65	87.4	-826.29	87.4	-0.64	0	
	Ferropericlase	FeO	-271.97	60.6	-272.6	59.59	-0.63	-1.01	**"NEA" FeO estimated from Fe2O3 and Fe3O4**
Cu	Tenorite	CuO	-156.1	42.6	x	x	0	0	
	Cuprite	Cu2O	-170.6	92.4	x	x	0	0	
C	CO2(g)	CO2	-393.51	213.7	-393.51	213.785	0	0.085	
	CO(g)	CO	-110.53	197.67	-110.53	197.66	0	-0.01	
S	H2S(g)	H2S	-20.3	205.77	-20.6	205.81	0.3	-0.04	
	SO2(g)	SO2	x	x	-296.81	248.223	0	0	
	Anhydrite	CaSO4	-1434.4	106.9	x	x	0	0	**This is the only sulfate mineral in HP11**
Cl	Halite	NaCl	-411.3	72.1	-411.26	72.15	0.04	0.05	**Problematic**
	Sylvite	KCl	-436.5	82.6	-436.461	x	0.039	0	**Problematic**

Two special cases are noted here. The first is about Na_2O and K_2O, neither of which is expressly present in either the HP11 or NEA data set. These oxides are implied in HP11 through the introduction of data for feldspar minerals ($NaAlSi_3O_8$ and $KAlSi_3O_8$) taken from Robie and Hemingway (1995). Using Na_2O and K_2O with no data essentially has the effective of assuming the feldspars as species representing Na and K on the HP11 side. Since neither the simple oxides nor the feldspars are represented in the NEA data set, no adjustments are possible. The second special case concerns NaCl and KCl, which we initially considered as possible substitutes for Na_2O and K_2O. The inclusion of these on the HP11 side is tied to the Holland and Powell aqueous model. Yet we know from the inclusion of the feldspars in HP11 that the data for those must trace to something else leading back to the elemental reference forms for Na and K. Nevertheless, we believe that it is generally reasonable to use these NaCl and KCl component data to address a small number of silicates that contain Cl.

It is worth comparing the calculated adjustment coefficients with uncertainties. Both HP11 and NEA provide uncertainty values. Their methods can be described in terms of the familiar "2σ." However, they are defined somewhat differently. Neither definition equates to the 2σ of real statistical mathematics. They can, however, be taken as proxies, with the general takeaway that an actual value is expected with high probability to lie between ±2σ of a specified value. Table 2 shows illustrative results. In general, the magnitude of adjustments is less than the corresponding 2σ values. This is good news, as it shows that HP11 is already fairly consistent with the NEA thermochemical standards. We prefer to make the adjustments, however, to achieve maximum consistency. This is in part due to the fact that the magnitudes of the adjustments are not much less than the uncertainties.

Table 2. Some adjustments compared with uncertainties.

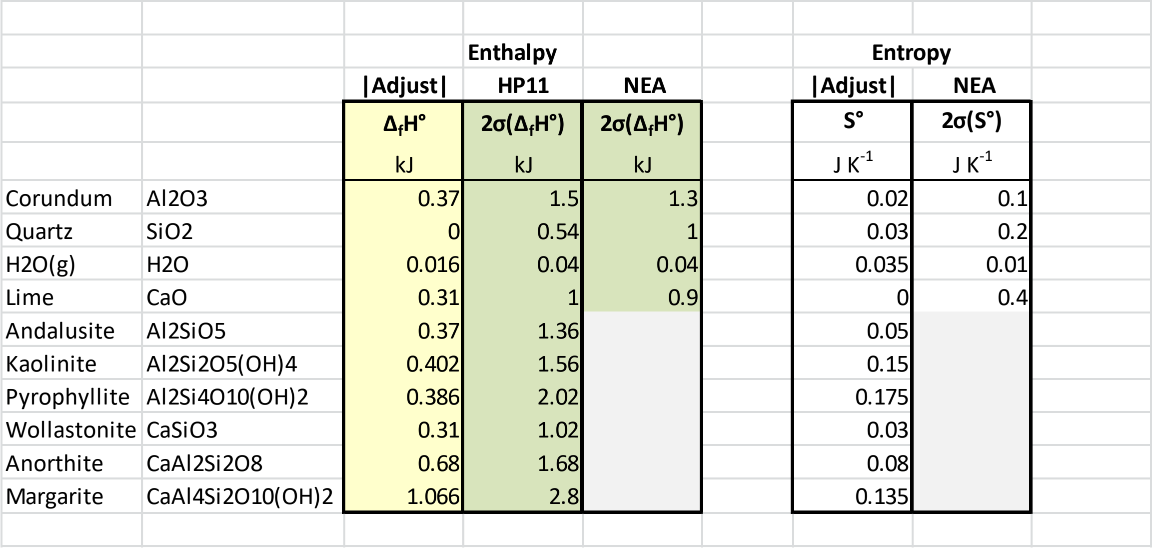

			Enthalpy				Entropy
		|Adjust|	HP11	NEA		|Adjust|	NEA
		$\Delta_f H°$	$2\sigma(\Delta_f H°)$	$2\sigma(\Delta_f H°)$		S°	$2\sigma(S°)$
		kJ	kJ	kJ		$J\ K^{-1}$	$J\ K^{-1}$
Corundum	Al2O3	0.37	1.5	1.3		0.02	0.1
Quartz	SiO2	0	0.54	1		0.03	0.2
H2O(g)	H2O	0.016	0.04	0.04		0.035	0.01
Lime	CaO	0.31	1	0.9		0	0.4
Andalusite	Al2SiO5	0.37	1.36			0.05	
Kaolinite	Al2Si2O5(OH)4	0.402	1.56			0.15	
Pyrophyllite	Al2Si4O10(OH)2	0.386	2.02			0.175	
Wollastonite	CaSiO3	0.31	1.02			0.03	
Anorthite	CaAl2Si2O8	0.68	1.68			0.08	
Margarite	CaAl4Si2O10(OH)2	1.066	2.8			0.135	

We have calculated the adjustments for the 210 species in the HP11 “minpet” data set. These have been entered in SUPCRTBL data blocks in place of the original HP11 values as part of our effort to build the SUPCRTNE data base.

On the NEA side, we have continued our efforts to obtain the NEA data in a useful text file form, with the goal of not having to re-enter data, which would undoubtedly introduce transposition and other errors. In FY22 we explored doing this starting with the auxiliary data table in the PDF version of volume 14 (Grenthe et al. 2020). This is the latest known version of this table. The PDF form was copy-pasted into a text document, which then required a lot of hand-editing to eliminate extraneous content, such as footnote markers and special notes. In FY23 we explored the idea of obtaining the NEA electronic data base. This is in the form of a relational database (Martinez et al. 2019), which not easily ported or used elsewhere by others. Instead, we obtained (with the help of Jesus Martinez of NEA) a set of .tsv files representing the NEA data. These are text files with extraneous content similar to that obtained using the PDF process. We note that spreadsheets and text files can be used by just about any scientific professional, in contrast to a relational database.

Our focus is to complete the paper on combining the HP11 and NEA data sets and the associated spreadsheet by the end of FY23, and also to complete some but by no means all of the data blocks for the SUPCRTNE database. We do expect to complete the modified data blocks for the HP11 data set, as all that is needed is replacing the Gibbs energies, enthalpies and entropies in the corresponding SUPCRTBL data blocks with our adjusted values. Completing the SUPCRTNE database will require a multi-year effort, especially as the NEA data lack most of the data needed to extrapolate to elevated temperatures and pressures (we will have to provide them), and the NEA development effort itself is still ongoing. There will also be a need to draw in data from other sources for species not covered by HP11 and NEA. This would include many compositions for clay minerals. One such source of data might be the THERMODDEM data base (Blanc et al., 2012) and technical papers written in support of it. However, all such data will need to be adjusted (if necessary) to the NEA thermochemical standard.

3. Planned Work for FY24

For FY24 we will create an initial SUPCRTNE data base and extensively test the SUPCRTNE code. We will include limited comparison testing with SUPCRT92 and SUPCRTBL. We will document this work in a report, with an eye to easing a future formal software qualification effort as was done on the Yucca Mountain Project for codes including SUPCRT92 and EQ3/6.

We note one problem pointed out to us by John Apps, our retired LBNL colleague. The Holland and Powell model treats two different models for phase transitions: Landau and Bragg-Williams (see Holland and Powell (2011)). The SUPCRTBL code as obtained from Chen Zhu's Indiana University web site lacks the full coding needed for the Bragg-Williams model, apparently due to an ambiguity in the documentation of it in the Holland and Powell (2011) paper. We were directed to a source code file created by one of Dr. Zhu's associates that is said to have fixed this. We will analyze the treatment of Bragg-Williams transitions as implemented in this revised SUPCRTBL source code.

As time permits, we will also extend the SUPCRTNE data base to include more species, mainly from the NEA volumes. We will add more data needed to extrapolate thermodynamic data to elevated temperatures and pressures. For a description of such data, see Johnson et al. (1992) and Holland and Powell (2011). Although NEA includes some data of this kind (for example heat capacity coefficients for some solids), it is generally not in the correct form to be included in the SUPCRTNE data base. We are using the four-term heat capacity model used by Holland and Powell (2011), whereas the NEA tabulations of heat capacity coefficients are often tied to other formulations. For aqueous species we will continue to use extrapolation to elevated temperatures and pressure using the HKF model built into SUPCRT92. The HKF model has recently been the subject of studies by Miron et al. (2019) and Awolayo and Tutolo (2022). There are various ways to estimate HKF coefficients. We will try to determine if an isocoulombic approach is capable of being used to estimate HKF parameters for aqueous ions. This could significantly accelerate database development. In developing the actual data blocks, we may draw on existing ones from say slop98.dat and the SUPCRTBL data file.

In contrast, a significant number of low temperature minerals will be missing at this point. We will evaluate the situation be referencing what is in data0.ymp, the Yucca Mountain database. Most clay minerals will be missing, and the more complex clays have properties that generally must be estimated.

With this in hand, we will be working on production of data files to directly support modeling codes. Initially we may be lacking data for full temperature and pressure dependence for many species, and the first attempts will be in EQ3/6 format and largely restricted to 25°C and 1 bar. The range of modeling code formats will be expanded, though this may require efforts extending beyond FY23.

We are hopeful that the NEA will provide an update of previously published data so as to be fully consistent with the anticipated Ancillary Data volume. If not, we might have to add that to our task list. We would use the approach described for our modification of the HP11 data set.

We will be watching for potentially impactful developments by others, such the paper by Miron et al. (2017) and the recent release of PyGeoChemCalc software (Awolayo and Tutolo, 2022). Integration of LLNL's databases with NEA-TDB will be pursued in coordination with the international work packages.

8. Acknowledgements

This work was supported by the Spent Fuel and Waste Science and Technology campaign of the Department of Energy's Nuclear Energy Program. Prepared by LLNL under Contract DE-AC52-07NA27344.

5 References

Anderson G. (2005) *Thermodynamics of Natural Systems*. Cambridge University Press, New York.

Awolayo A. N. and Tutolo B. M. (2022) PyGeochemCalc: A Python package for geochemical thermodynamic calculations from ambient to deep Earth conditions. *Chemical Geology* **606**, 120984.

Blanc P., Lassin A., Piantone P., Azaroual M., Jacquemet N., Fabbri A. and Gaucher E. C. (2012) Thermoddem: A geochemical database focused on low temperature water/rock interactions and waste materials. *Applied Geochemistry* **27**, 2107-2116.

Cox J. D., Wagman D. D. and Medvedev V. A. (1989) *CODATA Key Values for Thermodynamics*. Hemisphere Publishing Corp., New York.

Dick J. M. (2019) CHNOSZ: Thermodynamic Calculations and Diagrams for Geochemistry. *Frontiers in Earth Science* **7**.

Grenthe I., Fuger J., Konings R. J. M., Lemire R. J., Muller A. B., Nguyen-Trung C. and Wanner H. (1992) *Chemical Thermodynamics of Uranium*. North Holland Elsevier Science Publishers B. V., Amsterdam, The Netherlands.

Grenthe I., Palmer D. A., Taylor P., and Schlenz H. (2020) *Chemical Thermodynamics of Iron. Part 2*. OECD Nuclear Energy Agency, Boulogne-Billancourt, France.

Grenthe I., Gaona X., Plyasunov A. V., Rao L., Runde W. H., Grambow B., Konings R. J. M., Smith A. L. and Moore E. E. (2020) *Second Update on the Chemical Thermodynamics of Uranium, Neptunium, Plutonium, Americium and Technetium*. OECD Nuclear Energy Agency, Boulogne-Billancourt, France.

Helgeson H. C., Delany J. M., Nesbitt H. W. and Bird D. K. (1978) Summary and Critique of the Thermodynamic Properties of Rock-Formings Minerals. *American Journal of Science* **278**, 1-229.

Holland T. J. B. and Powell R. (2011) An improved and extended internally consistent thermodynamic dataset for phases of petrological interest, involving a new equation of state for solids. *Journal of Metamorphic Geology* **29**, 333-383.

IAPWS (2016) Revised Release on the IAPWS Formulation 1995 for the Thermodynamic Properties of Ordinary Water Substance for General and Scientific Use, p. 19.

Johnson J. W., Oelkers E. H. and Helgeson H. C. (1992) SUPCRT92: A software package for calculating the standard molal thermodynamic properties of minerals, gases, aqueous species, and reactions from 1 to 5000 bar and 0 to 1000°C. *Computers & Geosciences* **18**, 899-947.

Lanari P. and Duesterhoeft E. (2018) Modeling Metamorphic Rocks Using Equilibrium Thermodynamics and Internally Consistent Databases: Past Achievements, Problems and Perspectives. *Journal of Petrology* **60**, 19-56.

Martinez J. S., Santillan E.-F., Bossant M., Costa D. and Ragoussi M.-E. (2019) The new electronic database of the NEA Thermochemical Database Project. *Applied Geochemistry* **107**, 159-170.

Miron G. D., Leal A. M. M. and Yapparova A. (2019) Thermodynamic Properties of Aqueous Species Calculated Using the HKF Model: How Do Different Thermodynamic and Electrostatic Models for Solvent Water Affect Calculated Aqueous Properties? *Geofluids* **2019**, 5750390.

Miron G. D., Wagner T., Kulik D. A. and Lothenbach B. (2017) An internally consistent thermodynamic dataset for aqueous species in the system Ca-Mg-Na-K-Al-Si-OHC-Cl to 800 C and 5 kbar. *American Journal of Science* **317**, 755-806.

Swift P. N. Spent Fuel and Waste Science and Technology R&D Campaign Working Group Meeting Introduction.

USDOE (2011) Used Fuel Disposition Campaign Disposal Research and Development Roadmap.

Wagner W. and Pruß A. (2002) The IAPWS Formulation 1995 for the Thermodynamic Properties of Ordinary Water Substance for General and Scientific Use. *Journal of Physical and Chemical Reference Data* **31**, 387-535.

Walther J. V. (2009) *Essentials of Geochemistry*. Jones and Bartlett Publishers, LLC, Boston.

Wolery T. J. (1992) *EQ3/6, A software package for the geochemical modeling of aqueous systems, UCRL-MA-110662 Part I*. Lawrence Livermore National Laboratory, Livermore.

Wolery T. J. (2018) H2OI95: A Stand-Alone Fortran Code for Evaluating the IAPWS-95 Equation-of-State Model for Water. Lawrence Livermore National Laboratory, Livermore, p. 43.

Wolery T. J. (2020) H2OI95: A Stand-Alone Fortran Code for Evaluating the IAPWS-95 Equation-of-State Model for Water (Rev. 1). Lawrence Livermore National Laboratory, Livermore, p. 88.

Wolery T. J. and Jove-Colon C. F. (2007) Qualification of Thermodynamic Data for Geochemical Modeling of Mineral–Water Interactions in Dilute Systems. Sandia National Laboratories, OCRWM Lead Laboratory for Repository Systems, Las Vegas, p. 412.

Wolery T. J. and Jove-Colon C. F. (2017) Chemical thermodynamic data. 1. The concept of links to the chemical elements and the historical development of key thermodynamic data. *Geochimica Et Cosmochimica Acta* **213**, 635-676.

Zimmer K., Zhang Y., Lu P., Chen Y., Zhang G., Dalkilic M. and Zhu C. (2016) SUPCRTBL: A revised and extended thermodynamic dataset and software package of SUPCRT92. *Computers & Geosciences* **90**, 97-111.

Surface Complexation/Ion Exchange Hybrid Model for Radionuclide Sorption to Clay Minerals (LLNL) (Part V)

1. Introduction

The Argillite International Collaborations activity is focused on our long-term commitment to engaging our partners in international nuclear waste repository research. The focus of this part of the report is the establishment of international collaborations for surface complexation modeling and the associated impacts of unlocking larger, community-based datasets. More specifically, the LLNL team are developing a database framework for the SFWST campaign that is aligned with the Helmholtz Zentrum Dresden Rossendorf (HZDR) sorption database development group in support of the database needs of the SFWST program.

In our FY22 effort, we described a detailed analysis of U(VI) sorption to quartz through both traditional surface complexation modeling and through a hybrid ML framework. In FY23, effort was placed on publication of these results and expansion of the LLNL surface complexation and ion exchange database (L-SCIE) in order to assess mineral-based radionuclide retardation under a wider variety of geochemical conditions (e.g., ionic strength, varying electrolyte compositions). Efforts were initiated to expand L-SCIE to include radionuclide surface complexation and ion exchange to clays that are relevant to subsurface geochemical processes occurring at nuclear waste repositories. In particular, a large source of sorption data for clays resides at the Paul Scherrer Institute (PSI) (work primarily by Bradbury and Baeyens) and we initiated discussions on how to retrieve those data and apply FAIR principles to those datasets.

In addition to L-SCIE development, two hybrid models that incorporate AI/ML were investigated and compared to discern the most promising approaches for accurate and precise estimations of radionuclide retardation. Key considerations for future model development include (1) the ability to reduce computational burden on determining retardation coefficients for PA and (2) the ability to quantify and predict radionuclide-mineral partitioning at a more efficient, rapid pace due to automated workflows. Upon the careful consideration of the most effective modeling approaches, we are identifying ways to implement these approaches into PA.

Ultimately, the data science-based workflows will provide a major incentive for other institutions to adopt a FAIR-formatted, interoperable database. LLNL will play a key role in disseminating sorption data and acting as good data stewards by updating the database in a consistent format and assessing the quality of the newly assimilated data in an organized fashion. To this end, all data and workflows are open access and made available on the LLNL Seaborg research website (https://seaborg.llnl.gov/resources/geochemical-databases-modeling-codes).

2. Status of L-SCIE Sorption Database

To develop a comprehensive surface complexation database in support of the SFWST program, we continued to build a digital sorption database to support surface complexation database development. The LLNL Surface Complexation/Ion Exchange (L-SCIE) digital sorption database and workflow was developed in Microsoft Access with a series of linked tables as reported previously. The structure of the database was recently reported in Zavarin et al. (2022) and will not be reported here. The efforts in FY23 focused on applying the L-SCIE database to a number of problems rather than expanding the content of the database. In this capacity, various debugging efforts and database enhancements were performed. While the longterm goal is to provide all database and associated workflows in a web-accessible format, all materials associated with this project are presently made available by request to the authors. The materials made available include the following:

- Database: Contains the full access database and all linked files (zipped) that are necessary to fully implement the L-SCIE database. To work the full database, you should unzip the linked files and place them in the same directory as the access database.
- How-to videos: These videos explain the process of digitizing data from the literature and loading them into the L-SCIE database. They provide step-by-step instructions for selecting literature references, extracting figures and metadata, extracting data from figures using the DataThief software, and importing data into the L-SCIE database.
- L-SCIE unification code: This folder contains the R code (two files: Server.r and ui.r) that are used to run the unification code. The code is run using R Studio. The code takes the exported .csv files from the L-SCIE database (dataset.csv and data.csv) and performs numerous unit conversions, formatting, and other processes to "unify" all the data in the database (e.g. takes Kd data and converts it all to aqueous and sorbed concentrations). This yields a file called sc.dataset.csv: the file that contains all the sorption data in the database in a uniform format. You can also use the L-SCIE code to produce a subset file (e.g. extract all Sr-goethite sorption data) called sc.subset.csv. The L-SCIE code can also be used to produce input files for use in phreeqc/pest parameter estimation processes.

Our L-SCIE digital sorption database **includes 246 references, 2331 datasets, and 27,000 individual data points.** The database is also linked to a large Kd database available from the JAEA. A python code automates the import of JAEA Kd data into the L-SCIE workflow increased our total data holdings to 44,000 data points. Details regarding the L-SCIE database and associated workflows were reported in the FY22 annual reports and will not be repeated here.

In support of the Argillite work package, we began focusing on clay sorption data available in the literature. At present, the L-SCIE database, when combined with the JAEA database, contains approximately 16,000 data for radionuclide sorption to clay minerals. Discussions with Maria Marquez and Dan Miron (PSI) have been continuing since January, 2023, to establish a mechanism to share the vast clay data available at PSI. However, these data are not readily available at this time and require reworking into a digital format. We are assisting PSI in this process to ensure compatibility between the L-SCIE and PSI databases. Meanwhile, we are moving forward with digitizing other clay sorption data that are identified in the RES3T database (Helmholtz-Zentrum Dresden-Rossendorf, 2022). In total, this database contains 187 unique references to radionuclide sorption to bentonite, biotite, illite, kaolinite, montmorillonite, muscovite, smectite, nontronite, and beidellite clay. This is the starting point for our clay data digitization effort that will be initiated in FY24. We anticipate that a significant fraction of these data are from PSI and access to that digital resource will significantly reduce the burden of digitizing these datasets.

3. A Chemistry-Informed Hybrid Machine Learning Approach to Predict Metal Adsorption onto Mineral Surfaces

The information presented below is a summary from a manuscript published in June 2023 in Applied Geochemistry (Chang et al., 2023). The publication describes our L-SCIE sorption database (Zavarin et al., 2022) and the hybrid workflow used to fit sorption behavior using these data. Importantly, we show that the hybrid approach is sufficiently flexible to be applied to surface complexation and ion exchange dominated systems. This indicates that the approach, initially developed using a U(VI)-quartz test case, can be expanded to simulation of ion exchange on clays. This is tested for the case of U(VI) sorption to montmorillonite. The results were also published in the proceedings of the 2023 Waste Management conference (Zavarin et al., 2023).

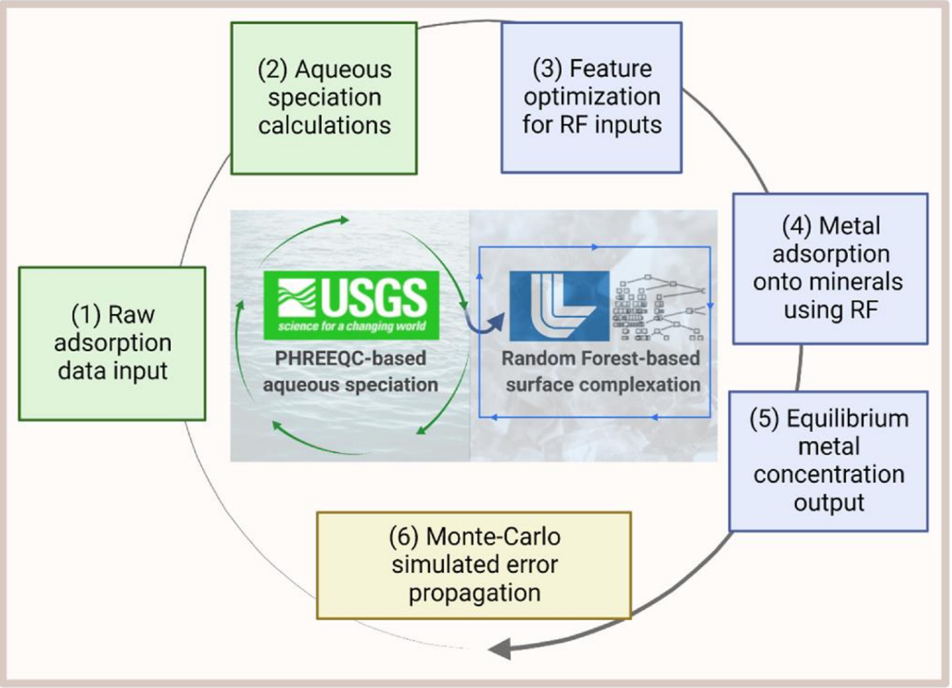

Figure1. L-SURF workflow chart with chronological steps: (1) Adsorption data and selected thermodynamic database are imported into L-SURF module, (2) Aqueous speciation calculations are conducted and all geochemical features are output, (3) Choice of most impactful geochemical features and hyperparameters are optimized, (4) Optimal features are used to train and test a random forest adsorption model, (5) Equilibrium aqueous metal sorbate concentrations are output, and (6) Steps 1–5 are repeated using Monte-Carlo simulations with randomly sampled input data ± experimentally-determined measurement uncertainty.

Historically, surface complexation model (SCM) constants and distribution coefficients (Kd) have been employed to quantify mineral-based retardation effects controlling the fate of metals in subsurface geologic systems. Our recent SCM development workflow, based on the L-SCIE database, illustrated a community FAIR data approach to SCM development by predicting uranium(VI)-quartz adsorption for a large number of literature-mined data. In this manuscript, we present an alternative hybrid machine learning (ML) approach that shows promise in achieving equivalent high-quality predictions compared to traditional surface complexation models. At its core, the hybrid random forest (RF) ML approach is motivated by the proliferation of incongruent SCMs in the literature that limit their applicability in reactive transport models. Our hybrid ML approach implements PHREEQC-based aqueous speciation calculations; values from these simulations are automatically used as input features for a random forest (RF) algorithm to quantify adsorption and avoid SCM modeling constraints entirely. Named the LLNL Speciation Updated Random Forest (L-SURF) model, this hybrid approach is shown to have applicability to U(VI) sorption cases driven by both ion-exchange and surface complexation, as is shown for quartz and montmorillonite cases. The approach can be applied to reactive transport modeling and may provide an alternative to the costly development of self-consistent SCM reaction databases.

The L-SURF code is available at https://ipo.llnl.gov/technologies/software/l-surf

The U(VI)-quartz dataset used in testing the workflow can be found at: https://seaborg.llnl.gov/resources/geochemical-databases-modeling-codes

Articles/presentations:

Chang, E., Zavarin, M., Beverly, L., and Wainwright, H. 2023. A Chemistry-Informed Hybrid Machine Learning Approach to Predict Metal Adsorption onto Mineral Surfaces, Applied Geochemistry, 155: 105731, https://doi.org/10.1016/j.apgeochem.2023.105731.

Zavarin, M., Chang, E., Beverly, L., Wainwright, H. 2023. A Data Mining and Hybrid Machine Learning Approach to Assess Mineral Retardation of Radionuclides, WM2023, February 26-March 2, 2023, Phoenix, AZ.

4. Aqueous Chemistry and Physics Constrained Autonomous-Closed-Loop Modeling for Quantifying Adsorption Processes as Applied to Metal-Mineral Interface Geochemistry

Chang, E. Beverly, L., and Wainwright, H. Submitted. Constrained Autonomous Modeling of Metal-Mineral Adsorption, *In* Methods and Applications of Autonomous Experimentation, Marcus Michael Noack and Daniela Ushizima, Eds.

The above manuscript was submitted as a book chapter for inclusion in Methods and Applications of Autonomous Experimentation, edited by Marcus Noack and Daniela Ushizima. The book chapter was prepared to illustrate the use of high-throughput, “big data” modeling approaches to investigate fluid-mineral interactions in subsurface geochemical processes. To this extent, working data in a FAIR formatted structure have been compiled using the Lawrence Livermore National Laboratory Surface Complexation/Ion Exchange (L-SCIE) database (Zavarin et al., 2022). Utilizing this consistently formatted set of data, the authors pose a test case using the mobility of the U(VI) exposed to quartz. The chapter illustrates the application of Gaussian process (GP) modeling that is informed by chemical aqueous speciation to develop predictive capabilities. A workflow is outlined based on autonomous optimization of the GP regressor, constrained by physics information - in this case mass conservation and statistical knowledge of high-variance regions. This approach demonstrates how chemistry and physics can be incorporated in the generation of a fine-tuned adsorption model through an autonomous, closed-loop process.

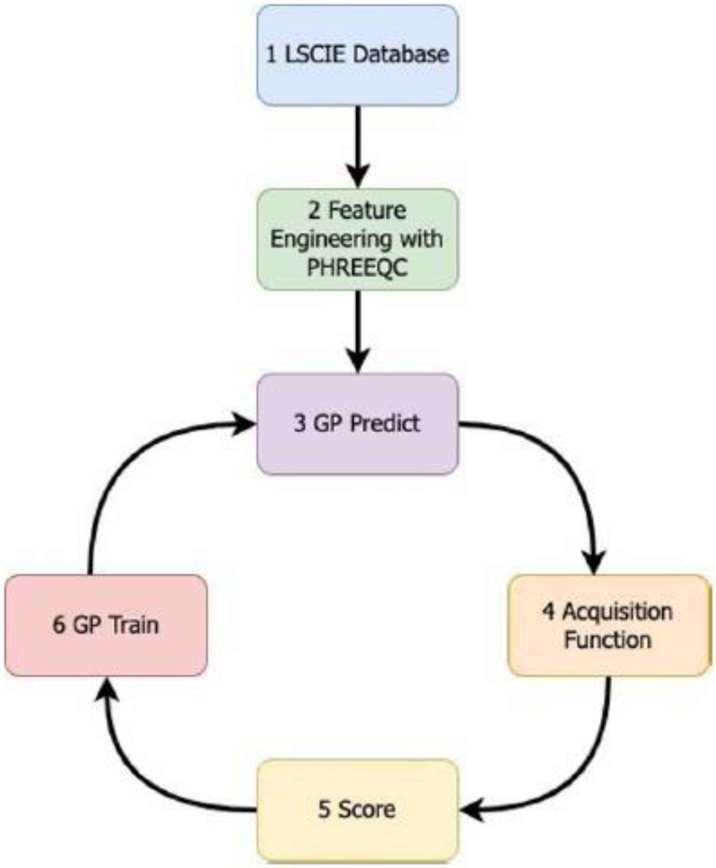

Figure 2. Autonomous experimentation loop for virtual instrument optimization

5. Planned FY24 Efforts

In FY24, effort will be placed on the growth of the surface complexation and ion exchange database (L-SCIE) with a particular focus on clay minerals relevant to argillite rock. First, we will assist our collaborators at PSI to digitize their clay sorption data in a format consistent with our L-SCIE database. Second, these data will be supplemented by sorption reference contained in the RES^{3}T database and the data already captured from the JAEA Kd database. Once these datasets are digitized and unified, we will begin developing high throughput automated workflows to model sorption of a series of radionuclides and clays. This effort will move us from workflows that focus on single radionuclide-mineral pairs to more comprehensive modeling workflows. This effort will include the testing of L-SURF to quantify K_d values for numerous different radionuclide-clay pairs under varying geochemical conditions. We will conduct direct comparisons of the L-SURF approach with various surface complexation (Non-electrostatic, diffuse layer, etc.) and ion exchange (Vanselow, Gapon, etc.) models. These important model inter-comparisons will provide a clearer path forward in incorporating traditional SCM or/and modern hybrid ML approaches into repository flow and transport models.

Key considerations for future modeling development will include (1) the ability to reduce computational burden on determining retardation coefficients and (2) a new capability to quantify and predict radionuclide-mineral partitioning at a more efficient, rapid pace due to automated workflows. We will begin discussing efforts for the integration of our new surface complexation/ion exchange constants or hybrid-ML models into PFLOTRAN.

In addition to the modeling effort described above, we plan to upgrade our L-SCIE database to make it web-accessible. This will require converting the database that is presently supported as a Microsoft Access database to a more portable SQL format that is open access and readily shared with the scientific community, following the FAIR data principles (Wilkinson et al., 2016).

6. Acknowledgments

This work was supported by the Spent Fuel and Waste Science and Technology campaign of the Department of Energy's Nuclear Energy Program. Prepared by LLNL under Contract DE-AC52-07NA27344.

7. References

Chang, E., Zavarin, M., Beverly, L., Wainwright, H., 2023. A chemistry-informed hybrid machine learning approach to predict metal adsorption onto mineral surfaces. Applied Geochemistry 155, 105731. doi.org/https://doi.org/10.1016/j.apgeochem.2023.105731.

Helmholtz-Zentrum Dresden-Rossendorf, 2022. RES³T-Rossendorf Expert System for Surface and Sorption Thermodynamics. www.hzdr.de/res3t. 2022).

Wilkinson, M.D., Dumontier, M., Aalbersberg, I.J., Appleton, G., Axton, M., Baak, A., Blomberg, N., Boiten, J.-W., da Silva Santos, L.B., Bourne, P.E., Bouwman, J., Brookes, A.J., Clark, T., Crosas, M., Dillo, I., Dumon, O., Edmunds, S., Evelo, C.T., Finkers, R., Gonzalez-Beltran, A., Gray, A.J.G., Groth, P., Goble, C., Grethe, J.S., Heringa, J., ’t Hoen, P.A.C., Hooft, R., Kuhn, T., Kok, R., Kok, J., Lusher, S.J., Martone, M.E., Mons, A., Packer, A.L., Persson, B., Rocca-Serra, P., Roos, M., van Schaik, R., Sansone, S.-A., Schultes, E., Sengstag, T., Slater, T., Strawn, G., Swertz, M.A., Thompson, M., van der Lei, J., van Mulligen, E., Velterop, J., Waagmeester, A., Wittenburg, P., Wolstencroft, K., Zhao, J., Mons, B., 2016. The FAIR Guiding Principles for scientific data management and stewardship. Scientific Data 3(1), 160018. doi.org/10.1038/sdata.2016.18.

Zavarin, M., Chang, E., Beverly, L., Wainwright, H., 2023. A Data Mining and Hybrid Machine Learning Approach to Assess Mineral Retardation of Radionuclides, WM2023. Phoenix, AZ.

Zavarin, M., Chang, E., Wainwright, H., Parham, N., Kaukuntla, R., Zouabe, J., Deinhart, A., Genetti, V., Shipman, S., Bok, F., Brendler, V., 2022. Community Data Mining Approach for Surface Complexation Database Development. Environmental Science & Technology 56(4), 2827-2838. doi.org/10.1021/acs.est.1c07109.